UNIVERSIDADE DE LISBOA
FACULDADE DE CIÊNCIAS

Mass movement processes in the Southwest Portuguese Continental Margin during the Late Pleistocene-Holocene: a multidisciplinary approach for volume quantification, estimation of recurrence times and hazard implications

"Documento Definitivo"

Doutoramento em Geologia

Especialidade de Geodinâmica Externa

Manuel António da Cunha Teixeira

Tese orientada por:
Professor Doutor Pedro António Gancedo Terrinha
Doutora Ana Cristina Freixo Pereira Roque

Documento especialmente elaborado para a obtenção do grau de doutor

2020

2020

UNIVERSIDADE DE LISBOA

FACULDADE DE CIÊNCIAS

Ciências
ULisboa

Mass movement processes in the Southwest Portuguese Continental Margin during the Late Pleistocene-Holocene: a multidisciplinary approach for volume quantification, estimation of recurrence times and hazard implications

Doutoramento em Geologia

Especialidade de Geodinâmica Externa

Manuel António da Cunha Teixeira

Tese orientada por:
Professor Doutor Pedro António Gancedo Terrinha e Doutora Ana Cristina Freixo Pereira Roque

Júri:

Presidente:

● **Doutora Maria da Conceição Pombo Freitas**, *Professora Catedrática*
Presidente do Departamento de Geologia da Faculdade de Ciências da Universidade de Lisboa

Vogais:

● **Doutora Estefanía Llave Barranco**, *Científico Titular*
Departamento de Investigación y Prospectiv Geocientífica do Instituto Geológico y Minero de España (Espanha);

● **Doutor Roger Urgeles Esclasans**, *Científico Titular*
Department Marine Geosciences do Institut de Ciències del Mar (Espanha);

● **Doutor José Luís Gonçalves Moreira da Silva Zêzere**, *Professor Catedrático*
Instituto de Geografia e Ordenamento do Território da Universidade de Lisboa;

● **Doutor Fernando Silva da Fonseca Marques**, *Professor Associado*
Faculdade de Ciências da Universidade de Lisboa;

● **Doutor Pedro António Gancedo Terrinha**, *Professor Auxiliar Convidado*
Faculdade de Ciências da Universidade de Lisboa (orientador).

Documento especialmente elaborado para a obtenção do grau de doutor

Doutoramento financiado pela Fundação para a Ciência e Tecnologia (SFRH/BD/110674/2015)

2020

2020

Whatever you can do or dream you can do, begin it.
Boldness has genius, power, and magic in it!

Goethe

ACKNOWLEDGEMENTS

This PhD thesis was possible with the support of some institutions and the collaboration of many people that were very important for me during this period (2016-2020).

My gratitude is firstly dedicated to my supervisors Pedro Terrinha and Cristina Roque, whom I acknowledge the orientation and the guidance they gave me.

Pedro Terrinha is thanked for the support and encouragement he always gave, as well as his suggestions, corrections, and opinions during this work and for being always available whenever I needed. I also thank the opportunity for learning many things related with Marine Geology techniques.

Cristina Roque is acknowledged for her support and encouragement, and for always being concerned about my performance. I also thank many advices, the suggestions, revisions and corrections and the numerous talks we had during the work. I also thank the opportunity to meet and join with international Marine Geology groups.

I want to express my special acknowledgement to FCT (Fundação para a Ciência e a Tecnologia) – the Portuguese Science Foundation for funding my PhD project through the PhD grant (**SFRH/BD/110674/2015**).

IDL – Instituto Dom Luiz – FCT's Associated Laboratory, and IPMA – Instituto Português do Mar e da Atmosfera – are acknowledged for being my host institutions and for providing me the support, equipment, and workspace. I also acknowledge the University of Lisbon and, particularly, the Faculty of Sciences of the University of Lisbon and the Department of Geology.

Thanks to CONDRIBER (FCT – PTDC/GEO-GEO/4430/2012) and MOWER (CTM (2012)-39599-C03-02) projects, for providing data for this work, and MAGICLAND (PTDC/CTA-GEO/30381/2017) for funding two AMS ^{14}C dating.

Landmark Graphic Corporation is thanked due to Landmark University Grant Program. ESRI is thanked for the student license of ArcMap©. GEBCO is acknowledged for proving bathymetry data. IVS-3D Fledermaus is also acknowledged.

SEISLAB from IPMA is also acknowledged for providing the facilities for the analyses of seismic data.

My gratitude also goes to the following persons:

Dr. Gemma Ercilla and Dr. David Casas, from CSIC-Barcelona, are acknowledged for always being available to help, and for the insightful scientific discussions and for constantly giving me good ideas. They are also thanked for their sympathy and for their constant support and encouraging words. I also thank them for allowing me to be part of the FAUCES-2 oceanographic survey, and especially for what I learnt from them at the sea, during this oceanographic survey.

Dr. Fátima Abrantes, from IPMA-Algés, is acknowledged for her constant willingness to help, her constant encouraging words and advices, and for assuring all material in the lab, allowing the work to be successfully accomplished.

Dr. Antje Voelker from IPMA-Algés is acknowledged for her support, for text revisions, the encouraging words, for the collaboration and for being always available to discuss about Palaeoceanography, and to clarify my many doubts during my work.

Prof. António Viana da Fonseca, from the Faculty of Engineering of the University of Porto (FEUP), for important lessons about geotechnics, for enlightening my doubts, and for being always available to discuss and to help.

Dr. Emília Salgueiro, and Dr. Filipa Naughton, from IPMA-Algés, for being always available to teach and to discuss with me about Paleoceanography, for their help and support in the lab and for their encouraging words.

Dr. Pedro Silva from ISEL for his encouraging words and for important lessons about rock magnetics.

Dr. Mariano Yenes, from University of Salamanca, who I met during the FAUCES 2 oceanographic survey on board of the research vessel Sarmiento de Gamboa, for always being accessible for a scientific discussion and for enlightening me about geotechnical issues. Dr. Belen Alonso, from CSIC, is thanked for her encouraging words and for her sympathy during FAUCES cruise. Thanks, are extensive to the whole FAUCES team.

Dr. Vítor Magalhães from IPMA, for bibliography, discussion of ideas and constant encouraging words and Dr. Carlos Ribeiro, from the University of Évora, for discussion of ideas and encouraging words. Dr. Rui Quartau from Instituto Hidrográfico is also thanked for encouraging words.

Dr. Javier Hernández-Molina, from Royal Holloway University of London (RHUL), for some discussions and for teaching some important lessons and ideas related with deep sea sedimentary processes and contourite activity, especially during my very first oceanographic campaign - GRACO. Thanks, are extensive to the Drifters group.

Dr. Marga García is acknowledged for allowing me to be part of the team of GRACO, an EUROFLEETS oceanographic survey on board of the research vessel L'Atalante. Dr. Estefanía Llave, from IGME for important conversations and scientific discussions, and for her encouraging words. Thanks, are extensive to the whole GRACO team.

To the team members of the MINEPLAT surveys (1, 3, and 5) for good moments and for important practical and technical lessons learnt at sea.

Dr. Célia Lee, from Faculty of Sciences of the University of Lisbon (FCUL), for always being available to help solving problems. Dr. João Cabral and Dr. João Duarte, from FCUL for encouraging words and help in bureaucratic issues. Dr. Rachid Omira and Dr. Filipe Rosas, from FCUL, for the encouraging words.

Dr. Conceição Freitas and Marta Antunes from the Department of Geology of FCUL are also acknowledged.

The actual and former members of the Marine Geology group of IPMA: Carlos Ribeiro, Débora Duarte, Henrique Duarte, Joana Santos, João Noiva, Luís Batista, Marcos Rosa, Margarida Henriques, Mariana Silva, Marta Neres, Pedro Brito, Rui Quartau, Sara Rodrigues, Sónia Silva, Vasco Valadares, and Alessandro Righetti. To the members of the Geophysics group: Davide Gamboa, Dina Vales, Inês Ramalho, and Jihwan Kim. Thank you all for your friendship and encouragement.

Ana Lopes, Andreia Rebotim, Cremilde Monteiro, Cristina Lopes, Dulce Oliveira, Lélia Matos, Mafalda Freitas, Mária Padilha, Mário Mil-Homens, Montserrat Alonso-García, Teresa Drago, Teresa Rodrigues, and Warley Soares, from IPMA-Algés, for always being available and for helping me in the laboratory tasks whenever I needed.

Finally, I would like to thank my family, especially my parents for always supporting me and believing in me, and for being an example of life. To my brother, my sister-in-law, and my nephew, for always encouraging me. To Maria do Carmo for her great support in the last period of this work.

ABSTRACT

The Alentejo Margin, in the Southwest Portuguese Continental Margin, is a very complex and dynamic geomorphological area, located near the Eurasia-Africa plate boundary and affected by the flow path of the Mediterranean Outflow Water (MOW). This margin comprises the Sines Contourite Drift (SCD), which is the most prominent depositional feature (~2311 km^2, 303.9 km perimeter, 98 km length and 35 km width), emplaced in the continental slope of this margin, evolving in four main phases by the action of MOW, since the Late Pleistocene.

The interaction between along-slope and downslope processes forms a mixed morphosedimentary setting, which is greatly affected by mass movement activity in the middle and lower continental slopes, during the Late Pleistocene-Holocene.

This work analyses the occurrence of mass movement processes in the southwest Portuguese margin, in a total extent of ~85 km×82 km and identifies the main triggering and conditioning factors promoting slope instability during the Late Pleistocene-Holocene and assesses the morphosedimentary evolution of the Sines Contourite Drift. This study was performed through geophysical, sedimentological, physical, geochemical, and geotechnical analyses, using multibeam bathymetry, multichannel seismic and sub-bottom profiler, and gravity cores data.

The Alentejo margin is an unstable area, where the presence of a contourite drift significantly contributes for slope instability in consequence of its sediment mechanical properties. The SCD hosts a cluster of dominantly small landslide scars, affecting both steep and smooth slopes. This scar concentration is mainly provided by local intrinsic conditions that favour slope instability in the area. Scars predominantly occur on slope angles steeper than 5º, however sediment properties, especially low consolidation, very low permeability, high pore-pressure, high compressibility and low shear strength greatly promote slope instability in the Alentejo Margin. The inherent instability conditions of the area are increased by frequent seismicity that promotes additional stress, leading to increased slope instability.

Keywords: *Mass movement processes; Alentejo Continental Margin (SW Portugal); Sines Contourite Drift; Mediterranean Outflow Water; Late Pleistocene-Holocene morphosedimentary evolution*

RESUMO

A ocorrência de movimentos de massa submarinos constitui a maior expressão de instabilidade de vertentes da superfície terrestre e representa uma forma privilegiada de evolução morfo-sedimentar do fundo marinho. A presença de movimentos de massa (deslizamentos) submarinos é muito comum em plataformas continentais como a margem sudoeste Portuguesa, onde coexistem atividade tectónica, correntes de fundo com padrões de circulação intensos, e deposição contornítica. Esta margem é uma área geomorfologicamente muito complexa e dinâmica, que se localiza próximo do limite de placas tectónicas Eurásia-África, sendo afetada por várias correntes oceânicas das quais se destaca a corrente vinda do Mediterrâneo, a Mediterranean Outflow Water (MOW) que circula, atualmente, entre os ~600 e os ~1200 metros de profundidade. Esta massa de água é responsável pela formação do Contornito de Sines, que se depositou no talude continental da margem imersa do Alentejo, entre os ~1000 e os ~2200 metros de profundidade, atingindo ~2311 km^2, 303.9 km de perímetro, 98 km de comprimento, e 35 km de largura. Este corpo sedimentar depositou-se ao longo de várias fases desde o Miocénico Superior, tendo sido constrangido pelas palaeo-morfologias do fundo do mar que resultaram dos processos de rifting, herdados das fases de rifting Mesozóicas. Este depósito contornítico corresponde à secção distal do Sistema Deposicional Contornítico do Golfo de Cádiz (GCCDS - *Gulf of Cadiz Contouritic Depositional System*) que se começou a formar após a reabertura do Estreito de Gibraltar, no final do Miocénico Superior pela ação da corrente saída do Mar Mediterrâneo, a MOW. Durante a Expedição 339 do IODP (*Integrated Ocean Drilling Program*) Programa Integrado de Perfuração Oceânica, em 2012, foi identificada a ocorrência de movimentos de massa associados à presença de depósitos contorníticos ao largo do Alentejo, na margem sudoeste de Portugal.

Neste sentido pretende-se perceber como a presença do Contornito de Sines pode afetar a instabilidade da área e quais os fatores que mais contribuem para essa instabilidade durante o Quaternário.

Este trabalho analisa a ocorrência de movimentos de massa ao longo da margem do Alentejo, no sudoeste de Portugal continental, numa extensão total de ~85 km×82 km, e identifica os principais fatores condicionantes e desencadeantes de instabilidade durante o Pleistocénico Superior e o Holocénico, considerando a evolução morfo-sedimentar do Contornito de Sines no mesmo período. Assim, para atingir os objetivos propostos, neste trabalho efetuou-se o estudo da área com base na análise das características geofísicas, e nas propriedades

sedimentológicas, físicas, geoquímicas e geotécnicas dos sedimentos, através de um conjunto variado de dados: i) batimetria multifeixe SWIM recolhida ao longo de várias campanhas de diferentes projetos; batimetria CONDRIBER e MOWER adquirida em 2014 na campanha MOWER/CONDIRBER; ii) linhas de sísmica de reflexão multicanal adquiridas durante a campanha MOWER/CONDRIBER 2014; iii) perfis de reflexão sísmica multicanal de projetos científicos anteriores e da indústria petrolífera: GSI 1984, STEAM 1994 e BIGSETS 1998; iv) perfis de sísmica de alta resolução (Parasound) adquiridos na campanha MOWER/CONDRIBER em 2014; e v) cores de gravidade preparados para análise sedimentológica, e para análise de propriedades físicas e geoquímicas, e ainda cores para análise de propriedades geotécnicas.

A margem do Alentejo apresenta uma grande interação de processos que resulta sobretudo da presença de sismicidade ativa, morfologia muito irregular e de uma dinâmica de correntes oceânicas bastante intensa. Da interação de processos resulta um enquadramento morfo-sedimentar misto e bastante complexo, que é muito afetado por movimentos de massa no talude continental médio e inferior, sobretudo durante o Pleistocénico Superior e o Holocénico. A margem do Alentejo apresenta múltiplas formas sedimentares de deposição, de erosão e de origem gravítica. Esta variedade de formas sedimentares está sobretudo relacionada com a presença do Contornito de Sines que, pelo seu caráter dinâmico sob ação da MOW, favorece o aparecimento e coabitação de formas sedimentares que se desenvolvem paralela e perpendicularmente à vertente. A ação direta da MOW sobre os sedimentos promove a formação de ondas de sedimento que apresentam várias orientações ao longo do contornito, quer à superfície, quer em profundidade em função da atividade desta massa de água. Também por ação da MOW, mas com caráter erosivo, se formou uma fossa ao longo da base do talude superior, paralelamente à vertente. Similarmente, a presença de múltiplas cicatrizes de deslizamento ao longo da superfície do Contornito de Sines indica o dinamismo morfo-sedimentar da área, bem como a presença de fenómenos de instabilidade de vertentes e sugere a interação de vários fatores que a condicionam. A presença de declives acentuados (> 10º) em alguns setores da margem do Alentejo, bem como as taxas de sedimentação consideravelmente altas, e bastante variáveis, são determinantes para a grande densidade de pequenas cicatrizes ao longo do bordo ocidental do Contornito de Sines. Os sedimentos instabilizados são deslocados sobre forma de fluxos de detritos, formando ravinas que intersectam o contornito e se depositam no Rincão do Lebre, onde se registam depósitos cuja fácies sísmica é mais transparente e irregular.

A evolução sedimentar deste contornito durante o Pleistocénico Superior e o Holocénico teve quatro fases principais ao longo dos últimos ~50 ka (mil anos). 1) A primeira fase ocorreu há mais de 43 ka, antes do Presente, e apresentou um regime sedimentar estável com deposição de sedimentos dominantemente finos, com algumas intercalações de sedimentação mais grosseira. 2) A segunda fase, entre os 42.9 ka e os 30.5 ka regista dois ciclos de deposição bastante pronunciados com fortes variações nas propriedades dos sedimentos e uma forte diminuição na taxa de sedimentação. 3) Na terceira fase, entre os 30 ka e os 17.1 ka antes do Presente, registou a mais baixa taxa de sedimentação efetiva, inferior a 3 cm ka^{-1}. Nesta fase, a sedimentação foi a mais irregular e a mais grosseira dos últimos ~50 ka, promovendo a formação de níveis grosseiros distintos dos níveis contíguos. A maior concentração de elementos terrígenos como o ferro e o silício, que se superiorizam em abundância aos elementos biogénicos como o cálcio e o estrôncio, associada a uma granulometria mais grosseira, que se regista num intervalo de idades em que se verificou um período de arrefecimento sugere que nesta fase houve uma forte contribuição de sedimentos com origem continental, depositados diretamente na plataforma continental, tendo em conta o nível do mar mais baixo. Nesta fase houve um forte arrefecimento que culminou com o Último Máximo Glaciar e com um fortalecimento da MOW. 4) A quarta fase ocorreu desde os 17.1 ka até ao Presente, caracteriza-se por ser uma fase com sedimentação mais fina até ~12.9 ka, perto do início do Younger Dryas. Após este período, a granulometria voltou a aumentar ligeiramente até ao Presente. Estas diferentes fases de sedimentação correspondem a variações climáticas e a variações na intensidade da MOW.

Os sedimentos do Contornito de Sines têm um alto teor de água e uma baixa permeabilidade devido ao elevado conteúdo de argila, apresentando uma baixa consolidação e uma elevada compressibilidade que se expressam numa baixa resistência ao corte. Estes sedimentos têm forte plasticidade que promove a instabilidade. As condições intrínsecas destes sedimentos promovem a ocorrência de movimentos de massa em condições estáticas, mesmo sem a presença adicional de fatores transientes como a sismicidade.

A margem imersa do sudoeste de Portugal é, pois, uma área bastante instável e a presença do contornito contribui para essa instabilidade devido às propriedades mecânicas dos sedimentos. A presença de uma aglomeração de cicatrizes de pequenas dimensões no bordo oeste deste contornito ocorre sobretudo em declives mais acentuados, mas também em declives mais suaves onde cicatrizes isoladas de maiores dimensões se formam ao longo da superfície mais plana do contornito. Esta concentração de cicatrizes é proporcionada pelas condições morfo-sedimentares intrínsecas que favorecem a instabilidade na área, quer através do declive, quer

através das propriedades mecânicas e do alto teor em água destes sedimentos pouco consolidados e muito pouco permeáveis, altamente compressíveis e muito pouco resistentes ao cisalhamento. A instabilidade inerente da área é amplificada pela presença de muitos focos de sismicidade que promove instabilidade dos sedimentos através de carga adicional.

Palavras – chave: *Movimentos de massa submarinos; Margem Continental do Alentejo (SW de Portugal); Contornito de Sines; Corrente do Mediterrâneo; Evolução morfológica e sedimentar do Pleistocénico Superior - Holocénico*

INDEX

FIGURES INDEX

TABLES INDEX

LIST OF SYMBOLS

a = Upslope contributing area (m^{-2})

$\boldsymbol{a_v}$ = Coefficient of compressibility

α = Slope

b = Terrain unit / pixel (m)

$\boldsymbol{B}$ **=** Skempton's coefficient B

a/b = Contributing area per unit area (Log^{10} m^2)

C' = Effective cohesion (kPa)

$\mathbf{C_c}$ = Compression index (dimensionless)

$\mathbf{C_v}$ = Coefficient of consolidation (m^2 yr^{-1})

$\boldsymbol{\Delta H}$ = Axial displacement

$\boldsymbol{\Delta u}$ = Pore pressure variation (kPa)

$\boldsymbol{\Delta \sigma_3}$ = Increment of confining pressure (kPa)

$\boldsymbol{e}$ = Void ratio (dimensionless)

εa = Axial strain (%)

εv = Volumetric strain (%)

F; FS; FoS = Factor of safety

∑ = Sum

$\boldsymbol{\phi'}$ = Effective angle of shearing resistance/Effective friction angle (º)

ϕ'_{cv} = Constant volume friction angle (º)

ϕ'_{dss} = Simple shear effective friction angle (º)

ϕ'_{tri} = Triaxial effective friction angle (º)

$\boldsymbol{\delta_H}$ = Horizontal displacement (mm)

$\boldsymbol{\delta_v}$ = Vertical displacement (mm)

$\boldsymbol{g}$ = Gravity ($m\ s^{-2}$)

$\boldsymbol{G_s}$ = Density of solid particles ($kN\ m^{-3}$)

$\boldsymbol{h}$ = Thickness of the potentially unstable sediment (m)

$\boldsymbol{H_0}$ = Initial height (m)

$\boldsymbol{k}$ = Pseudo-static coefficient

K = Coefficient of permeability ($m\ s^{-1}$)

kPa = Kilopascal

$\boldsymbol{m}$ = Saturated column to the potentially unstable sediment thickness above the failure plane

$\boldsymbol{m_v}$ = Coefficient of volume compressibility (MPa^{-1})

q = Deviator stress (kPa)

p' = Effective normal stress (kPa)

ρ_s = Sediment density (kg m^{-3})

ρ_w = Water density (kg m^{-3})

σ = Normal stress (kPa)

σ'_p = Pre-consolidation stress (kPa)

σ'_v = Effective vertical stress (kPa)

σ'_{v0} = Overburden effective stress (kPa)

σ'_{vi} = Initial effective vertical stress (kPa)

S = Shear strength

Su = Static undrained shear strength

τ = Shear stress (kPa)

θ, β = Slope angle (º)

u = Neutral pressure (kPa)

γ, γ_m = Sediment unit weight (kN m^{-3})

γ_d = Dry unit weigth

γ_s = Unit weight of solid particles (kN m^{-3})

γ_{sat} = Saturated sediment unit weight (kN m^{-3})

γ_{sub} = Submerged sediment unit weight (kN m^{-3})

γ_w = Mass density of water (kN m^{-3})

W = Water content (%)

W_d = Dry weight of the sample (kN m^{-3})

W_L = Liquid limit (%)

∂u = Pore-pressure variation

∂**t** = Time variation

∂**z** = Depth variation

z = Thickness of the sediment (m)

1 – INTRODUCTION

Landslides are major expressions of slope instability (Varnes, 1978; Selby, 1993; Cruden and Varnes, 1996), conveying with them important signs of morphosedimentary evolution. Slope instability is a quite common process both onshore (Varnes, 1978; Selby, 1993; Cruden and Varnes, 1996; Dikau *et al.*, 1996a; Soeters and Van Westen, 1996) as well as offshore (Morgenstern, 1967; Lee and Edwards, 1986; Bugge *et al.*, 1987; Moore *et al.*, 1989; Hampton *et al.*, 1996; Mulder and Cochonat, 1996; Locat, 2001; Masson *et al.*, 2006; Lee *et al.*, 2007; Gross *et al.*, 2014; Shanmugam, 2016). However, more attention has been given to onshore than to offshore slope instability, especially because of both the ease of data acquisition and the direct impact on society (Crozier and Glade, 2004). Nevertheless, landslide activity on subaqueous environments is an issue of growing importance, especially due to the complexity of the process (Mosher *et al.*, 2010; Piper *et al.*, 2012; Moscardelli and Wood, 2015) but also due to the hazard it presents for coastal populations and infrastructures (Seed *et al.*, 1988; Hampton *et al.*, 1996; Geist, 2000; Canals *et al.*, 2004; Lee *et al.*, 2007; Kawamura *et al.*, 2009; Cattaneo *et al.*, 2014). This may be particularly critical when landslide-induced tsunamis occur (ten Brink *et al.*, 2009; Omira *et al.*, 2016), being imperative to study and to understand the impact these natural geohazards can have in continental margins (Masson *et al.*, 2006).

Submarine landslides are common in continental slope and shelf, as well as along steep submarine canyons (Locat, 2001; Lee *et al.*, 2007). Submarine landsliding activity is particularly important on active depositional bodies like contourite drifts (Bryn *et al.*, 2005a; Hernández-Molina *et al.*, 2006; Roque *et al.*, 2012; Miramontes *et al.*, 2018), which are prone to submarine slope instability (Laberg and Vorren, 2000; Bryn *et al.*, 2005b; Kvalstad *et al.*, 2005a; Rebesco *et al.*, 2007; Laberg and Camerlenghi, 2008; Cattaneo *et al.*, 2014; Rebesco *et al.*, 2014). The occurrence of slope instability and associated landslides on contourite drifts has been reported in diverse continental margins (Laberg *et al.*, 2005; Ercilla *et al.*, 2008b; Laberg and Camerlenghi, 2008; Baeten *et al.*, 2014; Alonso *et al.*, 2016; Laberg *et al.*, 2016), being conspicuous in the Tyrrhenian Sea (Martorelli *et al.*, 2016; Miramontes, 2016) and around Iberia, in both the Mediterranean and the Alboran Seas (Casas *et al.*, 2015; Ercilla *et al.*, 2016; Juan *et al.*, 2016) and in the Sines Drift (Roque *et al.*, 2015; Teixeira *et al.*, 2017) off west Iberia.

The interplay between contourite deposition, erosion-, and slope instability constitutes an important matter from different perspectives and for different purposes like palaeoceanography, and palaeoclimatic studies as well as for economic purposes and geohazards assessment (Faugères *et al.*, 1993; Rebesco *et al.*, 2007). Once contourite drifts constitute potential hydrocarbon reservoirs (Rebesco, 2005; Viana and Rebesco, 2007; Stow *et al.*, 2013; Rebesco *et al.*, 2014) and since landslides can be superficial major expressions of subsurface reservoirs in contourite deposits, serious attention has been given, in the last decades, to the interaction between these two downslope and along-slope process-based features (Mulder *et al.*, 2003; Bryn *et al.*, 2005b; Laberg and Camerlenghi, 2008; Shanmugam, 2008), especially by the oil industry (Shanmugam, 2006).

In fact, contourites constitute important records to unveil the history of the depositional record, showing its morphosedimentary evolution and the regional palaeoceanography and paleoclimate evolution. These complex sedimentary bodies result from the bottom current circulation and its interaction with local geomorphologic features, determining the depositional evolution as well as the associated history of slope stability.

1.1 – RATIONALE

The Southwest Iberia Margin that encompasses the Sines Contourite Drift (SCD), has had significant mass movement activity that occurred from the Late Pleistocene to the Present (Lebreiro *et al.*, 1998; Terrinha *et al.*, 2003; Vizcaino *et al.*, 2006; Gràcia *et al.*, 2010; Masson *et al.*, 2011; Lo Iacono *et al.*, 2012; Neves *et al.*, 2016; Sanchez-Serra *et al.*, 2020). The complex pre-existing structure (Alves *et al.*, 2003; Terrinha *et al.*, 2009; Pereira and Alves, 2011; 2013; Terrinha *et al.*, 2019b) and related faulting and seismicity (Baptista *et al.*, 1998; Custódio *et al.*, 2016; Silva *et al.*, 2017; Veludo *et al.*, 2017) associated with major earthquakes, have been interpreted as one of the main causes for the occurrence of slope disruption (Terrinha *et al.*, 2003; 2009). High-resolution multibeam bathymetry and multichannel seismic reflection data, acquired in the Alentejo Margin (Teixeira *et al.*, 2019) show, respectively, the existence of landslide scars and deposits on the surface, as well as Pliocene-Quaternary progressive deformation and several past mass transport deposits (MTD) enclosed in the stratigraphic column (Roque *et al.*, 2015; Neves *et al.*, 2016; Teixeira *et al.*, 2019; 2020).

The WNW-ESE oriented horizontal compressional tectonic activity that the SW Iberia Margin has been subjected to, during Pliocene-Quaternary times, led to offshore extensive seismicity (Baptista *et al.*, 2014; Custódio *et al.*, 2015; Silva *et al.*, 2017; Veludo *et al.*, 2017), which acts as triggering mechanism of slope instability (Neves *et al.*, 2016). This together with bottom current activity in the SWIM highly contributes for the contourite drift deposition and slope instability through the complex interaction of along-slope and downslope processes (Teixeira *et al*., 2019).

Climate variations have impact on bottom current activity (Schönfeld and Zahn, 2000; Rogerson *et al.*, 2005; Toucanne *et al.*, 2007; Rogerson *et al.*, 2012; Hernández-Molina *et al.*, 2014b; Khélifi *et al.*, 2014; Kaboth *et al.*, 2016), determining the depositional evolution (Abrantes *et al.*, 1998; Voelker *et al.*, 2006; Roque *et al.*, 2012; Bahr *et al.*, 2014; Hernández-Molina *et al.*, 2016a), sedimentary integrity, erosional activity and slope stability due to depositional constraints. High sedimentation rates have been reported on the continental slope of Southwest Portugal (Stow *et al.*, 2013), associated with the Mediterranean Outflow Water (MOW), since Late Miocene/Pliocene times (Hernández-Molina *et al.*, 2014b), forming the Sines Contourite Drift (SCD).

During the Integrated Ocean Drilling Program (IODP) Expedition 339 (Mediterranean Outflow), the occurrence of landsliding activity was one of the main findings within the contourite depositional system (CDS) of the SW Iberia Margin (Hernández-Molina *et al.*, 2013; Ducassou *et al.*, 2016). This poses relevant questions with broad significance, regarding the interaction between along-slope deposition in contourite drifts and downslope processes in a tectonically active region, as the SW Iberia.

Landsliding activity is suggested to have already caused tsunamis off Portugal in the past (Terrinha *et al.*, 2003; Baptista and Miranda, 2009; Lo Iacono *et al.*, 2012; Baptista *et al.*, 2014; Omira *et al.*, 2016). Considering the seismicity of the SW Iberia Margin, the generation of landslide-induced tsunamis as a consequence of earthquakes should also be considered, as the SCD is located nearby a seismicity cluster in the SW Iberia (Silva *et al.*, 2017; Veludo *et al.*, 2017). Accounting for the devastation caused by the 1755 Lisbon earthquake and tsunami in the SW Iberia (Baptista *et al.*, 1998; Canals *et al.*, 2004) and the possible consequent generation of landslides, it is critical to understand and to study the submarine landsliding susceptibility of the area, and also to assess slope instability, which constitutes a major geohazard for the Sines area, both underwater as well as on land near the coast. Submarine

landslides may destroy cables and other submarine man-made infrastructures, as already seen for other areas overseas (Heezen and Ewing, 1952; Piper *et al.*, 1985; 1999a), whereas landslide-induced tsunamis may severely affect coastal areas and populations. This may have a special impact and serious consequences both in the Sines oil refinery as in the harbour. These infrastructures constitute a serious vulnerability, as they are highly exposed to those geohazards, constituting a tremendous risk for the area.

Thus, it is crucial to understand the geomorphologic and the morphosedimentary evolution of the area, as well as the interaction between along-slope and downslope processes occurring there. Furthermore, the evaluation of slope stability and landslide susceptibility in the Alentejo Margin (AM) is critical to assess the hazard of the area.

1.1.1 – PREVIOUS WORK ON THE ALENTEJO MARGIN

The Southwest Iberian Margin in general and the Alentejo Margin, in particular, have been studied from various perspectives, mostly since the 1970s, when, for example, Mougenot *et al.* (1979) studied the structural and sedimentary evolution of the south Portuguese continental margin. Later, Vanney and Mougenot (1981) did a geomorphological analysis of the Portuguese continental shelf through a broad bathymetric and geomorphologic characterization, using single beam and reflection seismic data. In the late 1980s Mougenot (1989) studied the geology of the Portuguese margin, updating that geomorphologic analysis. The Mesozoic and Cenozoic tectonic and sedimentary evolution of the area during the syn-rift and post-rifting phases has been studied by Terrinha *et al.* (2003); Pereira and Alves (2009; 2011); Pereira *et al.* (2011); Alves *et al.* (2013); Pereira and Alves (2013); Terrinha *et al.* (2019b); Terrinha *et al.* (2019c). The Alentejo Margin has also been subject of several studies related to Late Quaternary climatic and palaeoceanographic variations (Baas *et al.*, 1997; Skinner *et al.*, 2003) and consequent impact on bottom current activity (Schönfeld *et al.*, 1993; Schönfeld and Zahn, 2000; Hernández-Molina *et al.*, 2014b; Voelker *et al.*, 2015), past circulation (Salgueiro *et al.*, 2014) and further sedimentary evolution (Zahn *et al.*, 1997; Abrantes *et al.*, 1998; Hernández-Molina *et al.*, 2003). The palaeoceanographic reconstruction of the West Iberia Margin, encompassing the Alentejo Margin, has been carried out by Cayre *et al.* (1999).

The Pliocene through Present contourite deposition, that started in the latest Messinian (Hernández-Molina *et al.*, 2014b) along the Alentejo Margin has been analysed in different works, addressing the depositional evolution induced by the Mediterranean Outflow Water variations (Hernández-Molina *et al.*, 2011; 2013; 2016a), the seismostratigraphy of the Sines Drift (Rodrigues *et al.*, 2020) and the slope failure affecting this along-slope depositional body (Roque *et al.*, 2015; Teixeira *et al.*, 2017; 2019) and the surrounding area (Collico *et al.*, 2020).

1.2 – AIMS OF THE WORK

This work aims to study the mass movement processes in the Southwest Portuguese Continental Margin during the Late Pleistocene - Holocene period. It aims at contributing to the understanding of the morphosedimentary evolution and the interaction of the along-slope and downslope morphosedimentary processes affecting the Sines Contourite Drift. Thus, the main goals of this work are to:

1) Assess the impact of regional tectonics and seismicity, as well as bottom currents activity on the development of landsliding activity;

2) Understand the evolution of landslides and MTD events within contourite successions;

3) Identify the main triggering factors of landsliding activity;

4) Evaluate the impact that sediment properties (sedimentological, physical and geochemical) have on the morphosedimentary evolution of Sines Contourite Drift sediments;

5) Assess the geotechnical behaviour of the shallowest contourite sediments and its impact on slope stability;

6) Evaluate the present-day potential of slope failure with physically based and statistical modelling, in the contouritic sediments of Sines Contourite Drift.

1.3 – DATA AND WORKING GUIDELINES

To achieve this, a dataset constituted by high-resolution multibeam bathymetry, multichannel seismic data, sub-bottom profile data (Parasound), and gravity core data were used. Therefore, this work is essentially dedicated to geomorphological analysis and mapping (swath bathymetry and seismic data); interpretation of seismic lines and determination of potential slide planes; analyses of sedimentological, chemical, geochemical, physical, and geotechnical properties; assessment of landslide susceptibility and validation with known mass movement events.

1.4 – THESIS OUTLINE

This thesis is divided into ten chapters, each one comprising one specific part of this work:

Chapter 1 (*Introduction*) outlines the objectives and the scope of the work, introducing the problem and the rationale of the thesis. Previous works focusing on contourites and on landslides in the Southwest Iberia are outlined.

Chapter 2 (*Mass movement activity, contourite deposition and slope stability*) presents a state-of-the-art on (submarine) landslides, comprising their terminology, main properties and triggering mechanisms. Contourite formation and their main features are described and the state-of-the-art on slope stability analysis is also reviewed.

Chapter 3 (*Regional setting of the study area*) provides the geological and tectonic background, indicating the evolution of the study area through time. The area is described in the different phases of compressional and extensional evolution. Litho-stratigraphy is described according to the present-day situation.

Chapter 4 (*Materials and methods*) presents the data sets and the methodologies and procedures used in this work.

Chapter 5 (*Geomorphologic features and processes in the Alentejo Margin (SW Iberia): implications on landsliding activity*) provides a geomorphologic analysis of the morphologic evolution of the area, where the main morphosedimentary features are presented and described. Depositional, erosional, and gravity-driven features are presented based on the

interaction between along-slope and downslope processes and consequent impact on slope stability.

Chapter 6 (*Sediment properties as indicators of the Late Pleistocene-Holocene sedimentary evolution of the Sines Contourite Drift*) focuses on the sediment properties and the morphosedimentary evolution of the Sines Drift through the assessment of the sedimentological, chemical, physical, and geochemical properties of the sediments. Climate variations and bottom current activity are analysed, and their impact on the sedimentary depositional behaviour is discussed.

Chapter 7 (*Geotechnical characterization of sediments*) aims to show the mechanical properties and the behaviour of the Sines Drift sediments, when submitted to shear stress in static conditions, through different geotechnical tests.

Chapter 8 (*Submarine landslide susceptibility analysis*) this chapter provides the assessment of landslide susceptibility using the mechanical properties previously retrieved, through both physically based and statistical models. Validation of these results is done through the landslide scars inventory, previously performed in Chapter 5.

Chapter 9 (*Discussion*) summarizes the main interpretations derived from this study.

Chapter 10 (C*onclusions*) summarizes the main conclusions of this work, showing and discussing the clues for future work.

2 – MASS MOVEMENT ACTIVITY, CONTOURITE DEPOSITION AND SLOPE STABILITY

2.1 – MASS MOVEMENTS: LANDSLIDES CLASSIFICATION AND TERMINOLOGY

According to the UNESCO Working Party on World Landslides Inventory, landslide is the downslope movement of a mass of sediment or rock (WP-WLI, 1993a), in both onshore and subaqueous environments, that develops in time through different stages (Hungr *et al.*, 2014), triggered by both natural- and human-induced causes (Varnes, 1958; 1978). The thematic of landslides has several concepts and terms associated with the phenomena, being Anglo-Saxon terminology the most widely accepted and used by the scientific community, with special emphasis for the contributions of Varnes (1958, 1978) and Hutchinson (1968, 1988). The works with the highest scientific relevance, in the last decades, on this domain are the works of Cruden (1991), WP-WLI (1993a), Cruden and Varnes (1996) and Dikau *et al.* (1996a), which are based on the terminology developed by Varnes (1958); Hutchinson (1968); Skempton (1969); Záruba and Mencl (1969); Varnes (1978) and Hutchinson (1988).

Varnes (1978) classification is the source for the present-day most accepted landslides classifications by scientific community being updated by Cruden and Varnes (1996) and Hungr *et al.* (2014). However, it was in 1993 with the classification proposed by the *Working Party on World Landslide Inventory* (WP-WLI, 1993a), that the landslides terminology was standardized based on the typology; distribution; state and style of activity; morphology and dimensions of landslides. For these authors the object of classification is termed as *Landslides - "Slope Movements"*, whereas Hutchinson (1968), in turn, defines the object of classification as *"Mass Movements"*, in which slope movements are included. Mass movements include all gravity-induced downslope movements, from which are excluded those whose material is displaced by fluvio-torrential action of water, snow, ice and wind, also termed as mass transportation by Hutchinson (1968).

By *Landslide* or *"Landslip"* as Cruden (1991) defines it, it is understood "*The movement of a mass of rock, earth or debris down a slope*" (Cruden, 1991), by the action of gravity (Blasio, 2011), where there is a downwards displacement of material directed to the outside of its centre of gravity (Terzaghi, 1952). This definition excludes vertical movements of sinking and settlement or subsidence, as well as snow avalanches and expansion/shrinkage

phenomena of clay soils (Zêzere, 1997) and corresponds to the same as the *"Mass Movements"* definition adopted by Hutchinson (1968). To be recognized as landslides and therefore to be distinguished from other types of gravity-induced movements, the displaced material should present a density 10% higher than water's (Blasio, 2011). In what concerns to the classification method, primary and secondary criteria of discrimination are used. Varnes (1978), WP-WLI (1993a), Cruden and Varnes (1996) and Dikau *et al.* (1996a) consider the different types of failure mechanism as the main criterion and the affected material as a secondary criterion of classification. However, Cruden and Varnes (1996) consider velocity, activity and water content of displaced materials as a secondary criterion as well.

2.1.1 – TYPOLOGY OF LANDSLIDES

In this work, it will be used the terminology and classification of landslides defined from the concepts initially proposed by Varnes (1978) and applied by WP-WLI (1993a) –

TABLE 2.1 – Main Landslide Typologies. Adapted from VARNES (1978).

Type of Movement (Failure Mechanism)		***Affected Material***		
		Rock	***Debris*** (Coarse)	***Soil*** (Fine)
Type	***Subtype***			
Fall		*Rock fall*	*Debris fall*	*Earth fall*
Topple		*Rock topple*	*Debris topple*	*Earth topple*
Rotational Slide	Single (slump); multiple; successive	*Rock slump*	*Debris slump*	*Earth slump*
Translational Slide	Not Rotational	*Rock block slide*	*Debris block slide*	*Earth block slide*
	Planar	*Rock slide*	*Debris slide*	*Earth slide*
Lateral Spreads		*Rock spread*	*Debris spread)*	*Earth spread*
Flows		*Rock flow*	*Debris flow*	*Earth flow*
Complex Landslides		*Combination of two or more types of failure mechanisms*		

UNESCO working group; Cruden and Varnes (1996); and Dikau *et al.* (1996a) - Table 2.1. These authors present a set of concepts resulting from the distinction of the type of failure

mechanism and affected material: *Fall*; *Topple*; *Lateral Spreading; Slide* - Rotational and Translational; *Flows* and *Complex Landslides*. In what concerns to the affected material it is considered rock, debris (coarser material) and soil/earth (fine material) - Table 2.1. This work will be mainly focused on slides, especially translational slides as they are dominant both on submarine environment (Prior and Coleman, 1984) and on land (Selby, 1993). Flows will also be focused, on this work, as a great majority of translational slides evolve into debris or earth flows, spreading disrupted materials through long distances (Piper *et al.*, 1999a).

1) ***Fall*** occurs whenever natural slope angle exceeds the limit equilibrium of materials, implying *"a detachment of soil or rock from a steep slope along a surface on which little or no shear displacement takes place. The material then descends largely through the air by falling, saltation or rolling"* (WP-WLI, 1993a), along steep slopes, sometimes vertical as for example sea cliffs (Marques, 1997). The rupture may be planar, wedge, stepped or vertical (Flageollet and Weber, 1996). Some researchers make a distinction between rock fall, which implies the falling of isolated or groups of boulders or blocks, and rock avalanches of huge dimensions. The main causes for falling processes (fall) may be cryoclastic and thermoclastic phenomena and also the root growth, which widens even more the existing rock fractures (Flageollet and Weber, 1996).

FIGURE 2.1 – Rock fall (Teixeira, 2006).

2) ***Topple*** corresponds to a *"(…) forward rotation, out of the slope, of a mass of soil or rock about a point or axis below the centre of gravity of the displaced mass"* (WP-WLI, 1993a), which is preferably developed along irregular stratification planes, cleavages and tension fractures (Dikau *et al.*, 1996b). According to Varnes (1978), this kind of slope movement occurs by the action of gravity and lateral forces, which are exerted by adjacent units and by fluids present in the joints and fractures.

FIGURE 2.2 – Topple (USGS).

3) ***Lateral Spreading***, in the Anglo-Saxon terminology is an *"extension of a cohesive soil or rock mass combined with a general subsidence of the fractured mass of cohesive material into softer underlying material. (…) Spreads may result from liquefaction or flow (…) of the*

softer and underlying *material"* (WP-WLI, 1993a). This is a slow movement on rock but quite fast on soft sediments.

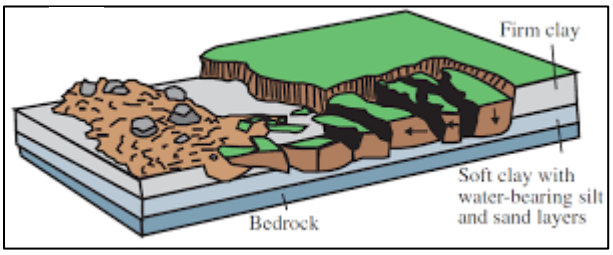

FIGURE 2.3 – Lateral spreading. Varnes, 1978

4) ***Slide*** is a *"downslope movement of a soil or rock mass occurring dominantly on surfaces of rupture or relatively thin zones of intense shear strain"* (WP-WLI, 1993a). Buma and Van Asch (1996) define slide as *"a movement of material along a recognizable shear surface"*. Slides can be rotational or translational and, according to Zêzere (1997), the displaced mass by the movement remains in contact with the underlying undisturbed material, presenting quite variable deformation stages, which vary with the type of slide. Slide scars start developing from stretch marks, previously created on the original topography, which indicate that the process of sliding is on the way and which direction it will take place. The sliding movement is a process that varies in time, lasting from a few minutes to some years until the slope stabilizes. Slides may be subdivided according to shear mechanism and the type of material affected by that mechanism (Varnes, 1978).

4a) *Rotational Slide* (***slump***) is by definition a *"more or less rotational movement, about an axis that is parallel to the slope contours, involving shear displacement (sliding) along a concavely upward-curving failure surface (...)"* (Varnes, 1978).

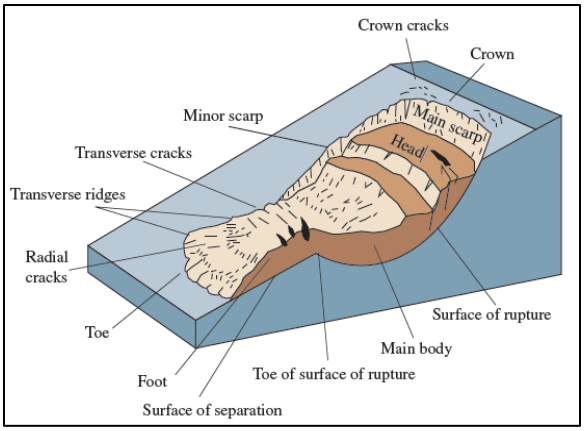

FIGURE 2.4A – Scheme of a Rotational Slide. Varnes (1978).

Rotational slides present a circular shear or "*spoon-shaped* surface" – concave – (Figure 2.4A) displaying a very low degree of internal deformation of the displaced material (Buma and Van Asch, 1996; Hampton *et al.*, 1996; Mulder and Cochonat, 1996). Rotational slides may be simple (*slumps*), when occurring along curve shear surfaces, in isotropic and homogeneous environments (Sirieys, 1984). The movement involves a rotation, materialized by a reduction on the slide's upstream sector and by a lifting on its frontal part forming more or less pronounced acclivities, according to Záruba and Mencl (1969) and Hutchinson (1988). Rotational slides are considered as multiple when they have a common basis and successive when they are chain-developed (Varnes, 1978), tending to evolve retrogressively by the loss of stability on the basis.

4b) *Translational Slides* are *"non-circular failures in which the landslide mass moves along a roughly planar surface with little rotation or backward tilting"* (Varnes, 1978), where there is a translational movement of weathered material on a shear zone close to the contact with underlying unweathered bedrock (Ibsen *et al.*, 1996) and generally with high internal deformation of displaced materials (Figure 2.4B).

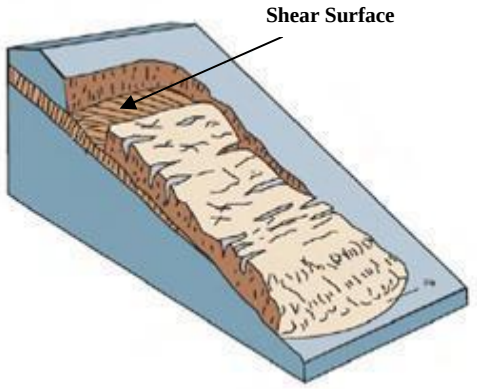

FIGURE 2.4B – Scheme of a Translational Slide. Varnes (1978).

Translational slides are the most common onshore but also offshore, especially on gentler slopes as there is a displacement of thin layers of mass over a slope-parallel failure surface (Prior and Coleman, 1984; Hampton *et al.*, 1996). According to Mulder and Cochonat (1996), translational slides evolve through well-defined failure surfaces and tend to occur in cohesive structured-materials and involve little displacement rates, comparing with debris flows.

FIGURE 2.4C - Shallow translational slide (Teixeira *et al.*, 2015).

The most common of translational slides (rock, soil, debris) are debris slides (shallow translational slides) which generally present an abrupt and well-defined shear surface (Figure 2.4C). These are very fast slides whose sliding speed and degree of run-out increase with slope angle (Hutchinson, 1988) and a great majority of these translational debris slides turn into debris flows (Corominas, 1996). Still according to Corominas (1996), debris slides take place mainly on topographic concavities where water and colluvium debris tend to accumulate, being available for disruption.

Translational landslides may be classified according to the failure plane type: planar translational slides and non-rotational translational slides (Dikau *et al.*, 1996a). Non-rotational translational slides are in the transition between rotational and the most typical translational (planar) landslides. These slides may also be classified according to the affected material.

Contrarily to rotational slides, translational ones develop over anisotropic materials with an evident structural control at the contact between colluvium cover and bedrock, in which the movement is controlled by low shear resistance failure surfaces (Corominas, 1996), essentially developing along normal faults, thrust faults, fractures, lithological contacts, sub-horizontal bedding planes and shear zones between bedrock and slope deposits. Planar translational slides have high topographic control (Montgomery and Dietrich, 1994), being mainly triggered when soil saturates in the contact between weathered materials and the underlying bedrock (Iverson, 2000).

5) ***Flow*** is a *"spatially continuous movement in which shear surfaces are short-lived, closely spaced and not usually preserved, where the distribution of velocities in the displacing mass resembles that in a viscous fluid"* (WP-WLI, 1993a), and showing free individual displacements of particles inside a moving mass. Flows *"involve whatever material is available to them and may therefore be high fractured rock, clastic debris in a fine matrix"* (Dikau *et al.*, 1996a). These movements have many stresses causing material internal deformation (Carson and Kirkby, 1975) and consequently differences in the run-out velocity specially near the surface, where they are higher (Bromhead, 1992). Flows may occur on rock - *rock flow* - (Bisci *et al.*, 1996); on soil or earth – *mudflow* - (Schrott *et al.*, 1996) and on debris – *debris flow* - (Corominas *et al.*, 1996). Debris flow is *"a gravity-induced movement somewhere between landsliding and water flooding"* (Johnson and Rodine, 1984), with torrential activity and consisting of a mass of a mixture of fine and coarse material chaotically disposed. These are very fast and destructive movements (Corominas *et al.*, 1996). Debris flows are commonly triggered by a sudden collapse of the stability of a slope by the action of both gravity and unusual presence of water and they are typically controlled by the topography which promotes their occurrence on topographic convergences (Figure 2.5), where subsurface flow drains to, hence promoting soil saturation provoking a loss on shear

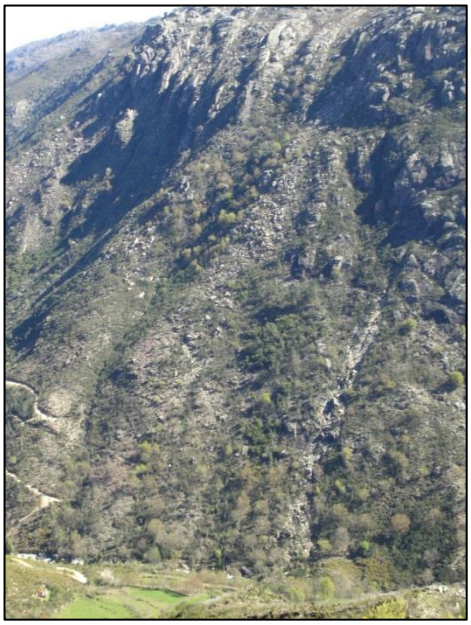

FIGURE 2.5 – Debris/rock flows (Teixeira, 2006)

strength (Montgomery and Dietrich, 1994). According to Johnson and Rodine (1984), debris flows start as translational or rotational slides and then develop into debris flows.

6) ***Complex Landslides*** *"combine two or more of the main landslide types either in different sections of the affected material or in different stages of the landslide"* (Varnes, 1978). This kind of landslide is very common as almost nothing is linear in nature. The occurrence of landslides displaying several mechanism types intervening is quite frequent (Laberg and Vorren, 2000), elapsing complex landslides precisely from the intersection of these different mechanisms, that is, as material moves downslope the initial mechanism that gave rise to it changes to another mechanism. Dikau *et al.* (1996a) use this designation to express situations in which it is occurring more than one landslide type with a well-defined temporal sequence. The landslide may start by fall and then turn into a debris flow (Figure 2.6) due to the breakdown of larger blocks, fragmented during the falling movement along the slope, like this example of the complex landslide (Teixeira, 2006).

FIGURE 2.6 – Complex landslide (Teixeira, 2006)

2.1.2 – LANDSLIDES' FEATURES AND DIMENSIONS

Landslides' (slides and slumps) internal features and dimensions are important elements to consider. Although recognised in nature as a whole, there are different parts of the landslides that must be clearly identified for a good interpretation of their dynamics and typology (Záruba and Mencl, 1969). Záruba and Mencl (1969), propose the existence of three main distinct sectors or areas on a landslide: rupture, transport and accumulation areas. Later on, Varnes (1978) created the most effective systematization for the identification of landslides' morphological features, which was adopted by the WP-WLI (1993a) and by the IAEG commission on landslides. This work also follows the nomenclature proposed by Varnes (1978) and adopted by WP-WLI (1993a).

The landslides' morphology and dimensions are thus presented as follows (Figure 2.7):

(1) - *Crown*: adjacent area to the highest parts of the main scarp; (2) – *Main scarp*: steep, generally concave surface on the undisturbed ground at the upper edge of the landslide; (3) – *Top*: the highest point of contact between the displaced material and the main scrap; (4) – *Head*: the upper parts of contact between the main scarp and the displaced material; (5) – *Minor scarp*: a steep surface on the displaced material originated by differential movements; (6) – *Main body*: the part of displaced material of the landslide that overlies the surface of rupture between the main scarp and the toe; (7) – *Foot*: the portion of the landslide that has moved beyond the toe of the surface of rupture, overlying the original ground surface; (8) – *Tip*: the point of the toe defining the downstream end of the displaced material; (9) – *Toe*: the lower, usually convex, margin of the displaced material most distant from the main scarp; (10) – *Surface of rupture*: sliding surface, the surface that forms the lower boundary of the displaced material, where occurs the shear movement; (11) – *Toe of surface of rupture*: downstream intersection between the surface of rupture and the original ground surface; (12) – *Surface of separation*: the original ground surface overlain by the foot of the landslide; (13) – *Displaced material*: material displaced from the original place by the action of a landslide; (14) – *Depletion area*: the area of the landslide within which the displaced material lies below the original ground surface; (15) – *Accumulation area*: the area of the landslide within which the displaced material lies above the original ground surface; (16) – *Depletion*: volume of lost material bounded by the main scarp, the depleted mass and the original surface; (17) – *Depleted mass*: the volume of displaced material overlying the sliding surface but underlying the original surface; (18) – *Accumulation*: the volume of displaced material; (19) – *Flank*: lateral limit of the landslide, non-displaced material adjacent to the sides of the rupture surface; (20) – *Original ground surface*: the original surface of the slope prior to the landslide.

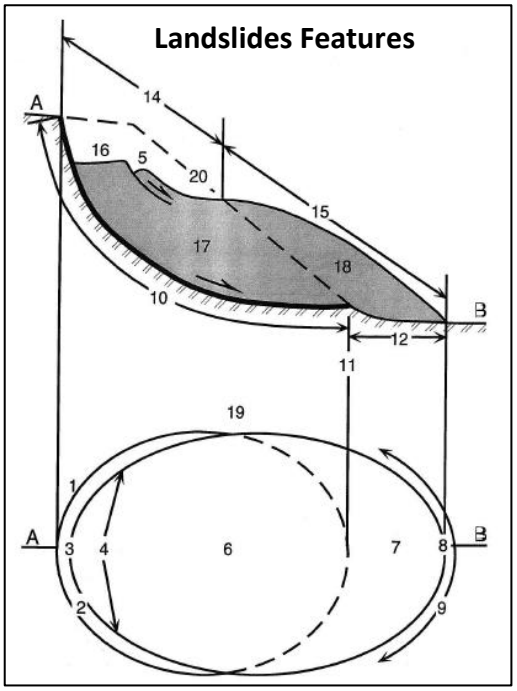

FIGURE 2.7 – Main morphological features of landslides. Modified from WP-WLI (1993a).

Some standardised dimensions (Figure 2.8) are also pertinent when studying landslides.

W_d – The width of the displaced mass that corresponds to the maximum breadth of the displaced mass perpendicular to the length, L_d.

W_r – Width of the rupture of surface is the maximum width between the flanks of the landslide, perpendicular to the length, L_r.

L – The total length is the distance from the crown to the tip of the landslide.

L_d – Length of the displaced mass, equivalent to the horizontal length of depletion and accumulation areas.

L_r – Length of the surface of rupture is the distance from the toe to the crown of the landslide.

D_d – Depth of displaced mass measured perpendicular to the plane.

D_r – Depth of the rupture of surface below the original ground.

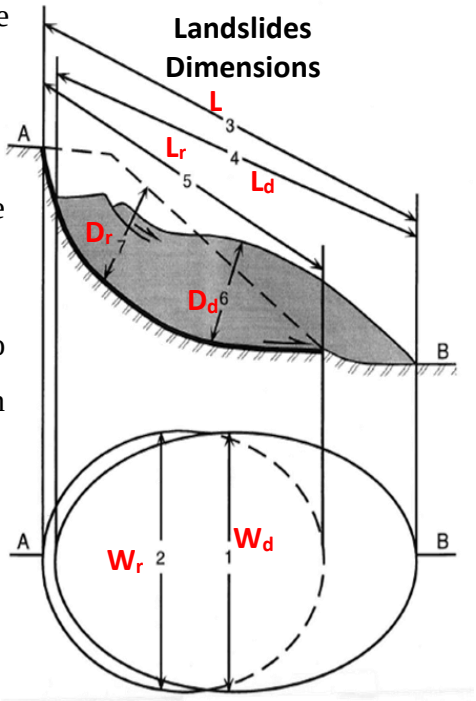

FIGURE 2.8 - Landslides' dimensions. Modified from WP-WLI (1993). Top – vertical section; bottom – top view.

2.1.3 – THE ACTIVITY OF LANDSLIDES

Landslides have a specific motion and present different activity according to the moment. In this sense following WP-WLI (1993b), based on the work of Varnes (1978), the activity of landslides may vary according to the style, state and distribution of activity.

2.1.3.1 – STYLES OF ACTIVITY OF LANDSLIDE

The style of activity *"indicates how different movements within the landslide contribute to its overall movement"*(WP-WLI, 1993b) - Figure 2.9.

1) *Single landslide* happens when there is only one single movement, or type of mechanism, of the displaced material, although as Zêzere (1997) states this is a very uncommon style as almost all landslides present more than one type of mechanism.

2) *Multiple landslides* show repeated developments of the same type of mechanism. These movements are more common on rotational slides (Hutchinson, 1988) in which they are characterized by a common basal surface of rupture and by a share of displaced material (Buma and Van Asch, 1996).

3) *Successive landslides* happen as a succession of individual movements of the same type that do not share displaced material or rupture surface. Generally, this type of activity is common on rotational landslides consisting of a succession of individual low deep slides (WP-WLI, 1993b).

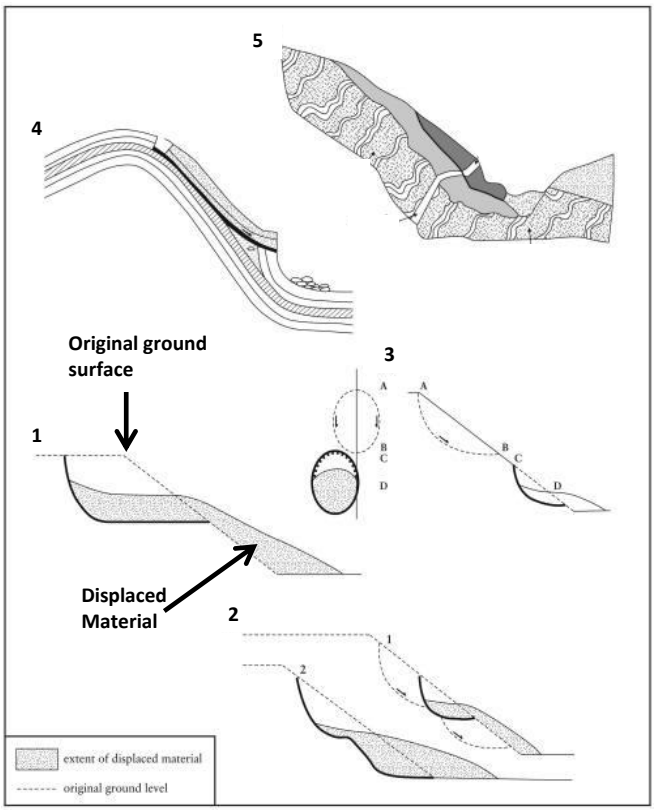

FIGURE 2.9 – Styles of landslide activity (WP-WLI, 1993a).

4) *Composite landslides* are movements with two or more types of simultaneous movements in different parts of the displaced material (WP-WLI, 1993b).

5) *Complex landslides* as stated before *"combine two or more of the main landslide types either in different sections of the affected material or in different stages of the landslide"* (Varnes, 1978). Following WP-WLI (1993b), Cruden and Varnes (1996) and Dikau *et al.* (1996a) complex landslides are those with two or more types of mechanisms sequentially developed in time.

2.1.3.2 – DISTRIBUTION OF ACTIVITY OF A LANDSLIDE

The distribution of activity (Figure 2.10) deals with the spatial motion of landslides – how they develop and what is their appearance on the field. Landslides may have several types of distribution of activity. In this work I will follow the terminology proposed by the *Working Party on World Landslides Inventory* (WP-WLI, 1993a; 1993b):

1) *Advancing* movements are those in which the rupture surface is propagating in the direction of the movement;
2) *Retrogressive* movements have the rupture surface propagating in the opposite direction to the movement of the displaced material, so in an opposite motion of the previous one;
3) *Enlarging* movements present the rupture surface extending in two or more directions, meaning these are in multiple advance;
4) *Diminishing* movements are those in which the volume of the displaced material is constantly decreasing at each reactivation of the movement;

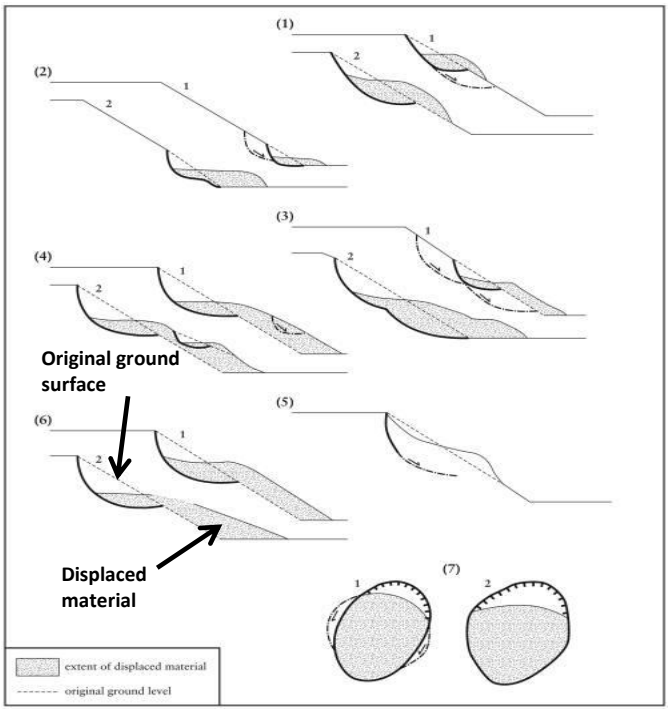

FIGURE 2.10 – Distributions of activity in landslides (WP-WLI, 1993a). Adapted.

5) *Confined* movements present a scarp but not a visible rupture surface on the foot of the displaced mass;
6) *Moving* landslides have constant movement of the displaced material without visible changes in the rupture surface or in the volume of the displaced mass;
7) *Widening* movements are those which are extending into one or both flanks of the landslide.

2.2 – SUBMARINE LANDSLIDES

Submarine slope instability is still poorly understood (Shanmugam, 2016), and although not as much studied as subaerial (Prior and Coleman, 1984; Piper *et al.*, 2012), it is a widespread and highly recognized phenomenon (Hampton *et al.*, 1996). Submarine landslides are recurrent and worldwide phenomena (Prior and Coleman, 1984; Hampton *et al.*, 1996; Masson *et al.*, 2006; Piper *et al.*, 2012; Shanmugam, 2016), and according to Mosher *et al.* (2010), these are the most important form and source of submarine erosion, displacing huge volumes of sediments that frequently transform into debris flows (Piper *et al.*, 1999a). This contributes for the deep-marine environments to be very complex systems (Figure 2.11),

where many processes interact (Shanmugam, 2016). Given the dynamic activity of these environments, displaced materials are reworked by bottom currents. Generally, landslides deposits coexist with other mass transported bodies such as turbidites and along-slope deposits as contourites (Laberg and Camerlenghi, 2008; Cattaneo *et al.*, 2014) - Figure 2.11. Submarine landslides constitute a matter of the highest concern especially for coastal areas (Moore *et al.*, 1989; Hampton *et al.*, 1996; Masson *et al.*, 2006). They may occur on different offshore environments, on very low-angle slopes (<5º) from shallow to deep-sea areas (Prior and Coleman, 1984). Commonly, they occur on continental slopes and spread to deep basins (Figure 2.11), where the interaction with bottom currents may promote the formation and the transformation of mass transport deposits into another type of depositional features as turbidity currents. There are examples where submarine slides occur at extremely low-angle slopes, < 1º, as it is the case of the Mauritania Slide Complex (Henrich *et al.*, 2008). Submarine landslides differ from subaerial landslides especially in dimension, as those can be ten times higher than these (Hampton *et al.*, 1996). For example, the Agulhas Slump in SE Africa is 20,333 km^3 in size (Dingle, 1977) and is ten times volumetrically larger than the world's largest subaerial landslide, the Markagunt landslide (Ikari *et al.*, 2011), in Utah, USA,

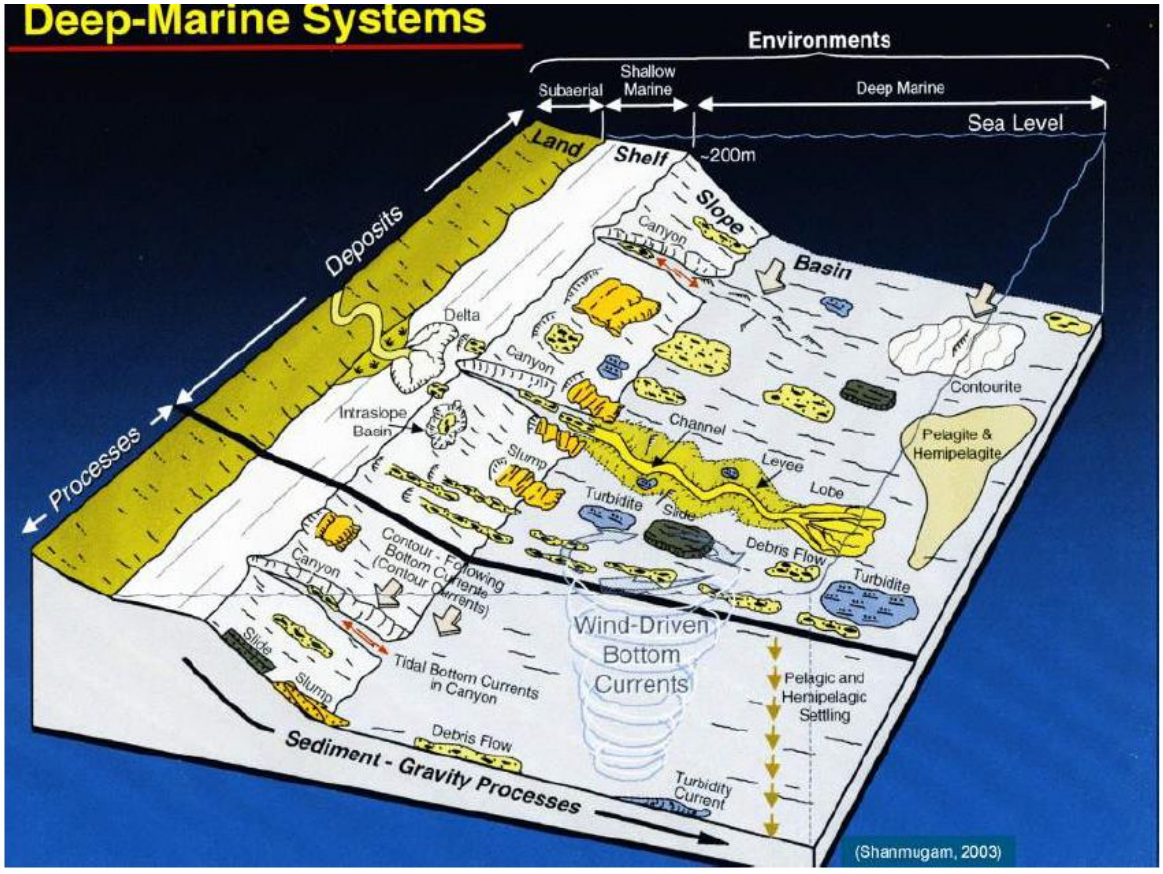

FIGURE 2.11 - Schematic diagram showing complex deep-marine sedimentary environments and processes occurring at water depths deeper than 200 m. From Shanmugam (2016).

which is 2,000 km^3. The rapid environmental transformations promoted by the complex deep-marine dynamics is another great difference (Shanmugam, 2015).

Unlike onshore, submarine slope instability may occur on slopes < 1º and sediments are generally fully water saturated, but the speed and strength of transient loadings like tides and currents as well as of earthquakes may act differently on slopes depending on the location, contributing to different instability degrees. In spite of this, the presence of gravity that persistently acts to pull sediment and rock downslope, is common to all of these environments, although submarine landslides have been identified in different areas presenting the most varied slope angles, stress environments as well as sedimentary thickness (Hampton *et al.*, 1996).

Research on this subject has some questions and duties to be solved. Some of the most important questions to be answered are put, for example, by Kawamura *et al.* (2009): what is the main triggering mechanism of submarine landslides? Where do they (preferably) occur?

2.2.1 – REFERENCE WORKS

Submarine landslides have been subject of analysis and important works have been done on different environments as continental slopes (Uchupi, 1967; Roberts and Stride, 1968; Almagor and Garfunkel, 1979; Bugge *et al.*, 1988; Canals *et al.*, 2004; Ercilla *et al.*, 2008a; Henrich *et al.*, 2008), in which one of the largest landslides on earth occurred – the Storegga slide - e.g., (Bugge *et al.*, 1987; Bugge *et al.*, 1988; Bryn *et al.*, 2005a; Kvalstad *et al.*, 2005a; Masson *et al.*, 2006). Particular attention has been given to submarine landslides also on submarine canyons, e.g. (Carlson and Karl, 1988), on oceanic volcanic islands and ridges, e.g., (Moore *et al.*, 1994; Hayward *et al.*, 2009), on river deltas (Sterling and Strohbeck, 1973; Terrinha *et al.*, 2019a) and on fjords, e.g. (Syvitski, 1987; Leroueil *et al.*, 1996). Research has been done also on the physics of landslides and on their behaviour after sliding, e.g. (Iverson, 1997; 2000; Blasio, 2011), as well as on the timing of their occurrence and possible effects, like tsunamis, for example, e.g., (ten Brink *et al.*, 2009; Urlaub *et al.*, 2013). This thematic has been also analysed from a point of view of Risk assessment, e.g., (Masson *et al.*, 2006; ten Brink *et al.*, 2009).

2.2.2 – TERMINOLOGY EVOLUTION

The typology of failures is similar both onshore and offshore (Piper *et al.*, 2012). During the last century, similarly to what happens onshore, several classifications have been proposed for submarine landslides (Shanmugam, 2015), despite the most popular and accepted classification, both onshore and offshore, being the one proposed by Varnes (1958; 1978), which determines the terms *landslide* and *slope movement* as those that better express the downslope movement of a mass of sediment. Nevertheless, no consensus has been reached so far and different terminology can be applied to submarine landslides (Hampton *et al.*, 1996). In this sense, Shanmugam (2015; 2016) considers the term mass transport deposit (MTD) as being more appropriate to describe a submarine downslope sliding mass. In 1963, Dott (1963) had already proposed a classification for subaqueous mass movement activity, quite similar to the one of Varnes (1958), in which turbidity currents are not included. According to Shanmugam (2015), Dott's (1963) classification seems to be among the most accurate.

More recently, Mulder and Cochonat (1996) adopted a terminology for submarine landslide activity, using the term *"Mass Movements"* based on the motion, on the architecture and on the shape of the failure surface. These authors mainly recognize three types of processes: slides and slumps; plastic flows and turbidity currents. For those authors, turbidity currents are considered as mass movements, by opposition to the classifications of Dott (1963), Varnes (1978) and Shanmugam (2015). Mulder and Cochonat (1996) essentially divide landslide activity in mass slides and gravity flows, where mass slides typically correspond to translational and rotational sliding processes; creeping; slab gliding and rock avalanche, whereas gravity flow activity can evolve as both mass flow with laminar regime and turbidity current with turbulent regime (Mulder and Cochonat, 1996). For example, Masson *et al.* (2006) define the turbidity current as a *gravity flow in which sediment grains are maintained in suspension by fluid turbulence*. In what concerns to the term landslide, these authors use it as a generic term that encompasses all the different forms of slope failure, regardless the process that gives rise to the instability. For these authors, slide is a *movement of a coherent mass of sediment bounded by distinct failure planes* (Masson *et al.*, 2006).

In this sense, Shanmugam's (2015) work has itself attempted for demystifying some terminological confusion in what concerns to submarine mass movement activity (Figure 2.12). This work distinguishes three types of mass based on its disaggregation: coherent; incoherent; and fluidal (Newtonian) masses. Slides and slumps are coherent material, where

the sediment concentration reaches ~100% of the volume, while debris flows are an incoherent mass of sediments with lower volume (25-100%) than slides and slumps, whose deposits reach further distances. Turbidity currents are fluid and less dense masses of suspended sediments with low concentration (<23%) (Figure 2.12).

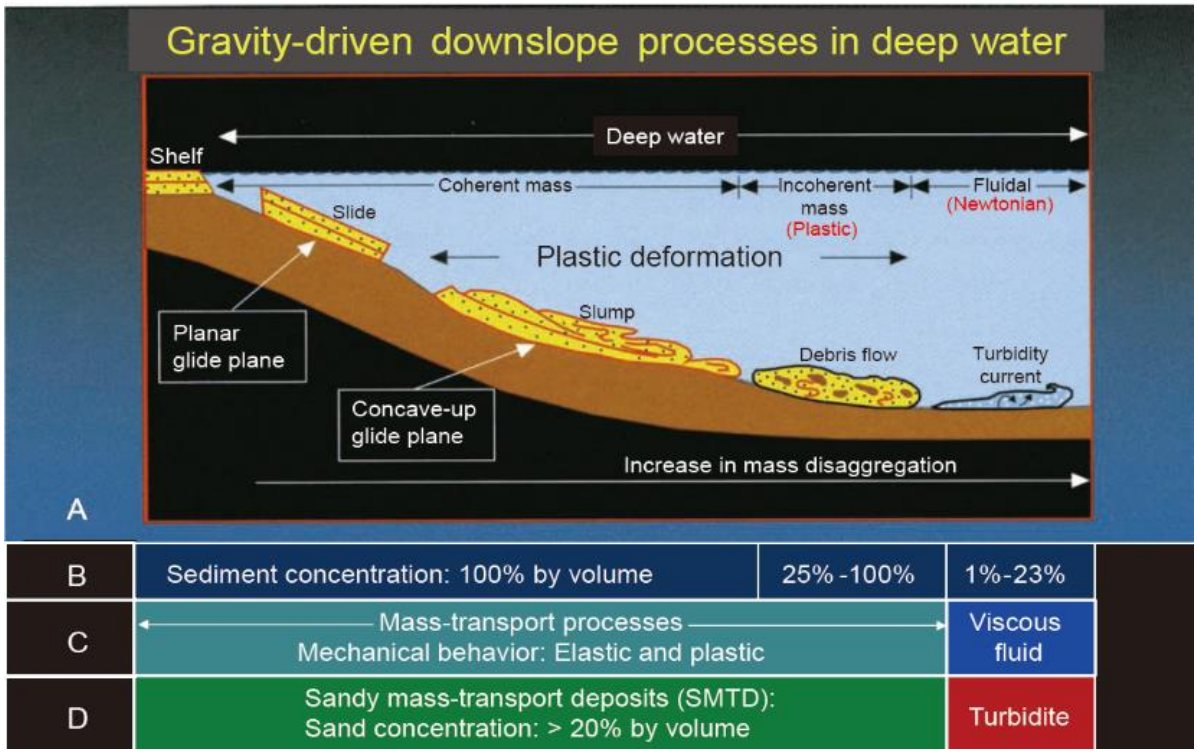

FIGURE 2.12 - Schematic diagram showing four common types of gravity-driven downslope processes that transport sediment into deep-marine environments. From Shanmugam (2015).

Although, some minor terminological variations may occur, the term *landslide*, originally defined by Varnes (1958) is generically adopted to define submarine mass movements (Hampton *et al.*, 1996; Shanmugam, 2015).

2.2.3 – FAILURE MECHANISMS: EVIDENCE FROM THE SEAFLOOR

Submarine landslides may occur at several scales (Shanmugam, 2012) and may vary in volume from few cubic meters, to thousands of cubic kilometres as the Storegga slide (3500 km^3) (Bugge *et al.*, 1988; Haflidason *et al.*, 2005; Kvalstad *et al.*, 2005a; Solheim *et al.*, 2005), to dozens of thousands of cubic kilometres as, for example, the Agulhas landslide (20 331 km^3) in the south-eastern Africa (Dingle, 1977; Shanmugam, 2012).

Slides, slumps, and debris flows are the most common types of submarine landslides (Masson *et al.*, 2006). These failure mechanisms leave scars, tracks and deposits that shape

the seabed (Figure 2.13) with distinctive bathymetric expression (Mosher *et al.*, 1994; 2004; Migeon *et al.*, 2012; Piper *et al.*, 2012; Shanmugam, 2016). They are also commonly noticeable at the subsurface (Piper *et al.*, 1999b; Bull *et al.*, 2009; Gamboa *et al.*, 2010; Piper *et al.*, 2012; Mosher *et al.*, 2017), where the resulting deposits are evident through seismic reflection (Figures 2.14 – 2.16).

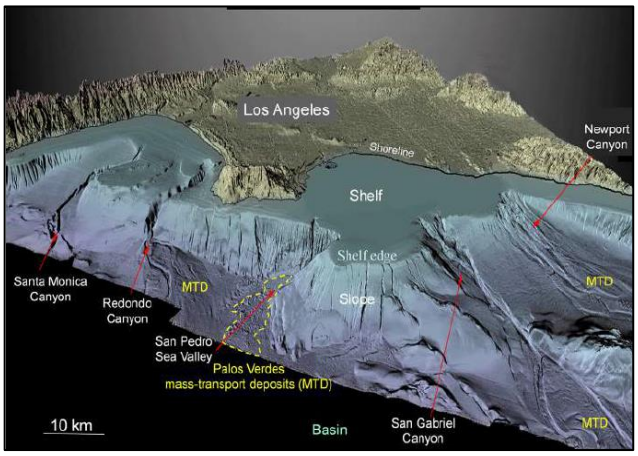

FIGURE 2.13 – Multibeam bathymetry offshore Los Angeles (California), showing well-developed mass-transport deposits (MTDs) on continental slopes. Shanmugam (2016).

Translational sliding is the most common and widespread type of submarine slope instability (Prior and Coleman, 1984), especially on shelf-edge slopes (Mosher *et al.*, 2017), on tectonic boundaries (Alves and Gamboa, 2019) and on areas of high pore-pressure (Locat, 2001). Translational slides are especially evident on gentler slopes (Hampton *et al.*, 1996; Kvalstad *et al.*, 2005a; Henrich *et al.*, 2008; Urlaub *et al.*, 2012) where thin sediment layers displace over slope-parallel failure surfaces (e.g., Prior and Coleman, 1984; Hampton *et al.*, 1996). However, they also occur on steeper slopes (Figure 2.14) as in the Scotian slope (Mosher *et al.*, 2017) or in the Iberia margins (Baraza *et al.*, 1999; Terrinha *et al.*, 2003; Teixeira *et al.*, 2019). According to Mulder and Cochonat (1996), translational slides evolve through well-defined failure surfaces and tend to occur in cohesive structured-materials and involve little displacement rates, contrarily to debris flows.

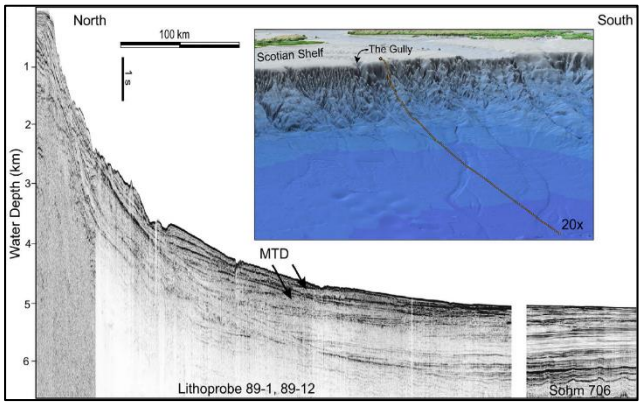

FIGURE 2.14 – Seismic profile and high-resolution bathymetry of the Scotian slope. From Mosher *et al.* (2017).

Rotational slides (Figure 2.12) are a kind of submarine mass movement in which blocks of failed material rotate along curved slip surfaces (Prior and Coleman, 1984; Hampton *et al.*, 1996; Mulder and Cochonat, 1996) and generally leave slump folds on the deposits (Bull *et al.*, 2009). Slumps usually involve failure over hundreds of square kilometres on the continental slope (Piper *et al.*, 2012), involving gradual, intermittent, downslope movement of thick coherent blocks (Moore *et al.*, 1989; Masson *et al.*, 2006) that slid along

well-defined curved rupture surfaces (Figure 2.4A). These mass transport processes form large deposits (Figures 2.13, 2.14, and 2.15) that are quite evident due to their dimension and morphology on the surface, but also well recognizable in depth through their acoustic pattern (Shanmugam, 2016) and kinematic indicators (Bull *et al.*, 2009). Generally, slides' deposits are identified in the acoustic data through their chaotic internal reflections (SD in Figure 2.15), which allow distinguishing those chaotic deposits from other non-turbulent ones, as contourites. The erratic pattern of these deposits is expressed by the hummocky configuration of seismic reflections (Figures 2.15 and 2.16). Moreover, these deposits are usually truncated at their limits, by discordant confining deposition, creating acoustic unconformities (Figures 2.15 and 2.16). This is quite evident in Storegga (Solheim *et al.*, 2005; Bull *et al.*, 2009) and in Vieste (Gamberi *et al.*, 2020) slide deposits.

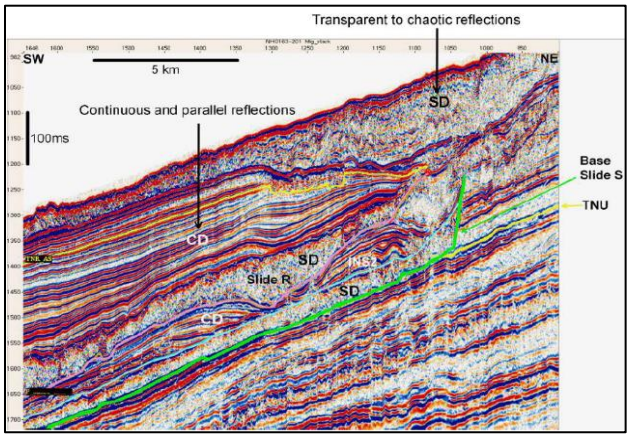

FIGURE 2.15 – Seismic profile of Storegga Slide on the mid-Norwegian continental margin, showing transparent (homogeneous) to chaotic internal reflections of slide deposits. SD = slide deposits; CD = contourite deposits. From *Solheim et al.* (2015).

Debris flows (Figure 2.12) and debris avalanches are very common offshore and correspond to rapid flow of cohesionless rock fragments and sediments with energy dissipation by grain contact (Masson *et al.*, 2006). Debris flows involve material with indistinct structure (Mulder and Cochonat, 1996), i.e., hummocky viscous matrix, where material is chaotically distributed (Laberg and Vorren, 1995; Laberg *et al.*, 2017). Normally, debris flows are subsequent to either slides or slumps being the downslope transport of debris released on the sliding process on a chaotic matrix of debris and fines that generally reaches velocities in the order of 100 m/s on steeper slopes (> 25º) (Masson *et al.*, 2006). Similarly to slides and slumps, debris-flows display near-vertical amphitheatre-shaped headwalls, an erosive chute on the upper part of the submarine slope and a pile of avalanche debris at the foot of the steepest slope (Masson *et al.*, 2006; Ercilla *et al.*, 2008a). Masson *et al.* (2006) refer that these landslides, similarly to the previous ones, can also initiate turbidity

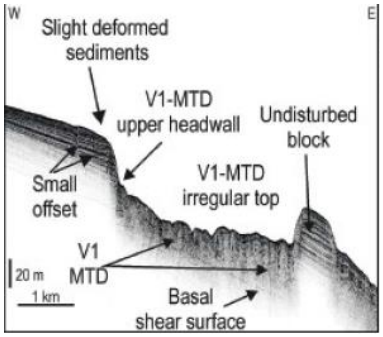

FIGURE 2.16 – PARASOUND profile of Vieste Slide in the southwestern Adriatic Sea, showing a slide scarp and an MTD with rugged surface and chaotic internal reflections. From Gamberi *et al.* (2020).

currents that are capable of having runout distances up to 130 km, as occurred for example off Canary Islands (Merle *et al.*, 2009). When flows are dominantly composed by silt and clay or by sand-like material it is respectively designated by liquefied flows or by fluidized flows (Mulder and Cochonat, 1996).

Turbidity currents are not assumed as a landslide by Varnes (1978), however it is still a matter of debate (Shanmugam, 2000). Turbidity currents, as the landslides, also correspond to gravity-driven processes (Heezen and Ewing, 1952; Wynn *et al.*, 2002; Shanmugam, 2016), which essentially consist on the downslope movement of the finest sediments through quite long distances (Masson *et al*., 2006). Like debris flows they tend to travel higher distances than slides (Bouma and Hollister, 1973), forming turbidites, the most abundant type of deep-sea deposit (Piper *et al.*, 2012), which are generally present in the distal parts of the unstable areas (Piper and Normark 2009). These are very common features, for example, in delta fans, but also on continental slopes (Alonso and Ercilla, 2003), volcanic islands, in submarine canyons (Laberg and Vorren, 1995) forming submarine fans and channel-levee systems (Hanquiez *et al.*, 2010) and in abyssal plains (Lebreiro *et al.*, 1997).

2.2.4 – TRIGERRING AND PRE-CONDITIONING FACTORS

Several factors control the development of submarine landslides, as well as their dimension and distribution (Piper *et al.*, 2012). Like for subaerial landslides, submarine landsliding activity may have both natural and anthropogenic triggering factors (Laberg and Camerlenghi, 2008), although natural triggers may be quite different from those observed onshore. Human activity is very limited and very unlikely to trigger submarine landslides (Masson *et al.*, 2006), although it may be present on shoreline, contributing to increase the consequences of landslides or even to trigger them, as it happened in Nice (Seed *et al.*, 1988) or in Norway (Merle *et al.*, 2006). In this sense, natural causes are the main triggering factors for submarine slope disruption and those may act both by decreasing the shear strength and by increasing shear stress, e.g., (Laberg and Camerlenghi, 2008).

Seismicity is perhaps the most important triggering factor of submarine slope instability generating horizontal and vertical accelerations (Lee and Edwards, 1986; Hampton *et al.*, 1996), especially in tectonically active areas as the Italian margins (Chiocci and Casalbore, 2017; Casalbore *et al.*, 2019), in the Gulf of Cadiz (Lee and Baraza, 1999; García *et al.*, 2020), in Southern Africa (Dingle, 1977), or in the western coast of North America

(McAdoo *et al.*, 2000). This is a transient factor that exerts intermittent additional pore-pressure to the slopes. Gas-charging, gas hydrate dissociation as well as low tides and seepage may also generate excess pore-pressure and thus play an important role on triggering slope instability (Sultan *et al.*, 2004). For example, submarine volcanic activity (Gross *et al.*, 2014) is held as an important landslide triggering mechanism as it is also salt diapirism (Tripsanas *et al.*, 2004) or glacial loading and eustatic changing (Mosher *et al.*, 2004). The occurrence of earthquakes – seismic loading, the tidal changes, and the presence of gas act more as strength reducers, while wave loading acts more as an increment of shear stress (Hampton *et al.*, 1996).

Slope gradient may be also considered as triggering factor (Piper *et al.*, 2012; Talling, 2014). Over-steepening has been worldwide recognized as being crucial for submarine slope instability, for example in the Grand banks (Piper *et al.*, 1999b; Piper *et al.*, 2012), in the Scotian slopes (Mosher *et al.*, 1994; 2004; 2017) in the Mediterranean (Casas *et al.*, 2015; Ercilla *et al.*, 2016), in the Tyrrhenian sea (Miramontes *et al.*, 2018) and in the Southwest Portuguese Margin (Teixeira *et al.*, 2019). Furthermore, over-steepening is also a key pre-conditioning factor, being perhaps the most evident static factor controlling submarine slope instability. Its control is due to gravity's action (Mulder and Cochonat, 1996) exerting influence over sediment weight, (Prior and Coleman, 1984; Montgomery and Dietrich, 1994), triggering slope instability. Notwithstanding this, there are other important pre-conditioning factors affecting submarine slope stability, especially on smooth slopes. Henrich *et al.* (2008) present the case of the Mauritania Slide Complex in which sliding activity occurred at slope gradients lower than 1º; Kvalstad *et al.* (2005a) also refer to sliding on extremely low sloping areas. Prior and Coleman (1978) refer the existence of landslides on slopes as steep as 0.01º, on the Mississippi River Delta. Notwithstanding this, in this last case it is important to bear in mind that in deltas there is a contrast and consequently a mixture of fresh water with salty water. Furthermore, there is a confluence between the river and the oceanic currents. These two factors certainly promote the formation of pycnoclines with contrasting temperature and salinity, in the contact between water and the top of the sediment column, contributing for slope instability. Moreover, the high sedimentation rates and the structure of the prograding deposits also contribute to the existence of landslides on deltas, as they generate excess pore water pressures inducing slope failure (Turmel *et al.*, 2016). According to Hampton *et al.* (1996) and bibliography therein, and according to the aforementioned ideas it is demonstrated

that except in steep slopes the force of gravity, *per se*, may be not enough to be the only cause of failure on continental margin slopes.

Rapid sedimentation and consequent generation of thick sedimentary deposits is another conditioning factor of slope instability (Hampton *et al.*, 1996), that contribute for the consequent low-consolidation of sediments and for high water content (Laberg and Camerlenghi, 2008). This is the case of clay-rich sedimentary deposits that have high water contents and plasticity (Kvalstad *et al.*, 2005a; Masson *et al.*, 2006), being more sensitive and weaker, losing strength more rapidly and thus being more susceptible to instability (Laberg and Camerlenghi, 2008). The susceptibility to slope instability may be increased when these sediments accumulate in preceding slide scars, as it happens in the Norwegian margin (Bryn *et al.*, 2005a).

High pore-pressure is known to be a fundamental pre-conditioning factor for subaqueous and submarine slope instability (Iverson, 1997). It is mainly caused by gravity-, seismic-, and storm wave-loading (Hampton *et al.*, 1996; Sultan *et al.*, 2004; Laberg and Camerlenghi, 2008). Pore-pressure is determinant when associated with weak layers (Hampton *et al.*, 1996; Locat, 2001; Bryn *et al.*, 2005a; Kvalstad *et al.*, 2005a; Locat *et al.*, 2014). Weak layers correspond to sediment or rock layers with lower strength than the adjacent units sufficiently enough to develop a surface of rupture (Locat *et al.*, 2014). Those generally correspond to clay-rich horizons with high pore-pressure that mainly result from normal depositional processes and from transient processes such as earthquake shaking, e.g., (Prior and Coleman, 1984; Hampton *et al.*, 1996; Masson *et al.*, 2006), as well as storm wave loading, although historical evidence suggests that some of the largest submarine landslides were essentially triggered by earthquakes (Masson *et al.*, 2006).

For Kawamura *et al.* (2009) pore fluid pressure is the main cause for slope disruption. However, the influence of pore-pressure is, for sure, different according to the different types of sediment, being necessary to predict and to test it. According to some authors (Kvalstad *et al.*, 2005a; Urlaub *et al.*, 2013) this demands information about sediments' compressibility and permeability and the way these parameters change with increasing overburden stress and compaction. According to Urlaub *et al.* (2013), compaction is also a crucial element leading to instability especially in low steep areas (<2º), by the control it exerts on destructuring the inner sediment structure and increasing pore-pressure.

According to Hampton *et al.* (1978), the time interval between accumulation and consolidation gives rise to pore-pressure increase, allowing the sediment to be prone to slide, which is more evident where there are high sedimentation rates. When these conditions are met there is propensity for submarine slope instability (Morgenstern, 1967; Hampton *et al.*, 1978).

2.2.5 – WORLDWIDE DISTRIBUTION AND TYPOLOGY OF SUBMARINE MASS-TRANSPORT DEPOSITS

Mass-movements are global phenomena, whose activity is recorded in distinct regions and environments (Hampton *et al.*, 1996; Laberg and Vorren, 2000; Kvalstad *et al.*, 2005a; Mosher *et al.*, 2010). The resulting mass-transport deposits comprise variable morphologies and morphometry (Moscardelli and Wood, 2015), according to the process and the geomorphologic setting where these events occur.

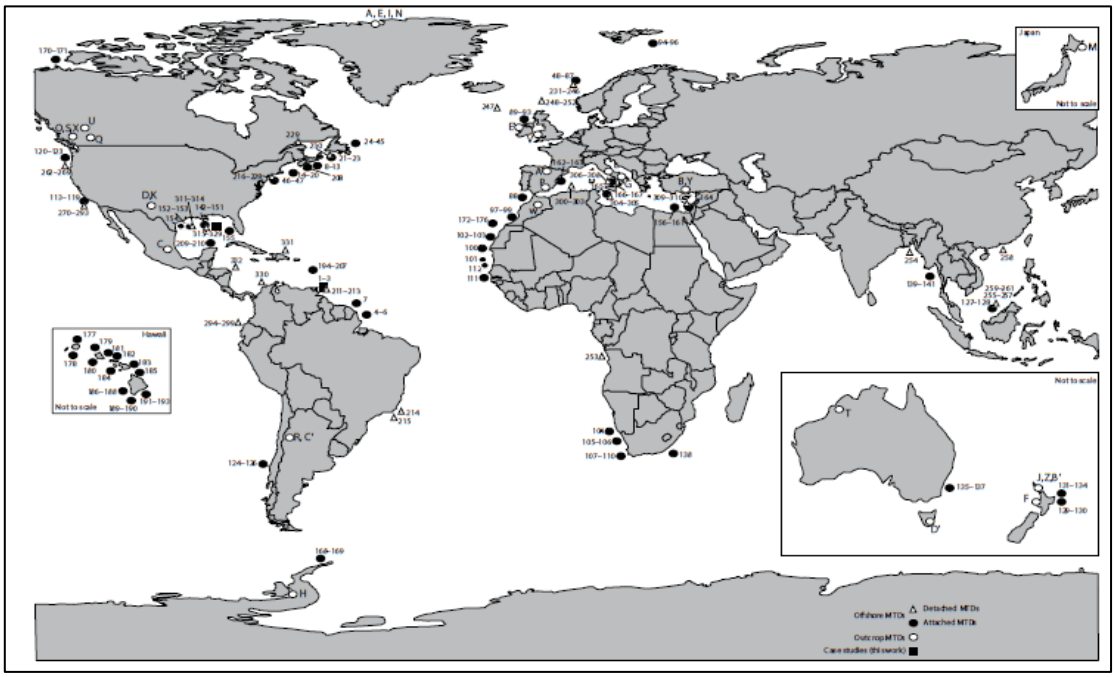

FIGURE 2.17 – Location of the worldwide most prominent mass-transport deposits (MTD) – from Moscardelli and Wood (2015). Black dots indicate the location of attached MTDs (offshore), white triangles the location of detached MTDs (offshore), white dots MTD outcrop localities, and squares areas where data was collected by the authors.

Two main types of MTDs are recognized – attached and detached MTDs (Moscardelli and Wood, 2015) – Figure 2.17. Attached MTDs sit close to the shelf and upper-slope depositional systems, being sourced from those areas (Moscardelli and Wood, 2015). These are bigger, reaching areas from 100 km^2 up to 120 000 km^2 and volumes between 1 km^3 and

>20 000 km^3. Detached MTD sit distally from the shelf break and are fed by several sources, being generally smaller, ranging between 0.3 and 100 km^2 and not exceeding 10 km^3 in volume (Moscardelli and Wood, 2015). These correspond to localized gravitational instabilities, being controlled by over-steepening or diapirism, whereas attached MTDs are controlled by extra-basin processes as tectonism and earthquakes, and volcanism. While the West African coast mainly presents attached MTDs (Wynn *et al.*, 2000; Henrich *et al.*, 2008), both the European and the American coasts show an hybrid concentration (Figure 2.17) of both detached-, like the Bjornoya Fan slide (Hjelstuen *et al.*, 2007), and attached MTDs as the Storegga slide, which comprises both detached and attached deposits (Haflidason *et al.*, 2005).

2.3 – CONTOURITES

Contourites are *sediments deposited or substantially reworked by the persistent action of bottom currents* (Stow *et al.*, 2002; Rebesco, 2005; Rebesco *et al.*, 2014), usually presenting poorly-sorted and muddy-rich facies with high levels of bioturbation and intercalations of thin horizons of fine-grained sand and silt in a rhythmic bedding deposition (Stow *et al.*, 2002; Rebesco *et al.*, 2014). Although dominantly composed of contourite sediments by the action of contour currents, contourite drifts may either be intercalated with turbidites and debris-flow deposits or even with deep-water facies, like hemipelagites, pelagites and glaciomarine sediments (Faugères and Stow, 2008).

Contourite deposits (Figure 2.18) are essentially affected and moulded by the persistent action of along-slope bottom currents (Stow *et al.*, 2002; Faugères and Stow, 2008; Hernández-Molina *et al.*, 2011; Rebesco *et al.*, 2014), whose dynamics is condition *sine qua non* for generating contourites. Bottom currents-derived deposition is one of the three main deep-sea sedimentary processes, in which are also included pelagic settling that generates pelagites, on very calm and deep environments, and density currents that origin turbidites (Rebesco *et al.*, 2014) – Figure 2.18.

According to these authors, contourite meaning has suffered some changes, since the term *contourite* (Heezen and Hollister, 1964; Heezen *et al.*, 1966) originally refers to deep-sea basin deposits generated by thermohaline circulation, having evolved to multi-facetted deposits (Faugères *et al.*, 1999). Nowadays, these deposits are ascribed to different current

types and can be found in deep ocean (Llave *et al.*, 2007; Hernández-Molina *et al.*, 2008b), on continental slopes (Hernández-Molina *et al.*, 2011), in shallow margins (Rebesco *et al.*, 2014) and in lakes (Ceramicola *et al.*, 2001).

Contourites research has long been being addressed by several authors (Heezen *et al.*, 1966; Faugères *et al.*, 1984; 1993; Rebesco *et al.*, 2014; Shanmugam, 2017), although the study of contourites as deep-sea forms generated by bottom currents has started in the end of the 1950s by Heezen (1959) and especially by Heezen and Hollister (1964). Nevertheless, other scientific contributions (Hollister, 1967; Hollister and Heezen, 1972; Bouma and Hollister, 1973; Stow and Lovell, 1979; Faugères *et al.*, 1984; Hollister and McCave, 1984) constitute reference works on the early stage of this scientific domain. Over the time, research on this subject has suffered some technical evolution and according to Shanmugam (2016), up

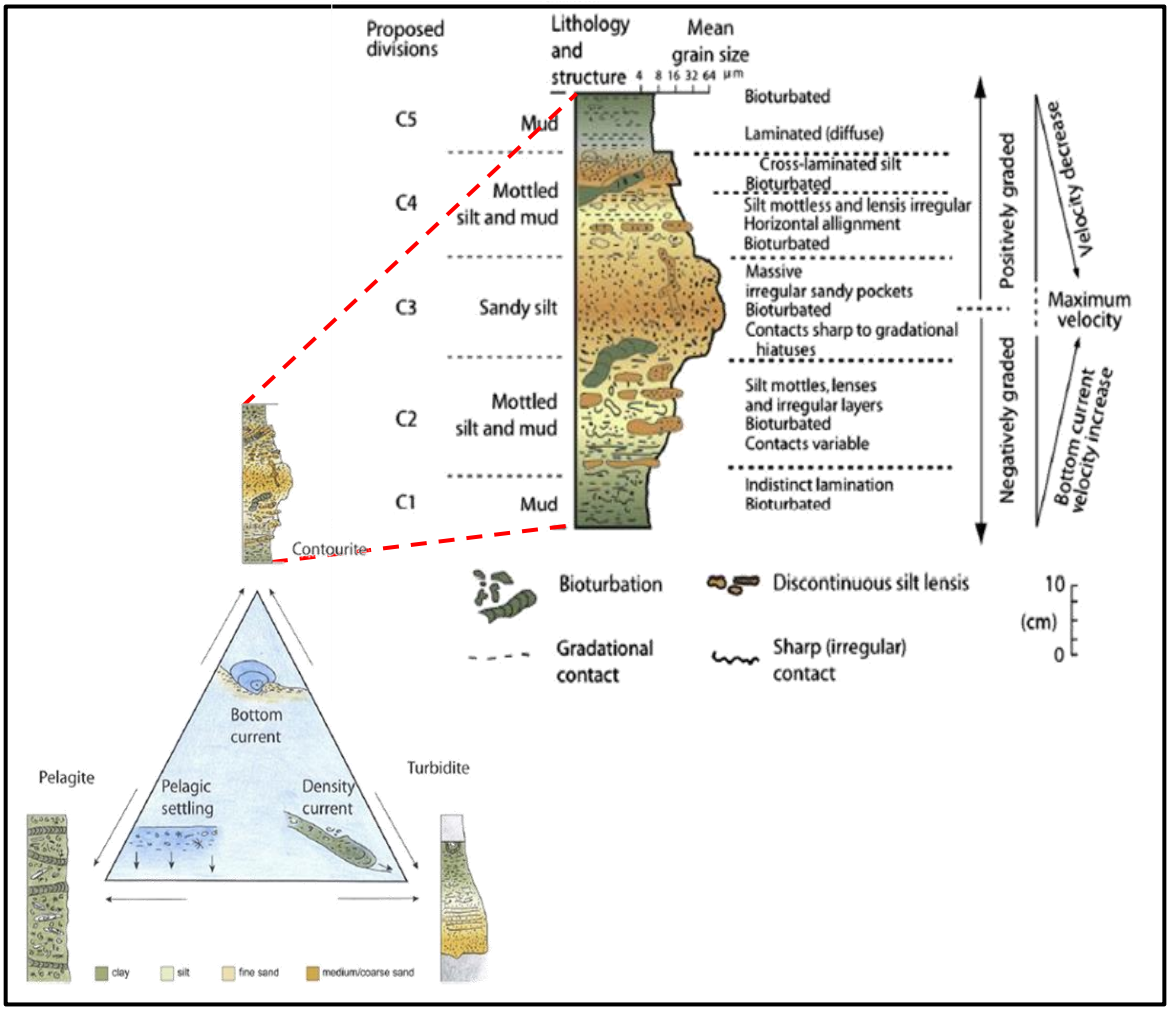

FIGURE 2.18 - Conceptual diagrams of the three main types of sedimentary processes occurring in the deep sea (within the triangle) and the facies model of the respective depositional products (from Rebesco *et al.*, 2014). standard facies model of contourite sequence, linked to variation in contour-current velocity. from Stow and Faugères (2008), based on the original figure from Gonthier *et al.* (1984). Adapted from Rebesco *et al.*, 2014.

to now, most of what is known about recent contourites is essentially based on features identified both on bathymetric and seismic data as well as on some core and drill data, thus encompassing different scales.

More recently, there have been new contributions focused on the main types of contourites and their spatial distribution (Faugères *et al.*, 1999; Rebesco and Stow, 2001; Faugères and Stow, 2008; Faugères and Mulder, 2011). Since the 1980s, there has been a great increment of works focused on contourite drifts evolution both in the Northern Atlantic (McCave and Tucholke, 1986; Laberg *et al.*, 2001; Pudsey and Howe, 2002), in the Eastern Atlantic (Van Rooij *et al.*, 2007; 2010; Liu *et al.*, 2019; 2020), in the Mediterranean and southwest Portugal margin (Llave *et al.*, 2001; Hernández-Molina *et al.*, 2003; 2006; Llave *et al.*, 2006; 2007; 2008a; Hernández-Molina *et al.*, 2008b; 2011; Llave *et al.*, 2011; Roque *et al.*, 2012; Hernández-Molina *et al.*, 2013; 2014b) as in Southern Atlantic, in Brazilian (Faugères *et al.*, 1998; Viana *et al.*, 1998a), Argentinean (Hernández-Molina *et al.*, 2009; Preu *et al.*, 2013) and Uruguayan coasts (Hernández-Molina *et al.*, 2016b). During the last decade, other works have come in, focusing on the contourites' terminology and morphology and on economic aspects related with contourites research (Viana and Rebesco, 2007; Shanmugam, 2008; Rebesco *et al.*, 2014). Notwithstanding this, during the last decades some issues have arisen involving contourites terminology (Shanmugam, 2017). The absence of sedimentological criteria for the classification of the contourite drifts is in the origin of the concept misunderstandings, as contourites can be generated by both wind-driven and thermohaline-driven bottom currents. So, Shanmugam (2017) proposes a replacement of the term "*contourite drift*" by "*sediment drift*". In this sense, a long path is on the way concerning contourites' terminology.

The study of contourites has been essential for three scientific domains (Rebesco *et al.*, 2014): palaeoclimatology and palaeoceanography (Rebesco, 2005; Rebesco *et al.*, 2007); hydrocarbon exploration (Shanmugam, 2006; 2012; Stow *et al.*, 2013), and slope stability and geological hazard assessment (Laberg and Vorren, 2000; Laberg *et al.*, 2001; 2002; Mulder *et al.*, 2003; Laberg and Vorren, 2004; Sultan *et al.*, 2004; Bryn *et al.*, 2005b; Evans *et al.*, 2005; Kvalstad *et al.*, 2005b; Laberg *et al.*, 2005; Rebesco, 2005; Laberg and Camerlenghi, 2008; Miramontes *et al.*, 2018).

2.3.1 – WORLDWIDE GEOGRAPHICAL DISTRIBUTION OF CONTOURITE DEPOSITS

Contourite drifts are natural features that differ morphologically according to the local seafloor morphology and bottom current activity. These sedimentary features are mainly associated with deep water masses like North Atlantic Deep Water (NADW) and the Antarctic Bottom Water (AABW) (Rebesco *et al.*, 2014) and the main differences can be seen in the North and South Atlantic Ocean basins - Figure 2.19 - where they are mostly found on (McCave and Tucholke, 1986; Viana *et al.*, 1998a; Pudsey and Howe, 2002). Most of the large contourite deposits and erosional features are found in the western side of those oceanic basins – Figure 2.19.

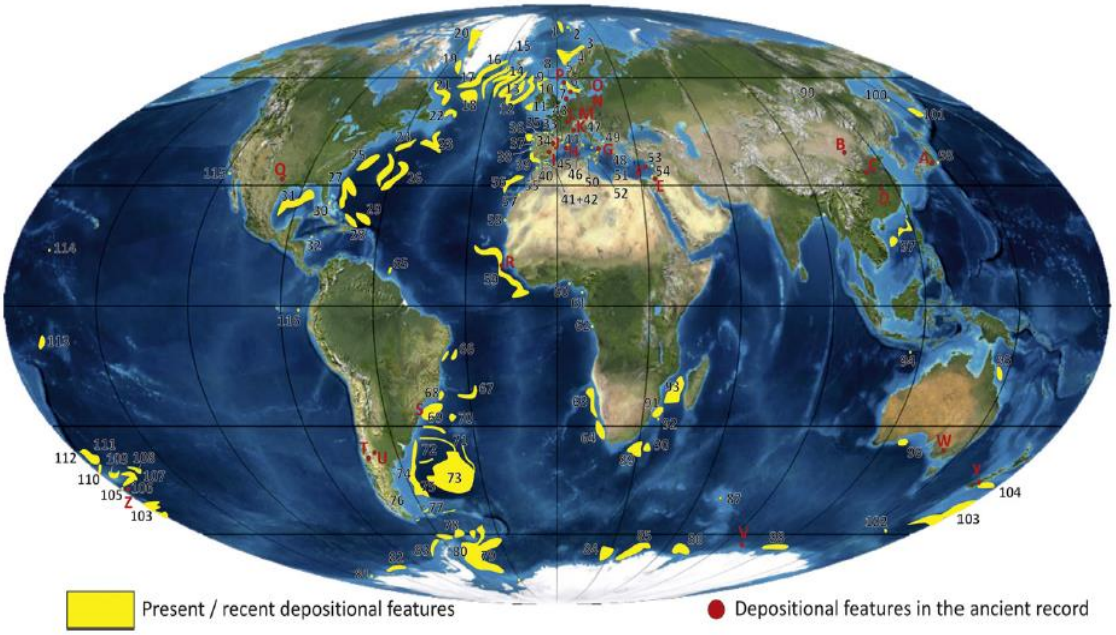

FIGURE 2.19 - Occurrence of large contourite deposits in the present (recent) ocean basins (yellow areas) and in the ancient sedimentary record (red dots) – from Rebesco *et al.*, 2014.

There are great differences between the types of drifts occurring in the North (Hollister and Heezen, 1972; Knutz *et al.*, 2002) and South Atlantic Ocean basins (Viana *et al.*, 1998b; Rebesco *et al.*, 2007), where giant marginal elongate drifts and contourite sheets and channel-related drifts are respectively predominant (Faugères *et al.*, 1993). In the North Atlantic, the Gulf of Cadiz is an example of the exhaustive study of contourites, being one of the most well studied areas in the world, where the first contourite facies model appeared (Faugères *et al.*, 1984; Gonthier *et al.*, 1984; Hernández-Molina *et al.*, 2013; 2014b; 2016a).

2.3.2 – CONTOURITE MORPHOLOGIES

Contourite bodies are mostly generated by the strong along-slope action of density-driven currents (Figure 2.20), involving large amounts of suspended sediments. These currents act as sediment conveyors, eroding when and where the current velocity is high and depositing suspended load when velocity decreases to a point that suspended material can settle down (Llave *et al.*, 2007; Hernández-Molina *et al.*, 2009).

The construction of these morphological features greatly depends on the regional geomorphology, as well as on the current's dynamics. From this it will result the formation of both large and small bedforms. The larger ones are known as drifts, being identifiable through seismic reflection data (Nielsen *et al.*, 2008), and may have many different associated types. Rebesco *et al.* (2014) point out that contourite drifts are better recognized when they have along-slope, elongated mounded shape and an adjacent moat (Figure 2.20).

According to Rebesco *et al.* (2014) – Figure 2.20A, contourite drifts may have several morphologies. The largest ones can be roughly classified as separated or detached: i) *Separated drifts* are elongated mounded drifts that essentially develop near steep slopes, being separated from these by a moat (Faugères and Stow, 2008; Hernández-Molina *et al.*, 2008a; Van Rooij *et al.*, 2010), a slope-parallel channel originated by non-deposition and localised erosion beneath the core of the bottom current, due to the Coriolis force (Rebesco *et al.*, 2014); ii) *Detached drifts* are isolated elongated-mounded drifts that become independent

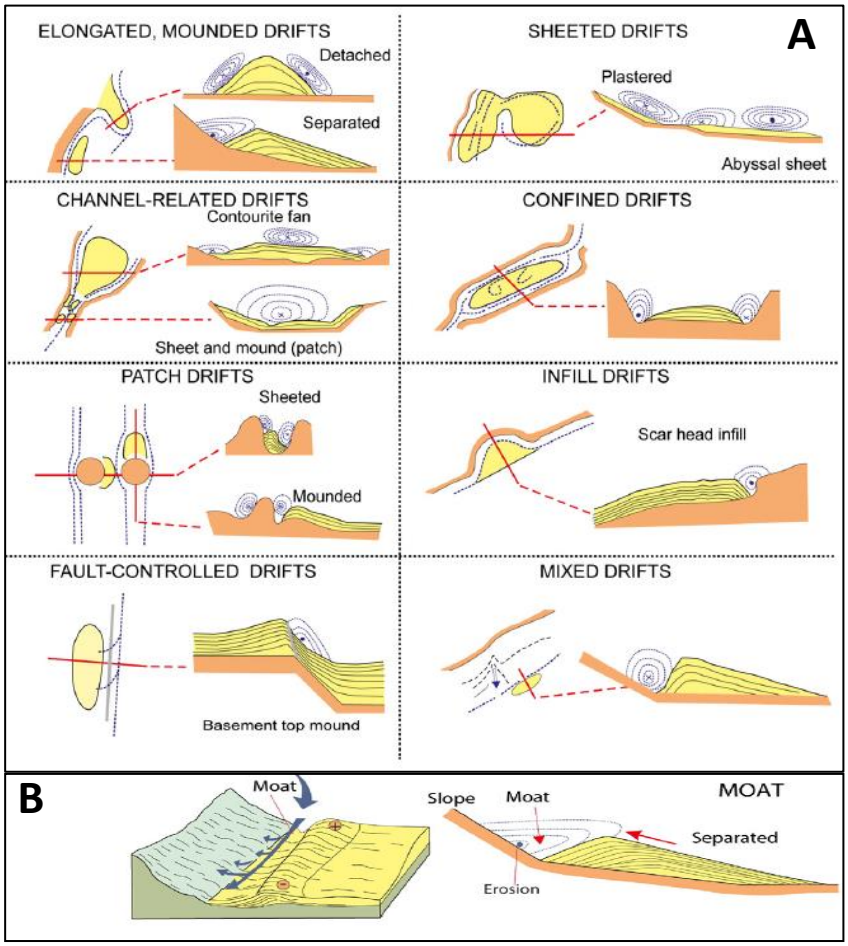

FIGURE 2.20 – Contourite drift morphologies. (A) - Sediment drift types and inferred bottom-current paths. (B) - Main characteristics of areal and linear, large-scale contourite erosional features. From Rebesco *et al.* 2014.

from the former slope, against which they form through a moat (Hunter *et al.*, 2007); iii) *Sheeted drifts* are typical in abyssal plains having a slight mounded geometry and uniform thickness that tends to thin towards the margins. These drifts exist in the Gulf of Cadiz and are described in Llave *et al.* (2007) and in Hernández-Molina *et al.* (2008b); iv) *Confined drifts* are mounded drifts having two moats, one at each side. These were identified, for example, by Ceramicola *et al.* (2001) in Lake Baikal (Russia); v) *Channel-related drifts* develop in gateways where flow velocities are high and currents forced (Maldonado *et al.*, 2005); vi) *Plastered drifts* are frequently smaller elongated-mounded features, normally found in shallower positions than sheeted drifts (Preu *et al.*, 2013; Rebesco *et al.*, 2013). Deposition occurs on one side or both, together with lateral migration of the drift axis (Faugères and Stow, 2008); vii) *Patched drifts* correspond to small and somewhat irregular drifts that form due to the interaction of bottom currents and irregular seafloor morphology (Hernández-Molina *et al.*, 2006); viii) *Infill drifts* (Laberg *et al.*, 2001) develop at the head of instability scars, have gentle reliefs and a slight mounded shape, which fills the depression opened by the instability. This kind of deposits was found in the Storegga area, accumulating at depths between 600 m and 1200 m (Bryn *et al.*, 2005b); ix) *Fault-controlled drifts* have the influence of faulting and; x) *mixed drifts* combine depositional processes with along-slope processes.

2.3.3 – SEDIMENTOLOGICAL TYPES OF CONTOURITE DEPOSITS

There are essentially two main types of contourite deposits: muddy and sandy contourites (Rebesco *et al.*, 2014; Shanmugam, 2017). Their composition varies essentially according to whether they formed, for example, in the mid-ocean where they present > 90% pelagic biogenic material, or at high latitudes, where > 90% of their composition is hemipelagic material (Rebesco *et al.*, 2014). For a better comprehension, Stow and Faugères (2008) present a compilation of several proposals of classification, according to which contourites may be classified in diverse groups: *clastic; volcaniclastic; shale-clast layers; calcareous, and chemiogenic contourites* (Rebesco *et al.*, 2014) - their figure 22.

Clastic contourites comprehend the following sub-types: (1) *Muddy Contourites* which have > 50% clay and < 15% of sand, high bioturbation and mottled appearance. These generally appear as homogeneous-thick, poorly-bedded features (Stow and Faugères, 2008); (2) *Silty contourites* that show similarities with muddy contourites constitute a transition between muddy and sandy contourites. Silt is the dominant grain size with about 40 to 60%,

having a mixed siliciclastic-biogenic composition (Stow and Faugères, 2008); (3) *Sandy contourites* range in thicknesses from a few centimetres to several meters (Rebesco *et al.*, 2014), sometimes serving as deep-water reservoirs for oil and gas (Stow and Lovell, 1979; Shanmugam, 2017); (4) *Bottom-current reworked sands* represent alternating events of traction and suspension deposition (Rebesco *et al.*, 2014) and have sand-mud rhythmites, double mud layers, cross-lamination, cross-bedding and internal erosion surfaces (Shanmugam, 2017) and lenticular and flaser bedding; (5) *Gravel contourites* are gravel-rich and result from the irregular spread of the seafloor erosion due to strong bottom currents, yielding irregular layers of poorly-to-very-poorly-sorted sandy gravel-lag (Rebesco *et al.*, 2014).

Volcaniclastic contourites consist of volcaniclastic material, being alike to clastic contourites. *Shale-clast layers*, which are millimetre-sized features mainly developed by strong currents action, in muddy and sandy contourites according to the current direction (Rebesco *et al.*, 2014).

Calcareous contourites may have also muddy, silty and sandy fractions. Rebesco *et al.* (2014) stress that calcareous contourites mainly occur on areas where biogenic input is dominant. (1) *Muddy* and *silty contourites* generally present poorly sorted facies and the main composition is pelagic-to-hemipelagic, including nannofossils and foraminifers. (2) *Calcareous sandy contourites* are equivalent of clastic sandy contourites (Rebesco *et al.*, 2014), but they are rich in foraminifers and bioclasts. (3) *Calcareous gravel-lag contourites* include microclasts derived from the erosion of the substrate being interpreted to be part of ancient contourite successions.

Siliceous bioclastic contourites can be muddy, silty and sandy being relatively rich in diatomaceous and radiolarian material (Rebesco *et al.*, 2014).

Chemiogenic contourites are mainly derived from seawater chemical precipitation and can be of manganiferous and chemiogenic gravel-lag type. *Manganiferous contourites* are rich in manganiferous and ferro-manganiferous horizons, which have very fine dispersed particles. Large quantities of these materials can form ferro-manganese nodules. *Chemiogenic gravel-lag contourites* occur when metal-carbonate chimneys, mounds and encrustations are available in the path of bottom currents.

2.3.4 – CONTOURITES AND SLOPE STABILITY

Contourites are sedimentary landslide-prone features (Laberg and Camerlenghi, 2008), whose distribution, composition and sediment properties constitute key elements for slope instability to occur (Bryn *et al.*, 2005b). The Storegga slide is perhaps the best and the most studied example of a submarine landslide formed in a contourite (Bugge *et al.*, 1988; Haflidason *et al.*, 2004; Bryn *et al.*, 2005a). It is known that contourites stability greatly depend on structural- and morphologic-related factors (Miramontes *et al.*, 2018). Amongst these are slope angle, -geometry and location but also others like high sedimentation rate; under-consolidation; high pore-pressure; seismic and storm loading; gas charging; well-sorted sediments and consequent high-water content (Laberg *et al.*, 2002; Kvalstad *et al.*, 2005a; Teixeira *et al.*, 2019). All these factors make contourites weak sedimentary bodies, as mentioned in subsection 2.2.4.

2.3.4.1 – CONTOURITES GEOTECHNICAL PROPERTIES

Slope instability depends mostly on sediment's geotechnical properties (Lee and Baraza, 1999). Contourites are sedimentary bodies with low shear strength, thus being landslide-prone features (Bryn *et al.*, 2005b; Miramontes *et al.*, 2018). Geotechnical analyses of marine sediments have been done in different areas with the purpose to analyse submarine slope instability. Lee and Baraza (1999) surveyed thirty-seven cores, in the Gulf of Cadiz, for textural, consolidation and shear strength analyses, using both static and cyclic triaxial tests in undrained conditions. Later on, in the Marquês de Pombal landslide, in the SW Portuguese margin, Minning *et al.* (2006) analysed the peak and residual shear strength of the sediments on the headwall, flow path and distal lobe through ring shear and falling cone penetrometer tests. In the Tyrrhenian sea, Miramontes *et al.* (2018) analysed the consolidation of contourite sediments and their undrained shear strength through vane shear tests. In the Gulf of Cadiz, Yenes *et al.* (2020) assessed the apparent over-consolidation of contouritic sediments through oedometer tests, using sediment samples recovered through box corer, and Yenes *et al.* (2021) analyse the link between contourite deposits and slope instability in the Alboran Sea, through the analysis of the geotechnical properties of the contourite drift sediments near the Guadiaro and Baños canyon walls.

2.4 – SLOPE (IN)-STABILITY

Slope instability is a mechanism of hillslope evolution by which material constituting a slope adjusts its surface angle and height to changes in the hydro-climatic, geomorphological and biotic conditions (Crozier, 1984).

The loss of stability mainly appears on active slopes by the action of natural landslides or by anthropic action, inducing changes, namely the base cutting of the natural hillslope (Selby, 1993). Instability is related to the inexistence or to the weak action of shear strength factors – Cohesion (C') and internal friction angle (ϕ). Slope stability may be determined by the Factor of Safety (FS), which corresponds to the capacity that a hillslope has to resist to gravitational stress and other external shear forces:

$$FS = \frac{Shear\ Strength}{Shear\ Stress}$$

When resisting forces or shear strength (S) equals driving forces - tangential or shear stress (τ), then FS = 1.0 and the hillslope is in its stability limit and slope disruption is imminent. When shear strength outweighs shear stress, then FS > 1.0 and the slope is likely to be stable. The higher the FS, the greater the stability of the hillslope, which is not absolute (Selby, 1993) but a probability that increases with the increase of the FS value. On the contrary, when FS < 1.0 the slope is unstable.

2.4.1 – SLOPE STABILITY ANALYSIS

Slope stability analysis aims at quantitatively determine the susceptibility of an area for slope instability, which corresponds to the moment when downslope driving forces (shear stress) exceed the resisting forces (shear strength) of the slope-forming material (Selby, 1993; Hampton *et al.*, 1996; Masson *et al.*, 2006; Ai *et al.*, 2014), which has been extensively strained, and the resulting strength is smaller than the downslope gravitational stress (Hampton *et al.*, 1996). During the ’50, ’60 and ’70 decades of the last century, some methods were used for slope stability analysis (Fredlund and Krahn, 1977), as it is the case of Fellenius Method; Simplified Bishop Method; Spencer’s Method; Janbu’s Simplified Method; Janbu’s Rigorous Method; Morgenstern-Price Method and General Limit Equilibrium (GLE). These methods are generally based on the slices’ method, which is well suited for deep landslides. Slope stability can also be analysed using the bi-dimensional Infinite Slope Stability Method,

e.g., (Morgenstern and Price, 1965; Selby, 1993), which is more suitable for the analysis of translational landslides.

2.4.1.1 – GENERAL LIMIT EQUILIBRIUM (GLE)

The analysis of slope stability is usually done through the determination of the Factor of Safety (FS), both for static and for transient conditions. For this purpose it can be used the General Limit Equilibrium (GLE) formulation (Fredlund and Krahn, 1977), which is based on the Mohr-Coulomb assumptions assuming that the cohesive and frictional components of strength are equal for all the soils and FS is assumed to be the same for all the sediments' slices, e.g., (Urgeles *et al.*, 2006). GLE satisfies force (equation 2.1) and moment equilibrium (equation 2.2), respectively through the following equations:

EQUATION 2.1

$$FS_f = \frac{\sum(c'l\cos\beta + (N - ul)\tan\phi'\cos\beta)}{\sum N\ \sin\beta + \sum k\,W}$$

EQUATION 2.2

$$FS_m = \frac{\sum(c'lR\ \cos\beta + (N - ul)R\ \tan\phi')}{\sum Wx + \sum Nf + \sum k\,We}$$

Where *c'* is the effective cohesion intercept; β is the angle between the tangent to of the base of each slice and the horizontal; *u* is the pore-water pressure; ϕ' is the effective angle of shear resistance; *k* is the pseudo-static coefficient (measured as a fraction of *g*, the acceleration due to gravity); *W* is the total weight of a slice of width (*l*) and height (*h*); *R* is the radius for a circular slip surface; *f* is the perpendicular offset of the normal force from the centre of rotation; *x* is the horizontal distance from the centreline of each slice to the centre of rotation; *e* is the vertical distance from the centroid of each slice to the centre of rotation; *N* is the total normal force (equation 2.3) on the base of the slice.

EQUATION 2.3

$$N = \frac{W + (X_R - X_L - \frac{c'\beta\sin\alpha + u\beta\sin\alpha\tan\phi\prime}{F}}{\cos\alpha + \frac{\sin\alpha\tan\phi\prime}{F}}$$

Where *X* is the interslice shear force:

EQUATION 2.4

$$X = E\lambda\, f(x)$$

f(*x*) is a function, λ is the percentage (in decimal form) of the function used, and *E* is the interslice normal force.

2.4.1.2 – INFINITE-SLOPE MODEL

Slope stability analysis is also assessed using the Infinite Slope Stability Method (Morgenstern and Price, 1965; Selby, 1993), which is more suitable for the analysis of translational landslides. This model is based on the assumptions that a failure plane is parallel to the surface of the sliding sediment (Figure 2.21) and that the edge effects, where this assumption is not valid, are insignificant (Selby, 1993).

The determination of FS applied to translational shallow landslides is, generally, analysed by the Infinite Slope method (Selby, 1993). In this method the gravitational stress (g) acts vertically along the shear plane (Selby, 1993; Blasio, 2011), while normal stress (σ) acts perpendicular to that plane, having the opposition of the subsurface pore-pressure. Shear stress acts along the shear plane and has the opposition of resisting stresses. As it can be seen in Figure 2.21, gravitational stress, shear stress and pore-pressure - (marked with *) contribute to the instability of the slope materials, whereas normal stress contributes to the slope stability, besides the direct opposition of hydrostatic pressure or pore water pressure (u).

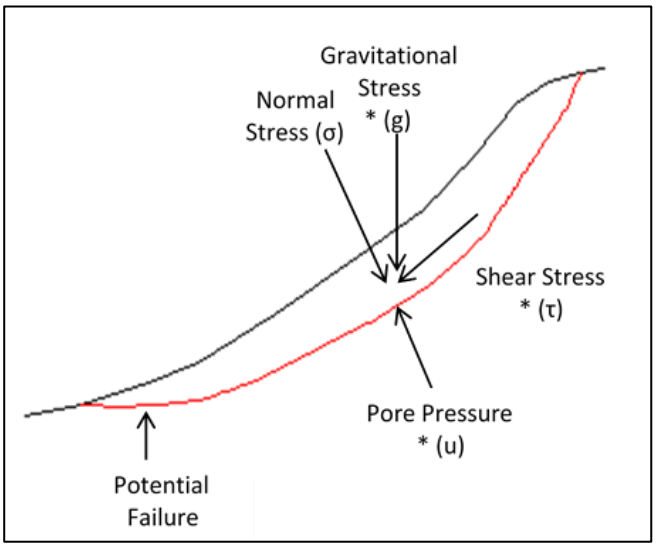

FIGURE 2.21 –Stresses acting on the potential sliding surface. Adapted from Selby (1993).

This model, originally created by Coulomb, in 1773, assumes that a section of the slope is homogeneous, with uniform mass and thickness, being representative of the slope as a whole, and ignoring irregularities both on its top and bottom. Sediment properties as well as water content are considered to be constant at any depth below the ground surface (Graham, 1984).

Concerning this, Mohr-Coulomb's equation (Equation 2.5) mathematically reproduces shear strength (S) on a hillslope as function of effective normal stress (σ - u), sediment cohesion (C') and the tangent of internal friction angle (ϕ').

EQUATION 2.5

$$S = C + (\sigma - u)tan\phi$$

On the failure plane σ will be $\gamma z \cos\beta^2$:

EQUATION 2.6

$$S = C' + (\gamma z cos^2\beta - u)tan\phi'$$

Pore-pressure (u) promotes normal stress reduction as well as sediment cohesion loss, especially when it is saturated.

Shear stress (τ) corresponds to the unit weight (γ) of the soil column (z) (mass x gravitational stress) multiplied by cosβ and sinβ.

EQUATION 2.7

$$\tau = \gamma g z . cos\beta . sin\beta$$

The stresses acting on a hillslope (Figure 2.21) are expressed by the Factor of Safety (Selby, 1993) – Equation 2.8:

EQUATION 2.8

$$FS = \frac{C' + (\gamma z cos\beta^2 - u)tan\phi'}{\gamma z cos\beta sin\beta}$$

As expressed on Figure 2.22, the product of mass (m) and gravitational stress (g) is the soil weight (w) which acts in two opposing ways: i) parallel to the failure plane (shear stress), promoting movement along that plane, causing rupture; ii) normal to the failure plane (shear strength), promoting an increase of friction between the failure plane and the overlying unstable soil (Selby, 1993), assuring stability to the hillslope. Soil thickness is a key parameter for determining the Factor of Safety. Once it is not

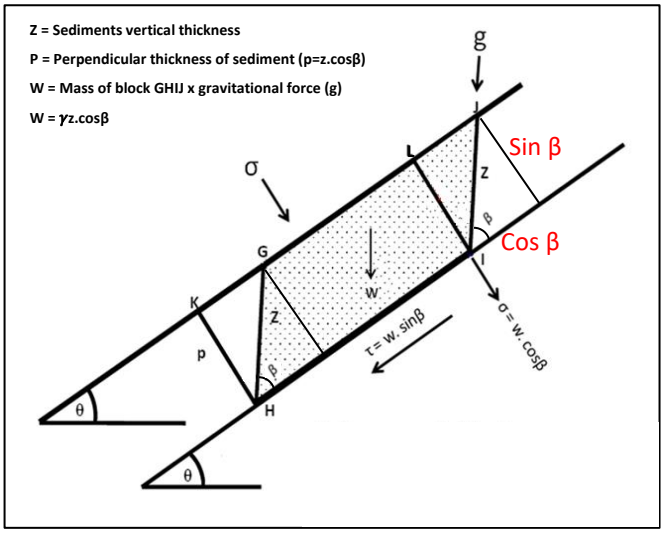

FIGURE 2.22 –Shear stress and strength acting on a slope. Modified from Selby (1993).

possible to assess it perpendicularly – KHIL block – it shall be calculated vertically to the failure plane in function of the soil thickness – z - in order to perform the GHIJ block.

Assuming that in submarine media sediments are water saturated, pore-pressure is one of the main causes for submarine sediment disruption (Hampton *et al.*, 1978; Kawamura *et al.*, 2009) as it reduces normal stress, infinite slope analysis may be addressed by deriving the pore-pressure, according to the Equation 2.9, assuming F = 1, as stated in Prior and Coleman (1984):

EQUATION 2.9

$$u = \frac{c' - F\ (\gamma' z\ sin\beta\ cos\beta) + \gamma' z\ cos^2\ \beta}{\tan \phi'}$$

Morgenstern and Price (1965) proposed the pseudo-static Factor of Safety (FoS), a 1D undrained model, for the ratio F = S/τ, during earthquake shaking (Stegmann *et al.*, 2016) – Equation 2.10 - where seismic-induced shear stresses are assumed to be constant during the period of shaking (Hampton *et al.*, 1996; Stegmann *et al.*, 2016).

EQUATION 2.10

$$FoS = \frac{S_u}{\sigma'_{vO}\left(\sin(\alpha)\cos(\alpha) + k\ \left(\frac{\gamma}{\gamma'}\right)\ cos^2(\alpha)\right)}$$

Where S_u is the resisting force, α is the slope angle, γ′ the effective unit weight, σ'_{vO} is the effective vertical stress, and *k* is the seismic coefficient.

According to Lee and Edwards (1986), most of the works studying the submarine slope instability have used the infinite-slope simplification for stability analysis, because the observed failures were so large in area that the infinite-slope assumptions are nearly met and parameters and dimensions are not known well enough to justify greater sophistication.

3 – GENERAL SETTING OF THE STUDY AREA

The study area is the Alentejo Margin in the Southwest Portuguese Continental Margin, as part of the broader West Iberia Margin (WIM), close to the Southwest Iberia Margin (SWIM). It is located in the transition between the Gulf of Cadiz and the Tagus Abyssal Plain. Bathymetrically, the study area spans from > 200 to < 3800 meters water depth (mwd) – Figures 3.1A and 3.1B. This area is near the tectonic boundary (Figure 3.1D) between the Africa (Nubia) and the Eurasia plates (Terrinha *et al.*, 2009; Zitellini *et al.*, 2009; Duarte *et al.*, 2011; Rosas *et al.*, 2012; Terrinha *et al.*, 2019c), presenting a slow convergence rate of ~4mm/year (Argus *et al.*, 1989). That boundary extends from the Northern Africa (Buforn *et al.*, 1995), until the Azores (Jiménez-Munt *et al.*, 2001). This margin presents one of the most complex geologic and tectonic structures (Sartori *et al.*, 1994) of the North Atlantic margins, due to the combination of several phases of extension, convergence and strike-slip motions (Maldonado *et al.*, 1999).

3.1 – GEOLOGIC EVOLUTION OF THE (SOUTH)WEST IBERIA MARGIN

During the last ~200 Ma, the WIM went through diverse tectonic phases, which determined the present-day configuration of its margins (Alves *et al.*, 2003). The WIM has been affected by three distinct and sequential tectonic events either extensional or compressional (Maldonado *et al.*, 1999), from the Late Triassic (Pinheiro *et al.*, 1996; Barrier and Vrielynck, 2008) up to the Quaternary (Alves *et al.*, 2009b; Terrinha *et al.*, 2019c), becoming a complex area, mainly constrained by the relative motion of the Eurasia-Nubia-America tectonic plates (Sartori *et al.*, 1994). The WIM started to form in the early phase of the northwards propagating continental rifting between Iberia and the Grand Banks of Newfoundland, from the Triassic throughout the Early Cretaceous (Whitmarsh and Sawyer, 1996; Maldonado *et al.*, 1999), leading to the opening of the North Atlantic Ocean (Mougenot, 1989; Alves *et al.*, 2003; Terrinha *et al.*, 2003; Pereira and Alves, 2011).

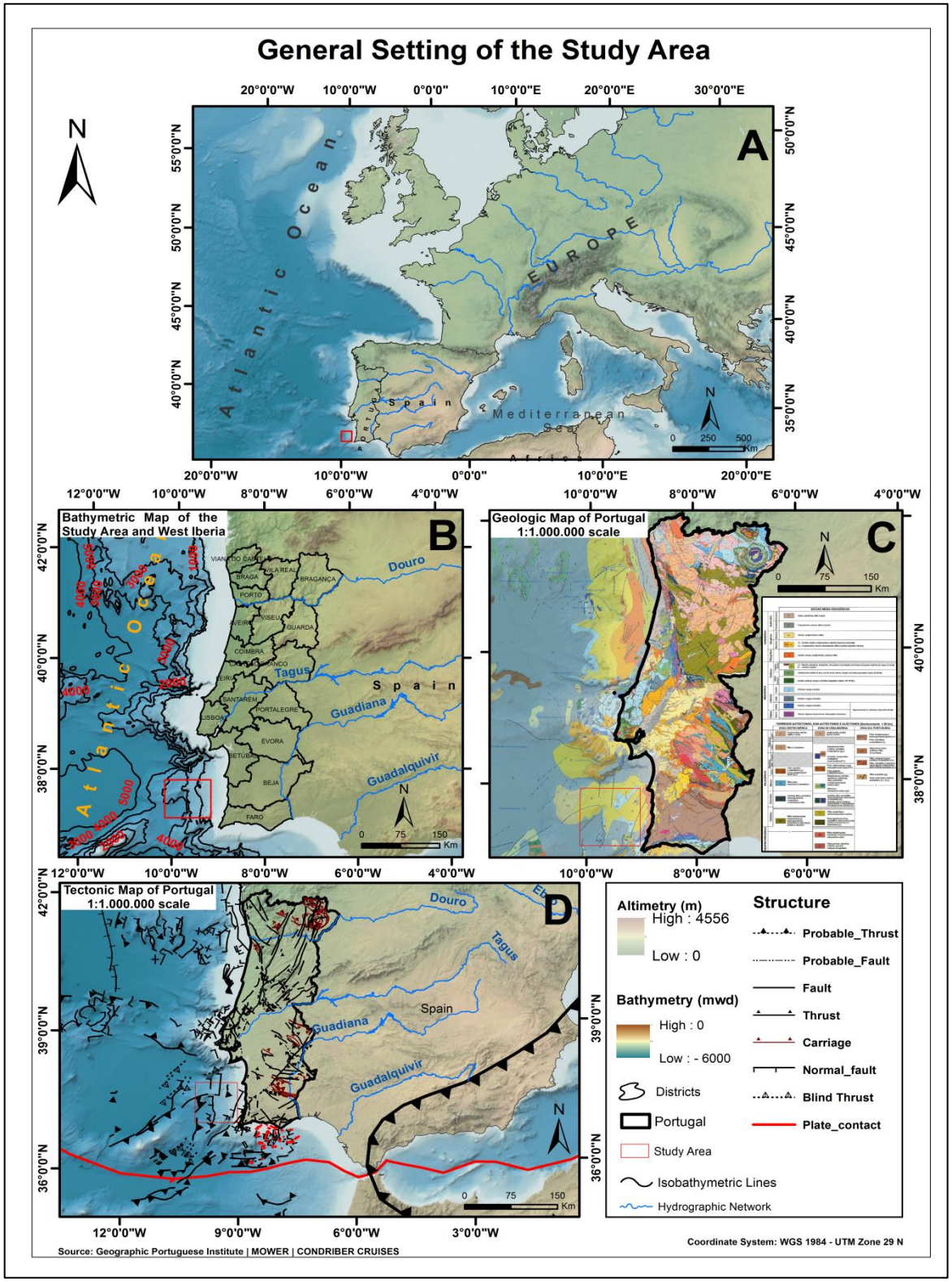

FIGURE 3.1 – General setting of the study area. (A) – General view of the actual display of Iberia and Europe; (B) – Morpho-bathymetric map of the West Iberia and the Alentejo Margin; (C) – Geological map of Portugal mainland and offshore at 1 Million scale (LNEG, 2010); (D) – General structural setting of the Iberia. Iberia and Nubia plate contacts identified by the red line, with the identification of converging and diffuse contacts. Big black-arrowed line in the West Mediterranean Sea (Alboran) refers to back-arc thrusting.

3.1.1 – LATE PALAEOZOIC EVOLUTION

The collision of the Laurasia and Gondwana major continents during the Late Palaeozoic, generated the Variscan orogeny during Devonian and Carboniferous periods (von Raumer *et al.*, 2002), forming the supercontinent Pangaea. This has also promoted the formation of the Hesperian Massif as part of the broader Variscan Orogenic Belt that extends across the Europe. According to Ribeiro (2013a), the basement of the WIM corresponds to the deformed rocks generated during that compressional event. In general, those are essentially metamorphic rocks (schists, quartzites, gneiss) with igneous intrusions (granitoids) – Figure 3.1C.

3.1.2 – MESOZOIC RIFTING

The Mesozoic is characterized by generalized extensional tectonics, which promoted intense rifting in the WIM (Srivastava *et al.*, 1990; Terrinha *et al.*, 2019b), subsidence and ocean transgression (Mougenot, 1989; Alves *et al.*, 2003; Terrinha *et al.*, 2003; Roque, 2007; Pereira and Alves, 2011; 2013). The Mesozoic rifting, which started at ~200 Ma (Pinheiro *et al.*, 1996), reshaped and split the Pangaea (Srivastava *et al.*, 1990), originating WIM and SWIM intra-continental rifts in West Iberia (Terrinha *et al.*, 2019b).

The WIM is a non-volcanic asymmetric rifted continental margin (Pinheiro *et al.*, 1996; Whitmarsh and Sawyer, 1996; Tucholke *et al.*, 2007; Neves *et al.*, 2009) that evolved as the conjugate of the Grand Banks area during Mesozoic rifting (Boillot *et al.*, 1989; Hiscott *et al.*, 1990; Srivastava *et al.*, 1990; Alves *et al.*, 2003; Péron-Pinvidic *et al.*, 2007). The separation of Iberia and the Grand Banks occurred in the Early Cretaceous (Driscoll *et al.*, 1995; Tucholke *et al.*, 2007) leading to the formation of a cluster of six epi-continental basins in the WIM, chronologically and spatially formed from south to north (Alves *et al.*, 2009b; Pereira and Alves, 2011; 2013). Starting from South (Terrinha *et al.*, 2013a; Terrinha *et al.*, 2013b), the Alentejo Basin (Alves *et al.*, 2009b; Pereira and Alves, 2009; 2011; 2013), the Peniche Basin (Alves *et al.*, 2006), the Lusitanian Basin (Pinheiro *et al.*, 1996; Whitmarsh and Sawyer, 1996; Rasmussen *et al.*, 1998; Alves *et al.*, 2003; Azerêdo *et al.*, 2003), the Porto Basin (Alves *et al.*, 2006) and the Galicia Basin (Pinheiro *et al.*, 1996; Whitmarsh and Sawyer, 1996). In consequence of this tectonic extensional activity, the WIM has been segmented into different structural domains: inner proximal margin, the outer proximal

margin and distal margin (Pereira and Alves, 2011). This margin-parallel segmentation resulted from northwards propagation (Whitmarsh and Sawyer, 1996) of continental rifting and ocean break-up (Mauffret *et al.*, 1989; Pinheiro *et al.*, 1996; Alves *et al.*, 2006).

3.1.2.1 – RIFTING PHASES IN THE WEST IBERIA MARGIN

According to Pinheiro *et al.* (1996), Lusitanian and Galician Basins were affected by four rifting phases, as follows: i) Triassic-Callovian (~200-166 Ma) with generalized subsidence and evaporite deposition (Rasmussen *et al.*, 1998); ii) Oxfordian-Tithonian (~165-145 Ma), with carbonate deposition and intense basement subsidence rates (Hiscott *et al.*, 1990) making this a substantial transtentional rifting phase (Wilson *et al.*, 1989); iii) Valanginian-Early Aptian (~140-113 Ma), presents fluvial siliciclastic sands and conglomerates alongside with shallow water carbonates; iv) Late Aptian-Early Campanian (~113-83 Ma) presents an abrupt and widespread onset of coarse-grained siliciclastic sediments transported from the Hesperian Massif south-westwards (Figures 3.2 and 3.3).

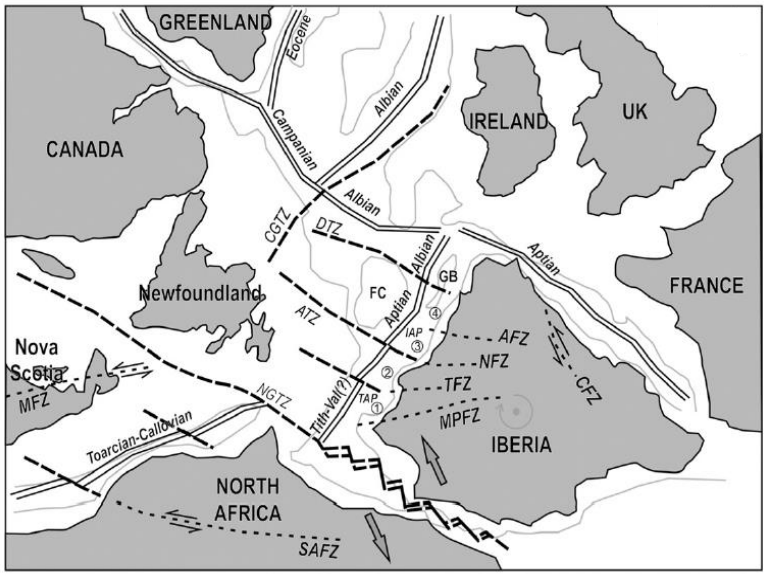

FIGURE 3.2 - Palaeogeographic reconstruction of the central and north Atlantic regions during continental rifting (adapted from Pereira and Alves, 2013). AFZ – Aveiro Fault Zone; ATZ – Atlantis Transform Zone; CFZ – Cantabria Fault Zone; CGTZ – Charlie-Gibbs Fault Zone; DTZ – Dominion Transform Zone; FC – Flemish Cap; GB – Galicia Bank; MFZ – Minas Fault Zone; MPFZ – Messejana-Plasencia Fault Zone; NFZ – Nazaré Fault Zone; NGTZ – Newfoundland-Gibraltar Fault Zone; SAFZ – South Atlas Fault Zone; TFZ – Tagus Fault Zone. Bold dashed line – Oceanic transform zone; Simple dashed line - First-order fault zone; Double line – Rift segment; Grey arrows – Relative direction of plate migration. 1,2,3,4 – margin segments.

At present, there is not yet a consensus about the number and magnitude of rifting events affecting the area (Pinheiro *et al.*, 1996; Alves *et al.*, 2009b). Tucholke and Sibuet (2007) have recognized the existence of two major phases of continental extension in the

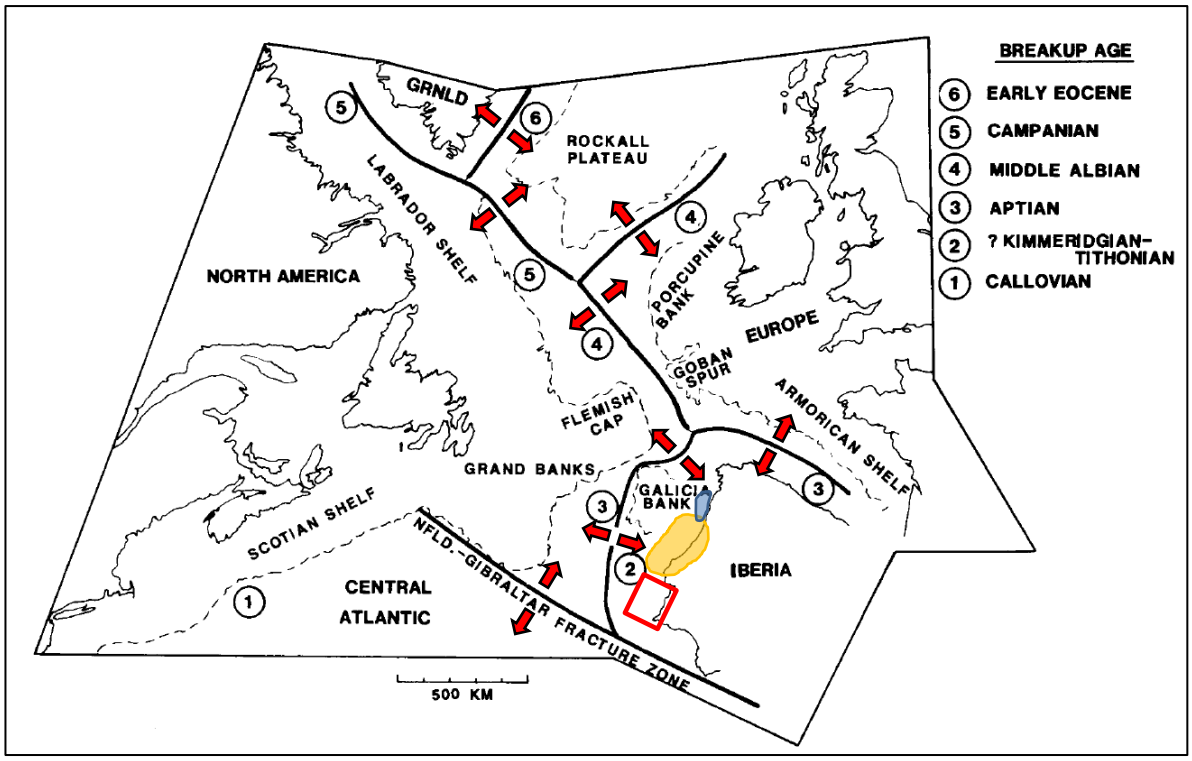

FIGURE 3.3 – North Atlantic break-up ages (Adapted from Hiscott *et al.*, 1990). Bold lines indicate sites of continental break-up. Red square: Alentejo Margin; Yellow area: Lusitanian Basin; Blue area: Porto Basin. Red arrows indicate break-up motion.

Newfoundland-Iberia rifting (Late Triassic - Early Jurassic, and Late Jurassic - Early Cretaceous) – Figure 3.2 – although it is generally accepted that four distinct rifting phases (Wilson *et al.*, 1989) have affected the Iberia Margin from Late Triassic to Early Cretaceous (Rasmussen *et al.*, 1998). These four phases occurred in the WIM and the SWIM in different geological ages (Pinheiro *et al.*, 1996; Pereira and Alves, 2009; 2011) – Figure 3.2. Comparing with the Lusitanian Basin (Pinheiro *et al.*, 1996; Whitmarsh and Sawyer, 1996; Rasmussen *et al.*, 1998; Alves *et al.*, 2003), rifting phases affecting the Alentejo Margin occur earlier (Hiscott *et al.*, 1990; Alves *et al.*, 2009b; Pereira and Alves, 2013) in result of the northwards advancing rifting (Figures 3.2 and 3.3).

Pereira and Alves (2011) identified three rifting phases affecting the Alentejo Basin, followed by a post-rifting phase (Pereira and Alves, 2013).

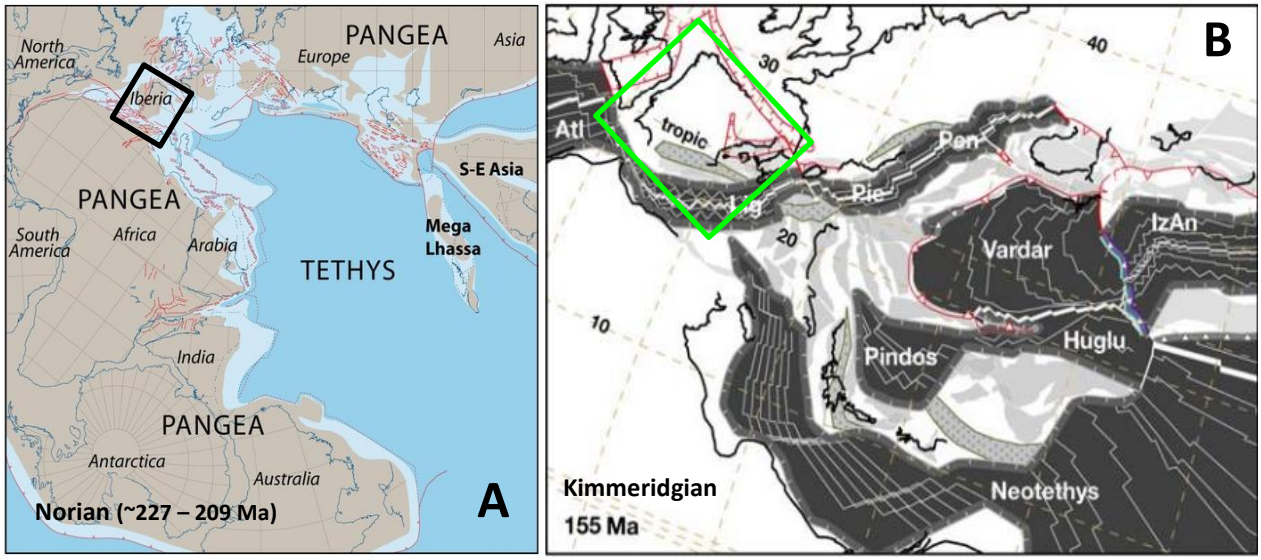

FIGURE 3.4 – (A) - The rifting in the future central Atlantic Ocean propagating eastwards during the Norian (adapted from Barrier and Vrielynck (2008). Black square points to Iberia; (B) – Spreading in the Tethyan Ocean during Kimmeridgian (adapted from Stampfli and Hochard, 2009). Green square bounds Iberia during Kimmeridgian.

3.1.2.1.1 – 1st RIFTING PHASE IN THE ALENTEJO BASIN

The first rifting phase occurs in the Late Triassic – Early Jurassic (Pereira and Alves, 2011) characterized by widespread subsidence as a consequence of the onset of the continental rifting in the North Atlantic and West Tethys (Figure 3.4). This phase is represented by a mega-sequence in the Alentejo Basin, where basal deposits include Norian continental red sandstones and shales of Silves formation, and the red Hettangian shales deposited in the Lusitanian Basin (Azerêdo *et al.*, 2003).

3.1.2.1.2 – 2nd RIFTING PHASE IN THE ALENTEJO BASIN

The second rifting phase spans from the Sinemurian (~180 Ma) in the Early Jurassic, up to Callovian (~162 Ma) in the Middle Jurassic (Pereira and Alves, 2013). This was a period of continental rifting (Alves *et al.*, 2009a) also affecting offshore Morocco and Nova Scotia (Tankard and Balkwill, 1989). During this rifting phase, the Newfoundland-Iberia continental extension pattern changed from a wide mode encompassing proximal margins focusing on the separation of continental crust on distal margins (Tucholke and Sibuet, 2007;

Pereira and Alves, 2013). During the initial stage of this phase a disperse magmatic activity occurred in the SWIM, generating volcano-sedimentary successions coeval with the Central Atlantic Magmatic Province (CAMP) (Martins *et al.*, 2008). Two regional uplift events occurred during Sinemurian and during Toarcian-Aalenian, promoting basin inversion (Azerêdo *et al.*, 2003). A third (Callovian-Oxfordian) uplift event occurred (Pereira and Alves, 2013) in the transition from the second to the third *syn-rift* phase, contemporaneously to the Callovian break-up at North Africa (Schettino and Turco, 2011) and Nova Scotia (Withjack *et al.*, 2009) that led to the formation of transfer-fault zones. Those uplift events are represented by the presence of hiatuses in the stratigraphic sequence, both in the inner and outer proximal margins (Pereira and Alves, 2013).

3.1.2.1.3 – 3rd RIFTING PHASE IN THE ALENTEJO BASIN

The third rifting phase lasted from the Late Jurassic (Oxfordian - ~160-164 Ma) until the Early Cretaceous (Berriasian - ~142 – 145 Ma). This phase hosts an intense tectonic subsidence with a maximum occurring nearby the Oxfordian-Kimmeridgian limit (Wilson *et al.*, 1989; Hiscott *et al.*, 1990; Stapel *et al.*, 1996; Stampfli and Hochard, 2009; Pereira and Alves, 2013) forming important first-order transfer lineaments as the Grândola fault and the Messejana-Plasencia Fault Zone, whose offshore prolongations separate the Alentejo Basin from the Estremadura Spur and from the Algarve Basin, respectively (Alves *et al.*, 2009a). In this phase, extensional faulting related to rifting activity exerted great control on the subsidence and geometry of sub-basins (Wilson *et al.*, 1989; Alves *et al.*, 2003). In the Alentejo Basin, this rifting phase shows evidences of regional uplift, in the Berriasian during the transition to the post-rifting (Pereira and Alves, 2013).

3.1.2.1.4 – POST-RIFT – ALENTEJO BASIN

The post-rifting phase occurred from the Early Cretaceous (Berriasian – ~142 Ma) up to Late Cretaceous (Pereira and Alves, 2013), although in Pereira and Alves (2011) from Late Berriasian and Late Aptian it is considered a syn-rift phase IV. This phase corresponds to a period of generalized rifting and consequent break-up at the Northern Newfoundland and Iberia. It is believed that seafloor spreading started near the Aptian-Albian boundary (Tucholke *et al.*, 2007). Subsequently, after the complete separation of the Iberian margin

from North America in the Late Aptian (Driscoll *et al.*, 1995; Pinheiro *et al.*, 1996), the Iberian plate developed as a separated micro-plate (Sibuet *et al.*, 2007; Ribeiro, 2013b) limited by four major rifting/fracture zones (Pinheiro *et al.*, 1996): the Mid-Atlantic Ridge (West); the Mid-Tethyan Ridge (East); the Azores-Gibraltar Fracture Zone (South) and the Charlie Gibbs Fracture Zone (North). The rotation of the Iberian micro-plate was accommodated by seafloor spreading in the Bay of Biscay also in this phase (Garcia-Mondejar, 1989; Srivastava *et al.*, 1990). This intense rifting activity promoted the collision of Iberia with Eurasia, in the Campanian-Maastrichtian, and has been accompanied by magmatic activity, with the intrusion of igneous bodies along the SWIM (Miranda *et al.*, 2009) – Figure 3.5.

Despite rifting activity is still active in the Northern Newfoundland and Iberia, evidences found in the Alentejo Basin point to the presence of a tectonic slow-down in this period (Alves *et al.*, 2013) in the Southwest Iberia, with marks of post-rift depositional activity. This phase has been defined as post-rift because of the presence of major sedimentary unconformities laying above the break-up unconformities (Pereira and Alves, 2013).

3.1.2.1.5 – MAGMATISM

During Late Cretaceous, important intrusive igneous activity occurred in the WIM spanning from ~92 Ma to 72 Ma (Ribeiro *et al.*, 1979; Storetvedt *et al.*, 1990; Silva *et al.*, 2008; Miranda *et al.*, 2009; Grange *et al.*, 2010), known as the Iberian Alkaline Igneous Province (Rock, 1982). This province post-dated the latest stages of the extensional phase. The Sines intrusive alkaline complex (Canilho, 1989) in the Alentejo Margin (Figure 3.5), form together with the Monchique and Sintra intrusive complexes a NNW-SSE striking lineament of alleged tectonic origin (Terrinha *et al.*, 2017). This lineament extends along the Estremadura Spur

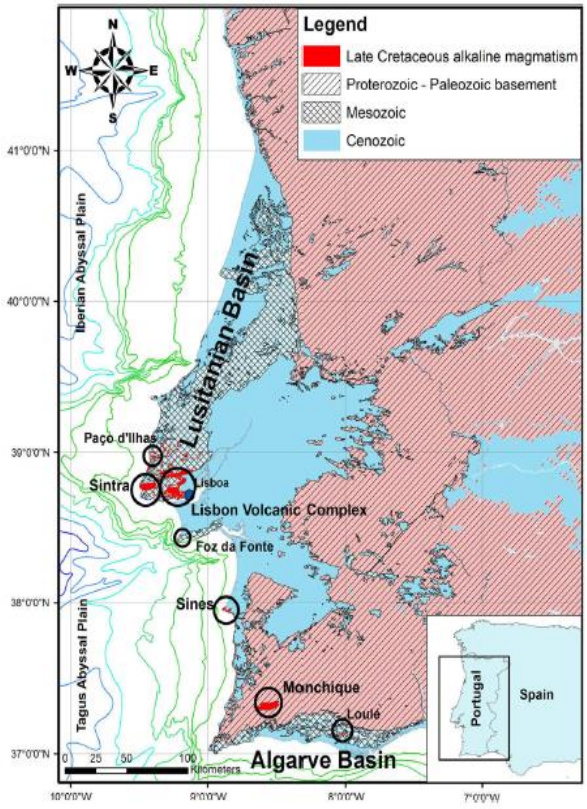

FIGURE 3.5 – Location of the igneous complexes, marked with a black circle, along Iberian Margin. Miranda *et al.* (2009).

(Neres *et al.*, 2014) towards the Madeira-Tore Rise, along which a series of volcanic seamounts from 100 Ma to 80 Ma have been reported (Geldmacher *et al.*, 2006; Merle *et al.*, 2009).

The Sines alkaline complex, whose isotopic age is 72 Ma (Macintyre and Berger, 1982) to 75 Ma (Neres *et al.*, 2014), is an E-W oriented elliptical pluton, being mostly submerged in the Atlantic (Rock, 1982). The major lithological components consist of syenites and basic rocks with basanite / lamprophyre minor intrusive suites.

3.1.3 – ALPINE OROGENY

The long period of >100 million years of extensional tectonics, from Late Triassic up to Late Cretaceous (Terrinha *et al.*, 2019b), was followed by a period of tectonic inversion, with considerable uplift, shortening events and formation of subduction zones through compressional activity, affecting the WIM (Mougenot, 1989; Wilson *et al.*, 1989; Pinheiro *et al.*, 1996; Terrinha *et al.*, 2003; Zitellini *et al.*, 2004; Terrinha *et al.*, 2019c). Compressional tectonics affected the Iberia passive margin during the Late Cretaceous through Present (Rosenbaum *et al.*, 2002a; Alves *et al.*, 2003; Pereira and Alves, 2013). Subduction and continental collision with Africa and Eurasia led to the formation of three important orogenic belts, the marginal Pyrenees and Betics and the intra-cratonic Iberian Chain and Iberian Central Massif. The general compressive phases were associated with the counter-clockwise rotation of Africa with respect to Eurasia that started in the Late Cretaceous (~92 Ma), e.g., Dewey *et al.* (1989) and the Tethyan subduction (Rosenbaum et al., 2002a).

The Alpine orogeny promoted the convergence of the Iberia micro-plate with Eurasia, and then with Nubia (Srivastava *et al.*, 1990) through compressional motion accommodated both along its northern and southern boundaries, respectively. The convergence between Nubia and Eurasia tectonic plates during the Eocene-Oligocene promoted the tectonic inversion of the Mesozoic rifting faults in the SWIM (Terrinha *et al.*, 2009; Duarte *et al.*,

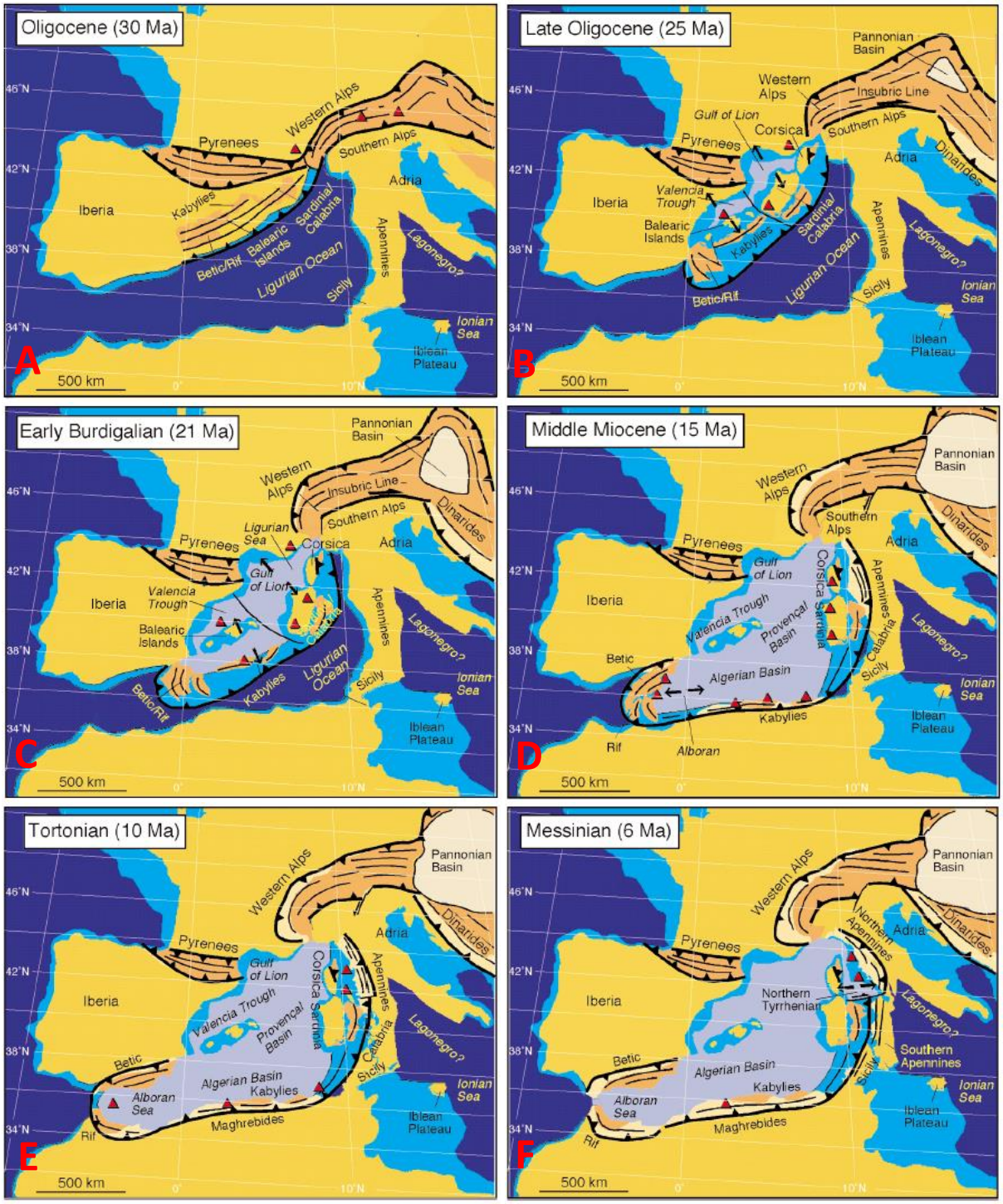

FIGURE 3.6 – Reconstruction of the tectonic evolution of the western Mediterranean since the Oligocene (adapted from Rosenbaum *et al.*, 2002a).

2013) and the reactivation of NE-SW inherited rift faults (Mougenot, 1989). Two main phases of tectonic inversion affected the Iberia: i) Late Cretaceous – Middle Eocene (Pyrenean phase) and ii) Oligocene – Late Miocene (Betic phase), which formed the Pyrenees and the Betic chains, respectively in the Eocene and the Miocene orogenic events (Terrinha *et al.*, 2019c).

The Pyrenean phase is characterized by a long period of shortening and inversion with N-S to NNE-SSW maximum compression, where the Iberian plate moved towards/collided against the Eurasian plate in the Middle Eocene (Ribeiro *et al.*, 1996), when the highest compression activity occurred, forming the Pyrenees. In the Eocene, northwards dipping subduction of the Alpine-Tethys oceanic lithosphere extending from the SE Iberia to the Alps, accommodated Nubia-Eurasia convergence (Rosenbaum *et al.*, 2002b; Duarte *et al.*, 2011; Rosas *et al.*, 2012; Duarte *et al.*, 2013).

During the Betic phase, when Iberia and Eurasia had already collided (Srivastava *et al.*, 1990), compression direction evolved to NNW-SSE (Ribeiro *et al.*, 1996). During this period, Nubia plate moved north-north-westwards colliding against Eurasia. This convergence had as immediate consequence the formation of the Gibraltar Arc, in the western end of the Mediterranean collision belt, during the Neogene Period (Duarte *et al.*, 2013), and the Betic-Rif orogen (Gutscher *et al.*, 2002) that is related to the northwards subduction of Tethyan Ligurian ocean (Figures 3.6C-3.6F). This led to the closure of the gateway that linked the Tethys and the Atlantic Ocean and to the formation of back-arc basins, in the western Mediterranean (Figure 3.6E). Roll-back of a sleeve of the Africa oceanic slab into the Atlantic Ocean led to the formation of the Gulf of Cadiz Accretionary Wedge (Gutscher *et al.*, 2002; Roque, 2007; Terrinha *et al.*, 2009; Duarte *et al.*, 2013). In the Late Miocene, this movement towards the west led to the closure of the connection of the Mediterranean Sea with the Atlantic (Haq *et al.*, 1987; Gargani and Rigollet, 2007; Govers, 2009; Hüsing *et al.*, 2010) and consequent desiccation of the Mediterranean in the Messinian, generating the Messinian salinity crisis, between 5.96 and 5.33 Ma (Krijgsman *et al.*, 1999; Govers, 2009; Roveri *et al.*, 2014; Flecker *et al.*, 2015). The connection of the Mediterranean Sea and the Atlantic Ocean was re-established in the early Pliocene with the opening of the Gibraltar strait (Blanc, 2002), resulting from transtensional tectonic activity (Garcia-Castellanos and Villaseñor, 2011), as well as climatic and oceanographic variations (Hernández-Molina *et al.*, 2014b; de Weger *et al.*, 2020) and fluvial erosion (Loget and Van Den Driessche, 2006).

3.1.4 – PLIOCENE-QUATERNARY REACTIVATION IN THE SWIM

The main tectonic shortening experienced in Iberia during the Alpine orogeny concentrated in the Palaeogene and lower and middle Miocene times (Maldonado *et al.*, 1999; Terrinha *et al.*, 2019c). The SWIM plate boundary was characterized as diffuse during this time interval (Sartori *et al.*, 1994) with a transpressive regime exerted through a main NNW-SSE oriented tectonic compression (Ribeiro et al., 1996) with an actual convergence rate between Nubia and Eurasia of ~4 mm/yr (Maldonado *et al.*, 1999). This NNW-SSE compression is promoting the inversion of many normal faults (Duarte *et al.*, 2011; 2013; Terrinha *et al.*, 2019c), creating a stair-like structure formed by several uplifted blocks (Mougenot, 1989; Rasmussen *et al.*, 1998; Pereira and Alves, 2011), disposed as successions of horsts and grabens (Figure 3.7). Most of those are tectonic inversion structures, generally

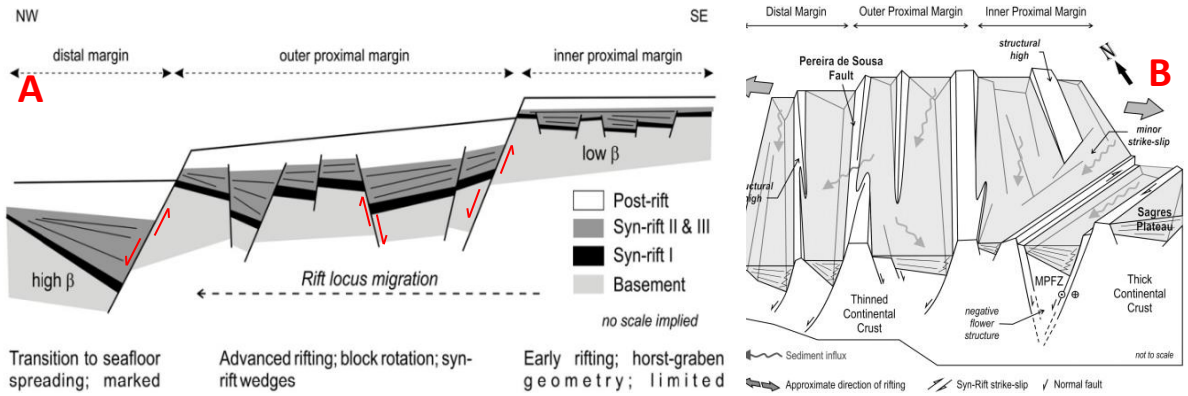

FIGURE 3.7 – (A) - Syn-rift segmentation of the proximal to distal margins of the Alentejo basin. Red arrows point to vertical tectonic movements (adapted from Pereira and Alves, 2011); (B) – 3D block diagram depicting Mesozoic segmentation (Pereira and Alves, 2013). Some of these faults, like the Pereira de Sousa Fault that limits to the west the Sines Contourite Drift, were reactivated in Pliocene-Quaternary times (Terrinha *et al.*, 2003).

anticlines, that are rooted in Mesozoic age extensional faults (Neves *et al.*, 2009). Several of these compressive structures have been identified in the offshore of the Iberia (Mauffret *et al.*, 1989; Wilson *et al.*, 1996), mostly through erosional unconformities (Alves *et al.*, 2003). Most of those faults are reactivations of Variscan faults that act now as reverse faults with main orientations between ENE–WSW and NE–SW (Ribeiro *et al.*, 1996; Terrinha *et al.*, 2003; Zitellini *et al.*, 2004). The continuation of the counter-clockwise rotation of Africa with respect to Eurasia in Pliocene-Quaternary times created a new transcurrent plate boundary in the SWIM, named the SWIM Fault plate boundary after Zitellini *et al.* (2009). The main tectonic compression also rotated clockwise towards WNW-ESE in the Alentejo Margin causing continental uplift of the SW Iberia, forming new oceanward directed thrusts (the

Marquês de Pombal thrust) and reactivating old Mesozoic graben bounding faults such as the >100 km long Pereira de Sousa Fault scarp (Terrinha *et al.*, 2003).

3.2 – STRATIGRAPHIC EVOLUTION OF THE SW IBERIAN MARGIN

3.2.1 – LITHOSTRATIGRAPHY

The post-Palaeozoic stratigraphic record of the Alentejo Margin spans from uncertain Triassic, to which correspond the earliest syn-rifting sediments, through Present. Several lithostratigraphic evidences (Figures 3.8A and B) document this evolution along the margin (Alves *et al.*, 2003; Azerêdo *et al.*, 2003; 2009b; Pereira and Alves, 2013), as the outcrops that have been compiled by Pereira *et al.* (2011), Alves *et al.* (2013), and Pereira and Alves (2013), both in inner and outer proximal margin. These sedimentary sequences span over the rifting, post-rifting, and tectonic inversion phases.

3.2.1.1 – MESOZOIC

The Mesozoic deposition of the Southwest Iberian margin started during the syn-rifting phase I. Deposition started in the Alentejo Basin with the Late Triassic siliciclastic sandstones of the Silves Formation (Azerêdo *et al.*, 2003), which spans in age from Carnian to Norian. These are quite visible in the Algarve, especially in Telheiro beach. These terrigenous sandstones, also known as *Grés de Silves* (Choffat, 1887), are interrupted at the top by an unconformity being overlain by the continental Dagorda Formation consisting of marls, shales, evaporites and dolomites, extending from Norian to Late Hettangian (Oliveira, 1984; Azerêdo *et al.*, 2003; Alves *et al.*, 2013). This transition is also visible onshore in Santiago do Cacém (Azerêdo *et al*., 2003), Carrapateira and Bordeira outcrops, as well as in Pescada-1 and Golfinho-1 boreholes (Figure 3.8B), all in the inner proximal margin, and correlated through the outer proximal margin (Pereira and Alves, 2011; 2013).

The end of the Hettangian brought another variation in the sedimentary deposition (Oliveira, 1984; Azerêdo *et al.*, 2003). The sedimentary record changed from terrigenous to marine in the beginning of the syn-rifting phase II, with the deposition of the Coimbra Formation, made up by dolomitic carbonates (Azerêdo *et al.*, 2003). According to these authors, that formation presents in the Alentejo Basin a low-energy carbonated ramp that

resulted from the regional uplift. During the syn-rifting phase II, the dominant sediments in Santiago do Cacém outcrop, Pescada-1 borehole and outer proximal margin are dolomite during the Lower Jurassic and limestones during the Middle Jurassic (Figure 3.8B). Both Bordeira and Carrapateira outcrops show an inverted succession with dolomites predominating during Middle Jurassic and overlaying Lower Jurassic shaly limestones (Pereira and Alves, 2011; 2013). Generalized subsidence is verified in the Southwest Iberian margin during that time interval leading predominantly to the deposition of limestones and dolomites (Inverno *et al.*, 1993; Azerêdo *et al.*, 2003). The Toarcian-Aalenian transition corresponds to a depositional hiatus caused by regional uplift (Cunha *et al.*, 2009; Pereira and Alves, 2011; 2013). Deposition resumed in Bajocian times in the outer proximal margin and in the end of Bajocian and beginning of Bathonian in the rest of the Alentejo Basin (Azerêdo *et al.*, 2003; Pereira and Alves, 2011). This deposition led to the formation of carbonate ramps that vary parallel to the palaeo-slope: Toarcian-Callovian dolomites in Carrapateira and Bordeira; Bathonian-Callovian marine limestones in Santiago do Cacém, where the Rodeado (200 m) and Monte Branco (50 m) Formations are present (Inverno *et al.*, 1993); Bajocian-Callovian limestones in Pescada-1 borehole and Bajocian(?)-Callovian(?) dolomites in Golfinho-1 borehole. The end of the syn-rifting phase II is again marked by a regional uplift during Callovian-Oxfordian times (Pereira and Alves, 2013) that led to generalized depositional unconformities in the transition between Middle and Upper Jurassic. These unconformities are present in the subsequent period of subsidence (Mougenot *et al.*, 1979). Inverno *et al.* (1993), for example, refer the presence of the Deixa-o-Resto Formation, composed of limestones, marls and conglomerates, in Santiago do Cacém, which is based on an Oxfordian-Kimmeridgian non-conformity. This unconformity is less expressive when going from south to north (Pereira and Alves, 2011; 2013).

FIGURE 3.8A – Location of outcrops near the Alentejo Basin. Modified from Pereira and Alves (2011).

The syn-rifting phase III starts in the Oxfordian with an unconformity on the sedimentary record, well recorded in Santiago do Cacém region (Figure 3.8B), where a thin

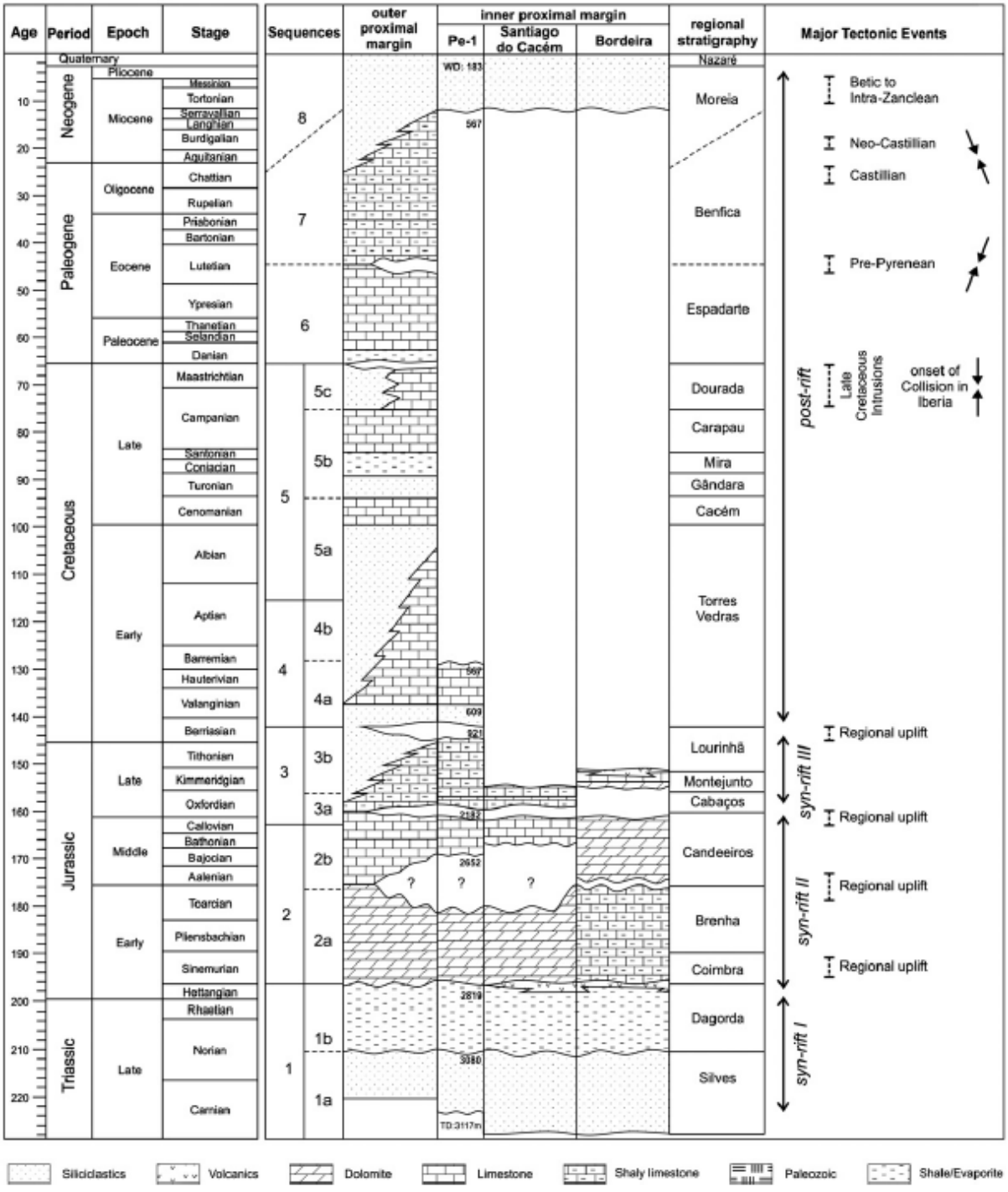

FIGURE 3.8B - Lithostratigraphy and seismic-stratigraphy of the Alentejo Basin relative to the main tectonic events (Pereira and Alves, 2013).

layer of shaly limestone is followed by a hiatus in the Early Kimmeridgian(?), and in Golfinho-1 borehole, where the hiatus spans from the base of the Oxfordian until Late Berriasian (Pereira and Alves, 2011; Alves *et al.*, 2013). The Oxfordian-Berriasian corresponds to the last syn-rifting episode (Pereira and Alves, 2011). During this phase the

Alentejo Basin formations are dominantly made up of shaly limestone (Pescada-1 and Santiago do Cacém). However, dolomites are topped by volcanic sediment at Carrapateira (Pereira and Alves, 2011). The Alentejo Basin formations mostly present sediment absence during this phase (Alves *et al.*, 2009b; Pereira and Alves, 2013).

Since the Early Cretaceous, the sedimentary record is absent in Santiago do Cacém (Inverno *et al.*, 1993) as well as in the Carrapateira and Bordeira outcrops, being only present in Pescada-1 and Golfinho-1 boreholes (Alves *et al.*, 2009b; Pereira and Alves, 2013). The sedimentary record of Pescada-1 borehole shows an intercalation of limestone, shaly limestone and siliciclastic sediments. This marks the start of a new phase in Berriasian with an unconformity in the sedimentary record of the Alentejo Basin (Alves *et al.*, 2009b; Alves *et al.*, 2013).

3.2.1.2 – CENOZOIC

During the Cenozoic, there are mostly carbonate sediments in the outer proximal margin (Mougenot *et al.*, 1979; Alves *et al.*, 2009b). However, in the inner proximal margin, Golfinho-1 sedimentary record presents siliciclastic sediments (Pereira and Alves, 2013). During most of the Palaeogene, sediments are essentially carbonates becoming more siliciclastic when passing from Eocene towards Oligocene (Figure 3.8). There is a transition from limestone and shaly limestone, contemporary with the Benfica Formation during Eocene to siliciclastic sediments, contemporary of Moreira Formation (Figure 3.8B).

The Neogene sediments are more difficult to recognize because they are covered by the Pliocene-Quaternary mobile sediments (Mougenot *et al.*, 1979). This is especially evident since the opening of the Gibraltar Strait (Flecker *et al.*, 2015) at the end of the Messinian Salinity Crisis - 5.96-5.33 Ma - (Cita, 2001; Garcia-Castellanos and Villaseñor, 2011) and consequent onset of the Mediterranean Outflow Water (MOW) (Hernández-Molina *et al.*, 2014b), which allowed for important contouritic sedimentary deposition (Hernández-Molina *et al.*, 2002).

3.2.1.3 – NEOGENE AND QUATERNARY SEISMOSTRATIGRAPHIC EVOLUTION

Important variations occurred in the stratigraphic evolution of the Alentejo Margin after the Late Miocene/Early Pliocene transition (Hernández-Molina *et al.*, 2016a). The

seismostratigraphic evolution of the area (Mougenot *et al.*, 1979; Mougenot, 1989) has been documented through seismostratigraphic correlation between sedimentary records and seismic data (Alves *et al.*, 2013; Pereira and Alves, 2013; Hernández-Molina *et al.*, 2014b; 2016a; Rodrigues *et al.*, 2020).

The end of Messinian is marked by an erosive discontinuity (Figure 3.9), which determined the beginning of new sedimentary dynamics in Southwest Iberia (Stow *et al.*, 2013; Hernández-Molina *et al.*, 2016a). This is demonstrated by the lithostratigraphy of IODP Site U1391 (http://iodp.tamu.edu/index.html). The correlation between seismic and sedimentary records (Rodrigues *et al.*, 2020) shows great variability in sedimentary deposition both in rate and grain-size (Figures 3.9 and 3.10).

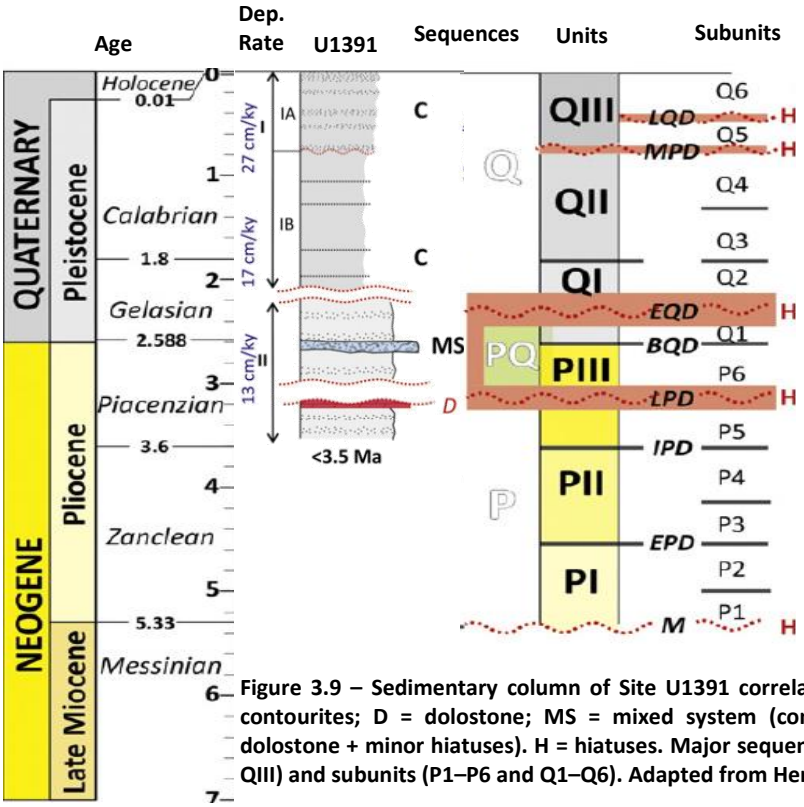

Figure 3.9 – Sedimentary column of Site U1391 correlated with seismostratigraphic units. C = contourites; D = dolostone; MS = mixed system (contourites, bio-siliceous muds, debrites, dolostone + minor hiatuses). H = hiatuses. Major sequences (P, PQ and Q), units (PI–PIII and QI–QIII) and subunits (P1–P6 and Q1–Q6). Adapted from Hernández-Molina *et al.* (2016).

Important depositional hiatuses occur in the Alentejo Margin both in Late Pliocene and Early Pleistocene (Figure 3.9), determining sharp discontinuities with upcoming sedimentation (Hernández-Molina *et al.*, 2016a). From the Early Quaternary discontinuity (EQD, Figure 3.9) and during the Pleistocene, deposition was irregular presenting variations between muddy and contourite deposition (Figures 3.9 and 3.10). These alternations are the result of strong variations in the bottom current enhancement (Stow *et al.*, 2013; Hernández-Molina *et al.*, 2016a; Rodrigues *et al.*, 2020).

The visual description of IODP Site U1391, from the Expedition 339 (Stow *et al.*, 2013), showed that the main lithology recognized at Site U1391 was calcareous silty mud with few intervals of coarse-grained deposits that mainly occur from Mid-Pleistocene onwards (Rodrigues *et al.*, 2020) – Figure 3.10. Since Pleistocene the grain-size evolution mostly denotes bi-gradational successions (Stow *et al.*, 2013; Rodrigues *et al.*, 2020).

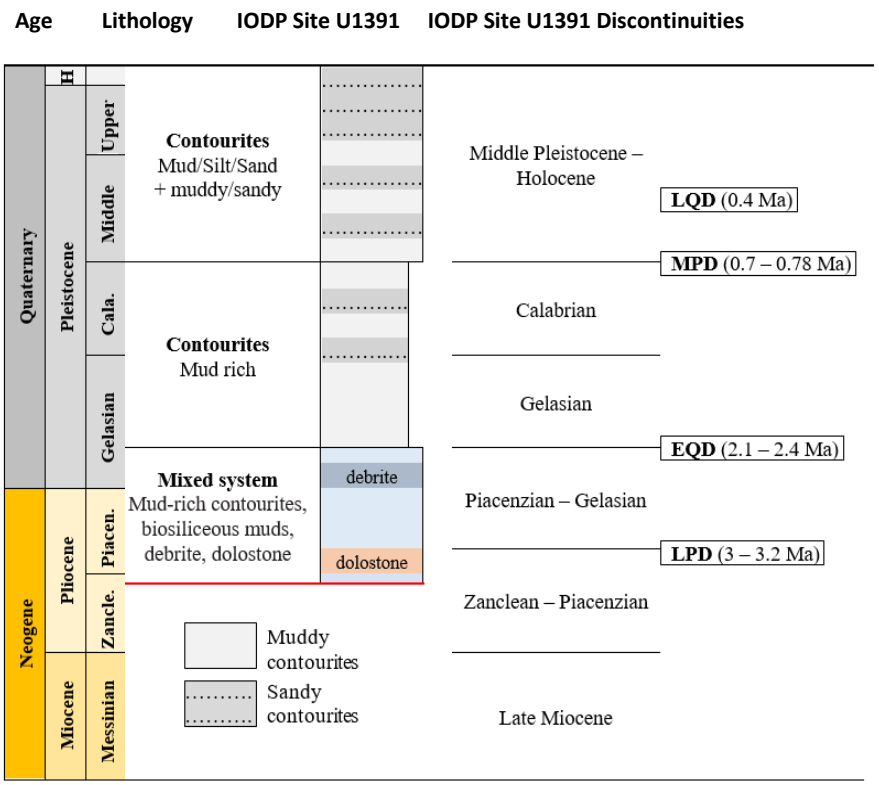

Figure 3.10 – Stratigraphic correlation between IODP Site U1391 and seismic data. Red line marks the bottom of the hole, while different colors indicate changes in lithology and dark grey denotes contourite beds; LPD – Late Pliocene Discontinuity; EQD – Early Quaternary Discontinuity; MPD – Middle Pleistocene Discontinuity; LQD – Late Quaternary Discontinuity. Adapted from Rodrigues (2017).

Although this sedimentary body offshore Alentejo is a distal part of the Gulf of Cadiz Contourite Drift System (Stow *et al.*, 2013), its evolution resembles that of other proximal drifts as Faro drift (Llave *et al.*, 2001; Roque *et al.*, 2012; Alonso *et al.*, 2016), although variable in time.

After the Palaeogene the stratigraphic column of the Alentejo Margin comprises six well-defined units (Rodrigues *et al.*, 2020), found through the correlation between seismic data and the sedimentary record of the IODP Site U1391. Starting from the Late Miocene, the unit 1 extends into the Early Pliocene. Unit 2 spans from Early to Late Pliocene, whereas Unit 3 comprises Late Pliocene to Early Pleistocene sediments. The units 4 and 5 are comprised in Early Pleistocene and unit 6 between Middle Pleistocene to Holocene. Based on this, a depositional evolution has been determined (Rodrigues *et al.*, 2020) for the period comprised between the Late Miocene and the Holocene.

3.2.2 – LITHOLOGY OF THE ALENTEJO MARGIN

Presently, the seafloor lithology in the study area is predominantly siliciclastic clayey, silty-clay, silty-sand Quaternary deposits, and hemipelagic clayey deposits, especially in the

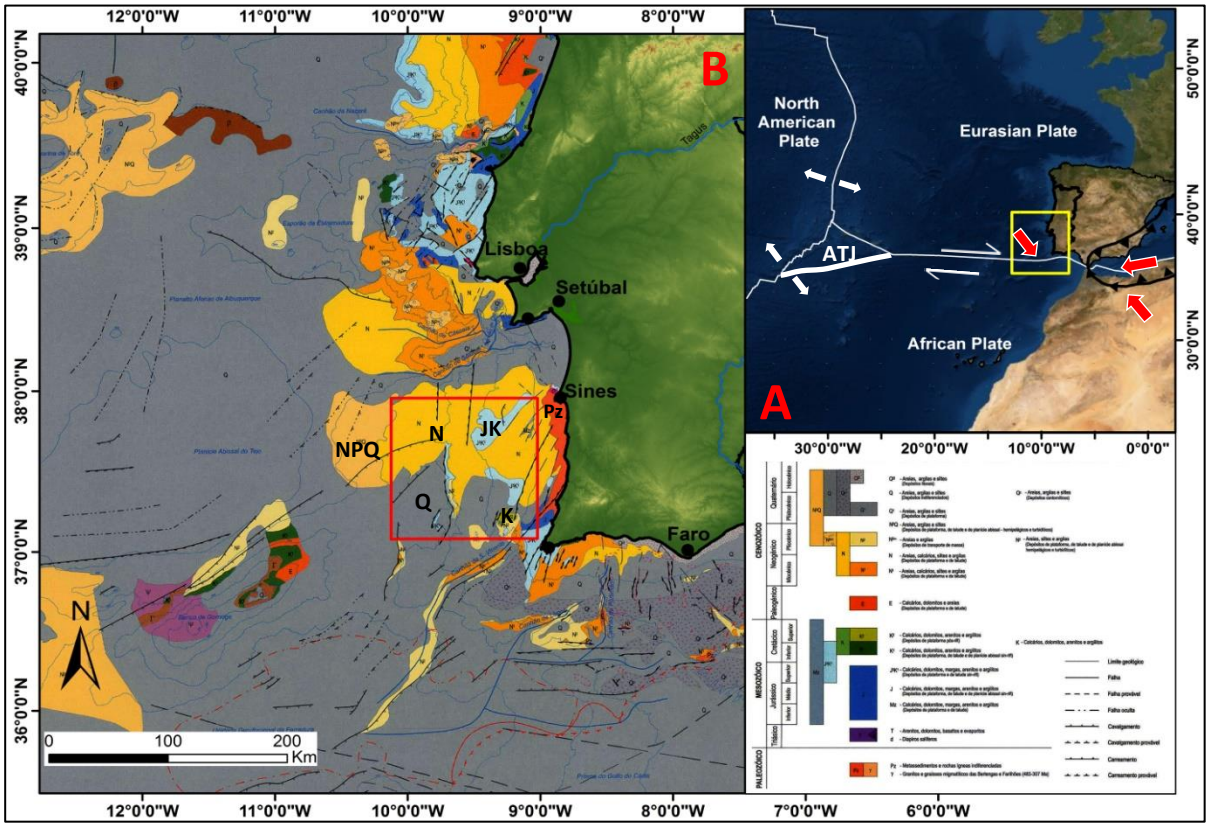

FIGURE 3.11 – Geological Map of Portugal offshore at 1: 1.000.000 scale. (A) - Yellow square: figure (B) encompassing SWIM area; Red arrows: direction of compression; White arrows: direction of rifting; White half-arrows: strike-slip direction, dextral motion. Black-arrowed line refers to thrust fault. ATJ – Azores triple junction. (B) - Red square: study area. Stratigraphy (colours): Greyish (Q) refers to Quaternary sediments; yellow (N and NPQ) refer respectively to Neogene, and Neogene and Pliocene-Quaternary sediments; Greenish (K) refers to Cretaceous sediments; JK refers to Late Jurassic and Early Cretaceous sediments; Dark blue refers to Jurassic sediments; Pz refers to Palaeozoic sediments.

bathymetrically most depressed areas (Figure 3.11B - red square). Neogene sediments drape the inherited reliefs, such as previous escarpments, as identified by Mougenot (1989). Cenozoic sediments, especially Neogene and Pleistocene-Holocene, prevail in the area, although some syn-rifting Mesozoic sediments outcrop in the upper continental shelf, dominantly dolomitic limestone, sandstone, and shale from the Late Jurassic and the Early Cretaceous (Figure 3.11). According to Mougenot (1989), there are Lower through Upper Jurassic (Oxfordian-Kimmeridgian) carbonated limestones, but also post-rifting gravelly limestones, in the Alentejo Basin. Few post-rifting Late Cretaceous deposits are present in the area, occurring in the hill tops. Near the shelf there are Jurassic limestones and dolomites overlying Palaeozoic igneous and metamorphic rocks (Figure 3.11). Most of the continental shelf, in the transition between the onshore and the upper continental slope, is floored by the

Palaeozoic and the upper continental slope presents Neogene sands, silts and clays, both being significant siliciclastic sources.

3.3 – SEISMOTECTONIC AND TSUNAMIGENIC ACTIVITY

The inherited faulted structure of the Alentejo Margin, formed during rifting phases (Pereira and Alves, 2011; 2013) and the Alpine compression (Pereira *et al.*, 2011; Terrinha *et al.*, 2019c) is now experiencing moderate frequency seismicity near the plate boundary (Baptista *et al.*, 1998; Baptista and Miranda, 2009; Baptista *et al.*, 2014; Custódio *et al.*, 2015; 2016; Silva *et al.*, 2017; Veludo *et al.*, 2017). The presence of low to moderate seismicity is mainly due to the proximity of the Eurasia-Africa plate boundary (Fukao, 1973; Roque, 2007; Zitellini *et al.*, 2009). The low-depth seismic foci present between the Gorringe bank and the Gulf of Cadiz (Roque, 2007) and especially in the Marquês de Pombal fault (Silva *et al.*, 2017) exert great impact in the Alentejo Margin contributing to continuously deform the seafloor and to keep faults active since the Pliocene until Present (Terrinha *et al.*, 2003). Notwithstanding this, there have been occasional large and mega earthquakes (M ~8.5 in 1755) affecting the area (Zitellini *et al.*, 2001) but also the Gulf of Cadiz (M 6.4 in 1964) and the Horseshoe Abyssal Plain (M 7.9 in 1969, and M 6.0 in 2007) (Fukao, 1973; Buforn *et al.*, 2004; Roque, 2007; Stich *et al.*, 2007).

The active seismicity recorded in the SW Iberia is presently associated with the Africa-Eurasia wrench collision (Zitellini *et al.*, 2009; Neres *et al.*, 2016). This tectonic regime caused the formation of various morpho-tectonic structures from 1.5 km to 5 km of vertical command, such as the Marquês de Pombal Fault and Gorringe Bank (Zitellini *et al.*, 2004). The Marquês de Pombal plateau and thrust results from various tectonic pulses from Oligocene through Present with a peak of activity in Pliocene times, rising the seafloor from 3200 to ~1800 mwd, as well as the São Vicente Canyon, and the Horseshoe scarp (Zitellini *et al.*, 2001; Gràcia *et al.*, 2003). These reliefs are part of a multiphase compressive tectonic regime (Mougenot, 1989; Alves *et al.*, 2003; Roque, 2007; Pereira *et al.*, 2011; Pereira and Alves, 2013). In the Alentejo Margin the 1400-m high escarpment of the Pereira de Sousa extensional fault (PSF) formed during the Triassic-Jurassic rifting is currently suffering uplift (Terrinha *et al.*, 2003). According to Roque (2007), the main focal mechanisms in the SW Iberia correspond to moderate-depth rupture events occurred in thrust- and strike-slip faults (Cabral, 1995).

3.3.1 – EVIDENCE OF TSUNAMI: ONSHORE AND OFFSHORE DEPOSITS

The high-magnitude earthquakes contributed for tsunamigenic activity in the SW Iberian margin (Fukao, 1973; Baptista *et al.*, 1998; Borges *et al.*, 2001; Zitellini *et al.*, 2004). The most studied is the 1755 seismic-induced tsunami whose most proposed location is the Marquês de Pombal Fault (Zitellini *et al.*, 1999), although other locations have been suggested with great uncertainty (Baptista *et al.*, 1998; Gutscher *et al.*, 2002; Terrinha *et al.*, 2003). Some sedimentary evidences of tsunami deposits, in the Algarve (Andrade, 1992; Dawson *et al.*, 1995; Costa *et al.*, 2011; Quintela *et al.*, 2016; Kümmerer *et al.*, 2020), have been attributed to the 1755 tsunami. Also related with the 1755 seismically-induced tsunami, are the testimonies found in the Tagus river delta (Abrantes *et al.*, 2005; Terrinha *et al.*, 2019a).

3.4 – MASS MOVEMENT ANALYSIS: AN OVERVIEW

As consequence of the seismotectonic activity, some large submarine landslides occurred in the SW Iberian margin, associated with major structures as the Gorringe thrust, the Hirondelle seamount and the Marquês de Pombal Fault (Terrinha *et al.*, 2003; Vizcaino *et al.*, 2006; Gràcia *et al.*, 2010). Most of the landslides occurred in the area have been ascribed to earthquake-induced activity (Gràcia *et al.*, 2003; Collico *et al.*, 2020). Some of these landslides as the Hirondelle and Gorringe landslides affecting the coasts of Portugal, Spain and Morocco were considered as being tsunamigenic (Lo Iacono *et al.*, 2012; Omira *et al.*, 2016). The same had already been proposed for the Marquês de Pombal landslides (Gràcia *et al.*, 2003; Terrinha *et al.*, 2003). Slope instability in the area has also been associated with climate variations and related sea-level oscillations, being especially evident during glacial periods (Lebreiro *et al.*, 2009; Gràcia *et al.*, 2010). In what concerns to the Alentejo Margin, the landsliding activity has been related with seismotectonic activity (Terrinha *et al.*, 2003) and with the presence of contourites (Roque *et al.*, 2015).

The presence of landslides has been assessed through quantitative analyses (Collico *et al.*, 2020; Mencaroni *et al.*, 2020) in the SW Iberia for a broader area, partially encompassing the southern part of the Alentejo Margin, but not including the Sines Contourite Drift or establishing any link between contourite deposition and landslide formation. The effects of

both seismic activity and sediment properties have been assessed and their impact on slope instability has been quantitatively analysed.

3.5 – GEOMORPHOLOGY OF THE ALENTEJO MARGIN: BRIEF REVIEW

The Alentejo Margin is limited by the Setúbal Canyon, in the north, and by the São Vicente Canyon, in the south. This margin develops over a low-dip stair-like structure of horsts and grabens (Coppier, 1982; Pereira and Alves, 2011), from the continental shelf until the Tagus Abyssal Plain (Vanney and Mougenot, 1981). According to Mougenot (1989), the continental shelf is an inherited feature from deep structure that is mainly composed by prograding Neogene deposits whose thickness decreases southwards, draping the Palaeozoic and Mesozoic basement (Boillot, 1979). This is a flattened erosional surface intersected by palaeo-valleys, filled by prograding Neogene sediments (Mougenot, 1989), many of them coming from proximal sources. This smoothed surface also hosts prodeltas and marine tide deltas and beaches (Brito, 2010; Terrinha *et al.*, 2019a).

The continental slope is under the effect of a dense water mass (Mougenot, 1989, and references therein), the Mediterranean Outflow Water (MOW), which contributes for the formation of distal quaternary deposits. Mougenot (1989) identified fosses and distal (contourite) deposits in the continental slope by the action of that water mass. These deposits are also present above 700 mwd. Between ~1000 and 2500 mwd, the presence of landslides is also verified.

Much of the sedimentation dynamics of this area is controlled by the presence of two canyons in both extremities. The Setúbal Canyon on the northern extremity (Terrinha *et al.*, 2003) contributes for moulding the northern sector of the Alentejo Margin through constant capture of sediments and regularization of the canyon walls. This constant sediment evacuation contributes for feeding the Tagus Abyssal Plain (Mougenot *et al.*, 1979; Terrinha *et al.*, 2003). In the southern extreme, another canyon contributes for moulding the area. The São Vicente Canyon (Sanchez-Serra *et al.*, 2020) is the offshore extension of the Odemira-Ávila fault. This deep trough greatly affects the morphosedimentary evolution of the Alentejo Margin as it captures sediments from the continental shelf and from the Sagres Plateau brought from SW by the MOW (Mougenot, 1989).

3.6 – OCEANOGRAPHIC CONDITIONS

The Alentejo Margin is an aisle for superficial, intermediate and deep-water masses circulation (Figure 3.12). The superficial water masses correspond to the North Atlantic Current (NAC) which extends down to 100 mwd and the underlying Eastern North Atlantic Central Water (ENACW) (Pollard *et al.*, 1996), whose temperature and salinity vary respectively from 12 - 16 ºC and 34.7 – 36.25 ‰ (Llave *et al.*, 2015). ENACW circulates in a cyclonic gyre at ~4 cm/s (Pingree and Le Cann, 1989) between 600 mwd and the surface with a main core at ~350 mwd (van Aken, 2000a). The intermediate circulation is dominated by the Mediterranean Outflow Water (MOW), which splits into two branches with distinct temperature and salinity flowing northwards between 600 and 1500 mwd at the latitude of the Cape St. Vicente (Ambar and Howe, 1979). The upper core flows at ~80 – 100 cm/s near the Cape St. Vicente (Cherubin *et al.*, 2000) along the upper continental slope between 600 and 950 mwd centred at ~800 mwd. This core is characterized by high temperature (13º-14ºC) and salinity (36.5-37.0‰) (Serra and Ambar, 2002). The lower core is colder (10.5º-11º C) and denser (36.5-37.5‰) meandering between 1000 and 1500 mwd, usually centred at about 1200 mwd in the middle continental slope (Zenk and Armi, 1990; Serra and Ambar, 2002) with an average velocity of 20–30 cm/s (Llave *et al.*, 2007). Below the MOW and between 1500-2200 mwd circulates the cold (3º - 4º C) and fresher (~34.88‰) Labrador Sea Water (LSW) with a main core at ~1800

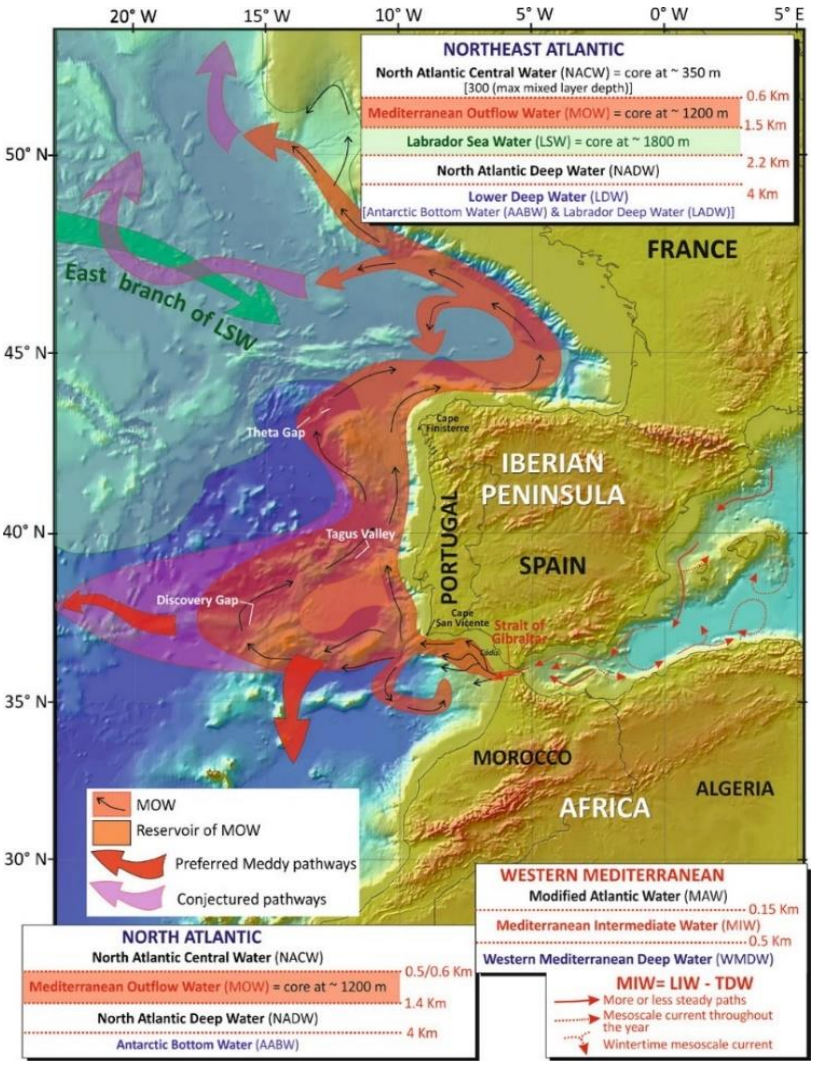

FIGURE 3.12 – Intermediate water circulation in the Western Mediterranean and North Atlantic (from Hernández-Molina *et al.*, 2011).

mwd (Talley and McCartney, 1982). The deep-water circulation involves the North Atlantic Deep Water (NADW) and the Lower Deep Water (LDW). The NADW flows southwards between 2200 and 4000 mwd and is characterized by lower temperature (3º- 8º C) and salinity (~35.0) (Caralp, 1988). The LDW is mainly composed by Antarctic Bottom Water (AABW) and flows northwards regionally below 4000 mwd, across the Horseshoe and Tagus abyssal plains (van Aken, 2000b). This water mass has a temperature of about 2ºC and a salinity of 34.76‰ (Reddy, 2001).

4 – MATERIALS AND METHODS

In this chapter, it is presented a description of the data as well as the methods used in this research. The dataset consists of multibeam bathymetry, multichannel reflection seismic profiles (MCS) and high-resolution seismic data, and gravity cores of sediments (Figure 4.1). Details on used equipment and methods for acquisition, processing and interpretation are presented.

4.1 – DATASET

Most of the data used in this work was acquired during the MOWER and CONDRIBER projects in 2014 (Hernández-Molina *et al.*, 2014a), although seismic data previously acquired in other academic and oil-industry surveys (GSI 1984; STEAM 1994; BIGSETS 1998), as well as bathymetry (SWIM - Diez *et al.*, 2006; Zitellini *et al.*, 2009) have also been used – Figure 4.1.

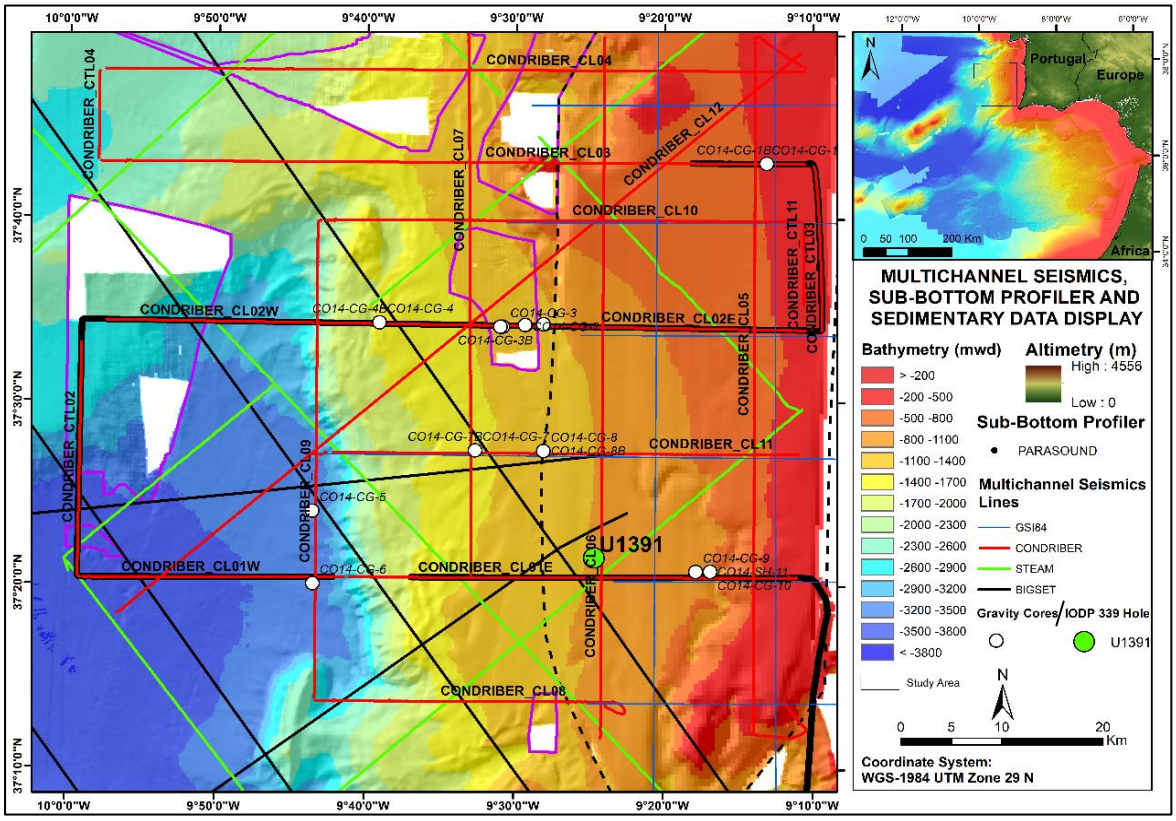

FIGURE 4.1 – General display of multibeam bathymetry, multi-channel seismic, sub-bottom profiles, and sedimentary data.
SWICONDRIMOW bathymetry is composed of three datasets: SWIM outside the dashed and purple polygons; inside black-dashed polygon corresponds to CONDRIBER bathymetry dataset. Bathymetry inside purple polygons refers to MOWER bathymetry dataset. Red lines correspond to CONDRIBER seismic profiles (2014); black lines correspond to BIGSETS seismic profiles (1998); green lines correspond to STEAM seismic profiles (1994) and blue lines correspond to GSI seismic profiles (1984). Thicker black line corresponds to a sequence of very high-resolution Parasound shotpoints. Blank holes correspond to no data. Some artefacts may appear in some bathymetric contacts due to the merging process.

4.1.1 – MULTIBEAM BATHYMETRY DATASET

Three different multibeam swath bathymetry datasets are available for the study area and were used in this work: SWIM dataset (Zitellini *et al.*, 2009), and CONDRIBER and MOWER multibeam bathymetry datasets, acquired during CONDRIBER and MOWER scientific cruises in 2014 (Hernández-Molina *et al.*, 2014a). These three datasets allowed for completing and filling almost completely all the study area with high-resolution bathymetry – designated in this work as SWICONDRIMOW (Figure 4.2).

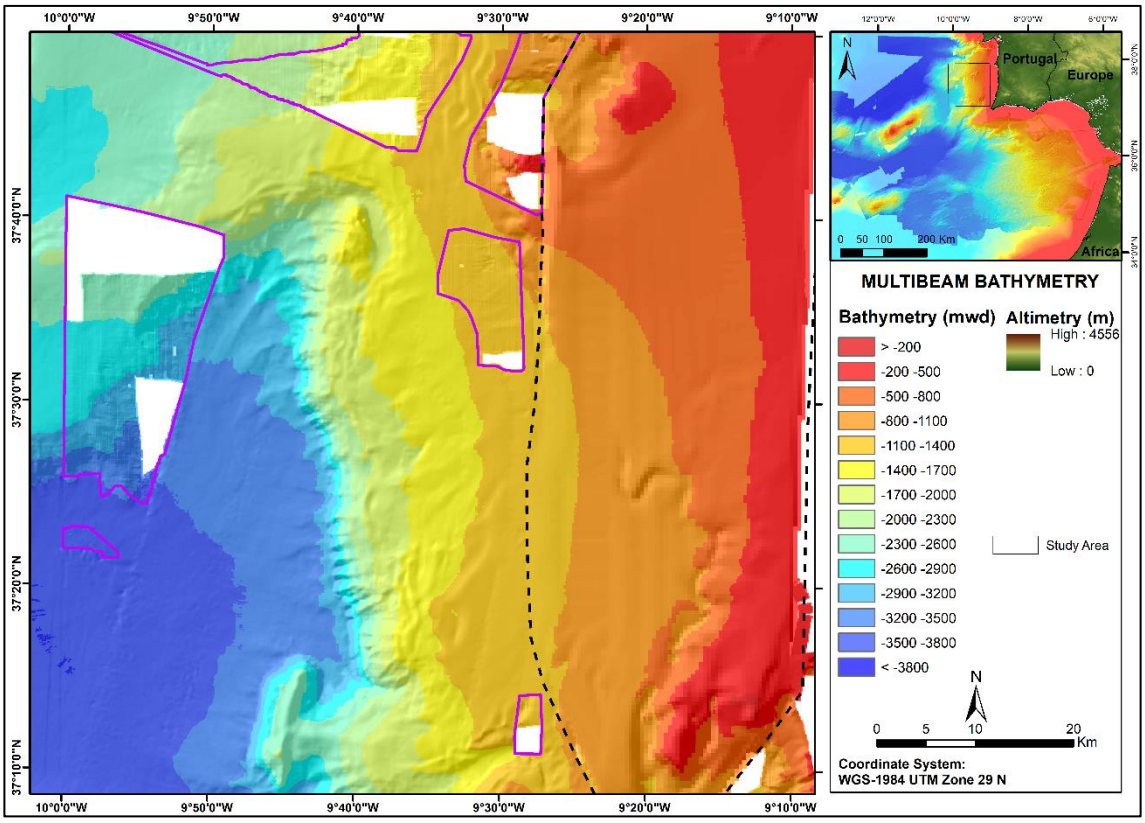

FIGURE 4.2 - SWICONDRIMOW bathymetry. Bathymetry inside purple polygons refers to MOWER bathymetry dataset. Inside black-dashed polygon corresponds to CONDRIBER bathymetry dataset. The remaining bathymetry outside the dashed and purple polygons corresponds to SWIM; Blank holes correspond to no data. Some artefacts may appear in some bathymetric contacts due to the merging process.

The **SWIM** dataset results from nineteen high-resolution multibeam swath bathymetry surveys, performed in the Gulf of Cadiz and SW Iberia, between 1978 and 2006, compiled into a single dataset (Diez *et al.*, 2006) – Table 4.1. This dataset covers an area exceeding 180,000 km^2, ranging from depths of 30 to 5200 mwd (Diez *et al.*, 2006; Zitellini *et al.*, 2009; Valadares, 2012) comprised between Parallels 34ºN and 38ºN and Meridians 12.5ºW and 5.5ºW. These data were acquired using different multibeam systems in these surveys depending on water depth. Multibeam echo-sounders Simrad EM3000 and EM1000 were used for shallow areas, and Simrad EM300, EM12S and EM120 have been used for deep

water areas, while Reson Seabat 8150 was used for intermediate deep waters, in the SWIM survey (Diez *et al.*, 2006) – Table 4.1.

TABLE 4.1 – Bathymetry acquisition surveys of the SWIM compilation. Adapted from Valadares (2012)

SURVEY		YEAR	INSTITUTION	VESSEL	DATA	ECHOSOUNDER
1	SISMER database	1978	IFREMER	R/V Jean Charcot	MB	GIC Seabeam
2		1990	IFREMER	R/V L'Atalante	MB	Simrad EM 12D
3	ESPICHEL	1991	IFREMER	R/V L'Atalante	MB	Simrad EM 12D
4	TASYO	2000	IGME	R/V Hesperides	MB	Simrad EM 12S
5	PARSIFAL	2000	CSIC-CMIMA	R/V Hesperides	MB	Simrad EM 12D
6	CADISAR 1	2001	Univ. Bordeaux	R/V Le Suroît	MB	Simrad EM 12D
7	HITS	2001	CSIC-CMIMA	R/V Hesperides	MB	Simrad EM 12D
8	CADIPOR	2002	Ghent Univ.	R/V Belgica	MB	Simrad EM 1002
9	GORRINGE	2003	IAMC – CNR	R/V Urania	MB	Reason Seabat 8101
10	TV-GIB	2003	UBO	R/V Le Suroît	MB	Simrad EM 12D
11	PICABIA	2003	CSIC-CMIMA	R/V Marion Dufresne	MB	Thompson Sea Falcon 11
12	GAP	2003	Bremen Univ.	R/V Sonne	MB	Simrad EM 120
13	MATESPRO	2004	CGUL	R/V D. Carlos I	MB, BSC	Simrad EM 120
14	CADISAR 2	2004	Univ. Bordeax	R/V Le Suroît	MB	Simrad EM 12D
15	DELILA	2004	IUEM/UBO	R/V D. Carlos I	MB, BSC	Simrad EM 120
16	DELSIS	2005	IUEM/UBO	R/V Le Suroît	MB	Simrad EM 12D
17	SWIM	2005	ISMAR	R/V OGS Explora	MB	Reason Seabat 8150
18	EMEPC data	2005	EMEPC	R/V D. Carlos I	MB	Simrad EM 120
19	HERMES	2006	NOC	R/V Charles Darwin	MB	Simrad EM 12S
20	SWIM	2006	CSIC-CMIMA	R/V Hesperides	MB	Simrad EM 120

MB – Multibeam bathymetry; BSC – BackSCatter data.

CONDRIBER bathymetry was acquired during the CONDRIBER cruise in 2014, on board of NRP Gago Coutinho, using SIMRAD EM 12, EM 1000 and EM 3000 multibeam echo-sounders (Table 4.2) and the seafloor deepness was determined using the SADO acquisition system.

MOWER bathymetric dataset, was acquired during MOWER cruise in 2014, on board of R/V Sarmiento de Gamboa through ATLAS HYDROSWEEP DS multibeam deep-water echo-sounder, with a frequency emission of 14.5 to 16 kHz, emitting until 960 echo-beams per shot in a wideness of 1º per 1º (Hernández-Molina *et al.*, 2014a). This echo-sounder can

reach the seafloor in the range between 10 m and 11,000 m bsl and a maximum resolution of 6.1cm (Table 4.2).

TABLE 4.2 – Characteristics of the bathymetry acquisition surveys of CONDRIBER and MOWER projects

SURVEY		YEAR	INSTITUTION	VESSEL	DATA	MB ECHOSOUNDER
1	CONDRIBER	2014	IDL – Univ. Lisboa	NRP/Gago Coutinho	MB, MCS, SBP	Simrad EM 12, EM 1000, EM 3000
2	MOWER	2014	Univ. Vigo, CSIC, IGME	R/V Sarmiento de Gamboa	MB, MCS, SBP	Atlas HYDROSWEEP DS

MB – Multibeam bathymetry; MCS – Multi-Channel Seismic; SBP – Sub-Bottom profiler.

These three bathymetric datasets (SWIM, CONDRIBER and MOWER) were compiled into a single 100 x 100 m-pixel dataset (SWICONDRIMOW) - Figure 4.2, in order to have a single dataset as much complete as possible, especially in the Sines Drift area (Figure 4.2). The merge of three datasets into one may have created small artefacts especially in the contacts (Figure 4.2), as these datasets were acquired through different multibeam systems and processed through different software suites. The coordinate system used on this bathymetry and on all the cartography is WGS-1984 with the UTM Zone 29N projection system. CONDRIBER and MOWER bathymetry data were firstly published in Teixeira *et al.* (2019).

4.1.2 – MULTI-CHANNEL SEISMIC DATASET

Several Multi-Channel Seismic (MCS) lines (Figure 4.3) have been acquired in the SW Iberia (Table 4.3), since the 1970's, during different scientific surveys. However, only a few of them cross totally the study area and were thus used in this work to identify the in-depth evolution of the geomorphologic features and to assess their relationship with morphotectonic evolution.

The MCS database used in this work consists of MCS profiles acquired in the Alentejo Margin shown in the Table 4.3 (identified with *). Thus, seismic lines acquired during GSI'84; BIGSETS'98; STEAM'94 and CONDRIBER 2014 surveys have been used in this work. The interpretation of the seismic data has been done using a software suite from Landmark™ Corporation, at the Portuguese Institute for the Sea and Atmosphere (IPMA).

TABLE 4.3 – Multi-channel seismic dataset acquired in the SW Iberia. Based in Sartori *et al.* (1994); Steam report (1994); Banda *et al.* (1995); Zitellini *et al.* (2001); Alves *et al.* (2003); Gràcia *et al.* (2006); Thiebot & Gutscher (2006); Valadares (2012); Hernández-Molina *et al.* (2014a).

SURVEY / DATASET	YEAR	RESEARCH VESSEL	SEISMIC SOURCE (AIR GUNS)	STREAMER LENGTH	TOTAL VOL.	CHANNELS	SAMPLING RATE (MS)	SHOOTING INTERVAL	ACQUIRED SEISMICS
***GSI**	1984	MV P.E. Haggerty	1 airgun	3000 m	2775 in.3 (2000 psi)	120	2 ms	25 m	4437 km
ARRIFANO	1992	RV Explora	32 air guns	3000 m		120	2 ms	50 m	-
IAM	1992		36 SWAG air gun	5000 m	120 L. (2000 psi)	192	4 ms	75 m	
***STEAM**	1994	MV Zirfae			10 in.3		25 ms	25 m	1095 km
***BIGSETS**	1998	RV Urania	4 Sodera GI guns	1200 m	150 - 250 in.3	48	4 ms	25 m	2823 km
SISMAR	2000	RV Nadir	1 airgun	-	-	360	4 ms	75-150 m	-
VOLTAIRE	2002	RV Urania	4GI guns	1200 m	-	48	1 ms	50 m	-
SWIM	2006	RV Hesperides	8	-	-	96	2 ms	25 m	-
***CONDRIBER**	2014	RV Sarmiento de Gamboa	4 G-Gun II Sercel airguns	250 m	610 - 910 in.3 (2000 psi)	3	0.5 ms	50 m	785 km

GSI84 lines were acquired in 1984 (Alves *et al.*, 2003), whose energy source was a 2775 in^3 airgun working at 2000 PSI. It was used a 3000-m length streamer with 120 channels of 27 hydrophones each, with a 25 m shooting interval and a sample rate of 0.5 ms.

BIGSETS lines (*Big Sources of Earthquake and Tsunami in Southern Iberia*) were acquired in 1998 (Zitellini *et al.*, 2001) with a 4-airgun – Sodera SSI GI-GUN - system with a total volume of 150–250 in.3 and a shooting interval of 25m and a 1200-m length streamer. Data were recorded through 48 channels at a sample rate of 1 ms (Zitellini *et al.*, 2010).

In 1994, STEAM lines used an airgun with a total volume of 10 in.3, with a shooting interval of 25m and a sample rate of 0.5 ms, using a 3000-m length streamer with 12 channels (Monteiro *et al.*, 1994).

CONDRIBER 2014 seismic dataset has been acquired on board of R/V Sarmiento de Gamboa (Hernández-Molina *et al.*, 2014a) with 4 G-Gun II SERCEL airguns at 3.5m depth, with a total volume of 610 and 910 in.3 (2000 psi) through a shot interval of 50 m, a sampling rate of 0.5 ms and a shooting frequency of 6, 7 and 10 s, using a 250-m length streamer composed by 3 channels and 40 hydrophones each (Hernández-Molina *et al.*, 2014a).

These seismic datasets present different penetrations (GSI and BIGSETS, up to 10 km depth) and (STEAM and CONDRIBER, up to 4 km depth), conferring medium to high resolutions, respectively. Most of these seismic datasets have already been published in the

scope of scientific works other than this thesis. CONDRIBER 2014 dataset has been firstly published in the scope of this thesis, in Teixeira *et al.* (2019).

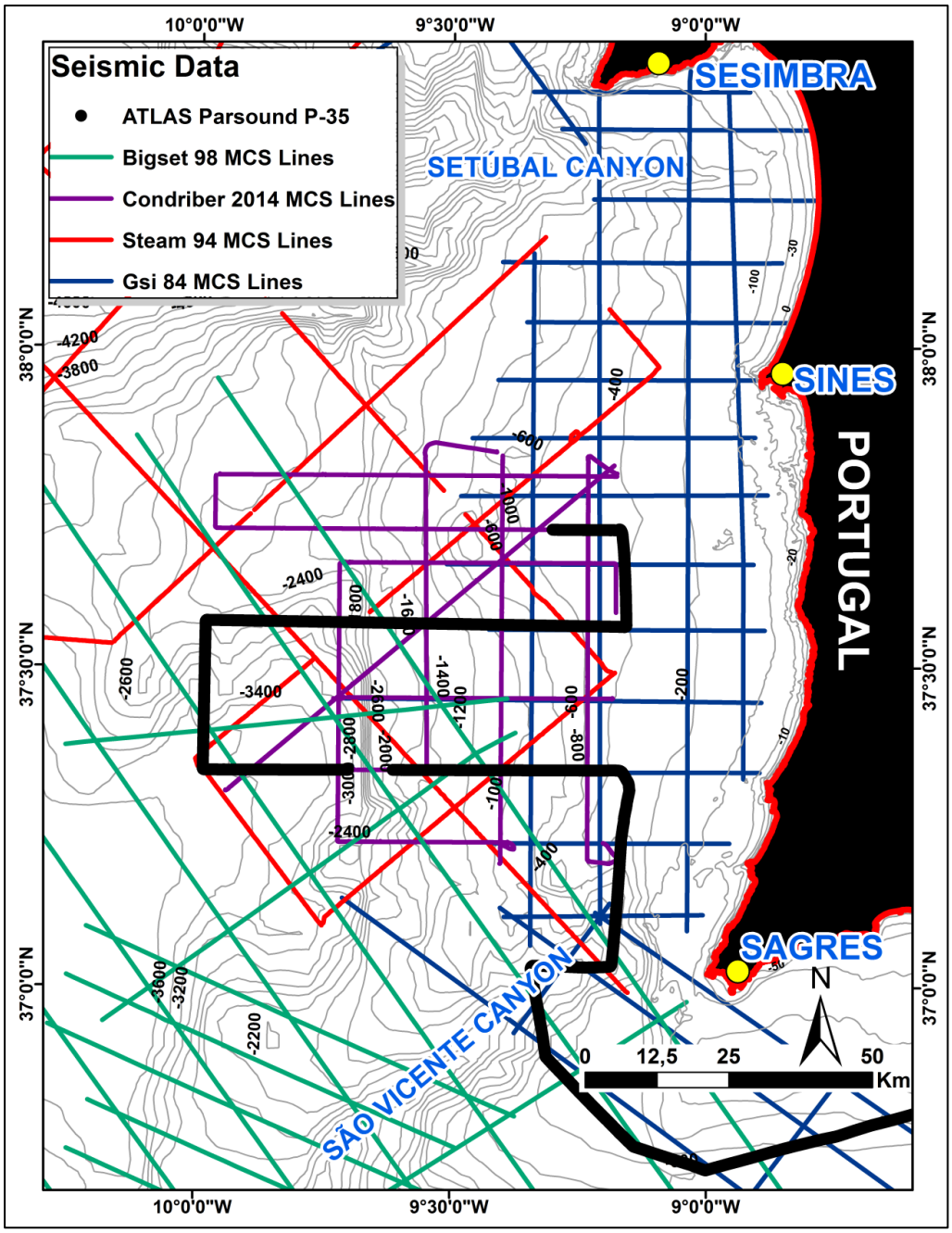

FIGURE 4.3 – Multi-Channel and High-Resolution Seismic dataset used in the present research.

4.1.3 – PARASOUND / SUB-BOTTOM PROFILER DATASET

Sub-bottom profiles (Figures 4.1 and 4.3) were also obtained in the 2014 MOWER/CONDRIBER campaign using a parametric ATLAS PARASOUND-P35 echo-sounder with a primary frequency of 18 kHz and secondary frequency of 4 kHz in a width of 200 m (Hernández-Molina *et al.*, 2014a), with a multi-ping emission, in a maximum of 16 pings per second and a maximum resolution of 6.1 cm. A total of 143 profiles were acquired

in the study area. Sub-bottom profile allows a shallower and more accurate analysis of the upper tens of meters of the sedimentary column, not achievable through multi-channel seismic analysis. Data processing was based on SEG-Y output data through filters, using *Hotshot* © (Hernández-Molina *et al.*, 2014a).

4.1.4 – SEDIMENTS DATASET

The sediments analysed in this work correspond to the unpublished CONDRIBER survey (2014) gravity cores retrieved from the Sines Contourite Drift (SCD) in the Alentejo Margin – Figure 4.4. During this scientific cruise, seventeen gravity cores were retrieved in the area, thirteen for sedimentary, physical, and geochemical analyses and six (those identified with number plus B) for geotechnical assessment.

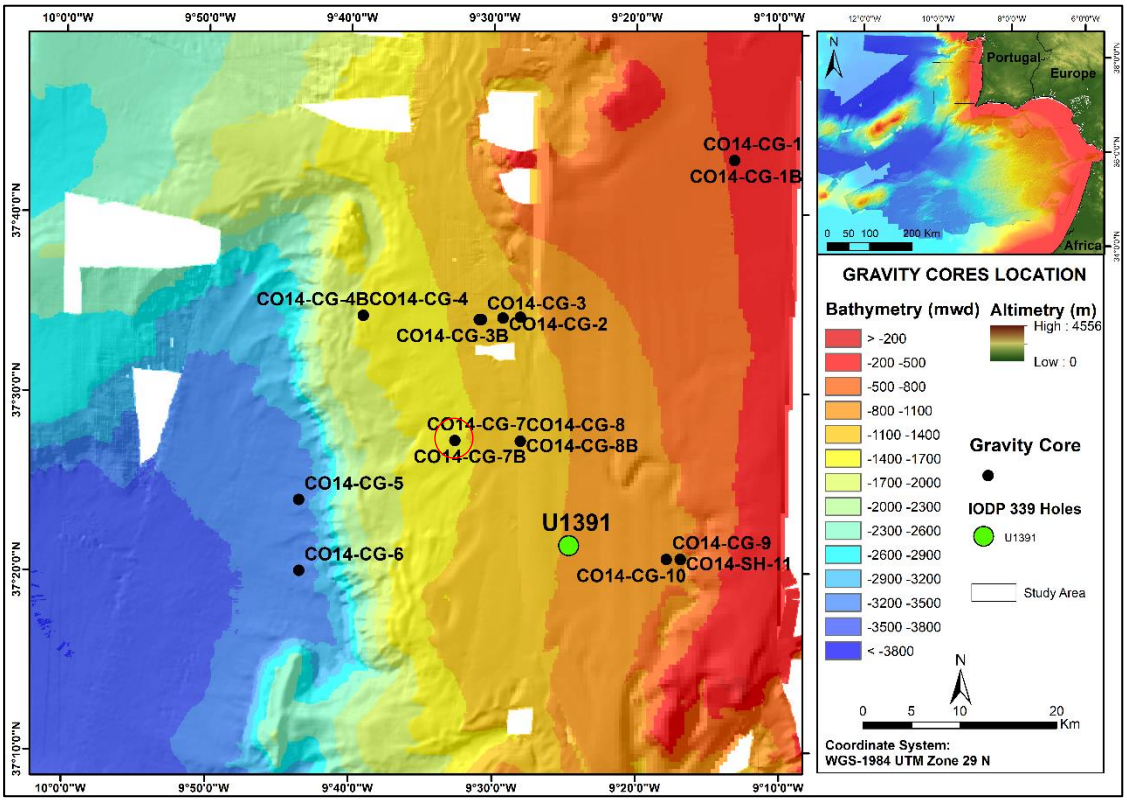

FIGURE 4.4 – Location of the gravity cores retrieved in CONDRIBER survey. Cores CO14-GC-7 and CO14-GC-7B (red circle) are used in this research.

From those cores, two are analysed in this work: cores CO14-GC-07 and CO14-GC-7B (Figure 4.4), whose main description is shown in Table 4.4. CO14-GC-07 is analysed for sedimentary, calcimetric, physical, and geochemical properties, whereas CO14-GC-7B was analysed for determination of geotechnical properties. These cores were retrieved from the SCD, near the Pereira de Sousa Fault (PSF) scarp headwall.

TABLE 4.4 – Coring summary of CO14-GC-07 and CO14-GC-7B gravity cores

Core ID	Coordinates		Depth (mwd)	Total Extension (m)	Seismic Line
	Longitude	Latitude			
CO14-CG-07	9,32,39.44 W	37,27,22.20 N	1425	3.51	CL11 / CL07 / BS07A
CO14-CG-7B	9,32,39.35 W	37,27,22.16 N	1425	3.46	CL11 / CL07 / BS07A

4.2 - METHODS

Several techniques and procedures have been used in order to prepare data to accomplish this work. Methods concerning to bathymetry acquisition and processing, seismic and echo-sounder data, as well as laboratory techniques associated with sediments' analyses – grain size, calcimetry, physical properties, geochemical properties, and geotechnical tests - are explained.

4.2.1 – MULTIBEAM BATHYMETRY

4.2.1.1 – ACQUISITION AND ECHO-SOUNDERS CHARACTERISTICS

Multibeam bathymetry is increasingly required for scientific projects, although a few decades ago single beam echo-sounders were the main tool for the acoustic mapping of the seafloor (Valadares, 2012). With the advent of multibeam bathymetry there was a qualitative and quantitative progress concerning the study of seafloor geomorphology, allowing to sample larger areas with greater detail than it was previously done with single beam. Instant acquisition with better vertical and horizontal resolution was a major improvement, as it has significantly reduced the amount of lines needed to cover an area and the time spent on the survey.

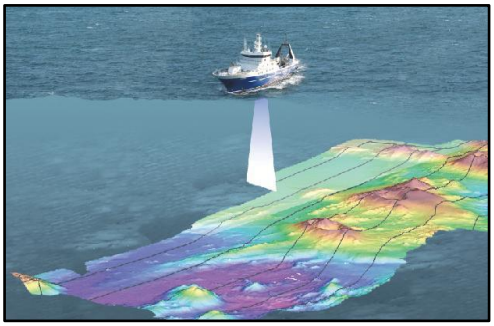

FIGURE 4.5 - Multibeam bathymetry acquisition. Source: gns.cri.nz

Multibeam bathymetry has been acquired using multibeam echo-sounders (Figure 4.5), which record data through the emission of acoustic impulses that travel through the water until reaching the seafloor and then return to the ship where they are recorded by

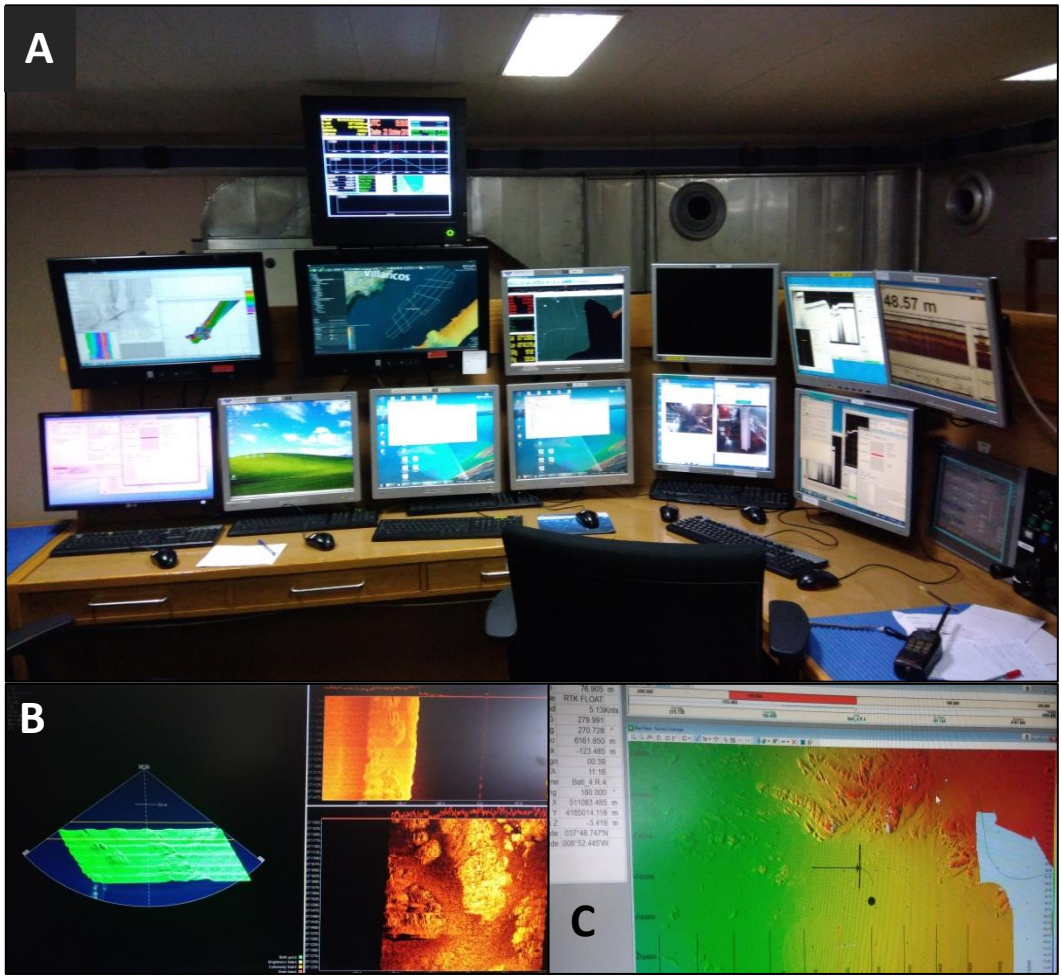

FIGURE 4.6 – (A) - Bathymetry survey room on the RV Sarmiento de Gamboa. (B) – Example of an acquisition panel in a campaign. (C) – Seafloor bathymetry covering map.

transducers (Hernández-Molina *et al.*, 2014a). This is a real-time acquisition method in which the beam returns to the transducers, after recording, and it is transposed to the monitors in the laboratory of the vessel (Figure 4.6). This is usually calibrated by sound velocity vertical profiles (SVP) that measure the speed of sound in the water (Figure 4.7), where depth (D) is equal to the speed of sound in water (S) x time (T) dividing by two: (D = S x T/2). Some multibeam systems can also record the acoustic intensity or backscatter, allowing to record acoustic reflectivity and sonar imagery of the seafloor.

FIGURE 4.7 – Sound velocity profiler (SVP), before measuring the sound velocity in the water.

The newly acquired CONDRIBER and MOWER multibeam bathymetry datasets have been respectively acquired using two different acquiring systems: Simrad EM© in NRP Gago Coutinho and Atlas HYDROSWEEP DS© in RV Sarmiento de Gamboa.

Simrad EM 3000 echo-sounder operated at a frequency between 11.25 and 12.6 kHz, with 191 beams covering 150º with a width of 1º, whereas Atlas HYDROSWEEP DS echo-sounder operated with an emission frequency of 14.5 to 16 kHz, emitting 960 beams by shot and a width of 1º. This echo-sounder operates from 10 to 11,000 mwd obtaining a maximum resolution of 6.1 cm.

4.2.1.2 – MULTIBEAM PROCESSING

After the acquisition (Figures 4.5, 4.6 and 4.7), raw data has been corrected because of external noise due to ship's balancing or shaking, heading, and irregularities in the incidence angle (Hernández-Molina *et al.*, 2014a). In this sense, filtering data is essential to obtain a good quality Digital Elevation Model (DEM), afterwards.

Raw data were processed using different software suites: SWIM dataset was processed using *CARAIBES*® system (Bourillet *et al.*, 1996), whereas CONDRIBER and MOWER were processed through *CARIS-HIPS*® (Caris-Hips, 2013).

CARAIBES is a software that allows seabed mapping and characterisation, enabling to process bathymetry and backscattered signal data sets from the multibeam echo-sounders (Seabeam, Simrad, Atlas, Thomson) and sidescan sonar images (Thomson, Egg, Dowty). All the processing steps were handled, from real time data acquisition and archiving to final seabed map production (Le Gal and Edy, 1997).

MOWER bathymetry was processed with CARIS-HIPS (Hydrographic Data Processing System – Caris-Hips (2013)). This is a software package that allows filtering bathymetric data through statistical algorithms.

Before processing the bathymetric data with CARIS-HIPS, some previous procedures were done. Thus, before filtering, it was created a ship file in which it is contained the corrections of roll, pitch, swath and positioning of the multibeam probe facing the ship's axis. After this, it is important to create a new project and configure the data structure and convert raw data in Hydrographic Data Cleaning System (HDCS) and then load tide data. It is then necessary to combine positioning and depth data through Total Propagated Uncertainty

(TPU), which applies Horizontal TPU (HzTPU) and Depth TPU (DpTPU) values to each sounding in the observed depths. The following step is the creation of a surface using CUBE. This process uses sounding propagation along with disambiguation to create and select hypotheses. The sound velocity profile is essential for the correction of the sound in water through a sound velocity correction. Then, data were ready for filtering (Caris-Hips, 2013; Hernández-Molina *et al.*, 2014a).

This filtering process can be either manual or automatic, being generally done first automatically and then manually (Valadares, 2012). These filters essentially constitute limits

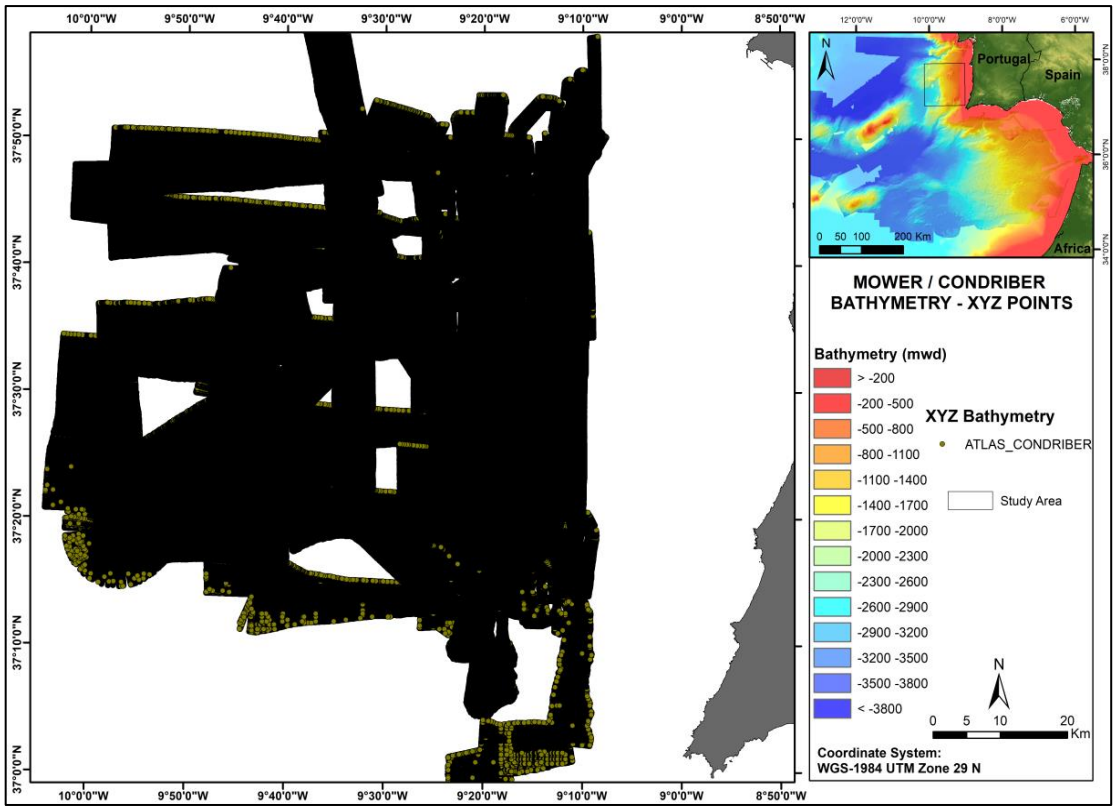

FIGURE 4.8 – XYZ points grid of CONDRIBER and MOWER multibeam bathymetry acquisitions

and conditions imposed to the data to eliminate the outlier elements and try to fit data as much as possible to the reality. After the filtering process and considering only the validated pings, it was generated a regularly spaced *XYZ* points grid (Figure 4.8).

4.2.1.3 – DEM PROCESSING

After data has been acquired and processed into *xyz* points (Figure 4.8), it was necessary to proceed to the generation of a bathymetric surface (DEM). This operation is very important because the quality of a lot of subsequently derived quantitative descriptors

depends on it. To obtain the best-fitted model to the reality it is essential to use the most adequate interpolation methods. There are several interpolation methods, which are more or less suitable for some types of analyses. Thus, depending on the aim of the study and on the goals to achieve, it is essential to select the interpolation method that best adapts to generate the DEM (Figure 4.2).

4.2.1.3.1 – INTERPOLATION METHODS

Interpolation can be either a raster- or a vector-based process, which consists of using points with known values to estimate values at other unknown points. It can be used to predict unknown values for any geographic data point, such as elevation, rainfall, chemical concentrations, and noise levels (Bekele *et al.*, 2003). In the process of creating digital elevation models there are several methods by which models can be derived from original bathymetry data (Table 4.5). In accordance with Smith *et al.* (2015), different interpolation methods present diverse characteristics depending on the purpose for which they are suitable for. In other words, each model has pros and cons depending on what it is intended to be done.

Depending on the dataset's dimensions it can be used different interpolation methods. For denser datasets the most common used methods are *Inverse Distance Weight* (IDW), *Natural Neighbour* and *Spline* (e.g., Valadares, 2012). Smith *et al.* (2015) point out that *IDW* and *Natural Neighbour* do not generate extrapolation, are fast executing the interpolation, are exact and are good for dense datasets (Table 4.5). *Nearest neighbour* is a fast and exact method that does not provide extrapolation either and is mostly used for datasets with missing values, while *Spline* is also fast in the execution of the interpolation and it is also exact and allows smoothing. *Spline* is a procedure that can be incorporated in other methods. *Kriging* is also frequently used and is especially suited for geostatistical models, sometimes providing extrapolation and prediction error estimates. *Triangulation with linear interpolation* is a Delaunay triangulation-based procedure, which is fast in terms of speed of execution and exact. *Topo to Raster* or *Topogrid* is also fairly used for topographic analysis onshore. This method, slow in execution, is based in iterative finite difference methods and interpolates hydrologically "correct" grid from sets of points, lines and polygons corresponding to the process of estimation of unknown values of an area through known values in neighbouring areas (Aronoff, 1989). The model is based on Hutchinson's *ANUDEM*™ model (Hutchinson,

1988). This model requires contour vector data as input (Smith *et al.*, 2015), aiming to the continuity on the DEM's surface and coherence in hydrological analyses.

TABLE 4.5 – Interpolation methods. Adapted from Smith *et al.* (2015)

Method	Speed	Type	Comments
Inverse distance weighting (IDW)	Fast	Exact, unless smoothing factor specified	Tends to generate bull's eye patterns. Simple and effective with dense data. No extrapolation. All interpolated values between data points lie within the range of the data point values and hence may not approximate valleys and peaks well
Natural neighbour	Fast	Exact	A weighted average of neighbouring observations using weights determined by Voronoi polygon concepts. Good for dense datasets. Typically, implementations do not provide extrapolation
Nearest neighbour	Fast	Exact	Most useful for almost complete datasets (e.g. grids with missing values). Does not provide extrapolation
Kriging -Geostatistical models (stochastic)	Slow/ Medium	Exact if no nugget (assumed measurement error)	Very flexible range of methods based on modelling variograms. Can provide extrapolation and prediction error estimates. Some controversy over aspects of the statistical modelling and inference. Speed not substantially affected by increasing number of data points. Good results may be achieved with <250 data points
Triangulation with linear interpolation	Fast	Exact	A Delaunay triangulation-based procedure. Requires a medium-large number of data point to generate acceptable results.
Spline functions	Fast	Exact (smoothing possible)	Available as a distinct procedure and incorporated into several other methods. Bicubic and biharmonic splines are commonly provided (see for example, Sandwell, 1987)
Topogrid/Topo to Raster	Slow/ Medium	Not specified	Based on iterative finite difference methods. Interpolates a hydrologically "correct" grid from a set of point, line and polygon data, based on procedures developed by Hutchinson (1988, 1989, 1996). Requires contour vector data as input. Based on Hutchinson's ANUDEM program

4.2.1.3.1.1 – IDW

Inverse Weighted Distance (IDW) was the interpolation method used in this work, because there is a dense dataset and this method is fast executing the interpolation and does not generate extrapolation. IDW - Figure 4.9 - is a raster-based interpolation method and one of the most used deterministic models in spatial interpolation (Smith *et al.*, 2015), assuming that the attribute values of any given pair of points are related to each other, but they are inversely related to the distance between the two locations (Lu and Wong, 2008). This model assumes that the value of the unknown points is the weighted average of the neighbouring known values, while the weights are inverse to the distance between known and unknown values. Notwithstanding this, this decline in the relationship is not simply proportional to

distance (Fotheringham and O'Kelly, 1989). To overcome this problem, Lu and Wong (2008) suggest that the value of the weighting parameter should vary according to the spatial pattern of the known points in the neighbourhood. This model is simple and effective when there are dense datasets, where no extrapolation exists and all interpolated values between points are comprised inside the range of the data point values (Smith *et al.*, 2015).

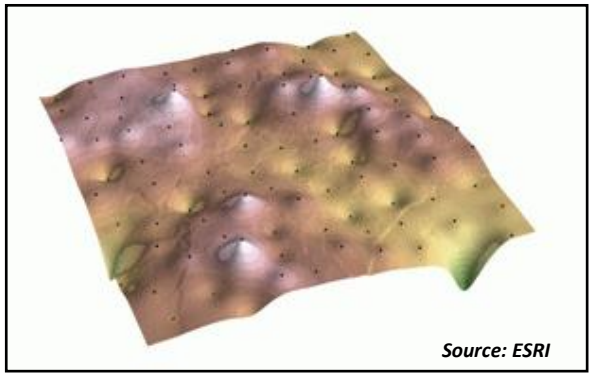

FIGURE 4.9 – IDW interpolated.

4.2.1.3.2 – BATHYMETRIC DERIVATIVE QUANTITATIVE PARAMETERS

Having the bathymetry mosaic for the whole area some seabed quantitative descriptors (Figure 4.10) were generated from the DEM to be possible a complete further morphological analysis.

4.2.1.3.2.1 – SHADED RELIEF (HYPSOMETRY)

Shaded relief (Figure 4.10A) represents the hypsometry through a hillshade map, providing a quick comprehension of the topography (Horn, 1981) of an area. This map highlights the relief and allows a more realistic perception of the real shape of the slopes. It is useful when used toghether with the other parameters, giving a more realistic view of the bathymetric envelope.

4.2.1.3.2.2 – SLOPE

Slope (Figure 4.10B) corresponds to the topographic dip of the surface with respect to a horizontal plane (Smith *et al.*, 2015). According to the notions mentioned by Horn (1981), slope is the amount of rise over run in some direction, i.e., the steepest path from one point to another. Slope is determined for a place where a local coordinate system is taken, and the cell centre has *x* and *y* values equal to zero, through the following equation:

EQUATION 4.1

$$S_t = tan^{-1}\left(\sqrt{e^2 + d^2}\right)$$

In terms of GIS it was computed the maximum rate of change between each cell and the neighbours in a 3 x 3 window around a centre cell. In GIS, slope is calculated in degrees according to the following algorithm/equation:

EQUATION 4.2

$$Slope = ATAN\left(\sqrt{\left(\left[\frac{dz}{dx}\right]^2 + \left[\frac{dz}{dy}\right]^2\right)}\right) * 57.29578$$

Where *dz*, *dx* and *dy* are directional derivatives (Burrough and McDonell, 1998). Through this equation slope was determined for the study area, using GIS.

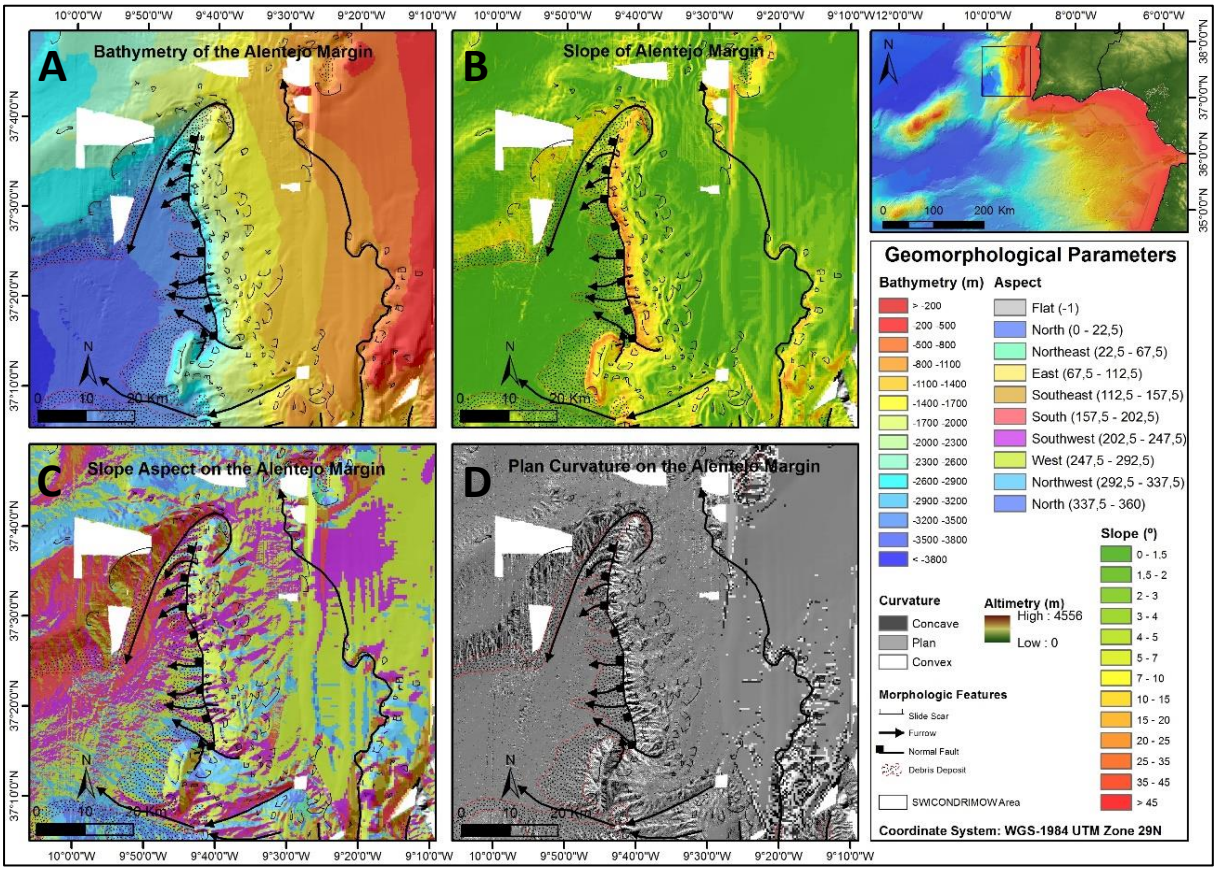

FIGURE 4.10 – Geomorphological parameters of the Alentejo Margin – quantitative descriptors derived from the DEM. (A) – Shaded relief (hypsometry); (B) – Slope angle; (C) – Slope aspect; (D) – Slope curvature.

4.2.1.3.2.3 – ASPECT

Slope aspect (Figure 4.10C) is the directional component of the gradient vector that corresponds to the direction of the maximum gradient of the surface at a given point (Smith *et al.*, 2015), and corresponds to a morphological feature that identifies the main downslope faces of a surface, being calculated for each cell through the DEM.

Generally, Aspect has 8 classes of 45º each, corresponding to the main cardinal directions. According to Smith *et al.* (2015), the equation for Aspect calculation is the following:

EQUATION 4.3

$$A = 270 - \frac{360}{2\pi}\, tan^{-1}\left(\frac{\partial z}{\partial x}, \frac{\partial z}{\partial y}\right)$$

Where, ∂x, ∂y, ∂z are directional derivatives. There are several ways to generate this parameter, depending on the model or software to work with. This parameter was derived according to the method of Horn (1981), which uses all the 8 immediate neighbours of z*, the resulting equation is as follows (equation 4.4). This method, used by GIS implies that for the x-direction the directly east and west positions are weighted 2 whereas the remaining 4 directions (NE, NW, SE, and SW) are weighted 1; the same process is used for the y-direction where north and south points are weighted 2 and the others are weighted 1.

EQUATION 4.4

$$A = tan^{-1}\left(\frac{e}{d}\right)$$

Where, *e* and *d* are constants to be estimated. With this formula, it was generated the aspect of the study area.

4.2.1.3.2.4 – CURVATURE

Curvature (Figure 4.10D) is a terrain parameter that refers to the way irregularities express in the geoid: terrain can be irregular by being depressed, concave relating to the plan, or by being elevated and thus convex relating to the plan. The surface can also be regular and hence can be plan, although this last condition is not very common, especially in very active areas due to erosion activity.

In GIS, both profile and planar curvature are calculated through Zevenbergen's equations (Zeverbergen and Thorne, 1987). This parameter is calculated in a cell-by-cell basis through a fourth-order polynomial, which can be expressed by the following equation:

EQUATION 4.5

$$Z = Ax^2y^2 + Bx^2y + Cxy^2 + Dx^2 + Ey^2 + Fxy + Gx + Hy + I$$

In a 3 x 3 cell basis, the curvature is calculated by the coefficients of all the cells, where elements A to I correspond to the elevation of each cell. In this sense, the output of the Curvature tool is the second derivative of the surface as expressed by the equation 4.6:

EQUATION 4.6

$$Curvature = -200\,(D + E)$$

Where, *D* and *E* are derivatives. Curvature can be also analysed both as plan curvature and as profile curvature. According to Smith *et al.* (2015), *planar curvature* is the shape of the surface viewed as if a horizontal plane has sliced through the surface at the target point. It is essentially the curvature of a contour line at height *z* and location (*x, y*).

For the calculation of the *planar curvature* different methods are used. In the case of *ArcGIS*©, the suite used here to generate these surfaces, it is used a fourth order surface model:

EQUATION 4.7

$$K_{pl} = \frac{-200\,(dh^2 + eg^2 - fgh)}{g^2 + h^2}$$

Profile curvature is the form of the surface near the sample point contained within the vertical plane. It represents the rate of change of the slope at that point in the vertical plane, and is negative if the shape is concave, positive if the shape is convex and zero if there is no slope (Smith *et al.*, 2015). To represent this parameter in a GIS system, the equation used for this purpose is:

EQUATION 4.8

$$K_{pr} = \frac{200\,(dh^2 + eg^2 - fgh)}{g^2 + h^2}$$

Where, *d*, *e*, *f*, *g* and *h* are coefficients of both quadratic and quartic forms (Smith *et al.*, 2015).

4.2.2 – SEISMIC DATA: ACQUSITION AND PROCESSING

The seismic lines used in this work perform a varied datset (Table 4.3) with diverse sources, acquisition and processing methods. All the seismic data have been through several steps during the acquisition and the processing procedures. Acquisition was fulfilled according to the parameters exposed in subsection 4.1.2 and Table 4.3. Processing also varied among the different datasets.

GSI 84 lines were processed through some steps: amplitude recovering was done by spherical divergence. Then, CMP (common midpoint) stack has been done by loading geometry and afterwards data were deconvoluted and migrated. It was applied a time-variant filtering of 15-65 *Hz* at 500 ms, 10-50 *Hz* at 2000 ms and 5-40 *Hz* at 3000 ms (Alves *et al.*, 2003).

The **STEAM 94 MCS lines** have been processed using *PROMAX*© software, in which it was defined the geometry of the system and were applied filtering frequencies of 60-90-400-600 kHz (Monteiro *et al.*, 1994). After, velocities were defined along time (depth) and data were stacked. Velocity was analysed through adequate peaks that were picked in function of the apparent velocity, allowing to show how CDP – common depth point – reacts when reflectors are aligned. Normal moveout (NMO) was removed and data was stacked according to the previously determined velocities.

BIGSETS 98 MCS lines have been processed using both *PROMAX*© and *DISCO-FOCUS*© software suites (Zitellini *et al.*, 2010). After recording data in SEG-D format, the processing flow began with the export of the headers and the calculation of a CDP. Data was input into the program in SEG-D format, using both 8048 and 8058 format codes. Then data was re-sampled at 4 ms. This process allows a consistent visual tie between different seismic surveys, according to Valadares (2012). After, it was applied a noise filter (band-pass filter: 6-9-58-62.5 Hz). This was to homogenize with the noise coming from the streamer (Zitellini *et al.*, 2010). This noise may come with the same or the inverted signal due to the multiple sources. Then, traces were edited to fix polarity reversals, and hand statics (-20 ms) were applied, as they are essential for converted waves, especially those whose receiver statics are larger than 100-200 ms (Yilmaz, 1987). The next step consisted in the loading of geometry with a common midpoint (CMP) folding between 6 or 16 or 24 (100 m, 37.5 m, 25 m distance between shots). Interactive Velocity Analysis was the next step, which is important for the efficient parameter testing that is crucial for processing sequences as filtering, deconvolution

and gain, but also for providing efficiency on the picking events, as first breaks on shot records for refraction statics, reflection times on migrated sections, and velocity functions from velocity spectra (Yilmaz, 1987). NMO correction and stacking, followd by Top mute and minimum phase predictive deconvolution (decon operator length: 300 ms; prediction distance: 20 ms) were applied. Time- and space-variant Ormsby band-pass filters have been applied. True Amplitude Recovery and Trace Mixing algorithm have been used for spherical spreading and for attenuation of valuable laterally changing information. Finally, automatic gain control has been used in this processing method (Zitellini *et al.*, 2010).

CONDRIBER 2014 MSC lines have been acquired in the MOWER/CONDRIBER cruise in 2014, through the acquistion system *DELF*© and processed in the Instituto de Ciencias Marinas of Barcelona (ICM-CSIC). The acquisition data were output in SEG-Y files.

These data processing started with the extraction of the original navigation of each shot and channel through *export headers* command from *Seisee*© software (Hernández-Molina *et al.*, 2014a). This was followed by the CDP calculation for each profile, using *CDP3* module (M. Farran, ICM-CSIC). The result was an ASCII file that can be imported to a SEG-Y file with shot, channel, CDP and UTM coordinates of both each shot and cdp.

Due to the presence of many noise sources and the existence of both same-signal and inverted-signal noises, it was crucial to apply a noise filter. Same-signal noise would be auto-eliminated itself when polarity of a channel is changed and summed, but this not always occurs due to differences in the magnitude of both channels (Hernández-Molina *et al.*, 2014a). Inverted-signal noise has been eliminated through a Matlab script (*Seg4King*) that replaces the values, in a certain time of the trace, when these are higher than a certain magnitude of the previous and next traces, by the mean of these.

Further processing has been done using *Hotshot*©. This software has been used for the creation of georreferenced bitmaps that allow the ulterior digitalization of the seafloor for the consequent elimination of the water column. Subsequently, it has been switched the signal (using *VNEG*) of the reflections from channels 2 and 3, which had an inverted polarity when compared with the reflections of the channel 1.

After, the *RABAL* function was applied to equalize the channels and shots plus a band-pass filtering to eliminate low frequencies (< 30 Hz). Subsequently, several progressive band-pass filters were applied downwards from the seafloor:

- 0 ms: 75.0 – 240.0 Hz
- 100 ms: 25.0 – 180.0 Hz
- 1000 ms: 25.0 – 100.0 Hz
- 9000 ms: 20.0 – 100.0 Hz

Then, it was applied a MUTE function to eliminate the signal below 0.4 s in the channel 3. For profiles with sedimentary cover it was also obtained another profile (version HF) with a different sequence. The upper 150 – 200 ms, below seafloor, of channels 1 and 2 have been removed to highlight the high frequencies of channel 3. Then, SORT and STACKM functions have been applied to the traces through the CDP in the upper lines and through the dominant shot in the further lines.

It has been applied another equalization to the traces resulting from the stack (BALANCE) and a resampling at 1 ms, while the originals were sampled at 500 μs. To normalize the traces, this was followed by an Automatic Gain Control (AGC) with a window of 0.7 seconds. Then, a SHIFT was applied to eliminate the first 50 ms of the file and to allow the synchronization between the register and the trigger. Afterwards, the SEG-Y file has been written (Hernández-Molina *et al.*, 2014a).

4.2.3 – SEDIMENTOLOGICAL ANALYSIS

The sedimentary analyses undertaken in this work have been done on the 350-cm long gravity core CO14-GC-07. Several analyses and tests have been performed for the determination of grain-size and calcimetry.

4.2.3.1 – GRAIN-SIZE ANALYSIS

As the grain-size analysis is a destructive test (Figure 4.11), the work has been carried out on the working half of the gravity core CO14-GC-07. Sediments were firstly sampled every 5 cm on ~10 g of bulk samples. After being retrieved from the core, the sediment samples were frozen at -20 ºC, and then freeze-dried to eliminate the wetness and to break the internal chains of the main minerals created by freezing, inside the sediment. This low temperature dehydration process consisted of removing the ice by sublimation through low pressures in a vacuum-chamber. The sediment sample becomes dried and with no internal chains.

The next step consisted of a "*chemical attack*", which consisted on the elimination of the organic matter of the sediments, through a combination of hydrogen peroxide (H_2O_2) and ammonia (NH_3O). Four consecutive dosages of 25, 50, 50 and 75 ml were added to each sample for 24 hours. After this, sediment samples were submitted to a 60 ºC warm water bath with distilled water (Figure 4.12). This process aimed at removal of molecular hydrogen acquired during the *chemical attack*.

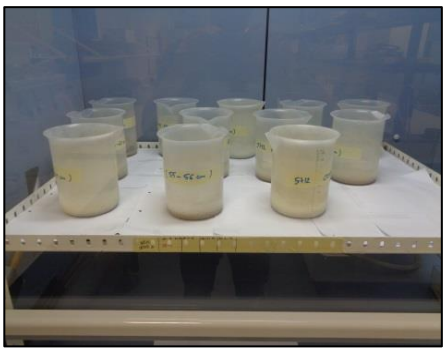

FIGURE 4.11 – Samples with H_2O_2 and NH_3O.

FIGURE 4.12 – Water-bath

FIGURE 4.13 – Ceramic candle filters

FIGURE 4.14 – Samples decanting

After this, the sediments had six consecutive washes with 1000 ml of distilled water, using ceramic candle filters (Figure 4.13), to purge the hydrogen peroxide and the ammonia. Then, the samples were left decanting (Figure 4.14). Samples were then sieved in order to obtain the fraction < 2 mm for further grain-size analysis in the grain-size analyser.

FIGURE 4.15 – LS 13 320 laser diffraction particle size analyser at IPMA

This analysis has been carried out in the sedimentology and micropaleontology laboratory of the Marine Geology Division at the Portuguese Institute for the Sea and the

Atmosphere (IPMA) by using a LS 13 320 Laser Diffraction Particle Size Analyser – COULTER® - Figure 4.15.

4.2.3.2 – CARBONATES ANALYSIS

Carbonate and organic carbon contents determination was done each 5 cm on sediment samples taken from the working half of the CO14-GC-07. Cylindrical sediment samples of 1 cm^3 (Figure 4.16) were weighted both in wet and dry states thus allowing to determine the wet and dry unit weights. To achieve the dry state the samples were kept in the furnace for 24 hours.

FIGURE 4.16 – Sediment sampling

After this, the samples were grinded using a Pulverisette 7® grinder (Figure 4.17) during 5 minutes at 600 rotations per minute. Then, each sample was divided into two sub-samples. One subset was directly run in a TruSpec® Micro CHNS LECO elemental analyser (Figure 4.18) to measure the total carbon content (TC), as weight percent (wt%). The other subset was subjected to combustion during 8 h on predefined steps of 1 h at 200 and 300 °C and 3 h at 400 °C, to remove the total organic carbon (TOC) and analysed for inorganic carbon content (IC; wt%). This corresponds to the carbonate carbon and is referred to as $CaCO_3$ in the text. The TOC was quantified by the difference between TC and IC (TOC = TC − IC). The carbonate (wt%) was calculated as the product of the inorganic carbon concentration by the factor of 8.332, as determined by Yamamoto *et al.* (2000). For each level the accepted value is the mean of 3 replicates unless the first two are equal to the millesimal. The analytical precision was <1% of relative standard deviation.

FIGURE 4.17 – Pulverisette 7 grinder - IPMA

FIGURE 4.18 – Micro CHNS LECO elemental analyser - IPMA

This work has also been undertaken in the Sedimentology and Micropaleontology laboratory of the Marine Geology Division at the Portuguese Institute for the Sea and the Atmosphere (IPMA).

4.2.4 – PHYSICAL AND GEOCHEMICAL PROPERTIES

Physical and geochemical properties of marine sediments are important indicators for slope stability and for palaeo-seismicity analysis (Gràcia *et al.*, 2010), for example. The analysis of marine sediments' physical and geochemical properties, comprising water content, sediment bulk density, and acoustic properties, for example, is done through core samples using different logging techniques (Zolitschka *et al.*, 2001).

The advent of automatic devices for the analysis of physical and geochemical properties brought the possibility of non-destruction of sediments and rapid analysis in a continuous way (Weaver and Schultheiss, 1990) with high resolution (Jansen *et al.*, 1998; Croudace *et al.*, 2006; Rothwell and Frank, 2006; Thomson *et al.*, 2006). These automated devices - Multi-Sensor Core Logger sensors (MSCL) – can measure both physical and geochemical properties – through X-ray fluorescence (XRF) sensors. Depending on the devices, MSCL analyses may be both on whole and split cores, whereas XRF analyses only accept split cores. Core splitting is an operation that affects the quality of the core, especially image data and all the measurements made on the split core's surface. It is very useful for further testing and high-resolution imaging with MSCL-CIS, colour spectrometry, X-ray fluorescence or magnetic susceptibility done through MSCL-XYZ and MSCL-XZ (Geotek, 2014).

Since the early 1980's, several works have already used different MSCL systems for physical analyses, e.g. (Schultheiss *et al.*, 1987; Weber *et al.*, 1997) and X-ray fluorescence (XRF) sensors for geochemical analyses, e.g. (Jansen *et al.*, 1998; Migeon *et al.*, 1998; Croudace *et al.*, 2006; Richter *et al.*, 2006; Sakamoto *et al.*, 2006; Thomson *et al.*, 2006).

In this work, physical and geochemical analyses have been conducted on the archive-half sediments of the CO14-GC-07 gravity core. Physical analyses were performed through a sampling-step of 1 cm using a MSCL at the University of Vigo, Spain. Geochemical analyses were performed through a sampling-step of 0.5 cm at the CACTI (*Centro de Apoio Científico e Tecnolóxico á Investigación*) of the University of Vigo.

4.2.4.1 – MULTI-SENSOR CORE LOGGER (MSCL)

Multi-sensor core logger (MSCL) is an automated logging device that allows the analysis of numerous different physical and geochemical properties of the sediments providing continuous measurements of parameters like gamma-ray attenuation, P-wave travel time and magnetic susceptibility on marine sediment cores (Weber *et al.*, 1997), by logging material at rates of 12 m/hr with sampling intervals up to 1mm in whole or split cores with 50

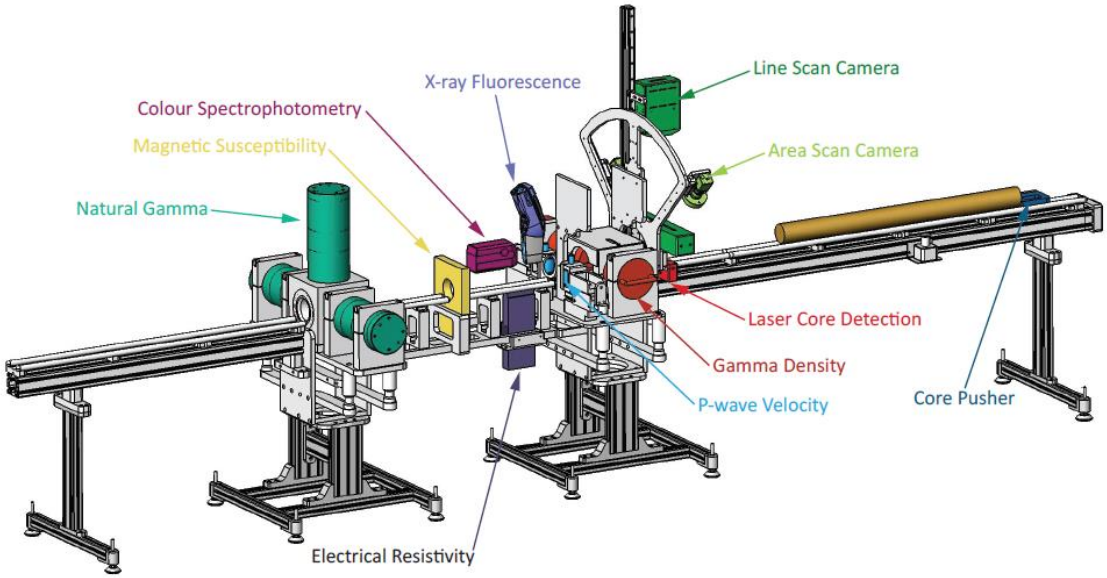

FIGURE 4.19 - MSCL schematic layout in whole core horizontal logging mode. Credits to Geotek.

to 150 mm in diameter cut into sections up to 1.5 m long. However, many other measurements can be done using this logging device. MSCL systems (Figure 4.19) - enable a suite of geophysical measurements to be obtained rapidly, accurately and automatically on sediment or rock half-cores (Figure 4.20).

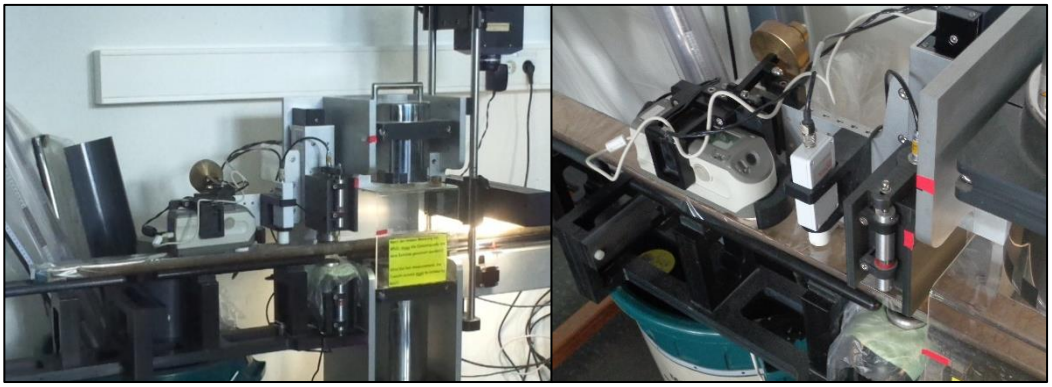

FIGURE 4.20 – Multi-Sensor Core Logger in activity, measuring physical properties in half-core sediments, at MARUM - Universität Bremen.

The different MSCL systems and sensors can cover a wide range of parameters that can be measured with detail (Weber *et al.*, 1997). MSCL can have several applications, allowing the analysis of high-resolution visual archives; chemistry; impedance, permeability, and water content profiles; seismic stratigraphy; synthetic seismograms; rapid assessment of core quality as well as rapid inter-core correlations; data rescue from existing core repositories and ice core logging (Geotek, 2014).

4.2.4.2 – PHYSICAL PROPERTIES - MSCL ANALYSES

There are various logging techniques to assess physical sediment properties using different and highly specialized sensors. Core sediment physical properties were tested and some important parameters as gamma-ray density, P-wave velocity, magnetic susceptibility, and electrical resistivity have been determined.

4.2.4.2.1 – GAMMA-RAY DENSITY

Gamma-ray attenuation is a method for measuring the wet bulk density, an elementary physical parameter of sediment cores (Zolitschka *et al.*, 2001). The main principle of this method consists in the attenuation of gamma rays, whose source is ^{137}Cs in a lead container, as they pass through sediments. According to Zolitschka *et al.* (2001), there are three main attenuation processes that may alter the intensity of gamma rays: photoelectric absorption, pair production and predominately Compton scattering that consists of partial energy loss due to the scattering of incident photons by electrons. The density (ρ) of a material measures how tight the matter is packed together and is given by the ratio of its mass (m) to its volume (V) being measured in kilograms per cubic metre - kg/m^3 (Geotek, 2014). Gamma-ray attenuation measurements allow the calculation of bulk density (ρB):

EQUATION 4.9

$$\rho B = (1/-\mu d)\ ln\ (I/I_0)$$

Where μ is the Compton attenuation factor (0.0795 cm^2/g); I is the intensity of gamma rays; I_0 the source intensity of gamma rays; d is the thickness.

Besides sediment's wet bulk density, gamma-ray density is used to estimate fractional porosity and fractional porosity in completely saturated samples (Zolitschka *et al.*, 2001).

That parameter can be calculated from bulk density whenever sediment is fully saturated and when mineral and fluid densities (ρg and ρf) are known (Equation 4.10):

EQUATION 4.10

$$\phi = (\rho g - \rho B)/(\rho g - \rho f)$$

The main purpose of wet bulk density is to measure the density and porosity of samples in order to better characterize the core lithology (Zolitschka *et al.*, 2001).

4.2.4.2.2 – FRACTIONAL POROSITY

Fractional porosity corresponds to the ratio of the void-space volume to the total volume of a material. This is a secondary calculated property that has been determined by the MSCL through bulk gamma density (γ), mean mineral grain density (γg) and air density (γa) (Bodwadker and Reis, 1994), as follows:

EQUATION 4.11

$$FP = \frac{\gamma g - \gamma}{\gamma g - \gamma a}$$

4.2.4.2.3 – P-WAVE VELOCITY

For a better understanding of the physical nature of seismic velocity and acoustic impedance of the reflectors it is applied the ultrasonic compressional wave (P-wave) method (Zolitschka *et al.*, 2001). P-wave values are expressed in *m/s* in a P-wave logger (PWL) which accurately and automatically measures the P-wave velocity of soft sediments inside a cylindrical plastic core liner (Schultheiss and McPhail, 1989). P-wave travel time was measured through a liner filled with distilled water and the calculation of P-wave velocity (V_P) may be as follows:

EQUATION 4.12

$$V_P = (d_R - 2d_L)/(t_R - t_L)$$

Where, d_R is the outer diameter of the liner (mm); d_L is the liner thickness (mm); t_R is the record pulse travel time (μ_S); and t_L is the pulse delay time (μ_S). There are many examples of applications of this method (Schultheiss *et al.*, 1987; Schultheiss and McPhail, 1989). In order to get good results, core samples' temperature should be in equilibrium with the laboratory (Zolitschka *et al.*, 2001), as this may cause variations in P-wave velocity results (Weber *et al.*, 1997).

4.2.4.2.4 – MAGNETIC SUSCEPTIBILITY

Magnetic susceptibility can be defined as the degree of magnetisation of a material according to a magnetic field. This parameter characterises the capacity of sediments to be magnetised according to the content of iron-bearing minerals, especially magnetite (Zolitschka *et al.*, 2001), being useful for inter-core correlation and for correlation of sedimentary provenance. This logging method is done either through whole-core or split-core logging, although it can be also performed in sub-cores and discrete samples from the core (Nowaczyk, 2001).

Two types of sensor may be used: (1) for split cores it is used point sensors which are mounted in an arm moving up and down to the sediment surface; (2) for whole core measurements loop sensors are stationary and the sediment moves through it. Point sensors are less sensitive, although they have higher spatial resolution. They cannot be used for whole cores as they have an influence field of about 1 cm in diameter (Geotek, 2014).

Magnetic susceptibility measurements should be made immediately after samples are collected to avoid losing data due to degradation generated by oxidation after the core is split.

4.2.4.2.5 – ELECTRICAL RESISTIVITY (NCR)

Non-contacting resistivity is a measure of how strongly a material opposes the flow of electric current, being the inverse of electrical conductivity. It is measured in ohm-meter (Ωm) (Jackson *et al.*, 2006; Geotek, 2014). It can be applied on whole-core or split-core for resistivity measurements (Jackson *et al.*, 2006). NCR is a technique that induces a high frequency magnetic field in the core, from a transmitter coil, which in turn induces electrical currents in the core that are inversely proportional to the resistivity (Geotek, 2014). As

pointed out by Jackson *et al.* (2006), this technique can be applied, for example, to studies of slope stability.

4.2.4.3 – GEOCHEMICAL PROPERTIES – XRF ANALYSES

XRF analyses can be essentially divided into two main general types: Wavelength Dispersive X-ray Fluorescence (WD-XRF) and Energy Dispersive X-ray Fluorescence (EDXRF). In this work, it was used the EDXRF analysis. For this reason, the focus will be only on EDXRF. Geochemical sediment properties have been analysed not in the MSCL but separately from physical properties in an individual ITRAX XRF-core scanner with Mo tube (Cox Analytical Systems).

4.2.4.3.1 – EDXRF SPECTROMETRY

Energy-dispersive X-ray fluorescence (XRF) spectrometry is a non-destructive technique that measures elemental abundances directly from the core surfaces (Schultheiss *et al.*, 1987; Schultheiss and McPhail, 1989; Jansen *et al.*, 1998; Migeon *et al.*, 1998; Zolitschka *et al.*, 2001; Morillas, 2016), allowing to observe different chemical tendencies on a sample. It consists on the interaction between radiation and the materials' atoms and the resulting X-rays allow detecting the abundance of the elements present in a sample (Migeon *et al.*, 1998).

The X-ray fluorescence has an extensive variety of applications being suited for the geochemical analysis of rocks, sediments, minerals and fluids through a spectrometer – X-ray spectrometry (Geotek, 2014). XRF measurements using MSCL X-rays have been used, for 30 years, as a non-destructive technique to analyse physical structures in sediment samples (Migeon *et al.*, 1998), being well-suited for bulk chemical analyses of major elements (Si, Ti, Al, Fe, Mn, Mg, Ca, Na, K, P) in rock and sediment and for bulk chemical analyses of trace elements (>1 ppm; Ba, Ce, Co, Cr, Cu, Ga, La, Nb, Ni, Rb, Sc, Sr, Rh, U, V, Y, Zr, Zn) in rock and sediment (Geotek, 2014). When measuring these properties, some problems may arise due to the presence of inhomogeneities like big clasts and veins and other irregularities on the core that may lead to misleading results. This creates additional difficulties in the conversion of core-scanner output to element concentrations (Weltje and Tjallingii, 2008). According to Richter *et al.* (2006), special care needs to be taken to remove surface irregularities from core slicing by carefully flattening the surface previously sliced. In order to

protect sediment from external influence and activity and to diminish surface roughness, half-core surfaces are covered with ultralene thin film (4μm).

EDXRF greatly differs from the conventional XRF analysis. Conventional XRF analysis was generally used by means of two different, destructive and semi-destructive, methods: fusion method in which about 0.5 g of sample in a lithium borate flux is dissolved in order to produce a solid solution like glass bead for determination of major and the more abundant trace elements; pelletization method is used to determine major trace elements. To accomplish this, it is created a briquette of 15-20 tonnes, from a compressed ground sample, over which the analysis is done (Croudace *et al.*, 2006).

4.2.4.3.2 – XRF-CORE SCANNERS

There are different types and models of XRF scanners, as for example CORTEX (Jansen *et al.*, 1998); SCOPIX (Migeon *et al.*, 1998); AVAATECH (Richter *et al.*, 2006); TATSCAN-F2 (Sakamoto *et al.*, 2006) and ITRAX (Croudace *et al.* 2006). Depending on the scanner model, it allows the measurement of elements covering atomic mass ranges from K to Sr (Jansen *et al.*, 1998), from Na to Fe (Sakamoto *et al.*, 2006), from Al (atomic nr. 13) to U (atomic nr. 92) (Richter *et al.*, 2006).

ITRAX core scanner (Figure 4.21) is an automated multi-function core scanning instrument, which analyses half cores up to 1.8 m length with a maximum resolution of 200μm (e.g., Streli *et al.*, 2004; Croudace *et al.*, 2006; Thomson *et al.*, 2006). According to Croudace *et al.* (2006), ITRAX can gather optical images, radiographic images and micro-X-ray fluorescence spectrometry (μXRF) elemental profiles, which are based on analysis of microscopically small areas of a larger sample (Streli *et al.*, 2004).

FIGURE 4.21 – ITRAX core scanner (Croudace *et al.*, 2006)

Like for the other scanners, during the analysis the split cores must be with the top pointing to the side of the scanning movement (Croudace *et al.*, 2006). Then, the core length has to be defined as well as

the excitation voltage to the X-ray tube in order to make a surface topographic scan of the core, relative to a horizontal reference plane, in order to avoid any subsequent collision of the XRF detector with the sediment surface (Croudace *et al.*, 2006). Then, there is a selection in the sample of the elements of the periodic table to be spectrally analysed. The spectral analysis was done using specific software – Q-Speq © (version 8.6.0).

ITRAX core scanner has an optical camera system with an incorporated light-sensitive device with a maximum resolution of 50µm, which allows defining the part of a sample to be analysed prior to scanning. A digital X-ray camera is also part of the instrumental components of ITRAX. This camera has a pixel resolution of about 20µ and is used for recording the intensity of X-radiation that passes through the sample, being able to operate with exposure times from 20 ms to several seconds (Croudace *et al.*, 2006). Also, a 3kW X-ray generator is incorporated for obtaining excitation for an array of elements.

ITRAX is a non-destructive core scanner that provides high resolution X-radiography and optical image. Furthermore, ITRAX has X-radiographic spatial resolution of ≥100µm and has the possibility to add other sensors to the scanner. To acquire data for a 1m-core at 200µm of resolution for Si, Al, S, Cl, K, Ca, Fe, As, Pb, Zn, Br, Rb, Sr and Zr elements, ITRAX takes 48h and only 2 hours for K, Ca, Fe and Sr, also for a 1m-core. The time to acquire optical image X-radiograph data, also on a 1m-core at 200µm of resolution is about 30 minutes. Beyond all this, ITRAX is also very useful for the identification of narrow zones of unusually high concentrations of specific elements (Thomson *et al.*, 2006).

Croudace *et al.* (2006) refer that a new ITRAX core scanner (second generation ITRAX) appeared with improvements on the sensitivity for the analysis of Si and above elements, but also improvements on the detector preamplifier and counting devices, which allow higher count rates almost without losing energy resolution.

4.2.5 – AMS ^{14}C DATING

Six planktonic foraminiferal samples of *Globigerina bulloides* (*G. bulloides*) species selected from the fraction >250 µm, and *Globorotalia inflata* for the sample at 200 cm, because *G. bulloides* were not enough (Table 4.6), were dated by accelerator mass spectrometer (AMS) ^{14}C by Beta Analytic Inc (Beta; USA). The AMS ^{14}C dates were calibrated to calendar years Before Present (BP) (before present: 1950 AD) through BetaCal 3.21, using the High Probability Density Range Method (HPD), through Bayesian analysis

(Bronk Ramsey, 2009) and the MARINE13 calibration data (Reimer *et al.*, 2013) without any additional local reservoir correction.

Previous works in the North Atlantic region have shown that the local reservoir age has changed in the past, e.g. Voelker *et al.* (1998), and in particular during the last glacial–interglacial transition at high latitudes of the eastern North Atlantic, e.g. Bard *et al.* (2004), and north of 41°N in its western part (Waelbroeck *et al.*, 2001). However, the precise spatial and temporal patterns in palaeo-reservoir ages during the last glaciation are still poorly understood. The Iberian margin is located far away from these sites where ^{14}C reservoir ages were large and variable during the last deglaciation.

It was used the 95.4% (2σ) confidence intervals and their relative areas under the probability curve as well as the median probability of the probability distribution as suggested by Stuiver *et al.* (2005).

TABLE 4.6 – AMS ^{14}C dates determined at Beta Analytic Inc (Miami, USA)

Lab ID	Core depth (cm)	Dated Material (Plankt. Foraminifera)	Conv. AMS ^{14}C (yr BP)	Error ±	95,4% (2σ) Cal BP Age ranges	Calendar age Cal kyr Median probability
Beta-532879	56	*G. bulloides*	11420	30	12997 - 12736	12870
Beta-532878	144	*G. bulloides*	14450	40	17292 - 16842	17070
Beta-548290	158	*G. bulloides*	18510	60	22197 - 21737	21970
Beta-548291	171	*G. bulloides*	26610	100	30846 - 30233	30540
Beta-532880	200	*G. bulloides* and *G. inflata*	36850	240	41594 - 40505	41050
Beta-532881	294	*G. bulloides*	39410	480	43637 - 42183	42910

4.2.6 – GEOTECHNICAL PROPERTIES

In addition to the previous analyses of sedimentological (grain-size and calcimetry), physical, and geochemical properties, this work also includes geotechnical analyses of sediments. The sediments used for these analyses were taken from the CO14-GC-7B, twin core of gravity core CO14-GC-07. In contrast with gravity cores retrieved for sedimentological, physical and geochemical analyses, which were sectioned into two halves (D-sections), gravity cores acquired for geotechnical analysis have been kept integral, being sealed and paraffin-insulated after being recovered from the seabed and then immediately stored in a fridge camera at 4ºC. These cores were stored at the University of Vigo.

This work has been conducted in the LabGeo (Figure 4.22) at Civil Engineering Department of the Faculty of Engineering of the University of Porto (FEUP). Geotechnical testing was prosecuted to assess sediments' mechanical behaviour on Alentejo Margin's slopes. These tests allowed to determine the sediments' strength (cohesion and internal friction angle), plasticity and consistency, as will be shown in Chapter 7 and Teixeira *et al.* (*under review*).

FIGURE 4.22 – General view of LabGeo – Faculty of Engineering of the University of Porto

A total of 25 geotechnical tests, encompassing triaxial-, oedometer-, direct shear and simple shear tests (Table 4.7) have been accomplished in 15 cm height and ~8 cm diameter cylindrical sediment samples. Five triaxial tests have been completed: four drained at 70-85 cm; 115-130 cm; 265-280 cm; and 295-310 cm, and one undrained at 145-160 cm, whereas three oedometer tests have been done at 160-175 cm; 175-190 cm; 280-295 cm. Once the values were already stabilized at the third test and as it is a long-lasting test, it was decided that this number of tests was enough. One direct shear test has been done in the topmost sediment layers (0 – 25 cm). Shear stress analysis has been continued through simple shear tests (DSS), which is more representative and more suitable for slope stability analysis. Fourteen DSS tests have been completed in five different sediment samples at 0 – 25 cm; 130

– 145 cm; 160-175 cm; 175-190 cm and 280-295 cm. Three tests per sample, with three different consolidation streses: 10; 50 and 200 kPa. Additionally, it was determined the density of the sediment particles in three different depths (0 – 25 cm; 70 – 85 cm and 280 – 295 cm). Granulometric analysis has also been done at the same depths (Table 4.7). The different tests were performed at different depths, encompassing varied granulometry, in order to assess the mechanical behaviour of finer sediments, coarser sediments and in the interfaces of both.

TABLE 4.7 – Summary of the geotechnical tests done for this work on CO14-GC-7B

Sample #	Core Depth (cm)	Geotechnical Test						
		Granulometric Analysis	Density of Solid particles	Water Content	Triaxial Test	Oedometer Test	Direct Shear Test (Conventional)	Simple Shear (DSS)
P1	0-25 cm	x	x	x			x	x
P5	70-85 cm	x	x		x			
P8	115-130 cm				x			
P9	130-145 cm			x				x
P10	145-160 cm				x			
P11	160-175 cm			x		x		x
P12	175-190 cm			x		x		x
P18	265-280 cm				x			
P19	280-295 cm	x	x	x		x		x
P20	295-310 cm				x			

4.2.6.1 – CONSOLIDATION TESTS

Consolidation tests were performed using a Wykeham Farrance® Oedometer (Figure 4.23) at LabGeo – FEUP, according to the specifications of CEN-ISO/TS-17892-5 (2004). This is a compressional device that allows draining sediment samples, which are inserted inside a metal ring-device and compression is exerted in by applying vertical loads over a steel top cap and a porous stone that involve the sample. Once the sediment sample is placed inside the cell, this was filled with salty water and the sample was saturated so as to dissipate the pore-pressure inside the sediment, and then the required load is transmitted to the sample, and amplified by 10 times, by a lever that is connected to a ram. The axial displacement is assessed by a 25 mm-range LVDT (Linear Variable Differential Transformer). In this test, the amount of sediment to be analysed on the oedometer depends

FIGURE 4.23 - Wykeham Farrance® Oedometer. LabGeo - FEUP

on the metal ring dimensions and the necessary void ratio. The confining rings used in this test were ~19.40 mm in height (H) and ~50 mm in diameter (Ø). This test was performed for each sample in a total of 12 steps of 24h applying a maximum vertical stress of 3200 kPa. Load increments were applied once the sample reached the equilibrium.

4.2.6.2 – DIRECT SHEAR TESTS

Direct shear stress tests were performed using shear box (ASTM-D3080, 1998). Prior to the analysis, in the shear box test, the sediments were saturated, and pore-pressure filled with water. After inserting sediment inside a 36-cm^2 shear box and protected by a grid plate and a porous stone below and above the sediment sample and then the shearing box was saturated and then it was placed in a vacuum chamber, where excess pore-pressure was dissipated. After this, the sample was kept 24h in consolidation so as to the repose effective stress can be reinstalled. One conventional shear box test has been done on the CO14-GC-7B gravity core, at 0-15 cm depth. This test has been performed using a Wykeham Farrance® shearing machine (Figure 4.24), with 60 X 60 X 20 mm cutting rings. As already verified by Viana da Fonseca (1996), the classic shear box is not the most suitable equipment for the shear strength analysis on residual sediments because it overstates the resistance of sediments.

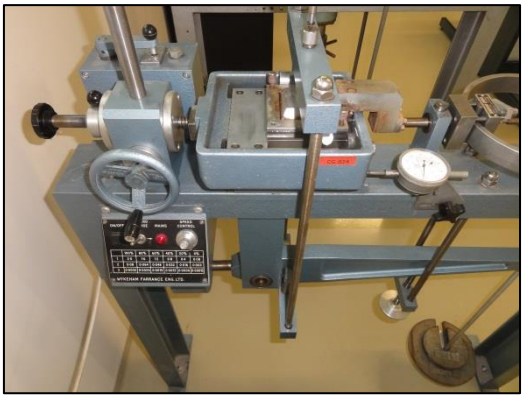

FIGURE 4.24 - Wykeham Farrance® Shear Box Machine

4.2.6.3 – DIRECT SIMPLE SHEAR TESTS (DSS)

Simple shear tests (DSS) were performed using a Willie® ring shear machine, from LabGeo – FEUP (Figure 4.25), using 63 mm in diameter and 24 mm in height samples, following the specifications of CEN-ISO/TS-17892-10 (2004). These were retrieved from the gravity core using a 63 X 24 mm cutting ring, and then it was placed inside a pile of rigid thin rings, preventing lateral extension but allowing further horizontal shearing

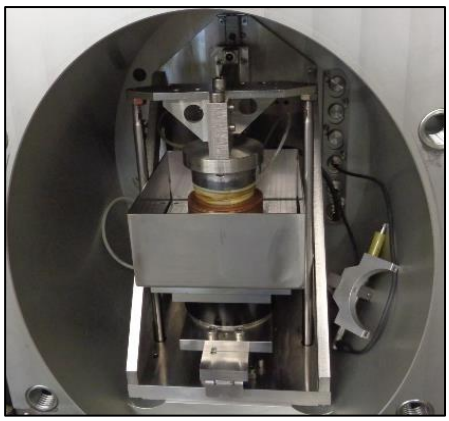

FIGURE 4.25 – Willie® ring simple shear test apparatus.

during the test. Five sets of three deformability tests were executed on the ~346 cm depth CO14-GC-7B gravity core, at different depths: 0-15 cm; 130-145 cm; 160-175 cm; 175-190 cm; and 280-295 cm, with effective vertical stress values ranging from 10 kPa up to 200 kPa. Samples were initially saturated and then consolidated at a vertical load of 10, 50 and 200 kPa, respectively for the different essays. The shearing process occurred in horizontal cycles, e.g. (Viana da Fonseca, 1996; Matos Fernandes, 2012; Pardo *et al.*, 2018).

4.2.6.4 – TRIAXIAL TESTS

Triaxial Compression Tests - Static and isotropically consolidated-drained triaxial compressive strength tests were performed in this work, according to CEN-ISO/TS-17892-9 (2004) and Viana da Fonseca *et al.* (2015). Five tests were executed on the ~346 cm depth CO14-GC-7B gravity core, at different depths: 70-85 cm; 115-130 cm; 145-160 cm; 265-280 cm; and 295-310 cm (Table 4.7). During these tests, all the sediment samples went through three main phases before inducing the shear stress: (1) Percolation, in which water flowed through the sediments' voids from the bottom to the top to expulse the air inside the pores; (2) Saturation promoted the dissolution of the air by applying crescent back-pressures and maintaining constant confining pressure. The assessment of saturation was done through P-wave measurement; (3) Consolidation occurred when the sediment was already saturated and confining pressure was applied.

A VJ Tech® Triaxial Cell with a pressure limiting capacity of 1700 kPa was used in this work, at LabGeo – FEUP (Figure 4.26). Silty to silty-clay cylindrical sediment specimens with 80 mm diameter and 150 mm height have been prepared and assembled in the triaxial chamber (Figure 4.26A). A rubber membrane was inserted on an expander and the sediment specimen was inserted and attached on the base of the chamber with two O-rings, being then the sediment specimen wrapped on with the rubber membrane and sealed on the cap with more two O-rings (Figure 4.26A). After this, the specimen was placed inside the chamber. Then the triaxial cylinder was assembled and closed, and placed in position in the axial loading device, which must be aligned with axial load-measuring device to avoid lateral forces to act on the piston during the measurements. When all this was set, pressure-maintaining and measurement device were attached, and the chamber was filled with the confining liquid – salty water. Confining pressure (CP) and back-pressure (BP) were determined in consequence of the vertical effective stress σ'_V values determined for these sediments (Equation 4.13). CP values varying between 300 and 310 kPa, and BP values

ranging from 310 to 325 kPa have been applied during percolation and consolidation processes. In order to keep positive effective stresses confining pressure values were kept slightly above back-pressure values.

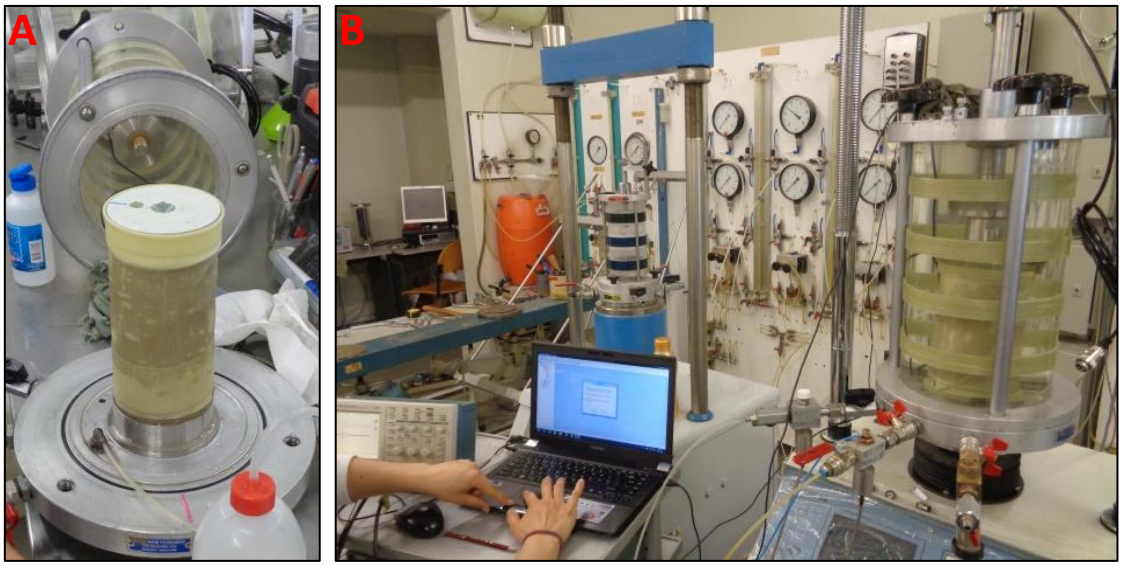

FIGURE 4.26 – (A) - Sediment sample assembled in the Triaxial chamber base with Bender elements mounted. (B) - Measurement of P- and S-waves on the sediment sample.

Vertical effective stress σ'_V has been calculated according to the following equation:

EQUATION 4.13:

$$\sigma'_V = \int_0^z \left(\gamma(z) - \gamma_w(z)\right) dz$$

Where γ corresponds to the sediment unit weight; z is the depth; γ_w is the unit weight of water and dz is the depth variation.

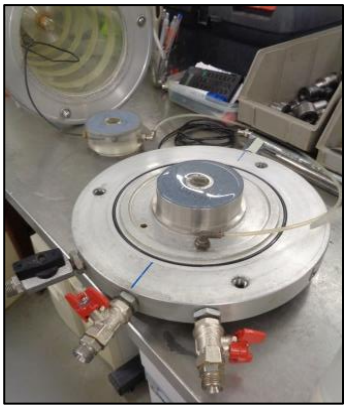

FIGURE 4.27 – Bender-extender elements mounted on a conventional Triaxial cell.

During saturation and aiming at measuring axial deformation and sediment stiffness, piezoelectric transducers were installed on the triaxial device at LabGeo – FEUP. These transducers implemented both on the base and on the top cap of the triaxial chamber, allow for the measurement of shearing and compressional waves (S- and P-wave) during the different stages of the triaxial test, and correspond to *bender/extender elements* type (Figure 4.27). *Bender elements* are piezoelectric transducers, composed by piezoceramic plates connected to a central metallic plate and to the external electrodes, which can transmit

and receive S-waves; *extender* transducers can transmit and receive P-waves velocities. These are base-top measurements, being the transmissor at the base and the receptor at the top of the specimen. For S-waves a 0.5 kHz increment was used between 0 and 2, whereas for P-waves it was used a 25 kHz increment, between 25 and 100 kHz. For seismic wave's measurement it was used an oscilloscope (Tektronix TDS220®), associated to the acquisition software WaveStar®, which allow for the acquisition and visualization of the travel time of signals; a function generator (Thurlby Thandar Instruments TTI TG 1010®) that generates an electrical signal; and signal output amplifiers. As has been done by Soares (2015), P-wave velocity has been measured and Skempton's coefficient B has been determined for assessing the degree of saturation of sediments. Velocities of propagation for P-wave (V_p) of 1500 m/s and values of 0.97 for Skempton's coefficient B have been achieved, indicating good degree of saturation of the sediments.

FIGURE 4.28 – Triaxial test.

After saturation and consolidation, and the consequent measurement of the Skempton coefficient B the triaxial test was initiated for the analysis of shear strength (Figure 4.28).

In this work direct shear, direct simple shear and triaxial tests have been performed according to different physical parameters, for each test at different depths. These values are listed for simple direct shear in Table 4.8.

TABLE 4.8 – Simple shear test values: shear strength and shear stress values for referenced sediment samples

Depth (cm)	Initial Normal Stress (σ'_{vi})	Final Normal Stress (σ'_{vf})	Shear Stress (τ)
	(kPa)	(kPa)	(kPa)
0-15	13*	14.4*	10.6*
	13	13.9	7.2
	200	212.2	92.8
130-145	10	10.8	13.3
	50	53.8	28.6
	200	216.3	101.2
160-175	10	10.7	5.9
	50	54.5	28.2
	200	217.9	106.4
175-190	10	10.9	10.7
	50	54.4	29.4
	200	217.7	114.8
280-295	10	16.3	14.8
	50	54.4	29.4
	200	217.9	103

Consolidated triaxial tests under axial compression were conducted for five different depths: three were drained (10, 11 and 35 kpa), respectively for 70-85, 115-130 and 265-280 cm depth; one undrained (16 kpa) at 145-160 cm, and one partially undrained (200 kpa) at 295-310 cm, with the pore-pressure (u) measurement on the two extremes and the centre in order to have the integral for the average of u. Four of these tests were performed according to the in situ effective vertical stress (10, 11, 16, and 35 kpa). Once the effective stress values of the deepest sample (295-310 cm) are < 50 kpa, it was confined at a higher value, 200 kpa, to assess the stress-strain and strength behaviour under higher stress. After all these tests, data were processed, and slope stability was assessed.

4.2.7 – SLOPE STABILITY / LANDSLIDE SUSCEPTIBILITY MODELLING

Slope stability has been assessed using both statistical and simple physically based models (Chapter 8). These models determine how favourable the area is to slope disruption. Modelling was performed through bivariate and multivariate statistical models as well as physically based models, knowing the main geomorphologic parameters and the key sediments' mechanical properties of the area.

Landslide susceptibility was validated using the landslides scars, which were recognized and inventoried in the Alentejo Margin through three different multibeam swath bathymetry datasets, with 100 m^2 resolution: SWIM, MOWER and CONDRIBER and through multichannel seismic reflection profiles (STEAM94; BIGSETS98 and CONDRIBER 2014) and high-resolution seismic profiles acquired with a parametric ATLAS PARASOUND-P35 echo-sounder - Figure 4.1. These data were used in this work for better in-depth interpretation of the unstable areas. Bathymetric, geotechnical, and sedimentological data have been used to fulfil the work's goals.

For statistical landslide susceptibility analysis, Information Value (IV) and Logistic Regression (LR) were applied using some bathymetric parameters derived from multibeam bathymetry datasets (slope angle; aspect, curvature, both plan and profile), and lithology – sediments mapped in the geological map at 1: 1 000 000 scale. These parameters were used as maps in both modelling: IV and LR.

5 - GEOMORPHOLOGIC FEATURES AND PROCESSES IN THE ALENTEJO MARGIN (SW IBERIA): IMPLICATIONS ON LANDSLIDING ACTIVITY[1]

In this chapter, new unpublished multibeam bathymetry and single- and multichannel seismic records are used to perform the geomorphological analysis of the Alentejo Margin, in the Southwest Portuguese Continental Margin, in a total extent of ~85 km×82 km.

The geomorphology of the Alentejo Margin results from the complex interaction between along-slope and downslope processes, which promote the formation of bottom current driven depositional and erosive features (moat) as well as gravity-driven features (gullies and landslides). The interplay between these processes contributes for the mixed and dynamic morphosedimentary pattern on the area.

Sines Contourite Drift (SCD) is a ~2311 km^2 sedimentary feature, being the most prominent depositional feature in the area with a perimeter of 303.9 km, 98 km length and 35 km width. The interaction between bottom currents and this sedimentary feature favours slope instability, with many landslide scars developing in the SCD, contributing for the instability of the contourite and to the downslope evacuation of sediments. These scars occur both on steep and on gentle slopes between ~200 and 3200 mwd (meters water depth). Scar concentration is higher in the middle- and lower-slope, whereas the thickest debris-flow deposits are found in the slope basin area - Lebre Basin (LB). Several triggering and pre-conditioning factors, some resulting from the interaction of along-slope and downslope processes, contribute for wide-ranging landslides scar concentration. Steep-slope and high sedimentation rates favour sediments low consolidation, promoting excess pore water pressure and weak layers formation.

It is shown that the interplay between bottom currents and pre-existing morphology performs the complex interaction of both along-slope and downslope processes thus promoting an active and diversified geomorphological evolution and generalised slope instability.

[1] This chapter has been published in **Marine Geology**:

TEIXEIRA, M., Terrinha, P., Roque, C., Rosa, M., Ercilla, G., & Casas, D. (2019) - Interaction of alongslope and downslope processes in the Alentejo Margin (SW Iberia) – Implications on slope stability. *Marine Geology*, 410, pp. 88-108. doi: https://doi.org/10.1016/j.margeo.2018.12.011

5.1 – INTRODUCTION

The Alentejo Margin, in the Southwest Portuguese continental margin, develops in an area of both tectonic plates interface (Figure 5.1A) and bottom currents confluence (Figure 5.1B). The Pliocene-Quaternary convergence (~4mm/yr) between Eurasia and Africa plates (Argus *et al.*, 1989; Zitellini *et al.*, 2009) greatly influences morphosedimentary processes (Stow *et al.*, 2013) and the seafloor morphology (Hernández-Molina *et al.*, 2014b) due to the vertical movements experienced in the area both during the Mesozoic rifting and subsequent Alpine orogeny (Zitellini *et al.*, 2004; Terrinha *et al.*, 2009). The re-opening of the Gibraltar gateway in the Messinian (Stow *et al.*, 2013; Roveri *et al.*, 2014) contributed for the onset of the Mediterranean Outflow Water (MOW) (Hernández-Molina *et al.*, 2014b), establishing a link between the circulation of the Mediterranean Sea with the Atlantic Ocean (Kaboth *et al.*, 2017a), allowing for a confluence and mixture of water masses, thus enhancing the bottom current circulation (Hernández-Molina *et al.*, 2011). This water mass exchange promoted the outflow of the saltier and warmer MOW from the Mediterranean Sea and an inflow of the fresher and cooler Atlantic Inflow Water (AIW), formed by the North Atlantic Superficial Water (NASW) and the North Atlantic Central Water (NACW), both sourced from the Atlantic (Ambar and Howe, 1979; Pingree and Le Cann, 1989; Pollard *et al.*, 1996; Cherubin *et al.*, 2000; van Aken, 2000b) – Figure 5.1B. The exit of MOW from the Mediterranean allowed for the increase of along-slope contourite sediments deposition along the Gulf of Cadiz and the Alentejo Margin (Hernández-Molina *et al.*, 2003; Roque *et al.*, 2012; 2015) and northwards along the Eastern Atlantic Margin (Llave *et al.*, 2007; Van Rooij *et al.*, 2010).

The Sines Contourite Drift (SCD) has been deposited in this area under the influence of the MOW since the Late Miocene (Hernández-Molina *et al.*, 2014b). The interaction of the MOW with structural reliefs brings additional complexity to the sedimentation patterns (Hernández-Molina *et al.*, 2011; 2014b; Roque *et al.*, 2015) representing a hazard for the slope stability in the moderate to high seismicity South West Iberian Margin (SWIM) (Gràcia *et al.*, 2003). Recent tectonic activity also plays an important role for landsliding activity in both Mediterranean and Atlantic Iberian margins (Ercilla *et al.*, 2008a; Casas *et al.*, 2015), but especially in SWIM where it seems to be prone to cause large landslides able to cause tsunamis (Terrinha *et al.*, 2003; Lo Iacono *et al.*, 2012; Omira *et al.*, 2016). Submarine landslides commonly occur on diversified submarine environments (Prior and Coleman, 1984; Moore *et al.*, 1994; Hampton *et al.*, 1996; Mulder and Cochonat, 1996; Masson *et al.*, 1997; Laberg *et al.*, 2005; Masson *et al.*, 2006; Ercilla *et al.*, 2008a; Henrich *et al.*, 2008;

Mosher *et al.*, 2010; Casas *et al.*, 2011; 2016; Chiocci and Casalbore, 2017; Casalbore, 2018). Landsliding activity is very common on continental margins with contouritic deposition, especially where the interaction between along-slope bottom currents and downslope gravitational processes takes place (Laberg and Vorren, 2000; 2004; Bryn *et al.*, 2005b; Kvalstad *et al.*, 2005a; Rebesco *et al.*, 2007; Laberg and Camerlenghi, 2008; Roque *et al.*, 2012; Rebesco *et al.*, 2014; Alonso *et al.*, 2016; Ercilla *et al.*, 2016; Martorelli *et al.*, 2016). Contouritic sediments can be prone to failure (e.g., Casas *et al.*, 2015) because of high-sedimentation rates of well-sorted and low consolidated sediments over a pre-existent irregular geomorphology, thus promoting differential stresses, overloading and consequent formation of sliding planes (Laberg *et al.*, 2002; Bryn *et al.*, 2005a; Laberg and Camerlenghi, 2008; Talling, 2014; Casas *et al.*, 2015). The Alentejo Margin is an interesting area to analyse the complex interactions of along-slope and downslope sedimentary processes, combining bottom currents action and tectonic activity in a contourite area. To date, no such analysis has been done for this area. The SCD is different from some other drifts (Wynn *et al.*, 2000; Bryn *et al.*, 2005b), because it is simultaneously near a plate boundary and thus in a seismically active region, and in the distal part of the Gulf of Cadiz Contourite Drift System. Does the presence of the drift deposited under the circulation of bottom currents in a tectonically active area give rise to landsliding activity?

This chapter aims to do an integrated analysis of the interaction of tectonic structures and bottom currents with a contourite drift willing to understand: first at local level i) the interaction of processes leading to the proneness of the study area to slope instability; ii) whether landslide occurrence is affecting differentially the SCD and the surrounding area; iii) if landslides vary in type and shape when affecting different geomorphologic areas; and second at a global level iv) the formation and origin of large scale along-slope and downslope sedimentary and non-sedimentary features; v) which are the main factors controlling slope instability on contourites formed in tectonically active areas.

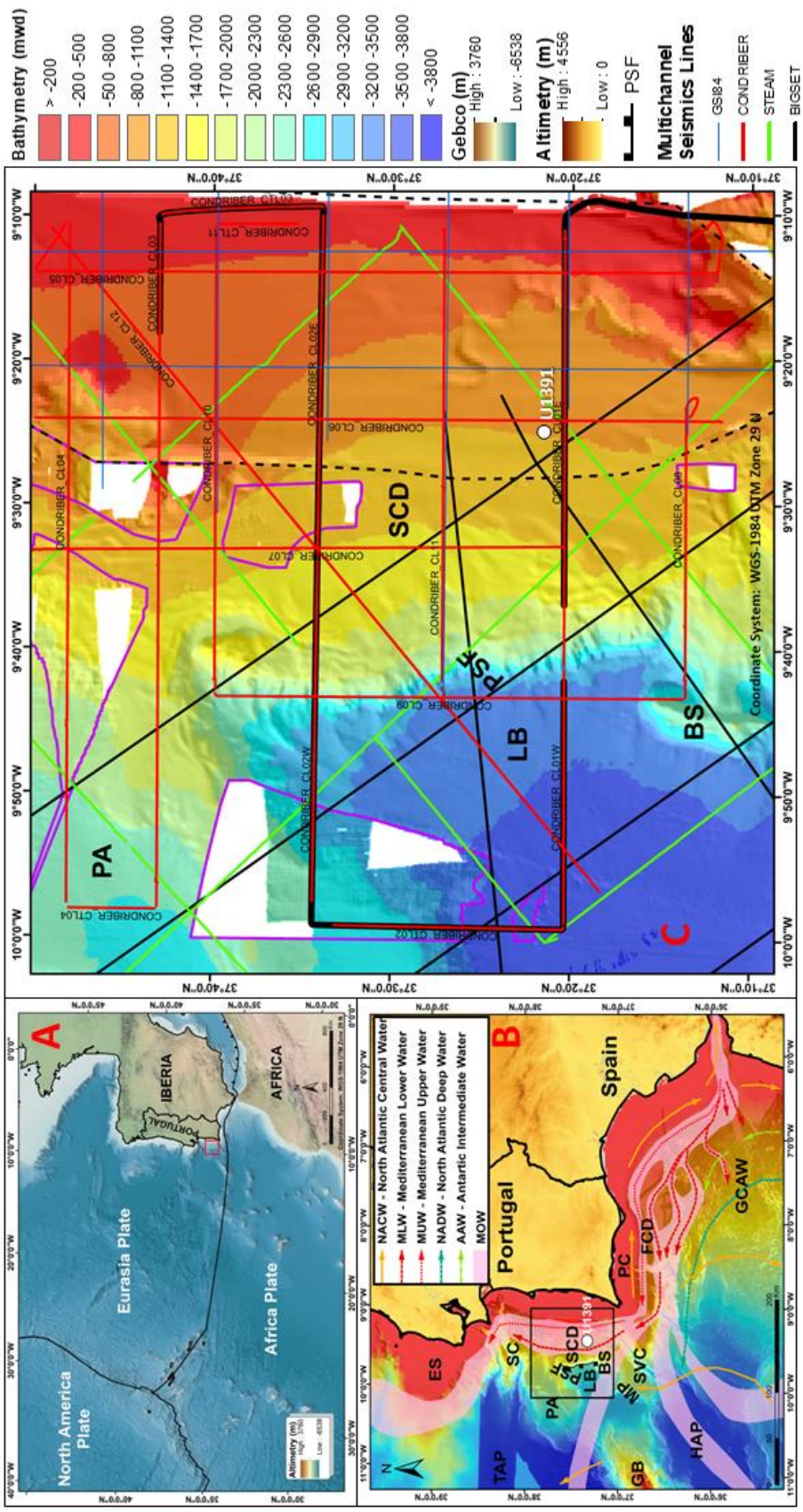

FIGURE 5.1 – The Alentejo Margin. (A) – General tectonic setting of the swim. (B) - Bathymetry of the area: SWIM, CONDRIBER, MOWER and GEBCO datasets with the main bottom currents affecting the area (after Hernández-Molina *et al.*, 2013 and Stow *et al.*, 2013). The black square corresponds to SWICONDRIMOW area. Main morphological features are identified in the map. ES – Estremadura Spur; FCD – Faro Contourite Drift; GB – Gorringe Bank; GCAW – Gulf of Cadiz Accretionary Wedge; HAP – Horseshoe Abyssal Plain; LB – Lebre Basin; MP – Marquês De Pombal fault; PA – Príncipes de Avis seamounts; PC – Portimão Canyon; PSF – Pereira de Sousa Fault; SC – Setúbal Canyon; SCD – Sines Contourite Drift; SVC – São Vicente Canyon; TAP – Tagus Abyssal Plain; Blank holes correspond to no data. (C) – Bathymetry of the study area - SWICONDRIMOW. Bathymetry is composed by three datasets. SWIM outside the dashed and purple polygons; Inside black-dashed polygon corresponds to CONDRIBER bathymetry dataset. Bathymetry inside purple polygons refers to MOWER bathymetry dataset. Acronyms in (C) correspond to the same in (B). Red lines correspond to CONDRIBER seismic profiles (2014); Black lines correspond to BIGSET seismic profiles (1998); Green lines correspond to STEAM seismic profiles (1994) and blue lines correspond to GSI SEISMIC PROFILES. Black line corresponds to a sequence of very high-resolution Parasound shotpoints that decal the CONDRIBER high-resolution profiles. Blank holes correspond to no data. Some artefacts may appear in some bathymetric contacts due to the merging process.

5.2 – DATA AND TECHNICAL CONSIDERATIONS

High-resolution multibeam swath bathymetry and multi-channel and high-resolution seismic datasets with different degrees of resolution (from a few metres to metric) have been analysed in this work (Figure 5.1C). Several multi-beam bathymetry datasets obtained with Simrad EM12, EM1000 and EM3000 and Atlas HYDROSWEEP DS multibeam echo-sounders were compiled and integrated for the present study from the SWIM (Zitellini *et al.*, 2009) and from CONDRIBER and MOWER projects (Hernández-Molina *et al.*, 2014a). A compilation of more than 30 profiles of multi-channel seismic records were analysed. These profiles were obtained from research projects: CONDRIBER 2014 (Hernández-Molina *et al.*, 2014a); STEAM 1994 (Monteiro *et al.*, 1994); BIGSETS 1998 (Zitellini *et al.*, 2001); and from oil-industry surveys - GSI'84 lines (see chapter 4). The identification and calibration of the seismic-stratigraphic horizons was based on the lithostratigraphic correlation with the ages of the major stratigraphic events obtained by Hernández-Molina *et al.* (2016a) from the IODP Site U1391 analysis. The lithostratigraphic units and hiatuses of similar age were identified in the seismic profiles through recognizing their lateral continuity. The multibeam bathymetry allowed for producing thematic maps: bathymetry, slope-angle, -aspect, -curvature in plane and profile (Figure 5.2), which were reclassified in discrete classes in the ArcGIS© software. Slope angle has 13 classes from < 1º up to > 45º. Discretization into many classes was made to better analyse how slope instability affects the lower slope angles, especially in the lower classes. The main reason for this is because submarine slope instability often occurs in slopes < 5º (e.g., Prior and Coleman, 1984; Hampton *et al.*, 1996). The inventory of morphosedimentary features and their interpretation were both based on bathymetry and seismic analysis. Features were firstly inventoried through bathymetric analysis and then confirmed in depth through multichannel and Parasound seismic data analysis. Landslide scars' areas and volumes were calculated for each scar. Volume was calculated through palaeo-bathymetric reconstruction of the disrupted area affected by each scar. The main statistical parameters referent to scars' area, volume and slope gradient were retrieved and the geographical distribution of scars was analysed through the directional distribution method (Yuill, 1971), which calculates the standard deviation of X- and Y- coordinates from the mean centre of a group of features, defining the axes of an ellipse and thus the main orientation and the distribution pattern of these features. The interpretation of the interaction of seafloor with bottom currents was based on water body salinity data (Schlitzer, 2018).

5.3 – RESULTS

The Alentejo Margin presents a varied morphology (Figures 5.2C and 5.3), having > 50% of the study area comprehended between 1100 and 3200 mwd (Figure 5.2A), ~95% of the slope gradient < 10º and a dominantly concave curvature (35%) (Figure 5.2D).

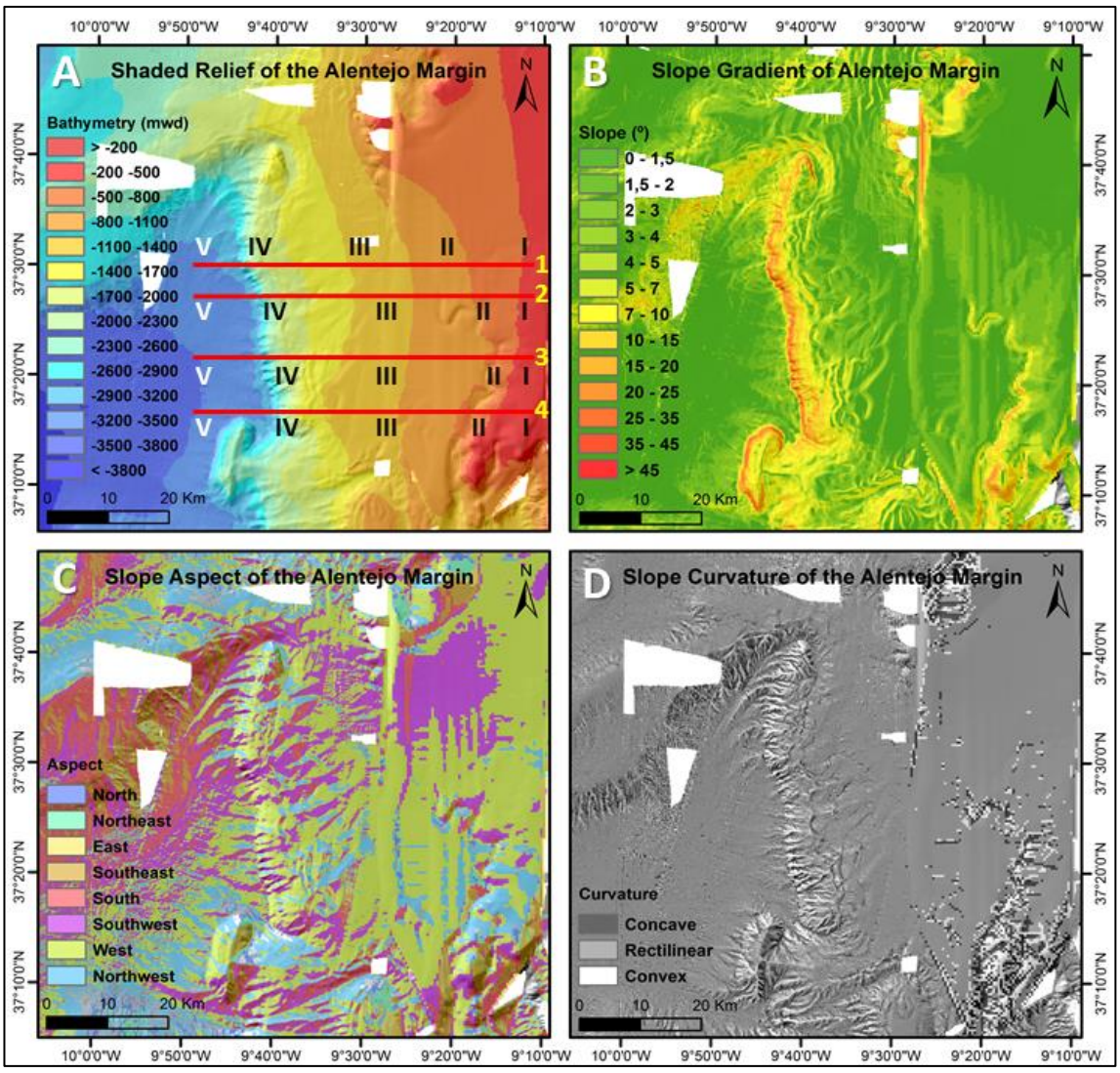

FIGURE 5.2 – Geomorphologic attributes of the study area. (A) – Shaded relief of the Alentejo Margin. Red lines in a correspond to the bathymetric profiles of Figure 5.3, where: I – Continental Shelf; Ii – Upper Continental Slope; Iii – Middle Continental Slope; IV – Lower Continental Slope; V – Slope Basin. (B) – Slope Gradient in degrees. (C) – Aspect indicating the slopes' compass. (D) – Plan curvature expressed as concave, rectilinear and convex surfaces. Blank holes present in all maps correspond to no data.

5.3.1 – PHYSIOGRAPHY

Three physiographic provinces were identified and devided into five segments: the continental shelf (I), the continental slope with its upper (II), middle (III) and lower (IV)

segments and the slope basin (V) - Figures 5.2 and 5.3. Each province has several geomorphologic features, encompassing tectonic- and also erosive and depositional along-slope and downslope process-driven bedforms (Figure 5.4). The continental shelf is the shallowest physiographic province (I) (Figures 5.2 and 5.3) extending until a depth of ~200 mwd (Figure 5.3) for ~33 km long. This province represents ~4% of the area and has low gradients (< 1º to 3-4º) (Figure 5.2B). An irregular and sharp shelf-break, mainly visible in the south, makes the transition from the continental shelf (I) to the upper continental slope (II) (Figure 5.3.4), between ~200-500 mwd.

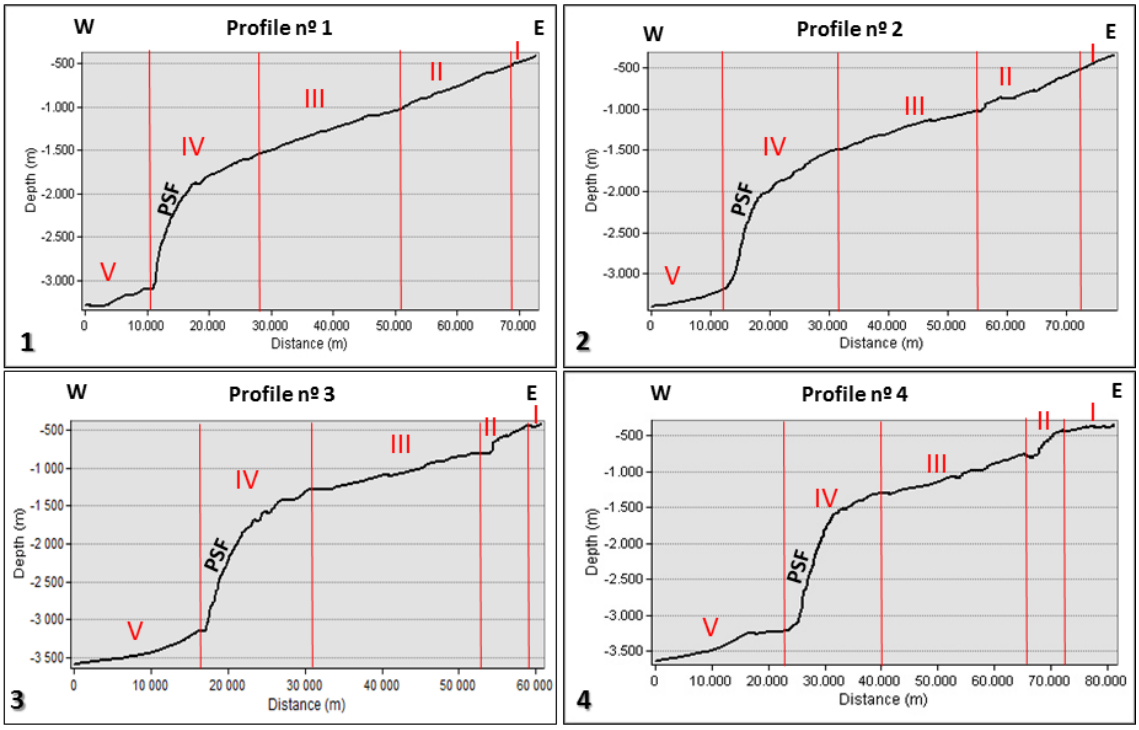

FIGURE 5.3 - Black line - West-East bathymetric profiles - See Figure 5.2A for location. I – Continental Shelf; II – Upper Continental Slope; III – Middle Continental Slope; IV – Lower Continental Slope; V – Slope Basin. PSF – Pereira de Sousa Fault.

The upper continental slope is a bathymetric step quite variable in depth, width and gradient and represents ~15% of the study area. Depth range increases from south to north, varying between ~500 – 800 mwd, in the south (Figures 5.3.3 and 5.3.4), and between ~500 and ~1000-1050 mwd in the north (Figures 5.3.1 and 5.3.2). Slope angles vary between 5º and 35º, being gentler in the north and steeper in the south (Figure 5.2B). Its width varies from 5 to 15 km. At its base, an irregular slope-break marks the transition from the upper- to the middle continental slope (III) - Figure 5.3.1.

The middle slope represents the largest physiographic province with 20-25 km width, corresponding to ~40% of the study area. It is a ~600-m high step that extends in the north

from ~1000 to ~1500 mwd (Figures 5.3.1 and 5.3.2) and in the south from ~700-800 mwd to ~1200-1300 mwd. This is the gentler sector of the whole area, displaying slope angles < 5º (Figure 5.2B). A slope-break at ~1500-1800 mwd makes the transition to the lower slope.

The lower slope occupies 36% of the study area, and has ~20 km width in the north narrowing southwards to about ~15 km. This area extends from ~1500 to ~3200 mwd, with gradients ranging from 15º to > 45º. It is controlled by tectonic reliefs, as the Pereira de Sousa Fault scarp and the southern flank of the Principe de Avis seamounts (Figures 5.1C and 5.4).

Lebre Basin (LB, a slope basin) sits at the base of the continental slope extending from 3200 mwd to < 3800 mwd, gently dipping to the west (from 1º to < 5º). This slope basin extends from the base of Pereira de Sousa fault scarp until the base of the Gorringe Bank (Figure 5.1B), with an area of 3449 km^2. This physiographic province can be considered as an equivalent of the marginal basin physiographic province defined by Heezen *et al.* (1959). The LB is bounded by the surrounding reliefs as the PSF scarp to the east, the Príncipes de Avis seamounts (PAS) to the northwest, and the Bow Spur (BS) to the southwest.

5.3.2 – STRUCTURAL AND MORPHOSEDIMENTARY FEATURES

The Alentejo Margin comprises three major groups of geomorphological features (Figure 5.4) that can be gathered into different groups, based on their origin: (i) tectonic (structural reliefs); (ii) bottom current driven: depositional (contourite drift and sediment waves) and erosive (moat); and (iii) gravity-driven (gullies and landslides).

5.3.2.1 – TECTONIC FEATURES

The most important tectonic features in the study area are PSF scarp, Bow Spur and the south-eastern flank of Príncipes de Avis seamounts, alongside with other minor structural features like the Infante Santo; Infante Dom Henrique; Estêvão Gomes; Fernão Mendes Pinto and Pêro Escobar hills.

The ~50-km long *Pereira de Sousa Fault (PSF) scarp* is the most prominent tectonic feature in the study area (Figures 5.1C and 5.4), trending NNW-SSE to N-S in its northern sector. This is a ~1400 to 2000-m high scarp (Figures 5.2A and 5.3), increasing in height

southwards. In the northern sector, the scarp top is at ~1300 mwd and its base is at ~2700 mwd in a mean height of ~1400 m and the gradients roughly vary from 10º to 25º. In this sector, the footwall of the scarp is concealed by downslope displaced sediments fed from the Sines Hook (SH) – Figure 5.4. The southern sector of PSF scarp is ~2000 m high, ranging from ~1200 mwd at the top and ~3200 mwd in the base. Slope gradients are steeper than in the northern section, varying from 15º to > 45º (Figure 5.2B).

The lower slope of south-eastern flank of the *Príncipes de Avis Seamounts (PAS)* extends for ~80 km until reaching the LB (Figure 5.4). This is a ~1000 m-high flank, whose top lies at ~2500 mwd and its base at ~3500 mwd. It presents quite steep slopes with gradients varying from 7º up to 35º.

The *Bow Spur (BS)* is a N-S tombolo-like morpho-tectonic structure ~15 km long, ~6 km width and ~1000 m height (Figures 5.2 and 5.4). It presents steep gradients that range from ~10º to > 45º. This elliptical relief is in the south-eastern boundary of slope basin (LB) - Figure 5.4.

The *Infante Santo* and *Infante Dom Henrique* hills (Figure 5.4) are part of a ~13 km long structure, in the northern sector of the area between ~500 and 800 mwd. The western face of these structures reaches slope gradients of ~15 to 20º (Figure 5.2B).

In the southern section of the study area the *Estêvão Gomes*, *Fernão Mendes Pinto* and *Pêro Escobar* hills (Figure 5.4) are structural highs whose tops range from ~200 to ~600 mwd, right in the headscarp of the *São Vicente Canyon*, SVC (Figure 5.1B), and gradients range from ~20 to 25º (Figure 5.2B).

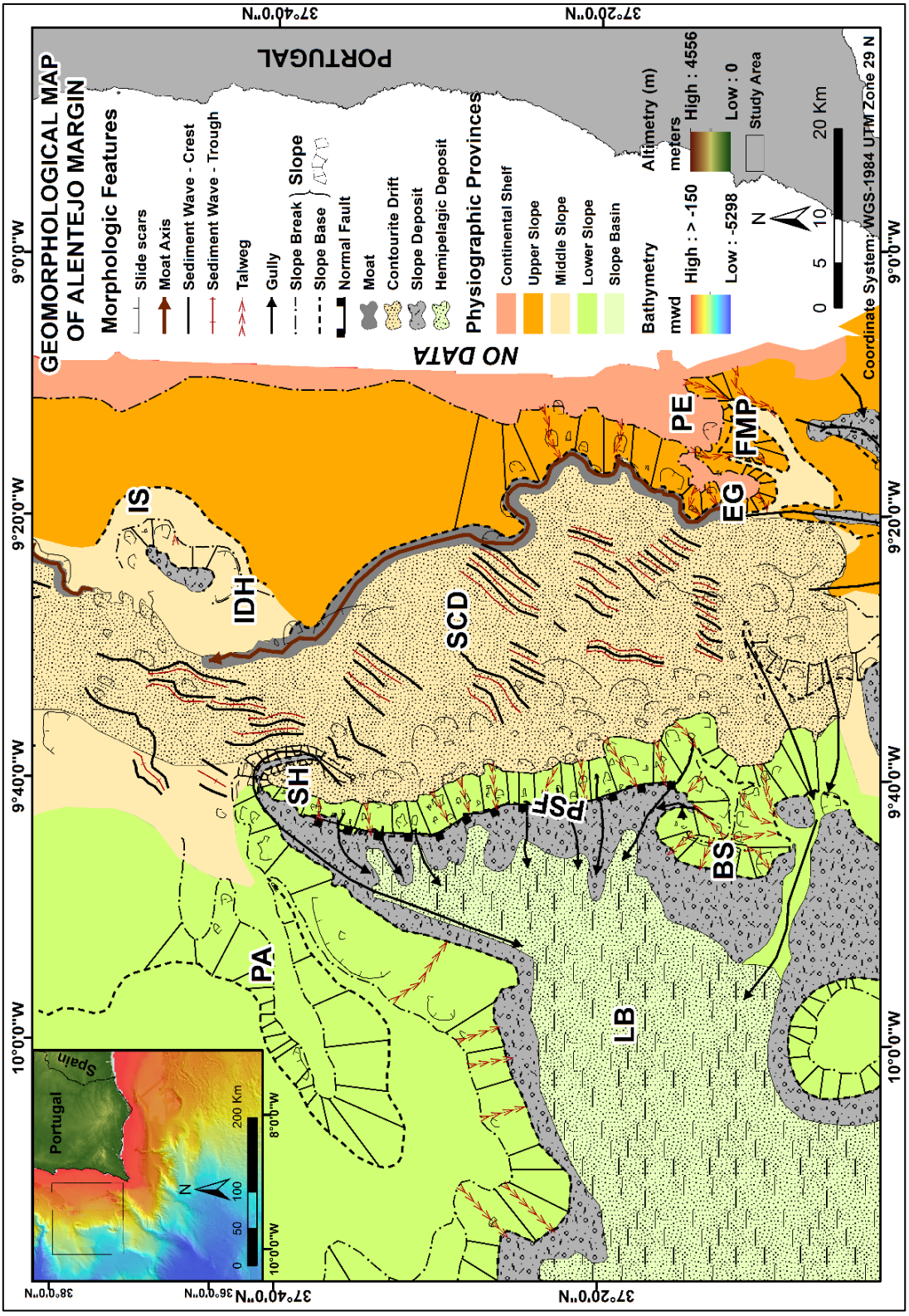

FIGURE 5.4 - Geomorphologic map of the Alentejo Margin. BS – Bow Spur; EG – Estêvão Gomes Hill; Fmp – Fernão Mendes Pinto Hill; IDH – Infante Dom Henrique hill; IS – Infante Santo hill; LB – Lebre Basin; PA – Príncipes de Avis Seamounts; PE – Pêro Escobar hill; PSF – Pereira De Sousa Fault; SCD – Sines Contourite Drift; SH – Sines Hook. Blank holes correspond to no data.

5.3.2.2 – BOTTOM CURRENT-DRIVEN FEATURES

5.3.2.2.1 – SINES CONTOURITE DRIFT (SCD)

The SCD is an aggradating plastered and elongated drift (Figures 5.5 and 5.7) emplaced in the middle continental slope (III) – Figure 5.4, whose onset started in the Late Miocene (Hernández-Molina *et al.*, 2014b). This depositional feature developed along ~2311 km^2 with a perimeter of 303.9 km, 98 km length and 35 km width (Figures 5.4, 5.5, 5.6) and is better developed from Late Pliocene discontinuity onwards (Figures 5.5 and 5.6). The SCD is geomorphologically constrained by the presence of other features: by PSF westwards; by Principe de Avis plateau and Principe de Avis seamounts, northwards; by São Vicente Canyon southwards and by the upper continental slope, eastwards. The SCD presents three abraded surfaces (AS) at different depths: at ~700-750 mwd is associated with a well-defined moat located at the base of the upper continental slope; at ~1200 mwd and at ~1350 mwd – Figure 5.5.

The stacking pattern of the SCD is composed of stratified packages of laterally continuous, high amplitude reflections alternating with packages characterized by low amplitude and low continuity reflections or semi-transparent facies. Within this depositional succession, three horizons characterized by high amplitude and continuity and denoting erosional character have been identified in the seismic profiles. Those horizons were correlated with the data from IODP Site U1391 (Hernández-Molina *et al.*, 2014b; 2016), which allowed to assign an age to them. These horizons are from top to bottom, Horizon H1 corresponding to the Middle Pleistocene Discontinuity (MPD, 0.9-0-7 Ma), Horizon H2 corresponding to the Early Quaternary Discontinuity (EQD, 2.4-2.0 Ma) and Horizon H3 corresponding to the Late Pliocene Discontinuity (LPD, 3.2-3.0 Ma) (e.g., Figure 5.5). Horizon H2 marks a major change in the seismic configuration of the SCD, from a predominant aggradating pattern during the Pliocene to slight progradating geometry during the Quaternary as shown by the mounded configuration and presence of palaeo-moats. Towards west, internal reflections are truncated against the sediment-rafted steep surface of the lower continental slope (Figure 5.5). SCD reaches 600 ms – 1300 ms (TWTT) in thickness (Figure 5.5).

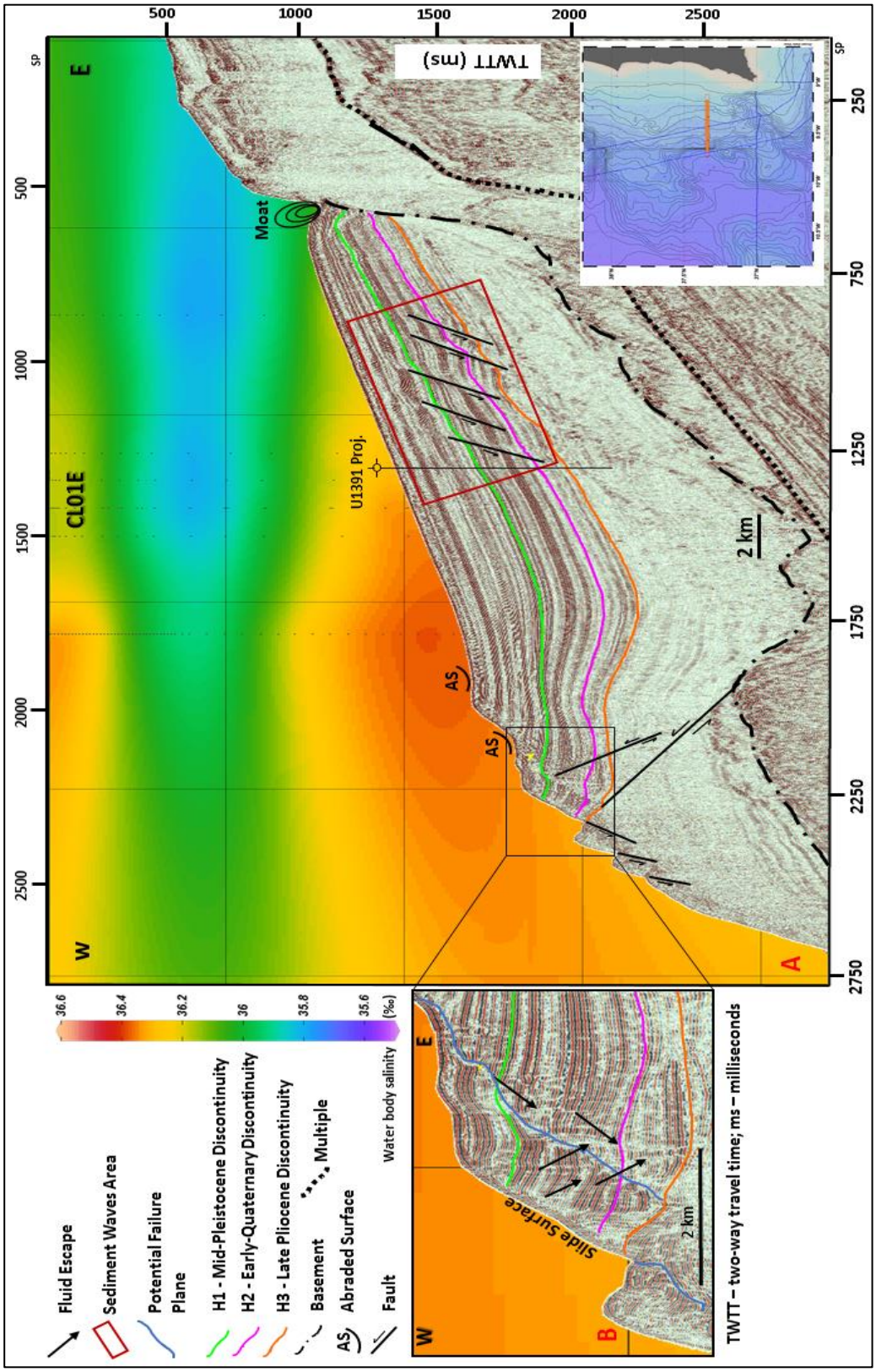

FIGURE 5.5 - (A) - East-West seismic line crossing the contourite drift (CL01E - see Figure 1C for location). Seismic and stratigraphic evidence of depositional, non-depositional, erosive and gravitational morphosedimentary features; Colour-coding: salinity (psu); Black dashed line marks the basement contact. U1391 Proj. – Projected site U1391 – IODP Expedition 339; the vertical doted-lines within the water column show the water depth to which the CTD was lowered; (B) - Detail of potential and effective slope instability.

5.3.2.2.2 – SEDIMENT WAVES

Sediment waves are smaller-scale sinuous-crest features affecting the surface of the SCD (Figure 5.4) from ~800 to ~1700 mwd (Figures 5.6 and 5.8). Sediment-waves were identified in three different sectors of the SCD surface, presenting different crest orientations and wave dimensions. These features have a N-S to NE-SW dominant crest orientation (Figure 5.4), being respectively parallel and oblique to the regional slope. In the northern sector, sediment waves extend for about 30 km and present a dominant N-S to NNE-SSW orientation. Recorded wave-length values are variable: ~906 m; 1208 m; 1811 m and 2415 m and wave amplitudes of 96 ms; 90 ms; 59 ms and 30 ms, respectively.

In the middle sector, the sediments-waves, preferentially NE-SW oriented, reach a total extension of 32 km (Figure 5.6), with wave-lengths with 664 m; 1811 m; 2113 m and 3018 m have been identified as well as wave amplitudes with 23 ms and 31 ms.

In the southern sector, NE-SW oriented sediment waves with lengths of ~9 to 11 km have been identified (Figure 5.8). The largest wavelength identified in this area has ~5100 m and the smallest ~930 m. Wave amplitude values of 50 ms (~38m), 75 ms (~56m) and 100 ms (~75m) have been identified.

Buried sediment waves were also found (Figure 5.6B). Stratigraphically, these features occur mainly between Late Pliocene (Horizon H3, ~3.2 Ma) and Middle Pleistocene (Horizon H1, ~0.8 Ma) discontinuities (Figures 5.5, 5.6 and 5.8C) showing an upslope migration towards east (Figures 5.8A and 5.8C) and south (Figure 5.6). Sediment waves are more concentrated between Early Quaternary (Horizon H2, ~2.4 Ma) and Middle Pleistocene (Horizon H1) discontinuities, constituting palaeo-waves sealed by overlaying continuous and well-stratified reflections (Figure 5.6E, 5.6F, 5.6G). In the northern sector, sediment waves occur above the Middle Pleistocene Discontinuity (Horizon H1) reaching the surface (Figure 5.6B), while in the middle sector sediment waves formed between Late Pliocene and Middle Pleistocene, with no superficial expression (Figures 5.6C, 5.6D, 5.6E and 5.6G). These sediment waves occur between ~1500 ms and 2200 ms, covered by overlying thick sediment layers. In the southern sector of the SCD (Figures 5.6F, 5.6G (zoomed section) and 5.8C), these features are closer to or even at the seafloor surface. These sediment waves present asymmetric structure with steeper faces exposed both to the west and to the north (Figure 5.6). Likewise, there is a decrease in the wavelength and wave-thickness from west and north

towards east and south (Figure 5.6), where SCD contacts with the upper slope eastwards and south-eastwards.

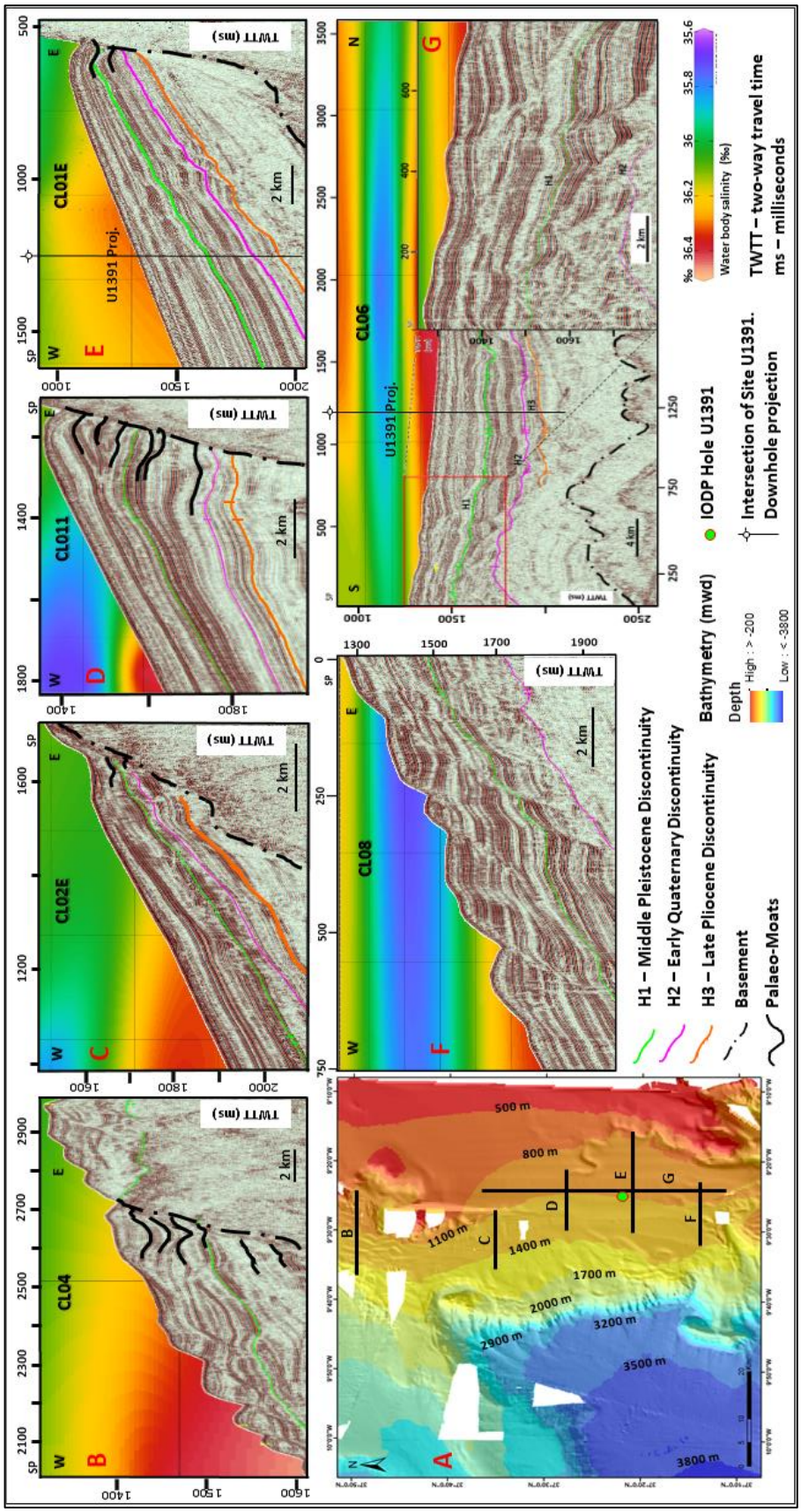

FIGURE 5.6 - Examples of sediment waves in the seismic record. (A) – Geographical display of seismic profiles. GREEN DOT = IODP HOLE U1391; (B) – Surficial and buried sediment waves. Palaeo-moats indicating different stages of the palaeo-currents; (C) - Buried sediment waves with large wave-lengths; (D) - Palaeo-sediment waves on the central section of the study area; (E) - Well-Defined sediment waves with no surficial expression; (F) - sediment waves with surficial expression; (G) - Upslope-migrating sediment waves toward south. Black dashed line defines the basement. Red square points to sediment wave bedforms. H1 - Middle Pleistocene Discontinuity; H2 - Early Quaternary Discontinuity; H3 - Late Pliocene Discontinuity. Black lines point to palaeo-moats that are recognised along East-West seismic profiles crossing the contourite drift (B. C. D and El. U1391 Proi. – Proiected site U1391 – IODP Expedition 339.

5.3.2.2.3 – EROSIONAL/NON-DEPOSITIONAL FEATURES (MOAT)

The SCD eastern flank is confined by an asymmetric roughly N-S oriented linear depression – a moat (Figures 5.7A, 5.7B, 5.7C and 5.7D). It extends from south (37º10'N) to

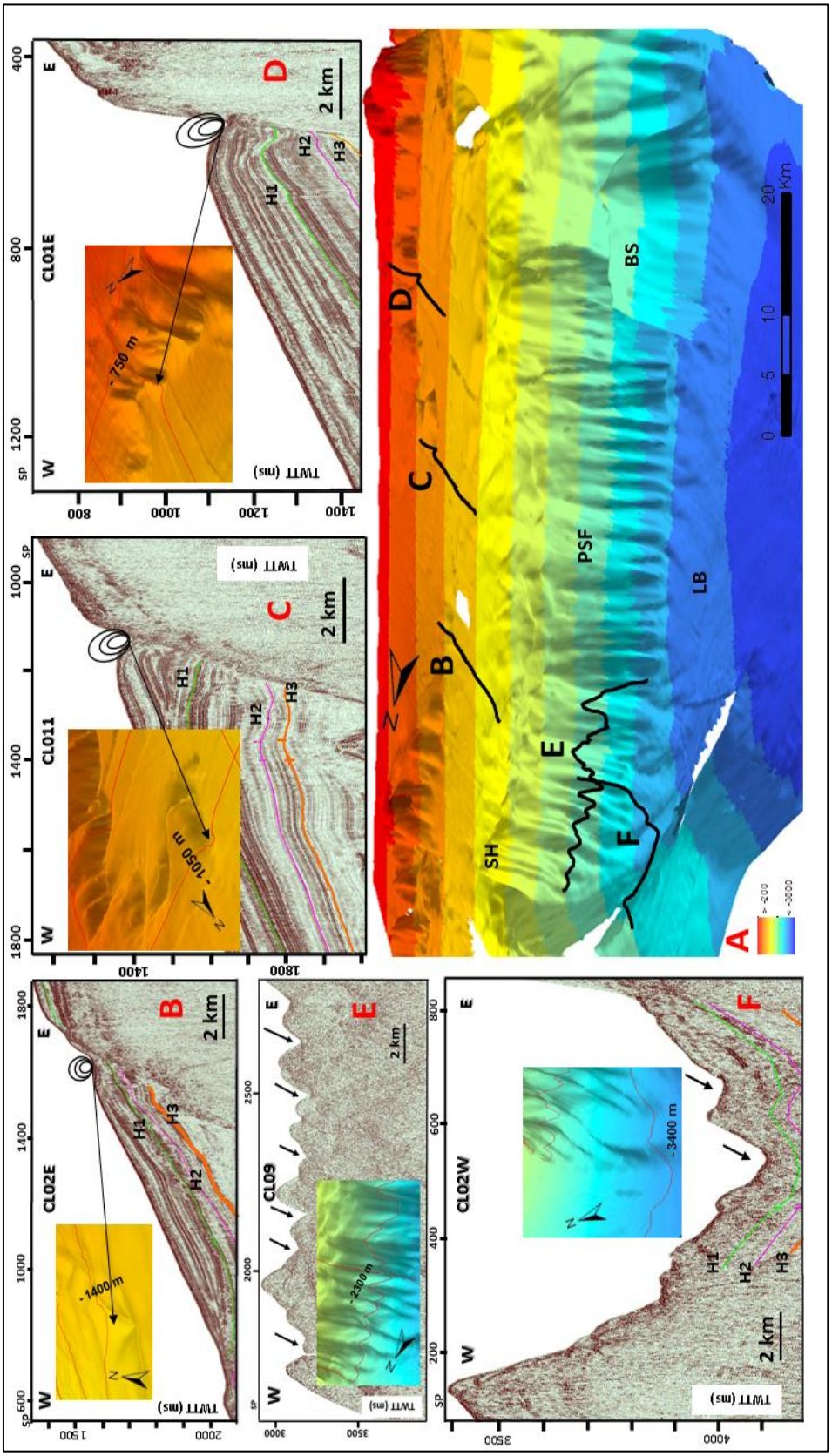

FIGURE 5.7 - Examples of erosional features in the seismic record. (A) – 3D bathymetry with the location of profiles shown in B, C, D, E and F; (B) – Moat crossed by seismic line CL02E. (C) – Moat with a more pronounced shape than in B, crossed by seismic line CL11. (D) – Moat Crossed By Seismic Line CL01E. (E) seismic line CL09 – gullies in the PSF (Pereira de Sousa Fault) represented by black arrows. (F) Seismic Line CL02W – deep gullies (black arrows) in the entrance of LB (Lebre Basin) affected by the passage of a deep trough that comes from the SH (Sines Hook). Black ellipses in (B), (C) and (D) point to the moaT. H1 - Mid-Pleistocene Discontinuity; H2 - Early-Quaternary Discontinuity; H3 - Late Pliocene Discontinuity.

north (37º 45' N) for 83.7 km, occupying an area of 145.1 km^2 and contouring the base of the upper continental slope and surrounding the SCD eastern flank (Figure 5.4). This channel-like feature deepens southwards showing a V-shaped and steep-sloped morphology (Figures 5.7C and 5.7D), whereas northwards it becomes less pronounced and more U-shaped (Figure 5.7B). Despite this, the moat migrates bathymetrically from ~700 until ~1400 mwd, and simultaneously westwards. This feature presents three main segments that change morphologically from south to north. The southern segment is an irregular N-S to NNE-SSW trending stretch that extends for ~45 km. The central segment is linear, trending NW-SE for an extension of ~39 km. The northern segment has an irregular trace with ~11 km trending NE-SW (Figures 5.4 and 5.7A). The moat path is interrupted locally in the transition between the central and the northern sections by landslide deposits (Figure 5.4).

5.3.2.3 – GRAVITY-DRIVEN FEATURES

5.3.2.3.1 – GULLIES

Gullies are narrow and elongated incisions, displaying pronounced V- and U- cross sections (Figure 5.7). They occur on the steepest slopes of both the upper slope, and the lower slope in the PSF scarp and Príncipes de Avis hillsides (Figures 5.4 and 5.8). Gullies morphology mainly varies with the slope gradient. On the steepest gradients (>10º) gullies are deeper, ranging from ~30 to ~120 m depth and from ~70 m to ~1000 m width (Figure 5.7A). In gently dipping areas (< 10º), as the Lebre Basin, gullies depths are less than 30 m and width varies from ~1300 m to ~2000 m (Figure 5.7F and 5.9D). In the PSF scarp, gullies are downslope erosional features with extensions from ~2 km to ~20 km long in a depth range of ~1800m (Figures 5.4 and 5.7E). These closely spaced (< 1 km) gullies link the middle-slope (III) with the downstream slope basin (V), crossing the lower continental slope (Figures 5.4 and 5.7A).

In the north-western flank of the SCD, the Sines Hook (SH) is the most prominent gully of the study area (Figures 5.4 and 5.7A). The SH is a 40-km long sharp and V-shaped feature with depths that reach ~700 m in the deepest sites (~2100 mwd). SH formed at ~1900 mwd as a S-N oriented along-slope feature that contours the northern flank of PSF escarpment, transforming then into a downslope feature (Figures 5.4 and 5.7A) connecting to the base of this scarp at ~3200 mwd. In the seismic profile the bottom of the V-shaped valley is blanketed with transparent seismic units with troughs and mounds, interpreted as channels and levees that can extend more than 14 km into the Lebre Basin (Figure 5.7F).

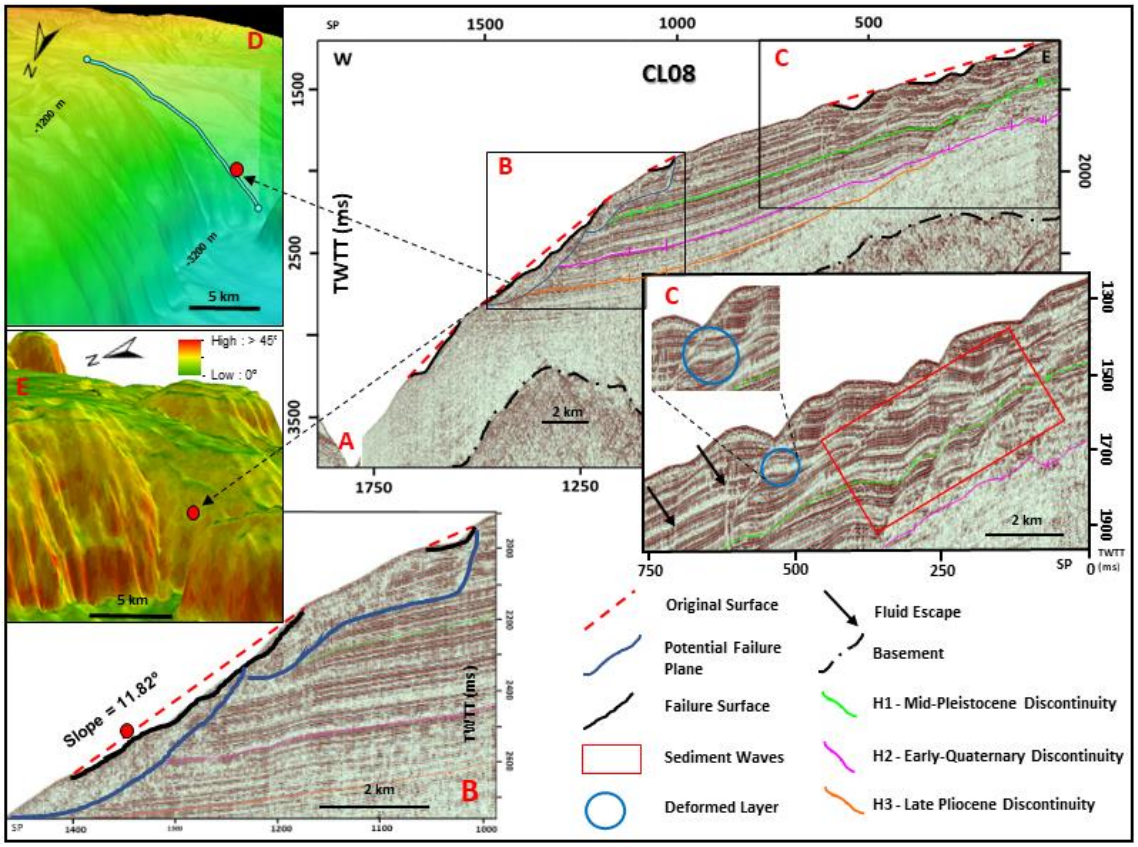

FIGURE 5.8 - (A) - Seismic line CL08. Slide scars on the seafloor and potential failure surfaces on the subsurface. Upslope-migrating sediment waves on the topmost layers of the contourite drift. H1 is the Middle Pleistocene Discontinuity; H2 corresponds to the Early Quaternary Discontinuity; H3 corresponds to the Late Pliocene Discontinuity. TWTT – two-way travel time; ms – milliseconds. (B) – Detail of slide scars and potential failure surfaces. (C) – Sediment waves mainly affecting quaternary sediments. (D) – Bathymetric map with the track of the seismic profile expressed in (A). Red dot marks a headscarp of a landslide scar. (E) – Slope gradient map.

5.3.2.3.2 – LANDSLIDES

A total of 169 landslide scars were identified in the Alentejo Margin (Figure 5.10), where they are widespread features. These mass wasting features can be recognized through two main distinct components – landslide scars and deposits. Landslides scars concentrate

mostly in the western limit of the SCD (Figures 5.4 and 5.10) near the middle slope-break, coinciding with the top of the PSF scarp. Here, slope disrupted sediments leave scars

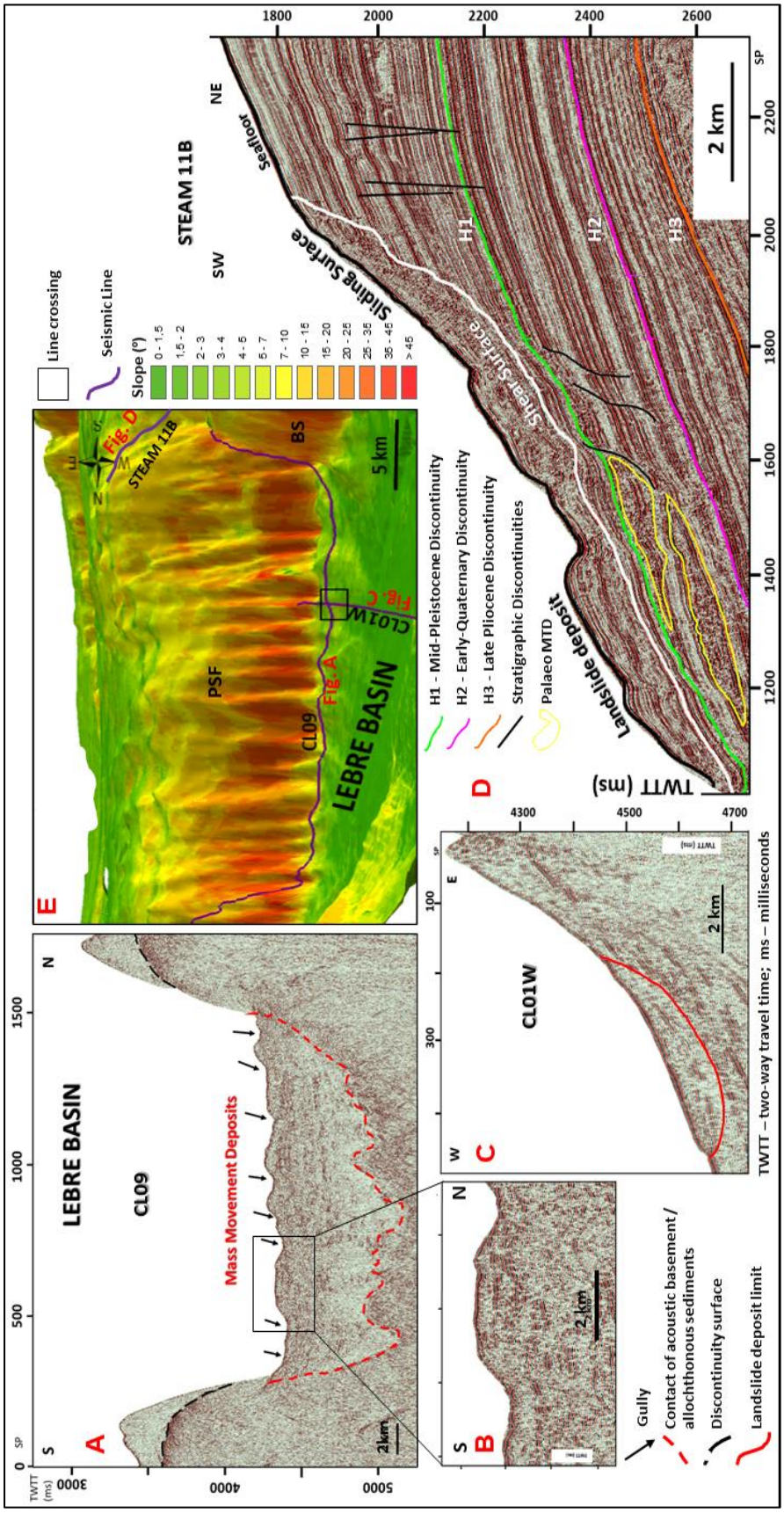

FIGURE 5.9 - (A) Seismic line CL09 with S-N orientation. Red dashed line represents the contact in depth of the acoustic basement with the sediments deposited in the Lebre Basin. Black arrows point to the gullies, which develop seawards from the reader's position. Black-dashed line points to the contact of the basement with the uppermost deposited sediments in the slopes surrounding lebre basin. (B) Zoom from the black square in Figure (A).. (C) Seismic line CL01W crossing CL09. Red line represents a mass movement deposit. (D) Seismic line STEAM 11B. Slope instability, with scars and deposits in active state. Palaeo-deposits found in the base of the slope, indicate presence of past instability. Black lines inside the profile indicate seismic reflection discontinuities and hence, sedimentary incoherencies. Lighter and less structured or structureless horizons indicate faded sediments, where excess pore-pressure and overloading seem to be acting. (E) - 3D slope gradient map with the location of the seismic profiles. BS – Bow Spur; PSF – Pereira de Sousa Fault.

(bathymetric hollows) and travel downslope through a pathway, accumulating then as landslide deposits in Lebre Basin (Figures 5.4 and 5.10). The slide scars are identified on the seismic reflection record as sediment-disturbed areas with truncated-layer parallel seismic reflections (Figure 5.8B and 5.9D).

Landslide deposits are present mainly on the base of seamounts and scarps, being displayed as mounded features (Figure 5.9D) with hummocky and transparent/fuzzy seismic facies and often with very disturbed and discontinuous internal reflections (Figure 5.9B and 5.9D). Palaeo-deposits are also found between Early Quaternary and Middle Pleistocene discontinuities, between 1800 and ~1990 mwd, with thickness from ~50 ms up to ~610 ms (TWTT) and a maximum extension of ~4.5km (Figure 5.9D). The mounded body recognized in the Lebre Basin near the foot of the PSF scarp (Figure 5.9A), is a ~75 km long deposit parallel to PSF, with ~11 km maximum width and an area of ~575 km^2. This deposit shows chaotic facies with the absence of continuous acoustic reflections (Figure 5.9B). Sediment's thickness (Figure 5.9) varies from 900 ms to 1300 ms (TWTT) near the PSF scarp and diminishes westwards. For example, westwards from Bow Spur, the maximum thickness recorded on the deposit is 400 ms.

5.3.2.3.2.1 – LANDSLIDE PRONE AREAS: DIMENSIONS AND SCAR CONCENTRATION

Scars concentration and their dimensions (area and volume) vary across the study area according to the bathymetric position and slope gradient (Figure 5.11).

TABLE 5.1 – Area and volume of the landslides' scars occurring both in the whole study area and in the contourite

Parameter	Alentejo Margin		SCD		Outside SCD	
	Scars Area (km^2)	*Scars Volume (km^3)*	*Scars Area (km^2)*	*Scars Volume (km^3)*	*Scars Area (km^2)*	*Scars Volume (km^3)*
Total	517.24	30.92	246.56	9.18	270.68	21.68
Average	3.06	0.18	2.47	0.09	3.92	0.32
Median	1.87	0.05	1.48	0.04	2.20	0.07
Max	40.33	6.34	14.03	1.06	40.33	6.34
Min	0.15	0.01	0.36	0.01	0.15	0.01

The 169 landslide scars identified in the Alentejo Margin, are comprised between > 300 mwd, in the upper slope, and ~3000 mwd, in the lower slope (Figure 5.10), corresponding to an overall area of 517.24 km^2 and a total volume of 30.9 km^3 (Table 5.1). The main cluster of disruptions is in the western border of the SCD, where most scars are concentrated, encompassing 68% of those (Figure 5.10B), which indicates a large concentration of scars on this morpho-bathymetric area. One hundred landslide scars affect the SCD between depths of 1100 and ~2500 mwd (Figures 5.10 and 5.11), occupying an area of 246.56 km^2 and 9.2 km^3 volume (Table 5.1), while 69 occur outside in the remaining area, performing a total area of 270.68 km^2 and 21.68 km^3 volume.

TABLE 5.2 – Statistics for scars' slope

Scars' Slope	Alentejo Margin (º)	SCD (º)	Outside SDC (º)
Average	7.48	7.83	6.98
Median	5.96	5.76	6.18
Max	28.34	23.66	28.34
Min	0.10	0.10	0.37

The average values for scars area and volume indicate that these values are higher outside than inside the SCD area (Table 5.1). Larger landslide scars affect the SCD, apart from three large scars with areas between 15 and 40 km^2 outside the SCD (Figure 5.10A), constituting outliers that lead to a positive difference for the area outside SCD of ~1.45 km^2 in average area and ~0.23 km^3 in average volume (Table 5.1).

TABLE 5.3 – Scars concentration by Class of slope

Scars' Slope	Alentejo Margin *(Scar Concentration)*	SCD *(Scar Concentration)*	Outside SCD *(Scar Concentration)*
> 20º	7.10	8.00	5.80
> 10º	28.40	34.00	20.29
< 10º	71.60	66.00	79.71
< 5º	43.20	45.00	40.58
2 - 5º	23.67	22.00	26.09
< 2º	19.53	16.00	14.49
< 1º	8.28	7.00	10.14

These outliers force the extremes, inducing the idea that smaller scars concentrate on the SCD area. Except those outliers, most of the larger scars are on the SCD surface (Figure 5.10). The smaller scars are mainly concentrated on the steepest slopes. The smallest scar lies outside the SCD area, where the extreme values, both the minimum and the maximum, are present. Hence, in the SCD the distribution of scars area values is less scattered and the difference between the biggest and the smallest scars is not as high as in the remaining area. The disrupted areas comprise variable slope angle values, whose average is lower for the remaining area (6.98º), than for the SCD (7.83º) - Table 5.2. The maximum and minimum slope angle values affecting landslide scars are outside the SCD (Table 5.2), indicating higher homogeneous slope conditions on the SCD.

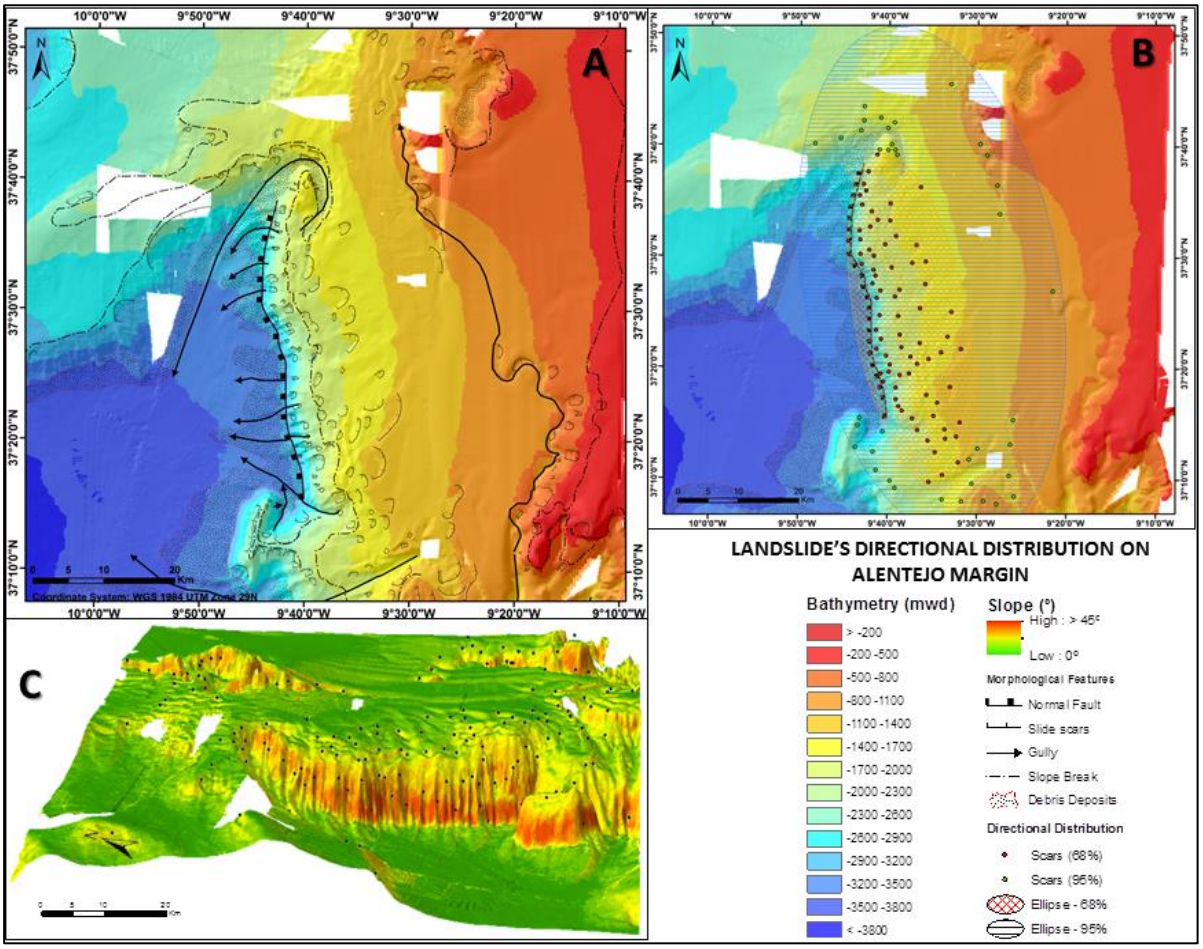

FIGURE 5.10 - (A) - slide scars map of Alentejo Margin. Landslides are represented by the head scarp, and not by the whole scar, to simplify the image interpretation. I – Continental Shelf; II – Upper Continental Slope; III – Middle Continental Slope; IV – Lower Continental Slope; V – Continental Basin. (B) - Landslides directional distribution on the study area. Dots correspond to landslide scars. (C) – Three-dimensional slope model of the study area with slide scars. Black dots correspond to landslide scars inventoried in the area.

A detailed analysis of the distribution of the scars is made in seven slope gradient classes varying between <1º and >20º (Table 5.3). Higher scar concentrations occur on slopes < 10º both in the SCD (66%) and in the remaining area (79.7%) – Table 5.3. Almost half

(45%) of the scars occurring on the SCD have gradients < 5º, whereas this scar concentration values fall to 40.6% in the remaining area. Scar concentration on gradients > 10º is higher for the SCD area (34%) than for the remaining area (~20.3%), as well as for gradients > 20º (8% against 5.8%) – Table 5.3, Figure 5.11B. These higher values for SCD reflect the high scar

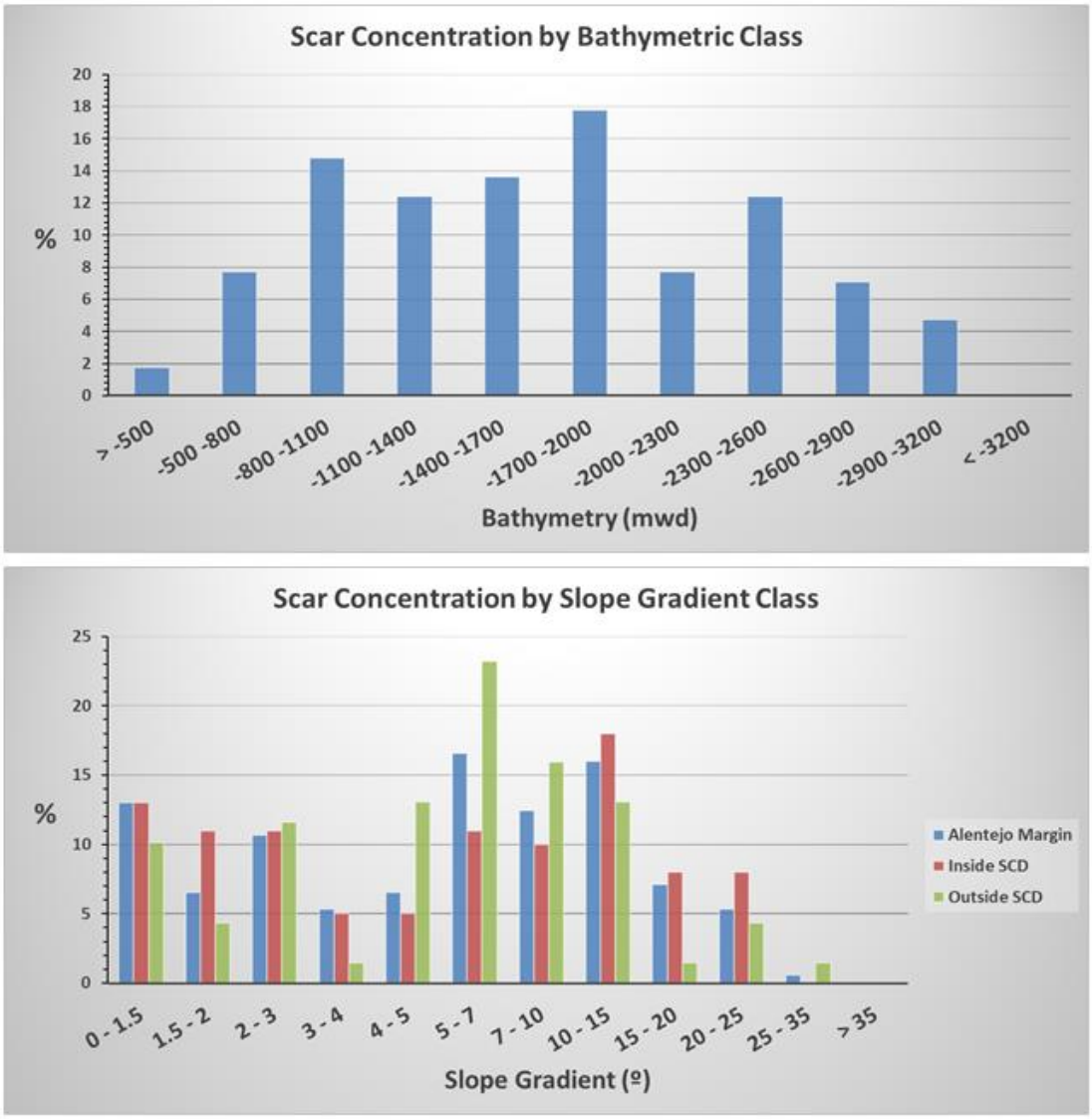

FIGURE 5.11 - Landslide scars concentration. (A) - Scar concentration by bathymetric class. (B) – Scar concentration by slope gradient class, for the whole study area and for inside and outside SCD.

concentrations on the western border of the contourite near the steep PSF scarp. Scar concentration varies by bathymetric class in a symmetric way. The shallowest areas (> 500 mwd) and the deepest areas (2900 - 3200 mwd) present scar concentrations < 5% (Figure 5.11) – lower than the neighbour classes. About 58% of the scars occur between ~800 and 2000 mwd, almost all in the SCD (Figures 5.10 and 5.11), where more sediment is available. The highest scar concentration occurs in the slope-break in the western boundary of the SCD (1700 – 2000 mwd) where 18% of the scars occurred (Figure 5.11). The heights of the head-scarps are heterogeneous, ranging from 10 m to 575 m height.

5.4 – DISCUSSION - INTERACTION OF ALONG-SLOPE AND DOWNSLOPE PROCESSES: IMPLICATIONS ON SLOPE STABILITY

The morphological map of the Alentejo Margin presents varied geomorphological along-slope and downslope erosional and depositional features such as contourite drift and moat, sediment waves, gullies, slide scars and slide deposits. The geomorphology of the area is strongly constrained by the interplay of three controlling-agents: tectonic-, oceanographic- and gravity-driven activity that create hybrid morphologies.

5.4.1 – TECTONICALLY-DERIVED FEATURES AND CONTROLLING-AGENTS IMPACT

Tectonic activity is a semi-permanent agent that exerts an indirect action on the geomorphological processes by deforming the seafloor at different space and time scales (Gràcia *et al.*, 2003; Terrinha *et al.*, 2003). Inherited tectonic structures are geomorphologic obstacles that interfere on the dynamics of both bottom currents' circulation and sediments transfer, leading to a complex geomorphological evolution and conditioning both along- and downslope processes. Variable cross-sectional profile heights of the PSF scarp, from north to south (Figure 5.3), indicate variable heights, suggesting that either tectonic activity has been affecting the area differently through the time or sediment removal acted with different impact along the scarp.

Several tectonic features have developed in the area, where the most prominent is the PSF scarp (Figures 5.4 and 5.7A). The neotectonic activity in the neighbouring onshore area indicates uplifting rates of 20 cm/kyr (Figueiredo *et al.*, 2013). This means an uplift of approximately 560 m for the Quaternary, assuming that this uplift rate extends basinwards until the continental slope. Inspection of figures 5.5 and 5.6 shows progressive unconformities from the lower Quaternary through present within the tilted SCD. At ~1500-1600 ms sediments are dragged upwards indicating relative uplift of the PSF footwall (Figure 5.5), which contributes for the decrease of sediment accommodation (Terrinha *et al.*, 2003) favouring landsliding activity (Roque *et al.*, 2015), due to steepening. This is quite evident both on the Atlantic and Mediterranean Iberian margins (Camerlenghi *et al.*, 2010; Casas *et al.*, 2015), where the most tectonically active areas display high number but small slope

failure events. Thus, as for the Águilas escarpment (Casas *et al.*, 2015), the uplifting of the Alentejo Margin (Terrinha *et al.*, 2003), associated with the high-angle PSF (Figures 5.3 and 5.7A) promotes the development of several small-scale retrogressive landslides. As a consequence, many landslide scars and gullies are present in the seabed between 1700 – 2000 mwd (Figure 5.10), not allowing the preservation of the along-slope derived features. This suggests that downslope activity is dominant over along-slope activity in this sector of the slope at least since the end of the last glaciation, when MOW's circulation migrated to upper depths (Schönfeld and Zahn, 2000).

The irregular and diversified steep-slope formation on the Alentejo Margin (Figure 5.3) points to both differential responses to tectonic activity and to differential sediment erosion, which will both affect the along-slope and downslope sedimentary activity. Besides, the palaeotopography, inherited from previous tectonic phases, greatly controls the local balance between erosion and deposition.

5.4.2 – ALONG-SLOPE PROCESS-DERIVED BEDFORMS AND CONTROLLING-AGENTS IMPACT

Bottom currents constitute semi-permanent agents (Stow *et al.*, 2013) whose impact plays a dynamic role on the seafloor morphology. The MOW began its activity with the re-opening of the Gibraltar Strait in Latest Miocene times (Messinian), and it is the most effective bottom current acting in the area (Hernández-Molina *et al.*, 2014b). The MOW underwent significant changes in composition and flow dynamics, impacting the North Atlantic circulation (Schönfeld and Zahn, 2000; Hernández-Molina *et al.*, 2014b; Kaboth *et al.*, 2017a). This water mass suffered two main phases of current intensification spanning from ~2.0 Ma to 1.0 Ma and from 0.9 Ma up to present times (Hernández-Molina *et al.*, 2014b). This intensification has geomorphologic expression both in the northern and southern sectors of the Alentejo Margin (Figure 5.6) where sediment waves appear well defined above the Middle Pleistocene discontinuity (H1) and reach the seabed surface. Furthermore, the sedimentary package appears much more continuous from Late Pliocene upwards in the middle-slope where the SCD is being formed (Figure 5.5A). MOW has two main cores (Schönfeld and Zahn, 2000) whose action centres at between 400 and 1400 mwd (Hernández-Molina *et al.*, 2014b). However, the SCD emplacement ranges bathymetrically from ~800 to ~1800 mwd in the study area (Figures 5.4 and 5.5A), probably due to geomorphological

constrictions (accommodation space) imposed by the morpho-structural setting to the bottom currents. Inspection of the morphology and tectonic structure show that the accommodation space is essentially controlled by inherited Mesozoic rifting structures, essentially horsts and grabens (e.g., Pereira and Alves (2011)), constrained by the PSF and the upper slope escarpment (Figures 5.4 and 5.5A) that favoured trapping of suspended MOW contourite sediments at a sedimentation rate of ~27cm/kyr since the Quaternary (Stow *et al.*, 2013).

The over-steepened PSF scarp prevents drift accumulation westwards by promoting the downslope evacuation of sediments through retrogressive landsliding activity (Figures 5.5 and 5.9D). Eastwards drift progradation is limited by a well-defined escarpment in the upper continental slope showing a well-developed moat (Figure 5.5A) at the base of the upper slope, avoiding the drift's lateral advance. Presently, the moat is formed in the base of the upper continental slope in the contact with the seawards contourite body (Figure 5.4), at ~750 - 800 mwd (Figure 5.5). This S-N trench-like feature is parallel to the MOW's path direction and it is eroding the footwall of the Upper Slope, depositing sediments westwards (Figures 5.5A, 5.6B, 5.6C, 5.6E and 5.7A, 5.7B, 5.7C, 5.7D).

There are three basinwards dipping abraded surfaces: at ~750-800 mwd; at ~1200 mwd and at ~1350 mwd (Figure 5.5A). Abraded surfaces (Figure 5.5) are sculpted by water-mass interfaces (Ercilla *et al.*, 2016) that constitute intense pycnoclines affected by baroclinic activity (McCave, 2001; Pomar *et al.*, 2012; Rebesco *et al.*, 2014; Ercilla *et al.*, 2016). At present, an active abraded surface is present at the base of the upper continental slope and corresponds to the actual moat at ~750-800 mwd (Figure 5.5A), where the current is carving the inherited Mesozoic rifting escarpment. The lower and upper ones contain the proposed position of the lower and upper branches of MOW, respectively (Hernández-Molina *et al.*, 2014b) that flow in the area at these depths, since the Holocene - ~10.000 yr - (Schönfeld and Zahn, 2000). Detailed inspection of the stratigraphy under the actual moat, at 1000 to 1200 ms (TWTT) shows erosive unconformities indicating strength variations in bottom currents carving activity (Figure 5.5A).

These observations suggest that the MOW lower branch is steadily eroding the sediments of the west edge of the SCD at the depth of the deeper abraded surface (~1350 mwd). The abraded surface at ~1200 mwd can result from slight fluctuations of the MOW lower core. The upper core probably experiences vertical fluctuations (or core splitting)

because it is steadily eroding both the harder fault escarpment at 400-550 mwd, as well as its footwall sediment wedge between ~750 and 800 mwd.

The deeper abraded surfaces (Figure 5.5) are not so carved as the shallower ones, indicating that either the lower core of MOW is presently weaker than the upper one (Llave *et al.*, 2007) or that the lower core might have already progressed upwards from its glacial position, leaving the carving activity in a suspended state. Moreover, these surfaces might have been also subjected to reworking activity by other agents, promoting the fade up of these features.

Sediment waves are dominantly oblique crest-oriented (Figure 5.4) rather than slope-parallel bedforms. These current-induced bedforms (Llave *et al.*, 2020) develop in the SCD, in the depth range of the MOW, ~800 and ~1700 mwd. However, sediment waves are also mapped deeper than these bathymetric levels, indicating the influence of bottom currents below the expected base of the MOW, indicating either the presence of the MOW at deeper bathymetric levels (Schönfeld and Zahn, 2000), but also suggesting the probable presence of other bottom currents at those levels. The concentration of sediment waves at surface levels (Figures 5.6B, 5.6F and 5.6G) mainly along MOW's pathway indicates a direct action of this water mass over sediment waves. Stratigraphically, these concentrate from the Pliocene discontinuity (H3) up to the Holocene, (Figures 5.5, 5.6, 5.7 and 5.8) towards the eastern and southern flanks of the SCD (Figure 5.6). This migration indicates different stages of the MOW during this period, both in terms of bottom current strength and depth of circulation, portrayed on the migration of sediment waves from lower to upper stratigraphic horizons and simultaneously spatial current displacement as the waves evolve from west and north to east and south. The intensification of sediment wave formation, especially from the Quaternary discontinuity (H2) upwards and near the Middle Pleistocene Discontinuity (H1) – Figures 5.5 and 5.6 - is coincident with the two latest (third and fourth) Hernández-Molina's (2014b) MOW's evolution phases that occurred during the Pliocene-Quaternary fault reactivation period and led to the intensification of the bottom currents' carving activity (Llave *et al.*, 2007; Zitellini *et al.*, 2009; Brackenridge *et al.*, 2013; Hernández-Molina *et al.*, 2014b). These phases roughly coincide with velocity perturbations of MOW (Ercilla *et al.*, 2016) and with the main stratigraphic discontinuities that correspond to the main foci of sediment waves (Figures 5.5 and 5.6). Furthermore, the interface, between MOW's upper and lower branches may have produced internal waves inducing large perturbations in the current's velocity as well as vertically displacing water parcels capable of generating sediment waves (Ercilla *et*

al., 2016). Above Middle Pleistocene Discontinuity (H1), the sedimentary column is thicker than in the units below (Figures 5.5, 5.6, 5.7B and 5.7D), demonstrating an increase in the sedimentation rate and a change in MOW's flow dynamics.

The variation of sediment wave's orientation from north to south along the SCD suggests variations in the MOW flow intensity and direction. The oblique orientation in the middle part of the study area (Figure 5.4), points to bottom currents' and internal waves action rather than structural. Contrasting with the main NE-SW crests orientation, in the northern and southern parts of the area there are crests roughly parallel to the regional slope, suggesting higher structural action rather than bottom currents. This may also possibly be due to a narrowing in the MOW's flow path between the Sines Hook and the eastern escarpment. This narrowing of the area may cause the lower branch of the current to accelerate and the presence of the Sines Hook may promote current diffraction and consequently the generation of wavy features at seabed surface.

5.4.3 – GRAVITY-DRIVEN PROCESSES AND THEIR INTERPLAY WITH BOTTOM CURRENTS AND PRE-EXISTING STRUCTURE

The morphosedimentary out-building of the Alentejo Margin points to considerable downslope activity, which results in numerous gravity-driven features (Figure 5.4). Most of these features are present both in the steeper slopes created by pre-existing structure and along bottom currents' (MOW) pathway (Figures 5.1B and 5.4). This suggests interdependence and interplay of gravity-driven processes with both bottom currents and pre-existing structure, which contribute for sculpting the morphology.

Pre-existing structure promotes gravity-driven activity through sediment deformation and oversteepening that acts in the study area as both triggering and pre-conditioning factor. The effect of gravity due to oversteepening on slope instability is evident in several sectors of the Iberia Margin (Canals *et al.*, 2004; Ercilla *et al.*, 2008a; Casas *et al.*, 2015). In the Alentejo Margin, this is evident especially in the PSF's surroundings where a dense concentration of landslide scars has formed (Figures 5.4 and 5.10). In these areas with gradients > 10º (Figure 5.10C), the effect of gravity seems to be strong enough to promote slope instability and sediments displacement. This is also evident in other working areas around the world (Mosher *et al.*, 1994; 2010; Ercilla *et al.*, 2011; Piper *et al.*, 2012). Although

steepness is not the only factor contributing for slope instability (Hampton *et al.*, 1996; Urlaub *et al.*, 2015), in the study area there is a considerable number of landslide scars occurring in steeper areas (Figure 5.10C), especially along the top of the PSF scarp (Figures 5.4 and 5.10). This steep normal-fault scarp, whose sedimentary building is being affected by inverse faults that constrain its accommodation space, at the top, and fold the contouritic sediments (Figure 5.5A), deforming their internal structure until near the surface, promoting the appearance of excess pore-pressure and consequent fluid escape (Figure 5.5B) that contribute for slope instability. Also, the depressed morphology in the central area (Figures 5.7A and 5.10C), between Setúbal and São Vicente canyons, where the main landslides cluster is present, suggesting the influence of palaeo-topography. The FMP, EG, PE hills in the southern area and IS and IDH hills in the northern area (Figure 5.4) present many landslide scars, suggesting the influence of the steepness of the tectonic structures in downslope processes. These morphosedimentary evidence indicate that the pre-existing structure constrains the sedimentary processes.

Bottom currents have critical role governing the sedimentary out-building throughout the Iberian margins (Hernández-Molina *et al.*, 2011; Alonso *et al.*, 2016; Ercilla *et al.*, 2016). Although bottom currents essentially favour along-slope processes (Hernández-Molina *et al.*, 2003; Llave *et al.*, 2007; Van Rooij *et al.*, 2010) they also contribute for slope instability through the high sedimentation rate (Stow *et al.*, 2013) that promotes an increase of stress in the sediments, leading to the decrease of sediment's strength (Casas *et al.*, 2015; Shanmugam, 2015), thus disturbing their internal cohesion. The presence of a dense field of sediment waves in the SCD seems to be the result of the interaction between subjacent structure, which promotes sediment folding and constrains sedimentary out-building (Figure 5.5), and bottom currents that act directly on the sediments surface, promoting wavy sequences (Figure 5.6). The formation of sediment waves seems to be promoting the occurrence of many small scars on the sedimentary package (Figure 5.5A), by favouring the differential deposition of the sediments brought by bottom currents. Furthermore, as also observed by Lee *et al.* (2002), sediment waves create discontinuity surfaces in the inner structure of the sedimentary package (Figures 5.5A and 5.6) that work as shear surfaces during the sedimentation process, when overloading and overpressure take place. These discontinuity surfaces are preferential paths for excess pore-pressure release (Figure 5.5A) and fluid escape (Figure 5.5B). In these areas, the development of shear strength reduction as well as potential failure planes (Figures 55.B and 5.8) is evident.

The presence of many seismicity clusters in the nearby area suggests that earthquakes might be an important triggering mechanism of slope instability in the sedimentary package, whereas the pre-existing structure created by tectonics constrains all the depositional evolution and the sequential sedimentary process, thus leading to the appearance of folded sedimentary sequences, which affect the ulterior depositional evolution of the drift. The constraints put by the bottom currents in the surface of the sedimentary package alongside with those put underneath by the structure are creating conditions for several other pre-conditioning factors to develop.

5.4.3.1 – SLOPE INSTABILITY: TRIGGERING AND PRE-CONDITIONING FACTORS

Two main types of scars exist in the study area: wide and elongated scars dominantly in gentler areas, and small, high-frequency scars in the steepest slopes. This suggests differential action and diverse factors affecting slope stability in the Alentejo Margin. Similar results have been obtained in other areas (Casalbore *et al.*, 2011; Ceramicola *et al.*, 2014).

Several elements affect submarine slope (in)stability, acting as triggering and pre-conditioning factors (Mosher *et al.*, 1994; Haflidason *et al.*, 2004). **Seismicity** is an important triggering factor of slope instability on the area (Figure 5.12) through its transient activity. Important historical and instrumental seismicity has been recorded in the SW Iberia (Baptista *et al.*, 1998; 2014; Silva *et al.*, 2017; Veludo *et al.*, 2017) along deep-rooted tectonically active faults, favouring slope disruption. According to the seismicity distribution on the area, from IPMA's catalogue 2000-2014 (Custódio *et al.*, 2016; Veludo *et al.*, 2017), there are many low-magnitude ($M < 4$) epicentres that mainly occur at depths >15 km (Veludo *et al.*, 2017, Fig. 3A), which probably contribute for the appearance of many small scars in the area, allowing for the sudden increase of overloading and excess pore fluid pressure (Lee and Baraza, 1999), leading then to internal bed disruption and consequent slope instability.

Slope angle (oversteepening) is quite important for submarine landsliding activity, e.g., (Piper *et al.*, 2012), and can be considered both as a triggering and pre-conditioning factor (Mosher *et al.*, 2010). On the steepest slopes of Alentejo Margin, tectonically derived oversteepening may be itself considered as a triggering factor of slope instability (Figure 5.12) once sediments can be detached by the effect of gravity, through the increase of shear stress. The effect of gravity can be an important triggering factor when associated with pre-conditioning factors in the inner structure of the sediments. This is particularly evident in the

PSF scarp, where discontinuity surfaces and fluid escape are observed (Figure 5.5). The presence of shear failure planes seems to capture and channelize fluids (Figure 5.5), which may lead to an increment of fluidization in the failure plane thus favouring sediment detachment. Oversteepening is particularly important in tectonically active margins (McAdoo *et al.*, 2000; Casas *et al.*, 2015; Chiocci and Casalbore, 2017; Casalbore *et al.*, 2019), as the Alentejo Margin, where steepness amplifies the effects of sediments' weakness. Oversteepening is also an important pre-conditioning factor (Figure 5.12), when associated with transient factors as seismicity that contributes for slope failure through earthquake acceleration (Lee and Baraza, 1999). The presence of a considerable number of scars (~30%) in the steeper areas (> 10º) leads to assume that steep slopes contribute for a regular landsliding activity. The western border of SCD is plenty of surface deformation, mainly small landslide scars (Figures 5.8A and 5.10C) and steepness seems to play an important role. The steeper are the slopes, the smaller are the scars and the greater their density (Figures 5.4 and 5.10). In the steepest slopes, the scars tend to be narrower and smaller because of the action of gravity that increases the shear stress and thus increases the sliding activity. This constant activity contributes to erase past scars, avoiding their enlargement, and to create new steep headwall scars, thus promoting fast retrogressive slope instability. Nevertheless, there

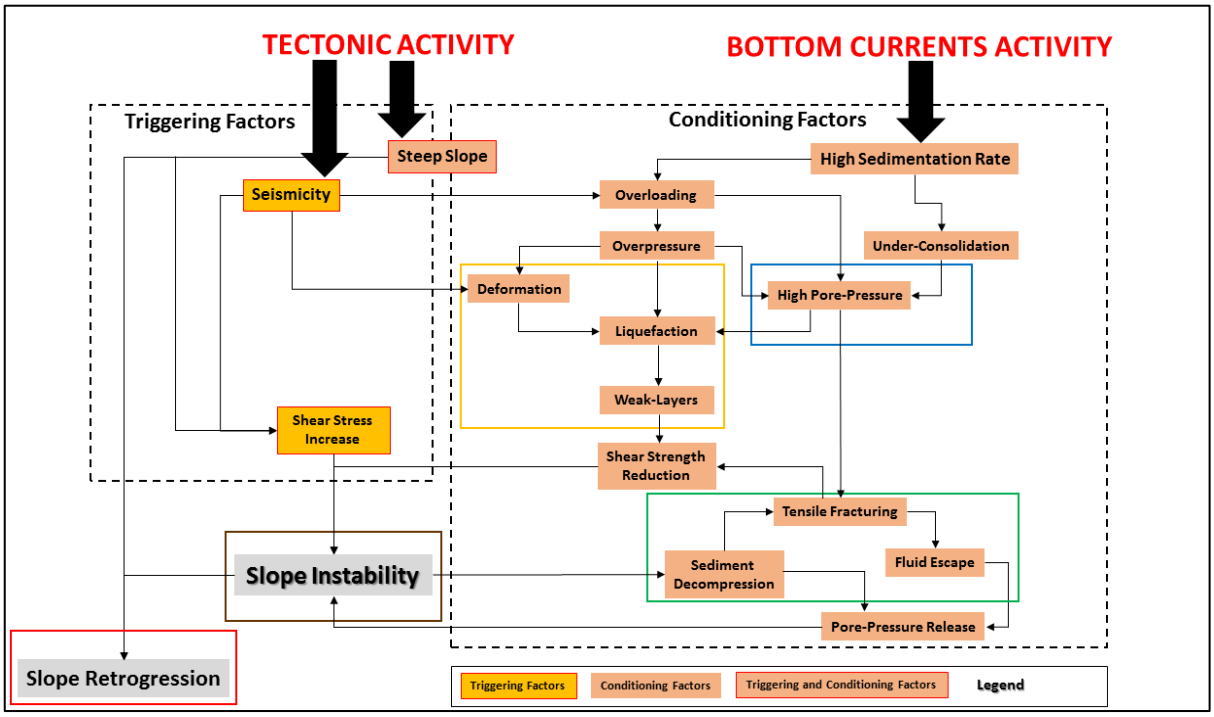

FIGURE 5.12 - Slope instability diagram and interaction of triggering and conditioning factors in the study area. Coloured squares and rectangles point to evidence of triggering and conditioning factors on the study area. Figures inside the coloured squares indicate sites where similar processes are suggested to explain the instability. Yellow square = Figure 5.8; Blue square = Figures 5.5 and 5.8B; Green rectangle = Figures 5.5B and 5.8B; Brown square = Figures 5.8 and 5.10; Red rectangle = Figures 5.7A and 5.8B.

are also examples worldwide, where submarine slides occur at extremely low-angle slopes, < 1º, as in the Mauritania Slide Complex (Henrich *et al.*, 2008) or Storegga Slide (Kvalstad *et al.*, 2005a). Landslides also occur in very low dip angles in the Alentejo Margin, where ~43% of the landslides were triggered in slopes < 5º and 8.3% occurred in slopes < 1º, while only 7% occurred in slopes > 20º (Table 5.3), corroborating that many submarine landslides occur also at very low-angle slopes as has been verified in different parts of the world (Prior and Coleman, 1984; Hampton *et al.*, 1996; Henrich *et al.*, 2008; Urlaub *et al.*, 2015). In low-gradient slopes, the low shear stress and consequent sliding rate, lower than in steeply dipping slopes, allow scars to laterally spread. The presence of large landslide scars in gentler areas (Figures 5.4 and 5.10) indicates that other factors than slope angle act on the sediments so as these to become unstable.

Another important pre-conditioning factor is the **sedimentation rate**. The presence of a contourite drift deposited at a moderately-high sedimentation rate, 17cm/kyr – 27cm/kyr (Stow *et al.*, 2013) contributes for the increase of overloading and under-consolidation of the sedimentary package (Figure 5.12), as verified in other areas (Laberg *et al.*, 2002; Laberg and Camerlenghi, 2008; Urlaub *et al.*, 2015), allowing the formation of pore-pressure in the sediments and favouring the development of weak layers (Sultan *et al.*, 2004) and consequent loss of shear strength and sediment disruption (Figure 5.5) through the loss of cohesion and lowering of the internal friction angle (Shanmugam, 2015). In PSF headwall slope instability, underlain by layers with excess pore-pressure, expressed by fluid escape pipes, is associated with the presence of bed discontinuities in the sediments (Figure 5.5). The rapid sedimentation alongside with seismicity, can promote excess pore-pressure (Masson *et al.*, 1997; Lee *et al.*, 2002), controlling the frictional resistance of slopes (Terzaghi, 1943) and forthcoming landslides' behaviour (Shanmugam, 2015). The combination of overloading and seismicity contributes for the internal rearrangement of the sediment's organization inside the sedimentary package, allowing the formation of **weak layers** (Figures 5.5B and 5.8C). These are pre-conditioning factors of slope instability (Figure 5.12), generally associated with bedding and discontinuity planes (e.g., Hungr *et al.* (2014)) that lead to future failure planes. Data suggest that the effect of weak layers may be also important on gentler slopes as the physiographic domain III (Figure 5.3), where landslides are wider and their evolution seems to be slower than in steeper slopes, suggesting that rapid sedimentation and high excess pore-pressure are probably the main triggering and pre-conditioning factors (Figure 5.12), which according to Urlaub *et al.* (2015) play an important role on developing wide scars in low

gradients. With such low gradients (< 5º) shear strength must be extremely low to cause slope disruptions. In the Alentejo Margin, weak layers mainly appear associated with excess pore-pressure (Figure 5.5), many times created by constraints put by pre-existing structure and syn-depositional forms as sediment waves (Figure 5.8C), whose irregular facets promote a differential pressure on the underlying sediment layers during post-depositional periods. In the western boundary of the SCD many potential failure surfaces develop in sectors affected by excess pore-pressure, where seismic horizons are partially disrupted and truncated by structureless layers (Figures 5.5B and 5.8). Pore-pressure contributes for sediments to become unstable (Urlaub *et al.*, 2013) and weak layers to easily develop (Locat *et al.*, 2014), especially along structural faults, starting new failure planes from there (Figures 5.5 and 5.8). In the Alentejo Margin, pore-pressure seems to be a cause but also a consequence of slope instability as it is common to detect fluid escape structures near and below disrupted sections of the slopes (Figure 5.5B). It seems that the release of weight in the slopes due to landsliding activity creates decompression, favouring then the pore-pressure escape and further slope instability. The effects of the presence of weak layers may be amplified by the action of transient load impacts (Lee and Baraza, 1999) released through seismicity. This leads to excess pore-pressure (Figure 5.5B) and sediment deformation (Figure 5.8C), reducing the shear strength (Skempton, 1960), especially when pore fluid cannot escape from sediment through fractures under saturation and stress (Shanmugam, 2015), promoting slope instability. All these factors contribute for shear strength reduction and even though there is not any shear stress acting on the slopes, promoted by gravity, earthquake or even storm surges, instability ends up appearing in the area.

5.5 – CONCLUSIONS

The analysis of multibeam bathymetry and high-resolution reflection seismic lines showed that the morphology of the Alentejo Margin results from the complex interplay between geology and oceanography. It is found in the area that this interplay favours the interaction between along-slope and downslope sedimentary processes, thus creating several erosional, depositional, and gravity-driven features. This interaction is a feedback mechanism that promotes the active sedimentary pattern of the area.

The presence of the MOW, a strong intermediate water mass, and its interaction with a rugged geomorphology promotes sediment erosion as well as deposition in the area, from

Pliocene up to present times, creating the SCD and associated bedforms. Tectonics plays an important role at both spatial and time scales due to crustal vertical movements and ground shakes, controlling the morphology and constraining the bottom currents pathway. Like in other areas the tectonic activity and high sedimentation rates, associated with bottom currents, control the landsliding occurrence and overall sedimentary dynamics.

The SCD is prone to landsliding activity in response to overpressure and under-consolidation. Landslides develop both on steep-slope and low-gradient areas, presenting two main morphologies: i) isolated, wide and elongated slide scars on low-gradient slopes, especially in the gentler areas, and; ii) contiguous, small slide scars on the steepest slopes, pointing to a reverse relationship between slope angle and scar area. The abundance of small landslides scars depends on active tectonics that promotes steep slopes and internal sediment deformation, but also quite frequent and low-magnitude seismicity foci, suggesting a continuous sliding activity. This differs from other drifts where landslides are larger and scarce. Furthermore, the presence of a field of sediment waves, whose interfaces constitute sedimentary discontinuity surfaces, promote the development of failure planes and consequent scar development.

The existence of excess pore-pressure near the unstable areas points to a feedback-like mechanism between strata-bounded fluids concentration and slope instability through the emplacement of fluids near failures and fluid structures, inducing layer-parallel sliding and hydraulic failure, mostly nearby free surfaces such as large fault escarpments. These semi-quantitative findings are important for further landslide susceptibility assessment in the study area.

6. SEDIMENT PROPERTIES OF THE LATE PLEISTOCENE-HOLOCENE SEDIMENTS OF THE SINES CONTOURITE DRIFT[2]

Since Late Pleistocene, multiple climate variations affected the Alentejo Margin constraining bottom current activity, and erosional and depositional evolution that promote variable sedimentation rates through different sediment sources. Cool-warm events cyclicity promoted diverse depositional rates and determined varying intrinsic sediments properties along the sedimentary column.

A combined analysis of grain-size, carbon content, physical-, and geochemical properties has been carried out on a 350-cm gravity core, retrieved in the Alentejo Margin, at 1425 mwd (meters water depth), to assess the morphosedimentary evolution of the Sines Contourite Drift (SCD) sedimentary package during Late Pleistocene-Holocene. According to AMS ^{14}C dating, sediments' ages vary from > 43 cal kyr BP to the present time.

Hemipelagic settling and along-slope deposition are dominant sedimentary processes during warmer events promoting calmer deposition, low erosion and more regularity on the signatures of sediments' properties. During cold climatic events, sediments' facies significantly change and coarse-grained, terrigenous Fe-rich sediments' layers with irregular limits are present along the sedimentary record associated with sea-level regression and the increase on terrigenous input.

The Alentejo Margin is a mixed sedimentary process-based area, where along-slope bottom current driven deposition and erosion, and downslope activity coexist.

The sedimentary record shows evidence of sediment deposition coeval with Heinrich Events (HE), quite eroded and reworked by Mediterranean Outflow Water (MOW) activity, which acts as a seabed shaping agent.

The presence of hiatuses on the sedimentary record, formed during cold-driven depositional events, which cause inversions and drastic variation on sediment properties' signatures reflect sharp variations on MOW erosional capacity, but essentially gravitational sediment displacement especially at depths where MOW does not reach the seabed.

[2] This chapter has been published in **Sedimentary Geology**:

TEIXEIRA, M., Terrinha, P., Roque, C., Voelker, A., Silva, P., Salgueiro, E., Abrantes, F., Naughton, F., Mena, A., Ercilla, G., Casas, D. (2020) - The Late Pleistocene-Holocene sedimentary evolution of the Sines Contourite Drift (SW Portuguese Margin): A multiproxy approach. *Sedimentary Geology*, 407, 105737. https://doi.org/10.1016/j.sedgeo.2020.105737

6.1 – INTRODUCTION

Sediment properties constitute important proxies for recording the palaeoclimatic and palaeoceanographic conditions, e.g., (Baas *et al.*, 1997; Abrantes *et al.*, 1998). This is valuable, especially on continental margins where considerable contouritic depositional activity occurs, e.g., (Stow and Faugères, 2008), as it happens along SW Iberia margin. There, contourite deposits mainly occur due to the action of the Mediterranean Outflow Water (MOW), which formed the Gulf of Cadiz contourite depositional system (GCCDS) that extends from the Gulf of Cadiz into the SW Portuguese margin (Hernández-Molina *et al.*, 2003; Voelker *et al.*, 2006; Hernández-Molina *et al.*, 2011; Roque *et al.*, 2015; Llave *et al.*, 2020), where the Sines Contourite Drift (SCD) has been formed (Figure 6.1). The GCCDS has been largely studied in the last 40 years especially the Guadalquivir, Huelva, Faro, Albufeira, Portimão and Sagres drifts, e.g., (Gonthier *et al.*, 1984; Nelson *et al.*, 1993; Hernández-Molina *et al.*, 2003; 2006; Llave *et al.*, 2006; 2007; Hernández-Molina *et al.*, 2011; Roque *et al.*, 2012; Hernández-Molina *et al.*, 2016a).

These along-slope depositional bodies are commonly ascribed to different current types (Rebesco *et al.*, 2014), thus the evolution of the SCD is greatly dependent on bottom current activity associated with climate change, e.g., (Baas *et al.*, 1997; Schönfeld and Zahn, 2000; Abrantes *et al.*, 2016). Bottom currents play a key role in the offshore Iberia, creating contourite depositional systems (Hernández-Molina *et al.*, 2003; Llave *et al.*, 2006; Hernández-Molina *et al.*, 2011) through strong transport and winnowing capacity, especially during glacial periods (e.g., Schönfeld and Zahn, 2000; Rogerson *et al.*, 2005; Llave *et al.*, 2006). Moreover, coarse contourite deposits generally form in response to bottom current intensification (Cacho *et al.*, 2000; Llave *et al.*, 2006; Voelker *et al.*, 2006; Llave *et al.*, 2007; Toucanne *et al.*, 2007; Juan *et al.*, 2016) during colder events such as the Last Glacial Maximum (LGM), the Younger Dryas (YD) and Heinrich Events (HE), when coarser material has been deposited and reworked along middle- (Llave *et al.*, 2006; Toucanne *et al.*, 2007) and upper slopes (Rogerson *et al.*, 2005; Voelker *et al.*, 2006; Rey *et al.*, 2014; Bahr *et al.*, 2015; Mena *et al.*, 2018). During these periods, MOW presented stronger outflow (e.g., Voelker *et al.*, 2006) and stronger erosional and depositional capacities leaving distinctive imprints (Schönfeld and Zahn, 2000) that correspond to coarse sediment layers in the contourite drift record. The effects of glacial and interglacial periods are documented on the sedimentary record in the Alentejo Margin (Baas *et al.*, 1997; Schönfeld and Zahn, 2000;

Skinner *et al.*, 2003), comprehending a wide range of biogenic and lithogenic sediments during the Late Quaternary (Zahn *et al.*, 1997).

Thus, contourite deposits constitute good records of bottom current variability. Some works have used contourite deposits stacking pattern to infer bottom current variability (Llave *et al.*, 2001; Hernández-Molina *et al.*, 2002; Llave *et al.*, 2011), but the analysis of sediment properties of these deposits have also been used to decipher bottom current behaviour based on climate change evidences (Rogerson *et al.*, 2005) represented on sediments properties (Bahr *et al.*, 2014; Kaboth *et al.*, 2016; Kaboth *et al.*, 2017a; 2017b) and on foraminiferal evidences (Schönfeld and Zahn, 2000; Salgueiro *et al.*, 2014).

Concerning to the SCD, little is still known about the (detailed) Pleistocene-Holocene sedimentary record, except for the IODP site U1391 (Stow *et al.*, 2013). However, the detailed relationship of the SCD sedimentary evolution with MOW and its interfaces with other water masses is still unknown.

Therefore, this chapter presents a multiproxy characterization of the Sines Drift sediments, which are in the present-day interface between the MOW and the NADW, based on the joint analysis of sedimentological, physical, geochemical, and environmental magnetic properties of sediments, and AMS ^{14}C dating. The aims of this chapter are the following: i) to understand the sedimentary evolution in the Alentejo Margin during the Late Pleistocene to Holocene, ii) to infer the variability of the MOW during this time interval, iii) to investigate the role of the interface MOW – NADW (North Atlantic Deep Water) in shaping the morphology of middle slope of the Alentejo Margin.

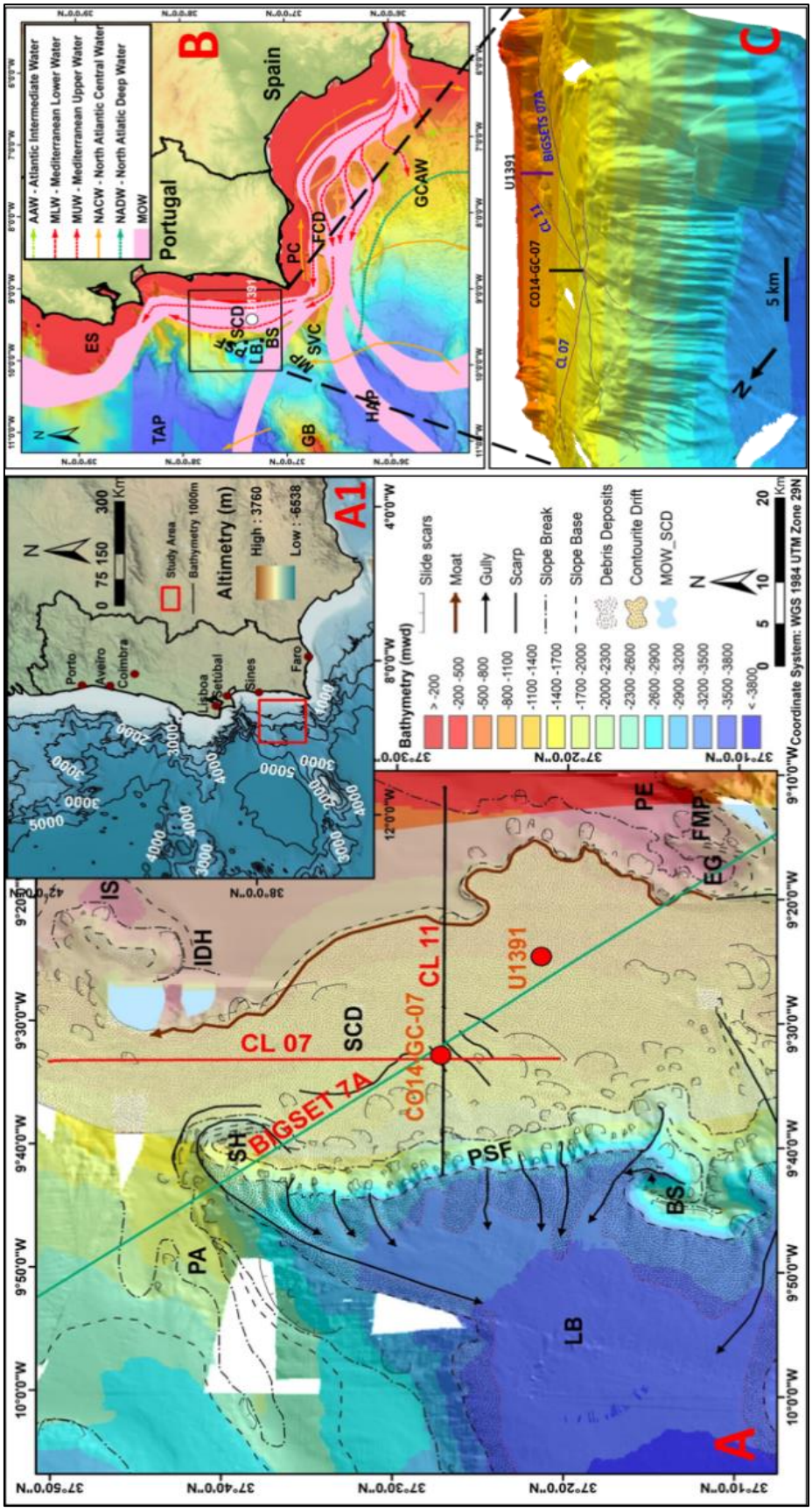

FIGURE 6.1 – Geomorphologic overview of the Sines Contourite Drift area. (A) – Bathymetry with geomorphologic interpretation. Black, red and green lines correspond to seismic lines CL 11, CL 07 and BIGSET 7A. Red dots refer to gravity core CO14GC-07 and IODP Site U1391. Blank holes correspond to no data. EG – Estêvão Gomes Hill; FMP – Fernão Mendes Pinto Hill; IDH – Infante Dom Henrique Hill; IS – Infante Santo Hill; PA – Príncipes De Avis Seamounts; SH – Sines Hook. (A1) – Geographic setting of the study area. Bathymetry obtained from GEBCO data (GEBCO, 2003). (B) – Bottom currents geographic display. BS – Bow Spur; ES – Estremadura Spur; FCD – Faro Contourite Drift; GB – Gorringe Bank; GCAW – Gulf of Cadiz Accretionary Wedge; HAP – Horseshoe Abyssal Plain; LB – Lebre Basin; MP – Marquês De Pombal Fault; PC – Portimão Canyon; PSF – Pereira De Sousa Fault; SC – Setúbal Canyon; SCD – Sines Contourite Drift; SVC – São Vicente Canyon; TAP – Tagus Abyssal Plain Bottom currents geographic display. (C) – 3D view of the area and the location of data.

6.2 – SEDIMENT PROPERTIES OF GRAVITY CORE CO14-GC-07

The SCD covers an area of ~2311 km^2, ~35 km wide and ~98 km long, within the study area (Figure 6.1), with a mean slope gradient of ~5º at the seafloor surface, > 1612 ms thick-TWTT, being limited eastwards by a moat that extends for ~84 km in the base of the upper continental slope, at ~800 mwd, and westwards by the Pereira de Sousa Fault scarp at ~1700 mwd (Figure 6.2A).

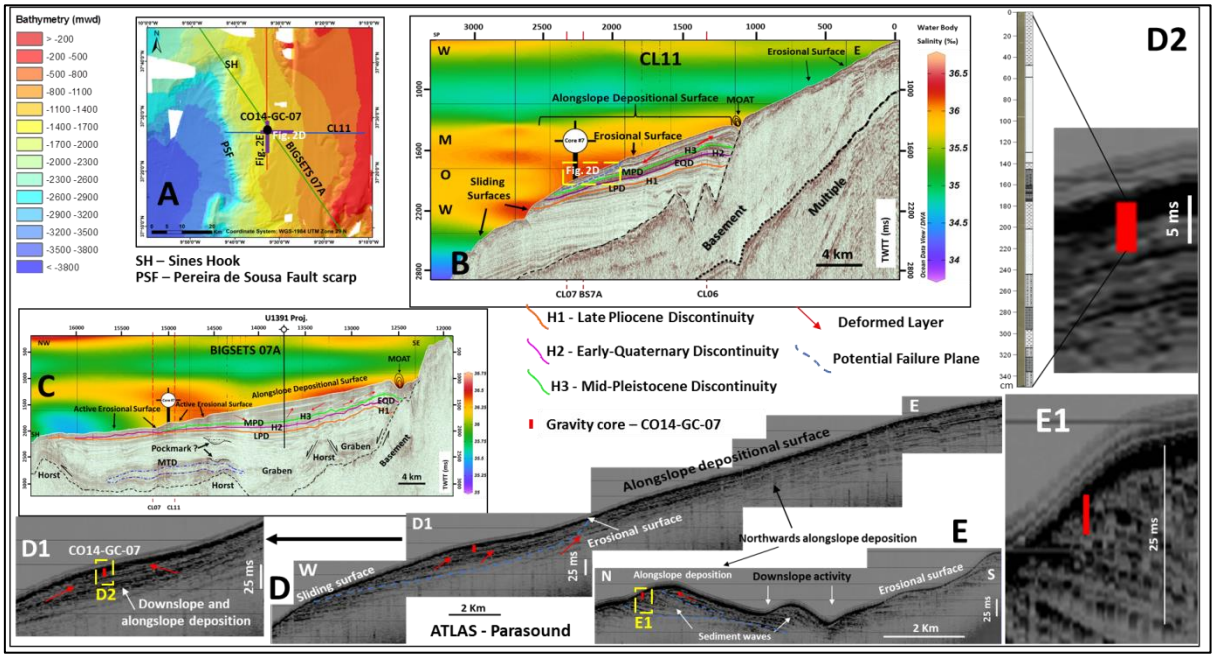

FIGURE 6.2 – Location of the CO14-GC-07 gravity core. (A) Study area with location of seismic lines and gravity core. Location of the gravity core CO14GC-07 and IODP site U1391, and the Seismic Lines CL11 and BIGSETS 07A, and ATLAS Parasound lines. SH – Sines Hook; PSF – Pereira de Sousa Fault scarp. (B) Seismic Line CL11. Blue-dashed line refers to probable sliding surface. Blue-dashed line refer to stratigraphic horizon discontinuities, corresponding to internal sediment deformation; MOW – Mediterranean Outflow Water. (C) Seismic Line BS07A. Black arrows refer to active erosional surfaces. Blue-edged features and red arrows refer to stratigraphic horizon discontinuities with chaotic facies, probably indicating sediment deformation; (D) East-West echofacies line (Atlas Parasound). Blue-dashed lines refer to potential failure plane and red arrows refer to deformed layers; (D1) Detail of the core surrounding area; (D2) Correlation of the core CO14-GC-07 with Parasound data. Visual description of the core on the left side; (E) North-South echofacies line. Lines and arrows as in (D); (E1) Detail of the core correlated with Parasound data. General - TWTT – two-way travel time; ms – milliseconds. H1 – Late-Pliocene Discontinuity (LPD, 3.2–3.0 Ma); H2 – Early Quaternary Discontinuity (EQD, 2.4–2.0 Ma); H3 – Middle Pleistocene Discontinuity (MPD, 0.9–0-7 Ma).

Gravity core CO14-GC-07 was retrieved in the western limit of the SCD, near the top of the Pereira de Sousa fault scarp (Figure 6.2A and B), in the transition between the middle and the lower continental slope of the Alentejo Margin and near the present-day interface of the MOW and the NADW. This core has been retrieved on a field of sediment waves (Figure 6.2D, E), where some discontinuities affect their internal structure. The depositional evolution on the core site seems to change the pattern at the middle of the core, according to the reflectors of the sub-bottom profiles (Figure 6.2D2, E1). This site is located in an area where

intense slope instability currently occurs (Teixeira *et al*., 2019), and where both along-slope and downslope activity coexist (Figure 6.2D, E). This is a west-dipping area, where multiple incisions occur on the top of the Pereira de Sousa fault scarp, laterally confining the core site (Figures 6.2D, E), thus indicating downslope activity. This is confirmed by the presence of 0.5- to ~11.5-km^2 landslide scars between ~1100 and ~1700 mwd (Figure 6.1A), which coincides with the depth range of MOW's present-day lower limit and the interface with NADW, at ~1500 mwd (Schönfeld and Zahn, 2000). Those erosional and sliding surfaces truncate subsurface sedimentary layers (Figure 6.2B, D, E). Beyond the surface instability (Figures 6.1A, 2B - D), subsurface potential failure planes and chaotic seismic facies also occur below the core site (Figures 6.2D, E), evidencing stratigraphic discontinuities that attest to slope instability. This mainly occurs above the Mid-Pleistocene discontinuity (Figure 6.2A). The present-day seafloor, between ~800-1700 mwd, is shaped by NE-SW oriented sediment waves (Figure 6.2D, E) with amplitudes ranging from 23 to 31 ms and wavelengths between 664 and ~3018 m. Such waves are also detected buried beneath Quaternary sediments (Figure 6.2B).

6.2.1 – COLOUR AND TEXTURE

Core CO14-GC-07 is mostly constituted of silty and clayey sediments with few fine and very fine sand sections (Figure 6.3B). Sediments' colour varies from yellowish olive- (10YR 5/4) to olive grey (5Y 5/7) according to Munsell's classification (Munsell, 1905), with brownish (olive brown) clayey and silty-clay layers, and greyish (olive grey) sandy and silty sandy layers – Figure 6.3B.

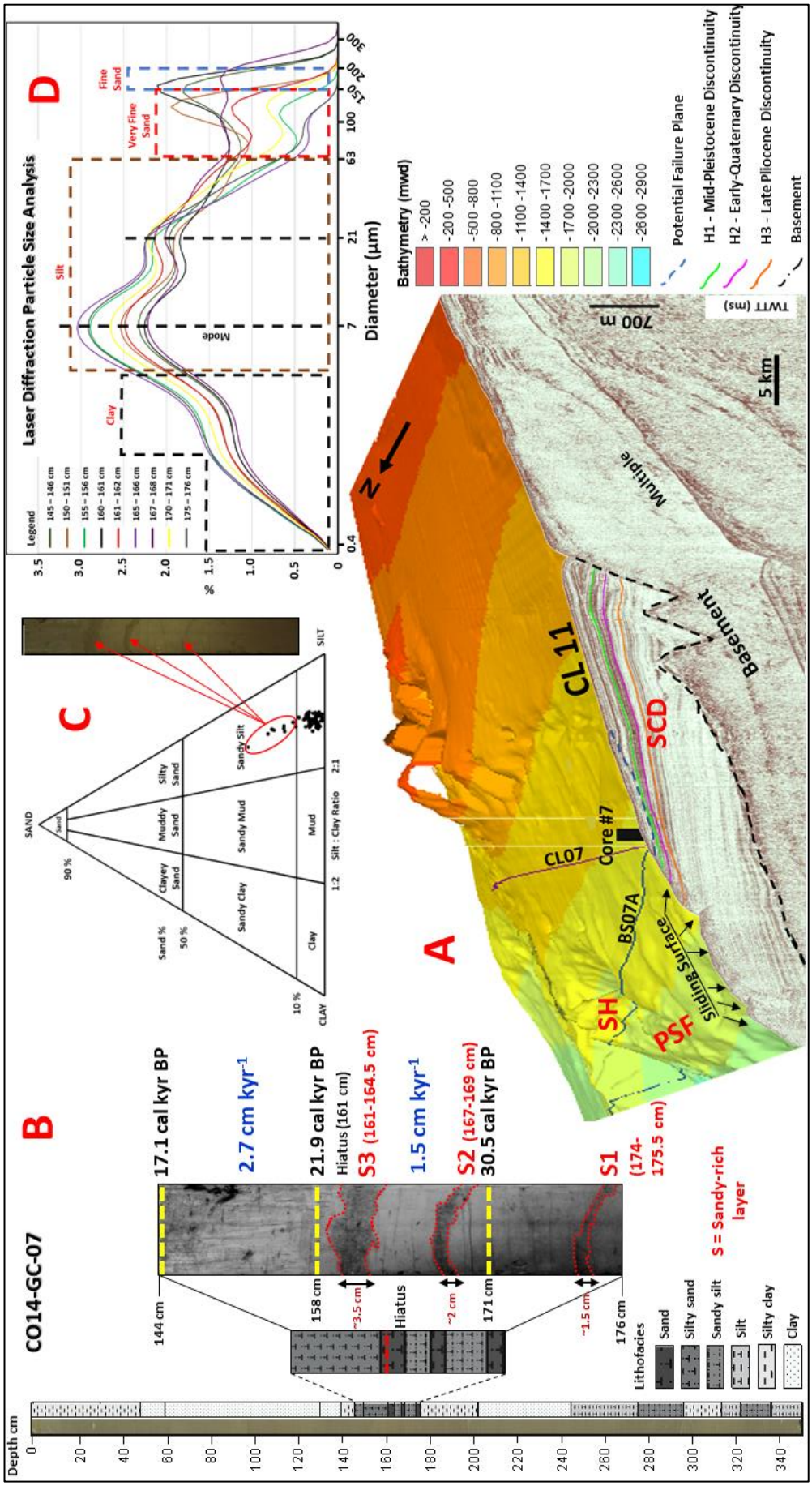

FIGURE 6.3 – CO14-GC-07 gravity core. (A) - General location of the core, with the main seismic lines (CL11, CL07 and BS07A) passing nearby, plotted in a 3D bathymetric block. CL11 seismic profile is plotted with the bathymetry. PSF – Pereira de Sousa Fault Scarp; SCD – Sines Contourite Drift; SH – Sines Hook. (B) – CORE 7 with the visual description. A section is highlighted through a black and white image. Brightness and contrast have been changed. Darker units (S1, S2 and S3) correspond to sandy-rich layers. Yellow dashed-lines represent the depths of AMS ^{14}C dating; Values in blue (cm kyr^{-1}) represent sedimentation rates in the intervals between yellow dashed-lines. (C) – Grain-size analysis in a sand-silt-clay trigonal diagram. Black dots refer to the core samples analysed in this work. Examples of coarser material are shown in the core through red arrows. (D) – Grain-size curves retrieved from the laser diffraction particle size analyser. Dashed rectangles/polygons: blue (fine sand); red (very fine sand); brown (silt); black (clay). Black-dashed lines point to diameter (µm) mode.

Most of the CO14-GC-07 sediments (93.5%) correspond to silt and clay fraction (<

63μm), ~5.8% to very fine sand (150>F>63 μm) and only 0.6% is > 150 μm, corresponding to fine sand (200>F>150 μm) - Figures 6.3B and C. Finer sediments are present in the upper ~145 cm, whereas below this depth, mainly down to ~176 cm sediments are coarser (Figure 6.3B). There is a dominant grain-size patern, for the whole sedimentary record: 46% of the samples present a bimodal curve, mostly pronounced on the diameters range ~6.5-7 μm (dominant mode) and ~21 μm. One third (33%) have trimodal curves with peaks on ~6.5-7; 21 and 110-120 μm. Only 17% of the curves are unimodal, with a peak on the ~7 μm. About 4% are polymodal, with more than 3 peaks, especially at the top of the upper ~20 cm and at the depth range of 144 – 176 cm (Figure 6.3D), where most of the curves are trimodal and polymodal, essentially corresponding to silty, and fine and very fine sandy samples.

6.2.2 – CARBONATE AND ORGANIC CARBON

Elemental chemical analyses demonstrate an upwards increase on carbon content (Figure 6.4). Total carbon (TC) content shows an overall increasing trend – Figure 6.4, ranging from 2.57 wt %, at 320-321 cm, and ~4.9 wt %, at 40-41 cm. Organic carbon (TOC) and inorganic carbon (IC) concentrations mostly have a symmetric behaviour (anti-correlation), with the later always having higher wt %. IC mostly increases on coarser sediment layers, whereas TOC typically shows the opposite behaviour (Figure 6.4). TOC ranges from 0.51 wt % at 20-21 cm to 1.41 wt % at 205-206 cm depth. In general, IC has a gradual increase from the base to the top, reaching the maximum (3.94 wt %) near the top, at 0-1 cm. The minimum IC recorded value (1.76 wt %) occurs at 320 cm depth, in the transition from coarser to finer sediment. The highest difference between IC and TOC increases above ~180 cm, especially in the core's topmost 40 cm (Figure 6.4).

6.2.3 – PHYSICAL PROPERTIES

Sediments' densities range between 1.49 and 1.67 g cm^{-3}, with ~90% laying in the $1.53 > \rho > 1.63$ g cm^{-3} interval and 53.5% in $1.58 > \rho > 1.60$ g cm^{-3}. About 7.5% is $\rho > 1.6$ g cm^{-3}, whereas only ~2% is $\rho < 1.53$ g cm^{-3}. CO14-GC-07's mean density is 1.59 g cm^{-3}, with the maximum (1.67 g cm^{-3}) occurring at 165 cm depth and the minimum (1.49 g cm^{-3}) near the bottom of the core (345 cm). This property shows a dual behaviour with higher cyclicity in the lower half (below 160 cm) with higher frequency (shorter cycles) and a smoother

behaviour in the upper 180 cm (Figure 6.4). Density increases from 1.49 g cm^{-3} to 1.62 g cm^{-3} between the core bottom and 320 cm depth, where a trend inversion occurs. This cyclic trend (Figure 6.4) maintains up to ~180 cm, where density reaches 1.6 g cm^{-3}, decreasing then ~0.08 g cm^{-3} until 1.52 g cm^{-3} at ~95 cm. From this depth up to the core top, density increases to 1.54 g cm^{-3}. Higher densities generally correspond to grain-size increases and vice-versa (Figure 6.4).

Fractional porosity – FP - (%) anti-correlates with density and varies between 71%, at 345 cm, and 60%, at 165 cm depth (Figure 6.4), growing up to 68% in the top of the core. Below 165 cm signature variations are more pronounced and evident (Figure 6.4). Likewise, FP changes the global trend around the 160-165 cm threshold.

Magnetic susceptibility (MS) increases from the bottom of the core until ~215 cm, rising from 55 to 127 units (>45%), followed by a decreasing pattern up to the top (Figure 6.4). Between ~215 cm and the top of the core, MS decreased from 127 to 11 units (<91%).

Resistivity (Ω.m) displays a dual behaviour as it starts at the uppermost layer with ~0.005 Ω.m and constantly decreases downwards, reaching negative values, at ~180 cm, returning to 0 Ω.m at ~230 cm (Figure 6.4). Below this depth the curve goes down to the end of the core close to 0.

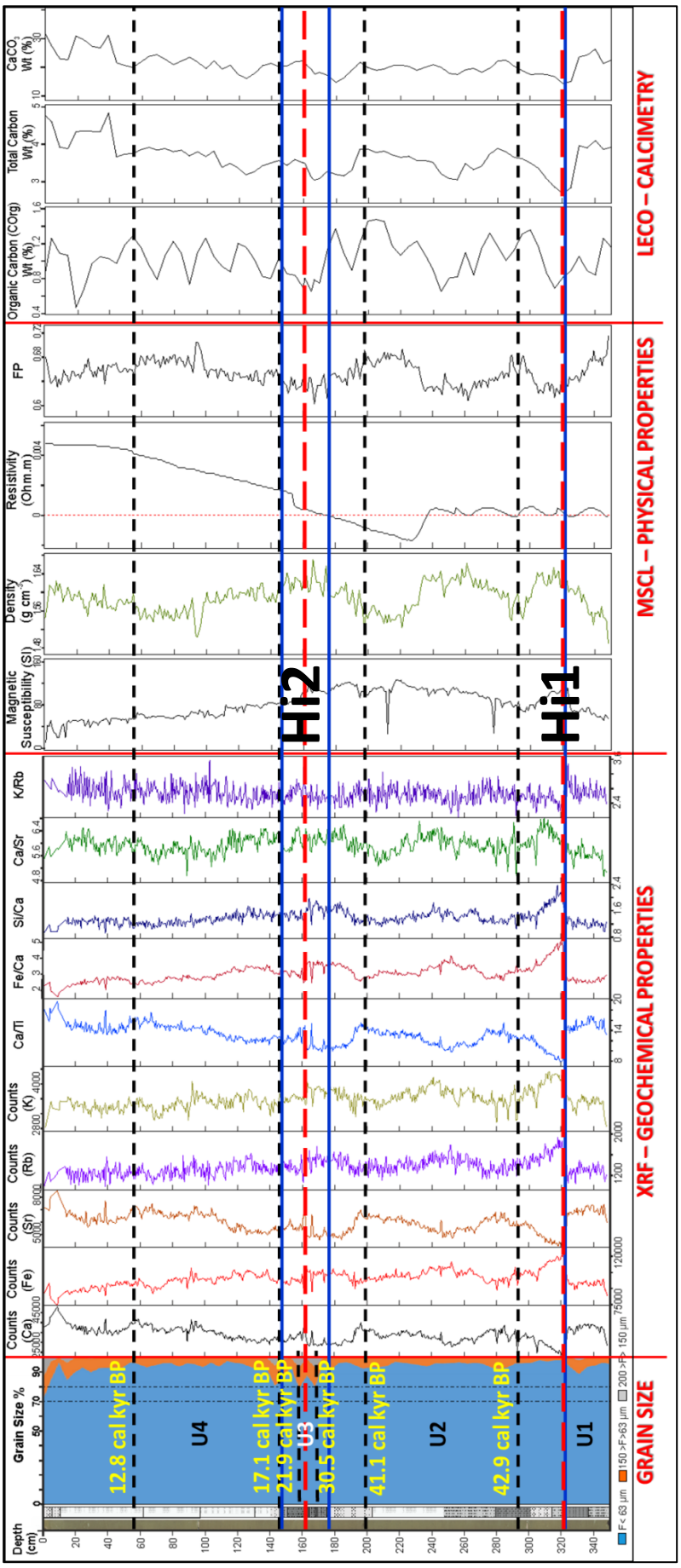

FIGURE 6.4 – Downcore plotting of geochemical, physical and calcimetric properties. Black dashed line corresponds to AMS ^{14}C dating. Dated ages are in yellow near the respective dashed line. Blue lines represent the limits of lithological units (U1-U4). Red dashed lines correspond to the hiatuses (Hi1 and Hi2) verified in the sediments' properties.

6.2.4 – GEOCHEMICAL PROPERTIES

Iron (Fe), calcium (Ca), strontium (Sr), potassium (K) and titanium (Ti) are among the most abundant elements in CO14-GC-07 gravity core. Generally, terrigenous and biogenic elements present symmetric disposition along the core (Figure 6.4). Terrigenous elements (Fe, K and Rb) present similar distribution pattern, increasing with depth, whereas biogenic elements Ca and Sr tend to decrease with depth. In what concerns to element ratios, terrigenous *vs* biogenic elements and vice-versa, Fe/Ca and Ca/Ti display a perfect anti-correlation and Si/Ca is very similar to Fe/Ca. Pearson correlation coefficient shows that correlations between elements are dominantly significant when using the *Two-Tailed* test of significance at the 0.01 level (Table 6.1). Strong correlations occur between elements as Ca and Sr or Ti and K (Table 6.1). Likewise, anti-correlations are evident in these data between terrigenous and biogenic elements as, for example, Fe and Sr, respectively (Table 6.1). There are some protuberances in the signature of properties that are common to all the elements along the core, especially at varying grain-size contacts (Figure 6.4). These sections present sharp inversion trends comparing with the contiguous ones. Some irregularities occur in core section breaks, constituting artefacts without sedimentary meaning.

TABLE 6.1 – Linear correlation (Pearson Coefficient) of the geochemical elements in the Alentejo Margin

	Si	Cl	K	Ca	Ti	Fe	Rb	Sr	Zr
Si	1								
Cl	-.566**	1							
K	.608**	-.603**	1						
Ca	*-0.059*	.155**	-.457**	1					
Ti	.531**	-.486**	.813**	-.561**	1				
Fe	.392**	-.392**	.811**	-.706**	.778**	1			
Rb	.296**	-.315**	.667**	-.610**	.619**	.724**	1		
Sr	-.264**	.329**	-.601**	.915**	-.684**	-.750**	-.637**	1	
Zr	.210**		*-0.072*	-.233**	.302**	.146**	.143**	-.323**	1

**. Correlation is significant at the 0.01 level (2-tailed). Values in italic correspond to not significant correlations.

6.3 – SEDIMENTS' PROPERTIES BY SEDIMENTARY UNIT

The sedimentary record of gravity core CO14-GC-07 was sub-divided into four sedimentary intervals from the base to the top. The main criterion used to define these intervals was the identification of discontinuities in the sedimentary record by correlation with all sediments' properties, i.e. colour variations, degree of bioturbation and changes in grain-size in agreement with calcimetry, physical and geochemical properties (Figure 6.4). AMS ^{14}C dating also helped in the definition of the intervals' boundaries.

6.3.1 – UNIT 1 (350 – 322 cm)

The top limit (322 cm) of this 28-cm thick interval coincides with an abrupt break observed in all properties (Figure 6.4), likely a hiatus (Hi1). This interval consists of light olive grey (5Y 5/7) coloured sandy mud and muddy sediments, with low to moderate bioturbation (BI=2-3) with an upwards increase in organic matter and shell fragments (Figure 6.4). Close to the upper limit, at 325 cm, grain-size varies between 0.375 µm and 282.1 µm with a mode of ~6-7 µm. In this interval, ~94% of the sediments are silt and clay (F<63 µm); ~6% correspond to very fine sand (150>F>63 µm); and only ~0.4% is fine sand (200>F>150 µm). Carbon content (organic, inorganic and total carbon) decreases 1.47 wt% from the base (340 cm) to the top (322 cm) of the unit (Figure 6.4). Magnetic susceptibility (SI) and density increase upwards, whereas FP anti-correlates with density (Figure 6.4). Density increases from 1.49 g cm^{-3} to 1.62 g cm^{-3} between the core bottom and 320 cm depth, where a trend inversion occurs. Inversely, FP reaches its maximum (71%) at 345 cm, presenting a decrease of ~8%, between the bottom and ~322 cm. Resistivity remains close to 0 throughout the unit (Figure 6.4). Geochemical properties present a global bottom-up constancy, with both terrigenous (Fe, Rb, K) and biogenic (Ca, Sr) elements presenting a regular pattern until the top of the unit (Figure 6.4). This interval comprises sediments older than 42.9 cal kyr BP, dated at 294 cm depth (Figure 6.5).

6.3.2 – UNIT 2 (322 – 176 cm)

This 146-cm interval comprises muddy layers (sandy silt, silt, silty-clay, and clay) ranging from light olive brown (5Y 5/5) to greyish brown (2.5Y 5/2) in colour, dominantly showing moderate bioturbation (BI=3). Ichnofossil traces (Zoophycus) occur at ~250 cm

depth, indicating biogenic activity. These sediments mostly present a massive structure with considerable presence of organic matter and shell fragments, as well as brown oxidation traces especially in the transition from finer to coarser layers. Grain-size varies between 0.375 and 194.2 µm. The mode occurs at 7.4 µm, where 96% of the sediments are silt and clay (F<63 µm), 4.4% are very fine sand (150>F>63 µm) and 0.03% are fine sand (200>F>150 µm). Carbon content presents a stable trend from the base to the top of the unit, although in the 195-180 and 180-160 cm range depths slight decreases (0.87 wt%) and increases (0.93 wt%) occur, respectively. This interval presents the lowest value of TC (2.57 wt %), at 320-321 cm. Conversely, maximum TOC (1.41 wt %) occurs at 205 cm. The minimum $CaCO_3$ value (1.76 wt %) of the whole core occurs at 320 cm. This occurs near the lower limit of this interval and coincides with an abrupt change in all properties. Magnetic susceptibility increases gradually towards the top, whereas density and porosity have a negative correlation, increasing and decreasing, respectively. The two negative magnetic peaks do not have a correspondence on the other measured properties. Density reaches its maximum (1.66 g cm^{-3}) at 259 cm and its minimum (1.52 g cm^{-3}) at 219 cm. Conversely, FP presents at those depths, respectively, its minimum (61%) and its maximum (69%) - Figure 6.4. Resistivity values oscillate around 0, falling below this threshold between 235 cm and 176 cm.

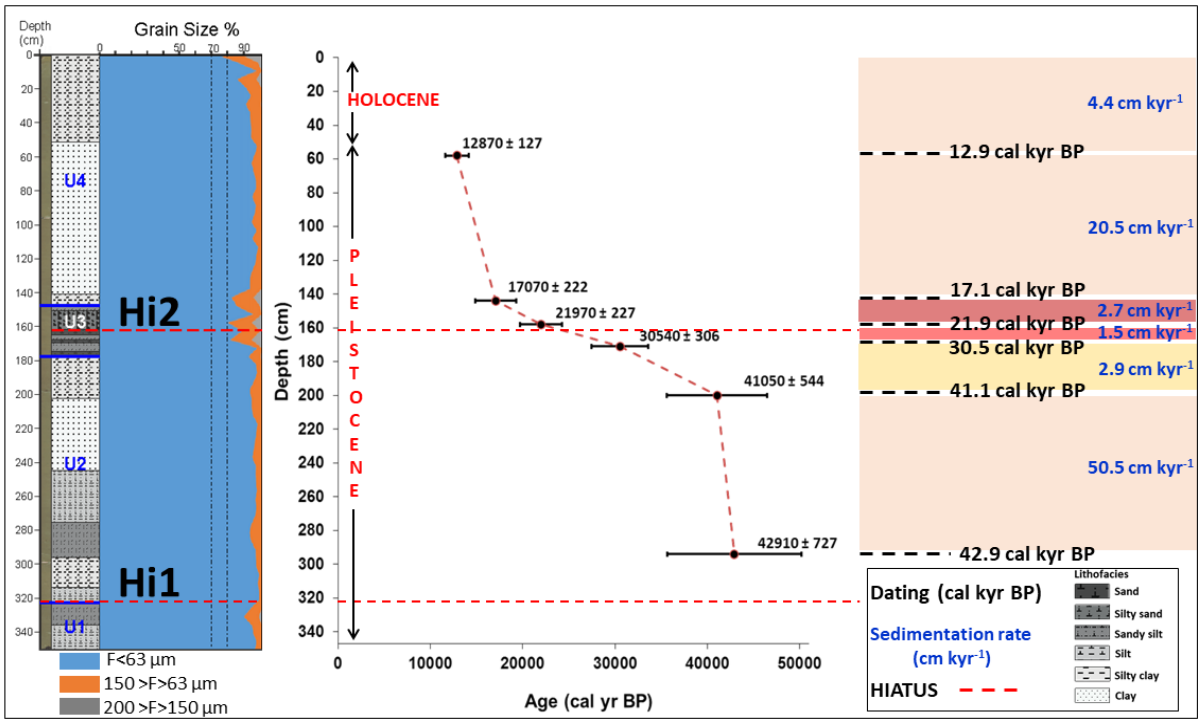

FIGURE 6.5 - Age-depth curve of the gravity core CO14-GC-07. Ages in cal yr BP with error bars (1 sigma error). Left panel: Downcore lot of grain-size; blue lines delimit the lithological units (U1-U4). Right panel: Coloured rectangles refer to sedimentation rates; black dashed lines indicate levels of listed calibrated AMS ^{14}C ages. Red dashed lines and Hi1 and Hi2 mark the two hiatuses identified based on the sediment properties.

The evolution of biogenic and terrigenous geochemical elements shows a general decrease of 5% for Ca and 14.4% for Sr, from 322 to 176 cm (Figure 6.4). Terrigenous elements present slight increases between 322 to 176 cm: 1.5% (Fe), 1.6% (Rb) and 0.1% (K).

Two AMS ^{14}C datings within this interval at 294 cm (42.9 cal kyr BP) and 200 cm (41.1 cal kyr BP) indicate high sedimentation rate of ~50.5 cm kyr^{-1}, with respect to the observed sedimentation rates in the core (Figure 6.5).

6.3.3 – UNIT 3 (176 – 144 cm)

This ~32 cm-long interval of sandy-mud and muddy layers with few shell fragments is olive- (5Y 5/2) and dark grey (5YR 4/1) in colour and moderately bioturbated (BI=3). It is distinguished from the other units by having layers with higher sand content (Figure 6.4). About 88% of the sediments in this section correspond to fine grain-size materials – silt and clay - (F<63 μm), whereas ~9.5% represent very fine sands (150>F>63μm) and 2.3% fine sands (200>F>150 μm). Grain-size in this interval varies from 0.38 up to 339.90 μm, with a dominant mode of 7.30 μm (Figure 6.3D), although most of the grain-size curves are trimodal (145-146; 150-151; 160-161; 161-162 cm) or even polymodal (165-166 cm). The mean grain-size of the sandy fraction is ~135.32 μm and the mode is ~166.73 μm. Coarser sands are present at 145 and 165 cm (~166.73 μm), whereas an intermediate sand size (~148.14 μm) occurs at 160 cm and a finer mean grain-size (111.50 μm) at 167 and 175 cm (Figure 6.3).

This interval defines a major transition at 160-161 cm depth, being common to all the remaining properties (Figure 6.4). TOC varies from 1.10 to 0.67 wt% between 175 and 165 cm. The $CaCO_3$ content increases from the minimum of this interval (17.46 wt%) at 175 cm, to 22.76 wt% at 160 cm, decreasing again to 20.79 wt% at 145 cm (Figure 6.4). There is a bottom up decrease in terrigenous elements and an increase on biogenic marine elements (Figure 6.4). In this unit, density reaches the maximum (1.67 g cm^{-3}), while fractional porosity records its minimum (60%), at 165 cm depth (Figure 6.4), increasing then towards the top of the unit. Resistivity reveals a drastic change in its behaviour, with a great increase of 0.002 Ω.m above 153 cm (Figure 6.4).

Three AMS ^{14}C dates provide the age control for this unit (Table 4.6, Figure 6.3B): 171 cm (~30.5 cal kyr BP); 158 cm (~21.9 cal kyr BP); 144 cm (~17.1 cal kyr BP). These

ages indicate lower sedimentation rates of 1.5 cm kyr^{-1} at the bottom of the unit increasing to 2.8 cm kyr^{-1} at its top (Figure 6.5).

Three sand-rich layers, hereafter designated as S1, S2 and S3, with erosive contacts are present within this interval. The thickness of these layers increases from the bottom to top (Figure 6.3B).

S1, at 175.5-174 cm, is a ~1.5-cm olive (5Y 5/2) fine silt layer, with irregular limits (Figure 6.3B), whose grain size varies between 0.38 and 234.00 µm (mode = 7.1 µm), with ~93% of the total fraction (F<63µm), ~6% (150>F>63 µm) and ~0.3% (200>F>150 µm). Sand mean grain-size is 111.50 µm (Figure 6.3).

S2 at 169-167 cm is a ~2-cm olive (5Y 5/2) coloured sandy mud layer with moderately irregular limits (Figure 6.3B). Grain-size varies between 0.38 and 340.00 µm, with a mode of 7.10 µm, where silt and clay (F<63µm) correspond to ~88%, while ~9% is very fine sand (150>F>63 µm) and ~3% is fine sand (200>F>150 µm). Sand mean grain-size is ~121.70 µm. This layer has more irregular boundaries than S1.

S3 consists of a ~3.5-cm olive (5Y 5/2) coloured sandy mud layer with very irregular limits (Figure 3B), between 164.5-161cm. In this layer, 83.5% of the fraction corresponds to silt and clay (F<63µm), while ~13% is very fine sand (150>F>63 µm) and ~3.5% is fine sand (200>F>150 µm). Grain-size varies between 0.38 and 282.10 µm with the mode between 7.00 and 7.50 µm. Sand mean grain-size is ~148.15 µm. The ages of S2 and S3 fall between ~30.5 cal kyr BP (171 cm) and ~21.9 cal kyr BP (158 cm).

6.3.4 – UNIT 4 (144 – 0 cm)

This is a silty-clay layer with shell fragments, and greyish olive (10Y 4/2) to moderate olive brown (5Y 4/4) colour and mottled structure, presenting moderate bioturbation (BI=3). The top 50 cm consist of a yellowish brown (10YR 5/4) to moderate olive brown (5Y 4/4) clay-silt layer with low bioturbation (BI=1). Ichnofossil traces (Zoophycus) are present at 42 and 25 cm depth, indicating biogenic activity. About 93% of the fraction is silt and clay (F<63 µm), 6.2% is very fine sand (150>F>63 µm) whereas only 0.74% corresponds to fine sand (200>F>150 µm). Grain-size varies between 0.38 and 373.10 µm, with a mode of ~6.46 µm, although some trimodal curves occur at the top of the record. $CaCO_3$ generally increases from the minimum (16.48 wt%) at 125 and the maximum (32.81 wt%) at the top of the core (Figure

6.4). Organic carbon reaches the minimum (~0.51 wt %) at 20 cm and the maximum ~1.23 wt% at 55 cm (Figure 6.4). Resistivity continuously increases from 144 up to 0 cm depth (Figure 6.4), while density and porosity have a regular trend upwards. FP has a peak (70%) at ~95 cm, whereas density reaches the lowest value (1.52 g cm^{-3}) of the whole record, at this depth. From this depth towards the core top, density increases to 1.54 g cm^{-3}. Magnetic susceptibility regularly decreases upwards. Geochemical elements show an increase on biogenic (Ca = 30%; Sr = 34%) and on terrigenous elements (K = 4%; Rb = 1.8%) but a bottom up decrease of 15% on Fe. This is corroborated by the upwards increasing Ca/Ti and the decreasing Fe/Ca ratios (Figure 6.4). This unit comprises two AMS ^{14}C dates: at the bottom, 144 cm (~17.1 cal kyr BP) and at 56 cm (~12.9 cal kyr BP), indicating a sedimentation rate of 20.5 cm kyr^{-1}, and 4.4 cm kyr^{-1} between 56 cm and the top (Figure 6.5).

6.4 – DISCUSSION - THE ACTION OF CLIMATE VARIATIONS AND MOW OSCILLATIONS ON (MORPHO) SEDIMENTARY EVOLUTION OF THE SINES CONTOURITE DRIFT

The CO14-GC-07 sediment's properties suggest that the SCD´s morphosedimentary evolution went through many climatic phases (Baas *et al.*, 1997; Schönfeld and Zahn, 2000; Bahr *et al.*, 2014), constricting both bottom currents circulation and depositional activity (Voelker *et al.*, 2006; Llave *et al.*, 2007; Hernández-Molina *et al.*, 2011), leading to several depositional stages.

6.4.1 – DEPOSITIONAL STAGES: EVIDENCE FROM SEDIMENT PROPERTIES

The analyses of the sediments' properties of gravity core CO14-GC-07 indicate that the SCD´s sedimentary evolution went through distinct sedimentation processes during four depositional stages from Marine Isotope Stage (MIS) 3 to Present, according to variations in grain-size and in the overall sediment properties.

6.4.1.1 – STAGE 1 (> 42.9 cal. kyr BP)

This stage comprehends the interval 350-322 cm and is composed by silt and sandy silt (Figure 6.3B). The constant and synchronised evolution of both terrigenous and biogenic elements (Figure 6.4), along this stage indicate a steady depositional environment, although

the coarse grain-size points to a strong energy environment probably swept by bottom currents, as suggested by Kaboth *et al.* (2017a). Conversely, the sharp variations in all properties at ~322 cm (Figure 6.4) mark a major change in the sedimentary conditions, generally associated with cold climatic conditions and sea-level drops (Rogerson *et al.*, 2005; Lebreiro *et al.*, 2009; Kaboth *et al.*, 2017a). Considering that stage 1 is older than 42.9 cal. kyr BP, coeval with MIS 3, it might be correlated with a cold climate period corresponding to a Greenland stadial (Llave *et al.*, 2006; Voelker *et al.*, 2006; Toucanne *et al.*, 2007) that occurred prior to 42.9 cal. kyr BP.

Although there is no dating for this interval, the sharp variation common to all sediments' properties at ~322 cm is interpreted as a hiatus (Figures 6.3 and 6.4) that is probably associated with a major erosional episode occurred in this period, the major sea-level fluctuation occurred between 60 - 45 cal. kyr BP that accounted for a sea-level drop of ~60 m (Lebreiro *et al.*, 2009). Given the impact climate cooling and sea-level drop have on sedimentary evolution (Kaboth *et al.*, 2017a) and given the sharp variation on sediments properties signature (Figure 6.4), the probable hiatus could result from a severe sea-level drop that drastically changed the local sedimentary dynamics.

6.4.1.2 – STAGE 2 (> 42.9 - >30.5 cal. kyr BP)

Stage 2 is comprehended between ~322 and 176 cm depth, with sediment ages comprised between > 42.9 and >30.5 cal. kyr BP, from the middle of MIS 3 through near its end. Two main oscillations occur during this stage, with two peaks and two lows quite evident on sediment's density and porosity (Figure 6.4), and on geochemical properties (Figure 6.4). In general, sediments tend to fine upwards, spanning from sandy silt and silt to silty clay and clay, although being coarser in both limits of this stage. This seems to be a transitional stage between two sea-level regressions. The boundaries of Stage 2 coincide approximately with major sea-level drops verified during MIS 3, at 45 kyr and 30.5 kyr (Voelker *et al.*, 2006; Lebreiro *et al.*, 2009). The effect of these eustatic variations might be recorded in SCD sediments by an increase of biogenic and calcium related elements (Figure 6.4).

According to AMS ^{14}C dating, the 1.8-cal. kyr interval between ~42.9 cal. kyr BP (294 cm) and ~41.1 cal. kyr BP (200 cm) spans from the end of the interstadial between HE5 and HE4 in the middle of MIS 3 (e.g., Voelker (2002)). This interval (HE5-HE4) presents an overall sedimentary uniformity, suggesting the absence of significant bottom current variations. Thus, during this period a high sedimentation rate (~50.5 cm kyr^{-1}) occurs,

dominantly by hemipelagic sediments (Figure 6.3B), suggesting quite stable depositional conditions, possibly associated with warmer climatic (interstadial) conditions and high sea-level stands.

6.4.1.3 – STAGE 3 (>30.5 – 17.1 cal. kyr BP)

This stage spans from > 30.5 to 17.1 cal. kyr BP, between ~176 and 144 cm, corresponding to the coarsest sedimentation regime (Figure 6.3). Great variability exists both on grain-size and sediments' physical and geochemical properties (Figure 6.4).

Three coarser layers (S1-S3) show increases in terrigenous concentrations with the thickest level (S3 at ~161 cm) showing the sharpest variation on sediment properties (Figure 6.4). The presence of higher Fe/Ca and Si/Ca ratios (Figure 6.4) on coarser sediment layers points to higher terrigenous contributions derived from continental fluxes, mainly during low-standing sea level stages (Baas *et al.*, 1997; Govin *et al.*, 2012). Sudden and sharp peaks on the magnetic susceptibility match with the peaks of Fe concentration. At these levels, sediments' density suddenly falls, and FP sharply increases (Figure 6.4), indicating either the presence of voids that favour the leakage of the fines after deposition, or even that fines have been winnowed away.

The sharp decrease of biogenic elements (Ca and Sr) and the increase of terrigenous elements in layers S1-S3 (Figure 6.4), indicate that these layers deposited under different processes from the remaining core. This shows a drop in organic carbon (OC) content, which is common to occur during colder periods (Ohkouchi *et al.*, 2002) pointing to low biogenic/marine contribution due to the influence of cold Arctic conditions, which according to Magill *et al.* (2018) promotes a decrease on total OC (TOC %).

Coarse sediment fractions and detrital sediment input can be associated with the increase of bottom current activity (Baas *et al.*, 1997; Kaboth *et al.*, 2017a). It is possible that the low sedimentation rates reflect sedimentary scarcity by both high winnowing activity of MOW, combined with hemipelagic settling still present in this period, thus justifying the low along-slope accumulation between these dated levels (>30.5-17.1 cal. kyr BP). The sudden and large variation in all properties at ~161 cm (Figure 6.4) suggests the existence of a hiatus (Hi2).

6.4.1.4 – STAGE 4 (17.1 cal. kyr BP - Present)

The high percentages (~80 to 90%) of <63 µm fraction (Figure 6.4), indicate a predominant deposition of clay and silty clay, probably due to less winnowing activity, as also verified for the Faro-Albufeira drift (Llave *et al.*, 2006). The lower and less variable magnetic susceptibility (SI) (Figure 6.4) correlates with the lower Fe content, and the increased biogenic elements when compared with depths below 160 cm, suggesting the predominance of marine contribution in the depositional events. Stable magnetic susceptibility points to steady depositional conditions being attested by the low irregularity in the general signature of almost all sediment properties. This indicates continuous and more constant, less disturbed, depositional environments. This may suggest both warmer climatic conditions and steadier bottom currents activity.

Between 144 (~17.1 cal. kyr BP) and 56 cm (~12.9 cal. kyr BP) there is a ~4.3 cal. kyr-period, with a sedimentation rate of ~20.5 cm kyr^{-1}. This period comprises the *Bølling-Allerød* (B-A) interstadial (warming event), which occurred between ~14.6 and 12.7 cal. kyr BP (Naughton *et al.*, 2016) to which correspond high-standing sea level stages that favoured calmer and vertical settling conditions and a decrease of MOW's strength. The lower velocity and strength of MOW during B-A interstadial (Voelker *et al.*, 2006; Sánchez Goñi *et al.*, 2016) is coeval with finer sedimentation in the CO14-GC-07 sedimentary record (Figure 6.4).

Above 56 cm depth (~12.9 cal. kyr BP) close to the Younger Dryas, silty clay is dominant (Figure 6.4). From this depth up to 0 cm, there is a Holocene sedimentary succession with a sedimentation rate of ~4.4 cm kyr^{-1} that probably occurred in a steady depositional environment as no great oscillations are shown in the sediment properties. Moreover, there is an increasing trend on biogenic elements, associated with abundant bioturbation represented for instance by *Zoophycus*.

6.4.2 – ORIGIN OF COARSE LAYERS (S1, S2, AND S3)

The three coarse sand layers S1, S2, and S3, occurring between 175 and 161 cm represent major variations in the depositional environment (Figure 6.3B), as they present coarser and heterogeneous sediments with very irregular contacts. Three hypotheses regarding their origin can be proposed:

i) IRD. The higher number of sand-sized grains could result from ice-rafted debris (IRD) deposited during HEs. IRD deposition has been recognized in the Portuguese Margin by several authors (Schönfeld *et al.*, 1993; Lebreiro *et al.*, 1996; Baas *et al.*, 1997; Zahn *et al.*, 1997; de Abreu *et al.*, 2003; Eynaud *et al.*, 2009). Baas *et al.* (1997) found that the ages of the IRD-rich layers match with the ages of HEs in the central North Atlantic. It is worth to note that Zahn *et al.* (1997) identified three discrete IRD layers corresponding to HE1, HE2 and HE4 (Figure 6.6C) in their core SO75-26KL, retrieved from 1099 mwd, ~41 km NNE from CO14-GC-07 (Figure 6.6A). Those three layers are thicker (~14 – 18 cm thick) than the three coarser ones found in CO14-GC-07, which only account for ~1.5 to 3.5 cm thickness (Figure 6.3B). Furthermore, and despite the occurrence of IRD in the nearby area (Baas *et al.*, 1997; Zahn *et al.*, 1997; Schönfeld and Zahn, 2000), mean sand grain-size in S1-S3 layers varies between 111.50 μm and ~148.15 μm (Figure 6.3D) not fulfilling the minimum fraction (~180 μm) proposed by Heinrich (1988) for IRD clasts. In addition, only the timing of S2 is close enough in age to potentially correspond to a HE, namely HE 3 for which Zahn *et al.* (1997) did not observe IRD deposition at the Alentejo Margin.

ii) Turbidites. Three different slope instability events could have occurred upslope (<1425 mwd) and the displaced sediments reached the area as turbidites, creating the S1-S3 thin-layered coarser levels. Some authors, e.g., (Baas *et al.*, 1997; Rasmussen *et al.*, 2003; Lebreiro *et al.*, 2009; Ducassou *et al.*, 2016), recognized that downslope mass transport processes were frequent in the Portuguese Margin, during glacial periods, led by substantial sea-level changes. Considering the mostly MIS 2 age constraints of the S1-S3 coarser layers they formed during a period of relative low sea-level. Such a period can be characterized by an increasing contribution of terrigenous input (Siddall *et al.*, 2008), favouring sediment coarsening as well as an increasing Fe content and magnetic susceptibility (Figures 6.3 and 6.4). The alternance between coarse layers (S1-S3) and finer sediments indicate a change in sediment source and the presence of hiatus Hi2, in the S1-S3 layers interval, could also be related with erosive processes due to sedimentary instability, which would reinforce the argument of gravitational deposition of these sediments. However, the absence of a fining-upward structure of these layers as indicated by Shanmugam (2016), and the thickening of the S1-S3 layers towards the hiatus point to an increase on contour current strength and winnowing activity.

iii) Intensification of the bottom / contour currents (especially MOW) activity, during colder periods.

Grain-size variability is a proxy for MOW flow speed and intensity, which is higher during cooler periods, e.g., (Rogerson *et al.*, 2005; Voelker *et al.*, 2006; Toucanne *et al.*, 2007). During cold periods, the lower core of the MOW, between ~1000 and 1500 mwd increased in strength (Schönfeld and Zahn, 2000; Rogerson *et al.*, 2005; Llave *et al.*, 2006), due to the increased salinity and density gradients (Voelker *et al.*, 2006; Rogerson *et al.*, 2012).

The increasingly coarser grain-size of S1-S3 layers and the irregular geometry of their limits (Figure 6.3B) towards the LGM, imply that they may be the result of high-energy events, such as bottom currents enhancement. The S1-S3 layers occurred prior to the LGM, with S3 presenting the coarsest mean sand size (~148.15 µm) and the most irregular limits (Figure 6.3B and 6.3D). S3 is also the thickest and the youngest layer (Figure 6.3B), thus being the closest one to the LGM. Thus, the closer to the LGM, the thicker the layer, the coarser the grain-size and more irregular are the limits (Figure 6.3B). These evidences point to the action of bottom current activity through the cooling transition to the LGM. Above S3,

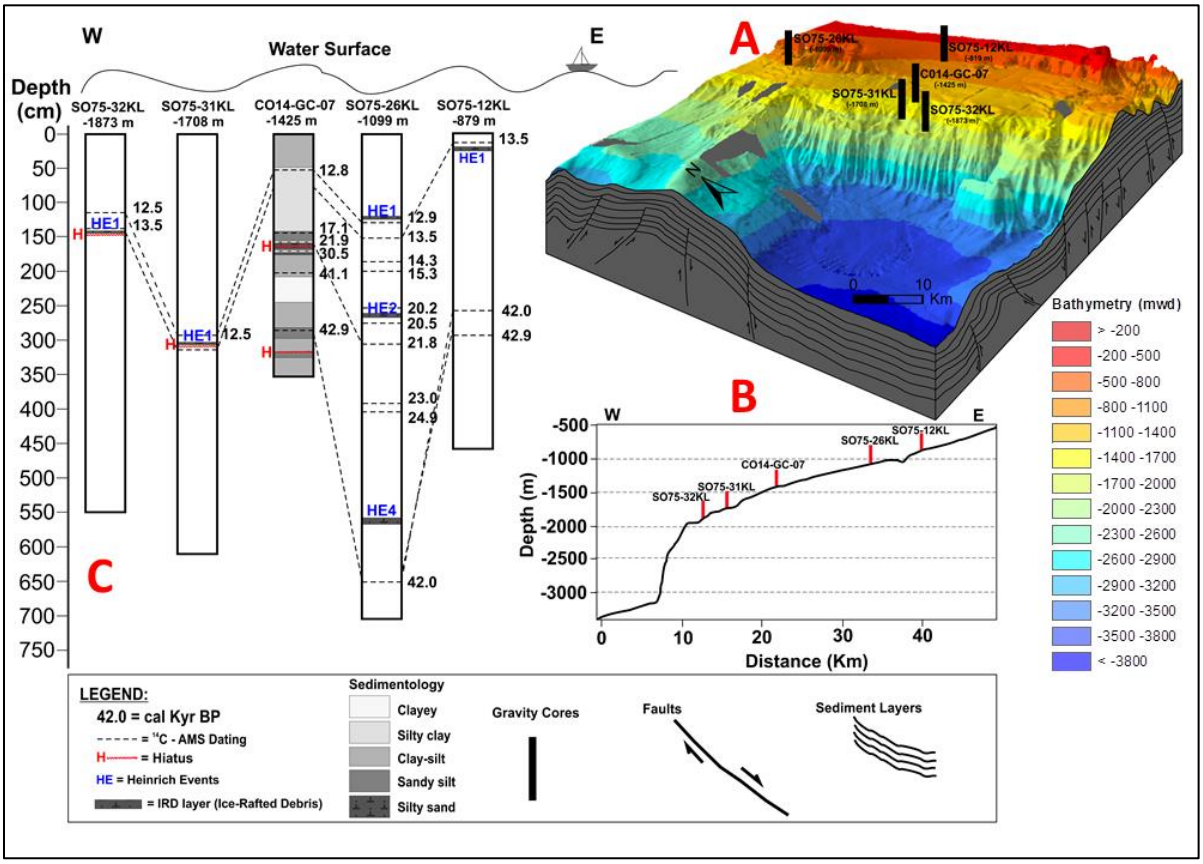

FIGURE 6.6 - Chronostratigraphic correlation between sedimentary cores retrieved from the Sines Contourite Drift. (A) – 3D diagram block, with bathymetry acquired in CONDRIBER project. Black bars correspond to cores retrieved in the area: CO14-GC-07 analysed in this work and four cores previously retrieved for other works. (B) – Longitudinal profile representing bathymetric position of each core. (C) – Chronostratigraphic core correlation based on AMS ^{14}C dates. Dated ages, stratigraphic hiatuses (H) and Heinrich events (HE) are marked along the cores. Data of cores SO75-12-, 26, 31, and 32KL retrieved from Baas *et al.* (1997), Zahn *et al.* (1997); Schönfeld and Zahn (2000).

sediments are still coarse, although not having the configuration of the S1-S3 layers, consistent with a lower influence of the MOW, which according to Schönfeld and Zahn (2000), during the LGM imprinted the continental slope of SW Portuguese margin between ~1600 and 2200 mwd, below the sedimentary record.

Considering the possible explanations previously addressed for the origin of the coarser layers S1-S3, the most plausible process is likely to be the enhanced bottom current activity that winnowed fine particles and sorted previously existing sandy sediments.

6.4.3 – MOW VARIABILITY DURING THE LAST ~50 cal. kyr: PALAEOCEANOGRAPHIC IMPLICATIONS

The multiproxy analysis of the sedimentary record of gravity core CO14-GC-07 allows to infer the variability and vertical migration of the MOW for the last ~50 cal. kyr, based on the current knowledge about the behaviour of this water mass (Rogerson *et al.*, 2005; Kaboth *et al.*, 2016). Currently, MOW circulates at < 10 cm s^{-1} along the Western Portuguese Margin (Ambar and Howe, 1979; Ambar *et al.*, 2002), although its intensity has been strengthened in the past (Bahr *et al.*, 2014; Kaboth *et al.*, 2017b), especially during Late Pleistocene glacial periods (Schönfeld and Zahn, 2000; Rogerson *et al.*, 2005; Voelker *et al.*, 2006; Toucanne *et al.*, 2007).

The advection of MOW left distinctive imprints, along the SW Portuguese margin (Schönfeld and Zahn, 2000), during glacial and interglacial bottom current oscillations. These are indicators of the intensifications of MOW's advection (Rogerson *et al.*, 2005) and vertical shifting of its path (e.g., Kaboth *et al.*, 2017b). Rogerson *et al*. (2005) found correlation between grain-size and MOW's flow strength, during glacial periods, indicating that sediment fraction coarsening reflects variations on MOW's intensity.

S1-S3 coarse layers (Figure 6.3B) are examples of those imprints, whose formation is coeval with the intensification of MOW (e.g., Rogerson *et al*., 2005; Voelker *et al.*, 2006). These layers are as coarser and present more irregular limits as they are closer in age to the peak of MIS 2, indicating the presence of a denser and enhanced MOW (Voelker *et al.*, 2015).

AMS ^{14}C dating reveals that in CO14-GC-07, from > ~50 cal. kyr to Present, deposition went through the last three MIS events. The general picture indicates that CO14-GC-07 went through two distinct climatic global trends: cooling from the bottom up to ~140

cm; warming from this depth up to the top, which led respectively to sea level retreat and advance. The multiproxy analysis of sediment properties (Figure 6.4) testifies several changes in the depositional conditions that can be interpreted as an indicator of the MOW strength and vertical variability. Therefore, four main phases of MOW's vertical oscillations during the last ~50 cal. kyr are proposed (Figure 6.7).

6.4.3.1 – PHASE I – (> 42.9 – ~30.5 cal. kyr BP)

This phase is comprised in MIS 3 (Figure 6.7). The presence of the S1 coarse layer (Figure 6.3B), immediately before 30.5 cal. kyr BP, suggests the strengthening of the MOW, inside a cooling period towards MIS 2 (~29 cal. kyr BP). The proximity to MIS 2 indicates glacial climate and sea level regression, promoting the MOW's enhancement and increase in density, verified in this region during colder periods (Schönfeld and Zahn, 2000; Kaboth *et al.*, 2017a) and corroborating the downslope shift of MOW verified by Kaboth *et al.* (2016).

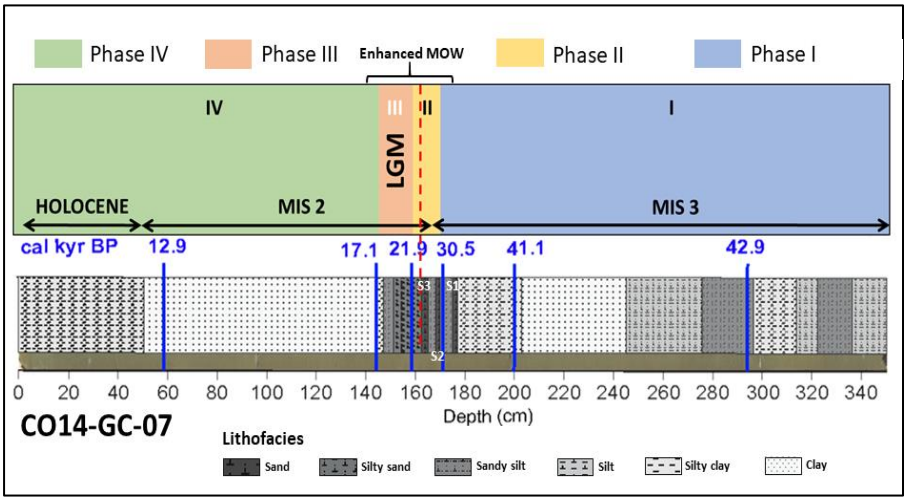

FIGURE 6.7 – The evolution of CO14-GC-07 through MOW phases during the Late Pleistocene-Holocene. S1-S3 are sand layers.

6.4.3.2 – PHASE II – (30.5 –21.9 cal. kyr BP)

This phase spans from the end of MIS 3 close to the LGM (Figure 6.7). The two coarse layers (S2 and S3) increase in thickness, together with mean grain size and irregularity of the boundaries towards the top (Figure 6.3B), indicating enhancement of the MOW, evident through the increasingly irregular boundaries, when getting closer to the LGM (~20 cal. kyr BP). During this phase the SW Portuguese margin faced an enhancement and sinking of the MOW (Schönfeld and Zahn, 2000; Rogerson *et al.*, 2005; Llave *et al.*, 2006; Voelker *et al.*, 2006; Bahr *et al.*, 2014; Kaboth *et al.*, 2017b), exerting great activity in the seafloor at

deeper depths (~1700 – 2200 mwd). Therefore, it is suggested that the coarse layers S2 and S3 testify two episodes of enhancement of the MOW, which reworked and sorted the middle slope's sediments, when this water mass was sinking towards its deepest position reached in the LGM. Furthermore, the presence of Hi2 at ~161 cm, closer to the LGM also suggests a stronger MOW and consequent high erosional activity reinforced by increasing colder conditions, as suggested by Kaboth *et al.* (2017b). Similarly, Schönfeld and Zahn (2000) found hiatuses close to and during the LGM, at sites nearby CO14-GC-07 (Figure 6.7). Their cores are ~300-400 m deeper than CO14-GC-07, which allows inferring that in this period MOW's activity was very intense and was shifting downwards. In CO14-GC-07 the hiatus (Hi2) marks the end of the visible effects of MOW on the sedimentary record, during this time interval.

6.4.3.3 – PHASE III – (21.9 - 17.1 cal. kyr BP)

The sedimentary record corresponding to this phase is homogeneous and is composed by sandy silt, (Figure 6.3B). These coarse sedimentation record suggests strong bottom current activity, although the depositional homogeneity and the absence of irregular contacts between sediment layers, points to the absence of MOW's activity at this site during the LGM. Thus, considering that Schönfeld and Zahn (2000) propose a deeper glacial MOW activity off southern Portugal, during LGM until 14 kyr, when MOW flowed ~800 m deeper than nowadays, between 1600 and 2200 mwd, it is inferred that CO14-GC-07 was not under the influence of the MOW during this phase. This means that MOW flowed below the depth of this core (1425 mwd) and its location was under the influence of the overlying ENACW, still allowing for the deposition of coarse sediments up to 17.1 cal. kyr BP (Figure 6.3B).

6.4.3.4 – PHASE IV – (17.1 cal. kyr BP – Present)

Close to 17.1 cal. kyr BP, the effects of the MOW were still absent on the middle continental slope of the Alentejo Margin, at core CO14-GC-07 depth (1425 mwd), as hemipelagic sedimentation (clay and silty-clay) is dominant (Figure 6.3B). However, after the LGM, the MOW suffered an upslope shifting, reaching its present-day circulation pattern and depth at 7.5 - 6.0 kyr BP (e.g., Schönfeld and Zahn, 2000). The gradual sediment coarsening, from clay to silty clay, after ~12.9 cal. kyr BP towards the core top (Figures 6.3 and 6.4) is interpreted as the probable upward shifting of the MOW / ENACW interface. This upward

shift promoted more impact on middle slope's sediments than during the LGM, when it was absent.

6.4.3.5 – MOW CIRCULATION AND SLOPE INSTABILITY

The depth of the interface between the upper and the lower MOW branches roughly shifted from its glacial position at 2200 mwd to present-day position at 1100 mwd, coinciding with the main cluster of landslides scars in the Alentejo Margin (Figures 6.1A and 6.1C). Their presence point to the effects of factors like slope angle and seismicity as triggering and conditioning factors, but also bottom current activity (Teixeira *et al.*, 2019) as an important conditioning factor for slope instability, essentially through overloading and under-consolidation, exerted on the sedimentary structure due to the high sedimentation rates.

Most of the slide scars present at the SCD, range in depth between 1100 and 2500 mwd, which partially coincide with the main cluster of sediment waves, between ~800 and ~1700 mwd (Teixeira *et al.*, 2019). Both clusters of landslides and sediment waves roughly match with the depth range (1100-2200 mwd) of the vertical shifting of MOW between glacial and interglacial periods. This vertical movement of MOW and its interfaces with NADW and ENACW may have had a key role creating this cluster of landslides and contributed to form the sediment wave fields.

Water-mass interfaces constitute important pycnoclines generated by salinity and temperature contrasts, which are generally affected by baroclinic activity (McCave, 2001; Pomar *et al.*, 2012), responsible for flow acceleration, e.g., (Rebesco *et al.*, 2014; Ercilla *et al.*, 2016). Under these conditions, water-masses' interfaces could be co-responsible for the higher slope instability in that depth range, through the impact on slopes surface caused by the acceleration generated by these water-masses' interfaces. Moreover, the presence of sediment waves favours the development of many small slide scars through the development of surface discontinuities, as also verified by Lee *et al.* (2002) in the margin of northern California. Those discontinuities are highly conditioned by the vertical shift of local water-mass interfaces, as also verified in the Ewing Terrace (Hernández-Molina *et al.*, 2009) and in La Plata Terrace in the Argentine margin (Preu *et al.*, 2013).

6.5 – CONCLUSIONS

The multiproxy – grain-size, calcimetry, physical, and geochemical properties of sediments, and AMS ^{14}C dating - analysis of the gravity core CO14-GC-07 has shown that the sedimentary evolution of the SCD went through four distinct stages between the last >43 cal kyr BP and the Present. The combined variation of these properties demonstrated that these stages have different and irregular sedimentary conditions, which are mainly dependent on variable climate conditions and bottom current speed variations and vertical oscillations.

The variability of the MOW represents major variations in the depositional conditions, which are represented in the sedimentary record by three coarse-grained layers, which are a proxy for MOW's enhancement. As bottom current enhancement is favoured by cold climatic episodes and S1-S3 layers are thicker and present coarser mean grain-size closer to Hi2, it is concluded that a major cold climatic episode occurred promoting sea-level regression and terrigenous input, with consequent augmentation in Fe content and magnetic susceptibility, typical of cooling events.

The vertical shifting of MOW associated with the presence of interfaces, between MOW and both ENACW and NADW, and the related contrasts of temperature and salinity constitute important focuses of flow acceleration and thus of greater impact on the seafloor/slope surface, creating morphosedimentary features as sediment waves and causing mechanical problems in the sedimentary stacking by favouring the development of landslide scars.

The multiproxy analysis of core CO14-GC-07 demonstrated a wide overview of the depositional environment on the SCD during the last >43 kyr. The correlation between multiple and diversified sediment properties showed an integrated evolution of both terrigenous- and biogenic-induced properties and glacial vs interglacial related events associated to those properties, thus allowing for a broad vision of the sedimentary evolution of the Sines Contourite Drift. This analysis can be very effective and very useful in other continental margins with contouritic activity.

7 – GEOTECHNICAL PROPERTIES OF THE LATE PLEISTOCENE-HOLOCENE SEDIMENTS OF THE SINES CONTOURITE DRIFT[3]

The Sines Contourite Drift (SCD), in the Alentejo Margin, is a middle continental slope plastered contourite deposit, whose Late Pleistocene-Holocene sediments have been deposited at a high sedimentation rate (27 cm kyr^{-1}), in different depositional phases controlled by palaeoceanographic and climatic variations, conferring low consolidation to these drift sediments. Given that these sediments are in a dynamic area, where the Mediterranean Outflow Water (MOW) has a key role on shaping the morphology and, given the presence of many landslides' scars both on steep and gentle slopes, it is imperative to understand the sediments' stability and how they behave mechanically under stress, through the assessment of their mechanical properties.

Geotechnical analyses were done through consolidation (oedometer), triaxial in compression, direct shear, and simple shear (DSS) tests on the sediments of the 346-cm long gravity core CO14-GC-7B, retrieved at 1425 meters water depth (mwd). The aim is to assess the resistance of these sediments through different methods to determine their consolidation, compressibility, and resistance to shear stress.

Results show that the upper 346 cm of the SCD, below seafloor, consist of low- to normally consolidated shallow-depth sediments, with high water content and void ratio, presenting *in situ* effective consolidation < 50 kPa. The high degree of compressibility of these sediments shows their low consolidation in consequence of the high sedimentation rates. Their low consistency and plastic behaviour are evident through the barrel-shaped disruption mode. Once under stress, the horizontal and vertical displacements of these sediments are generally constant with the increasing stress where almost no, or very smooth, peak strength is verified. Internal friction angle values vary between 23.6º and 30.9º with mean values of 25.7º and 28.5º, whether they are determined through simple shear or triaxial tests, respectively. The low consolidation of these sediments associated with the dynamism of the bottom current activity and the slope angle of the area are important triggers for landsliding activity.

[3] This chapter has been submitted for publication in **Engineering Geology**:

TEIXEIRA, **M**., Viana da Fonseca, A., Cordeiro, D., Terrinha, P., Roque, C. (2021) – Geotechnical properties of the Sines Contourite Drift sediments: conditions for triggering submarine landslides. *Engineering Geology*, under revision.

7.1 – INTRODUCTION

Contourites are along-slope depositional bodies highly susceptible to slope instability, especially because generally they are well-sorted sediment deposits, with high water content, e.g., (Bryn *et al.*, 2005a; Masson *et al.*, 2006; Laberg and Camerlenghi, 2008; Baeten *et al.*, 2014). This is particularly the case of the muddy drifts, e.g., (Laberg *et al.*, 2002; Bryn *et al.*, 2005b), whose high sorting (Miramontes *et al.*, 2018) and low angle of shear resistance (Baeten *et al.*, 2014), makes them weaker and prone to slope failure.

Submarine landslides are worldwide phenomena (Hampton *et al.*, 1996; Masson *et al.*, 2006; Laberg and Camerlenghi, 2008), with great incidence on contourites (Bugge *et al.*, 1988; Laberg and Vorren, 2000; Laberg *et al.*, 2002; Bryn *et al.*, 2005b; Laberg *et al.*, 2005) particularly on plastered drifts, e.g., (Krastel *et al.*, 2011; Preu *et al.*, 2013; Ercilla *et al.*, 2016; Martorelli *et al.*, 2016; Miramontes *et al.*, 2018; Teixeira *et al.*, 2019). However, little is known yet about the real impact mechanical properties have on submarine slope instability.

The Sines Contourite Drift (SCD) is a plastered drift, i.e., a giant and elongated drift (Rebesco *et al.*, 2014), fairly affected by slope instability (Teixeira *et al.*, 2019). This activity has been influenced by the millennial-scale climatic variation and bottom currents oscillations occurred during Late Pleistocene glacial and interglacial periods (Schönfeld and Zahn, 2000; Abrantes *et al.*, 2005; Rogerson *et al.*, 2005; Voelker *et al.*, 2006; Toucanne *et al.*, 2007; Hernández-Molina *et al.*, 2014b; Salgueiro *et al.*, 2014; Bahr *et al.*, 2015; Kaboth *et al.*, 2017a) promoting strong variations on depositional activity with highly varying sedimentation rates (Stow *et al.*, 2013). These are associated with periods of stable and abundant depositional activity and periods of sediment scarcity that caused strong variations on the signature of the sediment properties (Teixeira *et al.*, 2020). These geomorphological and sedimentary constraints might have impact on mechanical properties of the SCD, however it has never been neither analysed the geotechnical properties of this plastered drift, nor shown their impact on slope instability.

Geotechnical tests allow for measuring soil mechanical properties and can be performed both *in situ* and at the laboratory, although they are usually performed in laboratorial environment. Different geotechnical tests are performed in laboratorial conditions for measuring shear strength, compressibility, deformability and permeability, according to the scientific and technical needs (Head, 1982; Viana da Fonseca, 1996). Laboratory tests can be divided into two categories, according to Head (1982): classification tests that aim to

identify the general type of sediment; and tests for the assessment of the main engineering/mechanical properties.

Triaxial tests, direct- and simple-shear tests, and consolidation tests are among the most used laboratorial geotechnical testing procedures for determining the mechanical characteristics of sediments. Since long time ago, many studies have been using these tests for slope stability analysis with many different purposes as for engineering studies and landslide hazard assessment (Casagrande, 1936; Terzaghi and Peck, 1948; Kokusho, 1980; Head, 1982; Baraza *et al.*, 1992; Viana da Fonseca, 1996; Lee and Baraza, 1999; Casas *et al.*, 2004; Lee *et al.*, 2011; Matos Fernandes, 2012; Soares, 2015).

Geotechnical properties of sediments, both marine and non-marine, assume an extremely important role on slopes' mechanical behaviour (Lee and Baraza, 1999). This is particularly significant for the implementation of engineering projects, especially on the continental shelf, such as pipelines, internet cables, wind generators or even breakwaters, groins and jetties for coastal protection (Piper and Aksu, 1987; Hampton *et al.*, 1996). This knowledge of the geotechnical properties is also very useful for civil protection and natural hazards prevention in order to take better actions viewing future damaging events, which bring serious economic, social and environmental problems (Locat, 2001; Sultan *et al.*, 2004; Masson *et al.*, 2006). Submarine landslides often occur induced by sediment liquefaction in consequence of earthquakes (Baraza *et al.*, 1990; 1992; Lee and Baraza, 1999; Gràcia *et al.*, 2010) and excess pore-pressure, which constitute two important conditioning factors for landslide development (Schultheiss, 1989; Laberg *et al.*, 2002; Laberg and Camerlenghi, 2008; Urlaub *et al.*, 2015), being thus imperative to study the mechanical properties of the marine sediments for a feasible assessment of slope stability.

This chapter presents the theory, the procedures, the devices, and the results of the geotechnical analyses performed in the sediments of gravity core CO14-GC-7B, retrieved at 1425 mwd in the Alentejo Margin. This gravity core is the twin-core of CO14-GC-07, previously analysed in chapter 6. CO14-GC-7B gravity core was retrieved in the same location as CO14-GC-07 but unlike this, CO14-GC-7B was kept as a sealed whole core for the geotechnical analysis, to preserve the inner moisture of sediments, as explained in chapter 4. To understand the resistance of these sediments to shear stress, some tests were conducted on to assess their main geotechnical characteristics, as internal friction angle (ϕ') and cohesion (C').

In this chapter the aim is to assess the sediments' mechanical properties to evaluate the propensity of sediments to slope (in)stability when submitted to stress conditions.

7.2 – GEOTECHNICAL TESTS – THEORY AND TECHNIQUES

Geotechnical tests are used for shear strength assessment since long time ago (Casagrande, 1936; Terzaghi and Peck, 1948) until present times (Head, 1982; Viana da Fonseca, 1996; Matos Fernandes, 2012), serving multiple purposes as engineering works (Viana da Fonseca, 1996; Soares, 2015) and aiming to understand soil mechanics (Terzaghi, 1943) and slope stability (Lee and Edwards, 1986; Yenes *et al.*, 2020; 2021). The term soil is used here as a general term, once in this work the analysis is done on marine sediments.

7.2.1 – CONSOLIDATION - OEDOMETER TEST

Consolidation analysis through Oedometer tests (Terzaghi, 1943) are used for the determination of the consolidation characteristics of low permeability media (Head, 1982), such as marine sediments. The low permeability on clays has firstly been addressed by Terzaghi (1943), who has designed the first consolidation process (Head, 1982). The oedometer test is a manually-controlled one-dimensional compression test aiming to determine the sediment compressibility (Viana da Fonseca, 1996; Matos Fernandes, 2012; Soares, 2015), through vertical displacement by opposition to the constrained radial displacements (Matos Fernandes, 2012; Soares, 2015), allowing to measure the volume change. For the determination of consolidation two parameters are usually required (Head, 1982): the coefficient of volume compressibility and the coefficient of consolidation.

Consolidation is the process by which fine-grained sediments change in volume with changes in load (Baraza *et al.*, 1990). Oedometer test method aims to determine the magnitude and rate of consolidation of sediment when it is laterally restrained and drained axially while subjected to incrementally applied controlled-stress loading (ASTM-D2435, 1996). This test is also used for determining the sediment compressibility (compression index, Cc) and to estimate the stress history of the sediment (Terzaghi, 1943; Baraza *et al.*, 1992; Matos Fernandes, 2012), by offering a quantitative evaluation of sample disturbance (Head, 1982; Schultheiss, 1982).

According to Terzaghi (1943), consolidation corresponds to the dissipation of neutral pressure, i.e., when the pore water pressure regains the equilibrium and for this, time is a key value (Matos Fernandes, 2012). Terzaghi (1943) formulated the consolidation theory (Equation 7.1) assuming that the soil is homogeneous and saturated, that water and particles' compressibility are negligible, and stress and deformation states are uniform along any horizontal section of the sediment column, assuming that deformation only occurs vertically and so it does water flow, obeying to the Darcy's Law. In this theory it is also assumed that the coefficient of permeability k and the coefficients of compressibility (a_v) and volumetric compressibility (m_v) are constant (Terzaghi, 1943):

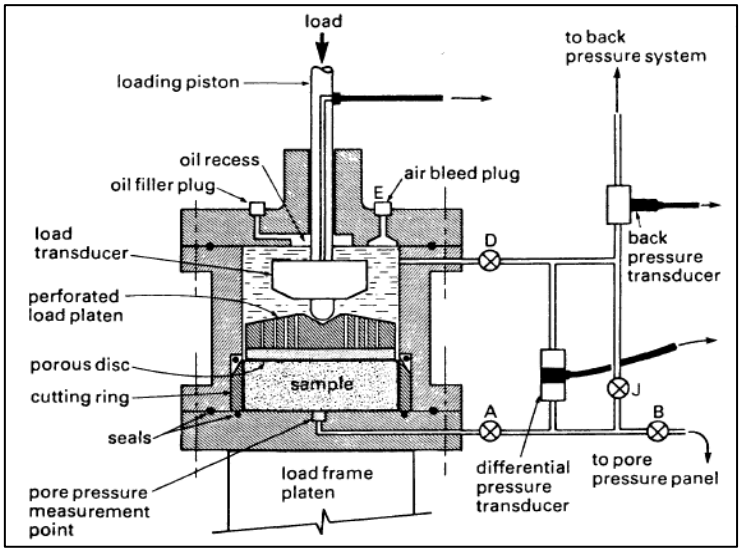

FIGURE 7.1 – Scheme of a sample and test oedometer chamber configuration (Head, 1982).

EQUATION 7.1:

$$\frac{\partial u_e}{\partial t} = c_v \frac{\partial^2 u_e}{\partial z^2}$$

Where, u_e is the neutral pressure, ∂t is time variation, ∂z is the depth variation and c_v is the coefficient of consolidation (Equation 7.2).

After testing the sediments' consolidation it is possible to calculate the over consolidation ratio (OCR), a ratio of the pre-consolidation stress (σ'_p) to the overburden effective stress (σ'_{v0}) (Baraza *et al.*, 1990; Casas *et al.*, 2004), and the coefficient of consolidation (C_v), which measures the rate at which the sediment consolidates (Baraza *et al.*, 1992). The coefficient of consolidation c_v is:

EQUATION 7.2:

$$C_v = \frac{k}{m_v \gamma_w}$$

Where, k is the coefficient of permeability of the clay, m_v is coefficient of volume compressibility of the clay and γ_w is the mass density of water.

When testing sediment's consolidation at the laboratory it is important to bear in mind that the results are dependent upon the magnitude of the load increments (ASTM-D2435, 1996), consisting of a reduction in sediment volume due to loading, which implies the removal of interstitial pore water in the case of saturated submarine deposits (Keller, 1982). In the laboratory it is normally used the oedometer (Figure 7.1), a device where an undisturbed sample, with at least 12 mm height and 50 mm diameter, is inserted inside a ring with a filter paper and two porous disks on each face of the specimen (ASTM-D2435, 1996). Then, the ring is submerged by water inside a cell and an apparatus is loaded over the top of the ring. When performing this test it is adverted that it should not be done with temperature variations ≥ to ± 4ºC (ASTM-D2435, 1996). Sunlight exposure is also not advisable so as not to promote water evaporation.

The results of oedometer tests come as compressional curves, resulting from the proportion of void ratio to the vertical confining stress for each load stage.

The oedometer tests allow for the compression curves to be drawn by plotting the vertical confining stress (Equation 7.3) against the void ratio (Equation 7.4), after the settlement is complete, for each load stage (e.g., Soares, 2015).

EQUATION 7.3:

$$\sigma'_v = \frac{F}{A}10$$

Where *F* and *A* correspond respectively to the total load and to the area of the sample and 10 is a value that corresponds to the amplification effect of the load exerted by the lever (Matos Fernandes, 2012; Soares, 2015). No horizontal displacement occurs in the sample during the test (Head, 1982; Viana da Fonseca, 1996; Soares, 2015), the area keeps constant, only varying the volume of the sample through the ratio between axial displacement and initial height: $\Delta H/H_0$. At the end of each loading stage, this ratio is determined, and the final volume is achieved. Having the volume, the void ratio (*e*) is calculated according to the following equation:

EQUATION 7.4:

$$e = G_s \frac{V_c}{W_d} - 1$$

Where, G_s is the density of solid particles; V_c the corrected volume (the product of the area to the difference between samples' height and samples' initial height) and W_d is the dry weight of the sample.

7.2.2 – DIRECT SHEAR STRESS TEST

Direct Shear Stress tests are used for determining the shear strength parameters – cohesion (C') and internal friction angle (ϕ') – of sediments. This is the oldest procedure for measuring short-term shear strength of soils in terms of total stresses (Head, 1982). This test aims to determine consolidated and unconsolidated shear strength by the deformation of a sediment sample through a controlled strain rate on a single shear plane (ASTM-D3080, 1998). Direct shear stress test can be done either under drained or undrained conditions, as it happens with triaxial tests. Although according to Schultheiss (1982), behaviours of the sediment in the direct shear stress test are similar to those of the triaxial test, stress states are not so well defined in direct shear stress test. Shear stress can be assessed either using a conventional shear box (Figure 7.2) or a ring shear apparatus (Figure 7.3).

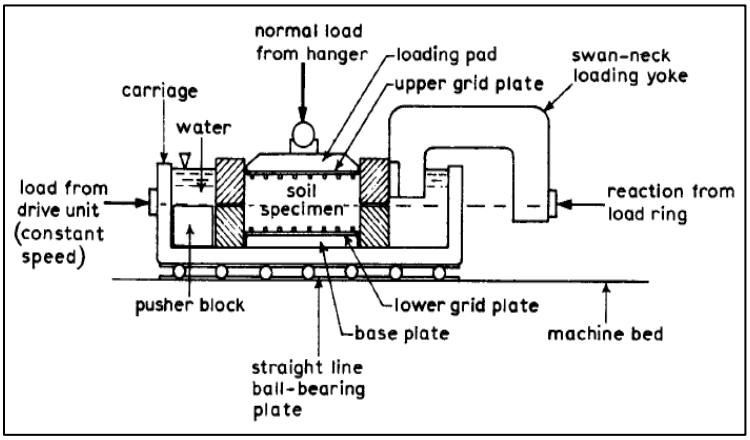

FIGURE 7.2 - Conventional 36 cm² shear box apparatus and displacement control. From Head (1982).

Direct shear tests assess the sediments response to the stress-strain relationship and strength forces (Viana da Fonseca, 1996), where the shear stress resisting sliding is determined on a horizontal surface through the following expression:

EQUATION 7.5:

$$\tau = \frac{F}{A_3}$$

Where, τ is the shear stress; F is the horizontal force; A_3 is the horizontal cross-sectional area.

Some drawbacks are present in direct shear stress tests (Tatsuoka *et al.*, 1988; Viana da Fonseca, 1996; Matos Fernandes, 2012), as they do not provide any control of the drainage and pore water pressure measurement (Head, 1982). With this method some regrets may appear, once it is only known the strain value on the shear plane not being possible to determine neither strain values nor strain directions on other planes. Conventional shear box test puts some limitations to the incremental deformation in the shear plane due to the box rigid edges, generating non-uniform stresses on the sediment sample (Viana da Fonseca, 1996).

This test consists in the insertion of a quadrangular section of soil that is cut across into two sections (ASTM-D3080, 1998), inside a shear box (Figure 7.2). A constant normal force (*N*) is applied vertically through a vertical weight (Matos Fernandes, 2012) in a way that it becomes slowly consolidated by squeezing out the water inside, before shearing and then the shear stress (*S*) is applied to the lower half of the split container at a constant velocity (ASTM-D3080, 1998; Matos Fernandes, 2012), causing the development of horizontal strain (Schultheiss, 1982). Meanwhile, the upper half of the split container is sustained by a reaction (*T*) whose value is measured by a dynamometric ring. The shear stress (τ) is obtained by the ratio of the mobilized reaction (*T*) by the shear section (*S*), which must be corrected during the analyses as it varies due to the reduction effect.

7.2.3 – DIRECT SIMPLE SHEAR TEST

The direct simple shear (DSS) test is similar to the conventional shear box test (Viana da Fonseca, 1996) as it only allows to know the vertical and horizontal stresses and does not allow to recognise the magnitude and direction of the main stresses acting on the sample (Soares, 2015; Pardo *et al.*, 2018). Direct simple shear test (Figure 7.3) is a laboratory test (CEN-ISO/TS-17892-10, 2004; ASTM-D6528, 2007), characterized by a horizontal motion imposed to a sediment sample at a constant velocity, in a similar way as it is done for the shear box (Matos Fernandes, 2012). This is a constant volume test that allows for the stress-

strain analysis, where the area and volume are kept constant (Soares, 2015). The strain analysis is performed through the ratio horizontal displacement – final height of sediments sample in the final stage of consolidation. The shear analysis is done through the vertical confining stress - σ_v (Equation 7.6) and the shear stress (τ) - (Equation 7.7).

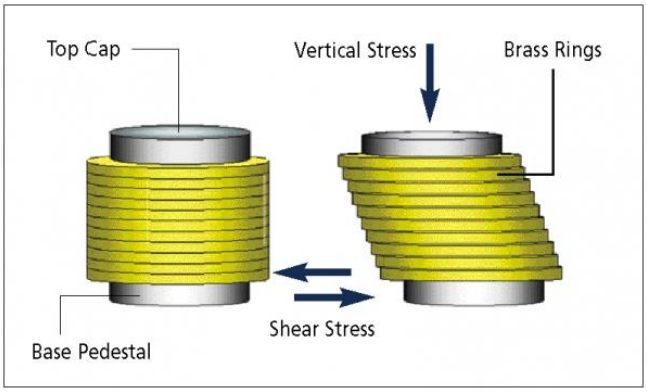

FIGURE 7.3 - Schematic diagram of cyclic simple shear test apparatus. Adapted from Pardo *et al.* (2018).

EQUATION 7.6:

$$\sigma_v = \frac{F_v}{A}$$

Where, F_v is the vertical load and A is the area of the sediment sample.

EQUATION 7.7:

$$\tau_{xy} = \frac{F_h}{A}$$

Where, F_h is the horizontal load and A is the area of the sediment sample.

7.2.4 – TRIAXIAL TEST

The triaxial test measures the drained and undrained stress-strain properties of sediments, being suitable to determine the strength and stress-strain relationships of cylindrical consolidated cohesive soil samples (ASTM-D4767, 1995; CEN-ISO/TS-17892-9, 2004). The sediments' shear strength that results from triaxial compression mainly depends on the applied stresses, the time allowed for consolidation, the strain rate, and the stress history of soil (Head, 1982; Winters, 1987; ASTM-D4767, 1995). The principle of this test consists of a cylindrical specimen of sediment that is subjected to an all-round confining pressure that is then kept constant as an axial load increases until the failure occurs (Head, 1982). This is the most popular test to study the geotechnical properties of sediments (Matos Fernandes, 2012), and the most suitable and complete for the study of shear strength (Fonseca, 2009). In the triaxial test the sediment specimen is saturated and confined via the

difference between the confining pressure (CP), and the back-pressure (BP) (Soares, 2015; Viana da Fonseca *et al.*, 2015).

Triaxial shear stress test is a common laboratory testing method that aims to obtain shear strength parameters for a variety of sediment types both as static and cyclic triaxial modes and as drained or undrained (Head, 1982; Viana da Fonseca, 1996; Matos Fernandes, 2012; Soares, 2015; Viana da Fonseca *et al.*, 2015). Cyclic triaxial tests are conducted to obtain the normalized strength degradation parameter A_r (Lee and Edwards, 1986), whereas static triaxial tests are generally used to estimate the normalized undrained shear strength, of normally consolidated sediments (Casas *et al.*, 2004), according to the following equation:

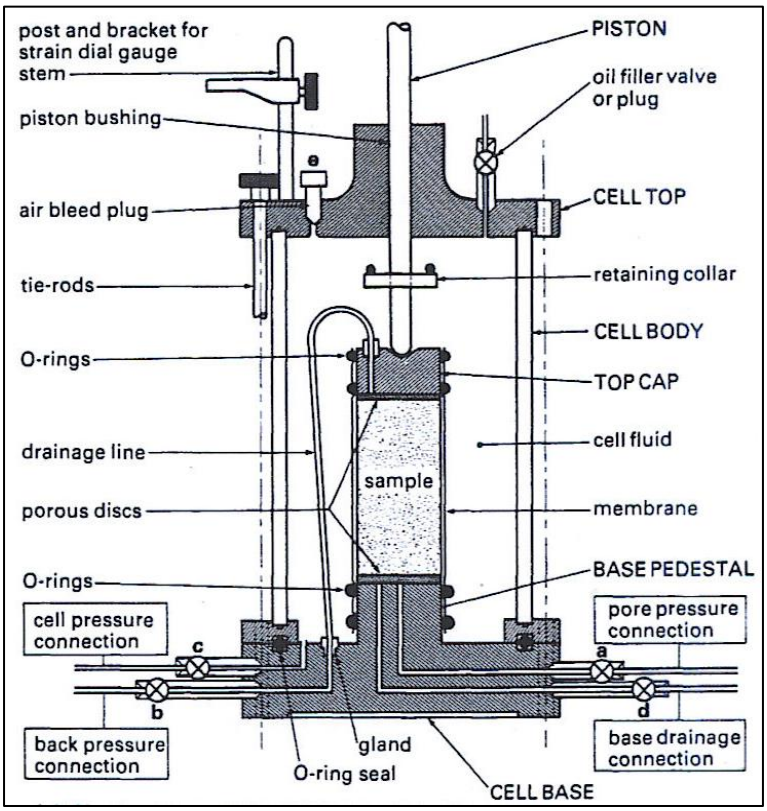

FIGURE 7.4 – Triaxial test device (Head, 1982).

EQUATION 7.8:

$$S = \frac{Su}{\sigma'_v}$$

Where *Su* corresponds to the static undrained shear strength; σ'_v is present overburden effective stress, calculated according to the Equation 4.13; *S* is the ratio of undrained shear strength to consolidation stress for normal consolidation.

Triaxial tests may be performed in three main types (Head, 1982): UU – Unconsolidated-Undrained is a low-shear strength test where strength and stress-strain relationships are determined without drainage; **CU** – **consolidated-undrained**, which determines the strength and stress-strain relationships of either an undisturbed or remoulded saturated cohesive sediment, by shearing without drainage at a constant rate of axial deformation (strain controlled) (ASTM-D4767, 1995); and **CD** – **consolidated-drained** a

slow test where drainage is allowed during consolidation, which is determined by normal loading. These are slow (< 0.5 mm/min) tests (Matos Fernandes, 2012), whose prosecution demands some procedures, which must be taken into account when assembling the triaxial device (ASTM-D4767, 1995). Most of these procedures are summarily described in subsection 4.2.6.4.

Sediment samples are confined to a triaxial chamber (Figure 7.4) with a fluid pressure (Lee and Baraza, 1999), generally distilled water (Takahashi *et al.*, 2014) and there is or there is not drainage depending on if it is a drained or an undrained test (Lee and Edwards, 1986) and then they are sheared in compression at a constant rate of axial deformation (ASTM-D4767, 1995) and the results are presented by an axial strain rate in percentage per hour (%/h). According to Head (1982), depending on the type of sediment, different types of failure occur as brittle failure for stiff sediment, where a shear plane develops, but also barrelling occurs through these tests on low consolidated sediments.

S- and P-wave measurements can be additionally performed on these sediment samples (Viana da Fonseca *et al.*, 2009; Soares, 2015), allowing to determine Skempton's coefficient B. This is the ratio of the induced pore-pressure to the change of stress loading (Skempton, 1954), which may be explained by the compressibility of rock and pore fluid (Bishop, 1966). Skempton's coefficient B is a significant pore-fluid parameter in poroelastic material (Skempton, 1954) that contain interconnected pore fluid saturated pores (Zhang *et al.*, 2009) as is the case of the hemipelagic marine sediments. This is usually determined by measuring the response of the pore water pressure inside a specimen through the increase of the confining pressure under undrained conditions, according to the following equation:

EQUATION 7.9:

$$B = \frac{\Delta u}{\Delta \sigma_3}$$

Where, Δu is the excess of pore pressure and $\Delta \sigma_3$ the increment of confining pressure applied in the triaxial apparatus. The value of B is always between 0 and 1 (e.g., Zhang *et al.*, 2009). When B = 0 no change on pore-pressure occurs due to the stress. When B = 1 the applied stress is completely transferred into the changing pore-pressure.

Previous works have already made these tests using piezoelectric transducers - bender/extender elements (Fonseca, 2009; Viana da Fonseca *et al.*, 2009; Soares, 2015). The

main role of these transducers is to measure the sediment stiffness (G_0 - read V_s), which is often used to evaluate soil liquefaction susceptibility. Bender element (BE) testing is a powerful and increasingly common laboratory technique for determining the shear S-wave velocity of geomaterials (Viana da Fonseca *et al.*, 2009).

7.3 – GEOTECHNICS RESULTS

The mechanical analysis of the sediments of the gravity core CO14-GC-7B was conducted in defined segments at variable depths that correspond to different effective consolidation stress values. The 346 cm-long gravity core CO14-GC-7B is mainly constituted by clayey and silty-clay fractions – (F < 63 μm), silty and silty sand (63 μm > F > 300 μm), of both hemipelagic and contourite sediments.

7.3.1 – PHYSICAL PROPERTIES: GRAIN-SIZE DISTRIBUTION AND ATTERBERG LIMITS

The grain-size distribution (Figure 7.5) and the Atterberg limits (liquid limit, and the plasticity index), as well as the unit weight, and water content, taken here as intrinsic physical properties of sediments, have been determined for three different samples (Table 7.1), representative of the top, middle and bottom sediments of the gravity core CO14-GC-7B.

The sediments of the gravity core CO14-GC-7B are very fine (Figure 7.5), with high percentages of clay and silt (> 90%), and a maximum grain-size of ~400 μm, although with a low percentage in the shallowest sample – 0-15 cm – (Figure 7.5). These samples have clay values between 40% and 50% ($D_{50} \approx 2$ μm for 70-85 cm and 280-295 cm; $D_{50} \approx 7$ μm for 0-15 cm), whereas the fraction < 63 μm is > 90% in both samples of 70-85 and 280-295 cm depth, being ~80% in the sample of 0-15 cm (Figure 7.5).

TABLE 7.1 – Unified soil classification, state properties, particles density and Atterberg limits for discrete samples at different depths of the gravity core CO14-GC-7B. As γ_s values are very similar, with minimal differences, they are represented with three decimals in order to better identify differences between samples

Depth (cm)	Sediment Classification (ASTM D2487-85)	Atterberg Limits		γ_s (kN m^{-3})	State Properties	
		W_L (%)	I_P (%)		w (%)	γ (kN m^{-3})
0-15	CL - Lean Clay	46	25	27.23	42.6	17.2
70-85	CL - Lean Clay	48	27	27.22	39.7	17.5
280-295	CH - Fat Clay	59	32	27.18	53.1	17.9

The silty fraction is also very significant, comprising values between 40 and 55% for the three sediment samples (Figure 7.5). Therefore, the sandy fraction is quite restricted, being thus almost incipient (< 5%) both in the samples of 70-85 cm and 280-295 cm. Contrarywise,

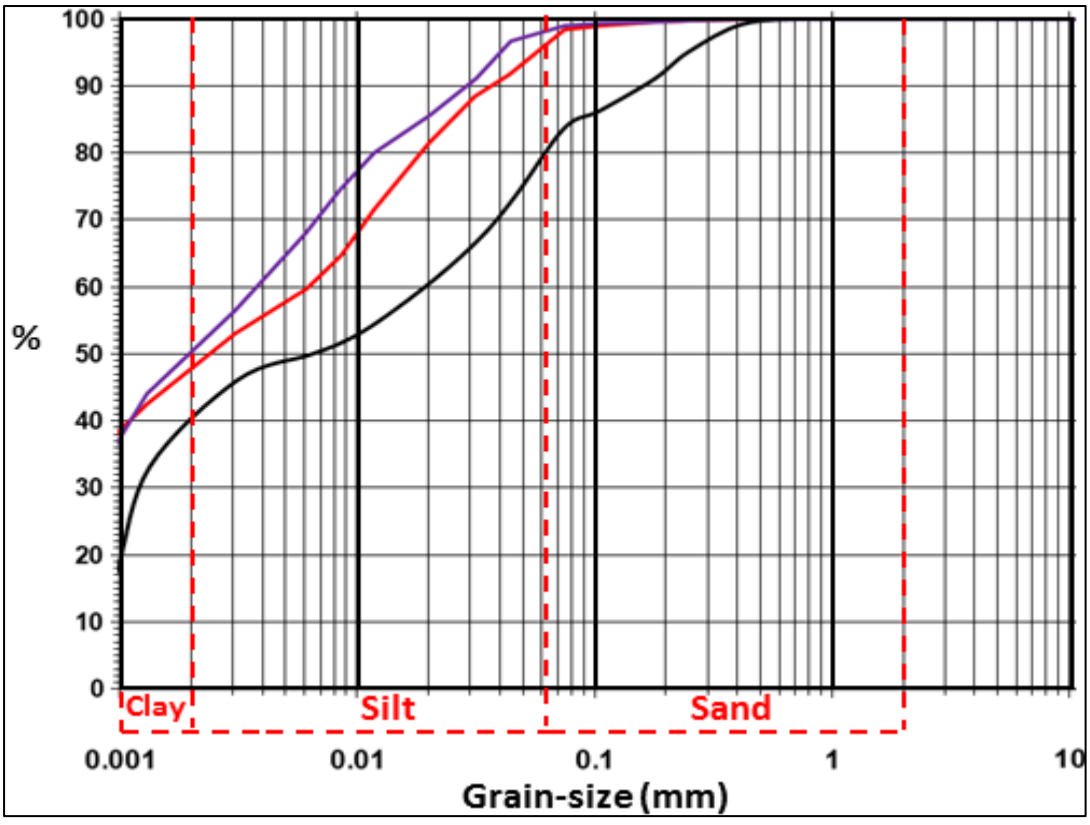

FIGURE 7.5 – Grain-size distribution. Grain-size curves: black (0 - 15 cm); red (70 - 85 cm); purple (280 – 295 cm). Red dashed lines delimit the main grain-sizes present in these sediment samples.

the shallowest sample (0-15 cm) presents a considerable percentage (~20%) of sand, when compared with the remaining samples. These data (Figure 7.5) show that although grain-size is dominantly fine, being concentrated in the fraction < 63 μm, there is a granulometric fining with depth.

These three samples present distinctive I_P values (Table 7.1), lower and higher than 30%, corresponding respectively to CL – lean clays (0-15 cm and 70-85 cm) and to CH – fat clays (280-295 cm), according to the Unified Soil Classification (ASTM-D2487, 1985). These sediments present significant (≥40%) water content (Table 7.1), rather variable with fine grain-size and clay content: finer sediments with > 90% of silty and clayey sediments, < 63 μm (Figure 7.5), present 53.1% of moisture (Table 7.1), whereas coarser grain-size material (0-15 cm) has ~43% of water content. However, despite presenting clayey material the sample of 70-85 cm has ~39.7%, less 13.4% than the sample of 280-295 cm, probably reflecting the lower silty-clay content (Figure 7.5), thus possibly indicating less ability of this sample to preserve water inside.

The consistency limits present higher values on coarser sediments (sandy silt) at lower depths and tend to decrease towards the top (Table 7.1). The liquid limit (W_L) percentages are quite similar to water content values, although higher, near the top of the core and more divergent in finer material (clayey content). These liquid limits (W_L) represent significant water content in these sediments. Both W_L and W_P decrease towards the top, thus inducing a decreasing plasticity index (I_P).

The gravity core CO14-GC-7B shows that the density of solid particles (G_S) is quite similar from the bottom to the top of the core (Figure 7.6). G_S varies between 2.77 and 2.78 g cm^{-3}. These G_S fit within the range of values (2.6 and 2.8 g cm^{-3}) described by Matos Fernandes (2012). Both unit weight, γ (kN m^{-3}), and dry unit weight γ_d (kN m^{-3}) range respectively from 17.2 to 18.4 kN m^{-3} and between 11.1 and 12.3 kN m^{-3} (Figure 7.6). These unit weight values for gravity core CO14-GC-7B are similar to the range of values obtained for the twin core CO14-GC-07 (16.4 - 16.7 kN m^{-3} - see chapter 6). Both unit weight and dry unit weight present a general bottom-up decreasing trend, although with some variations occurring near ~160 cm depth (Figure 7.6). These values of density vary in tune with void ratio, *e*, forming an almost perfect anti-correlation, as also verified with gamma-ray density and fractional porosity (Figure 6.4 – chapter 6). Figure 7.6 shows that there are great variations in all the properties between 145 and 175 cm. In this interval, sharp trending

inversions occur, marking a discontinuity in mechanical properties. Density properties (γ, and γ_d) increase from bottom up to ~175 cm and after this interval upwards they constantly decrease. Conversely, void ratio (e) decreases towards this limit, showing a pronounced increasing trend above 175 cm (Figure 7.6). The particles' density (G_S) is almost homogeneous along the whole record, however a break in this continuity occurs between 160 and 175 cm, being coincident with the remaining properties.

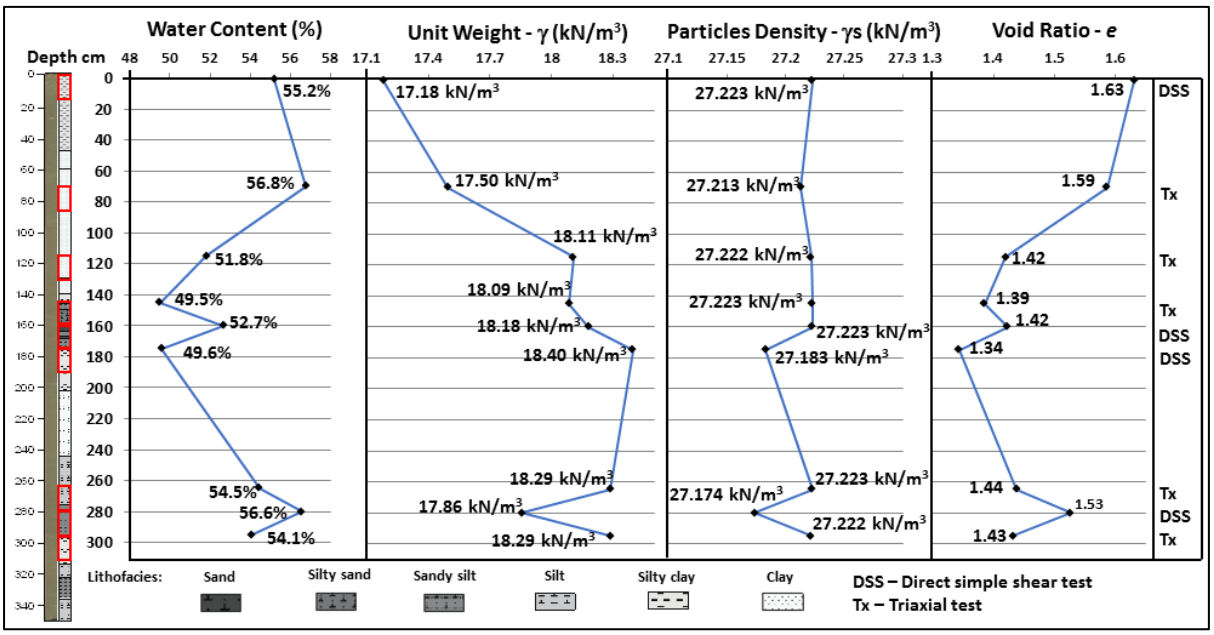

FIGURE 7.6 – Water content, unit weight, specific gravity/particles' density, and void ratio obtained from gravity core CO14-GC-7B through compressional and shear stress tests (red rectangles). Black dots refer to each analysis and correspond to each red rectangle. As γs values are very similar, with minimal differences, they are represented with three decimals in order to better identify differences between samples.

7.3.1.1 – COEFFICIENT OF PERMEABILITY

The overall coefficient of Permeability (k) of the sediments of the gravity core CO14-GC-7B is quite low and greatly decreases with increasing vertical load (Table 7.2). The general behaviour of this coefficient represents an almost constant decrease with the increasing applied vertical stress. Nevertheless, an outlier occurs in the transition of applied stress from 25 to 50 kPa (Table 7.2). At this loading transition there is generally an increase in k in the t_{50} consolidation factor at all depths and in t_{90} at the shallowest analysed sample (Table 7.2).

This increase corresponds to the fourth vertical stress increment imposed to the sediment sample, 96 hours after the test initiation. From the results of these samples, it seems

to be the lower consolidation factor (t_{50}) the one with the higher permeability values, although at deeper depths (280-295 cm) t_{90} has higher values than t_{50}. This coincides with the downwards increase in water content verified between these three samples (Table 7.2 and Figure 7.6). Comparing *k* in terms of depth variation, and according to t_{90}, it is in the depths comprised between 175 and 190 cm that permeability is higher, while for t_{50} the highest values are comprised between 160-175 and 175-190 cm.

TABLE 7.2 – Coefficient of permeability (*k*)

Vertical Stress, σ (kPa)	*k* (m/s)					
	160-175 cm		175-190 cm		280-295 cm	
	t50	t90	t50	t90	t50	t90
3	0	0	0	0	0	0
6	7.470E-11	3.950E-11	8.488E-11	8.410E-11	5.360E-11	8.540E-11
12	6.754E-11	5.590E-11	8.763E-11	5.230E-11	4.407E-11	5.740E-11
25	1.865E-11	3.230E-11	2.788E-11	5.230E-11	2.523E-11	4.860E-11
50	4.754E-11	7.130E-11	5.249E-11	5.090E-11	3.743E-11	4.520E-11
100	1.965E-11	1.560E-11	2.431E-11	3.650E-11	2.605E-11	2.920E-11
200	2.138E-11	1.840E-11	1.997E-11	2.350E-11	1.465E-11	2.000E-11
400	1.215E-11	1.190E-11	1.490E-11	1.470E-11	9.851E-12	1.330E-11
800	1.069E-11	8.720E-12	9.053E-12	8.860E-12	5.503E-12	8.250E-12
1600	6.270E-12	5.240E-12	5.904E-12	6.070E-12	3.603E-12	4.080E-12
3200	2.672E-12	2.350E-12	2.838E-12	2.920E-12	1.862E-12	2.570E-12
6400	1.342E-12	1.460E-12	1.188E-12	1.010E-12	8.660E-13	1.420E-12

7.3.2 – CONSOLIDATION (CLASSICAL OEDOMETER TEST)

The oedometer analysis determined the consolidation of sediments and allowed the characterization of these in terms of compressibility index (C_c) and over-consolidation (OCR). The evolution of both permeability and compressibility in response to vertical stress has a similar behaviour through time at different depths.

7.3.2.1 – SEDIMENTS' COMPRESSIBILITY

Sediments' compressibility is very similar along the sedimentary record, varying between 0.359 and 0.438 (Table 7.3). The compressibility analysis shows that the shallowest sediments (160-175 cm) have lower initial void ratios, both when load was firstly applied (Figure 7.7A), and when compressibility started (Table 7.3).

The initial void ratio obtained through oedometer test (Figure 7.7) is systematically greater with increasing depth: 1.42 (160 cm); 1.47 (175 cm), and 1.70 (280 cm). The slope verified in the upper part of all the three re-compressibility curves (I), shows that these are essentially normally consolidated sediments. In fact, they are slightly over-consolidated, with an OCR (σ'_p/σ'_{v0}) < 3, for the three samples, determined by Schmertmann's construction (Table 7.3). The pre-consolidation has never been higher than 30 kPa, as shown by the (Figure 7.7A, B, C). The compressibility index (II), corresponding to the virgin compression, shows a direct correlation between void ratio (*e*) and normal stress (σ'_v), presenting higher void ratio variations until 6400 kPa. The primary consolidation verified in the compression curve greatly varies when applied stress is > 30 kPa, and void ratio decreases during twelve (12) consecutive incremental vertical loads (Figure 7.7). The minimum void ratio at maximum vertical load is higher in the deepest sample (0.62; 280 cm) and decreases as the sediments are at shallower depths: 0.56 (175 cm) and 0.53 (160 cm). After the maximum vertical load (6400 kPa), the compressibility curve shows an increase in the void ratio in response to the sediment decompression. This is represented by a retroceding curve that corresponds to the swelling phase (III). The void ratio is higher in the deepest sediment sample (Figure 7.7C), indicating that this sample was the one with the lowest response to the applied load because it has the highest normal consolidation.

TABLE 7.3 – Compression and consolidation properties determined through oedometer testing: (e_i) initial void ratio, compression index (C_c) secondary consolidation ($C_c/1+e_0$), and over-consolidation ratio (OCR) for selected depths of the low consolidated sediments of the gravity core CO14-GC-7B. *OCR was determined by the Schmertmann's construction.

Depth (cm)	e_i	C_c	C_c / 1+ e_0	OCR*
160-175	1.176	0.365	0.168	2.92
175-190	1.208	0.359	0.154	1.67
280-295	1.332	0.438	0.188	0.65

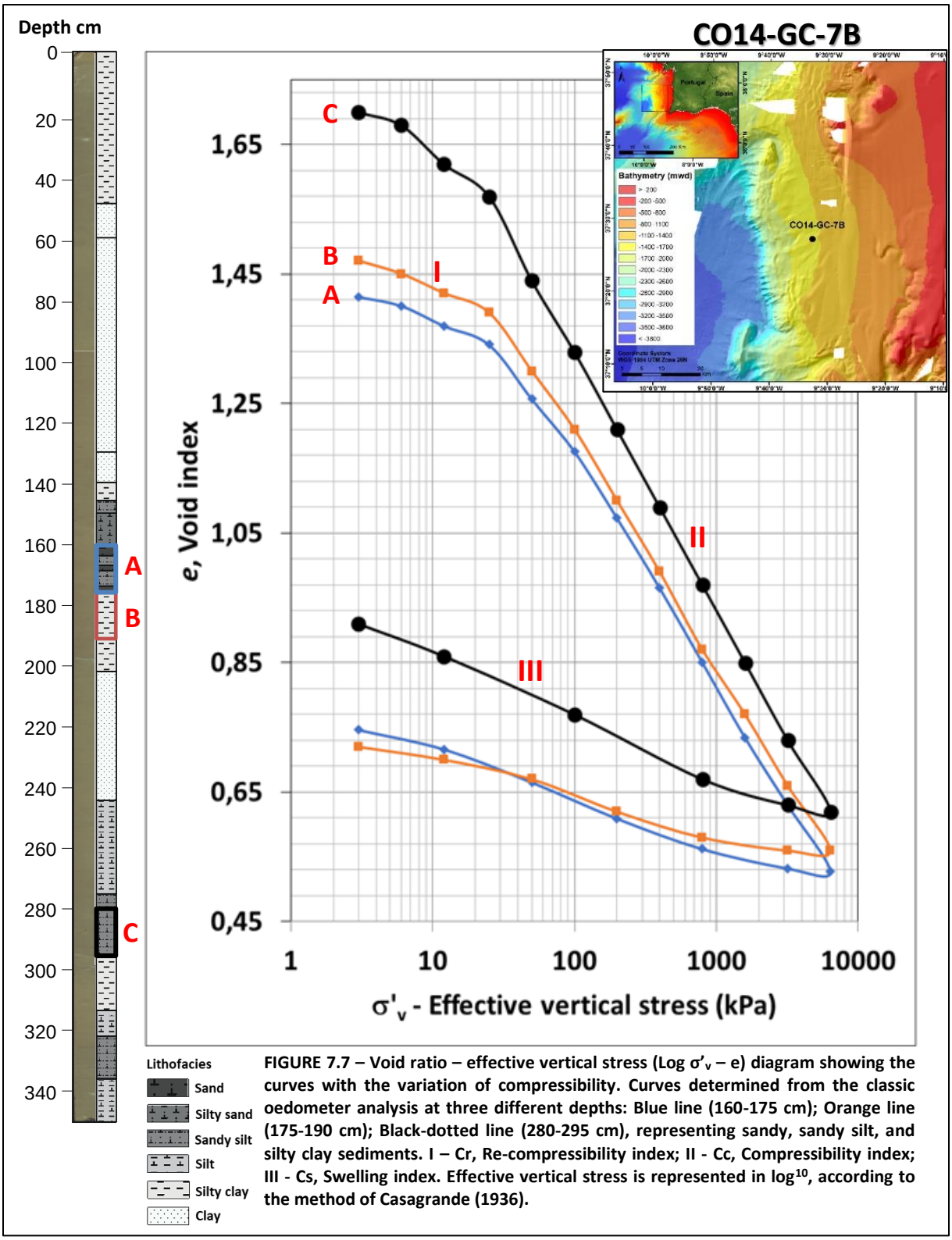

FIGURE 7.7 – Void ratio – effective vertical stress (Log σ'_v – e) diagram showing the curves with the variation of compressibility. Curves determined from the classic oedometer analysis at three different depths: Blue line (160-175 cm); Orange line (175-190 cm); Black-dotted line (280-295 cm), representing sandy, sandy silt, and silty clay sediments. I – Cr, Re-compressibility index; II - Cc, Compressibility index; III - Cs, Swelling index. Effective vertical stress is represented in $\log^{10}$, according to the method of Casagrande (1936).

7.3.3 – SHEAR STRENGTH – SIMPLE SHEAR ANALYSIS

Shear strength values have been obtained for the upper ~300 cm on the sediments of gravity core CO14-GC-7B, at five (5) different depths, through three increasing shear strength values (Table 7.4), at a very low average speed of 0.002 mm/min.

TABLE 7.4 – Simple shear test values: shear strength and shear stress values for referenced sediment samples.

***Determined through the classic shear box test.**

Depth (cm)	Initial Normal Stress ($\sigma'v_i$)	Final Normal Stress ($\sigma'v_f$)	Shear Stress (τ)	Horizontal Displacement (δH)	Friction Angle (ϕ')	Cohesion (C')	Friction Angle (ϕ')	Cohesion (C')
	(kPa)	(kPa)	(kPa)	(mm)	(º)	(kPa)	(º)	(kPa)
0-15	13*	14.4*	10.6*	4.9*	23.4	1.2	**36.4***	**0** (null cohesion) - set to intercept the origin
	13	13.9	7.2	4.3			**23.6**	
	200	212.2	92.8	5.5				
130-145	10	10.8	13.3	7.2	-	-	**25.3**	
	50	53.8	28.6	6.9				
	200	216.3	101.2	7.4				
160-175	10	10.7	5.9	6.3	27.0	3.7	**26.1**	
	50	54.5	28.2	8.0				
	200	217.9	106.4	8.0				
175-190	10	10.9	10.7	8.0	27.0	3.7	**27.9**	
	50	54.4	29.4	8.0				
	200	217.7	114.8	7.9				
280-295	10	16.3	14.8	7.9	23.8	6.6	**25.6**	
	50	54.4	29.4	8.0				
	200	217.9	103	8.0				

The shear strength values were derived from the horizontal maximum shear stress, applied accordingly with increasingly varying normal stress values. Given the low depths and the associated low effective stress of consolidation, confirmed by the pre-consolidation values, shear strength was assessed through three different increasing stress values (10, 50, 200 kPa). To the increasing shear stress values are generally associated increasingly higher horizontal displacement (δ_H) – Table 7.4.

The shear resisting parameters (cohesion *C'*, and internal friction angle ϕ') were firstly obtained by direct shear stress analysis. Given that the direct shear (shear box) test results were abnormally high for soft sediments, it was verified that this test is less suitable and less effective than simple shear for this analysis, having some drawbacks as the lack of control of drainage conditions (Viana da Fonseca, 1996), as also explained in the subsections 4.2.6.2 and 7.2.2. Thus, simple shear stress analyses were performed to assess shear strength. The friction angle (36.4º) for classic shear box test is quite high and different from DSS (Table 7.4). Thus, the results hereafter presented in this section for shear resistance are representative of simple shear tests.

According to the Mohr-Coulomb criterion, granular sediments present null effective cohesion. This is also the case of normally- to low-consolidated clays (Matos Fernandes, 2012), which have been previously confirmed in the SCD through the consolidation tests. Thus, null cohesion values and respective associated friction angle values will be used in this work.

7.3.3.1 – EVOLUTION BY DEPTH

Shear strength analyses on selected depths of the CO14-GC-7B gravity core show considerable variations according to the respective normal stress (Table 7.4). However, the global response of the sediments to shear stress and the curves' behaviour is quite similar along the whole record (Figures 7.8 – 7.12).

7.3.3.1.1 – SAMPLE 0-15 cm (13 - 200 kPa)

The shallowest sediment sample has been analysed through shear box and direct simple shear (DSS) tests. Shear stress was applied according to normal stress values of 13 and 200 kPa, for DSS test, and 13 kPa for the shear box test.

It is worth to note that, according to these results (Figure 7.8A, and C), the highest horizontal displacement, δ_H, (> 10 mm) occurs when sediments are submitted to classic shear box shear stress (Figure 7.8A). Horizontal displacement is higher as well even when lower shear stress is applied, since for a normal stress of 13 kPa the δ_H reaches 8 mm through shear box test and reaches only < 6 mm when submitted to the shear stress corresponding to a

normal stress of 200 kPa through DSS test (Figure 7.8A). However, in what concerns to the vertical displacement, δ_v, higher stresses allow for a higher and much more uniform evolution. For a normal stress of 200 kPa, δ_v increases gradually from the beginning to the end of the test, reaching a maximum of 0.6 mm, whereas for a 13-kPa normal stress, there is an extremely irregular δ_v that is negative in most of the time, for the DSS test. Nevertheless, for the classic shear box test, δ_v has a peak in the beginning of the test and then it keeps smoothing until the end of the test (Figure 7.8C). Also important is that the required shear stress needed to displace the sediment sample with 13 kPa is higher (≥ 10 kPa) for the shear box than for the DSS test (< 10 kPa).

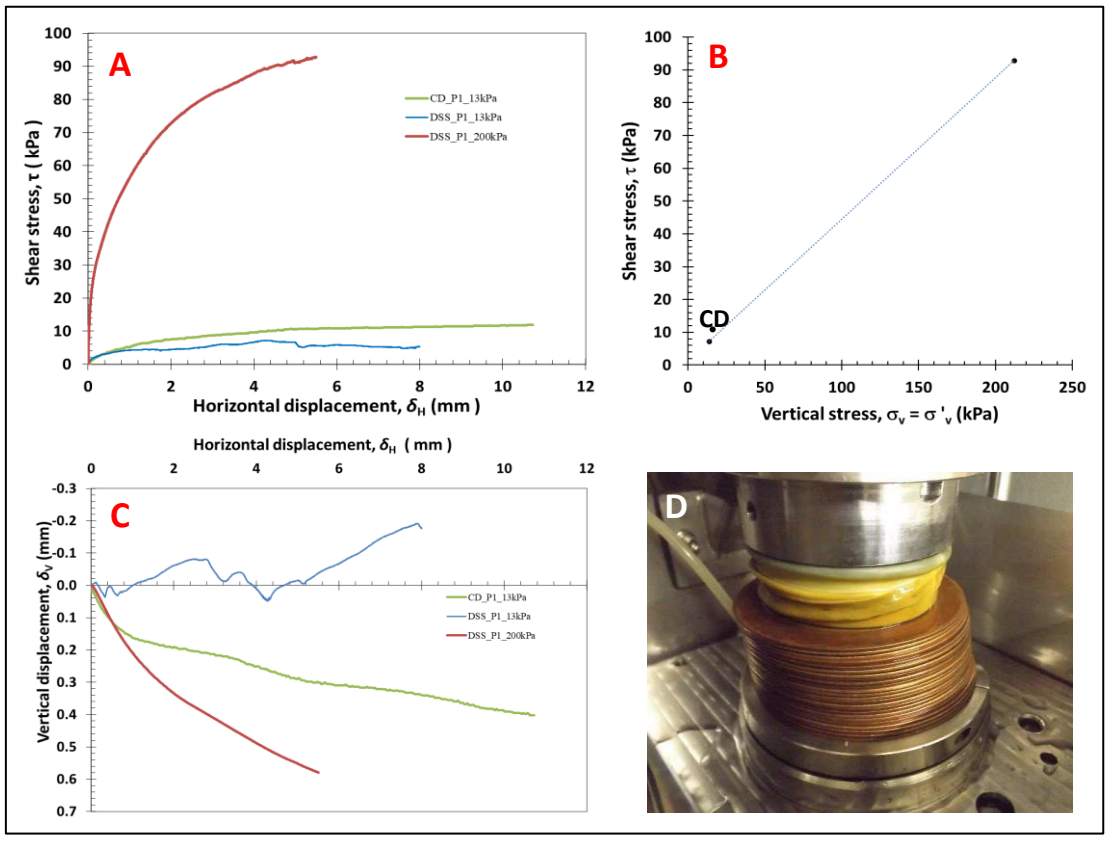

FIGURE 7.8 – Shear strength results from shear box and direct simple shear tests performed on sediments sample from 0-15 cm depth. (A) – Shear stress vs horizontal displacement progression. (B) – Shear stress vs vertical stress progression. CD – Direct shear (shear box) test. (C) – Vertical displacement vs horizontal displacement. (D) – Detail of the rupture in the laboratory.

7.3.3.1.2 – SAMPLE 130-145 cm (10, 50, 200 kPa)

The sample comprised between 130 and 145 cm depth has three distinct behaviour states in what concerns to the deformation derived from shear stress (Figure 7.9A). For a normal stress of 10 kPa, the horizontal displacement is achieved by a quite irregular shear

stress variation that leads to a horizontal deformation of 8 mm in the end. The shear stress increase is gradual with no well-defined peaks but pronounced fluctuations, especially after the ~4 mm of horizontal displacement (Figure 7.9A). For a normal stress of 50 kPa, the horizontal displacement is gradual and constant (Figure 7.9A), while the shear stress shows a small peak at ~25 kPa (τ), at δ_H = 4.4 mm, followed by a small decrease as signal of some elasticity, and then slowly increases until 30 kPa, followed again by a decreasing trend (Figure 7.9A). For 200 kPa, the evolution on the increase of the δ_H and τ is constant until δ_H of ~5.4 mm, where a peak strength occurs, close to the 100 kPa. After this, the evolution of the curve is quite irregular, indicating sediment deformation (Figure 7.9A).

Regarding to the δ_v, it is evident an extremely irregular progress of its curve. The curve is as more irregular as lower is the normal stress. On the other hand, the δ_v increases

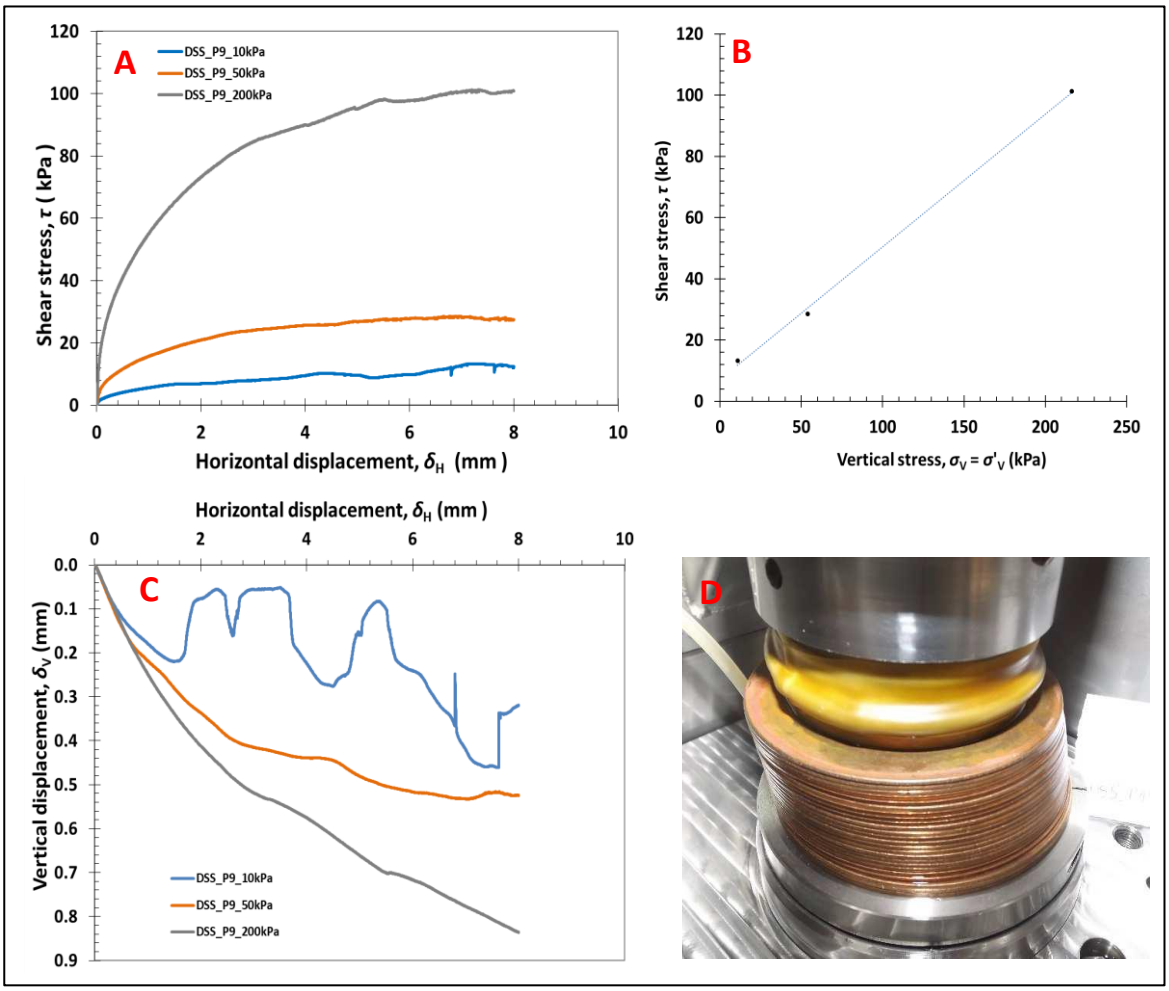

FIGURE 7.9 – Shear strength results from direct simple shear tests performed on sediments sample from 130-145 cm depth. (A) – shear stress vs horizontal displacement progression. (B) – Shear stress vs vertical stress progression. (C) – Vertical displacement vs horizontal displacement. (D) – Detail of the rupture in the laboratory.

with increasing normal stress, performing a positive correlation. This sample globally presents a much more irregular pattern than the previous one in all normal stress steps.

However, like the previous sample, the lower normal stress retrieves the most irregular vertical-horizontal displacement curve (Figure 7.9C).

7.3.3.1.3 – SAMPLE 160-175 cm (10, 50, 200 kPa)

The increase of the shear stress and the horizontal displacement (Figure 7.10A) are relatively correlative. The evolution of δ_H is constant, whereas the increase in τ has almost no oscillations for the curves of 10 and 50 kPa (σ') and few oscillations for the curve of 200 kPa, which presents a peak strength at ~110 kPa (τ), probably corresponding to the rupture, close

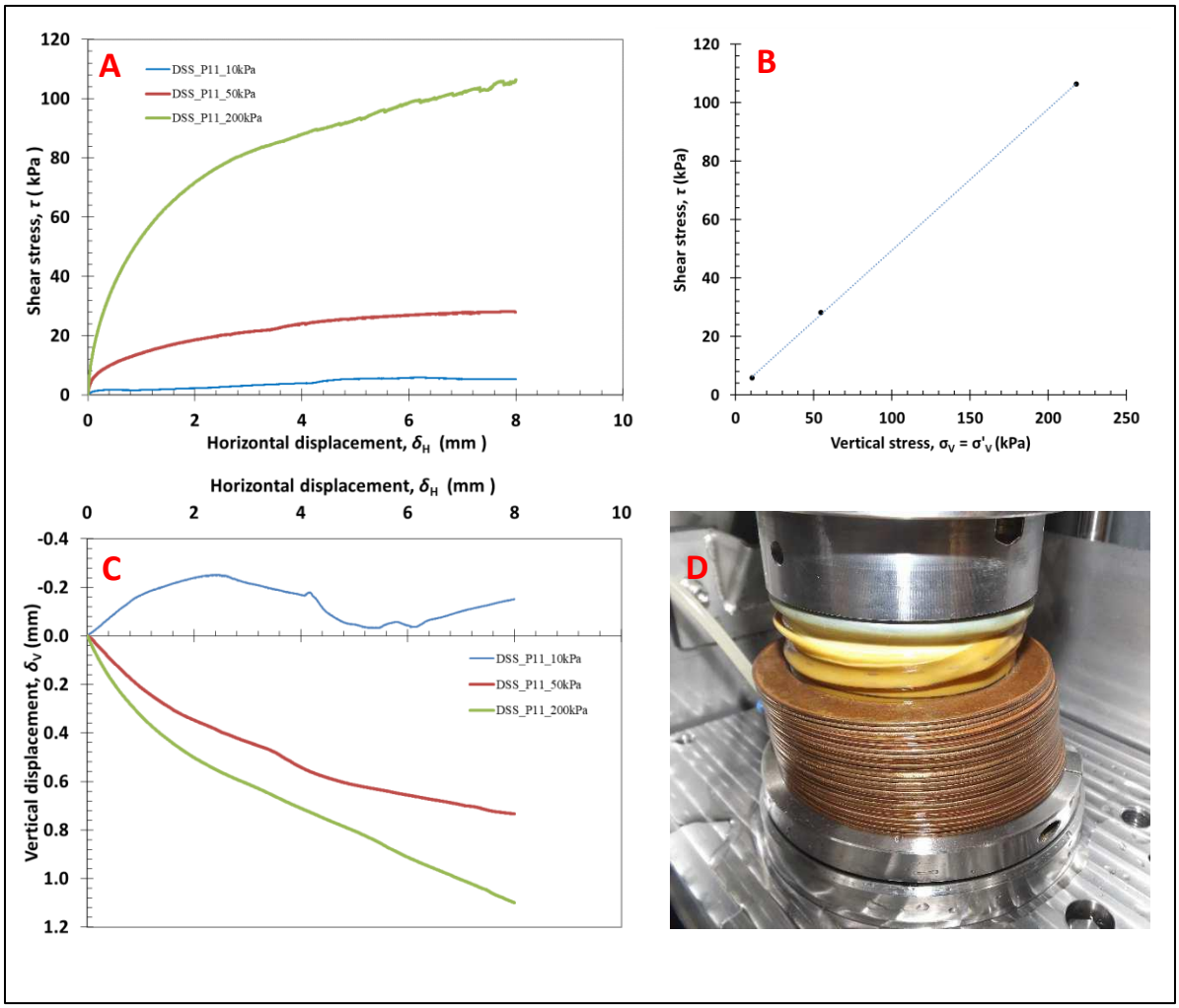

FIGURE 7.10 – Shear strength results from direct simple shear tests performed on sediments sample from 160-175 cm depth. (A) – Shear stress vs horizontal displacement progression. (B) – Shear stress vs vertical stress progression. (C) – Vertical displacement vs horizontal displacement. (D) – Detail of the rupture in the laboratory.

to the end of the curve (Figure 7.10A). The failure line of this sample (Figure 7.10B) is steeper than the previous ones (Figure 7.9B), and the peak strength was reached near the end of the test, indicating higher resistance to shear stress.

The δ_v vs δ_H has two positive curves and one negative (Figure 7.10C). The higher normal strength values (50 and 200 kPa) have a consistent and constant δ_v growth that is accompanied by δ_H. The δ_v of the curve of 50 kPa (σ') constantly increases from 0 until ~0.7 mm, presenting a small acceleration between 0.4 and 0.5 mm, and then a slowdown again (Figure 7.10C). The curve of 200 kPa follows a similar path, but with a higher increasing trend. While the curve of 50 kPa has a slowdown from 0.5 mm on, the curve of 200 kPa, on the contrary, has an increase until ~1.15 mm (Figure 7.10C). For the curve of 10 kPa (σ), δ_v is always negative, sometimes close, or even lower than -0.2 mm.

7.3.3.1.4 - SAMPLE 175-190 cm (10, 50, 200 kPa)

The horizontal displacement of the sediment sample 175-190 cm has a constant increase along the test and the increase on shear stress is also constant and continuous with

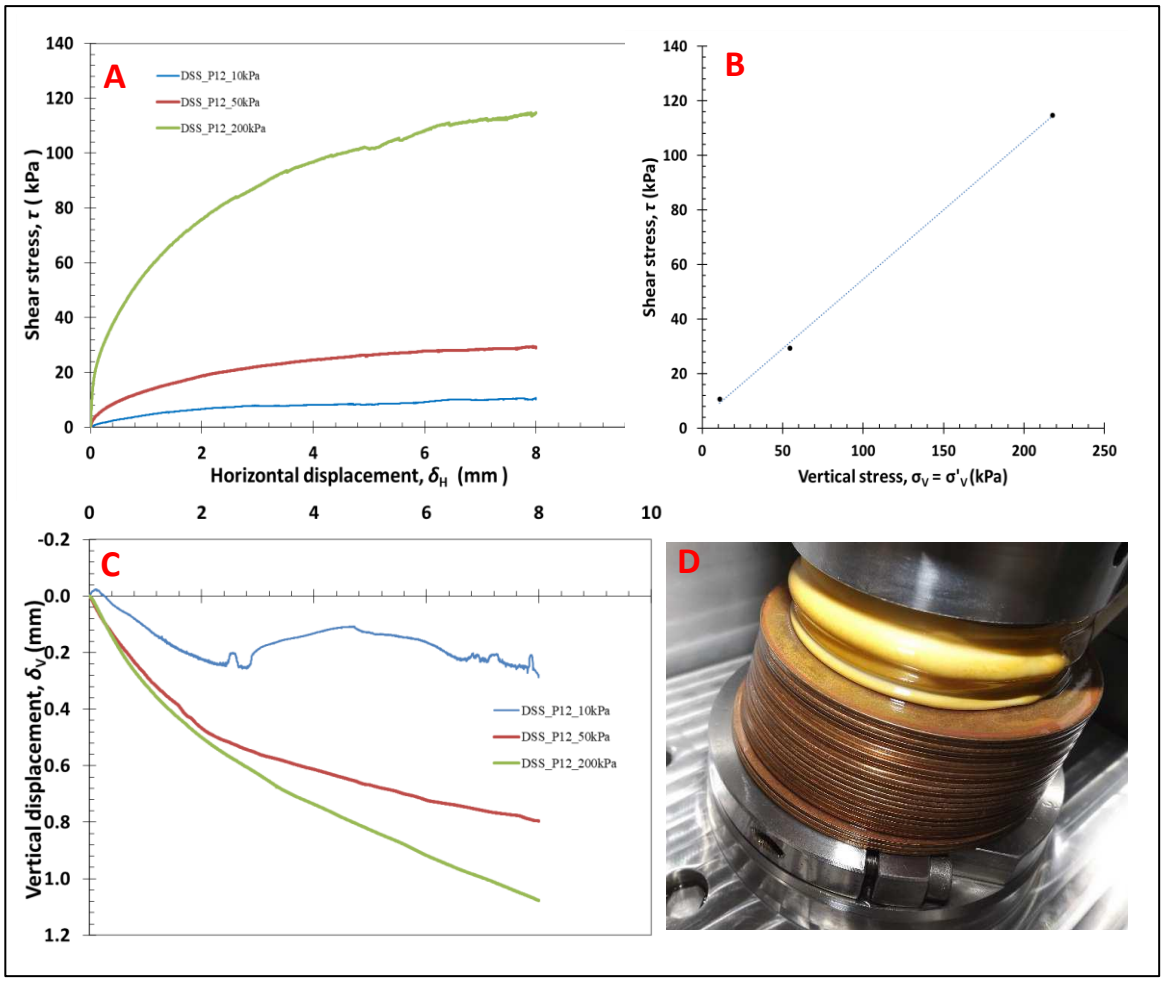

FIGURE 7.11 – Shear strength results from direct simple shear tests performed on sediments sample from 175-190 cm depth. (A) – Shear stress vs horizontal displacement progression. (B) – Shear stress vs vertical stress progression. (C) – Vertical displacement vs horizontal displacement. (D) – Detail of the rupture in the laboratory.

very small oscillations in the curve representing the 200 kPa normal stress. No peak strength is well-defined in this curve. However, at ~100 kPa (τ) there is a small peak (Figure 7.11A), followed by two more, that possibly indicates the beginning of the rupture. The curve representative of the 10 kPa (σ') has an oscillation close to the end, but always keeping stable (Figure 7.11A). The curve of the 50 kPa (σ') is the most stable and has the most perfect evolution, with a gradual increase until the end (Figure 7.11A). This is also common to all the previous tests.

The vertical displacement is quite constant for 50 and 200 kPa (σ'), ranging from 0 up to ~0.8 and 1.1 mm, respectively. These two curves develop aligned almost until 0.5 mm (δ_v), coinciding with ~2.2 mm of δ_H (Figure 7.11C). After this point, the curve of 50 kPa (σ') started to flatten, implying a slowdown on δ_v, while the curve of 200 kPa, although slowing down, increased its δ_v at a higher rate (Figure 7.11C). The curve of 10 kPa has a δ_v that ranges between -0.04 mm, in the beginning and 0.3 mm in the end of the curve (Figure 7.11C). This curve gradually grows from -0.04 until ~0.3 mm δ_v, until reaching 2.2 mm δ_H, where sudden decreases and increases occur (Figure 7.11C), indicating variations and rearrangement in the structure of the sediments sample skeleton. The 10-kPa δ_v/δ_H curve is the most irregular of all the curves, as has been common for all the tests. The overall sediment displacement and deformation can be seen in the detail of Figure 7.11D.

7.3.3.1.5 - SAMPLE 280-295 cm (10, 50, 200 kPa)

The τ vs δ_H evolution present stable and constant progressing curves, without oscillations (Figure 7.12A). The curves of 10 and 50 kPa (σ') are very smooth as no great shear stress was needed to move and to deform the sediments. The curves are always steadily increasing from the beginning towards the end (Figure 7.12A). The curve of the 200 kPa (σ') starts its deviation (δ_H) almost from the beginning and both the τ and the δ_H are constantly increasing. A very small peak strength occurs at ~80 kPa (τ) and 3.5 mm (δ_H), indicating the rupture of the sedimentary structure from this point on (Figure 7.12A).

Concerning to the δ_V/δ_H (mm) evolution, the curves of 50 and 200 kPa (σ') have almost the same path until ~0.64 mm (δ_V) and 5.4 mm (δ_H). After this point, the 50 kPa curve shows a slowdown on δ_V and although increasing until reaching 0.8 mm and 8.0 mm respectively for δ_V and δ_H (Figure 7.12C), whereas the curve of 200 kPa (σ') showed an

increasing trend on δ_V towards the end. The curve of 10 kPa is the most irregular in the δ_V/ δ_H and shows the highest δ_V in the first horizontally displaced 2 mm (Figure 7.12C), where a vertical movement of ~0.64 mm has been reached. Then, a sharp decrease on the δ_V to ~0.5 mm, coinciding with the other curves, occurs at ~2 mm (δ_H), falling then below this value (Figure 7.12C). Great oscillations occur towards the end, matching with the final value of the curve 50 kPa (Figure 7.12C). These oscillations are proper of the lower stress exerted on the sample that allow for higher vertical displacement variations and sediments rearrangement.

As it can be seen (Figure 7.12D), the sediment sample is fairly tilted, showing clearly both the horizontal and vertical displacement of the sediment sample.

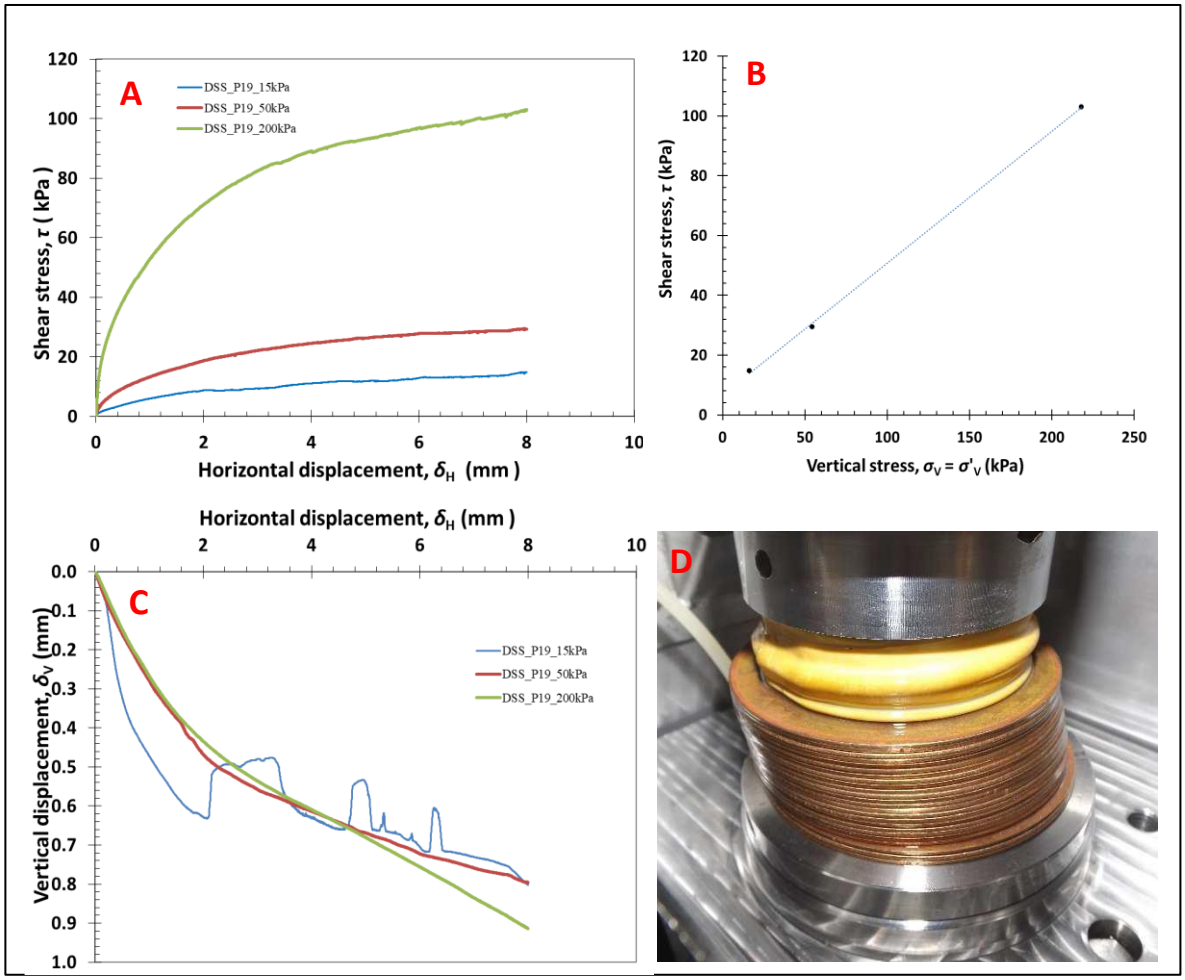

FIGURE 7.12 – Shear strength results from direct simple shear tests performed on sediments sample from 280-295 cm depth. (A) – Shear stress vs horizontal displacement progression. (B) – Shear stress vs vertical stress progression. (C) – Vertical displacement vs horizontal displacement. (D) – Detail of the rupture in the laboratory.

7.3.3.2 – INTERNAL FRICTION ANGLE

The friction angle for these sediments is very similar, ranging from 23.6º to 27.9º, with an average of ~25.7º, for null cohesion. For resisting values with cohesion, the average of friction angle values is 25.3º and cohesion varies from 1.2; 3.7; to 6.6, showing an average of 3.8 (Table 7.4).

7.3.4 – COMPRESSION RESULTS – TRIAXIAL TESTS

Compression tests have been performed for five different sediment specimens at different depths (Figure 7.13) at an average speed of 0.008 mm/min. Four drained-, and one undrained compressional tests have been performed according to the effective stress, calculated for each sample (Figure 7.13). Given that these samples are from shallow depths, the corresponding effective stress values are also very low. Once the *in situ* effective stress value of the deepest sample (295-310 cm) is < 50 kPa, it has been set to 200 kPa (Figure 7.13) to assess the stress-path behaviour under higher stress. These low effective stress values result from the low consolidation verified in this Late Pleistocene to Holocene sedimentary package, as already seen in the consolidation analysis.

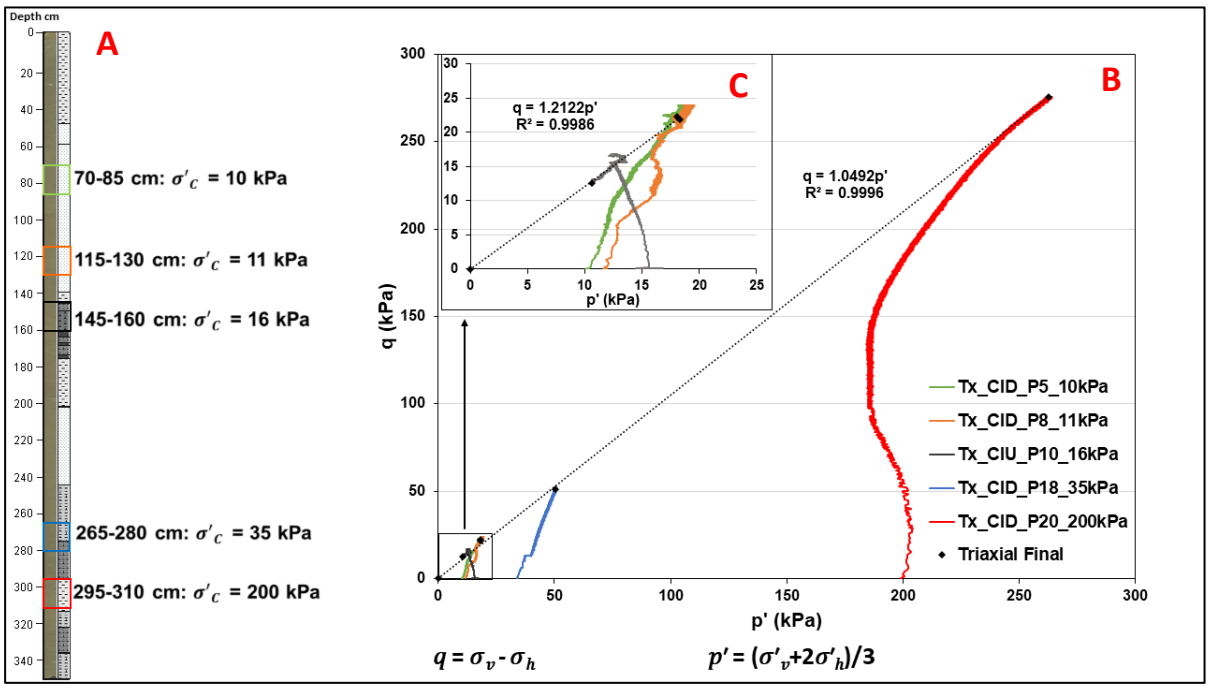

FIGURE 7.13 – Stress-path behaviour of five 80x150 mm sediment samples of the gravity core CO14-GC-7B. (A) – Gravity core with visual description. Coloured rectangles refer to sediments' samples analysed, by triaxial compression, whose depth is in cm and the effective vertical stress in kPa. (B) – Global stress-path ratio for the whole core. σ'c and *p'* refer to the effective normal stress, and *q* is the deviator stress. (C) – Stress-path ratio for the lower effective stress values.

The increasingly higher stress-path values (Figure 7.13) show a higher deviation, in response to the higher effective stress. This means that deeper sediments are subjected to higher compressional activity and need high shear stress to be affected by instability and consequent disruption. The stress-path for the first two samples (70-85 cm and 115-130 cm) is very similar, as they present quite similar vertical stress (Figure 7.13C). The sample at 145-

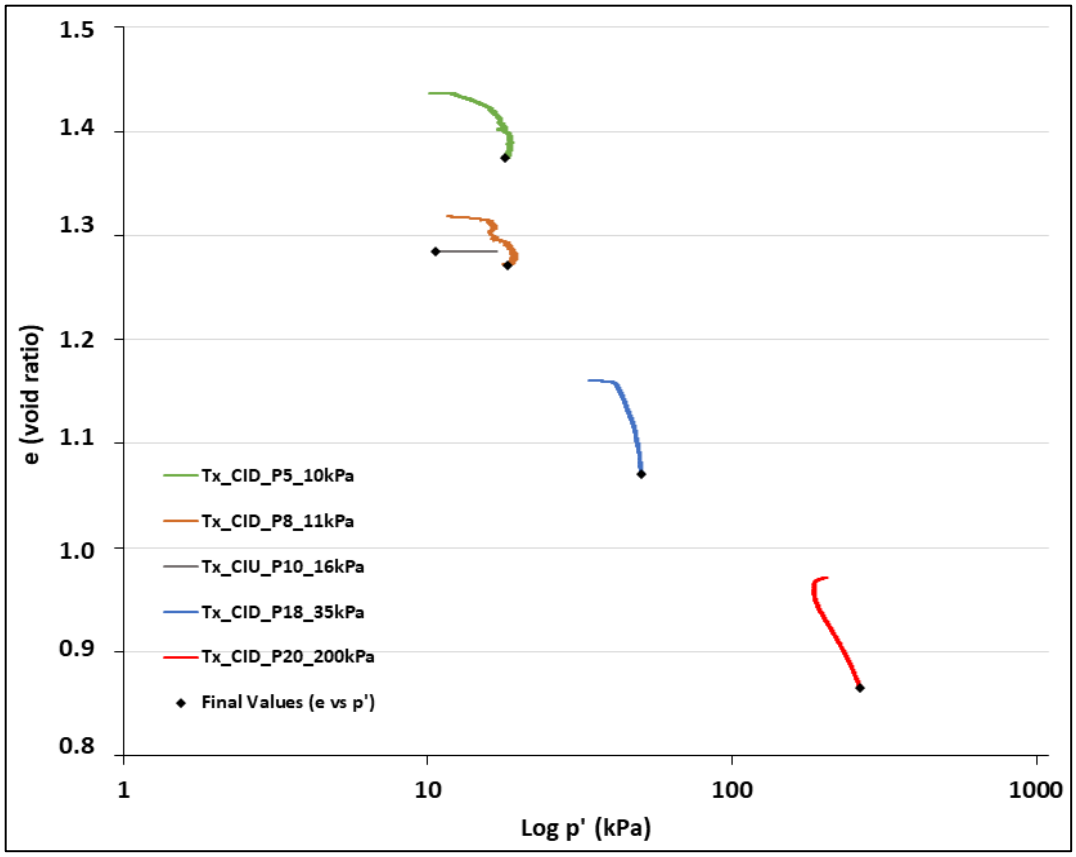

FIGURE 7.14 – Void - stress ratio of all sampled sediments.

160 cm depth, which was assessed as a CIU test, shows a decrease in mean effective stress indicative of pore-pressure build-up. The void ratio of each sample greatly decreases with the increasing normal stress (Figure 7.14). The decrease on interparticle free space is, as expected, greater on sediments submitted to higher stress values. Shallower sediment samples have more irregular void decreasing evolutions, also presenting less difference between higher and lower void ratio. Furthermore, the greater the normal stress, the less sinuous and the higher is the decrease of the void ratio on the sediment samples (Figure 7.14). This means that these sediments are normally to low-consolidated, allowing for a positive relationship between increasing stresses and decreasing space. Void ratio retrieved from the sample at 145-160 cm depth shows no variation. This is related with the fact that this has been an undrained test, which did not allow for fluid drainage and thus for void reduction.

7.3.4.1 – COMPRESSIONAL EVOLUTION BY DEPTH

The analysis of the stress-path, stress-strain, void-strain, and volumetric-axial strain evolution by compressional analysis, shows that there are diverse reactions to shear stress, along the sedimentary record (Figures 7.15, 7.16, 7.17, 7.18 and 7.19). However, similar effective consolidation stresses, verified in some of these sediment samples, allow determining a common pattern along the core.

7.3.4.1.1 – SAMPLE 70-85 cm (10 kPa)

The compressional analysis of this ~80 x 150 mm sediment sample started with a confining pressure (CP) of 311.02 kPa and a backpressure (BP) of 300.85 kPa. The Skempton

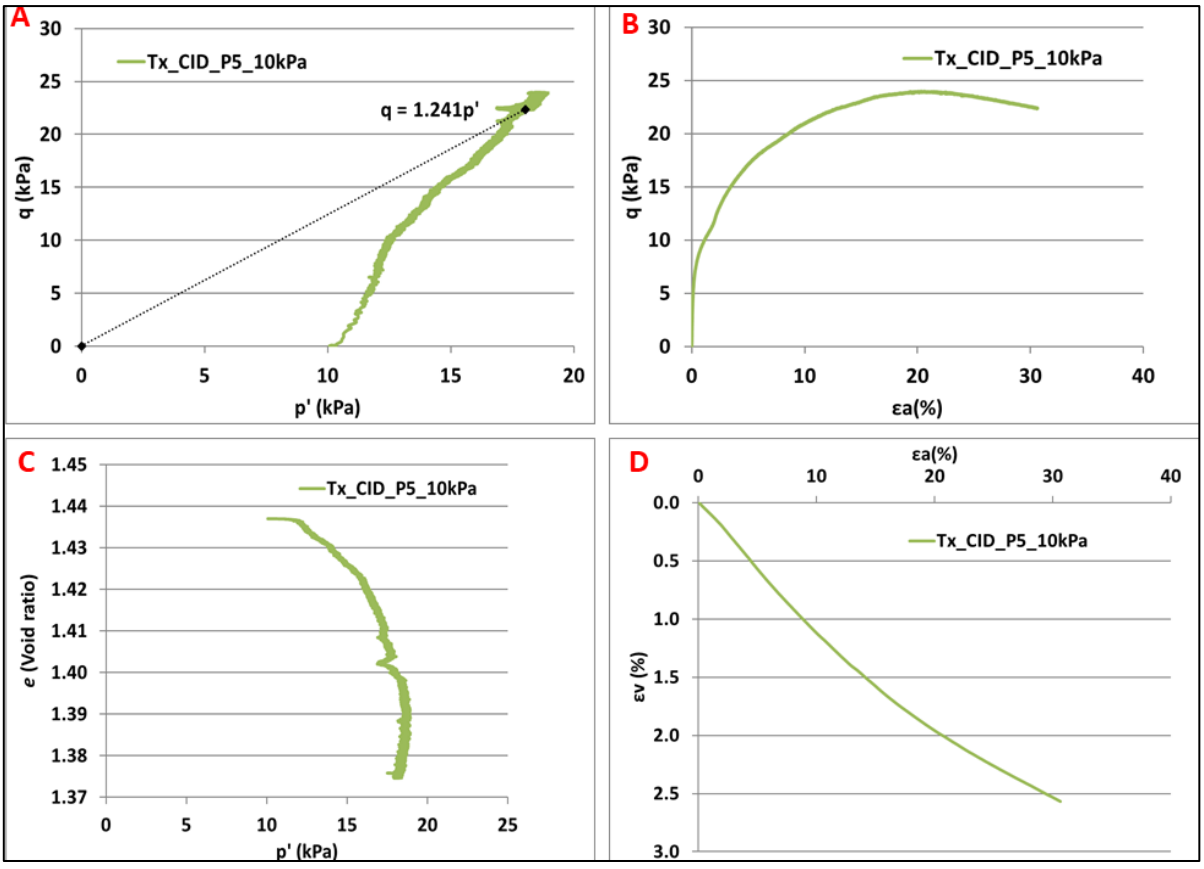

FIGURE 7.15 – Compressional results from triaxial tests performed on sediments sample retrieved from 70-85 cm depth. (A) – Stress-path evolution. (B) – Stress-strain evolution. (C) – Void-stress ratio. (D) - Volumetric-strain.

parameter B, corresponding to the saturation degree of this specimen, determined through the bender-elements, is > 0.9.

The behaviour of the shallowest sample demonstrates that its stress-path towards failure is quite irregular, stabilizing after reaching a vertical stress > 17 kPa (Figure 7.15A). After this, there is a somewhat regular alignment with the failure line, indicating that failure has been reached. The resulting stress-strain shows that the ultimate stress (~24 kPa), led to 20% deformation, after which deformation occurred with lower shear stress. At this point sediment was already in plastic behaviour towards the final rupture, at ~30 % εa (Figure 7.15B). The regularity in the curve and its smooth slope increasing in deformation from ~7 kPa onwards, lets to foresee low sediment elasticity and considerable plasticity.

Void ratio kept almost invariable from 10 to 13 kPa (Figure 7.15C). This stress range seems not to be enough to eliminate void space inside the sedimentary package. An increase on stress from 13 to ~17 kPa caused a decrease on sediments' empty space, from > 1.43 to 1.41 (Figure 7.15C). This decreasing trend on void space has been softened between void ratios of 1.41 and 1.40, and the increasing stress trend was interrupted with a small decrease (Figure 7.15C), possibly associated with a rearrangement in the internal structure of sediments. Empty space continued to diminish down to ~1.375 and the associated stress also suffered a decrease from 18.8 to 17.9 kPa. The maximum stress necessary to cause sediment shrinkage in this sample due to void dissipation was ~19 kPa. The volumetric-axial strain presents a quasi-uniform and constant evolution (Figure 7.15D) during the compressional activity, indicating low consolidation.

7.3.4.1.2 – SAMPLE 115-130 cm (11 kPa)

The compressional analysis of this ~80 x 150 mm sediment sample started with a confining pressure (CP) of 312.28 kPa and a backpressure (BP) of 300.71 kPa. The saturation degree determined through the Skempton parameter B is > 0.9.

The stress-path evolution of this sediment sample reveals a very irregular track. Shear stress rapidly advanced from 0 to ~7 kPa and then a slow-down occurred between 7 and 10 kPa, by the increase on shear strength. Then, an increase on shear stress led to the path inversion, which accelerated towards failure through a decrease on shear strength from 16.7 to 15.9 kPa (Figure 7.16A). The ultimate tensile strength occurred at 20.98 kPa (the shear stress maximum) and the final strain was 33.02 %, despite the sample being almost broken at 20% of strain (Figure 7.16B). This appears to have a degree of plasticity quite similar to the

previous one, as strain continued its increase after the peak strength, despite the decreasing stress (Figure 7.16B).

Void-stress ratio has an extremely irregular evolution, although smaller than the sediments of the upper sample, with *e* varying from 1.32 to 1.27 and *p'* varying between 11.6

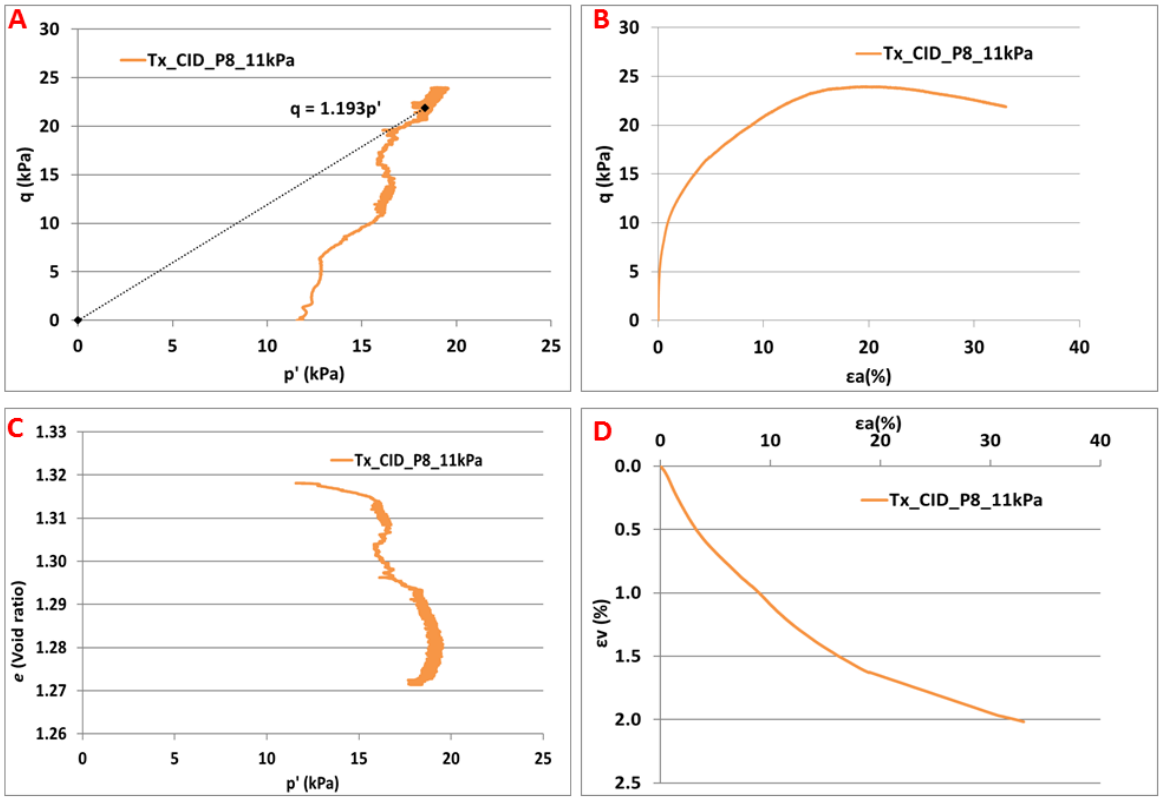

FIGURE 7.16 – Compressional results from triaxial tests performed on sediments sample retrieved from 115-130 cm depth. (A) – Stress-path evolution. (B) – Stress-strain evolution. (C) – Void-stress ratio. (D) - Volumetric-strain.

and 18.3 kPa (Figure 7.16C). This is significantly lower than in the previous sample, whose highest stress needed to dissipate interparticle sediment void was 19.41 kPa. Volumetric-axial strain shows a constant increase during the compressional activity (Figure 7.16D), although a volumetric slowdown occurs near εa (18%) and εv (1.6%) pointing to the constant axial deformation, despite the slowing down of the volumetric deformation, indicating that the sample was almost broken at that point.

7.3.4.1.3 – SAMPLE 145-160 cm (16 kPa)

The compressional analysis of this sediment sample started with a confining pressure (CP) of 316.98 kPa and a backpressure (BP) of 300.95 kPa. The saturation degree of this sample determined through the Skempton parameter B is > 0.9.

The compressional evolution of this sediment sample is totally different from the remaining samples, as it was assessed through an undrained triaxial test. The stress-path of this sample shows a retrogression towards the failure line, showing a decrease on effective stress from 16 kPa in the beginning to 11 kPa in the failure (Figure 7.17A). This decrease on the shear strength led to the fast disruption of the sediment sample. This sample presents a peak strength close to q=15.43 kPa (Figure 7.17B), being followed by a small reduction to 15.36 kPa that evinces an elastic state through a small recovery to the previous state. The ultimate tensile stress (16.77 kPa) provoked ~13.3% deformation (εa). After this, the sediments were already failed and the dominant plastic behaviour allowed for the continuous deformation of the sample, evinced by the loss of shear strength (Figure 7.17B).

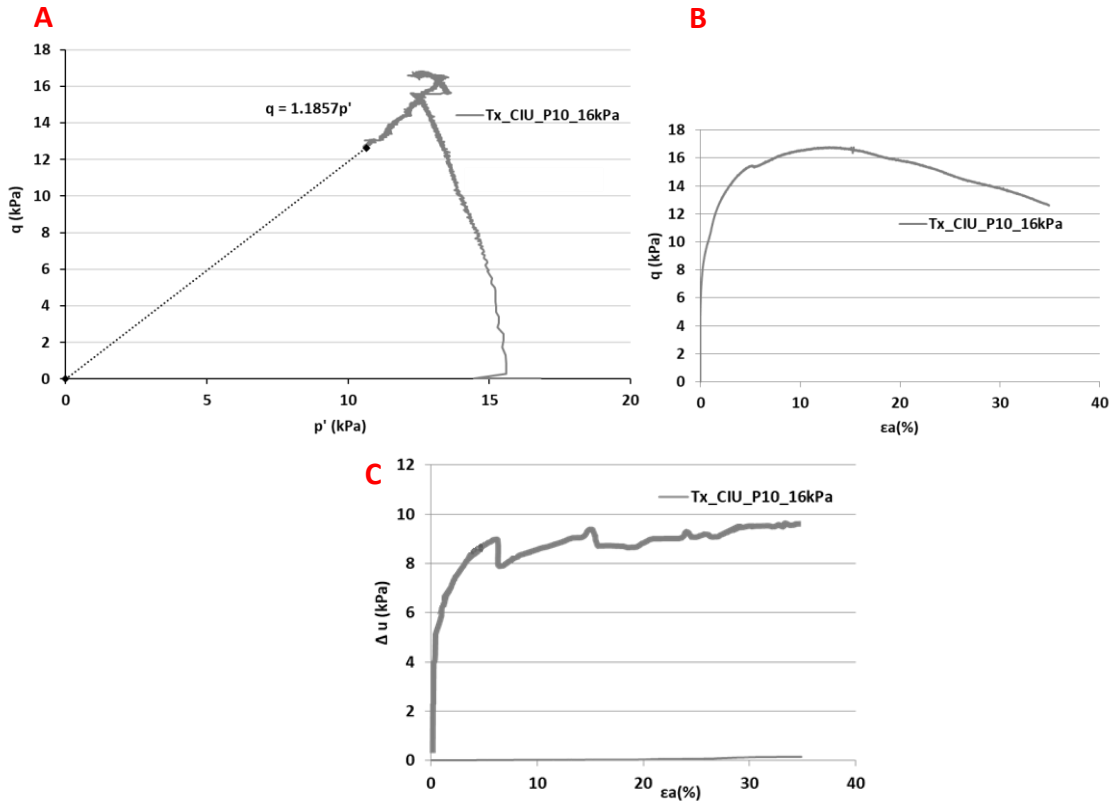

FIGURE 7.17 - Compressional results from triaxial tests performed on sediments sample retrieved from 145-160 cm depth. (A) – Stress-path evolution. (B) – Stress-strain evolution. (C) – Pore-pressure – strain ratio.

As this is a strain-controlled test, no void variation occurred (Figure 7.14) for this sample, but there was axial deformation associated with pore-pressure variation (Δu). Pore-pressure drastically increases in the beginning of the test until ~9 kPa (Figure 7.17C), coeval with the occurrence of a first peak strength (Figure 7.17B). Then, a sharp drop on pore-pressure occurs indicating the recovery of the previous state. After, a second increase on pore-

pressure (Figure 7.17C) is coincident with the maximum strength, >16 kPa (Figure 7.17B), which starts to slightly decrease then, despite the constant increase on axial deformation (Figure 7.17B). It is worth to note that the higher deformation state implied increasing pore-pressure (Figure 7.17C) in response to the stress exerted over the sedimentary structure.

7.3.4.1.4 – SAMPLE 265-280 cm (35 kPa)

This sediment sample started the compression with a confining pressure (CP) of 335.91 kPa and a backpressure (BP) of 301.71 kPa. The Skempton parameter B, reached 0.903.

The stress-path of this sample is very regular. Starting from 35 kPa, the stress increases almost regularly until ~37 kPa (*p'*) and ~13 kPa (q). Then, stabilization occurs with an increase to ~40 kPa (*p'*). After this point, an increase of shear stress and strength occurred proportionally until failure (Figure 7.18A).

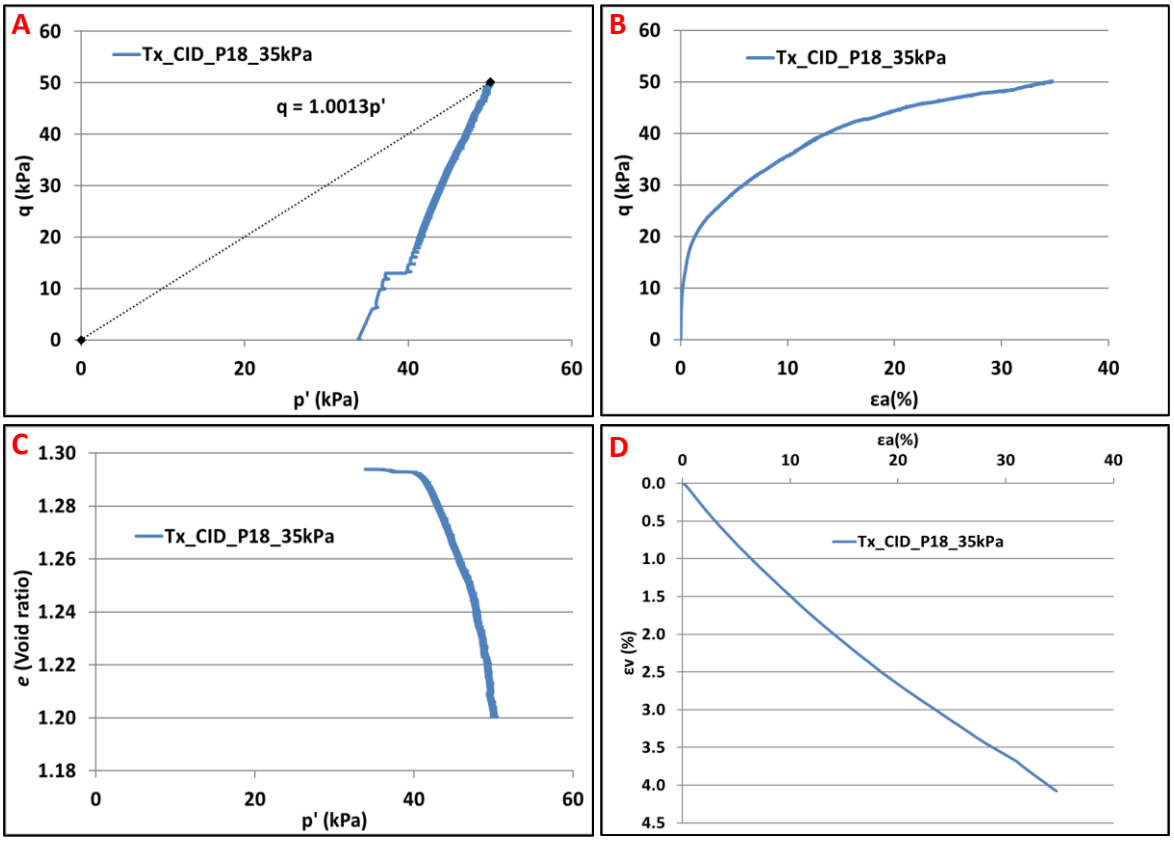

FIGURE 7.18 - Compressional results from triaxial tests performed on sediments sample retrieved from 265-280 cm depth. (A) – Stress-path evolution. (B) – Stress-strain evolution. (C) – Void-stress ratio. (D) - Volumetric-strain.

The stress-strain evolution shows that deformation starts almost in the beginning of the compression. By opposition to the previous examples, this one does not evince the presence of well-marked peak strength, indicating little elasticity, in consequence of the induced consolidation state. The rupture occurred with ~50 kPa stress, although when the deformation reached 30%, the specimen was already almost disrupted (Figure 7.18B).

The void-stress evolution was nearly constant and regular. After some stagnation in the void reduction, between 35 and ~41 kPa, the decrease on available interparticle space was quite rapid, from 1.29 to 1.20 between 41 and 50 kPa (Figure 7.18C).

The volumetric-axial strain shows a constant increase, an almost proportional variation between volumetric and axial strain, during compression (Figure 7.18D). The final εa (35%) and εv (4.1%) values point to a regular deformation along the compressional movement.

7.3.4.1.5 – SAMPLE 295-310 cm (200 kPa)

The compressional analysis of this sediment sample started with a confining pressure (CP) of 500.63 kPa and a backpressure (BP) of 301.45 kPa. The saturation degree of this sediment sample, corresponding to the Skempton parameter B, determined through the bender-elements, reached > 0.90.

The stress-path of this sample is quite irregular, as it starts with p' = 200 kPa and then retreated to 187 kPa when reaching q = 87 kPa. This implied a decrease on the shear strength and a compressional acceleration. However, after this point, p' kept constant and q increased up to 145 kPa, forcing a shear stress increase towards failure. After this, the stress-path went on a proportional increase until failure (Figure 7.19A). During the last phase of the compression, the stress-path clearly aligns with the failure line, indicating a normally consolidated sediment sample.

The stress-strain curve, as the previous example, presents a constant increasing curve and deformation starts much before compression gets 200 kPa, at ~75 kPa. Like the previous example, this one does not evince the presence of clear peak strength, showing instead a constant increase on stress-strain, indicating constant deformation by the action of the increasing stress. This is the most continuous stress-strain curve of all the tests. After 20% deformation, the curve starts to smooth pointing to a slow-down on the stress increase and a

constant sediment deformation (Figure 7.19B). This suggests that the sediment was partially disrupted after 20% deformation.

The void-stress evolution is nearly constant and regular. After some stagnation in the void reduction, between 180 and ~200 kPa, the decrease on available interparticle space is quite rapid, from 0.97 to 0.87 between 180 and ~270 kPa (Figure 7.19C).

The volumetric-axial strain shows a constant increase, an almost proportional variation between volumetric and axial strain, during compression (Figure 7.19D). The final εa (35%) and εv (5.4%) values indicate a regular deformation along the test, indicating a plastic behaviour.

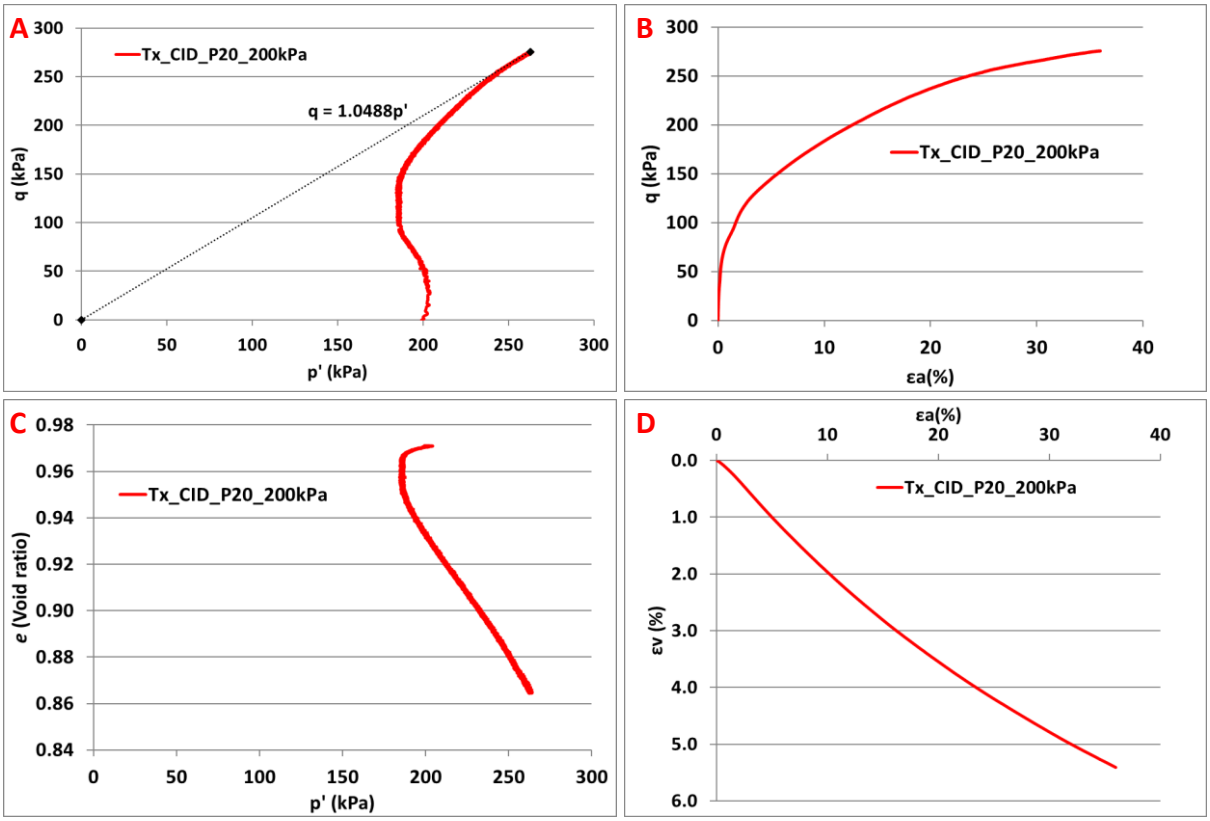

FIGURE 7.19 - Compressional results from triaxial tests performed on sediments sample retrieved from 295-310 cm depth. (A) – Stress-path evolution. (B) – Stress-strain evolution. (C) – Void-stress ratio. (D) - Volumetric-strain.

7.3.4.2 – TYPE OF FAILURE

Almost all the sediment samples submitted to compressional analysis were broken between 20 and 30% of axial strain. Moreover, all the samples are soft sediments as all present barrelling (Figure 7.20) as the failure mode. In the end of the test, the sediment

samples were laterally bulged, in result of the considerable strain imposed by the increasing stress.

As observed, no brittle failure occurred and thus no well-defined shear surface is detected on the sediment samples after testing. In contrast, compression marks are visible along the sample, attesting for the great axial deformation.

FIGURE 7.20 – Barrel-shaped disrupted specimen after triaxial compression.

7.3.4.3 – CONSTANT VOLUME FRICTION ANGLE (ϕ'_{cv})

The shear strength parameters determined for all the previous tests are summarized in Figure 7.21, where are all the friction angles determined by compressional analysis that show a top-down decreasing on the resisting parameters. There are 5º separating the highest from the lowest friction angles, with an average of 28.5º. The closest value and simultaneously the median correspond to 29.7º, which can be assumed as the most representative value of the whole record, according to the obtained data.

There is a decrease of 1º on the resisting properties between 70 and 115 cm, although no great variations occur on grain-size. Between 115 and 160 cm, the friction angle varies 0.2º, allowing to infer that the mechanical properties are pretty much similar, despite some grain-size and facies variations. The greatest decrease on friction angle occurs between 145-160 and 265-280 cm, with a drop of 4.1º. Then, an increase of ~1º is present between 265 and 310 cm.

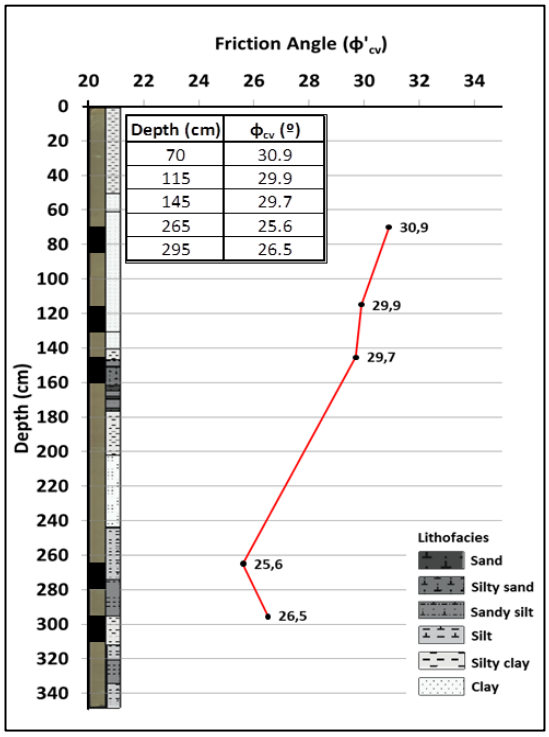

FIGURE 7.21 – Constant volume friction angle (ϕ'_{cv}). Black squares represent the samples used for triaxial tests. Lithofacies were obtained for twin core CO14-GC-07.

7.4 – DISCUSSION: EFFECTS ON SUBMARINE SLOPE STABILITY

7.4.1 – ATTERBERG LIMITS, WATER CONTENT, AND PERMEABILITY

Grain-size analysis shows a bottom-up decrease of clay content (Figure 7.5), which is partially reflected on water content (Table 7.1). The water content of the gravity core CO14-GC-7B is inhomogeneous and its variation is not linear with the increase of depth, but rather it matches with void ratio (Figure 7.6) and grain-size variation (Table 7.1), as also verified by Lee and Baraza (1999) for the Gulf of Cadiz. It is widely assumed that recent and shallower clayey sediments have higher water content, close to the liquid limit (Matos Fernandes, 2012), due to low pre-consolidation values, and that fine sediments present higher water content (Lee and Baraza, 1999). This is the case of both the Sines- (Figure 7.6) and the Pianosa ridge (Miramontes *et al.*, 2018) plastered drifts, which have homogeneous, well-sorted and high water content muddy contourite sediments, with clay and silt volumes of ~90%. Additionally, the coarse grain-sized sediments (sandy silt and silty sand), which are dominantly present between 140 and 180 cm depth, present lower water content than the finer silty clay and clayish fractions, both above and below (Figure 7.6). Likewise, the plasticity limit is higher for sandy silt, reflecting lower water content in coarser than in finer sediments.

According to the analyses done in core CO14-GC-7B, while the unit weight (both dry and natural) has a general decreasing trend towards the top (Figure 7.6), water content and void ratio increase, contrariwise. However, all these are smooth variations occurring in a small depth range that probably would be greater if they ranged between depths of several meters. This allows inferring that sediments are very similar, with very tiny physical variations along the core. This is confirmed by the particles' density that is very similar, with few variations of decimal kN m^{-3} along the whole sedimentary record (Figure 7.6). The depth between ~120 and 180 cm is the section where unit weight is higher and water content is lower. The sample at 280-295 cm is among those with the highest void ratio and water content, and simultaneously it has one of the lower unit weights. This seems to be favoured by the high void ratio, which may promote the loss of mass density by the lack of fine sediments, allowing the filling in the inner void space by water.

The very low permeability values (8.6×10^{-13} to 8.8×10^{-11} m s^{-1}) found in CO14-GC-7B gravity core, are typical of fine-grained sediments, e.g. (Head, 1982; Matos Fernandes, 2012; Urlaub *et al.*, 2012). However, this range of values is lower than the range of *k* found by Miramontes *et al.* (2018) for both mounded contourites (5×10^{-8} to 3×10^{-9} m s^{-1}) and for

the Pianosa Ridge plastered drift (4 x 10^{-9} and 9 x 10^{-9} m s^{-1}). This confirms that the very fine Late Pleistocene-Holocene sediments of the SCD have great amounts of clay, leading to such low permeability values. The highest permeability occurs between 160 and 190 cm, suggesting higher porosity and/or sediment heterogeneity at this depth, coinciding with lower water content. More permeability tests in the upper sediments, above 160 cm, where void ratio is higher (Figure 7.6), would better clarify about the correlation between voids and permeability of sediments.

7.4.2 – COMPRESSIBILITY

The three steep-slope compressibility curves of the CO14-GC-7B core indicate high compressibility index along the record, which is testified by the constant decreasing void ratio through the increasing vertical stress (Figure 7.7). The homogeneous compressibility behaviour of the three curves indicates that the sediments are low-consolidated, with very low pre-consolidation values. The presence of a quite similar lithology, rich in clay and silt, along the whole record may serve as a partial explanation for this homogeneity. Furthermore, these are organic-rich sediments (Teixeira *et al.*, 2020), and according to Urlaub (2013) and references therein, higher organic content tends to increase compressibility values. However, despite the similarity between the two first shallower samples (160-175; 175-190), the sample retrieved ~100 cm below has a greater void ratio at all vertical stress values (Figure 7.7C). Notwithstanding this, the overall performance of all curves is similar, as they have similar paths (Figure 7.7). The low effective pre-consolidation stress (σ'_p) of these sediments, demonstrates that the maximum effective vertical stress over them has never been higher than 30 kPa, as shown by the re-compressibility lines (I – Figure 7.7). Nevertheless, when the effective stress equals 6 kPa the degree of settlement accelerates (Figure 7.7). When submitted to effective stress values higher than ~25 kPa the compressibility starts, and above this vertical stress, the compressibility line greatly increases (Figures 7.7 A, B, C). This very low stress provokes a considerable settlement that leads to an intense decrease on void ratio from ~25 kPa until 6400 kPa (Figure 7.7). This steep slope section of the curve, with a constant decrease of sediments' inner void space, indicates that the sediments of all these depths have never been subjected to such effective stress. During this destruction period, sediments are rearranged, and spaces are reformatted and reduced with the increasing vertical stress.

These muddy sediments present a very scattered OCR (0.65 up to 2.92) – Table 7.3, being mostly normally consolidated (Figure 7.7), resulting in the presence of very low or even the absence of effective cohesion, as it is typical for low consolidated young clays (Matos Fernandes, 2012), as also evident abroad in other muddy drifts (Miramontes *et al.*, 2018). These authors found OCR values ranging between 0.5 and 1.1 for mounded- and plastered drifts, hemipelagites and on a moat in the Corsica Trough (Tyrrhenean Sea). The OCR range for these sediments is lower than of the OCR values (0.9 – 1.88) found by Yenes *et al.* (2021), and lower than the values of the CO14-GC-7B gravity core that ranges between 0.65 and 2.92. This may be probably explained by the higher diversity of sediments, higher data amount and the analysis on the moat, where erosion, compaction and consolidation are greater. Comparing these results with those of Yenes *et al.* (2020) for the Gulf of Cadiz, where OCR varies between 6.63 and 25.03, it is possible to conclude that CO14-GC-7B sediments have no over-consolidation. Contouritic sediments are more over-consolidated in the Gulf of Cadiz (Yenes *et al.*, 2020), than in the SW Portuguese Margin (this work), and in the Tyrrhenian Sea (Miramontes *et al.*, 2018), or even in the Alboran Sea (Yenes *et al.*, 2021). These differences may probably be explained by the location of the analysed cores in the Gulf of Cadiz, westwards of the Gibraltar Strait, where multiple morphological features as moats and channels are formed due to the stronger bottom current activity that contributes for higher erosion, and consequently leads to higher sediment compaction and consolidation. Conversely, the sediment samples analysed both in this work and in Pianosa Ridge (Miramontes *et al.*, 2018) are distal and in calmer areas, comparing with the Gulf of Cadiz, in what concerns to bottom current activity. In the analysed samples of the gravity core CO14-GC-7B, the OCR is higher between 160 and 190 cm (from 2.94 to 1.67). Below this depth, sediments at 280 cm are finer and clearly much more under-consolidated, with a lower OCR (0.65), higher C_c (Table 7.3) and lower coefficient of permeability, which is higher for the interval of 160-190 cm (Table 7.2). The sediments of this interval, unlike the interval 280-295 cm, have been deposited during a cooling period (beginning of the MIS 2 and Last Glacial Maximum) with associated bottom current enhancement and erosion that culminated with a hiatus at 161 cm below seafloor (Teixeira *et al.*, 2020). This ~30 cm transect is thus heterogeneous with more compaction, and higher deformation. This is coincident with the findings of Miramontes *et al.* (2018), for the Pianosa drift, where OCR and σ'_v are higher for the deformed zones. As found by Yenes *et al.* (2020), and references therein, apparent over-consolidation (AOC) is higher with low sedimentation rates. This is the case of the sediments of SCD deposited in the depth range of 160-190 cm, between 41.1 and 21.9 cal kyr BP, with

low (< 3 cm kyr^{-1}) sedimentation rates (Teixeira *et al.*, 2020). The higher compaction and lower sedimentation rates verified at these depths may thus justify the higher OCR for this section.

7.4.3 – SHEAR STRESS-STRAIN BEHAVIOUR

Contourite deposits may contain sediments with diverse geotechnical properties (Miramontes *et al.*, 2018), especially shear resistance. However, the CO14-GC-7B sedimentary record does not show great shear strength variations. The low *in situ* consolidation of these sediments promoted a steep evolution of the compressibility curves accordingly with the increasing normal stress (Figure 7.7). This mostly results from the considerable depositional rate (~27 cm kyr^{-1}) since the early Quaternary (Stow *et al.*, 2013), which promotes a rapid deposition and a weak accommodation in this contourite drift that favour under-consolidation and excess pore pressure, derived from overloading. As stated by Baeten *et al.* (2014), excess pore-pressure from rapid loading of fine-grained sediments is hardly dissipated, making the sediments to be more prone to slope instability. This is the case for the SCD, where the low consolidation of contourite sediments seems to be the main responsible for the sediment instability on gentle slopes. Nonetheless, this has been also verified off Norway (Laberg and Vorren, 2000; Bryn *et al.*, 2005a; Kvalstad *et al.*, 2005b), in contouritic deposits intercalated with glaciogenic sediments, despite higher sedimentation rates being needed to cause instability (Baeten *et al.*, 2014) because of their higher internal friction angle and their ability to expulse pore-pressure. The considerable water content, void ratio and compressibility attest this softness and even weakness of the Late Pleistocene – Holocene sediments of the SCD.

The recent sediments of the gravity core CO14-GC-7B are comprised in age between ~43 cal kyr BP and the Present (Teixeira *et al.*, 2020), whose maximum consolidation is <50 kPa. Thus, the behaviour of the curves in response to shear stress is somewhat variable especially for normal stress values lower than 50 kPa (Figures 7.8 - 7.12). The evolution of the τ-δ_H 10 kPa curves for all the samples is (the most) more irregular than the 50 and 200 kPa. However, when submitted to a normal stress of 200 kPa, the response of all the sediment samples to stress is very similar (Figure 7.22), showing a quasi-equal path, meaning that at these stress values the sediments of the whole record behave almost equally, thus attesting the very low-consolidation of the whole Late Pleistocene-Holocene sedimentary record.

The shear stress-strain analysis also shows that despite the inner properties of the sediments, results greatly vary according to the test, as with the classic shear box the horizontal displacement is higher than with the simple shear test (Figure 7.8). The reason for this lies in the fact that shear box test has only one shear surface, whereas DSS has several shear surfaces. However, for the same consolidation, greater shear stress is needed by the shear box to reach the same displacement as DSS (Figure 7.8). This is expressed in the internal friction angle values through a difference of 12.8º (Table 7.1). The shear box test seems to be less reliable, as it determines the stress exerted in only one point, where all the stress is concentrated, while the DSS distributes the stress for the whole sediment sample.

Higher stress induces greater vertical displacements, δ_V, with more regular curves, whereas lower stress presents more irregular curves (Figures 7.8 – 7.12). At some depths, the δ_V - δ_H curves of 10 kPa (σ) decreased to negative values (Figure 7.8C) or have been always negative (Figure 7.10C) indicating contraction on the sediment sample. Thus, these analyses recall the attention to the fact that these sediments are more sensitive to low shear stress, i.e., their response to the stress is best fitted with low stress. When the stress overpasses the *in-situ* consolidation, these sediments become highly deformable, and present a constant horizontal displacement. Therefore, the reaction of all the samples to the same stress (200 kPa), at different depths is almost the same (Figure 7.22).

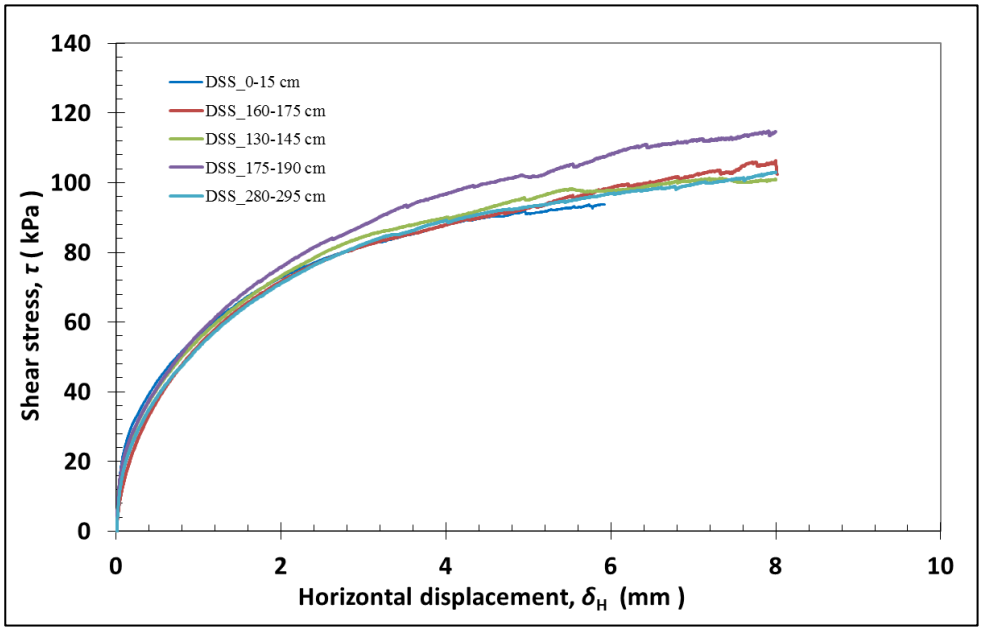

FIGURE 7.22 – Stress-strain behaviour of sediments at 200 kPa (σ'_V)

As verified in Figure 7.13, deeper sediments endure higher stress, thus having higher shear resistance. However, the stress-void ratio, *Log p'- e* (Figure 7.14) suggests low consolidation and presence of void space that indicates bad accommodation of sediments along the whole record and successive rearrangement whenever an increased stress is applied.

Furthermore, the rupture of these sediments is essentially a plastic failure, where the sediment sample bulges into a *barrel-shape*, rather than splitting, as it happens in brittle failure. As pointed out by Head (1982), failure normally occurs at 20% of axial strain for very plastic sediments. The very low-consolidated sediments of the plastered SCD clearly show that after reaching 20% of axial strain, deformation continued even with lowering stress. This shows the significant plasticity of these sediments (≥25%), which are quite mouldable even by the hand touch, thus having low ϕ'. Moreover, when the applied stress exceeds the *in situ* normal stress of sediments, the stress-strain curve tends to present a regular evolution, rapidly growing and moving away from the axis at the beginning of the curve (Figure 7.22). Additionally, the total absence of pronounced peak strengths on both q-εa and τ-δ_H plots, respectively for triaxial and simple shear tests, confirms the low consolidation of the sediments, which deform immediately and get reshaped under stress.

The considerable water content of these sediments also results from this and helps to diminish their resistance. Taking the example of the undrained triaxial compressional test, even with higher *p'* (16 kPa) than the two previous samples (10 and 11 kPa), assessed by drained tests, it reaches a peak strength at ~15.4 kPa and after ~13% (εa), the plastic deformation was already reached (Figure 7.17B). Thus, the type of test influences the results and whether samples are tested through drained or undrained compression, shear strength greatly varies, being quite smaller through undrained compression.

7.4.3.1 – SHEAR RESISTANCE: VARIATION BY DEPTH AND METHOD

The shear strength presents variable results according to shear strength test (Table 7.4; Figure 7.23). In CO14-GC-7B, the friction angle (ϕ') determined by triaxial compression tests (ϕ'_{tri}) ranges between ~25.6º and 30.9º, with a mean of 28.5º, whereas the friction angle determined by the DSS test (ϕ'_{dss}) varies from ~23.6º to 27.9º, with a mean value of 25.7º.

The ϕ'_{tri} shows a top-down decrease on friction angle (Figure 7.21), whereas the ϕ'_{dss} has a tendency for increasing with depth (Figure 7.23). However, below 170 cm the ϕ' values

tend to become closer (Figure 7.23). For similar depths, the ϕ' determined by the triaxial test is generally higher than that determined by DSS test. The shear movement is substantially different between triaxial and DSS tests. It seems likely that the horizontal shear movement promoted by DSS on the sediments is more effective in dissipating their resisting ability. The existence of several shear planes promoted by this test gives a higher homogeneity to the shearing movement. By opposition, the compressional movement, although combined with the confining movement (p'), seems to allow sediments to have a higher resistance probably because it does not have a shear movement, but rather the shear is got through compressive activity.

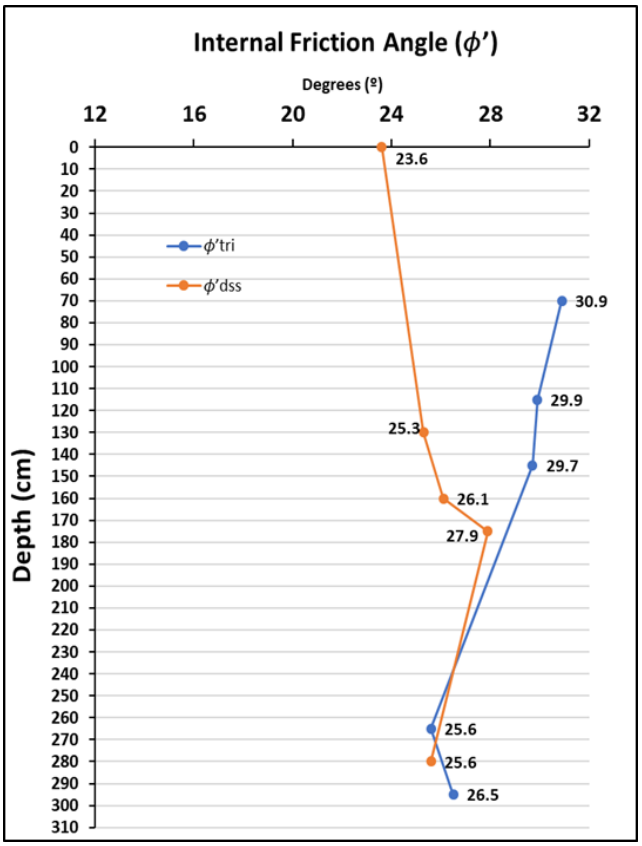

FIGURE 7.23 – Internal friction angle determined by triaxial and simple shear tests, by depth.

7.4.3.2 – SHEAR STRENGTH AND SLOPE INSTABILITY

The ϕ'_{tri} values for the Late Pleistocene-Holocene sediments of the SCD are quite coincident with the ϕ'_{tri} range found by Terzaghi and Peck (1948), for loose inorganic silt (27º to 30º) and very similar to the ϕ'_{tri} (28º) of the Late Pleistocene-Holocene sediments of the Ursa Basin (Urgeles *et al.*, 2010), in the Gulf of Mexico. The average ϕ'_{tri} (28.5º) for CO14-GC-7B is higher than the average ϕ'_{tri} of fine sediments (~23.8º) of Pianosa drift, but quite similar to the ϕ'_{tri} (28.8º) of the coarser material of the Corsica Trough (Miramontes *et al.*, 2018). Probably, this may have to do with grain-size whose mean (56 µm) in the SCD is similar to the mean grain-size of the coarser material (60 µm) of the Pianosa drift, but quite higher than that of the fine sediments (35 µm) of that drift (Miramontes *et al.*, 2018). The average ϕ'_{tri} for the SCD sediments is also quite similar to the ϕ'_{tri} determined by Soares

(2015) for silty tailings (28.2º). The average ϕ'_{dss} (25.7º) of the SCD is more coincident with the ϕ'_{tri} (23.8º) of fine sediments of Pianosa drift.

These differences in the ϕ' values may be explained by the dynamics on the depositional area. One possible explanation for this difference may be the fact that the plastered drift sediments are constantly under the winnowing effect of the contour current activity, which contributes for the sediment calibration and sphericity. By opposition, tailings are deposited in the base of the dams (Soares, 2015), suffering almost no transport. Once deposited, these sediments keep quit, as usually low or no turbulence exists in the base of the dams. Comparing the ϕ' values (34.2º) of silty sand tailings (Soares, 2015) with ϕ' values (27.9º) of sandy silt (coarser) sediments of the SCD, in the depth range of 144 - 176 cm of CO14-GC-7B, the explanation for the difference of values seems to be related to the transport and winnowing of the enhanced bottom current activity that promoted severe erosional activity, leading to the formation of a coarser sediment section and a hiatus (Teixeira *et al.*, 2020). The relatively low ϕ' found for these plastered drifts, SCD and Pianosa Ridge, can be related with the presence of high sedimentation-rate deposits of fine and well-calibrated sediments with high water content. Generally, these sediments present low consolidation and high pore-pressure, being thus prone for slope instability, as commonly verified abroad in other contourite drifts (Sultan *et al.*, 2004; Laberg and Camerlenghi, 2008). The presence of relatively low ϕ' in the moderately steep-slope ($\leq$10º) SCD (Teixeira *et al.*, 2019), where exists a combination of high sedimentation rates (Stow *et al.*, 2013) with strong bottom current-related variations on sediment properties (Teixeira *et al.*, 2020), may thus suggest that this area is quite susceptible to slope instability. Although slope gradient and seafloor morphology are key factors for slope instability (Talling, 2014; Miramontes *et al.*, 2018), landslides are also common on low-dip slopes (Hampton *et al.*, 1996), both on high sedimentation-rate contourites (Bryn *et al.*, 2005a; Kvalstad *et al.*, 2005a; Baeten *et al.*, 2014) and in low sedimentation-rate areas (Urlaub *et al.*, 2012). For this reason and given the low average ϕ'_{dss} (25.7º) of the low-consolidated (or cohesionless) sediments of the SCD, slope instability may be triggered despite the moderate slope angles (< 10º) of the SCD. Moreover, the hiatus in the section 160-175 cm, where ϕ'_{dss} is 26.1º, may act as a sliding plane and intensify or trigger slope instability at this point, because of the discontinuity on the sediment properties. This lithologic discontinuity associated with the low consolidation of sediments may thus be critical for their stability.

7.5 – CONCLUSION

The Late Pleistocene-Holocene contouritic and hemipelagic deposits of the SCD are constituted by fine-, normally to very low consolidated sediments, with considerable water content and low permeability. These are highly compressible sediments whose increase in shear stress promotes high and constant sediment settlement, as well as constant deformation (creep) with negligible strength peaks as consequence of their low consolidation. Compressibility for $\sigma'_v > 25$ kPa, is high, as expected in normal consolidated sediments and low, purely frictional, shear strength without any effective cohesive intercept. Thus, once under deviatoric stress, these sediments deform under steady and high shear strains. The barrel-shape of all the disrupted triaxial specimens signalize the soft state of these sediments (wet side on the critical state soil mechanics concepts) and tend to creep, which is a consequence of their plasticity and moderate sensitivity.

The depth range of 160-190 cm presents the highest values of permeability and therefore coefficient of consolidation, a slight sign of over-consolidation that may be due to some slight densification in sampling, pointing to distinct mechanical behaviour from more granular sediments. This sedimentary discontinuity confirmed by grain-size, chemical, geochemical, physical, and magnetic properties due to the presence of a hiatus at 161 cm, is also verified for the geotechnical properties.

These sediments have low values of the angle of shearing resistance, converging to critical friction angles, being this associated with high water contents (wet side of the critical state locus) and very low permeability, due to the significant fines content. The high and irregular sedimentation rate affecting the area seems to have a significant role on the mechanical behaviour of these sediments recovered in gravity core CO14-GC-7B at 1425 mwd. The low values of ϕ' near the discontinuity layer (~160 cm bsf) suggest this is a potential failure surface once it expresses a sedimentary discontinuity. Slope angle and seafloor morphology have a key role on slope instability in the area. However, instability occurs both at steep- and gentle slopes and mechanical properties of these sediments confirm the low resistance of sediments to shear stress and the proneness of the area for sliding activity. The intrinsic normal consolidation properties of these sediments, with high void ratio and high-water content and compressibility reveal fragility able to promote slope disruption even with low slope angles. These properties associated with climatic-induced varying sedimentation rates are important conditioning factors for slope instability in the area.

8. SUBMARINE LANDSLIDE SUSCEPTIBILITY ANALYSIS[4]

The Alentejo Margin off Southwest Portuguese continental margin is a rough, steep-slope area, affected by bottom current activity, especially Mediterranean Outflow Water (MOW). This intermediate bottom current contributes for the deposition of Sines Contourite Drift (SCD), over a pre-existing irregular Mesozoic through Miocene substrate structured during the Atlantic rifting and Alpine orogeny, respectively. The MOW also contributes for slope instability through the high depositional rates that lead to under-consolidation and overpressure, and through erosional activity by the impact exerted on the contouritic sediments. This contributes for localized highly irregular morphology, promoting natural propensity to slope failure, mainly shallow landslides.

This chapter aims to assess shallow landslide susceptibility, in the Alentejo Margin, using two statistical- and two physically based models. Statistical methods, Information Value (IV) and Logistic Regression (LR), use essentially bathymetric data and the landslides inventory to perform the modelling. Physically based models - SHALlow Landslide STABility (SHALSTAB) and FACTOR of SAFETY (FS), have been used for the physically based landslide susceptibility modelling, using a set of mechanical parameters, determined through geotechnical laboratory testing of a gravity core collected in the SCD, as well as accurate topographic information derived from a high-resolution digital elevation model (DEM). Internal friction angle values vary between 23.6º and 30.9º with mean values of 25.7º and 28.5º.

This modelling consists of a spatial zonation of the propensity for landslides occurrence. The validation of modelling results was done using shallow landslide scars, inventoried through DEM and multi-channel seismic (MCS) analysis. Both the results of statistical and physically based models were validated by the area under the curve (AUC) and the confusion matrix.

[4] This chapter is partially included in a manuscript that has been submitted for publication in **Engineering Geology**: **TEIXEIRA**, **M**., Viana da Fonseca, A., Cordeiro, D., Terrinha, P., Roque, C. (2021) – Geotechnical properties of the Sines Contourite Drift sediments: conditions for triggering submarine landslides. *Engineering Geology*, under revision.

8.1 - INTRODUCTION

Contourites are sediment deposits highly susceptible to submarine slope instability (Laberg and Vorren, 2000; Kvalstad *et al.*, 2005a; Laberg and Camerlenghi, 2008; Baeten *et al.*, 2014; Alonso *et al.*, 2016; Miramontes *et al.*, 2018; Teixeira *et al.*, 2019). Submarine landslides constitute serious hazards on coastal areas (Canals *et al.*, 2004; Kawamura *et al.*, 2009; Cattaneo *et al.*, 2014), from both economical costs and human casualties point of view (Locat, 2001; Sultan *et al.*, 2004; Masson *et al.*, 2006). However, spatial zonation of slope instability is not yet usually analysed in contourites, despite these being preferentially placed on continental margins (Stow and Faugères, 2008), causing serious impacts on coastal areas (Seed *et al.*, 1988). Hence, it is imperative the study, analysis and modelling of slope instability and landslide susceptibility of submarine landslides, for future hazard prevention and mitigation.

Landslide susceptibility is the spatial probability of landslide occurrence, based on the terrain's setting (Guzzetti *et al.*, 1999), allowing to determine if an area has the necessary conditions to trigger landslides (Carrara *et al.*, 1991). This probability is expressed by a spatial estimate of landslide occurrence and corresponds to the chance of an area to be affected (Aleotti and Chowdhury, 1999; Guzzetti, 2005). Susceptibility does not take into account neither the temporal probability of slope failure nor its magnitude, being mathematically expressed as the spatial probability of landslide occurrence according to a specific set of geo-environmental conditions (Carrara *et al.*, 1991; Zêzere, 1997; Guzzetti *et al.*, 1999). The product of spatial and temporal probabilities is the Hazard (Guzzetti, 2005).

Several quantitative methods have been developed for landslide susceptibility analysis, being applied worldwide in the last decades, especially onshore, with statistically based methods being the most frequently used (Yin and Yan, 1988; Carrara *et al.*, 1991; Soeters and Van Westen, 1996; Aleotti and Chowdhury, 1999; Guzzetti *et al.*, 1999; Süzen and Doyuran, 2004; Guzzetti, 2005) but also offshore (Piedade *et al.*, 2018). During the last decades, some physically based models have been used to analyse the landslides post-failure dynamics as the BING, a 1-D model (Imran *et al.*, 2001), the retrogressive model (Kvalstad *et al.*, 2005b), and the debris flow initiation- and run-out model Cemagref 1-D (Malet *et al.*, 2005). Other steady-state simple physically based models were also applied worldwide for the assessment of landslide susceptibility especially onshore: FS – *Factor of Safety* (Sharma, 2002); SINMAP - *Stability INdex MAPping* (Pack *et al.*, 1998; Calcaterra *et al.*, 2004; Pack *et al.*, 2005); SHALSTAB – *SHAllow Landslide STABility* (Montgomery and Dietrich, 1994; Dietrich and

Montgomery, 1998). All these models are based on the infinite slope, aiming to predict shallow translational landslides, and assuming the sediment column is totally water saturated. Thus, the use of physically based models should be confined to small and well defined areas, generally drainage basins (Montgomery and Dietrich, 1994; Teixeira, 2012; Teixeira *et al.*, 2015) to be possible the use of the Infinite Slope equation and because it is important to know the physical parameters in detail (Pack *et al.*, 1998; Van Westen *et al.*, 2003).

Once most of the submarine landslides are translational landslides (Hampton *et al.*, 1996) and the spatial variability of mass movement processes still remains poorly understood (Minning *et al.*, 2006), the assessment of shallow translational submarine landslide susceptibility for the Alentejo Margin is performed using physically based models. The assumption of fully water saturated sediments is fulfilled in submarine low consolidated sediments, allowing these models to be applied. In this sense, SHALSTAB and FACTOR of SAFETY are used in the mostly affected area by slide scars of the Sines Contourite Drift (SCD).

This chapter aims to assess translational submarine landslide susceptibility, through both statistical and physically based models, using the bathymetric and the sediments' geotechnical properties of the area.

8.2 – METHODS FOR ASSESSING LANDSLIDE SUSCEPTIBILITY

Different indirect methods are used for assessing and ranking slope instability factors and assigning the different hazard levels (Figure 8.1). These methods can be both qualitative or quantitative and direct or indirect (Guzzetti *et al.*, 1999).

Qualitative methods are subjective and attempt to portray the susceptibility zoning in descriptive terms (Guzzetti *et al.*, 1999), entirely depending on the judgement of the person who is carrying out the susceptibility assessment (Aleotti and Chowdhury, 1999). Quantitative analysis has been used (Fredlund and Krahn, 1977; Selby, 1993; Hampton *et al.*, 1996; Masson *et al.*, 2006; Urgeles *et al.*, 2006) through different models (Bishop, 1955; Morgenstern and Price, 1965; Morgenstern, 1967; Janbu, 1973), especially the simplified infinite slope model (Hampton *et al.*, 1978) much used in landslide susceptibility analysis. Landslide susceptibility is the function between hillslope stability and instability factors, which are able to reduce the shear strength and trigger landslides (Crozier and Glade, 2004).

Landslide susceptibility assessment may be also divided as direct and indirect mapping methods (Figure 8.1). According to Carrara *et al.* (1991); Guzzetti *et al.* (1999); Van Westen *et al.* (2003), those methods can be subdivided into Direct mapping (Geomorphological Method) and Indirect mapping: e.g., statistically based Methods and physically-based/mathematical models (Stochastic, Probabilistic and Deterministic). Deterministic models include, for example, SHALSTAB, SAFETY FACTOR, BING and CEMAGREF 1-D, while SINMAP is a probabilistic approach (Figure 8.1).

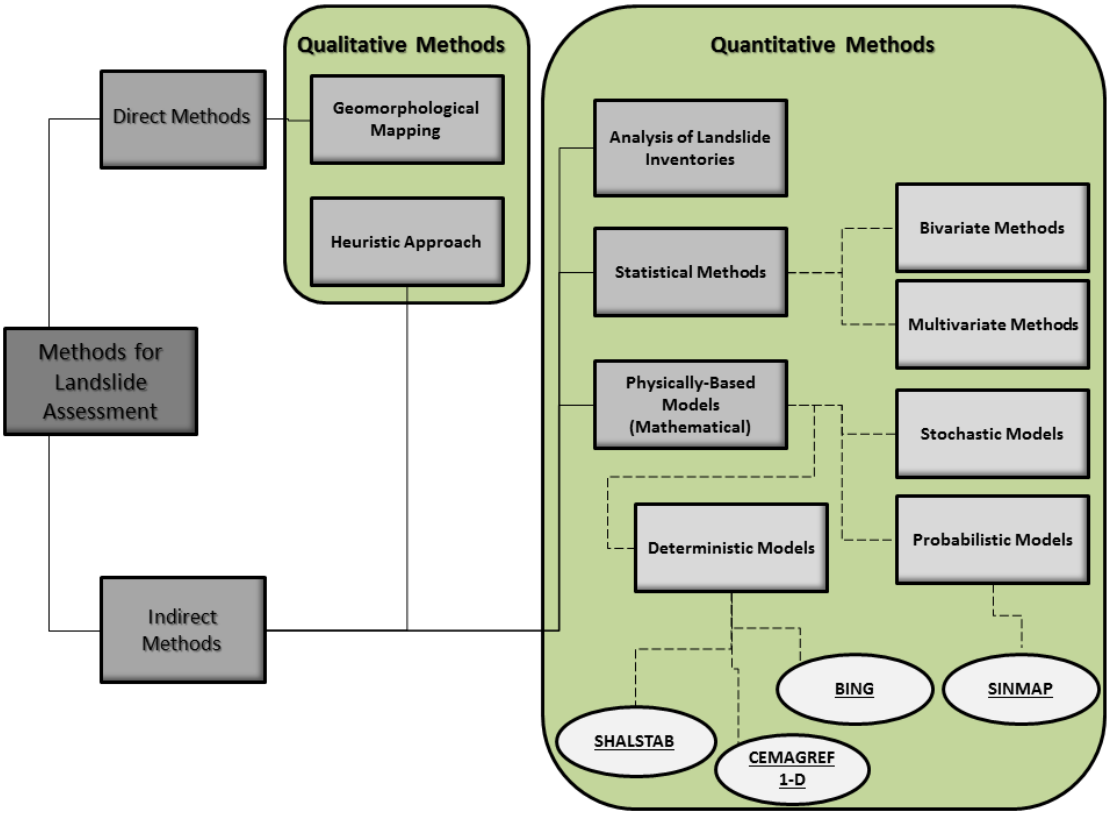

FIGURE 8.1 – Methods for assessing landslide susceptibility. Based on Aleotti and Chowdhury (1999) and Guzzetti *et al.* (1999). BING is used for landslide post-failure dynamic behaviour.

8.2.1 – STATISTICAL SUSCEPTIBILITY MODELLING

There are several statistical methods of calculation, both bivariate and multivariate, as it is the case of *Information Value* (Yin and Yan, 1988); *Weights of Evidence*; *Bayesian* combination rules; *Dempster-Shafer* method; *Fuzzy Logics* (Soeters and Van Westen, 1996) and *Logistic Regression* (Carrara *et al.*, 1991; Süzen and Doyuran, 2004).

Information Value (Yin and Yan, 1988) is a bivariate method for landslide susceptibility analysis, that aims to determine the landslide occurrence densities for each parameter, which will give the driven weights (scores of favourability) based on the class

distribution and the landslide density (Süzen and Doyuran, 2004). In this method each factor is individually compared with landslide scars inventory, being the score of favourability of each class of each parameter (e.g., lithology, slope angle, aspect, curvature) determined based on landslide density in each individual class (Aleotti and Chowdhury, 1999). The total number of landslides is divided in two aleatory subsets of equal number, of which one will serve for modelling and the other will serve for validation purposes. These aleatory subsets were obtained in ArcGIS© through subset feature tool. Information Value (Yin and Yan, 1988) consists on the determination of the logarithm ratio of the area affected by landslides to the total area:

EQUATION 8.1

$$Ii = \log \frac{Si/Ni}{S/N}$$

Where *Ii* is the Information Value of variable *i*; *Si* corresponds to the terrain units with landslides (number of unstable pixels by class) on the variable *i*; the number of terrain units, by class, of the variable *i* is expressed by *Ni*. When *Ii* is negative it is considered that there is not landslide proneness. Positive values show a direct relationship between the presence of a variable and the appearance of instability, which will be directly proportional to the *Ii* score (Yin and Yan, 1988; Zêzere, 1997). The total Information Value of a terrain unit *j* is determined according to the equation 8.2:

EQUATION 8.2

$$Ij = \sum_{i=1}^{m} Xji.Ii$$

Where *m* is the number of variables; *Xji* = if the variable has the value 0 it is absent of the terrain unit and if it has the value 1 it is present. Susceptibility of each terrain unit is directly proportional to the total Information Value, *Ij*. Some steps were considered: i) terrain units were defined on a matrix basis; ii) binary matrixes from each variable of each terrain unit were produced; iii) then the Information Value for each class of all variables was calculated, and iv) a final Information Value was obtained by summing all partial values of the independent variables of each terrain unit. The final susceptibility map has been reclassified into five susceptibility classes, according to the natural breaks of the distribution.

The Logistic Regression is a Multivariate Statistical Method (Dai *et al.*, 2001; Süzen and Doyuran, 2004) that allows forming a multivariate regression relation between a dependent variable (landslides) and several independent variables (morphologic parameters) that might affect the probability of landslide occurrence. Causative factors controlling slope stability are weighted indicating relative contribution of each factor on landslide susceptibility for each terrain unit. These statistical analyses are based on the presence or the absence of landslides inside each terrain unit (Süzen and Doyuran, 2004). In this model landslides are assumed as points, divided in two groups: real scars corresponding to 1 and non-events corresponding to 0. These non-events, which serve for validation purposes, are random points, automatically created in the GIS. This model is mathematically expressed in the simplest form as:

EQUATION 8.3

$$P = \frac{1}{1 + e^{-z}}$$

Where P corresponds to the estimated probability of landslide occurrence. The probability varies from 0 to 1 and z ($z = B_0 + B_1X_1 + B_2X_2 + B_3X_3 + \ldots + B_nX_n$) varies from -∞ to ∞, (linear logistic model). In an extended form the equation of logistic regression could be written as:

EQUATION 8.4

$$P = \frac{1}{1 + e^{-B0 + B1X1 + B2X2 + B3X3 + \ldots.. + BnXn}}$$

Where B_0 is the intercept of the model, n is the number of independent variables, Bi (i = 1,2, 3, ..., n) is the slope coefficient of the model and Xi (i = 1,2, 3, ..., n) is the independent variable.

The final landslide susceptibility map has been reclassified into five classes of susceptibility (very low, low, moderate, high, and very high) through the scores of Logistic Regression, according to the following boundaries: 0 – 0.2 represents very low susceptibility; 0.2 – 0.4 is low susceptibility; 0.4 – 0.60 is moderate susceptibility; 0.6 – 0.8 is high susceptibility; and > 0.8 is very high susceptibility.

8.2.2 – PHYSICALLY BASED SUSCEPTIBILITY MODELLING FOR SHALLOW TRANSLATIONAL LANDSLIDES

Simple physically based models have been used for the assessment of shallow landslide susceptibility and are based on the infinite slope model in which slope angle and sediments' internal friction angle, sediment's thickness and unit weight play a key role. SHALSTAB and FACTOR of SAFETY are among those models using these parameters.

8.2.2.1 – SHALSTAB MODEL

SHALSTAB - *Shallow Landslide Slope Stability* (Dietrich and Montgomery, 1998) is a slope-parallel failure plane model that aims to assess shallow translational landslides susceptibility through the coupling of a Infinite Slope Stability module based on the Coulomb's (1773) Infinite Slope equation (chapter 2) and a *steady-state* hydrological module. This combination originates a coupled model, which calculates the slope stability under steady-state saturated conditions (Montgomery and Dietrich, 1994; Dietrich and Montgomery, 1998; Montgomery *et al.*, 1998) i.e, it assumes that the sedimentary column is fully saturated. The stability module is based in geotechnical properties (cohesion, C'; sediment thickness, z; sediment bulk density $\rho s/\rho w$; and internal friction angle of an unstable column of sediment on the failure plane, $tan\phi'$) - equation 8.6. It is then assumed that hydraulic conductivity and transmissivity are constant with depth on a saturated sediment (Dietrich and Montgomery, 1998).

8.2.2.1.1 – STABILITY MODEL

In this model, stability is expressed by the ratio of the saturated- to the total sediment column (h/z) and may or may not include sediment cohesion on its analysis. The use of the cohesionless model consists of a simplification, due to the variability of the parameter over time and space, which may be applied to purely frictional and normally consolidated clays (see chapter 7). Since cohesion increases shear strength, one of the cohesionless outcomes is the increase of the potential unstable area, and the exclusion of this parameter may result in gross simplifications in the final result (Dietrich and Montgomery, 1998). Stability model without cohesion is expressed mathematically as follows:

EQUATION 8.5

$$\frac{h}{z} = \frac{\rho_s}{\rho_w}\left(1 - \frac{tan\theta}{tan\phi}\right)$$

With cohesion:

EQUATION 8.6

$$\frac{h}{z} = \frac{C'}{\rho_w g z cos^2\theta tan\phi} + \frac{\rho_s}{\rho_w}\left(1 - \frac{tan\theta}{tan\phi}\right)$$

In the stability model (equations 8.5 and 8.6), *h/z* corresponds to the sediment saturation necessary to trigger slope instability. As the sediment is fully saturated, this ratio will always be *h/z* = 1 and stability will essentially depend on morphologic characteristics of the area, especially slope angle. Hence, the stability is inversely proportional to the slope of the area. This may be expressed by the topographic ratio (*a/b.sinθ*):

EQUATION 8.7

$$\frac{h}{z} = \frac{Q}{T}.\frac{a}{bsin\theta}$$

Where *Q/T* is the steady-state saturation; (*a/b*) is contributing area per unit area and *sin θ* is the slope angle of the area, where *h* corresponds to the thickness of saturated potentially unstable sediment and *z* corresponds to the total sediment thickness (Dietrich and Montgomery, 1998; Montgomery *et al.*, 1998).

The final SHALSTAB equation consists of the slope stability model (Dietrich and Montgomery, 1998):

EQUATION 8.8

$$\frac{Q_c}{T} = \frac{sin\theta}{a/b}\left[\frac{C'}{\rho_w g z cos^2\theta tan\phi} + \frac{\rho_s}{\rho_w}\left(1 - \frac{tan\theta}{tan\phi}\right)\right]$$

Where θ is the slope angle, *a/b* the contributing area per contour width, C' is the effective soil cohesion (kN m^{-2}), ϕ is the effective sediment internal friction angle (°), ρ_s is the soil bulk density (kN m^{-3}), ρ_w is water density (kN m^{-3}), g is the gravity acceleration $m.s^{-2}$), and z is the thickness of the sediment, in metres.

This model (SHALSTAB) calculates the steady-state sliding potential per unit area, quantitatively identifying areas where shallow translational landslides may be triggered (Montgomery and Dietrich, 1994). Stability classes may vary from *Chronic Instability*, when ($tan\theta \geq tan\phi$), to *Unconditionally Stable* when ($tan\theta \leq tan\phi\ (1- \rho_w /\rho_s)$).

8.2.2.2 – FACTOR of SAFETY

The factor of safety, FS (Sharma, 2002) is also a ratio based on the application of the infinite slope limit equilibrium analysis, that quantitatively measures the stability of an area (equation 8.9). The FS may assume unstable (< 1) or stable (> 1) conditions. The sections of an area modelled as <1, even though not having landslide scars, may have already been previously affected by instability. When FS = 1, there is partial equilibrium between shearing and resisting forces. When FS > 1, there is stability and whenever an area is gradually increasing FS values its stability increases and vice-versa (Segoni *et al.*, 2009). FS is expressed through the following equation:

EQUATION 8.9

$$FS = \frac{c' + h \times cos^2\beta\ [(1-m)\gamma_m + m\gamma_{sub}] \times tan\phi'}{h \times sin\beta \times cos\beta[(1-m)\gamma_m + m\gamma_{sat}]}$$

Where c' is the effective sediment cohesion (kN m^{-2}); h is the thickness of potentially unstable sediment (in metres); β is the slope angle (º); ϕ' is the effective internal friction angle (º); γ_m is the sediment (natural) unit weight (kN m^{-3}); γ_{sub} is the submerged unit weight (kN m^{-3}); γ_{sat} is the saturated unit weight (kN m^{-3}); m is the ratio of the saturated sediment to the potentially unstable sediment ($\frac{q}{t}$ x ($\frac{a}{bxsin\beta}$)). Considering that the ground water table is at the seafloor (m = 1), the equation 8.9 (Sharma, 2002) is not totally suitable for the submarine environment. Thus, m can be ignored as both height and weight of water have no influence, it is considered the submerged unit weight of the sediment and the FS was solved through the following equation, considering a low c', h, γ, and ϕ':

EQUATION 8.10

$$FS = \frac{c' + h \times cos^2\beta \times \gamma_{sub} \times tan\phi'}{h \times sin\beta \times cos\beta \times \gamma_{sat}}$$

For a pure frictional analysis neglecting cohesion, sediment unit weight, and thickness FS could simply be solved as:

EQUATION 8.11

$$FS = \frac{tan\phi'}{tan\beta}$$

8.2.3 – SUSCEPTIBILITY VALIDATION

After landslide susceptibility modelling, results must be validated in order to determine the representativity of the modelled data. Thus, the validation group of the landslide inventory is used for this validation, which consists of determining how many pixels are in each class of instability, thus assessing the quality of the models' prediction (Bi and Bennett, 2003). Commonly, validation results are assumed to be good when > 75% (Guzzetti *et al.*, 1999). With these assumptions, validation is done in this work through the Area Under the Curve (AUC) – Equation 8.12) individually for statistical analyses, and in a comparison mode through a Confusion Matrix (Kohavi and Provost, 1998; Fawcett, 2006).

EQUATION 8.12

$$AUC = \sum_{i=1}^{n} \left[(Lsi - Li) \times \frac{ai + bi}{2} \right]$$

Where, (*Lsi*-*Li*) refers to the class amplitude, whereas *ai* refers to the value of the ordinate value corresponding to *Li*, while *bi* refers to the value of the ordinate value corresponding to *Lsi*. The model is as reliable as higher is the slope of the AUC curve.

The Confusion Matrix, used for both statistical and mathematical modelling, allows establishing an accurate relationship between predicted instability and existing landslides, by determining TPR, FPR, ACC and PPV. TPR (True-Positive Rate) is a ratio of the affected area by landslides by class to the total affected area predicted by the model (Fawcett, 2006), corresponding to the scar concentration by class of susceptibility; FPR (False Positive Rate) is the ratio of the wrongly predicted unstable area, to the total not slid area; ACC (Accuracy) is the ratio of the well predicted area to the total area; PPV (Positive Predictive Value) is the ratio of the true positives to the total unstable area.

8.3 – LANDSLIDE SUSCEPTIBILITY MODELLING FOR THE ALENTEJO MARGIN

8.3.1 – STATISTICAL ANALYSES

Statistically based shallow landslide susceptibility analyses, achieved by both Information Value and Logistic Regression, indicate good modelling predictions determining quite well the most unstable areas.

8.3.1.1 – INFORMATION VALUE

Information Value predicts 55% of the area as stable and 45% as unstable – area with Moderate, High, and Very High landslide susceptibility (Figure 8.2). Logistic Regression models ~65% of stable area and ~35% as unstable area (Figure 8.3).

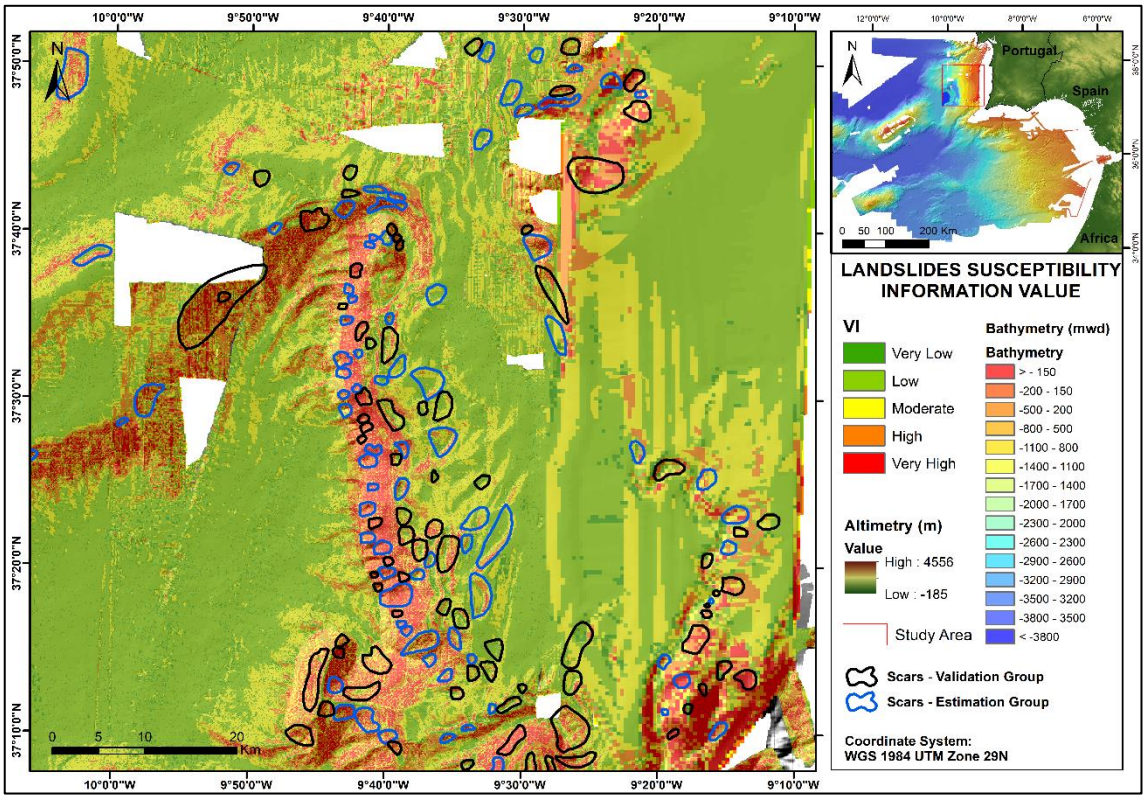

Figure 8.2 - Landslide susceptibility – Information Value. Landslide scars represented through the Estimation group (blue) and the Validation group (black).

Information Value calculation (Figure 8.2) classifies ~50% of the area as having Low landsliding susceptibility, and only 5.8% is modelled as Very Low susceptible to landslide occurrence. About 25% corresponds to Moderate susceptibility that is found on transitional areas, i.e., transitions from smoother to steeper areas. High susceptibility is attributed to 12% of the area and ~8% is classified as Very High susceptibility.

Table 8.1 – Scores of the Information Value

Thematic Map	ID	Class	*IV Score*
SLOPE ANGLE	1	< 1,5	-1.59355
	2	1,5 - 2	-0.91312
	3	2 - 3	-0.53205
	4	3 - 4	0.15208
	5	4 - 5	0.73512
	6	5 - 7	1.05381
	7	7 - 10	1.21511
	8	10 - 15	1.41153
	9	15 - 20	1.30733
	10	20 - 25	1.46629
	11	25 - 35	1.21202
	12	35 - 45	1.56414
	13	> 45	-1.62111
SLOPE ASPECT	1	Plane	-2.589
	2	N	-0.091
	3	NE	0.317
	4	E	0.673
	5	SE	0.502
	6	S	0.232
	7	SW	0.115
	8	W	0.543
	9	NW	-0.137
CURV PROFILE	1	Concave	0.588
	2	Plane	0.530
	3	Convex	-0.612
CURV PLAN	1	Concave	1.037
	2	Plane	-0.344
	3	Convex	0.546
LITHOLOGY	1	Pliocene sandy silt	0.859
	2	Calcareous sandstones	0.262
	3	Cretaceous sandstones	0.648
	4	Neogene sands	-0.108
	5	Quaternary silty mud	-0.143
	6	Miocene deposits	-0.151
	7	Plio-Quaternary sediments	-0.161

About 45% of the area is classified as moderate-, high- and very high susceptible areas that concentrate in the medium to steep areas (> 10º). According to Table 8.1, steeper areas (10º - 45º) present higher scores of favourability. On the other hand, east- and southeast-facing slopes have higher scores of favourability, and concave slopes are the most favourable to the development of landslides in plan and profile curvature (Table 8.1). This occurs in areas where sediments and internal pore-pressure mostly concentrate and is intensified by gravity effect, i.e., gravity, sediment availability, and internal fluids greatly determine instability, as explained in chapter 5. Pliocene sandy silt and Neogene sands are the most susceptible sediments (Table 8.1). These sediments occupy most of the area where scars mostly concentrate.

8.3.1.2 – LOGISTIC REGRESSION

Logistic Regression (LR) modelling (Figure 8.3) assesses ~37% of the area as having Low susceptibility and ~28% as Very Low susceptibility, which is found in the deeper and

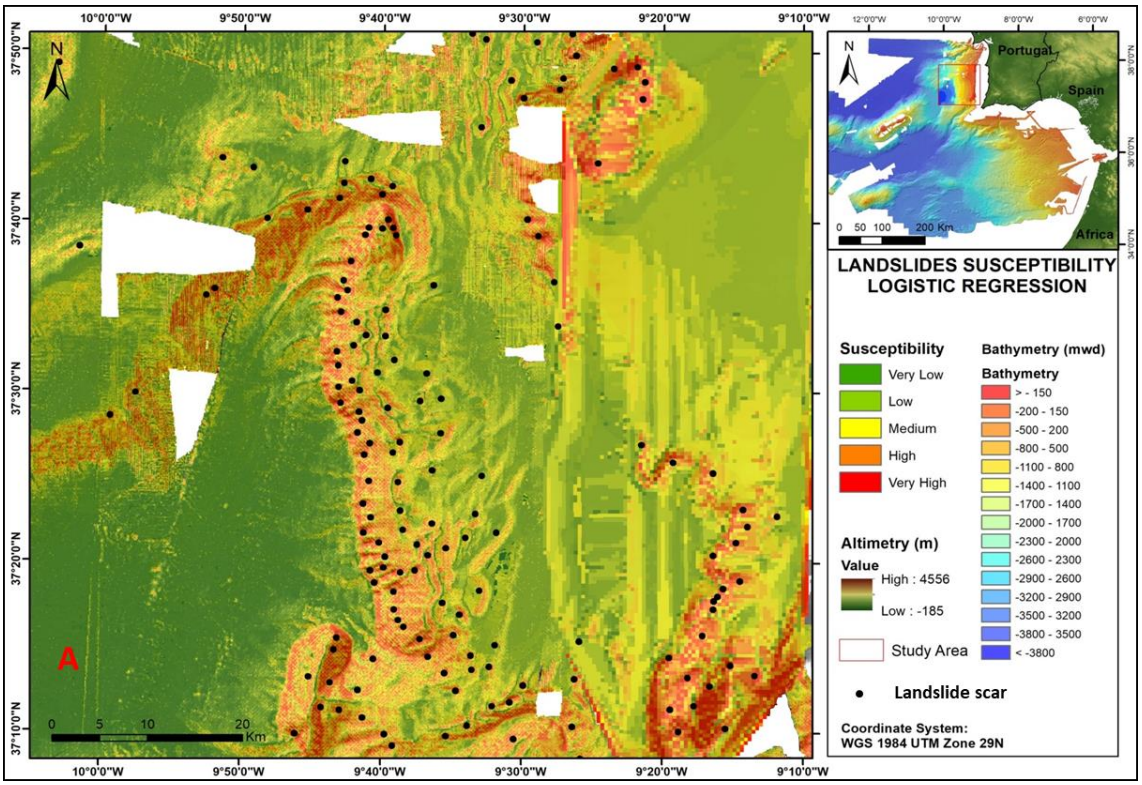

Figure 8.3 – Landslide susceptibility - Logistic Regression.

smoother areas as the *Lebre* Basin. Moderate susceptibility is found in 18% of the area, corresponding to medium-steep areas of the Middle Slope. About 10% of the area is modelled as High susceptibility and ~8% is modelled as having Very High susceptibility, essentially occurring on the steepest slopes.

8.3.1.3 – VALIDATION

Validation results for Information Value, through the AUC (Area Under the Curve) determine ~90% of fitness between model prediction and landslide scars inventory (Figure 8.4). In what concerns to scar concentration, ~29% of the scars are found in the area modelled as High susceptible, 25% in the Very High susceptible area and 24% in Moderate susceptibility, meaning that 78.8% of the scar concentration is well predicted as unstable area.

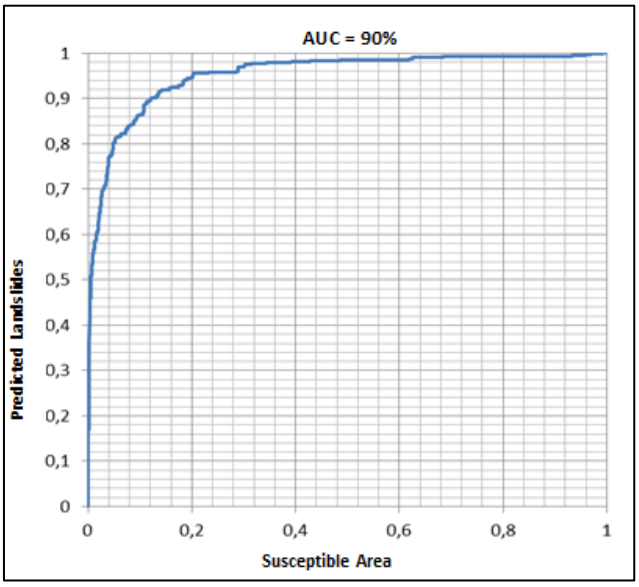

Figure 8.4 - Validation graph: Success Rate analysis. AUC (Area under the Curve)

LR validation results through Receiving Operating Characteristic (ROC) curves (Figure 8.5) indicate a success rate of 84%, meaning a good suitability of the model prediction with the landslide scars inventory. Scar concentration is higher in Very High susceptibility class with ~41% of the scars being found in this class. About ~22% of the scars are found in the class of High susceptibility and ~21% in the Moderate susceptibility class, accomplishing about 84% of well predicted unstable area.

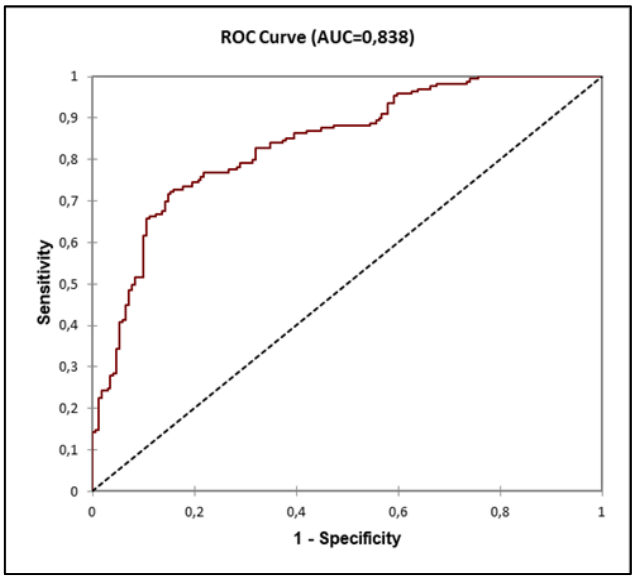

Figure 8.5 - Validation graph using ROC (Receiver Operating Characteristic) curve.

The Information Value presents greater scar concentration in High (29.3 %), Very High (25%), and Medium (24.4%) landslide susceptibility classes. Low (16.1%) and Very Low (5%) susceptibility only account ~21% of the area. Analysing validation results through a confusion matrix (Table 8.2), TPR ratio is slightly better in Logistic Regression (84.6) than in Information Value (78.8) modelling. Additionally, False Positive Rate (FPR) indicates that Logistic Regression is wrongly predicting susceptible area by a ratio of (35.5), less than Information Value (42.8). Accuracy values suggest better analysis retrieved by Logistic Regression (64.5) comparing with Information Value (57.9), indicating that the real unstable area to the well predicted area (Table 8.2) is better assessed in LR.

Table 8.2 - Confusion Matrix for statistical landslide susceptibility validation

MODEL	TPR (SC)	FPR	ACC	PPV (LP)	TPR/FPR
IV	**78,84**	**42,80**	**57,94**	**6,16**	**1,84**
LR	**84,62**	**35,54**	**64,46**	**0,03**	**2,38**

Contrarily to the previous parameters, Positive Predictive Value (PPV) indicates better modelling for Information Value than for Logistic Regression. This parameter always returns low values (< 10) as it is used only the area counted as unstable. TPR/FPR is > 1 for both modelling, although higher for Logistic Regression.

8.3.2 – PHYSICALLY BASED ANALYSES

A simple physically based landslide susceptibility analysis has been carried out to determine the most susceptible areas of the SCD, based on the geotechnical properties of the upper 3.5 m of the Late Pleistocene – Holocene sediments (chapter 7). A simple physically based modelling has been addressed, assuming a depth range (z) of 3.5 m; sediment density (γ) ranging between 17.2 and 18.4 kN m^{-3}; friction angle (ϕ') ranging between 24 and 31º and cohesion (c') ranging between 0 and 1.5 kN m^{-2} (Table 8.3).

Table 8.3 - Parameter range of values for landslide susceptibility modelling

PARAMETER	RANGE
Internal friction angle (ϕ'- º)	24 – 31
Cohesion (C' - kN m^{-2})	0 – 1.5
Sediment thickness (z - m)	0 – 3.5
Sediment unit weight (γ - kN m^{-3})	17.2 – 18.4

8.3.2.1 – SHALSTAB

According to these parameter values, SHALSTAB© modelling determines that 14.6% of the area is both chronically unstable and unstable, whereas 7.7% is partially stable, and ~6.6% is modelled as stable and ~71.2% as unconditionally stable. This means that more than 3/4 of the area is predicted to be stable (Figure 8.6). This prediction coincides with the gentler slopes, once most of the slope gradient of the area is < 10º (Figure 8.6). Landslide

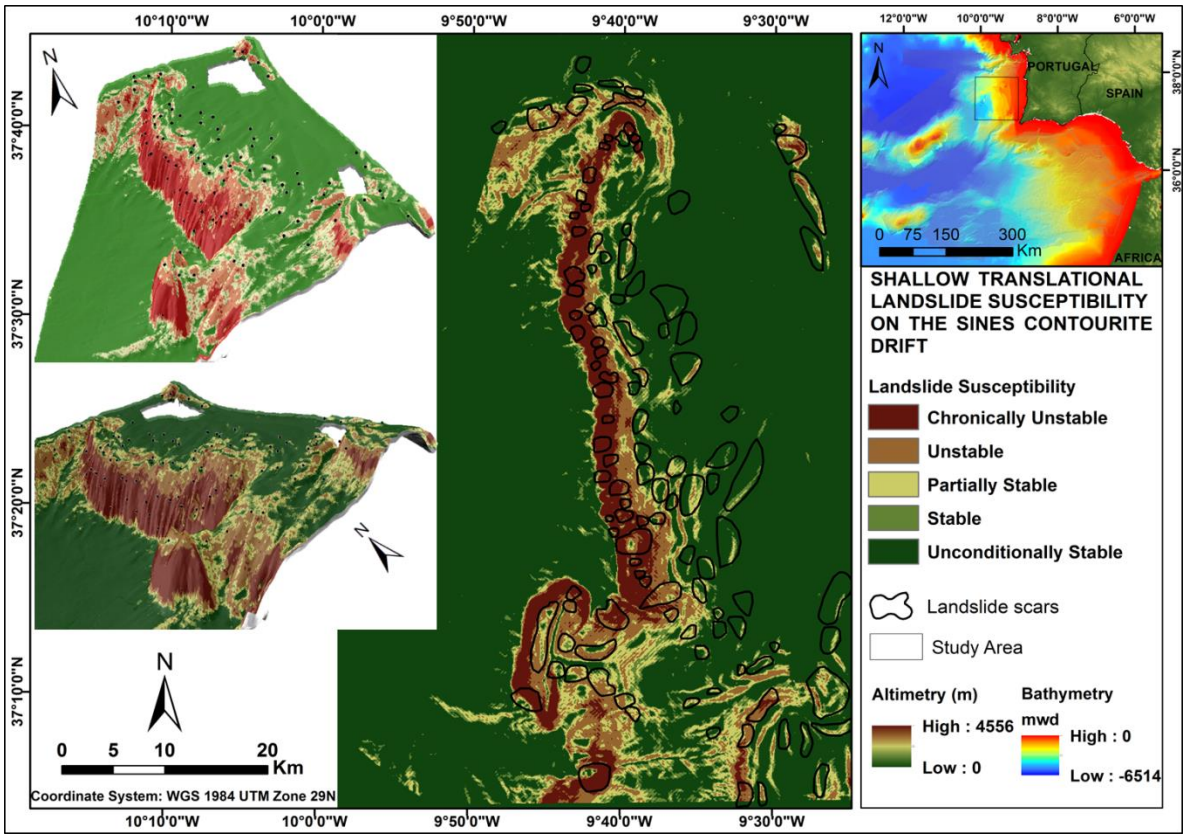

Figure 8.6 – SHALSTAB landslide susceptibility modelling

susceptibility analysis points to the steeper areas (> 10º) to be unstable. Thus, both the main body of the SCD and the Lebre Basin where slope gradient is < 5º are classified as stable, whereas the westernmost area of the SCD, the Pereira de Sousa Fault scarp, the Sines Hook,

the Bow Spur, and the northern sector of the Marquês de Pombal fault scarp are classified as the most unstable areas.

8.3.2.2 – FACTOR of SAFETY

Factor of Safety modelling determines that 15.3% of the area is unconditionally unstable (FS < 0.75) and unstable (FS < 1), mainly corresponding to steeper areas, whereas 14.6% is partially unstable (1 < FS < 1.5). About 12.4% and 57.8% were modelled as stable and unconditionally stable, respectively (Figure 8.7), performing 70% of the area as stable. Like in previous modelling, steeper areas are assigned with more instability, while the gentler surface of the SCD is modelled as a dominantly stable area. The Pereira de Sousa Fault scarp, the Sines Hook and the Bow Spur are the most susceptible areas, according to this modelling. The western side of the SCD close to that scarp is also quite unstable (Figure 8.7).

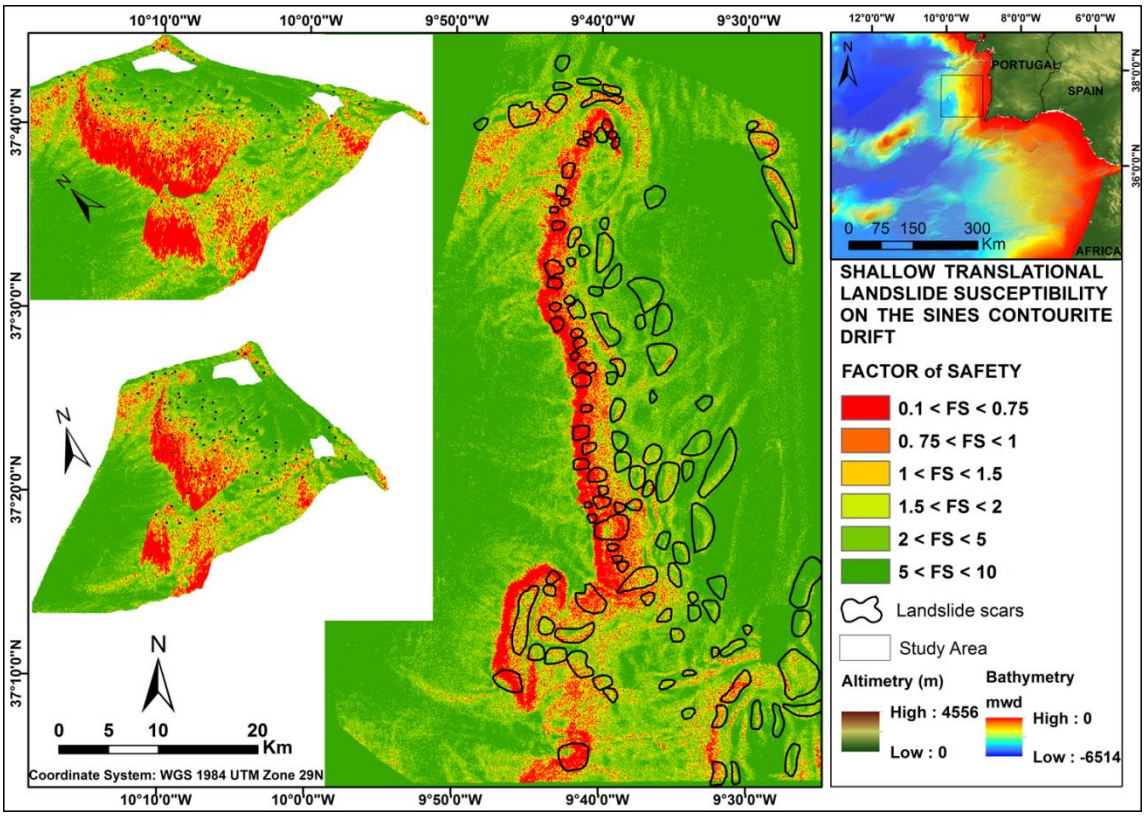

Figure 8.7 – Factor of Safety landslide susceptibility modelling

8.3.2.3 – VALIDATION

The SHALSTAB modelling validation through landslides scars concentration (SC) shows that ~37% of the area affected by landslide scars is both chronically unstable and

unstable, of which 18.7% are affected by chronic instability, and 18.4% to the unstable class. About 13.7 and 9.3% of the scars area is respectively affected to partially- and stable classes, while 39.8% of the scars is affected to unconditionally stable (Table 8.4). The landslide potential or Positive Predictive Value (PPV), gradually decreases from unstable to stable classes (Table 8.4), reflecting the lower proportion of disrupted area in stable classes, decreasing from a cumulative value of 20.58 on unstable classes to 19.97 in partially unstable, reaching only 5.09 in stable classes. In general, the true-positive rate (TPR) shows that 50% of area modelled as unstable was affected by landslide scars (Table 8.5), but that 20% of the modelling was wrongly (FPR) classified by this model, as no landslides occurred there. The accuracy (ACC) of the model is ~78%, 3% more than the minimum advisable (Guzzetti *et al.*, 1999). The global PPV is ~18.5 (Table 8.5).

Table 8.4 - Comparative modelling results

	SHALSTAB			**FACTOR of SAFETY**		
INDEX	**Unstable**	**Partially Unstable**	**Stable**	**Unstable**	**Partially Unstable**	**Stable**
SC	37.19	13.70	49.11	26.47	19.72	53.81
PPV	20.58	19.97	5.09	21.77	17.01	9.62

The scar concentration for the FS modelling retrieves ~27% of the scar area to be unstable, 19.7% partially unstable and ~54% to be stable (Table 8.4). The PPV, like in the previous modelling, decreases progressively from unstable to stable classes (Table 8.4), due to the fewer stable disrupted area, with 21.8% on unstable classes, 17% in partially unstable, and 9.6% in stable classes. The well-predicted instability (TPR) through FS is lower than 50% and the wrongly predicted (FPR) reaches ~20%. The accuracy of this model is 78%, while the global PPV is ~17.9% (Table 8.5).

Table 8.5 – Confusion matrix for validation of physically based landslide susceptibility

MODEL	**TPR**	**FPR**	**ACC**	**PPV**	**TPR/FPR**
SHALSTAB	50.89	19.70	77.93	18.47	2.58
FACTOR of SAFETY	48.65	19.29	78.16	17.90	2.52

As the TPR/FPR is > 1 (Table 8.5), both prediction modelling may be considered as acceptable, according to Fawcett (2006).

8.4 – DISCUSSION

The highest instability for static conditions occurs on steep and concave areas (Figures 8.2 to 8.7). The topographic/bathymetric parameters as slope angle, slope curvature and contributing area are important pre-conditioning factors for slope instability, as confirmed by these modelling. Topographic parameters are crucial for subaerial slope stability, e.g., (Montgomery and Dietrich, 1994; Teixeira, 2012), where slope angle, contributing area, and sediment thickness are considered the three main factors for slope instability (Okimura and Ichikawa, 1985), being also very important on submarine environments (Mosher *et al.*, 2010; Piper *et al.*, 2012) where seafloor morphology plays an essential role (Miramontes *et al.*, 2018; Collico *et al.*, 2020). According to the modelling in Sines Contourite Drift, both steep scarps and topographic concavities (*hollows*) are the most affected by instability. However, and despite being mainly triggered on the steepest slopes, landslides also occur on gentler slopes, confirming that landslide disruption on contourite drifts is also greatly controlled by mechanical properties, as already verified abroad (Laberg *et al.*, 2002; Haflidason *et al.*, 2004; Bryn *et al.*, 2005b; Laberg and Camerlenghi, 2008).

8.4.1 – LANDSLIDE SUSCEPTIBILITY

Landslide susceptibility analysis for static conditions for both statistical and mathematical modelling assign the highest scar concentrations to the most irregular geomorphology (Figures 8.2 to 8.7).

8.4.1.1 – STATISTICALLY BASED

The results of the statistically based landslide susceptibility modelling, for the Alentejo Margin, are similar for both Information Value (IV) and Logistic Regression (LR). The highest landslide susceptibility occurs on the steepest slope gradient, indicating that this has the highest weight among all variables and greatly impacts on this modelling. Furthermore, as some of the biggest landslides take place in steep areas (Figure 8.3), this confers higher scores (Table 8.1) to these areas and thus higher weight on the final assessment. In what concerns to the slope aspect, higher scores are achieved in the East- and southeast-facing slopes. These scores seem to be biased by the big landslides occurring in the southeast

facet of Príncipes de Avis Sea Mountains (PAS) (Figure 8.3). Once the number of pixels inside landslide scars determines the higher or lower favourability and hence the landsliding susceptibility, larger features end up by determining more favourability in each parameter. West-facing slopes have considerable score of favourability because most of the slides occur in west-facing slopes. The landslide susceptibility retrieved by these two methods (Figures 8.2 and 8.3) is similar to the probabilistic one determined for a broad area, also in the SW Iberian margin by Collico *et al.* (2020), as in both cases steeper, concave, and west-facing slopes are modelled as the most susceptible ones to be affected by slope instability.

Considering Very Low and Low susceptibility classes as stable areas (Figures 8.2 and 8.3), where probably (almost) no instability occurs, the general trend is similar between both models, with slight differences concerning to susceptibility classes. Both models retrieve validation values > 75% (Table 2), using the Area under the Curve (AUC) method (Figures 8.4 and 8.5). Nonetheless, both models present a common drawback: almost no instability is modelled for the gentler areas (Figures 8.2 and 8.3). Despite LR has better validation results, through confusion matrix (Table 8.2), IV seems to retrieve a more realistic assessment as it uses the landslide scar area to validate the susceptibility, whereas LR uses the scar as a single point. In this sense, LR may have misleading assignment of a scar to a landslide susceptibility class as it is represented by the centroid, which is seldom representative of the whole scar. Other validation methods also pinpoint the centroid of the scar but identify the most unstable terrain unit inside the scar (e.g., Montgomery and Dietrich, 1994; Teixeira *et al.*, 2015). Differently, in IV the susceptibility is validated through the area of the whole scar, cross-checking the modelled area and the area affected by instability. Nevertheless, IV has some drawbacks such as the fact of presenting some subjectivity when the scores are assigned to the variables, and the fact of not considering possible self-correlations between the different variables (Zêzere *et al.*, 2009). Besides, a common drawback exists in both methods: both use a part of the landslide inventory to model the susceptibility. Notwithstanding this, the statistically based results fit well to the real slope instability present in the study area, being essentially a topographically driven analysis.

8.4.1.2 – PHYSICALLY BASED

In order to overcome these constraints, physically based modelling has been addressed, combining bathymetric and geotechnical data (Table 8.3) on the susceptibility analysis

(Figures 8.6 and 8.7). The fact that this modelling uses landslide inventory only for validation purposes and includes geotechnical data of sediments in the susceptibility assessment, confers it higher reliability. Both physically based models present True-Positive Rates (TPR) ~50% (Table 8.5), presenting very similar FPR (~20%), ACC (~78%) and PPV (18 to 19%), with few differences between both physically based models. This validation confirms that these models assess satisfactorily the susceptibility of this rough geomorphology and is corroborated through the scar concentration by class of slope. The average slope of the area where landslides developed varies between 7 and 8º, although almost 10% of the scars occur on slopes > 20º, and 25% occur on slopes 10º - 20º. This is considerable for submarine landslides, whose slopes required for triggering instability are much lower than on subaerial slides (Hampton *et al.*, 1996). This is particularly relevant when comparing the SCD with other areas where translational sliding occur in very smooth slopes (Urlaub *et al.*, 2012), with slope gradients < 1º (Prior and Coleman, 1984; Henrich *et al.*, 2008). Like in statistical predictions, physically based modelling also determines the slope instability/landslide susceptibility to be especially concentrated on irregular morphology, i.e., on steep and concave slopes (Figures 8.6 and 8.7). Mathematical modelling yields more continuous landslide susceptibility scenarios than statistical models, which are more scattered. This is justified by the fact that the inclusion of geotechnical data on these models allows higher modelling accuracy, given by the mechanical numerical data, conferring greater precision to the analysis. With the geotechnical data determined for the upper 3.5 m of the SCD sedimentary package, stability is a constant on gentler areas for static conditions. This situation results from the low *c'* and ϕ' values of these sediments that suggest stability in the area. Physically based models have very good prediction ability for areas, where $tan\ \theta > tan\ \phi$', however not for areas where $tan\ \phi' > tan\ \theta$.

8.4.2 – SLOPE INSTABILITY IN STATIC CONDITIONS AND SCARS EVOLUTION

The natural propensity to instability of steep and concave-shaped areas in the SCD (Figures 8.2, 8.3, 8.6, and 8.7) comes from the gravity's action, which is recognized as a predisposing factor that greatly impacts on slope instability (Montgomery and Dietrich, 1994), and shows that shear stress as a result of the sediment weight and seafloor curvature are dominant factors. In static conditions, this is therefore a key element on slopes' stability. Additionally, concave slopes both in plan and profile curvature present higher landslide

susceptibility, indicating that it is in *hollows*, bathymetric concavities that more instability occurs, due to the local steepness increase and due to the high pore-pressure promoted by higher concentration of fluids in sediments' internal structure on these depressed areas. Upslope disrupted sediments preferentially accumulate in these sections, forming steep and allochthon deposits of cohesionless sediments that have lower shear strength, higher void ratio and greater water content, being thus prone for slope disruption. Besides, these depressed areas concentrate the internal sub-surface flow, creating higher pore-pressure on sediments that is as high as steeper is the slope. This is similar to and confirms the analysis done by Miramontes *et al.* (2018) for a contourite drift in the Tyrrhenian Sea, where the stability of the area is mainly controlled by the morphology of the sedimentary body. However, in the case of the SCD, this is valid for static conditions, without the additional action of bottom current activity, which is considerably higher in the SW Iberia due to the action of the MOW.

8.4.3 – THE IMPACT OF TRANSIENT FACTORS ON GENTLE-SLOPE GRADIENT INSTABILITY

Although modelling for static conditions suggests instability to be mainly allocated to steeper areas, the predominance of gentle slope angles in the SCD, and the presence of 66% of the scars inside the contourite occurring in slopes < 10º, stress the role of other conditioning factors on slope instability, such as the softness of sediments that present low consolidation, low cohesion, and low internal friction angles (< 32º), that together promote the sediment intrinsic weakness. This means that there are factors other than morphometric, especially transient factors like seismicity and bottom current activity, which are generating overburden stress, and triggering slope instability in the SCD. The presence of low magnitude (M< 4) seismicity epicentres in the area (Baptista and Miranda, 2009; Custódio *et al.*, 2016; Silva *et al.*, 2017; Veludo *et al.*, 2017), may promote the appearance of many small scars in the area. Bottom current activity exerts its direct impact on the sedimentary column through erosion, leading to a disequilibrium on the sedimentary column and indirectly through the formation of hiatuses (Teixeira *et al.*, 2020), which may constitute sliding planes. This is in agreement with the geotechnical analyses that show large variations of water content, void ratio, particles' density (Figure 7.5), as well as through the > OCR and the higher variation of the ϕ', coinciding with the hiatus detected in CO14-GC-07 at 161 cm (Teixeira *et al.*, 2020). This suggests the presence of a palaeo-sliding surface and a possible actual surface of

weakness acting as a boundary layer. Whenever transient triggering activity occurs, slope instability seems also very likely to occur, probably starting from this depth, even though the local (CO14-GC-7B) slope is < 5º.

8.5 – CONCLUSION

A landslide susceptibility analysis of the Late Pleistocene-Holocene contouritic sediments of the SCD has been done, in order to quantitatively determine the natural predisposition of the area to be affected by landslides in static conditions. Statistical and physically based methods, based on the bathymetric conditions and the geotechnical properties of the sediments, have been used to accomplish this analysis.

The landslide susceptibility in static conditions is greatly constrained and determined by seafloor morphology (slope angle, -aspect and –shape), which associated with the mechanical properties of the sediments, greatly determine the slope instability of the area. The importance of this analysis in static conditions consists on the assessment of the inherent/natural susceptibility of these sediments, without external triggers. These results constitute a starting point to assess the influence on instability caused by external transient triggers, such as seismicity and bottom currents.

These SCD contourites are naturally unstable sediments, whose under-consolidation due to low effective stress predisposes them to instability. This is intensified by the local steepness, which highly favours landslide instability even without external triggers. However, instability occurs both at steep- and gentle slopes. The fragile intrinsic mechanical properties of these soft sediments, confirmed by their low resistance to shear stress due to low pre-consolidation, leads the area to be quite prone for sliding activity even with low slope angles. Additionally, the mechanical resistance of the sediments is greatly diminished by the impact of external triggers as seismicity and bottom current activity. The low effective consolidation of these sediments without additional overburden stress, provoked by external agents, shows that these contouritic sediments are susceptible to disruption, once they are both on a seismically active region and under the impact of very dynamic bottom current activity. This is confirmed by the several scars occurring in very gentle slopes that are not predicted by these models.

9 – DISCUSSION

The southwest Portuguese continental margin is prone to landslide activity (Gràcia *et al.*, 2003; Terrinha *et al.*, 2003; Lo Iacono *et al.*, 2012; Collico *et al.*, 2020). The presence of the SCD, a plastered contourite drift, along this margin contributes for the increase of slope instability in the area, due to the intrinsic properties of the sediments. To better understand this, the morphosedimentary evolution of the SCD was assessed, from the Late Pleistocene onwards, by analysing the geomorphology, the sediment properties and the depositional phases that characterize this contourite drift, as well as the mechanical properties of the sediments, respectively through geophysical, sedimentological, physical and geochemical analyses, and geotechnical tests. In this sense, this study aims to assess slope instability on a contourite depositional setting in the Alentejo Margin, through the analysis of the main conditioning and triggering factors. The Late Pleistocene-Holocene sedimentary evolution and the morphosedimentary dynamics of the SCD is also analysed considering the interaction between along-slope and downslope processes.

9.1 – THE DEPOSITIONAL EVOLUTION OF THE SINES CONTOURITE DRIFT AND RELATED BOTTOM CURRENT VARIATIONS DURING THE LATE PLEISTOCENE-HOLOCENE

During the Late Pleistocene-Holocene there has been a relatively high mean deposition rate, varying between ~27 and 17 cm kyr^{-1} (Stow *et al.*, 2013), that corresponds to an increased bottom current activity (Hernández-Molina *et al.*, 2002; 2014b; Lofi *et al.*, 2016). This is testified by the core data of the IODP Site U1391, Expedition 339 (https://iodp.tamu.edu/index.html), which shows greater variations in colour and grain-size during that period, than previously (Stow *et al.*, 2013; Hernández-Molina *et al.*, 2014b). The reported intermittency on sediment's properties points to variations on sedimentary deposition derived from consecutive changes on MOW's regime. During this period, the SCD morphology and stacking pattern evolved from a mounded into a plastered drift (Rodrigues *et al.*, 2020).

The SCD has been through four main depositional stages during the last ~50 cal kyr BP, which correspond to four climatic-driven construction phases (Teixeira *et al.*, 2020). Throughout those stages, the climatic and sea-level changes greatly determined the MOW's strength, which influenced the sediment's supply and balance in the area. The sedimentary

evolution of this contourite is coded in the sediment properties (Teixeira *et al.*, 2020), creating layers with varying grain-size, carbonate and organic contents, physical, geochemical, and geotechnical properties (Figures 6.3, 6.4, 7.7 and 7.13). Between >43 and ~31 cal kyr BP, during the Marine Isotope Stage (MIS) 3, the sediment deposition has been quite regular, pointing to calmer and steadier oceanographic conditions, comparing with the previous phase. This is in agreement with the predominance of hemipelagic biogenic over coarse terrigenous elements, which suggests warmer and calmer depositional conditions, probably associated with high-standing sea-level.

However, with the end of MIS 3, the climatic conditions changed, and in MIS 2 (between 30.5 and 17.1 cal kyr BP) the depositional conditions significantly changed: it is verified a very low effective accumulation (2.7 to 1.5 cm kyr^{-1}) occurred during this period (Figure 6.5). This might have resulted from lower deposition or increased erosional activity, or perhaps the combination of both. The irregular effective deposition is demonstrated by the irregular limits between coarse and fine sediment layers (Figure 6.3B). This lower sedimentation rate is coeval with colder climatic conditions, which led to a sea-level retreat (Baas *et al.*, 1997) and consequent enhancement and downward shifting of the MOW (Schönfeld and Zahn, 2000). This climatic-induced downward shifting of the MOW promoted the cease of its direct action on the sedimentary record (where the gravity core CO14-GC-07 was retrieved). This helps to explain the lower sediment accumulation associated with climate cooling. As a consequence, during climate cooling, close to the LGM, and before the MOW sank below the depth of CO14-GC-07 (1425 mwd), sediment coarsened and formed three heterogeneous layers (Figures 6.4 and 6.7), enriched in terrigenous elements as iron (Fe), indicating that sediment supply likely had an increased inland source contribution, and that bottom currents enhanced and winnowed the finer sediments away. The presence of a hiatus at ~22 cal kyr BP and the irregular boundaries of the coarser layers, also suggest the presence of erosional activity events. The coarser and quite irregular deposition formed those heterogeneous layers, mostly comprising downslope displaced terrigenous-rich sediments reworked by bottom currents. Given the dynamism of the area in terms of bottom current activity (Cacho *et al.*, 2000; Rogerson *et al.*, 2005; Voelker *et al.*, 2006; Toucanne *et al.*, 2007), it seems that terrigenous elements, even though mostly originated from inland sources, they might not come exclusively from the Alentejo Margin. They rather seem to be mostly displaced along the SW Iberia margin, being then deposited along the west Iberia by the MOW, as contourites interbedded with finer, hemipelagic, sediment layers (Llave *et al.*, 2001;

2005; Hernández-Molina *et al.*, 2006; Llave *et al.*, 2006; Voelker *et al.*, 2006; Llave *et al.*, 2007; Hernández-Molina *et al.*, 2011; Hernández-Molina *et al.*, 2014b; Ducassou *et al.*, 2016; Ercilla *et al.*, 2016; Juan *et al.*, 2016; Rodrigues *et al.*, 2020; Teixeira *et al.*, 2020). These displaced sediments essentially come from source areas in the Mediterranean and Alboran Seas (Ercilla *et al.*, 1992; Estrada *et al.*, 1997; Pérez-Belzuz *et al.*, 1997; Alonso and Ercilla, 2003; García *et al.*, 2006; Casas *et al.*, 2011; Casas *et al.*, 2015; Yenes *et al.*, 2021), from the Gulf of Cadiz (Baraza *et al.*, 1999; Lee and Baraza, 1999; García *et al.*, 2009; 2020), close to the Gibraltar gateway, and the area around the São Vicente Canyon (Terrinha *et al.*, 2003; Gràcia *et al.*, 2010; Collico *et al.*, 2020; Mencaroni *et al.*, 2020). River discharges into the Mediterranean Sea and Gulf of Cadiz (Lobo *et al.*, 2006; Alonso *et al.*, 2016) were very important especially during glacio-eustatic low-stands, bringing larger terrigenous deposition directly into the continental slope. These are important sources of siliciclastic sediments (Ercilla and Alonso, 1996) that are captured by bottom currents and reworked in along the Iberia margin (Ercilla *et al.*, 2008a; Alonso *et al.*, 2016; Ercilla *et al.*, 2016; Juan *et al.*, 2016).

The climate and climatic-induced bottom current variations during the last ~50 cal kyr BP, along the Alentejo Margin, favoured an irregular sedimentary evolution of the SCD where diverse depositional rhythms and sediment sources are represented in the contourite body.

9.2 – THE EVOLUTION OF MASS TRANSPORT DEPOSITS (MTD) SINCE THE LATE PLEISTOCENE

As demonstrated by the combined analysis of multibeam bathymetry and multichannel seismic data, the western area of the SCD is the most affected by slope instability, and consequently mass transport deposits (MTD) accumulate in the Lebre Basin, at the base of the PSF scarp (Figure 9.1). Given the morphosedimentary constraints, the Lebre Basin is a natural repository for the displaced sediments resulting from slope failure. Most of the middle and lower continental slopes' sediments are drained into this basin (Figure 9.1). Moreover, several gullies are sculpted by debris flows and capture the suspended sediments and drain them as turbidite flows that deposit as apron-like deposits with hummocky architecture (Figures 5.9 and 9.1). These MTD, identified both in bathymetry and in seismic records (Figures 5.9 and 5.10), are mixed deposits of chaotically disposed sediments that result from gravity-driven activity triggered either as slides, slumps or debris flows. MTDs have been identified inside

the contouritic package since the Late Pliocene. However, slope instability has been mainly verified in the SCD sedimentary record during the Late Pleistocene-Holocene (Roque *et al.*, 2015; Teixeira *et al.*, 2019), coinciding with periods when an intensified MOW with higher erosive capacity (Voelker *et al.*, 2006; Toucanne *et al.*, 2007; Kaboth *et al.*, 2017b) was present. This increased activity of MOW might have also favoured slope instability and consequent intensification of deposition, suggesting a more dynamic morphosedimentary activity during this period. Although the buried scars can seldom be clearly identified and related with a specific age, there are many examples of deposits in the SCD that can be clearly identified in the acoustic data (Roque *et al.*, 2015) through hummocky and transparent seismic facies (Figure 5.9). In the Lebre Basin, these deposits reach more than 20 km from the footwall of the PSF scarp towards west (Terrinha *et al.*, 2003). In the Alentejo Margin, the mass transport deposits are mainly found since the Late Pleistocene (Teixeira *et al.*, 2019) and sedimentary evidences point to this instability to be mainly correlative with sea-level retreat (Teixeira *et al.*, 2020) and associated with the increase of terrigenous sediment input.

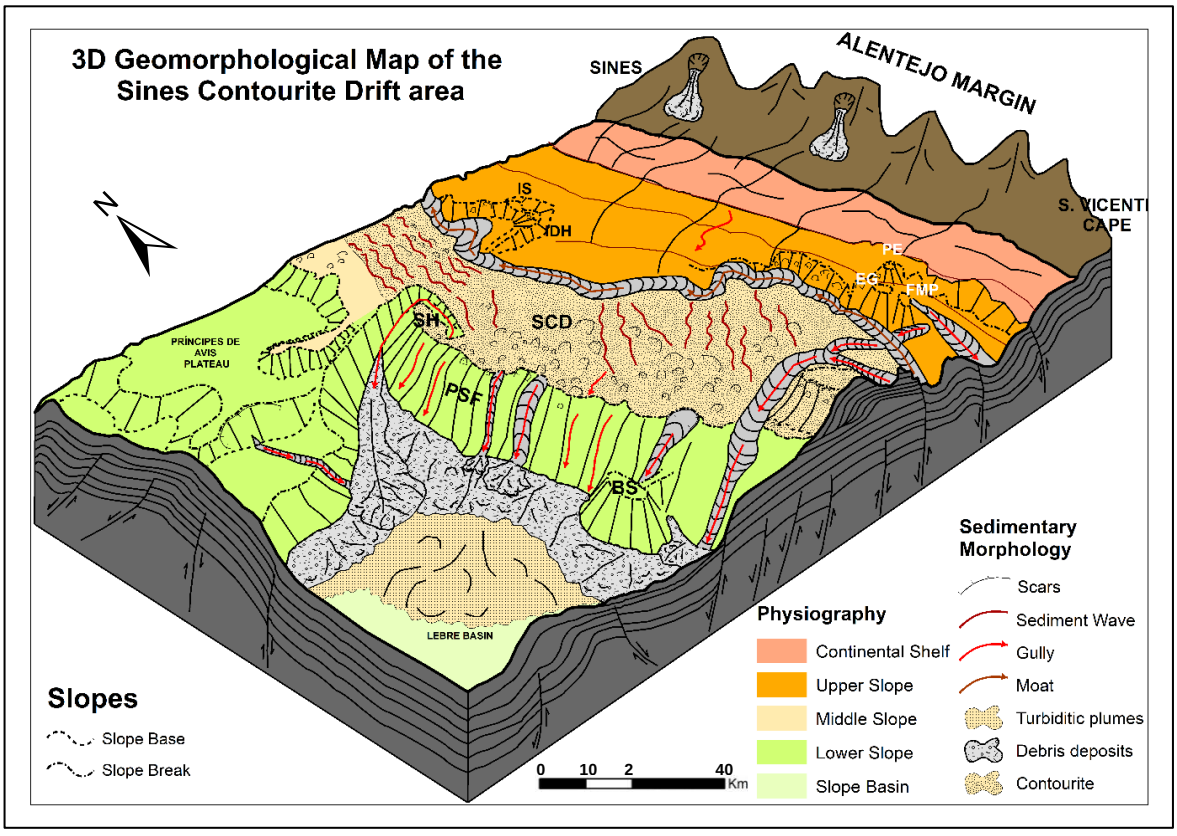

FIGURE 9.1 – 3D Geomorphological map of the Sines Contourite Drift area with the main morphosedimentary processes and deposits represented. The main processes mainly occur at the Upper and Middle Continental Slopes and the accumulation preferentially occurs at the Lebre Basin at > 3200 mwd. Accronyms: BS – Bow Spur; EG – Estêvão Gomes Hill; FMP – Fernão Mendes Pinto Hill; IDH – Infante Dom Henrique Hill; IS - Infante Santo Hill; LB – Lebre Basin; PE – Pêro Escobar Hill; PSF – Pereira De Sousa Fault; SCD - Sines Contourite Drift; SH – Sines Hook.

9.3 – THE IMPACT OF TECTONIC AND BOTTOM CURRENTS ACTIVITY ON LANDSLIDING ACTIVITY AND CONTOURITE DEPOSITION ALONG THE SOUTHWEST PORTUGUESE CONTINENTAL MARGIN

The tectonic activity of the Southwest Iberia Margin promoted a heterogeneous seafloor morphology inherited from Mesozoic rifting (Pereira and Alves, 2011; Terrinha *et al.*, 2019b), post-rifting and Alpine orogeny events (Terrinha *et al.*, 2019c). This structural control created a heterogeneous palaeo-morphology (Figure 9.1), which constrained and allowed for the differential sedimentation of the SCD in the southwest Portuguese continental margin. This tectonic setting has been suggested to be responsible for controlling MOW's pathways and to constrain bottom-current activity in the SW Iberia (Hernández-Molina *et al.*, 2016a). Moreover, the recent tectonic activity highly controls the regional seismicity pattern (Silva *et al.*, 2017), which probably is a key driving factor for triggering slope instability in the area.

9.3.1 – TECTONIC ACTIVITY

The palaeo-morphology inherited from the Mesozoic rifting, oceanic drifting thermal subsidence and tectonic inversion created the accommodation conditions for the deposition of the SCD, as an aggradating elongated drift, from the Late Miocene onwards (Hernández-Molina *et al.*, 2014b). This occurred since the reopening of the Gibraltar Strait (Maldonado *et al.*, 1999; Flecker *et al.*, 2015) at the end of the Messinian Salinity Crisis - 5.96-5.33 Ma - (Cita, 2001; Garcia-Castellanos and Villaseñor, 2011; Bache *et al.*, 2012) that led to strong changes in the oceanic circulation (Ambar and Howe, 1979; Hernández-Molina *et al.*, 2002; Rogerson *et al.*, 2012) and to the consequent onset of the Mediterranean Outflow Water (MOW).

The overall shape of the SCD is a wedge that thickens to the East towards the upper continental slope (Figure 5.5). Lateral constrictions in the eastern side of the drift especially at the base of the upper continental slope, where the moat is presently placed, do not allow the SCD eastwards progradation. To the west, the western flank of the drift is thinner, being permanently affected by slope instability mainly because of its proximity with the steep PSF scarp, which is a major tectonic and morphologic constraint, and perhaps the major restriction for the westwards morphosedimentary evolution of the Sines Contourite Drift. Thus, the morphology of the substrate is indirectly moulding the contouritic body and the local

morphosedimentary evolution. Also contributing for this is the fact that the SW Iberia has experienced uplift since the Lower Miocene (Roque, 2007). Additionally, Terrinha *et al.* (2003) reported reactivation under compression of the PSF scarp by the increase of its differential uplift with respect to the Lebre Basin and scarp dissection by strike-slip faults, while Figueiredo *et al.* (2013) reported a rate of ~20 cm kyr^{-1} for the Quaternary uplift of the SW Iberia Atlantic façade. These neotectonic constraints together with the frequent seismicity clustered in the SW Iberia (Custódio *et al.*, 2015; Silva *et al.*, 2017) are certainly major conditionings for slope instability verified in the offshore Alentejo. The determination of the dynamics of these competing processes (neotectonics, seismicity and sediment accumulation on the SCD) constitutes a challenge for a better comprehension of the morphosedimentary evolution in the area.

9.3.2 – BOTTOM CURRENTS CIRCULATION

The intense and enhanced bottom current circulation in the SW Iberia since the Late Pliocene (Talley and McCartney, 1982; Schönfeld and Zahn, 2000; Ambar *et al.*, 2002; Serra and Ambar, 2002) especially during global cooling periods (Zachos *et al.*, 2001), had great impact on the sedimentary building of the SCD, determining considerable variations in the depositional conditions and thus changes in the sediment fraction (Teixeira *et al.*, 2020) and consequently on slope stability. The activity of the MOW (Stow *et al.*, 2013), has a dual role on the morphosedimentary evolution of the seafloor in the area: either building-up a sedimentary body and sculpting sediment waves on its surface or destroying and reshaping it through its reworking activity.

Bottom current circulation seems to have considerable impact on slope stability, especially in the western boundary of the SCD, where the main cluster of landslide scars (1100 – 2500 mwd, Figure 5.10) is present. This roughly coincides with the depth range of the vertical shifting of MOW during interstadials and stadials, between ~1100 and 2200 mwd (Schönfeld and Zahn, 2000). This dynamism certainly creates additional stress on the sedimentary building and leads to seafloor instability. The presence of a cluster of landslide scars in the SCD, partially affected by the MOW's pathway (Figure 6.1), emphasises the role of the shaping and sculpting activity of this water mass over the seafloor.

Moreover, the activity of MOW is responsible for the contourite deposition and for the formation of sediment waves with different orientations, all over the SCD. Simultaneously,

downslope features as gullies and landslide scars form on this drift, resulting from the gravity-driven activity, induced by the interaction between bottom currents and palaeo-morphology. Slope instability seems also to benefit from the sedimentary discontinuities created by the sediment waves' interfaces that can act as preferential sliding planes. The irregular accommodation of the sedimentary body promoted by the combined action of the underlying structure and bottom current activity favours the presence of these discontinuities and thus favours slope instability. The coexistence of along-slope and downslope sedimentary processes greatly determines the morphosedimentary building in the area, as it does along the whole Iberia (Ercilla *et al.*, 2008a; García *et al.*, 2015; Alonso *et al.*, 2016; Ercilla *et al.*, 2016; 2019), leading to the formation of a mixed geomorphology, where along-slope and downslope-induced morphosedimentary features are interleaved and promote each-other.

9.4 – THE CONTRIBUTION OF THE MAIN TRIGGERING AND CONDITIONING FACTORS FOR SLOPE INSTABILITY IN THE SINES CONTOURITE DRIFT

The SCD is an unstable sedimentary body, which presents considerable permanent conditions for landslide susceptibility, due to the combination of multiple intrinsic factors. A simple physically based modelling, considering the geotechnical properties (c', ϕ', γ_s, and z) of local sediments, shows that steeper areas are quite unstable, even without external triggers (Figures 8.6 and 8.7). Regarding the sediment's mechanical properties, the geotechnical analyses showed that these are very low-consolidated and highly compressible sediments with excess pore-pressure, which contribute for reducing the factor of safety.

Considering these conditioning factors plus the significant tectonic and oceanographic dynamics of the area, a considerable propensity for slope instability and great probability for slope failure to be recurrent should be expected. The combination of moderate (M< 4) seismicity (Silva *et al.*, 2017; Veludo *et al.*, 2017) with normal to very low sediment consolidation favours the presence of multiple dominantly minor (< 5 km^2) landslide scars in the area. Moreover, the loading and shaping activity of the MOW has a crucial role on the permanent slope morphosedimentary evolution and constant sediment unstabilizing effect, by adding further stress. This is probably smoothing the impact of seismicity and is also probably contributing to prevent the formation of big landslide scars.

9.4.1 – SLOPE GRADIENT

Steep slopes are the most prone to slope failure worldwide (Mosher *et al.*, 2010; Piper *et al.*, 2012) and the SCD in the southwest Portuguese margin, is no exception. Most of the landslide scars affecting the SCD are near the PSF scarp, where a cluster of about a hundred slide scars concentrate (Teixeira *et al.*, 2019). These scars are mainly controlled by local rough morphology and steepness (slope gradients ≥ 5º). Gravity's action is more effective in these sectors increasing the shear stress and accelerating the sliding propensity. This is especially important both in tectonically active areas (Casas *et al.*, 2015; Chiocci and Casalbore, 2017) and in contourite deposits (Laberg *et al.*, 2002; Bryn *et al.*, 2005a; Kvalstad *et al.*, 2005a; Laberg and Camerlenghi, 2008; Laberg *et al.*, 2016; Miramontes *et al.*, 2018). Nevertheless, this is even more critical on contourite deposits affected by active tectonics as the SCD. Contrarily to what occurs offshore Mauritania (Henrich *et al.*, 2008), for example, or in most of the areas affected by submarine landslides at very gentle slope gradients (Prior and Coleman, 1984; Hampton *et al.*, 1996; Urlaub *et al.*, 2012), the SCD does not present large landslides as in other contourite areas (Bugge *et al.*, 1988; Haflidason *et al.*, 2004; Bryn *et al.*, 2005b), but a large number of small scars especially in the steepest slopes (>10º), instead. However, the largest slide scars of the area, not exceeding 6.3 km^3, occur on the gentlest slopes (<5º). These are wider and isolated scars that develop at a lower rate due to the weaker and less effective action of gravity promoted by the gentler steepness. This suggests that although slope is very important, it is not the only factor acting in the development of slope instability in the SW Portuguese margin, as also observed in other regions (McAdoo *et al.*, 2000; Urlaub *et al.*, 2012). In the SCD, like in the Oregon Coast (McAdoo *et al.*, 2000) the landslide scars are predominantly small and do not leave remarkable signatures, especially because of the recurrent slope instability that frequently evacuates sediments available to be displaced and may also contribute for local steepening.

Different conclusions have been reached worldwide about the main causes of slope instability. Miramontes *et al.* (2018), for example, found the geomorphology and steepness as the main conditions for slope instability, while Urlaub *et al.* (2013) found instability to be mostly determined by the sediment's mechanical properties as the compressibility. In the SCD, landslide susceptibility analysis at static conditions (Figures 8.6 and 8.7) shows that instability derives from the combined action of both geomorphology and sediment properties, promoting greater instability especially at the steepest slopes. Thus, higher instability is associated with steep areas. Furthermore, the Late Pleistocene-Holocene contourite deposits

of the SCD present normal to low consolidated sediments with high compressibility (Table 7.3), which intensify slope instability in the steepest slopes. However, these sediment properties also contribute for the development of landslide scars, even at very low gradients. This indicates that sediment mechanical properties also have an important role on slope instability in the SCD.

9.4.2 – SEDIMENTATION

Sedimentation is rather a conditioning factor that acts at variable rates during the formation of the SCD. The sedimentary pattern of this contouritic body although not fully understood, is best known since the Late Pleistocene. Ever since, the main depositional phases performed an irregular evolution with effective depositional rates varying from 1.5 to 50.5 cm kyr^{-1}, in response to climatic variations and climatic-induced bottom current oscillations (Teixeira *et al.*, 2020). The SCD morphology rather reflects the structural constraints and bottom current activity on the seafloor, while variations in the sedimentary package reveal great variations on deposition, as well as on the sedimentary input. The presence of coarse layers mainly reflects a change in depositional conditions promoted by climatic variations. These variations permit and favour the formation of boundary layers, inside the sedimentary building, which may act as failure surfaces. As also verified by Stegmann *et al.* (2007) and Laberg and Camerlenghi (2008), the existence of peak sedimentation rates and rapid loading greatly impacts on slope failure. The presence of weak layers and fluid escape (Figure 5.8.C) on the sedimentary record is mainly due to depositional and accommodation constraints that generate excess pore-pressure and low-consolidation, especially in sediment layers' interfaces leading to consequent proneness to submarine slope failure.

However, there are different scientific visions on the role of the sedimentation rate. While some authors (Hampton *et al.*, 1996; Masson *et al.*, 2006; Leynaud *et al.*, 2007) consider high sedimentation rates as being crucial for slope instability on continental slopes, others (Urlaub, 2013) found sediment intrinsic properties such as high compressibility at low sedimentation rates as promoting slope failure, once compressibility controls the magnitude of excess pore-pressure. In the case of the SCD, sedimentation rate is an important conditioning factor for the stability of the area, especially because of the depositional variability and irregularity that promote high compressibility and excess pore-pressure. These variations on

sedimentation rate also contribute for the formation of heterogeneous layers and respective boundaries that lead to varying shear strength and thus to instability.

The vision of this work, concerning to sedimentation rate is that more important than having high or low deposition, the most important is the variability on depositional patterns, once the main contacting surfaces, resulting from depositional variations and the contact between depositional/erosional surfaces are the most susceptible to act as sliding surfaces. These heterogeneous surfaces promote strong variations on physical and mechanical properties, and then variations on slope equilibrium.

9.4.3 – MECHANICAL PROPERTIES

Slope instability in the SCD greatly results from the mechanical properties, determined by the constraints imposed by the interplay between the bottom currents and the local palaeo-morphology that promotes differential deposition. The main consequence of the irregular sedimentation rate is the irregular sediment accommodation that leads to the low consolidation and high compressibility verified in these Late Pleistocene-Holocene sediments. This promotes high-water content (≥40%) and saturation (Skempton´s Coefficient B > 0.90), which, associated with the low permeability of these sediments, favour excess pore-pressure and, by consequence, slope instability at low gradients. According to Hampton *et al.* (1996), elevated pore-pressures, which contribute for fluidizing the shear planes, promote the reduction of the shear strength of sediments even at low gradients. This occurs in the gentlest slopes of the western boundary of the SCD, mainly due to the high deformation revealed by these sediments that endure low normal stresses (<50 kPa), resulting from their low effective consolidation (Teixeira *et al.*, *under review*). Moreover, the geotechnical tests performed in the scope of this work also reveal that the topmost 350 cm of the Late Pleistocene-Holocene sediments of the SCD present very low cohesion values between particles as well as low over-consolidation. This helps to explain their high susceptibility to slope instability. Although some authors, as Urlaub (2013) and references therein, state that marine sediments present high over-consolidation ratios, due to structural bonding, even in areas not affected by erosion, and cohesion is assumed as the main source of shear strength of marine sediments (Ikari and Kopf, 2015), the truth is that, in SCD's Late Pleistocene-Holocene sediments, cohesion between particles and over-consolidation are truly incipient, attesting that the sediments of the SCD are mechanically weak.

This favours high compressibility and rapid volume loss, which depends on the initial grade of structure (Burland, 1990), and is generally attributed to destructuring (Urlaub, 2013), a mechanical effect that leads to high values of compressibility and produces high pore-pressures. Nevertheless, some underestimation may occur from the compressibility analysis due to some remoulding of marine sediments during recovering manoeuvres (Urlaub, 2013). One of the causes for destructuring of the sediments in the southwest Portuguese continental margin might be the presence of active seismicity, which weakens the sediment's internal structure.

Saturated sediments reduce the overall shear strength, leading to slope instability (Moernaut *et al.*, 2017). The interstitial fluid pressure can also be itself the cause of sediment deformation by hydraulic fracturing, which is a key point in extensional failure deformation areas (Cosgrove, 2001). The fact of being on a seismically active region, this area is prone to sediment deformation by excess pore-pressure, which may lead to fluid escape, as it occurs in other places (Hovland and Judd, 1988; Bøe *et al.*, 1998; Mulder *et al.*, 2003; Mienert *et al.*, 2005; Ribeiro and Terrinha, 2007; Magalhães *et al.*, 2012; Duarte *et al.*, 2017). The presence of those fluids is consequence of high compressibility, as also verified by Urlaub (2013), promoting rapid volume loss and excess pore fluid pressure in the sedimentary building, in response to the increased shear stress, especially in the steepest areas.

Thus, the inner mechanical properties of the SCD sediments such as low over-consolidation, low permeability, and high compressibility associated with the tectonics of the area create the perfect environment for the presence of excess pore-pressure and the formation of weak layers that lead to sediment instability and consequent formation of many landslide scars.

9.4.4 – SEISMICITY

Earthquakes are considered as the most likely triggering factor of slope failure in seismically active regions (McAdoo *et al.*, 2000; Gràcia *et al.*, 2003; Stigall and Dugan, 2010; Ikari *et al.*, 2011) and probably it is also in the southwest Portuguese margin. The presence of multiple foci of dominantly moderated instrumental (M< 4) seismicity in the area (Baptista *et al.*, 1998; Silva *et al.*, 2017; Veludo *et al.*, 2017) with utmost epicentres occurring > 15 km deep (Veludo *et al.*, 2017), should allow for the formation of multiple, rather small than big, slide scars. This prevents the occurrence of big landslides with tsunamigenic potential as

those southwards of the study area, in the Marquês de Pombal Plateau, Gorringe Bank and Hirondelle South Bank (Gràcia *et al.*, 2003; Lo Iacono *et al.*, 2012; Omira *et al.*, 2016). The presence of great earthquakes ($M \geq 8.0$) that affected the SW Iberia (Fukao, 1973; Johnston, 1996) would be able to produce giant landslide scars in the SCD as those ones. However, no giant scars are present in the SCD area. Considering the proximity between the SCD and the remaining SW Iberia, the impact of seismicity might be similar, so the differences concerning to landslide scars dimensions between the SCD and the surrounding area might be also related with both the sediment properties (physical, geochemical and geotechnical) of the SCD, especially the lower consolidation and high compressibility that favour slope instability, and with the interaction of morphosedimentary processes occurring in the contourite drift area.

The generation of a large number of small landslide scars, which is also common in other areas of the Iberia margin (Camerlenghi *et al.*, 2010; Casas *et al.*, 2015), seems to be highly constrained by the tectonic activity. Seismicity, which has a key role for shear stress increments (Stigall and Dugan, 2010), acts as a cause for transient, additional pressure that increases the shear stress, promoting instability through the peak acceleration (Lee and Edwards, 1986) and promoting overloading, which imply sediment deformation and increase of pore-pressure that can lead to liquefaction and ultimately to shear strength reduction (Lee and Baraza, 1999). Its dual role, by triggering instability and by regularizing slopes through constant unroofing, confers the Alentejo Margin a constant but "controlled" instability. It is argued here that the permanent instability "cleans-up" the slopes and prevents major sediment displacements to occur, as in the Oregon coast, where few large failures occur despite that being also a seismically active margin (McAdoo *et al.*, 2000).

In fact, it is possible that this seismicity may be also contributing for an increasing stability of the southwest Portuguese margin in the long-term in what respects to landslide occurrence, as it happens in the Alboran Sea (Yenes *et al.*, 2021). Some authors (Urgeles and Camerlenghi, 2013; ten Brink *et al.*, 2016) demonstrated that slope stability increases with earthquake frequency and sedimentation rate decrease. The frequent ground shaking that contributes for the development of small, dominantly translational landslide scars seems to contribute for a long-term stabilization of the gentler slopes in the SCD through dynamic compaction of sediments as already verified by Locat and Lee (2002) and Lee *et al.* (2007) for other areas. If it is true that in the short term, seismicity promotes excess pore-pressure and overloading (Lee and Baraza, 1999) that lead to a proliferation of small landslide scars, which constantly sweep the highly-compressible, unstable sediments away in the SCD (Teixeira *et*

al., 2019), it is also true that large landslide scars will seldom develop in the area because of the inability of the low magnitude seismicity (Silva *et al.*, 2017) to trigger giant scars. As a matter of fact, inspection of the bathymetry of the Alentejo Margin did not show any evidence for the occurrence of any large landslide despite the occurrence of the M7.9 Horseshoe Abyssal Plain, 1969 earthquake (Fukao, 1973) with epicentre at only 160 km of distance nor the M>8, 1st November 1755 Lisbon earthquake (Johnston, 1996), possibly at similar distance.

The earthquake-driven sediment strengthening (Ikari and Kopf, 2015) seems to be more effective in low-gradient slopes, because, given the effect of gravity on steeper slopes this stabilization through compaction is less effective, being mainly got through the permanent evacuation of any deposited sediments in the slopes. The seismicity pattern occurring in the SW Iberia margin acts as a permanent slope unstabilizing factor, however in the long-term it may act as a slope stabilizer, once it is permanently regularizing slopes, through failure overprinting. On the other hand, as observed by McAdoo *et al.* (2000), larger landslides tend to concentrate on weaker sediments, and in fact this is happening in the smoother slopes of the SCD, which is constituted by very low-consolidated hemipelagic and contouritic sediments. Thus, the frequent, low-magnitude (M<4) seismicity may itself be contributing for the coalescence of scars in the smoother slopes of the SCD, where sediment consolidation is low and compressibility is high (Teixeira *et al., under review*). In this sense, many landslides' scars may not be detected, and probably most of the deposits result from many more disruption events than those estimated by this work.

10 – CONCLUSIONS

This thesis presents a multidisciplinary analysis of the factors and processes contributing for slope instability and mass movement activity during the Late Pleistocene-Holocene in the Alentejo Margin - Southwest Portuguese continental margin. Furthermore, this work also consists of an analysis of the Late Pleistocene-Holocene morphosedimentary evolution of the Sines Contourite Drift, during the last ~50 cal kyr BP. This work thus constitutes an innovative scientific approach for: i) the determination of the morphosedimentary evolution of the Sines Contourite Drift and adjacent area, through the use of multidisciplinary techniques, and ii) the assessment, for the first time, of the landslide susceptibility for the Sines Contourite Drift. The main conclusions of this study are summarized as follows:

- The morphosedimentary evolution of the Sines Contourite Drift and adjacent area, in the Southwest Portuguese continental margin, results from the complex interplay between morphology and bottom currents, which promotes the interaction between along-slope and downslope sedimentary processes, leading to the formation of a mixed morphology. The along-slope activity is responsible for the formation of the contourite drift and the sediment waves through deposition, and for the creation of a moat through erosion, whereas the downslope processes are responsible for the formation of several landslide scars and gullies.

- During the last > 43 cal kyr BP, the Sines Contourite Drift has been through four main depositional phases that resulted from climatic-induced bottom current variations: 1) > 42.9 cal kyr BP, there was a steady deposition of both hemipelagic and contouritic silty to sandy silty sediments; 2) from > 42.9 to > 30.5 cal kyr BP, during middle to late Marine Isotope Stage (MIS) 3, it is characterized by deposition of dominantly hemipelagic sediments with variable granulometry, ranging from silt to silty clay and clay; 3) > 30.5 to 17.1 cal kyr BP, mostly during MIS 2, is dominantly characterized by deposition of contouritic sediments varying from sandy silt to fine sand, which have great variability on sediment properties; 4) 17.1 cal kyr BP to Present, corresponds to the steadiest depositional phase, with the deposition of mostly hemipelagic sediments with high percentages (80 to 90%) of silty clay and clay.

- The enhancement of the Mediterranean Outflow Water during the end of MIS 3 and during MIS 2, due to climate cooling, left imprints in the sedimentary record as

discontinuities and coarse sediment layers with significant variations on grain-size, chemical, physical, geochemical, magnetic, and geotechnical properties, which reproduce climatic-induced bottom current varying intensities and vertical oscillations. The hiatus that occurred at ~22 cal kyr BP, marks the transition to the Last Glacial Maximum, when Mediterranean Outflow Water started to sink below 1425 mwd, ceasing its direct activity on the sedimentary record analysed in gravity core CO14-GC-07 until ~17.1 cal kyr BP, in the last deglaciation.

- The geotechnical analyses of the Late Pleistocene-Holocene fine sediments of the Sines Contourite Drift showed that they have high water content, low permeability, and plastic behaviour. These recent sediments present moderate to very low consolidation (≤ 0.01) and high compressibility (> 0.35), performing low shearing resistance and constant deformation.

- Landslide susceptibility modelling at steady state conditions shows that the Sines Contourite Drift is fairly susceptible to slope instability, especially in consequence of the steep morphology and the mechanical properties of its sediments.

- The Sines Contourite Drift is an unstable sedimentary body, which hosts a cluster of ~100 dominantly small landslide scars in its western boundary, near the headwall of the Pereira de Sousa Fault scarp, between 1100 and 2500 mwd. These scars are mostly affected by steepness and by the mechanical action of the climatic-induced vertical shifting of MOW.

- Slope instability mainly concentrates along the Alentejo Margin on steep areas with gradients comprehended between >5º and < 10º, where small landslide scars are predominant. On gentler areas, landslide scars are wider and slope instability is mainly conditioned by the mechanical properties of sediments. Slope angle is the main pre-conditioning factor for slope instability in static conditions.

- Highly variable effective sedimentation rates (1.5 to 50.5 cm kyr^{-1}) during the Late Pleistocene and Holocene (> 43 cal kyr BP to Present) promoted an irregular sedimentation pattern, which favoured sediment overloading and under-consolidation, leading to excess pore-pressure and to the formation of weak-layers, mostly near the headwall of the Pereira de Sousa Fault scarp.

- The normal to low consolidation, high compressibility and low shear resistance of the sediments, can promote instability in the Sines Contourite Drift, even without external triggers. The inclusion of transient conditions, as seismicity, in the analyses would further reduce the factor of safety and increase the landslide susceptibility of the area.

- The combination of steep-slope morphology, high density of moderate seismicity foci, persistent bottom currents circulation and low sediment consolidation favours the recurrence of instability, promoting the frequent development of predominantly small slide scars (< 5 km^2).

The complex morphosedimentary evolution the Alentejo Margin, in the Southwest Portuguese Continental Margin, and of the Sines Contourite Drift in particular, since the Late Pleistocene has been controlled by the complex interplay between tectonics, palaeo-morphology and bottom-current circulation, promoting sedimentary and gravity-driven processes. The interaction of steepness, sedimentation rate, sediment's physical and geotechnical properties, and seismicity control the regional susceptibility to slope instability.

10.1 – FUTURE WORK

The advances achieved by this work concerning to the knowledge of the mass movement activity and its main triggering and pre-conditioning factors, as well as on the morphosedimentary evolution of the Alentejo continental margin, arise new questions: i) how was the morphosedimentary evolution of the Alentejo Margin before the Pleistocene? Was it as prone to landslide susceptibility before Pleistocene as it has been during the Pleistocene-Holocene? ii) which are the main triggering factors of submarine slope instability in transient conditions in the Alentejo Margin? iii) which is the impact of seismicity on slope instability in the area, and which would be the minimum magnitude to trigger landslides on these sediments? iv) which is the impact the coarse layers have on slope stability? Do they constitute preferential shear planes that favour further slope instability?

To answer these questions, additional acoustic, sedimentological, seismicity and geotechnical data should be analysed for the sedimentary record prior to the Pleistocene in order to obtain:

- A complete and longer sedimentary record older than the Pleistocene;

- A broad analysis of the mechanical behaviour of the sediments;

- The analysis of landslide susceptibility in transient conditions, through seismicity-based modelling, integrating the seismicity data for a more consistent interpretation of the instability in the area and to better understand the impact of seismically induced landslides in the Alentejo Margin and surrounding area of the southwest Portuguese continental margin.

REFERENCES

Abrantes, F., Baas, J., Haflidason, H., Rasmussen, T., Klitgaard, D., Loncaric, N., Gaspar, L. (1998). Sediment fluxes along the northeastern European Margin: inferring hydrological changes between 20 and 8 kyr. *Marine Geology, 152*(1 - 3), pp. 7 - 23.

Abrantes, F., Cermeno, P., Lopes, C., Romero, O., Matos, L., Van Iperen, J., Rufino, M., Magalhães, V. (2016). Diatoms Si uptake capacity drives carbon export in coastal upwelling systems. *Biogeosciences, 13*, 4099 - 4109. doi: 10.5194/bg-13-4099-2016

Abrantes, F., Lebreiro, S., Rodrigues, T., Gil, I., Bartels-Jónsdóttir, H., Oliveira, P., Kissel, C., Grimalt, J. O. (2005). Shallow marine sediment cores record climate variability and earthquake activity off Lisbon (Portugal) for the last 2000 years. *Quaternary Science Reviews, 24*, pp. 2477 - 2494.

Ai, F., Kuhlmann, J., Huhn, K., Strasser, M., Kopf, A. (2014). Submarine Slope Stability Assessment of the Central Mediterranean Continental Margin: The Gela Basin. In S. Krastel & J.-H. Behrmann, Völker, D., Stipp, M., Berndt, C., Urgeles, R., Chaytor, J., Huhn, K., Strasser, M., Harbitz, C.B. (Eds.), *Submarine Mass Movements and Their Consequences, Advances in Natural and Technological Hazards Research* (Vol. 37, pp. 225 – 236).

Aleotti, P., Chowdhury, R. (1999). Landslides hazard assessment: summary review and new perspectives. *Bullettin Eng. Geol. Env/Springer-Verlag, 58*, 21 - 44.

Almagor, G., Garfunkel, Z. (1979). Submarine slumping in the continental margin of Israel and northern Sinai. *AAPG Bulletin, 63*, 324 - 340.

Alonso, B., Ercilla, G. (2003). Small turbidite systems in a complex tectonic setting (SW Mediterranean Sea): morphology and growth patterns. *Marine Petroleum Geology, 19*(10), pp. 1225 - 1240.

Alonso, B., Ercilla, G., Casas, D., Stow, D., Rodríguez-Tovar, F., Dorador, J., Hernández-Molina, J. (2016). Contourite vs gravity-flow deposits of the Pleistocene Faro Drift (Gulf of Cadiz): Sedimentological and mineralogical approaches. *Marine Geology, 377*, pp. 77 - 94. doi: 10.1016/j.margeo.2015.12.016

Alves, T., Cunha, T., Moita, C., Terrinha, P., Monteiro, J. H., Manupella, G. (2013). A evolução de bacias sedimentares tipo-rift em margens continentais passivas: o exemplo da Margem Ocidental Ibérica. In R. Dias, A. Araújo, P. Terrinha & J. Kullberg (Eds.), *Geologia de Portugal: Geologia Meso-cenozóica de Portugal* (Vol. II, pp. 349 - 404). Lisboa: Escolar Editora.

Alves, T., Gamboa, D. (2019). Mass-Transport Deposits as Markers of Local Tectonism in Extensional Basins. In K. Ogata, A. Festa & G. A. Pini (Eds.), *Submarine Landslides:*

Subaqueous Mass Transport Deposits from Outcrops to Seismic Profiles (pp. 71 - 90): John Wiley & Sons.

Alves, T., Gawthorpe, R., Hunt, D., Monteiro, J. H. (2003). Cenozoic Tectono-Sedimentary Evolution of the Western Iberian Margin. *Marine Geology, 195*(1), pp. 75 - 108. doi: 10.1016/S0025-3227(02)00683-7

Alves, T., Moita, C., Cunha, T., Monteiro, J. (2009a). *Structural Evolution and Timing of Continental Rifting in the Northeast Atlantic, West Iberian Margin*. Paper presented at the 71st EAGE Conference and Exhibition incorporating SPE EUROPEC 2009.

Alves, T., Moita, C., Cunha, T., Ullnaess, M., Myklebust, R., Monteiro, J., Manuppella, G. (2009b). Diachronous evolution of Late Jurassic–Cretaceous continental rifting in the northeast Atlantic (west Iberian margin). *Tectonics, 28*, TC4003. doi: 10.1029/2008TC002337

Alves, T., Moita, C., Sandnes, F., Cunha, C., Monteiro, J. H., Pinheiro, L. (2006). Mesozoic-Cenozoic evolution of North Atlantic continental-slope basins: The Peniche basin, western Iberian margin. *American Association of Petroleum Geologists Bulletin, 90*(1), pp. 31 - 60.

Ambar, I., Howe, M. (1979). Observations of the Mediterranean outflow-II. The deep circulation in the vicinity of the Gulf of Cadiz. *Deep-Sea Research, 26*, pp. 555 - 568.

Ambar, I., Serra, N., Brogueira, M., Cabeçadas, G., Abrantes, F., Freitas, P., Gonçalves, C., Gonzalez, N. (2002). Physical, chemical and sedimentological aspects of the Mediterranean Outflow off Iberia. *Deep-Sea Research, 49*(19), pp. 4163 - 4177.

Andrade, C. (1992). Tsunami generated forms in the Algarve Barrier Islands (South Portugal). *Sc. Tsunami Hazards, 10*(1), pp. 21 - 34.

Argus, D., Gordon, R., DeMets, C., Stein, S. (1989). Closure of the Africa-Eurasia-North America plate motion circuit and tectonics of the Gloria fault. *Journal of Geophysical Research, 94*, pp. 5585 - 5602.

Aronoff, S. (1989). *Geographic Information Systems: A Management Perspective*. Ottawa: WDL Publications. 294 pp.

ASTM-D2435. (1996). Standard Test Method for One-Dimensional Consolidation Properties of Soils. *ASTM International. West Conshohocken, PA.*

ASTM-D2487. (1985). Standard Practice for Classification of Soils for Engineering Purposes (Unified Soil Classification System). *ASTM International. West Conshohocken, PA.*

ASTM-D3080. (1998). Standard Test Method for Direct Shear Test Under Consolidated Drained Conditions. *ASTM International. West Conshohocken, PA.*

ASTM-D4767. (1995). Standard Test Method for Consolidated Undrained Triaxial Compression Test for Cohesive Soils. *ASTM International. West Conshohocken, PA.*

ASTM-D6528. (2007). Standard Test Method for Consolidated Undrained Direct Simple Shear Testing of Cohesive Soils. *ASTM International*.

Azerêdo, A., Duarte, L., Henriques, M., Manupella, G. (2003). Da dinâmica continental no Triásico aos mares do Jurássico Inferior e Médio. *Cadernos de Geologia de Portugal* (pp. 1 - 43). Lisboa: Instituto Geológico e Mineiro.

Baas, J., Mienert, J., Abrantes, F., Prins, M. (1997). Late Quaternary sedimentation on the Portuguese continental margin: climate-related processes and products. *Palaeogeography, Palaeoclimatology, Palaeoecology, 130*, pp. 1 - 23.

Bache, F., Popescu, S.-M., Rabineau, M., Gorini, C., Suc, J.-P., Clauzon, G., Olivet, J.-L., Rubino, J.-L., Melinte-Dobrinescu, M., Estrada, F., Londeix, L., Armijo, R., Meyer, B., Jolivet, L., Jouannic, G., Leroux, E., Aslanian, D., Tadeu dos Reis, A., Mocochain, L., Dumurdzanov, N., Zagorchev, I., Lesic, V., Tomic, D., Catagay, M., Brun, J.-P., Sokoutis, D., Csato, I., Ucarkus, G., Cakir, Z. (2012). A two step process for the reflooding of the Mediterranean after the Messinian Salinity Crisis. *Basin Research, 24*, pp. 125 - 153.

Baeten, N., Laberg, J., Vanneste, M., Forsberg, C., Kvalstad, T., Forwick, M., Vorren, T., Haflidason, H. (2014). Origin of Shallow Submarine Mass Movements and their Glide Planes - Sedimentological and Geotechnical Analyses from the Continental Slope Off Northern Norway. *Journal of Geophysical Research: Earth Surface, 119*, 26 pp. doi: 10.1002/2013JF003068

Bahr, A., Jimenez-Espejo, F., Kolasinac, N., Grunert, P., Hernández-Molina, F. J., Röhl, U., Voelker, A., Escutia, C., Stow, D., Hodell, D., Alvarez-Zarikian, C. (2014). Deciphering bottom current velocity and paleoclimate signals from contourite deposits in the Gulf of Cádiz during the last 140 kyr: An inorganic geochemical approach. *Geochemistry Geophysics Geosystems, 15*, 16 pp. doi: 10.1002/2014GC005356

Bahr, A., Kaboth, S., Jiménez-Espejo, F., Sierro, F., Voelker, A., Lourens, L., Röhl, U., Reichart, G., Escutia, C., Hernández-Molina, F. J., Pross, J., Friedrich, O. (2015). Persistent monsoonal forcing of Mediterranean Outflow Water dynamics during the late Pleistocene. *Geology, 43*, pp. 951 - 954. doi: 10.1130/G37013.1

Baptista, M. A., Miranda, J. M. (2009). Revision of the Portuguese catalogue of tsunamis. *Natural Hazards and Earth Systems Science, 9*(1), pp. 25 - 42. doi: http://www.nat-hazards-earth-syst-sci.net/9/25/2009/

Baptista, M. A., Miranda, J. M., Batlló, J. (2014). The 1531 Lisbon Earthquake: A Tsunami in the Tagus Estuary? *Bulletin of the Seismological Society of America, 104*(5), pp. 2149 - 2161. doi: https://doi.org/10.1785/0120130316

Baptista, M. A., Miranda, P., Miranda, J. M., Mendes-Victor, L. (1998). Constrains on the source of the 1755 Lisbon tsunami inferred from numerical modelling of historical data. *Journal of Geodynamics, 25*, pp. 159-174.

Baraza, J., Ercilla, G., Lee, H. (1992). Geotechnical Properties and Preliminary Assessment of Sediment Stability on the Continental Slope of the Northwestern Alboran Sea. *Geo-Marine Letters, 12*, 150 - 156.

Baraza, J., Ercilla, G., Nelson, C. H. (1999). Potential geologic hazards on the eastern Gulf of Cadiz slope (SW Spain). *Marine Geology, 155*, pp. 191 - 215.

Baraza, J., Lee, H., Kayen, R., Hampton, M. (1990). Geotechnical characteristics and slope stability on the Ebro margin, western Mediterranean. *Marine Geology, 95*, 379 - 393.

Bard, E., Rostek, F., Ménot-Combes, G. (2004). Radiocarbon calibration beyond 20,000 14C yr B.P. by means of planktonic foraminifera of the Iberian Margin. *Quaternary Research, 61*(2), pp. 204 - 214. doi: 10.1016/j.yqres.2003.11.006

Barrier, E., Vrielynck, B. (2008). Palaeotectonic maps of the Middle East *Tectono-sedimentary-palinspastic maps from Late Norian to Pliocene*. Paris: CGMW/CCGM.

Bekele, A., Downer, R., Wolcott, M., Hudnall, W., Moore, S. (2003). Comparative evaluation of spatial prediction methods in a field experiment for mapping soil potassium. *Soil Science, 168*, pp. 15-28. doi: https://doi.org/10.1097/01.ss.0000049735.22043.96

Bi, J., Bennett, K. P. (2003). *Regression Error Characteristic Curves.* Paper presented at the Proceedings of the Twentieth International Conference on Machine Learning (ICML-2003), Washington D.C.

Bisci, C., Drams, F., Sorriso-Valvo, M. (1996). Rock Flow (Sackung). In R. Dikau, D. Brunsden, L. Schrott & M.-L. Ibsen (Eds.), *Landslide Recognition. Identification, Movement and Causes*: John Wiley & Sons. Chichester.

Bishop, A. W. (1955). The use of the Slip Circle in the Stability Analysis of Slopes. *Géotechnique, 5*, 7 - 17. doi: 10.1680/geot.1955.5.1.7

Bishop, A. W. (1966). Soils and soft rocks as engineering materials *Imperial College of Sci Tech 6* (Vol. 6, pp. 189 - 213).

Blanc, P.-L. (2002). The opening of the Plio-Quaternary Gibraltar Strait: assessing the size of a cataclysm. *Geodinamica Acta, 15*(5 - 6), pp. 303 - 317.

Blasio, F. V. (2011). *Introduction to the Physics of Landslides*. Rome: Springer.

Bodwadker, S., Reis, J. (1994). Porosity measurements and of core samples using gamma-ray attenuation. *Nuclear Geophysics, 8*, pp. 61 - 78.

Bøe, R., Rise, L., Ottesen, D. (1998). Elongate depressions on the southern slope of the Norwegian Trench (Skagerrak): morphology and evolution. *Marine Geology, 146*, pp. 191 - 203.

Boillot, G. (1979). *Géologie des Marges Continentales*. Paris: Masson.

Boillot, G., Girardeau, J., Kornprobst, J. (1989). Rifting of the West Galicia continental margin: a review. *Bulletin de la Société Géologique de France, 8*(4), pp. 393 - 400.

Borges, J., Fitas, A., Bezzeghoud, M., Teves-Costa, P. (2001). Seismotectonics of Portugal and its adjacent Atlantic area. *Tectonophysics, 331*, pp. 373 - 387. doi: http://dx.doi.org/10.1016/S0040-1951(00)00291-2

Bouma, A., Hollister, C. (1973). Deep ocean basin sedimentation. In G. Middleton & A. Bouma (Eds.), *Turbidites and Deep-water Sedimentation* (pp. 79 - 118): SEPM Pacific Section Short Course. SEPM, Anaheim, CA.

Bourillet, J., Edy, C., Rambert, F., Satra, C., Loubrieu, B. (1996). Swath Mapping System Processing: Bathymetry and Cartography. *Marine Geophysical Researches, 18*, 487 - 506 pp.

Brackenridge, R., Hernández-Molina, F. J., Stow, D., Llave, E. (2013). A Pliocene mixed contourite-turbidite system offshore the Algarve Margin, Gulf of Cadiz: seismic response, margin evolution and reservoir implications. *Marine Petroleum Geology, 46*, 36 - 50.

Brito, P. (2010). *Impactos da elevação do nível médio do mar em ambientes costeiros: O caso do estuário do Sado.* PhD Thesis, University of Lisbon, Lisbon, Portugal.

Bromhead, E. (1992). *The Stability of Slopes - 2nd ed.* London: Blackie Academic & Professional.

Bronk Ramsey, C. (2009). Bayesian analysis of radiocarbon dates. *Radiocarbon, 51*(1), pp. 337 - 360.

Bryn, P., Berg, K., Forsberg, C. F., Solheim, A., Kvalstad, T. J. (2005a). Explaining the Storegga slide. *Marine and Petroleum Geology, 22*, 11–19. doi: 10.1016/j.marpetgeo.2004.12.003

Bryn, P., Berg, K., Stoker, M., Haflidason, H., Solheim, A. (2005b). Contourites and their relevance for mass wasting along the Mid-Norwegian Margin. *Marine and Petroleum Geology, 22*, pp. 85 - 96.

Buforn, E., Bezzeghoud, M., Udías, A., Pro, E. (2004). Seismic sources on the Iberia-African plate boundary and their tectonic implications. *Pure and Applied Geophysics, 161*, pp. 623 - 646.

Buforn, E., Degaldeano, C., Udias, A. (1995). Seismotectonics of the Ibero-Maghrebian region. *Tectonophysics, 248*(3 - 4), pp. 247 - 261.

Bugge, T., Befring, S., Belderson, R. H., Eidvin, T., Jansen, E., Kenyon, N. H., Holtedahl, H., Sejrup, H. (1987). A giant three-stage submarine slide off Norway. *Geo-Marine Letters, 7*, 191 - 198. doi: 10.1007/BF02242771

Bugge, T., Belderson, R., Kenyon, N. (1988). The Storegga slide. *Philosophical Transactions of the Royal Society A, 325*, 357 – 388.

Bull, S., Cartwright, J., Huuse, M. (2009). A review of kinematic indicators from mass-transport complexes using 3D seismic data. *Marine and Petroleum Geology, 26*, pp. 1132 - 1151.

Buma, J., Van Asch, T. (1996). Slide (Rotational). In R. Dikau, Brunsden, D., Schrott, L., Ibsen, M-L. (Ed.), *Landslide Recoginition. Identification, Movement and Causes* (pp. 29 - 42): John Wiley & Sons. Chichester.

Burland, J. (1990). On the compressibility and shear strength of natural clays. *Geotechnique, 40*(3), pp. 329 - 378.

Burrough, P., McDonell, R. (1998). *Principles of Geographical Information Systems*. New York: Oxford University Press.

Cabral, J. (1995). Neotectónica em Portugal Continental. *memórias do Institutito Geológico e Mineiro, 31*, 265 pp.

Cacho, I., Grimalt, J., Sierro, F. J., Shackleton, N., Canals, M. (2000). Evidence for enhanced Mediterranean thermohaline circulation during rapid climatic coolings. *Earth and Planetary Science Letters, 183*, pp. 417 - 429.

Calcaterra, D., de Riso, R., Di Martire, D. (2004). *Assessing shallow debris slide hazard in the Agnano Plain (Naples, Italy) using SINMAP, a physically based slope stability model*. Paper presented at the Symposium on landslides, Rio de Janeiro.

Camerlenghi, A., Urgeles, R., Fantoni, L. (2010). A Database on Submarine Landslides of the Mediterranean Sea. In D. Mosher, L. Moscardelli, R. Shipp, J. Chaytor, C. Baxter, H. Lee & R. Urgeles (Eds.), *Submarine Mass Movements and Their Consequences, Advances in Natural and Technological Hazards Research* (Vol. 28, pp. 491 - 501). Dordrecht (The Netherlands): Springer.

Canals, M., Lastras, G., Urgeles, R., Casamor, J., Mienert J., Cattaneo, A., De Batist, M., Haflidason, H., Imbo, Y., Laberg, J., Locat, J., Long, D., Longva, O., Masson, D., Sultan, N., Trincardi, F., Bryn, P. (2004). Slope failure dynamics and impacts from seafloor and shallow sub-seafloor geophysical data: case studies from the COSTA project. *Marine Geology*, *213*, 9 – 72. doi: 10.1016/j.margeo.2004.10.001

Canilho, M. (1989). Elementos de geoquímica das rochas do macIço igneo de Sines. *Ciências da Terra, 10*, pp. 65 - 80.

Caralp, M. (1988). Late Glacial to Recent deep-Sea benthic foraminifera from the Northeastern Atlantic Cadiz Gulf and Western Mediterranean Alboran Sea. Paleoceanographic results. *Marine Micropaleontology*, *13*, pp. 265 - 289.

Caris-Hips. (2013). User Guide. In N. Fredericton, Canada (Ed.), (pp. 552 pp.).

Carlson, P., Karl, H. (1988). Development of large submarine canyons in the Bering Sea, indicated by morphologic, seismic, and sedimentologic characteristics. *Geologic Society American Bulletin, 100*, 1594 - 1615.

Carrara, A., Cardinali, M., Detti, R., Guzzetti, F., Pasqui, V., Reichenbach, P. (1991). GIS techniques and statistical models in evaluating landslide hazard. *Earth Surf Process Landf., 16*, 427–445.

Carson, M. A., Kirkby, M. J. (1975). *Hillslope Form and Processes - 2nd ed.* Malta: Cambridge University Press.

Casagrande, A. (1936). Characteristic of cohesionless soils affecting the stability of slope and earth fill. *Journal of the Boston society of Civil Engineering*, pp. 13 - 32.

Casalbore, D. (2018). Volcanic Islands and Seamounts. *Submarine Geomorphology Springer Geology. Cham: Springer*, pp. 333 - 347. doi: https://doi.org/10.1007/978-3-319-57852-1_17

Casalbore, D., Bosman, A., Casas, D., Chiocci, F., Martorelli, E., Ridente, D. (2019). Morphological Variability of Submarine Mass Movements in the Tectonically–Controlled Calabro–Tyrrhenian Continental Margin (Southern Italy). *Geosciences, 9*(43). doi: 10.3390/geosciences9010043

Casalbore, D., Romagnoli, C., Bosman, A., Chiocci, F. (2011). Potential tsunamigenic landslides at Stromboli Volcano (Italy): Insight from marine DEM analysis. *Geomorphology, 126*, pp. 42 - 50.

Casas, D., Casalbore, D., Yenes, M., Urgeles, R. (2015). Submarine mass movements around the Iberian Peninsula. The building of continental margins through hazardous processes. *Boletín Geológico y Minero, 126*(2 - 3), pp. 257 - 278.

Casas, D., Chiocci, F., Casalbore, D., Ercilla, G., Ortiz De Urbina, J. (2016). Magnitude-frequency distribution of submarine landslides in the Gioia Basin (Southern Tyrrhenian Sea). *Geo-Marine Letters, 36*, pp. 405 - 414. doi: 10.1007/S00367-016-0458-2

Casas, D., Ercilla, G., Estrada, F., Alonso, B., Baraza, J., Lee, H., Kayen, R., Chiocci, F. (2004). Physical and Geotechnical Properties and Assessment of Sediment Stability on the Continental Slope and Basin of the Bransfield Basin (Antarctica Peninsula). *Marine Georesources & Geotechnology, 22*(4), 253 - 278.

Casas, D., Ercilla, G., Yenes, M., Estrada, F., Alonso, B., García, M., Somoza, L. (2011). The Baraza Slide: model and dynamics. *Marine Geophysical Research, 32*(1-2), pp. 245 - 256.

Cattaneo, A., Jouet, G., Charrier, S., Théreau, E., Riboulot, V. (2014). Submarine Landslides and Contourite Drifts along the Pianosa Ridge (Corsica Trough, Mediterranean Sea). In S. Krastel & J.-H. Behrmann, Völker, D., Stipp, M., Berndt, C., Urgeles, R., Chaytor, J., Huhn, K., Strasser, M., Harbitz, C.B. (Eds.), *Submarine Mass Movements and Their Consequences, Advances in Natural and Technological Hazards Research* (Vol. 37, pp. 435 – 445).

Cayre, O., Lancelo, Y., Vincent, E., Hall, M. (1999). Paleoceanographic reconstructions from planktonic foraminifera off the Iberian Margin; Temperature, salinity, and Heinrich Events. *Paleoceanography, 14*, pp. 384 - 396.

CEN-ISO/TS-17892-5. (2004). Geotechnical Investigation and Testing - Laboratory Testing of Soil - Part 5: Incremental loading oedometer test *CEN, Brussels*.

CEN-ISO/TS-17892-9. (2004). Geotechnical Investigation and Testing - Laboratory Testing of Soil - Part 9: Consolidated Triaxial Compression on Water Saturated Soil. *CEN, Brussels*.

CEN-ISO/TS-17892-10. (2004). Geotechnical Investigation and Testing - Laboratory Testing of Soil - Part 10: Direct Shear Tests. *CEN, Brussels*.

Ceramicola, S., Praeg, D., Coste, M., Forlin, E., Cova, A., Colizza, E., Critelli, S. (2014). Submarine Mass-Movements along the Slopes of the Active Ionian Continental Margins and Their Consequences for Marine Geohazards (Mediterranean Sea). In S. Krastel & J.-H. Behrmann, Völker, D., Stipp, M., Berndt, C., Urgeles, R., Chaytor, J., Huhn, K., Strasser, M., Harbitz,

C.B. (Eds.), *Submarine Mass Movements and Their Consequences, Advances in Natural and Technological Hazards Research* (Vol. 37, pp. 295-306).

Ceramicola, S., Rebesco, M., De Batist, M., Khlystov, O. (2001). Seismic evidence of small-scale lacustrine drifts in Lake Baikal (Russia). *Marine Geophysical Researches, 22*, pp. 445 - 464.

Cherubin, L., Carton, X., Paillet, J., Morel, Y., Serpatte, A. (2000). Instability of the Mediterranean Water undercurrents southwest of Portugal: effects of baroclinicity and topography. *Oceanological Acta, 23* (5), pp. 551 - 573.

Chiocci, F., Casalbore, D. (2017). Unexpected fast rate of morphological evolution of geologically-active continental margins during Quaternary: examples from selected areas in the Italian seas. *Marine and Petroleum Geology, 82*, pp. 154 - 162.

Choffat, P. (1887). Recherches sur les terrains secondaires au Sud du Sado. *Comunicações da Comissão de Trabalhos Geológicos de Portugal, I*, pp. 222 - 312.

Cita, M. B. (2001). The Messinian salinity crisis in the Mediterranean. In U. Briegel & W. Xiao (Eds.), *Paradoxes in Geology* (pp. 353 - 360): Elsevier Science.

Collico, S., Arroyo, M., Urgeles, R., Gràcia, E., Devincenzi, M., Peréz, N. (2020). Probabilistic mapping of earthquake-induced submarine landslide susceptibility in the South-West Iberian margin. *Marine Geology, 429*. doi: https://doi.org/10.1016/j.margeo.2020.106296

Coppier, G. (1982). *Tectonique et sédimentation tertiaires sur la marge sud-portugaise.* Thèse 3ème cycle, Université Paris VI.

Corominas, J. (1996). Debris Slide. In R. Dikau, Brunsden, D., Schrott, L., Ibsen, M-L. (Ed.), *Landslide Recognition. Identification, Movement and Causes* (pp. 97 - 102): John Wiley & Sons. Chichester.

Corominas, J., Remondo, J., Farias, P., Estevão, M., Zêzere, J., Diaz de Terán, J., Dikau, R., Schrott, L., Moya, J., González, A. (1996). Debris Flow. In R. Dikau, Brunsden, D., Schrott, L., Ibsen, M-L. (Ed.), *Landslide Recognition. Identification, Movement and Causes* (pp. 161 - 180): John Wiley & Sons. Chichester.

Cosgrove, J. (2001). Hydraulic fracturing during the formation and deformation of a basin: a factor in the dewatering of low-permeability sediments. *AAPG Bulletin, 85*, pp. 737 - 748.

Costa, P. J. M., Andrade, C., Freitas, M. C., Oliveira, M. A., Silva, C., Omira, R., Taborda, R., Baptista, M. A., Dawson, A. (2011). Boulder deposition during major tsunami events. *Earth Surface Processes and Landforms, 36*, pp. 2054 - 2068.

Croudace, I. W., Rindby, A., Rothwell, R. G. (2006). ITRAX: description and evaluation of a new multi-function X-ray core scanner. In R. G. Rothwell (Ed.), *New techniques in sediment core analysis* (pp. 51 - 63): Geological Society Special Publication.

Crozier, M. J. (1984). Field Assessment of Slope Instability. In D. Brunsden & D. Prior (Eds.), *Slope Instability* (pp. 103 – 142): Wiley. Chichester.

Crozier, M. J., Glade, T. (2004). Landslide Hazard and Risk: Issues, Concepts and Approach. In T. A. Glade, M; Crozier, M. J (Ed.), *Landslide Hazard and Risk* (pp. 802). Chichester: John Wiley & Sons Ltd,.

Cruden, D. (1991). A Simple Definition of a Landslide. *Bulletin of the international Association of Engineering Geology, No. 43*, pp. 27– 29.

Cruden, D., Varnes, D. J. (1996). Landslide Types and Processes. In K. Turner & R. Schuster (Eds.), *Landslides Investigation and Mitigation* (Vol. 3, pp. 129 - 177). Washington: National Academy Press.

Cunha, T., Watts, A., Pinheiro, L., Alves, T. (2009). *West Iberia margin subsidence - uplift history: constraints from seismic data and well and pseudo-well backstripping*. Paper presented at the 6° Simposio sobre el Margen Ibérico Atlántico, Spain, Oviedo.

Custódio, S., Dias, N., Carrilho, F., Gongora, E., Rio, I., Marreiros, C., Morais, I., Alves, P., Matias, L. (2015). Earthquakes in western Iberia: improving the understanding of lithospheric deformation in a slowly deforming region. *Geophysical Journal International 203*, pp. 127–145. doi: 10.1093/gji/ggv285

Custódio, S., Lima, V., Vales, D., Cesca, S., Carrilho, F. (2016). Imaging active faulting in a region of distributed deformation from the joint clustering of focal mechanisms and hypocentres: Application to the Azores–western Mediterranean region. *Tectonophysics, 676*, pp. 70 - 89.

Dai, F., Lee, C., Xu, Z. (2001). Assessment of landslide susceptibility on the natural terrain of Lantau Island, Hong Kong. *Environ Geology, Vol. 40*(3), pp. 381 - 391.

Dawson, A., Hindson, R., Andrade, C., Freitas, M. C., Parish, R., Bateman, M. (1995). Tsunami sedimentation associated with the Lisbon earthquake of November 1st 1755 AD: Boca do Rio, Algarve, Portugal. *Holocene, 5*(2), pp. 209 - 215.

de Abreu, L., Shackleton, N., Schönfeld, J., Hall, M., Chapman, M. (2003). Millennial-scale oceanic climate variability off the W Iberian margin during the last two glacial periods. *Marine Geology, 196*, pp. 1 - 20.

de Weger, W., Hernández-Molina, F. J., Flecker, R., Sierro, F. J., Chiarella, D., Krijgsman, W., Amine Manar, A. (2020). Late Miocene contourite channel system reveals intermittent overflow behavior. *Geology, 48*. doi: https://doi.org/10.1130/G47944.1

Dewey, J., Helman, M., Turco, E., Hutton, D., Knott, S. (1989). Kinematics of the Western Mediterranean. In M. Coward, D. Dietrich & R. Park (Eds.), *Alpine Tectonics* (Vol. 45, pp. 265 - 283): Geological Society Special Publication.

Dietrich, W., Montgomery, D. (1998). SHALSTAB: A digital terrain model for mapping shallow landslide potencial. *National Council of the Paper Industry for Air and Stream Improvement (NCASI). Technical Report*, 26 p.

Diez, S., Gràcia, E., Gutscher, M.-A., Matias, L., Mulder, T., Terrinha, P., Somoza, L., Zitellini, N., De Alteriis, G., Henriet, J.-P., Dañobeitia, J. (2006). *Bathymetric map of the Gulf of Cadiz, NE*

Atlantic Ocean: The SWIM multibeam compilation. Paper presented at the 250th anniversary of the 1755 Lisbon earthquake. 5th Symposium on the Iberian Atlantic Margin, Aveiro, Portugal.

Dikau, R., Brunsden, D., Schrott, L., Ibsen, M.-L. (1996a). *Landslide Recognition. Identification, Movement and Causes*. Chichester: John Wiley & Sons.

Dikau, R., Schrott, L., Dehn, M. (1996b). Topple. In R. Dikau, D. Brunsden, L. Schrott & M.-L. Ibsen (Eds.), *Landslide Recognition. Identification, Movement and Causes* (pp. 29 - 41): John Wiley & Sons. Chichester.

Dingle, R. (1977). The anatomy of a large submarine slump on a sheared continental margin (SE Africa). *Geological Society of London Journal, 134*, pp. 293 - 310.

Dott, R. (1963). Dynamics of subaqueous gravity depositional processes. *AAPG Bulletin, 47*, pp. 104 - 128.

Driscoll, N., Hogg, J., Christie-Blick, N., Karner, G. (1995). Extensional tectonics in the Jeanne d'Arc Basin, offshore Newfoundland: implications for the timing of breakup between Grand Banks and Iberia. In R. Scrutton, M. Stoker, G. Shimmield & A. Tudhope (Eds.), *The Tectonics, Sedimentation and Paleoceanography of the North Atlantic Region* (Vol. 90, pp. 1 - 28): Geological Society Special Publication.

Duarte, D., Magalhães, V. H., Terrinha, P., Ribeiro, C., Madureira, P., Pinheiro, L., Benazzouz, O., Kim, J.-H., Duarte, H. (2017). Identification and characterization of fluid escape structures (pockmarks) in the Estremadura Spur, West Iberian Margin. *Marine and Petroleum Geology, 82*, pp. 414-423.

Duarte, J., Rosas, F., Terrinha, P., Gutscher, M.-A., Malavieille, J., Silva, S., Matias, L. (2011). Thrust-wrench interference tectonics in the Gulf of Cadiz (Africa-Iberia plate boundary in the north-east Atlantic): insights from analog models. *Marine Geology, 289*, 135 - 149 pp.

Duarte, J., Rosas, F., Terrinha, P., Schellart, W., Boutelier, D., Gutscher, M. A., Ribeiro, A. (2013). Are subduction zones invading the Atlantic? Evidence from the SW Iberia margin. *Geology, 41*, 839 – 842. doi: 10.1130/G34100.1

Ducassou, E., Fournier, L., Sierro, F., Alvarez Zarikian, C., Lofi, J., Flores, J., Roque, C. (2016). Origin of the large Pliocene and Pleistocene debris flows on the Algarve margin. *Marine Geology, 377*, pp. 58 - 76

Ercilla, G., Alonso, B. (1996). Quaternary siliciclastic sequence stratigraphy of western Mediterranean passive and tectonically active margins: the role of global versus local controlling factors. *Geological Society of London, Special Publication, 117*(1), pp. 125 - 137.

Ercilla, G., Alonso, B., Baraza, J. (1992). Sedimentary evolution of the Northwestern Alboran Sea during the Quaternary. *Geo-Marine Letters, 12*, pp. 144 - 149.

Ercilla, G., Casas, D., Estrada, F., Vázquez, J., Iglesias, J., García, M., Gómez, M., Acosta, J., Gallart, J., Maestro-González, A., Team, M. (2008a). Morphosedimentary features and recent

depositional architectural model of the Cantabrian continental margin. *Marine Geology, 247*, 61 – 83. doi: 10.1016/j.margeo.2007.08.007

Ercilla, G., Casas, D., Vázquez, J. T., Iglesias, J., Somoza, L., Juan, C., Medialdea, T., León, R., Estrada, F., García-Gil, S., Farran, M., Bohoyo, F., García, M., Maestro, A., ERGAP, P., Cruise, T. (2011). Imaging the recent sediment dynamics of the Galicia Bank region (Atlantic, NW Iberian Peninsula). *Marine Geophysical Research, 32*(1 - 2), pp. 99 - 126. doi: http://dx.doi.org/10.1007/s11001-011-9129-x

Ercilla, G., García-Gil, S., Estrada, F., Gràcia, E., Vizcaino, A., Váquez, J., Díez, S., Vilas, F., Casas, D., Alonso, B., Dañobeitia, J., Farran, M. (2008b). High-resolution seismic stratigraphy of the Galicia Bank Region and neighbouring abyssal plains (NW Iberian continental margin). *Marine Geology, 249*, pp. 108 - 127.

Ercilla, G., Juan, C., Hernández-Molina, J., Bruno, M., Estrada, F., Alonso, B., Casas, D., Farran, M., Llave, E., García, M., Vázquez, J., D'Acremont, E., Gorini, C., Palomino, D., Valencia, J., El Moumni, B., Ammar, A. (2016). Significance of bottom currents in deep-sea morphodynamics: An example from the Alboran Sea. *Marine Geology, 378*, pp. 157 - 170.

Ercilla, G., Juan, C., Periáñez, R., Alonso, B., Abril, J. M., Estrada, F., Casas, D., Vázquez, J. T., d'Acremont, E., Gorini, C., El Moumni, B., Do Couto, D., Valencia, J. (2019). Influence of alongslope processes on modern turbidite systems and canyons in the Alboran Sea (southwestern Mediterranean). *Deep Sea Research. Part I: Oceanographic Research Papers, 144*, pp. 1 - 16.

Estrada, F., Ercilla, G., Alonso, B. (1997). Pliocene–Quaternary tectonic–sedimentary evolution of the NE Alboran Sea (SW Mediterranean Sea). *Tectonophysics, 282*, pp. 423 - 442.

Evans, D., Harrison, Z., Shannon, P., Laberg, J., Nielsen, T., Ayers, S., Holmes, R., Hoult, R., Lindberg, B., Haflidason, H., Long, D., Kuijpers, A., Andersen, E., Bryn, P. (2005). Palaeoslides and other mass failures of Pliocene to Pleistocene age along the Atlantic continental margin of NW Europe. *Marine and Petroleum Geology, 22*, pp. 1131 - 1148.

Eynaud, F., de Abreu, L., Voelker, A., Schönfeld, J., Salgueiro, E., Turon, J.-L., Penaud, A., Toucanne, S., Naughton, F., Sánchez Goñi, M., Malaizé, B., Cacho, I. (2009). Position of the Polar Front along the western Iberian margin during key cold episodes of the last 45 ka. *Geochemestry, Geophysics, Geosystems, 10*(7), 21 pp. doi: https://doi.org/10.1029/2009GC002398

Faugères, J.-C., Gonthier, E., Stow, D. (1984). Contourite drift molded by deep Mediterranean Outflow. *Geology, 12*, pp. 296 - 300.

Faugères, J.-C., Imbert, P., Mézerais, M. L., Cremer, M. (1998). Seismic patterns of a muddy contourite fan (Vema Channel, South Brazilian Basin) and a sandy distal turbidite deep-sea fan (Cap Ferret system, Bay of Biscay): a comparison. *Sedimentary Geology, 115*, pp. 81 - 110.

Faugères, J.-C., Mezerais, M. L., Stow, D. (1993). Contourite drift types and their distribution in the North and South Atlantic Ocean basins. *Sedimentary Geology, 82*, pp. 189 - 203.

Faugères, J.-C., Mulder, T. (2011). Contour Currents and Contourite Drifts. In H. Hüneke & T. Mulder (Eds.), *Deep-Sea Sediments* (Vol. 63, pp. 750): Elsevier.

Faugères, J.-C., Stow, D., Imbert, P., Viana, A. (1999). Seismic features diagnostic of contourite drifts. *Marine Geology, 162*, pp. 1 - 38.

Faugères, J., Stow, D. (2008). Contourite drifts: Nature, evolution and controls. In M. Rebesco, . & A. Camerlenghi (Eds.), *Contourites. Developments in Sedimentology* (Vol. 60, pp. 258 - 288).

Fawcett, T. (2006). An introduction to ROC analysis. *Pattern Recogn. Letters, 27*, pp. 861 – 874.

Figueiredo, P., Cabral, J., Rockwell, T. (2013). Recognition of Pleistocene marine terraces in the southwest of Portugal (Iberian Peninsula): evidences of regional Quaternary uplift. *Annals of Geophysics, 56*(6), pp. 1 - 19. doi: 10.4401/ag-6276

Flageollet, J. C., Weber, D. (1996). Fall. In R. Dikau, D. Brunsden, L. Schrott & M.-L. Ibsen (Eds.), *Landslide Recognition. Identification, Movement and Causes* (pp. 13 - 28): John Wiley & Sons. Chichester.

Flecker, R., Krijgsman, W., Capella, W., Martins, C., De, C., Demitrieva, E., Mayser, J., Marzocchi, A., Modestu, S., Ochoa Lozano, D., Simon, D., Tulbure, M., Van den Berg, B., Van der Schee, M., de Lange, G., Ellam, R., Govers, R., Gutjahr, M., Hilgen, F., Kouwenhoven, T., Lofi, J., Meijer, P., Sierro, F., Bachiri, N., Barboun, N., Chakor Alami, A., Chacon, B., Flores, J., Gregory, J., Howard, J., Lunt, D., Ochoa, M., Pancost, R., Vincent, S., Yousfi, M. (2015). Evolution of the late Miocene Mediterranean-Atlantic gateways and their impact on regional and global environmental Change. *Earth-Science Reviews, 150*, pp. 365 - 392.

Fonseca, M. (2009). *The use of seismic wave velocities in the measurement of stiffness of a residual soil*. Msc Thesis, Faculty of Enginnering of the University of Porto, Porto.

Fotheringham, S., O'Kelly, M. (1989). *Spatial Interaction Models: Formulations and Applications*. Dordrecht / Boston / London: Kluwer Academic Publishers.

Fredlund, D., Krahn, J. (1977). Comparison of slope stability methods of analysis. *Canadian Geotechnical Journal, 14*, 429 – 439.

Fukao, Y. (1973). Thrust faulting at a lithospheric plate boundary the Portugal earthquake of 1969. *Earth and Planetary Science Letters, 18*(2), pp. 205 - 216.

Gamberi, F., Dalla Valle, G., Foglini, F., Rovere, M., Trincardi, F. (2020). Submarine Landslides on the Seafloor: Hints on Subaqueous Mass-Transport Processes From the Italian Continental Margins (Adriatic and Tyrrhenian Seas, Offshore Italy). In K. Ogata, A. Festa & G. A. Pini (Eds.), *Submarine Landslides: Subaqueous Mass Transport Deposits from Outcrops to Seismic Profiles* (Vol. 246, pp. 339 - 356): John Wiley & Sons.

Gamboa, D., Alves, T., Cartwright, J., Terrinha, P. (2010). MTD distribution on a 'passive' continental margin: The Espírito Santo Basin (SE Brazil) during the Palaeogene. *Marine and Petroleum Geology, 27*(7), pp. 1311 - 1324.

Garcia-Castellanos, D., Villaseñor, A. (2011). Messinian salinity crisis regulated by competing tectonics and erosion at the Gibraltar arc. *Nature, 480*, pp. 359 - 365.

Garcia-Mondejar, J. (1989). Strike-slip subsidence of the Basque-Cantabrian Basin of northern Spain and its relationship to Aptian-Albian opening of Bay of Biscay. In A. Tankard & H. Balkwill (Eds.), *Extensional tectonics and stratigraphy of the North Atlantic margins* (Vol. 46, pp. 395 - 409): American Association of Petroleum Geologists.

García, M., Alonso, B., Ercilla, G., Gràcia, E. (2006). The tributary valley systems of the Almeria Canyon (Alboran Sea, SW Mediterranean): sedimentary architecture. *Marine Geology, 226*(3 - 4), pp. 207 - 223.

García, M., Hernández-Molina, F. J., Alonso, B., Vázquez, J., Ercilla, G., Llave, E., Casas, D. (2015). Erosive sub-circular depressions on the Guadalquivir Bank (Gulf of Cadiz): Interaction between bottom current, mass-wasting and tectonic processes. *Marine Geology, 378*, pp. 5 - 19.

García, M., Hernández-Molina, F. J., Llave, E., Stow, D., León, R., Fernández-Puga, M., Díaz del Río, V., Somoza, L. (2009). Contourite erosive features caused by the Mediterranean Outflow Water in the Gulf of Cadiz: Quaternary tectonic and oceanographic implications. *Marine Geology, 257*, pp. 24 - 40.

García, M., Llave, E., Hernández-Molina, F. J., Lobo, F., Ercilla, G., Alonso, B., Casas, D., Mena, A., Fernández-Salas, L. (2020). The role of late Quaternary tectonic activity and sea-level changes on sedimentary processes interaction in the Gulf of Cadiz upper and middle continental slope (SW Iberia). *Marine and Petroleum Geology, 121*. doi: https://doi.org/10.1016/j.marpetgeo.2020.104595

Gargani, J., Rigollet, C. (2007). Mediterranean Sea level variations during the Messinian Salinity Crisis. *Geophysical Research Letters, 34*(10), L10405. doi: 10.1029/2007GL029885

Geist, E. (2000). Origin of the 17 July 1998 Papua New Guinea tsunami; earthquake or landslide. *Seismological Research Letters, 71*, 344 – 351.

Geldmacher, J., Hoernle, K., Klügel, A., Wombacher, F., Berning, B. (2006). Origin and geochemical evolution of the madeira-tore rise (eastern north atlantic). *Journal of Geophysical Research: Solid Earth (1978-2012), 111*(B9).

Gonthier, E., Faugères, J.-C., Stow, D. (1984). Contourite facies of the Faro Drift, Gulf of Cadiz. In D. Stow & D. Piper (Eds.), *Fine Grained Sediments, Deepwater Processes and Facies. Special Publication* (Vol. 15, pp. 275 - 291). London: Geological Society.

Govers, R. (2009). Choking the Mediterranean to dehydration: The Messinian salinity crisis. *Geology, 37*(2), pp. 167–170. doi: 10.1130/G25141A.1

Govin, A., Holzwarth, U., Heslop, D., Keeling, L., Zabel, M., Mulitza, S., Collins, J., Chiessi, C. (2012). Distribution of major elements in Atlantic surface sediments (36°N - 49°S): Imprint of terrigenous input and continental weathering. *Geochemistry Geophysics Geosystems, 13*(1), 23 pp. doi: 10.1029/2011GC003785

Gràcia, E., Dañobeitia, J., Vergés, J., Cordoba, D., Parsifal. (2003). Mapping Active Faults at the SW Iberia Margin (38º - 36º) from High-resolution Swath-Bathymetry Data. Implications for Earthquake Hazard Assessment. *Geology 31*(1), pp. 83 - 86.

Gràcia, E., Vizcaino, A., Escutia, C., Asioli, A., Rodés, A., Pallàs, R., Garcia-Orellana, J., Lebreiro, S., Goldfinger, C. (2010). Holocene earthquake record offshore Portugal (SW Iberia): testing turbidite paleoseismology in a slow-convergence margin. *Quaternary Science Reviews, 29*, 1156 – 1172.

Graham, J. (1984). Methods of Stability Analysis. In D. Brunsden & D. Prior (Eds.), *Slope Instability* (pp. 171 - 215): Wiley. Chichester.

Grange, M., Scharer, U., Merle, R., Girardeau, J., Cornen, G. (2010). Plume - Lithosphere Interaction during Migration of Cretaceous Alkaline Magmatism in SW Portugal: Evidence from U-Pb Ages and Pb-Sr-Hf Isotopes. *Journal of Petrology, 51*(5), pp. 1143 - 1170.

Gross, F., Krastel, S., Chiocci, F., Ridente, D., Bialas, J., Schwab, J., Beier, J., Cukur, D., Winkelmann, D. (2014). Evidence for Submarine Landslides Offshore Mt. Etna, Italy In S. Krastel & J.-H. Behrmann, Völker, D., Stipp, M., Berndt, C., Urgeles, R., Chaytor, J., Huhn, K., Strasser, M., Harbitz, C.B. (Eds.), *Submarine Mass Movements and Their Consequences, Advances in Natural and Technological Hazards Research* (Vol. 37).

Gutscher, M.-A., Malod, J., Rehault, J.-P., Contrucci, I., Klingelhoefer, F., Mendes-Victor, L., Spakman, W. (2002). Evidence for active subduction beneath Gibraltar. *Geology, 30*(12), pp. 1071 - 1074.

Guzzetti, F. (2005). *Landslide hazard and risk assessment.* PhD Thesis, University of Bonn.

Guzzetti, F., Carrara, A., Cardinali, M., Reichenbach, P. (1999). Landslide hazard evaluation: a review of current techniques and their application in a multi-scale study, Central Italy. *Geomorphology, 31*, 181 - 216.

Haflidason, H., Lien, R., Sejrup, H., Forsberg, C., Bryn, P. (2005). The dating and morphometry of the Storegga Slide. *Marine and Petroleum Geology, 22*, pp. 123 - 136. doi: 10 .1016 /j .marpetgeo .2004 .10 .008

Haflidason, H., Sejrup, H., Nygard, A., Mienert, J., Bryn, P., Lien, R., Forsberg, C., Berg, K., Masson, D. (2004). The Storegga slide: architecture, geometry and slide development. *Marine Geology, 213*, pp. 201 - 234.

Hampton, M., Bouma, A., Carlson, P., Molnia, B., Clukey, E., Sangrey, D. (1978). *Quantitative study of slope instability in the Gulf of Alaska*. Paper presented at the 10th Annual Offshore Technology Conference, Houston, Texas.

Hampton, M., Lee, H., Locat, J. (1996). Submarine landslides. *Reviews of Geophysics, 34*, pp. 33 – 59. doi: 10.1029/95RG03287

Hanquiez, V., Mulder, T., Toucanne, S., Lecroart, P., Bonnel, C., Marchès, E., Gonthier, E. (2010). The sandy channel-lobe depositional systems in the Gulf of Cadiz: Gravity processes forced by contour current processes. *Sedimentary Geology, 229*, pp. 110 - 123.

Haq, B., Hardenbol, J., Vail, P. (1987). Chronology of Fluctuating Sea Levels since the Triassic. *Science, 235*, pp. 1156 -1167.

Hayward, B., Sabaa, A., Kawagata, S., Grenfell, H. (2009). The Early Pliocene recolonisation of the deep Mediterranean Sea by benthic foraminifera and their pulsed Late Pliocene-Middle Pleistocene decline. *Marine Micropaleontology, 71*, pp. 97 - 112.

Head, K. (1982). *Manual of Soil Laboratory Testing - Permeability, Shear Strength and Compressibility Tests* (Vol. 2). New York: John Wiley & Sons.

Heezen, B. (1959). Dynamic processes of abyssal sedimentation: erosion, transportation and redeposition on the deep-sea floor. *Geophysical Journal, 2*, pp. 142 - 163.

Heezen, B., Ewing, M. (1952). Turbidity currents and submarine slumps, and the 1929 Grand Banks Earthquake. *American Journal of Science, 250*, 775 - 793.

Heezen, B., Hollister, C. (1964). Deep sea current evidence from abyssal sediments. *Marine Geology, 1*, pp. 141 - 174.

Heezen, B., Hollister, C., Ruddiman, W. (1966). Shaping of- the Continental Rise by Deep Geostrophic Contour Currents. *Science, 12*, 502 - 508.

Heezen, B., Tharp, M., Ewing, M. (1959). The floors of the ocean. *The North Atlantic Geological Society America, Special Papers, 65*, 122 pp.

Heinrich, H. (1988). Origin and consequences of cyclic rafting in the northeast Atlantic Ocean during the past 130,000 years. *Quaternary. Research, 29*, pp. 142 - 152.

Henrich, R., Hanebuth, T., Krastel, S., Neubert, N., Wynn, R. (2008). Architecture and sediment dynamics of the Mauritania Slide Complex. *Marine and Petroleum Geology, 25*, 17 - 33.

Hernández-Molina, F. J., Ercilla, G., Casas, D., team, M. (2014a). Rasgos erosivos y depósitos arenosos generados por la MOW alrededor de iberia: implicaciones paleoceanográficas, sedimentarias y económicas *Informe Científico Campaña Oceanográfica MOWER* (pp. 111 pp).

Hernández-Molina, F. J., Llave, E., Somoza, L., Fernández-Puga, M. C., Maestro, A., León, R., Medialdea, T., Barnolas, A., García, M., Díaz del Río, V., Fernández-Salas, L. M., Vázquez, J. T., Lobo, F., Alveirinho Dias, J. M., Rodero, J., Gardner, J. (2003). Looking for clues to paleoceanographic imprints: a diagnosis of the Gulf of Cádiz contourite depositional systems. *Geology, 31*, pp. 19 - 22. doi: 10.1130/0091- 7613(2003)0312.0.CO;2

Hernández-Molina, F. J., Llave, E., Stow, D. (2008a). Continental slope contourites. In M. Rebesco & A. Camerlenghi (Eds.), *Contourites. Developments in Sedimentology*. (pp. 379 - 408). Amsterdam: Elsevier.

Hernández-Molina, F. J., Llave, E., Stow, D., García, M., Somoza, L., Vázquez, J., Lobo, F., Maestro, A., Díaz del Río, V., Léon, R., Medialdea, T., Gardner, J. (2006). The contourite depositional system of the Gulf of Cadiz: a sedimentary model related to the bottom current activity of the Mediterranean outflow water and its interaction with the continental margin. *Deep-Sea Research, 53*(II), 1420 - 1463.

Hernández-Molina, F. J., Maldonado, A., Stow, D. (2008b). Abyssal plain contourites. In M. Rebesco & A. Camerlenghi (Eds.), *Contourites. Developments in Sedimentology* (pp. 345 - 378). Amsterdam: Elsevier.

Hernández-Molina, F. J., Paterlini, M., Violante, R., Marshall, P., de Isasi, M., Somoza, L., Rebesco, M. (2009). Contourite depositional system on the Argentine slope: an exceptional record of the influence of Antarctic water masses. *Geology, 37*, pp. 507 - 510.

Hernández-Molina, F. J., Serra, N., Stow, D., Llave, E., Ercilla, G., Van Rooij, D. (2011). Along-slope oceanographic processes and sedimentary products around the Iberian margin. *Geo-Marine Letters, 31*(5), 315 - 341.

Hernández-Molina, F. J., Sierro, F., Llave, E., Roque, C., Stow, D., Williams, T., Lofi, J., Van der Schee, M., Arnáiz, A., Ledesma, S., Rosales, C., Rodríguez-Tovar, F., Pardo-Igúzquiza, E., Brackenridge, R. (2016a). Evolution of the gulf of Cadiz margin and southwest Portugal contourite depositional system: Tectonic, sedimentary and paleoceanographic implications from IODP expedition 339. *Marine Geology, 377*, pp. 7 - 39. doi: https://doi.org/10.1016/j.margeo.2015.09.013

Hernández-Molina, F. J., Somoza, L., Vázquez, J. T., Lobo, F., Fernández-Puga, M. C., Llave, E., Díaz del Río, V. (2002). Quaternary stratigraphic stacking patterns on the continental shelves of the southern Iberian Peninsula: their relationship with global climate and palaeoceanographic changes. *Quaternary International, 92*(1), pp. 5 - 23.

Hernández-Molina, F. J., Soto, M., Piola, A., Tomasini, J., Preu, B., Thompson, P., Badalini, G., Creaser, A., Violante, R., Morales, E., Paterlini, M., De Santa Ana, H. (2016b). A contourite depositional system along the Uruguayan continental margin: Sedimentary, oceanographic and paleoceanographic implications. *Marine Geology, 378*, pp. 333 - 349. doi: https://doi.org/10.1016/j.margeo.2015.10.008

Hernández-Molina, F. J., Stow, D., Alvarez-Zarikian, C., Acton, G., Bahr, A., Balestra, B., Ducassou, E., Flood, R., Flores, J., Furota, S., Grunert, P., Hodell, D., Jimenez-Espejo, F., Kim, J., Krissek, L., Kuroda, J., Li, B., Llave, E., Lofi, J., Lourens, L., Miller, M., Nanayama, F., Nishida, N., Richter, C., Roque, C., Pereira, H., Sanchez Goñi, M., Sierro, F., Singh, A., Sloss,

C., Takashimizu, Y., Tzanova, A., Voelker, A., Williams, T., Xuan, C. (2014b). Onset of Mediterranean Outflow into the North Atlantic. *Science, 344*(6189), 1244 - 1250.

Hernández-Molina, F. J., Stow, D., Alvarez-Zarikian, C., Scientists, E. I. (2013). IODP Expedition 339 in the Gulf of Cadiz and off West Iberia: decoding the environmental significance of the Mediterranean outflow water and its global influence. *Scientific Drilling, 16*, 1 - 11. doi: 10.5194/sd-16-1-2013

Hiscott, R., Wilson, R., Gradstein, F., Pujalte, V., García-Mondéjar, J., Boudreau, R., Wishart, H. (1990). Comparative stratigraphy and subsidence history of Mesozoic rift basins of North Atlantic. *AAPG Bulletin, 74*, pp. 60 - 76.

Hjelstuen, B., Eldholm, O., Faleide, J. (2007). Recurrent Pleistocene mega-failures on the SW Barents Sea margin. *Earth and Planetary Science Letters, 258*, pp. 605 - 618. doi: 10 .1016 /j .epsl .2007 .04 .025

Hollister, C. (1967). *Sediment distribution and deep circulation in the western North Atlantic.* PhD thesis, Columbia University, New York.

Hollister, C., Heezen, B. (1972). Geological effects of bottom currents: western North Atlantic. In A. Gordon (Ed.), *Studies in Physical Oceanography* (Vol. 2, pp. 37 - 66). New York: Gordon and Breach.

Hollister, C., McCave, I. N. (1984). Sedimentation under deep-sea storms. *Nature, 309*, pp. 220 - 225.

Horn, B. (1981). *Hill shading and the reflectance map.* Paper presented at the Proceedings IEEE.

Hovland, M., Judd, A. (1988). *Seabed Pockmarks and Seepages: Impact on Geology, Biology and the Marine Environment*. London: Graham & Trotman.

Hungr, O., Leroueil, S., Picarelli, L. (2014). The Varnes classification of landslide types, an update. *Landslides, 11*, 167 - 194.

Hunter, S., Wilkinson, D., Louarn, E., McCave, I. N., Rohling, E., Stow, D., Bacon, S. (2007). Deep Western Boundary Current dynamics and associated sedimentation on the Eirik Drift, Southern Greenland Margin. *Deep-Sea Research. Part I: Oceanographic Research Papers, 54*, pp. 2036 - 2066.

Hüsing, S., Oms, O., Agustí, J., Garcés, M., Kouwenhoven, T., Krijgsman, W., Zachariasse, W.-J. (2010). On the late Miocene closure of the Mediterranean - Atlantic gateway through the Guadix basin (southern Spain). *Palaeogeography, Palaeoclimatology, Palaeoecology, 291*(3 - 4), pp. 167 - 179.

Hutchinson, J. N. (1968). Mass Movement. In R. W. FAIRBRIDGE (Ed.), *Encyclopedia of Geomorphology* (pp. 688 - 695): Reinhold. New York.

Hutchinson, J. N. (1988). General Report: Morphological and Geotechnical Parameters of Landslides in Relation to Geology and Hydrogeology. In C. Bonnard (Ed.), *Landslides, Proceedings of the Fifth International Symposium on Landslides, Lausanne, 1988* (Vol. I, pp. 3 - 35): Balkema. Rotterdam.

Ibsen, M.-L., Brunsden, D., Bromhead, E., Collison, A. (1996). Block Slide. In R. Dikau, D. Brunsden, L. Schrott & M.-L. Ibsen (Eds.), *Landslide Recognition. Identification, Movement and Causes* (pp. 64 - 77): John Wiley & Sons. Chichester.

Ikari, M., Kopf, A. (2015). The role of cohesion and overconsolidation in submarine slope failure. *Marine Geology, 369*, pp. 153 - 161. doi: https://doi.org/10.1016/j.margeo.2015.08.012

Ikari, M., Strasser, M., Saffer, D., Kopf, A. (2011). Submarine landslide potential near the megasplay fault at the Nankai subduction zone. *Earth and Planetary Science Letters, 312*, pp. 453 - 462. doi: http://dx.doi.org/10.1016/j.epsl.2011.10.024

Imran, J., Parker, G., Locat, J., Lee, H. (2001). 1d numerical model of muddy subaqueous and subaerial debris flows. *Journal of Hydraulic Engineering, 959*, 959 – 968.

Inverno, C., Manupella, G., Zbyszewski, G., Pais, J., Ribeiro, M. L. (1993). Notícia explicativa da folha 42-C, Santiago do Cacém, 1:50.000. Lisboa: Serviços geológicos de Portugal.

Iverson, R. M. (1997). The physics of debris flows. *Review Geophysics, 35*, 245 - 296. doi: 10.1029/97RG00426

Iverson, R. M. (2000). Landslide triggering by rain infiltration. *Water Resources Research 36*, 1897-1910.

Jackson, P., Lovell, M., Roberts, J., Schultheiss, P., Gunn, D., Flint, R. C., Wood, A., Holmes, R., Frederichs, T. (2006). Rapid non-contacting resistivity logging of core. In R. G. Rothwell (Ed.), *New techniques in sediment core analysis* (Vol. 267, pp. 209 - 217): Geological Society of London Special Publication.

Janbu, N. (1973). Slope stability computations. In R. Hirschfeld & S. Poulos (Eds.), *Embankment-dam Engineering* (pp. 40 pp.). NY: John Wiley and Sons Inc.

Jansen, J., Van der Gaast, S., Koster, B., Vaars, A. (1998). CORTEX, a shipboard XRF-scanner for element analyses in split sediment cores. *Marine Geology, 151*(1-4), 143 - 153.

Jiménez-Munt, M., Fernandez, M., Torné, M., Bird, P. (2001). The transition from linear to diffuse plate boundary in the Azores–Gibraltar region: results from a thin sheet model. *Earth and Planetary Science Letters, 192*, pp. 175 - 189.

Johnson, A. M., Rodine, J. R. (1984). Debris flows. In D. Brunsden & D. Prior (Eds.), *Slope Instability* (pp. 257 - 361). Norwich, U.K.: John Wiley & Sons.

Johnston, A. (1996). Seismic moment assessment of earthquakes in stable continental regions – III, New Madrid 1811-1812, Charleston 1886, and Lisbon 1755. *Geophysical Journal International, 126*, pp. 314 - 344.

Juan, C., Ercilla, G., Hernández-Molina, J., Estrada, F., Alonso, B., Casas, D., García, M., Farran, M., Llave, E., Palomino, D., Vázquez, J., Medialdea, T., Gorini, C., D'Acremont, E., El Moumni, B., Ammar, A. (2016). Seismic evidence of current-controlled sedimentation in the Alboran Sea during the Pliocene and Quaternary: palaeoceanographic implications. *Marine Geology, 378*, pp. 292 - 311. doi: 10.1016/j.margeo.2016.01.006

Kaboth, S., Bahr, A., Reichart, G.-J., Jacobs, B., Lourens, L. (2016). New insights into upper MOW variability over the last 150 kyr from IODP 339 Site U1386 in the Gulf of Cadiz. *Marine Geology, 377*, pp. 136 - 145. doi: http://dx.doi.org/10.1016/j.margeo.2015.08.014

Kaboth, S., de Boer, B., Bahr, A., Zeeden, C., Lourens, L. (2017a). Mediterranean Outflow Water dynamics during the past ~570 kyr: Regional and global implications. *Paleoceanography, 32*, pp. 634 - 647. doi: 10.1002/2016PA003063

Kaboth, S., Grunert, P., Lourens, L. (2017b). Mediterranean Outflow Water variability during the Early Pleistocene. *Climate of the Past, 13*, pp.1023 - 1035. doi: https://doi.org/10.5194/cp-13-1023-2017

Kawamura, K., Yamada, Y., Ikehara, K., Yamamoto, Y., Kanamatsu, T., Sakaguchi, A. (2009). White paper for Geohazard (Submarine landslides and mass movements) at INVEST09 from Japanese research group.

Keller, G. (1982). Organic matter and the geotechnical properties of submarine sediments. *Geo-Marine Letters Vol. 2*, pp. 191 - 198.

Khélifi, N., Sarnthein, M., Frank, M., Andersen, N., Garbe-Schönberg, D. (2014). Late Pliocene Variations of the Mediterranean Outflow. *Marine Geology, 357*, pp. 182 - 194.

Knutz, P., Jones, E., Austin, W., van Weering, T. (2002). Glacimarine slope sedimentation, contourite drifts and bottom current pathways on the Barra Fan, UK North Atlantic margin. *Marine Geology, 188*, pp. 129 - 146.

Kohavi, R., Provost, F. (1998). On Applied Research in Machine Learning. In C. University (Ed.), *Special Issue on Applications of Machine Learning and the Knowledge Discovery Process* (Vol. 30). New York.

Kokusho, T. (1980). Cyclic triaxial test of dynamic soil properties for wide strain range. *Soils and Foundations, 20*(2), pp. 45 - 60.

Krastel, S., Wefer, G., Hanebuth, T., Antobreh, A., Freudenthal, T., Preu, B., Schwenk, T., Strasser, M., Violante, R., Winkelmann, D., MSS, P. (2011). Sediment dynamics and geohazards off Uruguay and the de la Plata River region (northern Argentina and Uruguay). *Geo-Marine Letters, 31*(4), 271 - 283. doi: https://doi.org/10.1007/s00367-011-0232-4

Krijgsman, W., Hilgen, F., Raffi, I., Sierro, F., Wilson, D. (1999). Chronology, causes and progression of the Messinian salinity crisis. *Nature, 400*, pp. 652 - 655.

Kümmerer, V., Drago, T., Veiga-Pires, C., Silva, P., Magalhães, V., Mena, A., Lopes, A., Rodrigues, A. I., Schmidt, S., Terrinha, P., Baptista, M. A. (2020). Exploring offshore sediment evidence of the 1755 CE tsunami (Faro, Portugal): Implications for the study of outer shelf tsunami deposits. *Minerals, 10*(9). doi: https://doi.org/10.3390/min10090731

Kvalstad, T., Andresen, L., Forsberg, C., Berg, K., Bryn, P., Wangen, M. (2005a). The Storegga slide: evaluation of triggering sources and slide mechanics. *Marine and Petroleum Geology, 22*(1-2), pp. 245 - 256. doi: 10.1016/j.marpetgeo.2004.10.019

Kvalstad, T., Nadim, F., Kaynia, A., Mokkelbost, K., Bryn, P. (2005b). Soil conditions and slope stability in the Ormen Lange area. *Marine Petroleum Geology, 22*(1-2), pp. 299 - 310. doi: 10.1016/j.marpetgeo.2004.10.021

Laberg, J., Baeten, N., Vanneste, M., Forsberg, C., Forwick, M., Haflidason, H. (2016). Sediment failure affecting muddy contourites on the continental slope offshore northern Norway: lessons learned and some outstanding issues. In G. Lamarche, J. Mountjoy, S. Bull, T. Hubble, S. Krastel, E. Lane, A. Micallef, L. Moscardelli, C. Mueller, I. Pecher & S. Woelz (Eds.), *Submarine mass movements and their consequences. Advances in Natural and Technological Hazards Research* (pp. 281-289): Springer.

Laberg, J., Camerlenghi, A. (2008). The significance of contourites for submarine slope stability. In M. Rebesco & A. Camerlenghi (Eds.), *Contourites. Developments in Sedimentology* (Vol. 60, pp. 537 - 556): Elsevier, Amsterdam

Laberg, J., Dahlgren, T., Vorren, T., Haflidason, H., Bryn, P. (2001). Seismic analyses of Cenozoic contourite drift development in the Northern Norwegian Sea. *Marine Geophysical Researches, 22*, pp. 401 - 416.

Laberg, J., Stoker, M., Dahlgren, K., de Haas, H., Haflidason, H., Hjelsteun, B., Nielsen, T., Shannon, P., Vorren, T., van Weereing, T., Ceramicola, S. (2005). Cenozoic alongslope processes and sedimentation on the NW European Atlantic Margin. *Marine and Petroleum Geology, 22*(9 - 10), pp. 1069 - 1088. doi: 10.1016/j.marpetgeo.2005.01.008

Laberg, J., Strasser, M., Alves, T., Gao, S., Kawamura, K., Kopf, A., Moore, G. (2017). Internal deformation of a muddy gravity flow and its interaction with the seafloor (site C0018 of IODP Expedition 333, Nankai Trough, SE Japan). *Landslides, 14*, pp. 849 - 860. doi: 10.1007/s10346-016-0766-7

Laberg, J., Vorren, T. (1995). Late Weichselian submarine debris flow deposits on the Bear Island Trough Mouth Fan. *Marine Geology, 127*, pp. 45 - 72.

Laberg, J., Vorren, T. (2000). The Trænadjupet Slide, offshore Norway - morphology, evacuation and triggering mechanisms. *Marine Geology, 171*, 95 - 114.

Laberg, J., Vorren, T. (2004). Weichselian and Holocene growth of the northern high-latitude Lofoten Contourite Drift on the continental slope of Norway. *Sedimentary Geology, 164*, pp. 1 - 17.

Laberg, J., Vorren, T., Mienert, J., Bryn, P., Lien, R. (2002). The Trænadjupet Slide: a large slope failure affecting the continental margin of Norway 4,000 years ago. *Geo-Marine Letters, 22*(1), pp. 19 - 24.

Le Gal, L., Edy, C. (1997). *CARAIBES: an integrated software for multibeam echosounder and sidescan sonar data mapping.* Paper presented at the Oceans '97. MTS/IEEE Conference Proceedings.

Lebreiro, S., McCave, I. N., Weaver, P. (1997). Late Quaternary emplacement of turbidites on the Horseshoe Abyssal Plain (Iberian Margin). *Journal of Sedimentary Research, 67*, pp. 856 - 870.

Lebreiro, S., Moreno, J., McCave, I. N., Weaver, P. (1996). Evidence for Heinrich layers off Portugal (Tore Seamount: 39N, 12W). *Marine Geology, 131*, pp. 47 - 56.

Lebreiro, S., Voelker, A., Vizcaino, A., Abrantes, F., Alt-Epping, U., Jung, S., Thouveny, N., Gràcia, E. (2009). Sediment instability on the Portuguese continental margin under abrupt glacial climate changes (last 60 kyr). *Quaternary Science Reviews, 28*, pp. 3211 - 3223. doi: 10.1016/j.quascirev.2009.08.007

Lebreiro, S., Weaver, P., Howe, R. (1998). Sedimentation on the Madeira abyssal plain: Eocene-Pleistocene history of turbidite infill. In P. Weaver, H.-U. Schmincke, J. Firth & W. Duffield (Eds.), *Proceedings of the Ocean Drilling Program: Scientific Results* (Vol. 157, pp. 523 - 531).

Lee, C., Yun, T., Lee, J.-S., Bahk, J., Santamarina, C. (2011). Geotechnical characterization of marine sediments in the Ulleung Basin, East Sea. *Engineering Geology, 117*, 151 - 158.

Lee, H., Baraza, J. (1999). Geotechnical characteristics and slope stability in the Gulf of Cadiz. *Marine Geology, 155*, 173 – 190.

Lee, H., J., Edwards, B. (1986). Regional method to assess offshore slope stability. *Journal of Geotechnical Engineering, American Society of Civil Engineers, 112*, 489 - 509.

Lee, H., Locat, J., Desgagnés, P., Parsons, J., McAdoo, B., Orange, D., Puig, P., Wong, F., Dartnell, P., Boulanger, E. (2007). Submarine mass movements on continental margins. In Nittrouer & e. al. (Eds.), *Continental Margin Sedimentation: From Sediment Transport to Sequence Stratigraphy* (pp. 213 - 273): Blackwell, Oxford, U. K.

Lee, H., Syvitski, J., Parker, G., Orange, D., Locat, J., Hutton, E., Imran, J. (2002). Distinguishing sediment waves from slope failure deposits: field examples, including the 'Humboldt slide', and modelling results. *Marine Geology, 192*, 79 – 104.

Leroueil, S., Locat, J., Vaunat, J., Picarelli, L., Lee, H., Faure, R. (1996). Geotechnical characterization of slope movements. In K. Senneset (Ed.), *Landslides* (Vol. 1, pp. pp. 53 - 74): Balkema, Rotterdam.

Leynaud, D., Sultan, N., Mienert, J. (2007). The role of sedimentation rate and permeability in the slope stability of the formerly glaciated Norwegian continental margin: the Storegga Slide model. *Landslides, 4*, pp. 297 - 309.

Liu, S., Hernández-Molina, F. J., Ercilla, G., Van Rooij, D. (2020). Sedimentary evolution of the Le Danois contourite drift systems (southern Bay of Biscay, NE Atlantic): A reconstruction of the Atlantic Mediterranean Water circulation since the Pliocene. *Marine Geology*. doi: 10.1016/j.margeo.2020.106217

Liu, S., Van Rooij, D., Vandorpe, T., González-Pola, C., Ercilla, G., Hernández-Molina, F. J. (2019). Morphological features and associated bottom-current dynamics in the Le Danois Bank region (southern Bay of Biscay, NE Atlantic): A model in a topographically constrained small basin. *Deep-Sea Research. Part I: Oceanographic Research Papers, 149*, pp. 1 - 17.

Llave, E., Hernández-Molina, F. J., García, M., Ercilla, G., Roque, C., Juan, C., Mena, A., Preu, B., Rooij, D., Rebesco, M., Brackenridge, R., Jané, G., Gómez-Ballesteros, M., Stow, D. (2020). Contourites along the Iberian continental margins: conceptual and economic implications. In K. McClay & J. Hammerstein (Eds.), *Passive Margins: Tectonics, Sedimentation and Magmatism* (Vol. 476, pp. 403 - 436). London: Geological Society London Special Publications.

Llave, E., Hernández-Molina, F. J., Somoza, L., Díaz del Río, V., Stow, D., Maestro, A., Alveirinho Dias, J. M. (2001). Seismic stacking pattern of the Faro-Albufeira contourite system (Gulf of Cádiz): A Quaternary record of paleoceanographic and tectonic influences. *Marine Geophysics Research, 22*, 487 - 508. doi: 10.1023/A:1016355801344

Llave, E., Hernández-Molina, F. J., Stow, D., Somoza, L., Díaz del Río, V. (2005). The contourite depositional system in the Gulf of Cadiz: an example of drifts with reservoir potential characteristics. *25 Aniversario de la AAGEP Special Publication*, pp. 53 - 73.

Llave, E., Hernández-Molina, J., Somoza, L., Stow, D., Díaz Del Río, V. (2007). Quaternary evolution of the contourite depositional system in the Gulf of Cádiz. In A. Viana & M. Rebesco (Eds.), *Economic and Paleoceanographic Importance of Contourites* (Vol. 276, pp. 49 - 79): Geological Society of London, Special Publication.

Llave, E., Matias, H., Hernandez-Molina, F. J., Ercilla, G., Stow, D., Medialdea, T. (2011). Pliocene–Quaternary contourites along the northern Gulf of Cadiz margin: sedimentary stacking pattern and regional distribution. *Geo-Marine Letters, 31*, pp. 377 - 390.

Llave, E., Schönfeld, J., Hernández-Molina, F. J., Mulder, T., Somoza, L., del Rio, V. D., Sanchez-Almazo, I. (2006). High-resolution stratigraphy of the Mediterranean outflow contourite system in the Gulf of Cadiz during the late Pleistocene: the impact of Heinrich event. *Marine Geology, 227*, pp. 241 - 262.

LNEG (Cartographer). (2010). Geological Map of Portugal at 1 000 000 scale.

Lo Iacono, C., Gràcia, E., Zaniboni, F., Pagnoni, G., Tinti, S., Bartolomé, R., Masson, D. G., Wynn, R., Lourenço, N., Pinto Abreu, M., Dañobeitia, J., Zitellini, N. (2012). Large, deepwater slope failures: Implications for landslide-generated tsunamis. *Geology, 40*(10), 931 - 934. doi: 10.1130/G33446.1

Lobo, F. J., Fernández-Salas, L., Moreno, I., Sanz, J. L., Maldonado, A. (2006). The sea-floor morphology of a Mediterranean shelf fed by small rivers, northern Alboran Sea margin. *Continental Shelf Research, 26*, pp. 2607 - 2628.

Locat, J. (2001). Instabilities along ocean margins: a geomorphological and geotechnical perspective. *Marine and Petroleum Geology, 18*, 503 - 512.

Locat, J., Lee, H. (2002). Submarine landslides: advances and challenges. *Canadian Geotechnical Journal, 39*, pp. 193 - 212. doi: https://doi.org/10.1139/t01-089

Locat, J., Leroueil, S., Locat, A., Lee, H. (2014). Weak Layers: Their Definition and Classsification from a Geotechnical Perspective. In S. Krastel, J.-H. Behrmann, D. Völker, M. Stipp, C. Berndt, R. Urgeles, J. Chaytor, K. Huhn, M. Strasser & C. Harbitz (Eds.), *Submarine Mass Movements and Their Consequences. Advances in Natural and Technological Hazards Research* (Vol. 37, pp. 3 - 12): Springer.

Lofi, J., Voelker, A. H. L., Ducassou, E., Hernández-Molina, F. J., Sierro, F., Bahr, A., Galvani, A., Lourens, L., Pardo-Igúzquiza, E., Pezard, P., Rodríguez-Tovar, F., Williams, T. (2016). Quaternary chronostratigraphic framework and sedimentary processes for the Gulf of Cadiz and Portuguese Contourite Depositional Systems derived from Natural Gamma Ray records. *Marine Geology, 377*, pp. 40-57.

Loget, N., Van Den Driessche, J. (2006). On the origin of the Strait of Gibraltar. *Sedimentary Geology, 188 - 189*, pp. 341 - 356. doi: https://doi.org/10.1016/j.sedgeo.2006.03.012

Lu, G., Wong, D. (2008). An adaptive inverse-distance weighting spatial interpolation technique. *Computers and Geosciences, 34*(9), pp. 1044 - 1055. doi: https://doi.org/10.1016/j.cageo.2007.07.010

Macintyre, R., Berger, G. (1982). A note on the geochronology of the Iberian AlkaIine Province. *Lithos, 15*, pp. 133 - 136.

Magalhães, V., Pinheiro, L., Ivanov, M., Kozlova, E., Blinova, V., Kolganova, J., Vasconcelos, C., McKenzie, J., Bernasconi, S., Kopf, A., Díaz-del-Río, V., González, F., Somoza, L. (2012). Formation processes of methane-derived authigenic carbonates from the Gulf of Cadiz. *Sedimentary Geology, 243 - 244*, pp. 155 - 168.

Magill, C., Ausín, B., Wenk, P., McIntyre, C., Skinner, L., Martínez-García, A., Hodell, D., Haug, G., Kenney, W., Eglinton, T. (2018). Transient hydrodynamic effects influence organiccarbon signatures in marine sediments. *Nature Communications, 9*(4690), 8 pp. doi: 10.1038/s41467-018-06973-w

Maldonado, A., Barnolas, A., Bohoyo, F., Escutia, C., Galindo-Zaldívar, J., Hernández-Molina, F. J., Jabaloy, A., Lobo, F. J., Nelson, C. H., Rodríguez-Fernández, J., Somoza, L., Vázquez, J.-T. (2005). Miocene to Recent contourite drifts development in the northern Weddell Sea (Antarctica). *Global and Planetary Change, 45*, pp. 99 - 129.

Maldonado, A., Somoza, L., Pallarés, L. (1999). The Betic orogen and the Iberian-African boundary in the Gulf of Cadiz: geological evolution (central north Atlantic). *Marine Geology 155*, pp. 9 - 43

Malet, J.-P., Laigle, D., Remaître, A., Maquaire, O. (2005). Triggering conditions and mobility of debris flows associated to complex earthflows. *Geomorphology, 66*, pp. 215 - 235. doi: 10.1016/j.geomorph.2004.09.014

Marques, F. (1997). *As Arribas do Litoral do Algarve. Dinâmica, Processos e Mecanismos.* Tese de Doutoramento em Geologia, Departamento de Geologia da Faculdade de Ciências da Universidade de Lisboa.

Martins, L., Madeira, J., Youbi, N., Munhá, J., Mata, J., Kerrich, R. (2008). Rift-related magmatism of the Central Atlanticmagmatic province in Algarve, Southern Portugal. *Lithos, 101*(1-2), pp. 102 - 124.

Martorelli, E., Bosman, A., Casalbore, D., Falcini, F. (2016). Interaction of downslope and alongslope processes off Capo Vaticano (southern Tyrrhenian Sea, Italy), with particular reference to contourite-related landslides. *Marine Geology, 378*, 43-55.

Masson, D., Arzola, R., Wynn, R., Hunt, J., Weaver, P. (2011). Seismic triggering of landslides and turbidity currents offshore Portugal. *Geochemistry Geophysics Geosystems, 12*(12).

Masson, D., Harbitz, C., Wynn, R., Pedersen, G., Løvholt, F. (2006). Submarine landslides: processes, triggers and hazard prediction. *Philosophical Transactions of the Royal Society London, 364*, 2009 – 2039.

Masson, D., Van Niel, B., Weaver, P. (1997). Flow processes and sediment deformation in the Canary Debris Flow on the NW African Continental Rise. *Sedimentary Geology, 110*(3 - 4), pp. 163 - 179 doi: 10.1016/S0037-0738(96)00089-9

Matos Fernandes, M. (2012). *Mecânica dos solos: conceitos e princípios fundamentais* (3rd ed.): FEUP Edições.

Mauffret, A., Mougenot, D., Miles, P., Malod, J. (1989). Cenozoic deformation and Mesozoic abandoned spreading centre in the Tagus Abyssal Plain (west of Portugal): Results of a multichannel seismic survey. *Canadian Journal of Earth Sciences, 26*, pp. 1101 - 1123. doi: 10.1139/e89-095

McAdoo, B., Pratson, L., Orange, D. (2000). Submarine landslide geomorphology, US continental slope. *Marine Geology, 169*, pp. 103-136.

McCave, I. N. (2001). Nepheloid Layers. In J. Steele, S. Thorpe & K. Turekian (Eds.), *Encyclopedia of Ocean Sciences* (Vol. 4, pp. 1861–1870). London: Academic Press.

McCave, I. N., Tucholke, B. (1986). Deep current-controlled sedimentation in the western North Atlantic. In P. Vogt & B. Tucholke (Eds.), *The Geology of North America. The Western North Atlantic Region, Decade of North American Geology* (pp. 451 - 468): Geological Society of America, Boulder.

Mena, A., Francés, G., Pérez-Arlucea, M., Hanebuth, T., Bender, V., Nombela, M. (2018). Evolution of the Galicia Interior Basin over the last 60 ka: sedimentary processes and

palaeoceanographic implications. *Journal of Quaternary Science, 33*(5), pp. 536 - 549. doi: 10.1002/jqs.3032

Mencaroni, D., Llopart, J., Urgeles, R., Lafuerza, S., Gràcia, E., Le Friant, A., Urlaub, M. (2020). From gravity cores to overpressure history: the importance of measured sediment physical properties in hydrogeological models. *Geological Society, London, Special Publications*. doi: https://doi.org/10.1144/SP500-2019-176

Merle, R., Jourdan, F., Marzoli, A., Renne, P. R., Grange, M., Girardeau, J. (2009). Evidence of multi-phase Cretaceous to Quaternary alkaline magmatism on Tore-Madeira Rise and neighbouring seamounts from Ar-40/Ar-39 ages. *Journal of the Geological Society, 166*, pp. 879 - 894.

Merle, R., Schärer, U., Girardeau, J., Cornen, G. (2006). Cretaceous seamounts along the continent-ocean transition of the Iberian margin: U-Pb ages and Pb-Sr-Hf isotopes. *Geochimica et cosmochimica acta, 70*(19), pp. 4950 - 4976.

Mienert, J., Vanneste, M., Bünz, S., Andreassen, K., Haflidason, H., Sejrup, H. P. (2005). Ocean warming and gas hydrate stability on the mid-Norwegian margin at the Storegga Slide. *Marine and Petroleum Geology, 22*(1-2), pp. 233 - 244.

Migeon, S., Cattaneo, A., Hassoun, V., Dano, A., Casedevant, A., Ruellan, E. (2012). Failure Processes and Gravity-Flow Transformation Revealed by High-Resolution AUV Swath Bathymetry on the Nice Continental Slope (Ligurian Sea). In Y. Yamada, K. Kawamura, K. Ikehara, Y. Ogawa, R. Urgeles, D. Mosher, J. Chaytor & M. Strasser (Eds.), *Submarine Mass Movements and Their Consequences, Advances in Natural and Technological Hazards Research* (Vol. 31, pp. 1 - 12).

Migeon, S., Weber, O., Faugeres, J.-C., Saint-Paul, J. (1998). SCOPIX: A new X-ray imaging system for core analysis. *Geo-Marine Letters 18*(3), 251-255. doi: doi: 10.1007/s003670050076

Minning, M., Hebbeln, D., Hensen, C., Kopf, A. (2006). Geotechnical and geochemical investigations of the Marquês de pombal landslide at the Portuguese continental margin. *Norwegian Journal of Geology, 86*, pp. 187-198.

Miramontes, E. (2016). *Submarine landslides in the northern Tyrrhenian Sea and relationship with the contouritic and turbiditic deposits: morphology, stratigraphy, geotechnics and modelling.* PhD Thesis, Université de Bretagne Occidentale.

Miramontes, E., Garziglia, S., Sultan, N., Jouet, G., Cattaneo, A. (2018). Morphological control of slope instability in contourites: a geotechnical approach. *Landslides, 15,* 1085 - 1095 doi: 10.1007/s10346-018-0956-6

Miranda, R., Valadares, V., Terrinha, P., Mata, J., Azevedo, M., Gaspar, M., Kullberg, J., Ribeiro, C. (2009). Age constraints on the Late Cretaceous alkaline magmatism on the West Iberian Margin. *Cretaceous Research, 30,* pp. 575 - 586.

Moernaut, J., Van Daele, M., Strasser, M., Clare, M., Heirman, K., Viel, M., Cardenas, J., Kilian, R., Ladrón de Guevara, B., Pino, M., Urrutia, R., De Batist, M. (2017). Lacustrine turbidites

produced by surficial slope sediments remobiliation: a mechanism for continuous and sensitive turbidite paleoseismic records. *Marine Geology, 384*, pp. 159 - 176.

Monteiro, J., Gaspar, L., Abrantes, F., Rebelo, L., Teixeira, F., Moura, R. (1994). STEAM 94 research cruise to the continental margin of SW Portugal *Report from IGM*.

Montgomery, D. R., Dietrich, W. (1994). A Physically Based Model for the Topographic Control on Shallow Landsliding. *Water Resources Research, Vol. 30* (No. 4), 1153 - 1171.

Montgomery, D. R., Sullivan, K., Greenberg, H. (1998). Regional Test of a Model for Shallow Landsliding. *Hydrological Processes, 12*, pp. 943 - 955.

Moore, J., Clague, D., Holcomb, R., Lipman, P., Normark, W., Torresan, M. (1989). Prodigious submarine landslides on the Hawaiian Ridge. *Journal of Geophysical Research, 94*(17).

Moore, J., Normark, W., Holcomb, R. (1994). Giant Hawaiian landslides. *Annual Review Earth and Planetary Science, 22*, 119 - 144.

Morgenstern, N. R. (1967). Submarine slumping and the initiation of turbidity currents. In A. F. Richards (Ed.), *Marine Geotechnique* (pp. 189 - 210): University of Illinois Press, Urbana.

Morgenstern, N. R., Price, V. (1965). The analysis of the stability of general slip surfaces. *Geotechnique, 15*(1), 79 - 93.

Morillas, H., Maguregui, M., Madariaga, J. M. (2016). Spectroscopic evidences to understand the influence of marine environments on Built Heritage. *Spectroscopy Europe, 28*(3), 6 - 11.

Moscardelli, L., Wood, L. (2015). Morphometry of mass-transport deposits as a predictive tool. *Geological Society of America Bulletin, 128*(1 - 2), pp. 47 - 80. doi: https://doi.org/10.1130/B31221.1

Mosher, D., Campbell, D., Gardner, J., Piper, D., Chaytor, J., Rebesco, M. (2017). The role of deep-water sedimentary processes in shaping a continental margin: The Northwest Atlantic. *Marine Geology, 393*, pp. 245 - 259.

Mosher, D., Moran, K., Hiscott, R. (1994). Late Quaternary sediment, sediment mass flow processes and slope stability on the Scotian Slope, Canada. *Sedimentology, 41*, pp. 1039 - 1061.

Mosher, D., Piper, D., Campbell, D., Jenner, K. (2004). Near surface geology and sediment failure geohazards of the central Scotian Slope. *American Association of Petroleum Geologists Bulletin, 88*, 703 - 723.

Mosher, D. C., Moscardelli , L., Shipp, R., Chaytor, J., Baxter, C., Lee, H. J., Urgeles, R. (2010). Submarine mass movements and their consequences: Introduction. In D. C. Mosher, C. Shipp, L. Moscardelli, J. Chaytor, C. Baxter, H. Lee & R. Urgeles (Eds.), *Submarine Mass Movements and Their Consequences: IV* (pp. 1-8). Dordrecht, Netherlands: Springer.

Mougenot, D. (1989). *Geologia da Margem Portuguesa.* PhD Thesis, Université Pierre et Marie Curie, Lisbon.

Mougenot, D., Monteiro, J. H., Dupeuble, P., Malod, J. (1979). La marge continentale sud-portugaise: évolution structurale et sédimentaire. *Ciências da Terra, 5*, pp. 223 - 246.

Mulder, T., Cochonat, P. (1996). Classification of Offshore Mass Movements. *Journal of Sedimentary Research, 66*(1), 43 - 57.

Mulder, T., Voisset, M., Lecroart, P., Le Drezen, E., Gonthier, E., Hanquiez, V., Faugères, J.-C., Habgood, E., Hernandez-Molina, F. J., Estrada, F., Llave-Barranco, E., Poirier, D., Gorini, C., Fuchey, Y., Voelker, A., Freitas, P., Sanchez, F. L., Fernandez, L., Kenyon, N., Morel, J. (2003). The Gulf of Cadiz: an unstable giant contouritic levee. *Geo-Marine Letters, 23*, pp. 7 - 18.

Munsell, A. (1905). A Color Notation. Boston: G. H. Ellis Co.

Naughton, F., Sanchez Goñi, M., Rodrigues, T., Salgueiro, E., Costas, S., Desprat, S., Duprat, J., Michel, E., Rossignol, L., Zaragosi, S., Voelker, A., Abrantes, F. (2016). Climate variability across the last deglaciation in NW Iberia and its margin. *Quaternary International, 414*, pp. 9 - 22.

Nelson, C., Baraza, J., Maldonado, A. (1993). Mediterranean undercurrent sandy contourites, Gulf of Cadiz, Spain. *Sedimentary Geology, 82*, pp. 103 - 131.

Neres, M., Bouchez, J. L., Terrinha, P., Font, E., Moreira, M., Miranda, R., Launeau, P., Carvallo, C. (2014). Magnetic fabric in a Cretaceous sill (Foz da Fonte, Portugal): flow model and implications for regional magmatism. *Geophysics Journal International, 199*, pp. 78 - 101.

Neres, M., Carafa, M., Fernandes, R., Matias, L., Duarte, J., Barba, S., Terrinha, P. (2016). Lithospheric deformation in the Africa-Iberia plate boundary: Improved neotectonic modeling testing a basal-driven Alboran plate. *Journal of Geophysics Research: Solid Earth, 121*, pp. 6566 - 6596. doi: 10.1002/2016JB013012

Neves, M., Roque, C., Luttrel, K., Vazquez, J.-T., Alonso, B. (2016). Impact of sea-level rise on earthquake and landslide triggering offshore the Alentejo margin (SW Iberia). *Geo-Marine Letters, 36*(6), 415 - 424 pp.

Neves, M., Terrinha, P., Afilhado, A., Moulin, M., Matias, L., Rosas, F. (2009). Response of a multi-domain continental margin to compression: study from seismic reflection – refraction and numerical modelling in the Tagus Abyssal Plain. *Tectonophysics, 468*, pp. 113 - 130. doi: org/10.1016/j.tecto.2008.05.008

Nielsen, T., Knutz, P., Kuijpers, A. (2008). Seismic expression of contourite depositional systems. In M. Rebesco & A. Camerlenghi (Eds.), *Contourites. Developments in Sedimentology* (pp. 301 - 322).

Nowaczyk, N. R. (2001). Logging of magnetic susceptibility. In W. M. Last & J. Smol (Eds.), *Tracking Environmental Change Using Lake Sediments. Basin Analysis, Coring and Chronological Techniques, Developments in Paleoliminological Research*: Kluwer Academic Publishers, Dordrecht, The Netherlands.

Ohkouchi, N., Eglinton, T., Keigwin, L., Hayes, J. (2002). Spatial and Temporal Offsets Between Proxy Records in a Sediment Drift. *Science, 298*(5596), pp. 1224-1227. doi: 10.1126/science.1075287

Okimura, T., Ichikawa, R. (1985). A Prediction Method for Surface Failure by Movements of Infiltrated Water in a Surface Soil Layer. *Natural Disaster Science, 7 (1)*, 41 - 51.

Oliveira, J. (1984). Notícia explicativa da carta geológica de Portugal, folha 7, 1:200.000 (pp. 77). Lisboa, Portugal: Serviços Geológicos de Portugal.

Omira, R., Ramalho, I., Terrinha, P., Baptista, M. A., Batista, L., Zitellini, N. (2016). Deep-water seamounts, a potential source of tsunami generated by landslides? The Hirondelle Seamount, NE Atlantic. *Marine Geology, 379*, 267 - 280.

Pack, R., Tarboton, D., Goodwin, C. (1998). SINMAP – a stability index approach to terrain stability hazard mapping. User's manual. *http://hydrology.neng.usu.edu/sinmap/*. 68 pp.

Pack, R., Tarboton, D., Goodwin, C. (2005). SINMAP 2 – a stability index approach to terrain stability hazard mapping. . *http://hydrology.neng.usu.edu/sinmap/. User's manual. Terratech Consulting Ltd.*, (Salmon Arm, B.C., Canada), 73 p.

Pardo, G., Orense, R., Sarmah, A. (2018). Cyclic strength of sand mixed with biochar: Some preliminary results. *Soils and Foundations, 58*, pp. 241 - 247.

Pereira, R., Alves, T. (2009). *Mesozoic Rifting of the SW Iberian Margin - Implications to the Hydrocarbon Potential of Alentejo Basin*. Paper presented at the 71st EAGE Conference & Exhibition, Amsterdam - The Netherlands.

Pereira, R., Alves, T. (2011). Margin segmentation prior to continental break-up: A seismic–stratigraphic record of multiphased rifting in the North Atlantic (Southwest Iberia). *Tectonophysics, 505*(1), pp. 17 - 34. doi: 10.1016/j.tecto.2011.03.011

Pereira, R., Alves, T. (2013). Crustal deformation and submarine canyon incision in a Meso-Cenozoic first-order transfer zone (SW Iberia, North Atlantic Ocean). *Tectonophysics 601*, pp. 148 - 162. doi: 10.1016/j.tecto.2013.05.007

Pereira, R., Alves, T., Cartwright, J. (2011). Post-rift compression on the SW Iberian margin (eastern North Atlantic): a case for prolonged inversion in the ocean-continent transition zone. *Journal of the Geological Society, 168*, pp. 1249 - 1263. doi: 10.1144/0016-76492010-151

Pérez-Belzuz, F., Alonso, B., Ercilla, G. (1997). History of mud diapirism and trigger mechanisms in the Western Alboran Sea. *Tectonophysics 282*, pp. 399 - 422.

Péron-Pinvidic, G., Manatschal, G., Minshull, T., Sawyer, D. (2007). Tectonosedimentary evolution of the deep Iberia-Newfoundland margins: Evidence for a complex breakup history. *Tectonics, 26*, pp. 1 - 19. doi: 10.1029/2006TC001970, 2007

Piedade, A., Alves, T., Zêzere, J. (2018). A new approach to assess ancient marine slope instability using a bivariate statistical method. *Marine Geology, 401*, pp. 129 - 144.

Pingree, R., Le Cann, B. (1989). Celtic and Armorican slope and shelf residual currents. *Progress in Oceanography, 23*, pp. 303 - 338.

Pinheiro, L., Wilson, R., Pena dos Reis, R., Whitmarsh, R., Ribeiro, A. (1996). The Western Iberia Margin: a geophysical and geological overview. In R. Whitmarsh, D. Sawyer, A. Klaus & D. Masson (Eds.), *Proceedings of the Ocean Drilling Program, Scientific Results* (Vol. 149, pp. 3 - 23).

Piper, D., Aksu, A. (1987). The source and origin of the 1929 grand banks turbidity current inferred from sediment budgets. *Geo-Marine Letters, 7*, pp. 177 - 182.

Piper, D., Cochonat, P., Morrison, M. (1999a). The sequence of events around the epicentre of the 1929 Great Banks earthquake: initiation of debris flow and turbidity current inferred from sidescan sonar. *Sedimentology, 46*, pp. 79 - 97.

Piper, D., Cochonat, P., Morrison, M. (1999b). Sidescan sonar evidence for progressive evolution of submarine failure into a turbidity current: The 1929 Grand Banks event. *Sedimentology, 46*, pp. 79 - 97.

Piper, D., Mosher, D., Campbell, D. (2012). Controls on the distribution of major types of submarine landslides. In J. Clague & D. Stead (Eds.), *Landslides: Types, Mechanisms, and Modeling* (pp. 95-107). Cambridge, UK: Cambridge University Press.

Piper, D., Normark , W. (2009). The processes that initiate turbidity currents and their influence on turbidites: A marine geology perspective. *Journal of Sedimentary Research, 79*, pp. 347 - 362.

Piper, D., Shor, A., Farre, J., O'Connell, S., Jacobi, R. (1985). Sediment slides around the epicentre of the 1929 Great Banks earthquake. *Geology, 13*, pp. 538 - 541.

Pollard, S., Griffiths, C. R., Cunningham, S. A., Read, J. F., Perez, F. F., Ríos, A. F. (1996). Vivaldi 1991 - A study of the formation, circulation and ventilation of Eastern North Atlantic Central Water. *Progress in Oceanography, 37*, pp. 167-192.

Pomar, L., Morsilli, M., Hallock, P., Bádenas, B. (2012). Internal waves, an under-explored source of turbulence events in the sedimentary record. *Earth Sciences Review, 111*(1 - 2), 56 - 81. doi: http://dx.doi.org/10.1016/j.earscirev.2011.12.005

Preu, B., Hernández-Molina, F. J., Violante, R., Piola, A. R., Paterlini, C. M., Schwenk, T., Voigt, I., Krastel, S., Spiess, V. (2013). Morphosedimentary and hydrographic features of the northern Argentine margin: the interplay between erosive, depositional and gravitational processes and its conceptual implications. *Deep-Sea Research. Part I: Oceanographic Research Papers, 75*, pp. 157 - 174.

Prior, D. B., Coleman, J. (1978). Disintegrative retrogressive landslides on very-low-angle subaqueous slopes, Mississippi delta. *Marine Geotechnology, 3*, 37 - 60.

Prior, D. B., Coleman, J. (1984). Submarine Slope Stability. In D. Brunsden & D. Prior (Eds.), *Slope Instability* (pp. 419 - 455): Jonh Wiley & Sons.

Pudsey, C., Howe, J. (2002). Mixed biosiliceous–terrigenous sedimentation under the Antarctic Circumpolar Current, Scotia Sea. In D. Stow, C. Pudsey, J. Howe, J.-C. Faugéres & A. Viana (Eds.), *Deep-water Contourite Systems: Modern Drifts and Ancient Series, Seismic and Sedimentary Characteristics* (Vol. 22, pp. 323 - 336): Geological Society, London, Memoir.

Quintela, M., Costa, P., Fatela, F., Drago, T., Hoska, N., Andrade, C., Freitas, M. C. (2016). The AD 1755 tsunami deposits onshore and offshore of Algarve (south Portugal): Sediment transport interpretations based on the study of Foraminifera assemblages. *Quaternary International, 408*(Part A), pp. 123 - 138. doi: https://doi.org/10.1016/j.quaint.2015.12.029

Rasmussen, E., Lomholt, S., Andersen, C., Vejbæk, O. (1998). Aspects of the structural evolution of the Lusitanian Basin in Portugal and the shelf and slope area offshore Portugal. *Tectonophysics, 300*, pp. 199 - 225.

Rasmussen, S., Lykke-Andersen, H., Kuijpers, A., Troelstra, S. (2003). Post-Miocene sedimentation at the continental rise of Southeast Greenland: the interplay between turbidity and contour currents. *Marine Geology, 196*(1-2), pp. 37-52.

Rebesco, M. (2005). Contourites. In R. Selley, L. Cocks & I. Plimer (Eds.), Encyclopedia of Geology (pp. 513 - 527). Oxford: Elsevier.

Rebesco, M., Camerlenghi, A., Volpi, V., Neagu, C., Accettella, D., Lindberg, B., Cova, A., Zgur, F., the MAGICO party, Society, G. (2007). Interaction of processes and importance of contourites: insights from the detailed morphology of sediment drift 7, Antarctica. In A. Viana & M. Rebesco (Eds.), *Economic and Palaeoceanographic Significance of Contourite Deposits* (Vol. 276, pp. 95 - 110): Geological Society, London, Special Publication.

Rebesco, M., Hernández-Molina, F. J., Van Rooij, D., Wåhlin, A. (2014). Contourites and associated sediments controlled by deep-water circulation processes: State-of-the-art and future considerations. *Marine Geology, 352*, 111 - 154.

Rebesco, M., Stow, D. (2001). Seismic expression of contourites and related deposits: a preface. *Marine Geophysical Research, 22*, pp. 303 - 308.

Rebesco, M., Wåhlin, A., Laberg, J. S., Schauer, A., Brezcynska-Möller, A., Lucchi, R. G., Noormets, R., Accettella, D., Zarayskaya, Y., Diviacco, P. (2013). Quaternary contourite drifts of the Western Spitsbergen margin. *Deep-Sea Research. Part I: Oceanographic Research Papers, 79*, pp. 156 - 168.

Reddy, M. (2001). *Descriptive physical oceanography*: A.A Balkema Publishers.

Reimer, P., Bard, E., Bayliss, A., Beck, J., Blackwell, P., Bronk Ramsey, C., Grootes, P., Guilderson, T., Haflidason, H., Hajdas, I., Hattz, C., Heaton, T., Hoffmann, D., Hogg, A., Hughen, K., Kaiser, K., Kromer, B., Manning, S., Niu, M., Reimer, R., Richards, D., Scott, E., Southon, J., Staff, R., Turney, C., van der Plicht, J. (2013). IntCal13 and Marine13 Radiocarbon Age calibration curves 0-50,000 Years cal BP. *Radiocarbon, 55*(4), pp. 1869 - 1887.

Rey, D., Álvarez-Iglesias, P., Araújo, M., Bernabeu, A. M., Comas, M., DeCastro, M., Druet, M., Ferreira da Silva, E., Ferrín, A., Gesteira, M., Martins, V., Mohamed, K., Rubio, B., Vilas, F. (2014). The NW Iberian continental shelf. In F. Chiocci & A. Chivas (Eds.), *Continental shelves of the world: Their evolution during the Last Glacio-Eustatic cycle* (Vol. 41, pp. 91 - 108). London: Geological Society, London, Memoirs.

Ribeiro, A. (2013a). Evolução geodinâmica de Portugal: os ciclos ante-mesozóicos. In R. Dias, A. Araújo, P. Terrinha & J. Kullberg (Eds.), *Geologia de Portugal: Geologia Pré-Mesozóica de Portugal* (Vol. II, pp. 15 - 58). Lisboa: Escolar Editora

Ribeiro, A. (2013b). Evolução geodinâmica de Portugal: os ciclos Meso-Cenozóicos. In R. Dias, A. Araújo, P. Terrinha & J. Kullberg (Eds.), *Geologia de Portugal: Geologia Meso-cenozóica de Portugal* (Vol. II, pp. 9 - 28). Lisboa: Escolar Editora.

Ribeiro, A., Antunes, M., Ferreira, M., Rocha, R., Soares, A., Zbyszewski, G., Almeida, F., Carvalho, D., Monteiro, J. (1979). Introduction à la Géologie Générale du Portugal. (pp. 1 - 114). Lisboa: Serviços Geológicos de Portugal.

Ribeiro, A., Cabral, J., Baptista, R., Matias, L. (1996). Stress pattern in Portugal mainland and the adjacent Atlantic region, West Iberia. *Tectonics, 15*, pp. 641-659.

Ribeiro, C., Terrinha, P. (2007). Formation, deformation and chertification of systematic clastic dykes in a differentially lithified carbonate multilayer. SW Iberia, Algarve Basin, Lower Jurassic. *Sedimentary Geology, 196*, pp. 201 - 215.

Richter, T., van der Gaast, S., Koster, B., Vaars, A., Gieles, R., de Stigter, H., De Haas, H., v, an Weering, T. (2006). The Avaatech XRF Core Scanner: technical description and applications to NE Atlantic sediments. *Geological Society of London. Special Publication, 267*(1), 9 - 50.

Roberts, D., Stride, A. (1968). Late Tertiary slumping on the continental slope of southern Portugal. *Nature 217*, 48 - 50.

Rock, N. (1982). The Late Cretaceous Alkaline Igneous Province in the Iberian Peninsula, and its tectonic significance. *Lithos, 15*, pp. 111 - 131.

Rodrigues, S., Roque, C., Hernández-Molina, F. J., Llave, E., Terrinha, P. (2020). The Sines Contourite Depositional System along the SW Portuguese Margin: onset, evolution and conceptual implications. *Marine Geology*(in press).

Rogerson, M., Bigg, G., Rohling, E., Ramirez, J. (2012). Vertical density gradient in the eastern North Atlantic during the last 30,000 years. *Climate Dynamics, 39*, pp. 589 - 598. doi: 10.1007/s00382-011-1148-4

Rogerson, M., Rohling, E., Weaver, P., Murray, J. (2005). Glacial to interglacial changes in the settling depth of the Mediterranean Outflow plume. *Paleoceanography, 20*, PA3007. doi: 10.1029/2004PA001106

Roque, C. (2007). *Tectonostratigrafia do Cenozóico das margens continentais sul e sudoeste portuguesas: Um modelo de correlação sismostratigráfica.* PhD Thesis, University of Lisbon, Lisbon, Portugal.

Roque, C., Duarte, H., Terrinha, P., Valadares, V., Noiva, J., Cachão, M., Ferreira, J., Legoinha, P., Zitellini, N. (2012). Pliocene and Quaternary depositional model of the Algarve margin contourite drifts (Gulf of Cadiz, SW Iberia): Seismic architecture, tectonic control and paleoceanographic insights. *Marine Geology, 303-306*, 42 - 62.

Roque, C., Hernández-Molina, F. J., Ercilla, G., Casas, D., Quartau, R., Llave, E., Alonso, B., Ferran, M., Mena, A., Francés, G., Party, M. C. (2015). *Slope failure and mass movements in the Sines Contourite Drift (West Portuguese Margin): preliminary results*. Paper presented at the VII Symposium MIA15, Malaga, Spain.

Rosas, F., Duarte, J., Neves, M., Terrinha, P., Silva, S., Matias, L., Gràcia, E., Bartolomé, R. (2012). Thrust–wrench interference between major active faults in the Gulf of Cadiz (Africa–Eurasia plate boundary, offshore SW Iberia): Tectonic implications from coupled analog and numerical modeling. *Tectonophysics, 548 - 549*, pp. 1 - 21. doi: 10.1016/j.tecto.2012.04.013

Rosenbaum, G., Lister G., Duboz, C. (2002a). Relative motions of Africa, Iberia and Europe during Alpine orogeny. *Tectonophysics, 359*, pp. 117 - 129.

Rosenbaum, G., Lister G., Duboz C. (2002b). Reconstruction of the tectonic evolution of the western Mediterranean since the Oligocene. In Rosenbaum G. & L. G. (Eds.), *Reconstruction of the evolution of the Alpine-Himalayan Orogen* (Vol. 8, pp. pp. 107 - 126): Journal of the Virtual Explorer.

Rothwell, R. G., Frank, R. R. (2006). New techniques in sediment core analysis: an introduction. In R. G. Rothwell (Ed.), *New Techniques in Sediment Core Analysis* (Vol. 267, pp. 1 - 29): Geological Society, London, Special Publications.

Roveri, M., Flecker, R., Krijgsman, W., Lofi, J., Lugli, S., Manzi, V., Sierro, F. J., Bertini, A., Carnerlenghi, A., De Lange, G., Govers, R., Hilgen, F. J., Huebscher, C., Meijer, P. T., Stoica, M. (2014). The Messinian salinity crisis: past and future of a great challenge for marine sciences. *Marine Geology, 352*(pp. 25 - 58).

Sakamoto, T., Kuroi, K., Sugawara, T., Aoike, K., Lijima, K., Sugisaki, S. (2006). Non-destructive X-ray fluorescence (XRF) core-imaging scanner, TATSCAN-F2. *Scientific Drilling, 2*, 37 - 39.

Salgueiro, E., Naughton, F., Voelker, A., Abreu, L., Alberto, A., Rossignol, L., Duprat, J., Magalhães, V., Vaqueiro, S., Turone, J.-L., Abrantes, F. (2014). Past circulation along the western Iberian margin: a time slice visionfrom the Last Glacial to the Holocene. *Quaternary Science Reviews, 106*, pp. 316 - 329. doi: http://dx.doi.org/10.1016/j.quascirev.2014.09.001

Sanchez-Serra, C., Martínez-Loriente, S., Gràcia, E., Urgeles, R., Vizcaino, A., Perea, H., Bartolome, R., Pallàs, R., Lo Iacono, C., Diez, S., Dañobeitia, J., Terrinha, P., Zitellini, N. (2020). Tectonic evolution, geomorphology and influence of bottom currents along a large submarine

canyon system: The São Vicente Canyon (SW Iberian margin). *Marine Geology, 426*, 106219. doi: 10.1016/j.margeo.2020.106219

Sánchez Goñi, M., Llave, E., Oliveira, D., Naughton, F., Desprat, S., Ducassou, E., Hodell, D., Hernández-Molina, F. J. (2016). Climate changes in south western Iberia and Mediterranean Outflow variations during two contrasting cycles of the last 1 Myrs: MIS 31–MIS 30 and MIS 12–MIS 11. *Global and Planetary Change, 136*, pp. 18 - 29.

Sartori, R., Torelli, L., Zitellini, N., Peis, D., Lodolo, E. (1994). Eastern Segment of the Azores-Gibraltar Line (Central-eastern Atlantic): An Oceanic Plate Boundary with Diffuse Compressional Deformation. *Geology, 22*, 555 - 558.

Schettino, A., Turco, E. (2011). Tectonic history of the western Tethys since the Late Triassic. *GSA Bulletin, 123*, pp. 89 - 105.

Schlitzer, R. (2018). Ocean Data View. *http://odv.awi.de*.

Schönfeld, J., Erlenkeuser, H., Zahn, R. (1993). Stratigraphy: preliminary results of piston core SO75 26KL. In H. Kudrass (Ed.), *SONNE CRUISE SO-75-3: Cruise Report 1992. Test of the Geological Equipment by Surveying and Sampling of the Southwestern Portuguese Continental Slope and the Ampere Seamount* (pp. 97 - 99). Hannover: Bundesanst. Geowiss. Rohstoffe.

Schönfeld, J., Zahn, R. (2000). Late Glacial to Holocene history of the Mediterranean Outflow. Evidence from benthic foraminiferal assemblages and stable isotopes at the Portuguese margin. *Palaeogeography, Palaeoclimatology, Palaeoecology, 159*, pp. 85 - 811.

Schrott, L., Dikau, R., Brunsden, D. (1996). Soil Flow (Mudflow). In R. Dikau, D. Brunsden, L. Schrott & M.-L. Ibsen (Eds.), *Landslide Recognition. Identification, Movement and Causes*: John Wiley & Sons. Chichester.

Schultheiss, P. (1982). Geotechnical properties of deep-sea sediments: A critical review of measurement techniques *Report, No . 134* (pp. 73 pp.): Institute of Oceanographic Sciences.

Schultheiss, P. (1989). Pore Pressures in Marine Sediments: An Overview of Measurement Techniques and Some Geological and Engineering Applications. *Marine Geophysical Researches, 12*, 153 - 168.

Schultheiss, P. J., McPhail, S. D. (1989). An automated P-Wave Logger for recording fine-scale compressional wave velocity structures in sediments. In W. Ruddiman, M. Sarnthein & al. (Eds.), *Proceedings of the Ocean Drilling Program, Scientific Results, 108* (pp. 407 - 413): Ocean Drilling Program, College Station, TX.

Schultheiss, P. J., Mienert, J., Party, S. S. (1987). Whole-core p-wave velocity and gamma-ray attenuation logs from Leg 108 (sites 657 through 668). In W. Ruddiman, M. Samthein & al. (Eds.), *Proceedings ODP Init. Rep., 108* (pp. 1015 - 1017).

Seed, H., Seed, R., Schlosser, F., Blondeau, F., Juran, I. (1988). The Landslide at the Port of Nice on October 16, 1979. Report No. UCB/EERC-88/10 (pp. 68): Earthquake Engineering Research Center - University of California, Berkeley.

Segoni, S., Leoni, L., Benedetti, A., Catani, F., Righini, G., Falorni, G., Gabellani, S., Rudari, R., Silvestro, F., Rebora, N. (2009). Towards a definition of a real-time forecasting network for rainfall induced shallow landslides. *Natural Hazards Earth System Sciences*.

Selby, M. J. (1993). *Hillslope: Materials and Processes*. Oxford, England: Oxford University Press.

Serra, N., Ambar, I. (2002). Eddy generation in the Mediterranean undercurrent. *Deep-Sea Research II, 49*, pp. 4225 - 4243.

Shanmugam, G. (2000). 50 years of the turbidite paradigm (1950s-1990s): deep-water processes and facies models - a critical perspective. *Marine and Petroleum Geology, 17*, pp. 285 - 342.

Shanmugam, G. (2006). Deep-water Processes and Facies Models: Implications for Sand-stone Petroleum Reservoirs. *Handbook of Petroleum Exploration and Production* (Vol. 5). Amsterdam: Elsevier Science.

Shanmugam, G. (2008). Deep-water bottom currents and their deposits. In M. Rebesco & A. Camerlenghi (Eds.), *Contourites, Developments in Sedimentology* (Vol. 60, pp. 59 - 81). Amsterdam: Elsevier.

Shanmugam, G. (2012). New perspectives on deep-water sandstones: origin, recognition,initiation, and reservoir quality. *Handbook of Petroleum Exploration and Production* (Vol. 9, pp. 524). Amsterdam: Elsevier.

Shanmugam, G. (2015). The landslide problem. *Journal of Palaeogeography, 4*(2), 109 - 166. doi: 10.3724/SP.J.1261.2015.00071

Shanmugam, G. (2016). Slides, Slumps, Debris Flows, Turbidity Currents, and Bottom Currents *Reference Module in Earth Systems and Environmental Sciences* (pp. 1 - 87).

Shanmugam, G. (2017). The Contourite Problem. In R. Mazumder (Ed.), *Sediment Provenance* (pp. 183 - 254): Elsevier.

Sharma, S. (2002). Slope Stability Concepts. In L. W. Abramson, T. S. Lee, S. Sharma & G. M. Boyce (Eds.), *Slope Stability and Stabilization Methods* (pp. 329 - 461). New York, : John Wiley & Sons, Inc.

Sibuet, J.-C., Srivastava, S., Manatschal, G. (2007). Exhumed mantle-forming transitional crust in the Newfoundland-Iberia rift and associated magnetic anomalies. *Journal of Geophysical Research, 112*(B06105), 23 pp. doi: 10.1029/2005JB003856.

Siddall, M., Rohling, E., Thompson, G., Waelbroeck, C. (2008). Marine isotope stage 3 sea level fluctuations: Data synthesis and new outlook. *Rev. Geophysics*(46), RG4003. doi: 10.1029/2007RG000226

Silva, P., Henry, B., Marques, F. O., Font, E., Mateus, A., Vegas, R., Miranda, J. M., Palomino, R., Palencia-Ortas, A. (2008). Magma flow, exsolution processes and rock metasomatism in the

Great Messejana - Plasencia dyke (Iberian Peninsula). *Geophysics Journal International, 175*(2), pp. 806 - 824.

Silva, S., Terrinha, P., Matias, L., Duarte, J., Roque, C., Ranero, C., Geissler, W., Zitellini, N. (2017). Micro-seismicity in the Gulf of Cadiz: Is there a link between micro-seismicity, high magnitude earthquakes and active faults? *Tectonophysics, 717,* pp. 226 - 241. doi: http://dx.doi.org/10.1016/j.tecto.2017.07.026

Sirieys, P. (1984). *Divers Types de Mecanismes de mouvements de terrains. Mouvements de Terrain.* Paper presented at the Colloque de Caen, Documents du B.R.G.M, 83, Paris.

Skempton, A. W. (1954). The Pore-Pressure Coefficients A and B. *Géotechnique, 4*, pp. 143 - 147.

Skempton, A. W. (1960). Terzaghi's discovery of effective stress. In L. Bjerrum, A. Casagrande, R. Peck & A. W. Skempton (Eds.), *From Theory to Practice in Soil Mechanics* (pp. 42-53). Hoboken, New Jersey: John Wiley.

Skempton, A. W., Hutchinson, J. N. (1969). *Stability of Natural Slopes and Embankment Foundations. State-of-the-Art Report.* Paper presented at the 7th International Conference on Soil Mechanisms and Foundation Engineering, Proceedings, Mexico City.

Skinner, L., Shackleton, N., Elderfield, H. (2003). Millennial-scale variability of deep-water temperature and δ18Odw indicating deep-water source variations in the Northeast Atlantic, 0-34 cal. ka BP. *Geochemistry Geophysics Geosystems, 4*(1098). doi: 10.1029/2003GC000585

Smith, M., Goodchild, M., Longley, P. (2015). Geospatial Analysis. A comprehensive guide to principles, techniques and software tools. 5th Edition

Soares, M. (2015). *Evaluation of soil liquefaction potential based on laboratory data: Major factors and limit boundaries.* PhD Thesis, Facultyof Engineering of the University of Porto, Porto.

Soeters, R., Van Westen, C. J. (1996). Slope Instability Recognition, Analysis and Zonation. In K. Turner & R. Schuster (Eds.), *Landslides Investigation and Mitigation*. Washington: National Academy Press.

Solheim, A., Berg, K., Forsberg, C., Bryn, P. (2005). The Storegga Slide complex: Repetitive large scale sliding with similar cause and development. *Marine and Petroleum Geology, 22*, pp. 97 - 107.

Srivastava, S., Schouten, H., Roest, W., Klitgord, K., Kovacs, L., Verhoef, J., Macnab, R. (1990). Iberian Plate kinematics - A jumping plate boundary between Eurasia and Africa. *Nature, 344*, pp. 756 - 759. doi: 10.1038/344756a0

Stampfli, G., Hochard, C. (2009). Plate tectonics of the Alpine realm. In J. Murphy, J. Keppie & A. Hynes (Eds.), *Ancient Orogens and Modern Analogues* (pp. 89 - 111): Geological Society London Special Publications.

Stapel, G., Cloetingh, S., Pronk, B. (1996). Quantitative subsidence analysis of the Mesozoic evolution of the Lusitanian Basin (western iberian margin). *Tectonophysics, 266*(1 - 4), pp. 493 - 507.

Stegmann, S., Kreiter, S., L'Heureux, J.-S., Vanneste, M., Völker, D., Baeten, N., Knudsen, S., Rise, L., Longva, O., Brendryen, J., Haflidason, H., Chand, S., Mörz, T., Kopf, A. (2016). First results of the geotechnical in situ investigation for soil characterisation along the upper slope off Vesterlen: Northern Norway. In G. Lamarche, J. Mountjoy, S. Bull, T. Hubble, S. Krastel, E. Lane, A. Micallef, L. Moscardelli, C. Mueller, I. Pecher & S. Woelz (Eds.), *Submarine mass movements and their consequences. Advances in Natural and Technological Hazards Research* (pp. 211 - 219): Springer.

Stegmann, S., Strasser, M., Anselmetti, F., Kopf, A. (2007). Geotechnical in situ characterization of subaquatic slopes: The role of pore pressure transients versus frictional strength in landslide initiation. *Geophysical Reasearch Letters, 34*. doi: 10.1029/2006GL029122

Sterling, G., Strohbeck, E. (1973). *The failure of the South Pass 70 'B' platform in Hurricane Camille.* Paper presented at the 5th Annual Offshore Technology Conference, Houston, Texas.

Stich, D., de Mancilla, F. L., Pondrelli, S., Morales, J. (2007). Source analysis of the February 12th 2007, Mw 6.0 Horseshoe earthquake: Implications for the 1755 Lisbon earthquake. *Geophysical Research Letters, 34*, L12308 doi: https://doi.org/10.1029/2007GL030012

Stigall, J., Dugan, B. (2010). Overpressure and earthquake initiated slope failure in the Ursa region, northern Gulf of Mexico. *Journal of Geophysical Research 115 - B04101*. doi: 10.1029/2009JB006848

Storetvedt, K., Mitchell, J., Abranches, M., Oftedahl, S. (1990). A new kinematic model for Iberia; further palaeomagnetic and isotopic age evidence. *Physics of the Earth and Planetary Interiors, 62*, pp. 109 - 125.

Stow, D., Faugères, J. (2008). Contourite facies and the facies model. In M. Rebesco & A. Camerlenghi (Eds.), *Contourites. Developments in sedimentology* (Vol. 60, pp. 223-256): Elsevier.

Stow, D., Hernández-Molina, J., Alvarez-Zarikian, C., Scientists, E. (2013). Expedition 339 summary. In IODP (Ed.), *Proceedings of the Integrated Ocean Drilling Program* (Vol. 339).

Stow, D., Lovell, J. (1979). Contourites: their recognition in modern and ancient sediments. *Earth Science Reviews, 14*, pp. 251 - 291.

Stow, D., Pudsey, C., Howe, J., Faugères, J.-C., Viana, A. (2002). *Deep-water Contourite Systems: Modern Drifts and Ancient Series, Seismic and Sedimentary Characteristics*. London.

Streli, C., Wobrauschek, P., Pepponi, G., Zoeger, N. (2004). A new total reflection X-ray fluorescence vacuum chamber with sample changer analysis using a silicon drift detector for chemical analysis. *Spectrochimica Acta, B59*, pp. 199 - 203.

Stuiver, M., Reimer, P., Reimer, R. (2005). CALIB 5.0. (WWW program and documentation).

Sultan, N., Cochonat, P., Canals, M., Cattaneo, A., Dennielou, B., Haflidason, H., Laberg, J., Long, D., Mienert, J., Trincardi, F., Urgeles, R., Vorren, T., Wilson, C. (2004). Triggering

mechanisms of slope instability processes and sediment failures on continental margins: a geotechnical approach. *Marine Geology, 213*, 291 - 321.

Süzen, M., Doyuran, V. (2004). A comparison of GIS based landslide susceptibility assessment methods: multivariate versus bivariate. *Environmental Geology, 45*, 665 - 679.

Syvitski, J., Burrell, D., Skei, J. (1987). *Fjords: Processes and Products*. New York.

Takahashi, M., Azuma, S., Ito, H., Kanagawa, K., Inoue, A. (2014). Frictional properties of the shallow Nankai Trough accretionary sediments dependent on the content of clay minerals. *Earth, Planets and Space, 66*, 13 pp.

Talley, L., McCartney, M. (1982). Distribution and circulation of Labrador Sea water. *Journal of Physical Oceanography, 12*(11), pp. 1189 - 1205.

Talling, P. (2014). On the triggers, resulting flow types and frequencies of subaqueous sediment density flows in different settings. *Marine Geology, 352*, 155 - 182. doi: http://dx.doi.org/10.1016/j.margeo.2014.02.006

Tankard, A., Balkwill, H. (1989). Extensional tectonics and stratigraphy of the North Atlantic margins: Introduction. In A. Tankard & H. Balkwill (Eds.), *Extensional tectonics and stratigraphy of the North Atlantic margins* (Vol. 46, pp. 1 - 6): American Association of Petroleum Geologist.

Tatsuoka, F., Pradham, T., Horil, N. (1988). Discussion on direct shear tests on reinforced sand. *Géotechnique, vol. 38*(1), pp. 148 - 153.

Teixeira, M. (2006). Movimentos de Vertente: Factores de Ocorrência e Metodologia de Inventariação. *Geonovas, Nº 20*, pp. 95 - 106.

Teixeira, M. (2012). *Avaliação da Suscetibilidade à Ocorrência de Deslizamentos Translacionais Superficiais. Utilização de Modelos Matemáticos de Base Física na Bacia de Tibo, Arcos de Valdevez.* Dissertação de Mestrado, Universidade do Porto.

Teixeira, M., Bateira, C., Marques, F., Vieira, B. (2015). Physically based shallow translational landslide susceptibility analysis in Tibo catchment, NW of Portugal. *Landslides, 12*(3), pp. 455 - 468. doi: 10.1007/s10346-014-0494-9

Teixeira, M., Roque, C., Terrinha, P., Rodrigues, S., Ercilla, G., Casas, D. (2017). *Evidence of slope failure in the Sines Contourite Drift area (SW Portuguese Continental Margin) – preliminary results*. Paper presented at the EGU General Assembly 2017, Vienna, Austria.

Teixeira, M., Terrinha, P., Roque, C., Rosa, M., Ercilla, G., Casas, D. (2019). Interaction of alongslope and downslope processes in the Alentejo Margin (SW Iberia) – Implications on slope stability. *Marine Geology, 410*, pp. 88 - 108. doi: https://doi.org/10.1016/j.margeo.2018.12.011

Teixeira, M., Terrinha, P., Roque, C., Voelker, A. H. L., Silva, P., Salgueiro, E., Abrantes, F., Naughton, F., Mena, A., Ercilla, G., Casas, D. (2020). The Late Pleistocene-Holocene sedimentary evolution of the Sines Contourite Drift (SW Portuguese Margin): A multiproxy

approach. *Sedimentary Geology, 407*, 105737. doi: https://doi.org/10.1016/j.sedgeo.2020.105737

ten Brink, U. S., Andrews, B. D., Miller, N. (2016). Seismicity and sedimentation rate effects on submarine slope stability. *Geology, 44*(7), pp. 563 - 566. doi: https://doi.org/10.1130/G37866.1

ten Brink, U. S., Lee, H., Geist, E., Twichell, D. (2009). Assessment of tsunami hazard to the U.S. East Coast using relationships between submarine landslides and earthquakes. *Marine Geology, 264*, 65 - 73.

Terrinha, P., Duarte, H., Brito, P., Noiva, J., Ribeiro, C., Omira, R., Baptista, M. A., Miranda, M., Magalhães, V., Roque, C., Tagusdelta. (2019a). The Tagus River delta landslide, off Lisbon, Portugal. Implications for Marine geo-hazards. *Marine Geology, 416*, 105983. doi: https://doi.org/10.1016/j.margeo.2019.105983

Terrinha, P., Kullberg, J., Neres, M., Alves, T., Ramos, A., Ribeiro, C., Mata, J., Pinheiro, L., Afilhado, A., Matias, L., Luís, J., Anton Muñoz, J., Fernández, O. (2019b). Rifting of the Southwest and West Iberia Continental Margins. In C. Quesada & J. Oliveira (Eds.), *The Geology of Iberia: A Geodynamic Approach, Regional Geology Reviews* (pp. 251 - 283). Switzerland: Springer Nature.

Terrinha, P., Matias, L., Valadares, V., Roque, C., Duarte, J., Rosas, F., Silva, S., Cunha, T., Batista, L., Duarte, H., Carrara, G., Gràcia, E., Zitellini, N., Lourenço, N., Pinto de Abreu, M. (2013a). A Margem Sul Portuguesa Profunda. In R. Dias, A. Araújo, P. Terrinha & J. Kullberg (Eds.), *Geologia de Portugal, Volume II: Geologia Meso-cenozóica de Portugal* (Vol. III.2, pp. 167 - 194). Lisboa: Escolar Editora.

Terrinha, P., Matias, L., Vicente, J., Duarte, J., Luís, J., Pinheiro, L., Lourenço, N., Diez, S., Rosas, F., Magalhães, V., Valadares, V., Zitellini, N., Roque, C., Mendes-Víctor, L., Team, M. (2009). Morphotectonics and strain partitioning at the Iberia – Africa plate boundary from multibeam and seismic reflection data. *Marine Geology, 267*, pp. 156 - 174.

Terrinha, P., Pinheiro, L., Henriet, J., Matias, L., Ivanov, M., Monteiro, J., Akhmetzhanov, A., Volkonskaya, A., Cunha, T., Shaskin, P., Rovere, M. (2003). Tsunamigenic–seismogenic structures, neotectonics, sedimentary processes and slope instability on the southwest Portuguese Margin. *Marine Geology, 195*(1 - 4), pp. 55 - 73.

Terrinha, P., Pueyo, E., Aranguren, A., Kullberg, J., Kullberg, M., Casas-Sainz, A., Azevedo, M. (2017). Gravimetric and magnetic fabric study of the Sintra Igneous complex: laccolith-plug emplacement in the Western Iberian passive margin. *International Journal of Earth Sciences*. doi: https://doi.org/10.1007/s00531-017-1573-7

Terrinha, P., Ramos, A., Neres, M., Valadares, V., Duarte, J., Martínez-Loriente, S., Silva, S., Mata, J., Kullberg, J., Casas-Sainz, A., Matias, L., Fernández, O., Anton Muñoz, J., Ribeiro, C., Font, E., Neves, C., Roque, C., Rosas, F., Pinheiro, L., Bartolomé, R., Sallarès, V., Magalhães,

V., Medialdea, T., Somoza, L., Gràcia, E., Hensen, C., Gutscher, M. A., Ribeiro, A., Zitellini, N. (2019c). The Alpine Orogeny in the West and Southwest Iberia Margins. In C. Quesada & J. Oliveira (Eds.), *The Geology of Iberia: A Geodynamic Approach, Regional Geology Reviews* (pp. 487 - 505).

Terrinha, P., Rocha, R., Rey, J., Cachão, M., Moura, D., Roque, C., Martins, L., Valadares, V., Cabral, J., Azevedo, M., Barbero, L., Clavijo, E., Dias, R., Matias, H., Matias, L., Madeira, J., Silva, C., Munhá, J., Rebelo, L., Ribeiro, C., Vicente, J., Noiva, J., Youbi, N., Bensalah, M. (2013b). A Bacia do Algarve: Estratigrafia, Paleogeografia e Tectónica. In R. Dias, A. Araújo, P. Terrinha & J. Kullberg (Eds.), *Geologia de Portugal: Geologia Meso-cenozóica de Portugal* (Vol. II, pp. 29 - 166). Lisboa: Escolar Editora.

Terzaghi, K. (1943). *Theoretical Soil Mechanics*: John Wiley & Sons, New York.

Terzaghi, K. (1952). Mecanismo dos Escorregamentos de Terra (Vol. Separata Nº 467). São Paulo: Instituto de Pesquisas Tecnológicas de São Paulo.

Terzaghi, K., Peck, R. (1948). *Soil mechanics in engineering practice*. New York: John Wiley & Sons.

Thomson, J., Croudace, I. W., Rothwell, R. G. (2006). A geochemical application of the ITRAX scanner to a sediment core containing eastern Mediterranean sapropel units. In R. G. Rothwell (Ed.), *New Techniques in Sediment Core Analysis* (Vol. 267, pp. 65 - 77): Geological Society, London, Special Publications.

Toucanne, S., Mulder, T., Schoenfeld, J., Hanquiez, V., Gonthier, E., Duprat, J., Cremer, M., Zaragosi, S. (2007). Contourites of the Gulf of Cadiz: A high-resolution record of the paleocirculation of the Mediterranean outflow water during the last 50,000 years. *Palaeogeography, Palaeoclimatology, Palaeoecology, 246*, pp. 354 - 366.

Tripsanas, E., Bryant, W., Phaneuf, B. (2004). Slope-instability processes caused by salt movements in a complex deep-water environment, Bryant Canyon area, northwest Gulf of Mexico. *American Association of Petroleum Geologists Bulletin, 88*, 801 - 824.

Tucholke, B., Sawyer, D., Sibuet, J. (2007). Breakup of the Newfoundland Iberia rift. In G. Karner, G. Manatschal & L. Pinheiro (Eds.), *Imaging, Mapping and Modelling Continental Lithosphere Extension and Breakup* (Vol. 282, pp. 9 - 46): Geological Society, London, Special Publications.

Tucholke, B., Sibuet, J.-C. (2007). Leg 210 synthesis: tectonic, magmatic, and sedimentary evolution of the Newfoundland-Iberia rift. In B. Tucholke, J.-C. Sibuet & A. Klaus (Eds.), *Proc. ODP, Sci. Results* (Vol. 210, pp. 1 - 56): College Station, TX (Ocean Drilling Program).

Turmel, D., Locat, J., Parker, G., Konrad, J. (2016). Knickpoint Migration Induced by Landslide: Evidence from Laboratory to Field Observations in Wabush Lake. In G. Lamarche, J. Mountjoy, S. Bull, T. Hubble, S. Krastel, E. Lane, A. Micallef, L. Moscardelli , C. Mueller, I. Pecher & S. Woelz (Eds.), *Submarine Mass Movements and their Consequences. Advances in Natural and Technological Hazards Research* (Vol. 41, pp. 239 - 249): Springer.

Uchupi, E. (1967). Slumping on the continental margin southeast of Long Island, New York. *Deep Sea Research, 14*, pp. 635 - 639.

Urgeles, R., Camerlenghi, A. (2013). Submarine landslides of the Mediterranean Sea: Trigger mechanisms, dynamics, and frequency-magnitude distribution. *Journal of Geophysical Research, 118*, pp. 2600 - 2618.

Urgeles, R., Leynaud, D., Lastras, G., Canals, M., Mienert, J. (2006). Back-analysis and failure mechanisms of a large submarine slide on the Ebro slope, NW Mediterranean. *Marine Geology, 226*, 185 – 206. doi: 10.1016/j.margeo.2005.10.004

Urgeles, R., Locat, J., Sawyer, D., Flemings, P., Dugan, B., Binh, N. (2010). History of pore pressure build up and slope instability in mud-dominated sediments of Ursa Basin, Gulf of Mexico Continental Slope. In D. Mosher, R. Shipp, L. Moscardelli, J. Chaytor, C. Baxter, H. J. Lee & R. Urgeles (Eds.), *Submarine Mass Movements and Their Consequences*. Dordrecht: Springer Netherlands.

Urlaub, M. (2013). *The role of sedimentation rate on the stability of low gradient submarine continental slopes.* PhD Thesis, University of Southampton.

Urlaub, M., Talling, P., Masson, D. (2013). Timing and frequency of large submarine landslides: implications for understanding triggers and future geohazard. *Quaternary Science Reviews, 72*, 63 - 82. doi: http://dx.doi.org/10.1016/j.quascirev.2013.04.020

Urlaub, M., Talling, P., Zervos, A., Masson, D. (2015). What causes large submarine landslides on low gradient (< 2º) continental slopes with slow (~ 0.15 m/kyr) sediment accumulation? *Journal of Geophysical Research: Solid Earth, 120*, pp. 6722-6739. doi: 10.1002/2015JB012347

Urlaub, M., Zervos, A., Talling, P., Masson, D., Clayton, C. (2012). How do ~2° slopes fail in areas of slow sedimentation? A sensitivity study on the influence of accumulation rate and permeability on submarine slope stability. In Y. Yamada, K. Kawamura, K. Ikehara, Y. Ogawa, R. Urgeles, D. Mosher, J. Chaytor & M. Strasser (Eds.), *Submarine Mass Movements and Their Consequences. Advances in Natural and Technological Hazards Research* (Vol. 31, pp. 277 - 287). Dordrecht: Springer.

Valadares, V. (2012). *The morphotectonics offshore Southwest Iberia and the origin and evolution of the South Portuguese submarine canyons. PhD Thesis.* Departament of Geology - University of Lisbon.

van Aken, H. (2000a). The hydrography of the mid-latitude Northeast Atlantic Ocean. I: The deep water masses. *Deep-Sea Research I, 47*, pp. 757 - 788.

van Aken, H. (2000b). The hydrography of the mid-latitude Northeast Atlantic Ocean. II: The intermediate water masses. *Deep-Sea Research I, 47*, pp. 789 - 824.

Van Rooij, D., Blamart, D., Kozachenko, M., Henriet, J.-P. (2007). Small mounded contourite drifts associated with deep-water coral banks, Porcupine Seabight, NE Atlantic Ocean. In A. Viana

& M. Rebesco (Eds.), *Economic and Palaeoceanographic Significance of Contourite Deposits* (Vol. 276, pp. 225–244). London: Geological Society, Special Publications.

Van Rooij, D., Iglesias, J., Hernandez-Molina, F. J., Ercilla, G., Gomez-Ballesteros, M., Casas, D., Llave, E., De Hauwere, A., Garcia Gil, S., Acosta, J., Henriet, J.-P. (2010). The Le Danois Contourite Depositional System: interactions between the Mediterranean outflow water and the upper Cantabrian slope (North Iberian margin). *Marine Geology, 274*, pp. 1 - 20.

Van Westen, C. J., Rengers, N., Soeters, R. (2003). Use of Geomorphological Information in Indirect Landslide Susceptibility Assessment. *Natural Hazards Volume 30* pp. 399 - 419

Vanney, J.-R., Mougenot, D. (1981). La plateforme continental du Portugal et les provinces adjacentes: analyse géomorphologique *Memórias Serviços Geológicos de Portugal* (Vol. 28, pp. 145).

Varnes, D. (1958) Landslide Types and Processes. *Vol. 29. Landslides and Engineering Practice* (pp. 20 - 47): Natural Academy of Science.

Varnes, D. (1978). Slope Movement Types and Processes. In R. L. Schuster (Ed.), *Special Report 176: Landslides: Analysis and Control* (pp. 11 - 33). Washington, D. C.: National Research Council.

Veludo, I., Dias, N., Fonseca, P., Matias, L., Carrilho, F., Haberland, C., Villaseñor, A. (2017). Crustal seismic structure beneath Portugal and southern Galicia (Western Iberia) and the role of Variscan inheritance. *Tectonophysics, 717*, pp. 645 - 664.

Viana, A., Faugères, J.-C., Stow, D. (1998a). Bottom-current controlled sand deposits: a review from modern shallow to deep water environments. *Sedimentary Geology, 115*, pp. 53 - 80.

Viana, A., Faugères, J., Kowsmann, R., Lima, J., Caddah, L., Rizzo, J. (1998b). Hydrology, morphology and sedimentology of the Campos continental margin, offshore Brazil. *Sedimentary Geology, 115*, pp. 133 - 157.

Viana, A., Rebesco, M. (2007). Economic and Palaeoceanographic Significance of Contourite Deposits. *Geological Society, London, Special Publications, 276*.

Viana da Fonseca, A. (1996). *Geomechanics in residual soils from Porto granite. Criteria for the design of shallow foundations.* PhD Thesis, Faculty of Engineering of University of Porto, Porto.

Viana da Fonseca, A., Ferreira, C., Fahey, M. (2009). A Framework Interpreting Bender Element Tests, Combining Time-Domain and Frequency-Domain Methods. *Geotechnical Testing Journal, Vol. 32*(2). doi: 10.1520/GTJ100974

Viana da Fonseca, A., Ferreira, C., Soares, M., Klar, A. (2015). *Improved laboratory technicques for advanced geotechnical characterization towards matching in situ properties.* Paper presented at the Deformation Characteristics of Geomaterials. Keynote lecture in 6th ISDCG, Buenos Aires.

Vizcaino, A., Gràcia, E., Pallàs, R., Garcia-Orellana, J., Escutia, C., Casas, D., Willmott, V., Diez, S., Asioli, A., Dañobeitia, J. (2006). Sedimentology, physical properties and ages of mass-transport deposits associated to the Marquês de Pombal Fault, southwest Portuguese margin. *Norwegian Journal of Geology, 86*, 177 - 186.

Voelker, A. (2002). Global distribution of centennial-scale records for Marine Isotope Stage (MIS) 3: a databse. *Quaternary Science Reviews, 21*(10), pp. 1185 - 1212.

Voelker, A., Lebreiro, S., Schönfeld, J., Cacho, I., Erlenkeuser, H., Abrantes, F. (2006). Mediterranean outflow strengthening during northern hemisphere coolings: A salt source for the glacial Atlantic? *Earth and Planetary Science Letters, 245*(1 - 2), pp. 39 - 55 doi: 10.1016/j.epsl.2006.03.014

Voelker, A., Salgueiro, E., Rodrigues, T., Jimenez-Espejo, F., Bahr, A., Alberto, A., Loureiro, I., Padilha, M., Rebotim, A., Röhl, U. (2015). Mediterranean Outflow and surface water variability off southern Portugal during the early Pleistocene: A snapshot at Marine Isotope Stages 29 to 34 (1020–1135 ka). *Global and Planetary Change, 133*, pp. 223 - 237.

Voelker, A., Sarnthein, M., Grootes, P., Erlenkeuser, H., Laj, C., Mazaud, A., Nadeau, M.-J., Schleicher, M. (1998). Correlation of marine 14C ages from the Nordic seas with the GISP2 isotope record: implications for 14C calibration beyond 25 ka BP. *Radiocarbon, 40*, pp. 517 - 534.

von Raumer, Stampfli, G., Borel, G., Bussy, F. (2002). Organization of pre-Variscan basement areas at the north-Gondwanan margin. *Interntional Journal of Earth Sciences, 91*, pp. 35 - 52.

Waelbroeck, C., Duplessy, J., Michel, E., Labeyrie, L., Paillard, D., Duprat, J. (2001). The timing of the last deglaciation in North Atlantic climate records. *Nature, 412*, pp. 724 - 727.

Weaver, P. P., Schultheiss, P. J. (1990). Current methods for obtaining, logging and splitting marine sediment cores. In E. Hailwood & R. Kidd (Eds.), *Marine Geological Surveying and Sampling* (pp. 85 - 101): Kluwer, Dordrecht.

Weber, M. E., Niessen, F., Kuhn, G., Wiedicke, M. (1997). Calibration and application of marine sedimentary physical properties using a multi-sensor core logger. *Marine Geology, 136*, pp. 151 - 172.

Weltje, G., Tjallingii, R. (2008). Calibration of XRF core scanners for quantitative geochemical logging of sediment cores: Theory and application. *Earth and Planetary Science Letters, 274*(3 - 4), pp.423 - 438.

Whitmarsh, R., Sawyer, D. (1996). The Ocean/Continent Transition Beneath the Iberia Abyssal Plain and Continental-Rifting to Seafloor-Spreading Processes. In R. Whitmarsh, D. Sawyer, A. Klaus & D. Masson (Eds.), *Proceedings of the Ocean Drilling Program, Scientific Results* (Vol. 149, pp. 713 - 733).

Wilson, R., Hiscott, R., Willis, M., Gradstein, P. (1989). The Lusitanian Basin of west-central Portugal: Mesozoic and Tertiary tectonic, stratigraphic and subsidence history. In A. Tankard

& H. Balkwill (Eds.), *Extensional Tectonics and Stratigraphy of the North Atlantic Margins* (Vol. 46, pp. 341 - 361): AAPG Memories.

Wilson, R., Sawyer, D., Whitmarsh, R., Zerong, J., Carbonell, J. (1996). *Seismic stratigraphy and tectonic history of the Iberia Abyssal Plain.* Paper presented at the Proceeding of the Ocean Drilling Program, Scientific Results, College Station, TX

Winters, W. (1987). Guidelines for handling, storing, and preparing soft marine sediment for geotechnical testing *Open-File Report 87-278* (pp. 11 pp.): U.S. Geological Survey.

Withjack, M., Schlische, R., Baum, M. (2009). Extensional development of the Fundy rift basin, southeastern Canada. *Geological Journal, 44*, pp. 631 - 651. doi: 10.1002/gj.1186

WP-WLI. (1993a). Multilingual Landslide Glossary. In U. Working Party on World Landslide Inventory (Ed.): International Geotechnical Societies.

WP-WLI. (1993b). A suggested method for describing the activity of a landslide. *Bulletin of the International Association of Engineering Geology, 47*, 53-57.

Wynn, R., Masson, D., Stow, D., Weaver, P. (2000). The Northwest African slope apron: a modern analogue for deep-water systems with complex seafloor topography. *Marine and Petroleum Geology, 17*, pp. 253- 265.

Wynn, R., Weaver, P., Stow, D., Masson, D. (2002). Turbidite depositional architecture across three interconnected deep-water basins on the northwest African margin. *Sedimentology, 49*, 1441–1462. doi: 10.1046/j.1365-3091.2002.00471.x

Yamamoto, M., Yamamuro, M., Tada, R. (2000). Late Quaternary records of organic carbon, calcium carbonate, and biomarkers from the Site 1016 off Point Conception, California margin. In M. Lyle, I. Koizumi, C. Richter & T. Moore Jr. (Eds.), *Proceedings of the Ocean Drilling Program, Scientific Results* (pp. 183 - 194).

Yenes, M., Casas, D., Nespereira, J., López-González, N., Casalbore, D., Monterrubio, S., Alonso, B., Ercilla, G., Juan, C., Bárcenas, P., Palomino, D., Mata, P., Martínez-Díaz, P., Pérez, N., Vázquez, J. T., Estrada, F., Teixeira, M. (2021). The Guadiaro-Baños contourite drifts (SW Mediterranean). A geotechnical approach for its stability analysis. *Marine Geology, 437*, 106505. doi: https://doi.org/10.1016/j.margeo.2021.106505

Yenes, M., Monetrrubio, S., Nespereira, J., Casas, D. (2020). Apparent overconsolidation and its implications for submarine landslides. *Engineering Geology, 264*, 11 pp. doi: https.//doi.org/10.1016/j.enggeo.2019.105375

Yilmaz, O. (1987). *Seismic data processing. Society of Exploration of Geophysics - Investigations in Geophysics* (Vol. 2).

Yin, K., Yan, T. (1988). Statistical Prediction Model for Slope Instability of Metamorphosed Rocks. In C. Bonnard (Ed.), *Proc. Fifth International Symposium in Landslides, Lausanne* (Vol. 2, pp. 1269-1272). Rotterdam, Holland: A.A. Balkema.

Yuill, R. (1971). The Standard Deviational Ellipse; An Updated Tool for Spatial Description. *Geografiska Annaler. Series B, Human Geography, 53*(No. 1), pp. 28 - 39.

Zachos, J., Pagani, M., Sloan, L., Thomas, E., Billups, K. (2001). Trends, rhythms, and aberrations in global climate 65 Ma to present. *Science, 292*, pp. 686-693.

Zahn, R., Schönfeld, J., Kudrass, H., Park, M., Erlenkeuser, H., Grootes, P. (1997). Thermohaline Instability in the North Atlantic during melt water events: stable isotope and ice-rafted detritus records from core SO07-26KL, Portuguese margin. *Paleoceanography, 12*, pp. 696 - 710.

Záruba, Q., Mencl, V. (1969). Landslides and their Control. *Elsevier, Amsterdam*.

Zenk, W., Armi, L. (1990). The complex spreading pattern of Mediterranean water off the Portuguese continental slope. *Deep-Sea Research, 37*, pp. 1805 - 1823.

Zeverbergen, L., Thorne, C. (1987). Quantitative Analysis of Land Surface Topography. *Earth Surface Processes and Landforms, 12*, pp. 47 - 56.

Zêzere, J. (1997). *Movimentos de Vertente e Perigosidade Geomorfológica na Região a Norte de Lisboa.* Tese de Doutoramento. Universidade de Lisboa, Lisboa.

Zêzere, J., Faleh, A., Sadiki, A., Garcia, R., Oliveira, S. C. (2009). Modelação da susceptibilidade a deslizamentos na bacia do Oued Sra (Rif central, Marrocos) com métodos estatísticos bi-variados. *Publicações da Associação Portuguesa de Geomorfólogos, VI*, 203 - 210.

Zhang, Y., Huang, F., Lai, G. (2009). Research on Skempton's coefficient B based on the observation of groundwater of Changping station. *Earthquake Science, 22*, pp. 631 - 638. doi: 10.1007/s11589-009-0631-z

Zitellini, N., Berton, E., Bortoluzzi, G., Calafato, N., Centorami, G., Chierici, F., Landuzzi, V., Ligi, M., Penitenti, D., Scipionii, E., Rovere, M., Casoni, L., Correggiari, A., Magagnoli, A., Marozzi, G., Vigliotti, L., Jornet, P., Rodriguez, P., Thompson, I., Zahinos, A., Bartolome, R., Gracia, E., Terrinha, P., Ribeiro, A. (2010). Project BIGSETS: report on seismic and magnetic investigations during cruise BS'98 with R/V Urania. *RAPPORTI ISMAR* (Vol. 1, pp. 1-17).

Zitellini, N., Chierici, F., Sartori, R., Torelli, L. (1999). The tectonic source of the 1755 Lisbon earthquake and tsunami. *Annals of Geophysics, 42*, 49 - 55.

Zitellini, N., Gràcia, E., Matias, L., Terrinha, P., Abreu, M., DeAlteriis, G., Henriet, J. P., Dañobeitia, J., Masson, D., Mulder, T., Ramella, R., Somoza, L., Diez, S. (2009). The quest for the Africa-Eurasia plate boundary west of the Strait of Gibraltar. *Earth and Planetary Science Letters, 280*(1 - 4), pp. 13 - 50.

Zitellini, N., Mendes, L. A., Cordoba, D., Danobeitia, J., Nichols, R., Pellis, G., Ribeiro, A., Sartori, R., Torelli, L., Bartolome, R., Bortoluzzi, G., Calafato, A., Carrilho, F., Casoni, L., Chierici, F., Corela, C., Correggiari, A., Vedova, B., Gracia, E., Jornet, P., Landuzzi, M., Ligi, M., Magagnoli, A., Marozzi, G., Matias, L., Penitenti, D., Rodriguez, P., Rovere, M., Terrinha, P., Vigliotti, L., Ruiz, A. (2001). Source of 1755 Lisbon earthquake and tsunami investigated. *Eos, Transactions American Geophysical Union, 82*(26), 285 - 296 pp.

Zitellini, N., Rovere, M., Terrinha, P., Chierici, F., Matias, L., BIGSETS, T. (2004). Neogene Through Quaternary Tectonic Reactivation of SW Iberian Passive Margin. *Pure and Applied Geophysics, 161*(3), pp. 565 - 587.

Zolitschka, B., Mingram, J., Van Der Gaast, S., Jansen, J. H. F., Naumann, R. (2001). Sediment logging techniques. In W. M. Last & J. Smol (Eds.), *Tracking Environmental Change Using Lake Sediments. Basin Analysis, Coring and Chronological Techniques, Developments in Paleoliminological Research* (pp. 1 - 17): Kluwer Academic Publishers, Dordrecht.